Evolution has strong medicine for antibiotics use *p. 758*

The personal costs of healing societies *pp. 766 & 787*

A call to counter hype in stem cell research *p. 776*

# Science

$15
13 MAY 2016
sciencemag.org

AAAS

## A MIGRANT'S PLIGHT

Arctic warming hurts red knots on their tropical winter range *pp. 775 & 819*

# CONTENTS

13 MAY 2016 • VOLUME 352 • ISSUE 6287

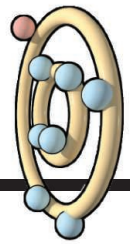

774 & 805
Targeting molecules with photonics

## NEWS

### IN BRIEF

748 News at a glance

### IN DEPTH

751 **NEW SCRUTINY FOR A SLOWING ATLANTIC CONVEYOR**
Researchers retrieve data from biggest effort yet to monitor currents that warm Europe *By E. Hand*

752 **ANIMALS SHOW HOW ZIKA HARMS FETUSES**
Mouse and monkey models detail viral attack on the placenta and the brain *By J. Cohen*

754 **UNEXPECTED REVELATIONS FOR STUDY VOLUNTEER**
Years after signing up for a cholesterol study, a woman learns she's central to a paper *By J. Couzin-Frankel*

755 **NSF DIRECTOR UNVEILS BIG IDEAS**
Plan is aimed at the next president and Congress *By J. Mervis*

756 **HOW THE VENUS FLYTRAP ACQUIRED ITS TASTE FOR MEAT**
Plant turned preexisting defenses against insect pests into tools for catching and eating prey *By E. Stokstad*

### FEATURES

758 **RESISTANCE FIGHTERS**
Evolutionary biologists are challenging old dogmas about the way antibiotics should be used *By K. Kupferschmidt*

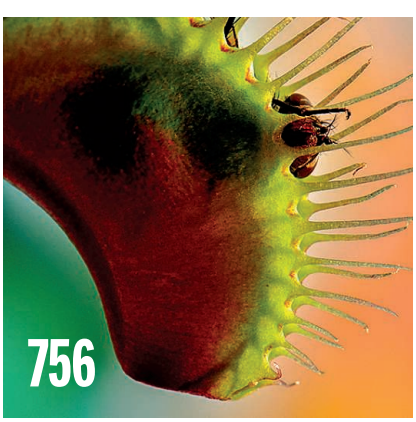


PHOTO (TOP RIGHT): C. CLARK/SMITHSONIAN

762 **MUSEUM DRAWERS GO DIGITAL**
New technology speeds efforts of museums to display billions of natural history specimens online
*By N. Rogers*

## INSIGHTS

### PERSPECTIVES

766 **RECONCILIATION IN SIERRA LEONE**
Short, low-cost interventions can help communities to recover from civil war
*By K. Casey and R. Glennerster*
▸ RESEARCH ARTICLE P. 787

768 **IDENTIFYING REMNANTS OF EARLY EARTH**
Isotope analysis reveals portions of Earth that have remained the same since accretion *By T. W. Dahl*
▸ REPORT P. 809

769 **TOWARD A PROSPECTIVE MOLECULAR EVOLUTION**
Fitness landscapes provide a prospective understanding of chance and necessity in evolution *By X. He and L. Liu*
▸ REPORTS PP. 837 & 840

770 **REMEMBERING WHAT YOU LEARNED**
Specific brain activity during REM sleep affects memory consolidation
*By B. Kocsis*
▸ REPORT P. 812

772 **REFUGEE PROTECTION AND RESETTLEMENT PROBLEMS**
Refugees face painful uncertainties that could be ameliorated by aid agency coordination *By E. C. Dunn*

774 **NANOPHOTONICS GETS TWISTED**
Simple structures process complex light beams that carry angular momentum
*By G. Molina-Terriza*
▸ REPORT P. 805

775 **LIVING SENTINELS FOR CLIMATE CHANGE EFFECTS**
Migrating birds affected by climate change in the Arctic may have lower survival chances in their tropical habitats *By M. Wikelski and G. Tertitski*
▸ REPORT P. 819

776 **CONFRONTING STEM CELL HYPE**
Against hyperbole, distortion, and overselling *By T. Caulfield* et al.

### BOOKS *ET AL.*

778 **STATES OF MIND**
*E. Sargent, curator; reviewed by G. Frazzetto*

779 **THE SEVEN PILLARS OF STATISTICAL WISDOM**
*By S. M. Stigler, reviewed by H. Wainer*

### LETTERS

780 **REMINDER TO DEPOSIT DNA SEQUENCES**
*By M. Blaxter* et al.

780 **CRIMEA REPORT LEAVES READERS IN THE COLD**
*By A. Goushcha* et al.

781 **RESPONSE**
*By T. Appenzeller*

781 **NEW ALLIES FIGHT FOR CHINA'S ENVIRONMENT**
*By S. Lu* et al.

Downloaded from http://science.sciencemag.org/ May 12, 2016



Published by AAAS

# CONTENTS

770 & 812
Sleep and memory

13 MAY 2016 • VOLUME 352 • ISSUE 6287

## RESEARCH

### IN BRIEF

783 From *Science* and other journals

### RESEARCH ARTICLES

786 **MUCOSAL IMMUNOLOGY**
IgA production requires B cell interaction with subepithelial dendritic cells in Peyer's patches *A. Reboldi* et al.
RESEARCH ARTICLE SUMMARY; FOR FULL TEXT: dx.doi.org/10.1126/science.aaf4822

787 **PSYCHOLOGY**
Reconciling after civil conflict increases social capital but decreases individual well-being *J. Cilliers* et al.
▸ PERSPECTIVE P. 766

### REPORTS

795 **NONLINEAR OPTICS**
Large optical nonlinearity of indium tin oxide in its epsilon-near-zero region *M. Z. Alam* et al.

797 **CATALYSIS**
Photochemical route for synthesizing atomically dispersed palladium catalysts *P. Liu* et al.

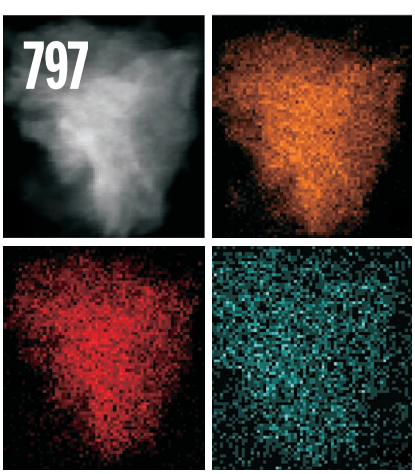


801 **ORGANIC CHEMISTRY**
A general alkyl-alkyl cross-coupling enabled by redox-active esters and alkylzinc reagents *T. Qin* et al.

805 **APPLIED PHYSICS**
On-chip noninterference angular momentum multiplexing of broadband light *H. Ren* et al.
▸ PERSPECTIVE P. 774

809 **GEOCHEMISTRY**
Preservation of Earth-forming events in the tungsten isotopic composition of modern flood basalts *H. Rizo* et al.
▸ PERSPECTIVE P. 768; PODCAST

812 **SLEEP RESEARCH**
Causal evidence for the role of REM sleep theta rhythm in contextual memory consolidation *R. Boyce* et al.
▸ PERSPECTIVE P. 770

816 **ZIKA VIRUS**
Zika virus impairs growth in human neurospheres and brain organoids *P. P. Garcez* et al.

819 **CLIMATE CHANGE**
Body shrinkage due to Arctic warming reduces red knot fitness in tropical wintering range *J. A. van Gils* et al.
▸ PERSPECTIVE P. 775

822 **METALLOPROTEINS**
Radical SAM catalysis via an organometallic intermediate with an Fe–[5′-C]-deoxyadenosyl bond *M. Horitani* et al.

825 **ATMOSPHERIC SCIENCE**
Empirical evidence of contrasting soil moisture–precipitation feedbacks across the United States *S. Tuttle and G. Salvucci*

828 **HIV-1 ANTIBODIES**
Fusion peptide of HIV-1 as a site of vulnerability to neutralizing antibody *R. Kong* et al.

833 **ORIGIN OF LIFE**
A high-yielding, strictly regioselective prebiotic purine nucleoside formation pathway *S. Becker* et al.

### MOLECULAR EVOLUTION

837 The fitness landscape of a tRNA gene *C. Li* et al.

840 Network of epistatic interactions within a yeast snoRNA *O. Puchta* et al.
▸ PERSPECTIVE P. 769

844 **CANCER**
Histone H3K36 mutations promote sarcomagenesis through altered histone methylation landscape *C. Lu* et al.

### DEPARTMENTS

747 **EDITORIAL**
Pursuit of integral ecology
*By Marcelo Sánchez Sorondo and Veerabhadran Ramanathan*

862 **WORKING LIFE**
My seismic career shift
*By Julia MacDougall*

### ON THE COVER

Red knots (*Calidris canutus canutus*) migrate between the high Arctic, where they breed during summer, and the West African tropics. Chicks born under rapidly warming conditions in the Arctic attain smaller sizes before migrating, and the shorter bills of these smaller birds hamper their ability to reach food on the wintering grounds. Similar warming-induced morphological changes with downstream survival effects may also extend to other Arctic migrants. See pages 775 and 819. *Photo: Jan van de Kam*

*Science* Staff ..... 746
New Products ..... 853
*Science* Careers ..... 854

**SCIENCE (ISSN 0036-8075) is published weekly on Friday, except the last week in December, by the American Association for the Advancement of Science, 1200 New York Avenue, NW, Washington, DC 20005.** Periodicals mail postage (publication No. 484460) paid at Washington, DC, and additional mailing offices. Copyright © 2016 by the American Association for the Advancement of Science. The title SCIENCE is a registered trademark of the AAAS. Domestic individual membership and subscription (51 issues): $165 ($74 allocated to subscription). Domestic institutional subscription (51 issues): $1522; Foreign postage extra: Mexico, Caribbean (surface mail) $55; other countries (air assist delivery) $89. First class, airmail, student, and emeritus rates on request. Canadian rates with GST available upon request, GST #1254 88122. Publications Mail Agreement Number 1069624. **Printed in the U.S.A.**
**Change of address:** Allow 4 weeks, giving old and new addresses and 8-digit account number. **Postmaster:** Send change of address to AAAS, P.O. Box 96178, Washington, DC 20090–6178. **Single-copy sales:** $15.00 current issue, $20.00 back issue prepaid includes surface postage; bulk rates on request. **Authorization to photocopy** material for internal or personal use under circumstances not falling within the fair use provisions of the Copyright Act is granted by AAAS to libraries and other users registered with the Copyright Clearance Center (CCC) Transactional Reporting Service, provided that $35.00 per article is paid directly to CCC, 222 Rosewood Drive, Danvers, MA 01923. The identification code for *Science* is 0036-8075. *Science* is indexed in the *Reader's Guide to Periodical Literature* and in several specialized indexes.



*Published by AAAS*

Downloaded from http://science.sciencemag.org/ on May 12, 2016

Science
AAAS
1200 New York Avenue, NW, Washington, DC 20005
Bateman House, 82-88 Hills Road, Cambridge, UK CB2 1LQ

**Editor-in-Chief** Marcia McNutt
**Executive Editor** Monica M. Bradford **News Editor** Tim Appenzeller
**Managing Editor, Research Journals** Katrina L. Kelner
**Deputy Editors** Lisa D. Chong, Andrew M. Sugden(UK), Valda J. Vinson, Jake S. Yeston

## Research and Insights

**DEPUTY EDITOR, EMERITUS** Barbara R. Jasny **SR. EDITORS** Caroline Ash(UK), Gilbert J. Chin, Julia Fahrenkamp-Uppenbrink(UK), Pamela J. Hines, Stella M. Hurtley(UK), Paula A. Kiberstis, Marc S. Lavine(Canada), Kristen L. Mueller, Ian S. Osborne(UK), Beverly A. Purnell, L. Bryan Ray, Guy Riddihough, H. Jesse Smith, Jelena Stajic, Peter Stern(UK), Phillip D. Szuromi, Sacha Vignieri, Brad Wible, Nicholas S. Wigginton, Laura M. Zahn **ASSOCIATE EDITORS** Brent Grocholski, Keith T. Smith **ASSOCIATE BOOK REVIEW EDITOR** Valerie B. Thompson **LETTERS EDITOR** Jennifer Sills **CHIEF CONTENT PRODUCTION EDITOR** Cara Tate **SR. CONTENT PRODUCTION EDITORS** Harry Jach, Lauren Kmec **CONTENT PRODUCTION EDITORS** Jeffrey E. Cook, Chris Filiatreau, Cynthia Howe, Barbara P. Ordway, Catherine Wolner **SR. EDITORIAL COORDINATORS** Carolyn Kyle, Beverly Shields **EDITORIAL COORDINATORS** Aneera Dobbins, Joi S. Granger, Lisa Johnson, Anita Wynn **PUBLICATIONS ASSISTANTS** Jeffrey Hearn, Dona Mathieu, Le-Toya Mayne Flood, Shannon McMahon, Scott Miller, Caitlyn Phillips, Jerry Richardson, Alice Whaley(UK), Brian White **EXECUTIVE ASSISTANT** Anna Bashkirova **ADMINISTRATIVE SUPPORT** Janet Clements(UK), Lizanne Newton(UK), Maryrose Madrid

## News

**NEWS MANAGING EDITOR** John Travis **INTERNATIONAL EDITOR** Richard Stone **DEPUTY NEWS EDITORS** Robert Coontz, Elizabeth Culotta, David Grimm, David Malakoff, Leslie Roberts **CONTRIBUING EDITOR** Martin Enserink(Europe) **SR. CORRESPONDENTS** Daniel Clery(UK), Jeffrey Mervis, Elizabeth Pennisi **NEWS WRITERS** Adrian Cho, Jon Cohen, Jennifer Couzin-Frankel, Carolyn Gramling, Eric Hand, Jocelyn Kaiser, Catherine Matacic, Kelly Servick, Robert F. Service, Erik Stokstad(Cambridge, UK), Emily Underwood **INTERNS** Patrick Monahan **CONTRIBUTING CORRESPONDENTS** John Bohannon, Warren Cornwall, Ann Gibbons, Mara Hvistendahl, Sam Kean, Eli Kintisch, Kai Kupferschmidt(Berlin), Andrew Lawler, Christina Larson(Beijing), Mitch Leslie, Charles C. Mann, Eliot Marshall, Virginia Morell, Dennis Normile(Shanghai), Heather Pringle, Tania Rabesandratana(London), Gretchen Vogel(Berlin), Lizzie Wade(Mexico City) **CAREERS** Donisha Adams, Rachel Bernstein(Editor) **COPY EDITORS** Julia Cole, Dorie Chevlen, Jennifer Levin (Chief) **ADMINISTRATIVE SUPPORT** Jessica Adams

**Executive Publisher** Rush D. Holt
**Interim Publisher** Bill Moran **Chief Digital Media Officer** Rob Covey

**BUSINESS OPERATIONS AND PORTFOLIO MANAGEMENT DIRECTOR** Sarah Whalen **PRODUCT DEVELOPMENT DIRECTOR** Will Schweitzer **PRODUCT DEVELOPMENT ASSOCIATE** Hal Moore **BUSINESS SYSTEMS AND FINANCIAL ANALYSIS DIRECTOR** Randy Yi **MANAGER OF FULFILLMENT SYSTEMS** Neal Hawkins **SYSTEMS ANALYST** Nicole Mehmedovich **ASSISTANT DIRECTOR, BUSINESS OPERATIONS** Eric Knott **MANAGER, BUSINESS OPERATIONS** Jessica Tierney **SENIOR BUSINESS ANALYST** Cory Lipman **BUSINESS ANALYSTS** Sandy Kim, Meron Kebede **FINANCIAL ANALYST** Robert Clark **DIRECTOR, COPYRIGHTS LICENSING SPECIAL PROJECTS** Emilie David **PERMISSIONS ASSOCIATE** Elizabeth Sandler **RIGHTS, CONTRACTS, AND LICENSING ASSOCIATE** Lili Kiser

**MARKETING DIRECTOR** Elise Swinehart **ASSOCIATE MARKETING DIRECTOR** Christina Schlecht **MARKETING MANAGER** Elizabeth Sattler **MARKETING ASSOCIATE** Steven Goodman **CREATIVE DIRECTOR** Scott Rodgerson **SENIOR ART ASSOCIATES** Seil Lee, Paula Fry **ART ASSOCIATE** Kim Huynh **PROGRAM DIRECTOR, AAAS MEMBER CENTRAL** Peggy Mihelich **FULFILLMENT SYSTEMS AND OPERATIONS** membership@aaas.org **MANAGER, MEMBER SERVICES** Pat Butler **SPECIALISTS** Terrance Morrison, Latasha Russell **MANAGER, DATA ENTRY** Mickie Napoleoni **DATA ENTRY SPECIALISTS** Brenden Aquilino, Fiona Giblin

**PUBLISHER RELATIONS MANAGER** Catherine Holland **PUBLISHER RELATIONS, EASTERN REGION** Keith Layson **PUBLISHER RELATIONS, WESTERN REGION** Ryan Rexroth **SALES RESEARCH COORDINATOR** Aiesha Marshall **MANAGER, SITE LICENSE OPERATIONS** Iquo Edim **SENIOR OPERATIONS ANALYST** Lana Guz **FULFILLMENT ANALYST** Judy Lillibridge **ASSOCIATE DIRECTOR, MARKETING** Christina Schlecht **MARKETING ASSOCIATE** Isa Sesay-Bah

**WEB TECHNOLOGIES SR. DEVELOPER** Chris Coleman **DEVELOPERS** Dan Berger, Jimmy Marks, Ryan Jensen **SR. PROJECT MANAGER** Trista Smith **PROJECT MANAGER** Nick Fletcher

**DIGITAL MEDIA DIRECTOR OF ANALYTICS** Enrique Gonzales **DIGITAL REPORTING ANALYST** Eric Hossinger **SR. WEB PRODUCER** Sarah Crespi **WEB PRODUCER** Alison Crawford **VIDEO PRODUCER** Nguyen Nguyen **SOCIAL MEDIA PRODUCER** Brice Russ

**DIRECTOR OF OPERATIONS PRINT AND ONLINE** Lizabeth Harman **DIGITAL/PRINT STRATEGY MANAGER** Jason Hillman **QUALITY TECHNICAL MANAGER** Marcus Spiegler **PROJECT ACCOUNT MANAGER** Tara Kelly **DIGITAL PRODUCTION MANAGER** Lisa Stanford **ASSISTANT MANAGER DIGITAL/PRINT** Rebecca Doshi **SENIOR CONTENT SPECIALISTS** Steve Forrester, Antoinette Hodal, Lori Murphy, Anthony Rosen **CONTENT SPECIALISTS** Jacob Hedrick, Kimberley Oster

**DESIGN DIRECTOR** Beth Rakouskas **DESIGN EDITOR** Marcy Atarod **SENIOR DESIGNERS** Garvin Grullón, Chrystal Smith **GRAPHICS MANAGING EDITOR** Alberto Cuadra **SENIOR SCIENTIFIC ILLUSTRATORS** Chris Bickel, Katharine Sutliff **SCIENTIFIC ILLUSTRATOR** Valerie Altounian **INTERACTIVE GRAPHICS EDITOR** Jia You **SENIOR ART ASSOCIATES** Holly Bishop, Nathalie Cary, Preston Huey **PHOTOGRAPHY MANAGING EDITOR** William Douthitt **PHOTO EDITORS** Leslie Blizard, Christy Steele

**DIRECTOR, GLOBAL COLLABORATION, CUSTOM PUBLICATIONS, ADVERTISING** Bill Moran **EDITOR, CUSTOM PUBLISHING** Sean Sanders: 202-326-6430 **ADVERTISING MARKETING MANAGER** Justin Sawyers: 202-326-7061 science_advertising@aaas.org **ADVERTISING SUPPORT MANAGER** Karen Foote: 202-326-6740 **ADVERTISING PRODUCTION OPERATIONS MANAGER** Deborah Tompkins **SR. PRODUCTION SPECIALIST/GRAPHIC DESIGNER** Amy Hardcastle **SR. TRAFFIC ASSOCIATE** Christine Hall **SALES COORDINATOR** Shirley Young **ASSOCIATE DIRECTOR, COLLABORATION, CUSTOM PUBLICATIONS/CHINA/TAIWAN/KOREA/SINGAPORE** Ruolei Wu: +86-186 0082 9345, rwu@aaas.org **COLLABORATION/CUSTOM PUBLICATIONS/JAPAN** Adarsh Sandhu + 81532-81-5142 asandhu@aaas.org **EAST COAST/E. CANADA** Laurie Faraday: 508-747-9395, FAX 617-507-8189 **WEST COAST/W. CANADA** Lynne Stickrod: 415-931-9782, FAX 415-520-6940 **MIDWEST** Jeffrey Dembksi: 847-498-4520 x3005, Steven Loerch: 847-498-4520 x3006 **UK EUROPE/ASIA** Roger Goncalves: TEL/FAX +41 43 243 1358 **JAPAN** Katsuyoshi Fukamizu(Tokyo): +81-3-3219-5777 kfukamizu@aaas.org **CHINA/TAIWAN** Ruolei Wu: +86-186 0082 9345, rwu@aaas.org

**WORLDWIDE ASSOCIATE DIRECTOR OF SCIENCE CAREERS** Tracy Holmes: +44 (0) 1223 326525, FAX +44 (0) 1223 326532 tholmes@science-int.co.uk **CLASSIFIED** advertise@sciencecareers.org **U.S. SALES** Tina Burks: 202-326-6577, Nancy Toema: 202-326-6578 **EUROPE/ROW SALES** Sarah Lelarge **SALES ASSISTANT** Kelly Grace **JAPAN** Hiroyuki Mashiki(Kyoto): +81-75-823-1109 hmashiki@aaas.org **CHINA/TAIWAN** Ruolei Wu: +86-186 0082 9345 rwu@aaas.org **MARKETING MANAGER** Allison Pritchard **MARKETING ASSOCIATE** Aimee Aponte

**AAAS BOARD OF DIRECTORS, CHAIR** Geraldine L. Richmond **PRESIDENT** Barbara A. Schaal **PRESIDENT-ELECT** Susan Hockfield **TREASURER** David Evans Shaw **CHIEF EXECUTIVE OFFICER** Rush D. Holt **BOARD** Cynthia M. Beall, May R. Berenbaum, Carlos J. Bustamante, Stephen P.A. Fodor, Claire M. Fraser, Michael S. Gazzaniga, Laura H. Greene, Elizabeth Loftus, Mercedes Pascual

**SUBSCRIPTION SERVICES** For change of address, missing issues, new orders and renewals, and payment questions: 866-434-AAAS (2227) or 202-326-6417, FAX 202-842-1065. Mailing addresses: AAAS, P.O. Box 96178, Washington, DC 20090-6178 or AAAS Member Services, 1200 New York Avenue, NW, Washington, DC 20005

**INSTITUTIONAL SITE LICENSES** 202-326-6730 **REPRINTS:** Author Inquiries 800-635-7181 **COMMERCIAL INQUIRIES** 803-359-4578 **PERMISSIONS** 202-326-6765, permissions@aaas.org **AAAS Member Services** 202-326-6417 or http://membercentral.aaas.org/discounts

*Science* serves as a forum for discussion of important issues related to the advancement of science by publishing material on which a consensus has been reached as well as including the presentation of minority of conflicting points of view. Accordingly, all articles published in *Science*—including editorials, news and comment, and book reviews—are signed and reflect the individual views of the authors and not official points of view adopted by AAAS or the institutions with which the authors are affiliated.

**INFORMATION FOR AUTHORS** See pages 624 and 625 of the 5 February 2016 issue or access www.sciencemag.org/authors/science-information-authors

**SENIOR EDITORIAL BOARD**
**Gary King,** *Harvard University,* **Susan M. Rosenberg,** *Baylor College of Medicine,*
**Ali Shilatifard,** *Northwestern University Feinberg School of Medicine*

**BOARD OF REVIEWING EDITORS** (Statistics board members indicated with **(S)**

**Adriano Aguzzi,** *U. Hospital Zürich*
**Takuzo Aida,** *U. of Tokyo*
**Leslie Aiello,** *Wenner-Gren Foundation*
**Judith Allen,** *U. of Edinburgh*
**Sonia Altizer,** *U. of Georgia*
**Sebastian Amigorena,** *Institut Curie*
**Kathryn Anderson,** *Memorial Sloan-Kettering Cancer Center*
**Meinrat O. Andreae,** *Max-Planck Inst. Mainz*
**Paola Arlotta,** *Harvard U.*
**Johan Auwerx,** *EPFL*
**David Awschalom,** *U. of Chicago*
**Clare Baker,** *University of Cambridge*
**Nenad Ban,** *ETH Zurich*
**Jordi Bascompte,** *University of Zurich*
**Franz Bauer,** *Instituto de Astrofisica*
**Ray H. Baughman,** *U. of Texas, Dallas*
**David Baum,** *U. of Wisconsin*
**Carlo Beenakker,** *Leiden U.*
**Kamran Behnia,** *ESPCI-ParisTech*
**Yasmine Belkaid,** *NIAID, NIH*
**Philip Benfey,** *Duke U.*
**May Berenbaum,** *U. of Illinois*
**Gabriele Bergers,** *U. of California, San Francisco*
**Bradley Bernstein,** *Massachusettes General Hospital*
**Peer Bork,** *EMBL*
**Bernard Bourdon,** *Ecole Normale Supérieure de Lyon*
**Chris Bowler,** *École Normale Supérieure*
**Ian Boyd,** *U. of St. Andrews*
**Emily Brodsky,** *U. of California, Santa Cruz*
**Ron Brookmeyer,** *U. of California Los Angeles* **(S)**
**Christian Büchel,** *U. Hamburg-Eppendorf*
**Joseph A. Burns,** *Cornell U.*
**Carter Tribley Butts,** *U. of California, Irvine*
**Gyorgy Buzsaki,** *New York U. School of Medicine*
**Blanche Capel,** *Duke U.*
**Mats Carlsson,** *U. of Oslo*
**Ib Chorkendorff,** *U. of Denmark*
**David Clapham,** *Children's Hospital Boston*
**Joel Cohen,** *Rockefeller U., Columbia U.*
**James J. Collins,** *MIT*
**Robert Cook-Deegan,** *Duke U.*
**Lisa Coussens,** *Oregon Health & Science U.*
**Alan Cowman,** *Walter & Eliza Hall Inst.*
**Robert H. Crabtree,** *Yale U.*
**Roberta Croce,** *Vrije Universiteit*
**Janet Currie,** *Princeton U.*
**Jeff L. Dangl,** *U. of North Carolina*
**Tom Daniel,** *U. of Washington*
**Frans de Waal,** *Emory U.*
**Stanislas Dehaene,** *Collège de France*
**Robert Desimone,** *MIT*
**Claude Desplan,** *New York U.*
**Dennis Discher,** *U. of Pennsylvania*
**Gerald W. Dorn II,** *Washington U. School of Medicine*
**Jennifer A. Doudna,** *U. of California, Berkeley*
**Bruce Dunn,** *U. of California, Los Angeles*
**William Dunphy,** *Caltech*
**Christopher Dye,** *WHO*
**Todd Ehlers,** *U. of Tuebingen*
**David Ehrhardt,** *Carnegie Inst. of Washington*
**Tim Elston,** *U. of North Carolina at Chapel Hill*
**Gerhard Ertl,** *Fritz-Haber-Institut, Berlin*
**Barry Everitt,** *U. of Cambridge*
**Ernst Fehr,** *U. of Zurich*
**Anne C. Ferguson-Smith,** *U. of Cambridge*
**Michael Feuer,** *The George Washington U.*
**Toren Finkel,** *NHLBI, NIH*
**Kate Fitzgerald,** *U. of Massachusetts*
**Peter Fratzl,** *Max-Planck Inst.*
**Elaine Fuchs,** *Rockefeller U.*
**Daniel Geschwind,** *UCLA*
**Karl-Heinz Glassmeier,** *TU Braunschweig*
**Ramon Gonzalez,** *Rice U.*
**Julia R. Greer,** *Caltech*
**Elizabeth Grove,** *U. of Chicago*
**Nicolas Gruber,** *ETH Zurich*
**Kip Guy,** *St. Jude's Children's Research Hospital*
**Taekjip Ha,** *U. of Illinois at Urbana-Champaign*
**Wolf-Dietrich Hardt,** *ETH Zurich*
**Christian Haass,** *Ludwig Maximilians U.*
**Sharon Hammes-Schiffer,** *U. of Illinois at Urbana–Champaign*
**Michael Hasselmo,** *Boston U.*
**Martin Heimann,** *Max-Planck Inst. Jena*
**Yka Helariutta,** *U. of Cambridge*
**James A. Hendler,** *Rensselaer Polytechnic Inst.*
**Janet G. Hering,** *Swiss Fed. Inst. of Aquatic Science & Technology*
**Kai-Uwe Hinrichs,** *U. of Bremen*
**David Hodell,** *U. of Cambridge*
**Lora Hooper,** *UT Southwestern Medical Ctr. at Dallas*
**Tamas Horvath,** *Yale University*
**Raymond Huey,** *U. of Washington*
**Fred Hughson,** *Princeton U.*
**Auke Ijspeert,** *EPFL Lausanne*
**Stephen Jackson,** *USGS and U. of Arizona*
**Steven Jacobsen,** *U. of California, Los Angeles*
**Kai Johnsson,** *EPFL Lausanne*
**Peter Jonas,** *Inst. of Science & Technology (IST) Austria*
**Matt Kaeberlein,** *U. of Washington*
**William Kaelin Jr.,** *Dana-Farber Cancer Inst.*
**Daniel Kahne,** *Harvard U.*
**Daniel Kammen,** *U. of California, Berkeley*
**Abby Kavner,** *U. of California, Los Angeles*
**Masashi Kawasaki,** *U. of Tokyo*
**V. Narry Kim,** *Seoul National U.*
**Joel Kingsolver,** *U. of North Carolina at Chapel Hill*
**Robert Kingston,** *Harvard Medical School*
**Etienne Koechlin,** *Ecole Normale Supérieure*
**Alexander Kolodkin,** *Johns Hopkins U.*
**Thomas Langer,** *U. of Cologne*
**Mitchell A. Lazar,** *U. of Pennsylvania*
**David Lazer,** *Harvard U.*
**Thomas Lecuit,** *IBDM*
**Virginia Lee,** *U. of Pennsylvania*
**Stanley Lemon,** *U. of North Carolina at Chapel Hill*
**Ottoline Leyser,** *Cambridge U.*
**Wendell Lim,** *U.C. San Francisco*
**Marcia C. Linn,** *U. of California, Berkeley*
**Jianguo Liu,** *Michigan State U.*
**Luis Liz-Marzan,** *CIC biomaGUNE*
**Jonathan Losos,** *Harvard U.*
**Ke Lu,** *Chinese Acad. of Sciences*
**Christian Lüscher,** *U. of Geneva*
**Laura Machesky,** *CRUK Beatson Inst. for Cancer Research*
**Anne Magurran,** *U. of St. Andrews*
**Oscar Marin,** *CSIC & U. Miguel Hernández*
**Charles Marshall,** *U. of California, Berkeley*
**C. Robertson McClung,** *Dartmouth College*
**Graham Medley,** *U. of Warwick*
**Tom Misteli,** *NCI*
**Yasushi Miyashita,** *U. of Tokyo*
**Mary Ann Moran,** *U. of Georgia*
**Richard Morris,** *U. of Edinburgh*
**Alison Motsinger-Reif,** *NC State U.* **(S)**
**Thomas Murray,** *The Hastings Center*
**Daniel Neumark,** *U. of California, Berkeley*
**Kitty Nijmeijer,** *U. of Twente*
**Helga Nowotny,** *European Research Advisory Board*
**Ben Olken,** *MIT*
**Joe Orenstein,** *U. of California Berkeley & Lawrence Berkeley National Lab*
**Harry Orr,** *U. of Minnesota*
**Pilar Ossorio,** *U. of Wisconsin*
**Andrew Oswald,** *U. of Warwick*
**Margaret Palmer,** *U. of Maryland*
**Steve Palumbi,** *Stanford U.*
**Jane Parker,** *Max-Planck Inst. of Plant Breeding Research*
**Giovanni Parmigiani,** *Dana-Farber Cancer Inst.* **(S)**
**John H. J. Petrini,** *Memorial Sloan-Kettering Cancer Center*
**Samuel Pfaff,** *Salk Institute for Biological Studies*
**Joshua Plotkin,** *U. of Pennsylvania*
**Albert Polman,** *FOM Institute AMOLF*
**Philippe Poulin,** *CNRS*
**Jonathan Pritchard,** *Stanford U.*
**David Randall,** *Colorado State U.*
**Felix Rey,** *Institut Pasteur*
**Trevor Robbins,** *U. of Cambridge*
**Jim Roberts,** *Fred Hutchinson Cancer Research Ctr.*
**Barbara A. Romanowicz,** *U. of California,Berkeley*
**Amy Rosenzweig,** *Northwestern University*
**Mike Ryan,** *U. of Texas, Austin*
**Mitinori Saitou,** *Kyoto U.*
**Shimon Sakaguchi,** *Kyoto U.*
**Miquel Salmeron,** *Lawrence Berkeley National Lab*
**Jürgen Sandkühler,** *Medical U. of Vienna*
**Alexander Schier,** *Harvard U.*
**Vladimir Shalaev,** *Purdue U.*
**Robert Siliciano,** *Johns Hopkins School of Medicine*
**Denis Simon,** *Arizona State U.*
**Uri Simonsohn,** *U. of Pennsylvania*
**Alison Smith,** *John Innes Centre*
**Richard Smith,** *U. of North Carolina* **(S)**
**John Speakman,** *U. of Aberdeen*
**Allan C. Spradling,** *Carnegie Institution of Washington*
**Jonathan Sprent,** *Garvan Inst. of Medical Research*
**Eric Steig,** *U. of Washington*
**Paula Stephan,** *Georgia State U. and National Bureau of Economic Research*
**Molly Stevens,** *Imperial College London*
**V. S. Subrahmanian,** *U. of Maryland*
**Ira Tabas,** *Columbia U.*
**Sarah Teichmann,** *Cambridge U.*
**John Thomas,** *North Carolina State U.*
**Shubha Tole,** *Tata Institute of Fundamental Research*
**Christopher Tyler-Smith,** *The Wellcome Trust Sanger Inst.*
**Herbert Virgin,** *Washington U.*
**Bert Vogelstein,** *Johns Hopkins U.*
**Cynthia Volkert,** *U. of Göttingen*
**David Wallach,** *Weizmann Inst. of Science*
**Ian Walmsley,** *U. of Oxford*
**Jane-Ling Wang,** *U. of California, Davis* **(S)**
**David A. Wardle,** *Swedish U. of Agric. Sciences*
**David Waxman,** *Fudan U.*
**Jonathan Weissman,** *U. of California, San Francisco*
**Chris Wikle,** *U. of Missouri* **(S)**
**Ian A. Wilson,** *The Scripps Res. Inst.* **(S)**
**Timothy D. Wilson,** *U. of Virginia*
**Rosemary Wyse,** *Johns Hopkins U.*
**Jan Zaanen,** *Leiden U.*
**Kenneth Zaret,** *U. of Pennsylvania School of Medicine*
**Jonathan Zehr,** *U. of California, Santa Cruz*
**Len Zon,** *Children's Hospital Boston*
**Maria Zuber,** *MIT*

**BOOK REVIEW BOARD**
**David Bloom,** *Harvard U.,* **Samuel Bowring,** *MIT,* **Angela Creager,** *Princeton U.,*
**Richard Shweder,** *U. of Chicago,* **Ed Wasserman,** *DuPont*

EDITORIAL

# Pursuit of integral ecology

Later this month (23 and 24 May), the United Nations will convene the first World Humanitarian Summit in Istanbul, where global and local leaders will commit to putting each and every person's safety, dignity, freedom, and right to thrive at the heart of decision-making. More than 125 million people are in need of humanitarian assistance, a level of suffering not seen since World War II. The social problems are wide and deep, from war and human trafficking to the gross inequality between the wealthy 1% and the poorest 3 billion of the population. Included in the summit's Agenda for Humanity are climate and natural disasters. Indeed, 1 year ago, Pope Francis emphasized, in the encyclical *Laudato Si*, that complex crises have both social and environmental dimensions. The bond between humans and the natural world means that we live in an "integral ecology," and as such, an integrated approach to environmental and social justice is required.

***"The real innovation is this new synergy between science, policy, and religion."***

The need for an integral ecology approach can be seen, for example, in the coupling of economic activities and wealth inequalities with environmental pollution and climate change. Climate pollutants come primarily from the wealthy 1 billion, but the worst consequences of associated climate change will be experienced by the bottom 3 billion, who had little to do with this pollution.

Last year brought two historic global agreements that renewed optimism about a sustainable future. The United Nations' (UN's) declaration of sustainable development goals called for the eradication of poverty and the improvement of human well-being. The Paris agreement was signed by 195 nations to limit global warming to well below a 2°C increase. These global acknowledgements of systemic ecological and social problems have opened a window of opportunity to focus on how problems of poverty, human well-being, and the protection of creation are interlinked. The real innovation is this new synergy between science, policy, and religion.

The origin, transformative potential, and future development of an alliance between science, policy, and religion is based on recent advances at the Holy See, which houses two Pontifical Academies devoted to science: one for natural scientists and the other for social scientists. The members of these academies are chosen not for their religious affiliations but for their scientific preeminence. In May 2014, the two academies of scholars, philosophers, and theologians met to contemplate the sustainability of humanity and nature, and came to a remarkable (for a scientific body) conclusion: The resolution of major environmental problems facing society requires a fundamental reorientation in our behavior and attitude toward nature and toward each other. Both academies convened faith leaders of the major religions, including Buddhism, Christianity, Hinduism, Islam (both Sunni and Shia), and Judaism to state that slavery and human trafficking are crimes against humanity. Although it is hard for different religions to pray at the same altar, it finally became possible and necessary for them to act together to defend the dignity of human beings and their common home. This new attitude spurred meetings in 2014 and 2015 between scientists, policy-makers, and religious leaders that included UN Secretary-General Ban Ki-moon and governors and mayors from more than 80 large cities. The groups agreed that the mitigation of climate change was a moral and religious imperative, and that the development of a sustainable relationship with the planet also requires a moral revolution. This new alliance also declared that extreme globalization of forms of indifference such as human trafficking and modern slavery should be acknowledged as crimes against humanity.

Pope Francis' effort to unite science, policy, and religion toward an integral ecology approach is just a start. We hope that other religions and moral and political leaders will join this new synergy and nudge society toward equitable solutions to ecological and social justice problems without losing sight of the values of the human person and the common good.

**– Marcelo Sánchez Sorondo and Veerabhadran Ramanathan**

*Monsignor Marcelo Sánchez Sorondo is the Chancellor of the Pontifical Academy of Sciences and the Pontifical Academy of Social Sciences. Email: pas@pas.va*

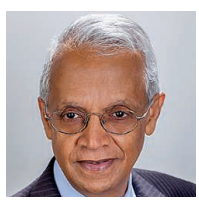

*Veerabhadran Ramanathan is a council member of the Pontifical Academy of Sciences and a distinguished professor of climate sciences at the University of California, San Diego. Email: vram@ucsd.edu*

10.1126/science.aag0826

PHOTOS: (TOP RIGHT) PONTIFICAL ACADEMY OF SCIENCES; (BOTTOM RIGHT) VEERABHADRAN RAMANATHAN; (INSET) RICCARDO LENNART NIELS MAYER/ISTOCKPHOTO.COM

Downloaded from http://science.sciencemag.org/ on May 12, 2016



Published by AAAS

# NEWS

> “The woman was concerned that I was a terrorist because I was writing strange things on a pad of paper.”

**University of Pennsylvania economist Guido Menzio** to The Associated Press last week, after his American Airlines flight was delayed while officials questioned him. Menzio’s seatmate had seen him solving a differential equation.

## IN BRIEF

### Research facility to release its chimps

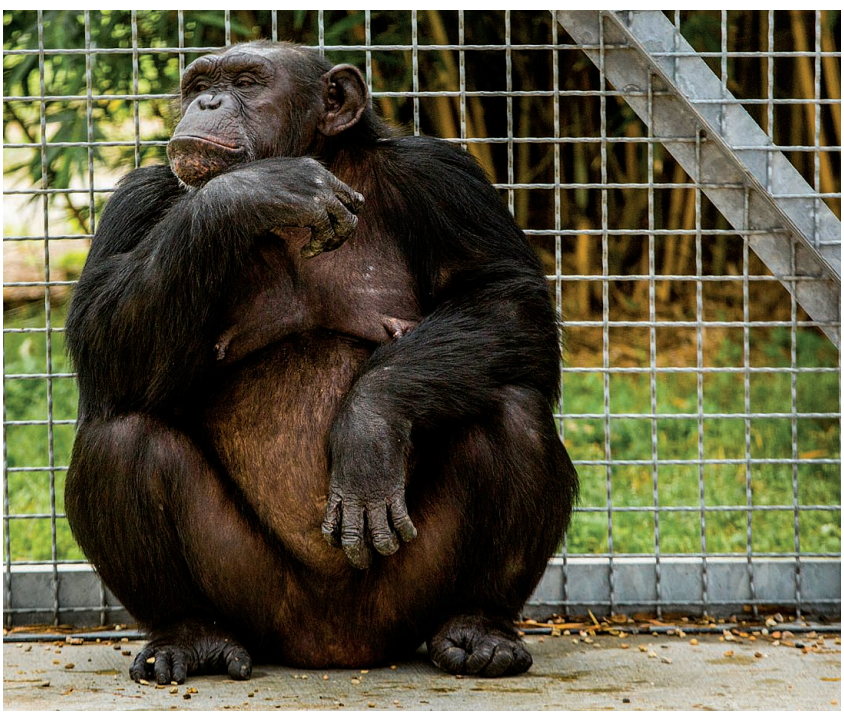

A now-retired chimpanzee at the New Iberia Research Center in Louisiana.

In what it is calling the largest resettlement of chimpanzees from a U.S. research center, Louisiana’s New Iberia Research Center (NIRC) announced 3 May that it will move all 220 of its chimps to Project Chimps, a 95-hectare sanctuary in Blue Ridge, Georgia. The animals include Hercules and Leo, which have been the subject of an intense legal battle over the legal rights of chimps. In 2013, the National Institutes of Health (NIH) began to phase out most government-funded chimp research, retiring the majority of its research chimps to sanctuaries; last November, NIH said it would end all support for invasive chimp research. Meanwhile, the U.S. Fish and Wildlife Service stated in June 2015 that all U.S. chimpanzees—including the more than 700 chimps used in research—would be classified as endangered under the Endangered Species Act. NIRC said in a statement that it will begin transferring the chimps in June, in groups of 10 animals at a time, to keep them in their current social groups. It expects to complete the transfer in 3 to 5 years. http://scim.ag/Iberiachimps

AROUND THE WORLD

### GM mosquitoes in Grand Cayman

GEORGE TOWN | Grand Cayman, the largest of the three Cayman Islands, is set to release millions of genetically modified (GM) insects in a bid to vanquish *Aedes aegypti*, the mosquito species that can spread Zika, dengue, and chikungunya. The U.K. territory announced on 5 May that it had inked a deal with biotech company Oxitec, the producer of the transgenic mosquitoes. A 2009 to 2010 study on Grand Cayman showed that releasing the GM insects, which don’t produce viable offspring, can cause the natural mosquito population to crash. The two other Cayman Islands have smaller *A. aegypti* populations and won’t participate. Oxitec’s mosquitoes have also been deployed in Brazil.

### FDA cracks down on e-cigarettes

SILVER SPRING, MARYLAND | The U.S. Food and Drug Administration last week took a long-anticipated step to regulate the e-cigarette industry by finalizing a document that requires manufacturers to seek the agency’s approval before marketing their products. Some research has concluded that e-cigarettes are a safer alternative to traditional cigarettes and a valuable quitting aid, but public health experts have warned that e-cigarettes’ appeal to children could entice a new generation of smokers. The new rule will give companies up to 3 years to comply with the premarket approval process, but its ban on selling to people under age 18—already in place for e-cigarettes in most

E-cigarettes may pose dangers to children.

PHOTOS: (LEFT TO RIGHT) DOUG DUGAS/UNIVERSITY OF LOUISIANA, LAFAYETTE; MAURO GRIGOLLO/ISTOCK PHOTO

Downloaded from http://science.sciencemag.org/ on May 12, 2016



Published by AAAS

states—begins in August. The rule will also require warning labels about the addictive nature of nicotine starting in May 2018.

## *Attenborough*, not *Boaty*

SWINDON, U.K. | The saga is over: The United Kingdom's new £200 million polar research ship, to launch in 2019, will be named the *RRS Sir David Attenborough*, after the famed naturalist. In March, the Natural Environment Research Council (NERC) announced the #NameOurShip campaign online; the runaway favorite quickly became *Boaty McBoatface*, a joking suggestion by a former BBC presenter. Last week, NERC announced that the winner had been chosen—and it wasn't *Boaty*. However, NERC said, the name *Boaty McBoatface* will "live on"—it will be given to one of the ship's remotely operated subsea vehicles. Attenborough, 90, said in a statement that he is "truly honoured" by the choice.

FINDINGS

## Making hornless cows

Each year, some 80% of dairy cattle in the United States have their horns removed. The horns can pose a risk both to humans and to the cattle themselves, but animal rights activists have protested the process of dehorning as cruel. Now, a team of researchers led by scientists with the St. Paul–based biotech startup Recombinetics offers a different solution: Hornless cows created with the genome-editing technique TALENs. Natural hornlessness is common in cattle breeds raised for beef, but rare in dairy cows, so the team edited into them genetic variants associated with hornlessness in beef cattle. In the end, the team reported last week in *Nature Biotechnology*, they created five live, hornless calves with no off-target effects.

## Teen trends in disease, injury

In the most far-reaching analysis of its kind, the Institute for Health Metrics and Evaluation (IHME) in Seattle, Washington, has evaluated global disease and injury prevalence among adolescents from 1990 to 2013. Published in the 9 May issue of *The Lancet* as part of the Global Burden of Diseases, Injuries, and Risk Factors Study, the study led by IHME epidemiologist Ali Mokdad found that the leading cause of death in 10- to 14-year-olds changed from drowning to HIV/AIDS during that time; for 15- to 25-year-olds, it continues to be road injuries. The leading mortality risk factor for the younger and older brackets did not change (unsafe drinking water and alcohol use, respectively), but unsafe sex jumped from 12th to 2nd place for 15- to 19-year-olds. A few surprising geographic findings stood out: For example, Brazil has one of the highest rates of birth in 15- to 19-year-old girls, and the countries with the biggest increases in obesity include China, Mali, and Niger.

PHOTO: AP PHOTO/RAJESH KUMAR SINGH

### The smallest planet, in silhouette

About 13 or 14 times a century, Mercury's orbit brings it between Earth and the sun, appearing to observers as a tiny black dot moving swiftly across a fiery backdrop. The planet's most recent transit, on Monday, drew audiences to observatories around the world, including these schoolchildren in Lucknow, India. Fittingly, NASA last week released the first full topographic map of the small rocky planet, using 10 terabytes of data collected from the 4-year MESSENGER mission. Mercury's last transit was in 2006; the next chance to see it will be in 2019.

## Organism ditches mitochondria

An organism that lives in the guts of chinchillas is challenging one prevailing bit of wisdom: that all eukaryotes require mitochondria to supply cellular energy. Eukaryotes are the group of organisms that includes humans, other animals, plants, fungi, and various microscopic creatures. While sequencing the genome of a single-celled species of *Monocercomonoides*, a type of eukaryote, researchers observed that it didn't show any signs of mitochondrial genes. (Mitochondria carry their own DNA.) It also lacked all the key proteins that enable the organelles to function, the scientists reveal online this week in *Current Biology*. The discovery "overturns the definition of the eukaryotic cell," says coauthor Anna Karnkowska of the University of British Columbia, Vancouver, in Canada. *Monocercomonoides* gets along fine without mitochondria by using enzymes in its cytoplasm to produce energy. Its closest relatives still have small mitochondria, suggesting that the microbe jettisoned the organelles fairly recently, in evolutionary terms. Karnkowska and her colleagues speculate that other undiscovered eukaryotes have also shed the powerhouses.
**http://scim.ag/nomitoeuk**

Downloaded from http://science.sciencemag.org/ on May 12, 2016



Published by AAAS

Last week, crew members hoisted an OSNAP mooring onto the deck of the *CCGS Hudson*.

PHOTO: IGOR YASHAYAEV/*CCGS HUDSON*/FISHERIES AND OCEANS CANADA

OCEANOGRAPHY

# *New scrutiny for a slowing Atlantic conveyor*

## Researchers retrieve data from biggest effort yet to monitor currents that warm Europe

*By* **Eric Hand**

Motoring among springtime ice floes—with the occasional seal resting on top—the Canadian ship was searching for oceanographic treasure. Just beneath the surface of the Labrador Sea, held taut by submerged buoys, were lines moored to the sea floor and studded with instruments monitoring a vital—and perhaps ailing—ocean circulatory system. In the morning on 5 May, the *CCGS Hudson* reached the first X on its map: mooring C2. The captain cleared the sea ice with a few brisk circles of the vessel. A technician sent an acoustic release code toward a sensor on the anchor 345 meters down. Minutes later, yellow flotation packs burbled up to the surface, and the crew hoisted the mooring on deck to swap out the instruments.

Mooring C2 is the first retrieval in a season of five research cruises this spring and summer that will fetch data from the 53 moorings in an array called the Overturning in the Subpolar North Atlantic Program (OSNAP), which stretches from Labrador to Greenland to Scotland. The array's measurements of temperature, salinity, and current velocity will be key to understanding the Atlantic Meridional Overturning Circulation (AMOC), a set of powerful currents with far-reaching effects on the global climate that has mysteriously slowed over the past decade.

Often called the Atlantic conveyor belt, the currents include the Gulf Stream, which brings shallow, warm waters north, nourishing fisheries and warming northwest Europe. The warm waters give up their heat in the bitterly cold regions monitored by OSNAP, become denser, and sink, forming ocean-bottom currents that return southward, hugging the perimeter of the ocean basins. Models suggest that climate change should weaken the AMOC as warmer Arctic temperatures, combined with buoyant freshwater from Greenland's melting ice cap, impede the formation of deep currents. But so far, limited ocean measurements show the AMOC to be far more capricious than the models have been able to capture.

"We really need some ground-truthing of the AMOC, and that will really help the climate models," says Susan Lozier, a physical oceanographer at Duke University in Durham, North Carolina, and the international project lead for the seven-nation OSNAP collaboration, which deployed the moorings in 2014. Researchers hope OSNAP and similar arrays in other parts of the Atlantic will shed light on how the deep currents make their way to the far southern end of the ocean, what forces pull them back to the surface there, and how climate change could affect each part of the enormous system.

The first hints of a fickle conveyor came from a U.K.-U.S.–supported array of moorings deployed in 2004 along a line at 26.5°N latitude, from Florida to the Canary Islands. Initial data from these subtropical moorings showed unexpectedly wild swings in the AMOC's strength from month to month. Then, in 2009 to 2010, the average strength of the AMOC plunged by about 30%. Heat remained in the tropics rather than being delivered to northern latitudes. The consequences included an unusually harsh European winter, a strong Atlantic Basin hurricane season, and—because a strong AMOC keeps water away from land—an extreme sea level rise of nearly 13 centimeters along the North American coast north of New York City.

Overall, the subtropical array has measured a decline in the AMOC from an average strength of 20 sverdrups in 2004 to about 15 sverdrups a decade later. (A sverdrup is a unit of flux of 1 million cubic meters of water per second—roughly the total flow of all the world's rivers into the oceans.) That decline is an order of magnitude more than models suggest could be due to climate change. Scientists suspect some natural cycle is to blame, such as the 60- to 70-year cycle of varying sea temperatures called the Atlantic Multidecadal Oscillation, says Meric Srokosz, an oceanographer at the University of Southampton in the United Kingdom, and the science coordinator for RAPID, the U.K.-funded portion of the 26.5°N array. Initial analysis of the latest unpublished data, from the 18 months through October 2015, shows the AMOC's average strength leveling out at about 15.5 sverdrups, Srokosz says. "It could

Downloaded from http://science.sciencemag.org/ on May 12, 2016



Published by AAAS

be a hiatus, or it could start coming back up," he says. It will take another decade of measurements to separate the climate change effect from natural variability, he says.

For years, the 26.5°N array was the only line of moorings crossing a messy, complicated system of ocean currents. Scientists have long wondered whether the AMOC is equally strong everywhere across the Atlantic Basin. And if climate change in the subpolar region is affecting it, "we want to be closer to where that forcing is taking place," says Amy Bower, an OSNAP principal investigator and a physical oceanographer at Woods Hole Oceanographic Institute in Massachusetts.

Getting close to the action was challenging. Whereas the ocean floor at 26.5°N is flat and wide, making it possible to gauge the strength of the AMOC with 18 widely spaced moorings, it is far more rugged in the subpolar North Atlantic. That forced the OSNAP team to cluster moorings along the walls of seafloor basins to get accurate readings. And like other arrays, OSNAP relies on costly, rare ship voyages to collect data. If the moorings had surface buoys, they could radio back their data, but the potential for damage by hungry fish or vandalism from fishermen made that impractical. As a partial remedy, OSNAP supplements the moorings with gliders: torpedolike drones that patrol the complicated currents and then surface to transmit their data.

The push of sinking, cold waters in the subarctic, which OSNAP aims to measure, is just one half of the AMOC's engine. Scientists also want to understand the "pull" in the Southern Ocean that girds Antarctica. There, winds and tides cause mixing that tugs deep waters to the surface, where they warm up and begin their journey northward in the Atlantic. Researchers have long debated which mechanism is more important and how climate change is likely to affect each of them, says Chris Meinen, an oceanographer at the National Oceanic and Atmospheric Administration's Atlantic Oceanographic and Meteorological Laboratory in Miami, Florida, and a leader for an array of moorings crossing the Atlantic at 34.5°S. Supported by the United States, Brazil, France, and South Africa, the southern array started pilot operations in 2009 and launched in earnest in 2013—although it still fields far fewer instruments than its northern counterparts. "There has always been a tendency for the North American and European countries to focus on the North Atlantic, because it's in their backyard," he says.

The stakes are high for all three arrays. Some theoretical models suggest that if the strength of the AMOC drops below a certain threshold, it could suddenly shut down—the doomsday scenario of a frozen Europe exploited in the 2004 disaster movie *The Day After Tomorrow*. Many climate models suggest that the AMOC should be stable over the long term in a warming world, but plenty of evidence from the recent geological past confirms that the conveyor belt can slow down significantly. Srokosz isn't alarmed by the slowdown RAPID has detected, but he is eager for more data. "We have no way of knowing whether we're near such a threshold," he says. "Over the next few years, we'll have a clearer picture of what's going on." ■

## Current events

Three arrays are monitoring a conveyor belt of powerful currents in the Atlantic, in which shallow warm waters move north (red), while deep, cold water moves south (blue).

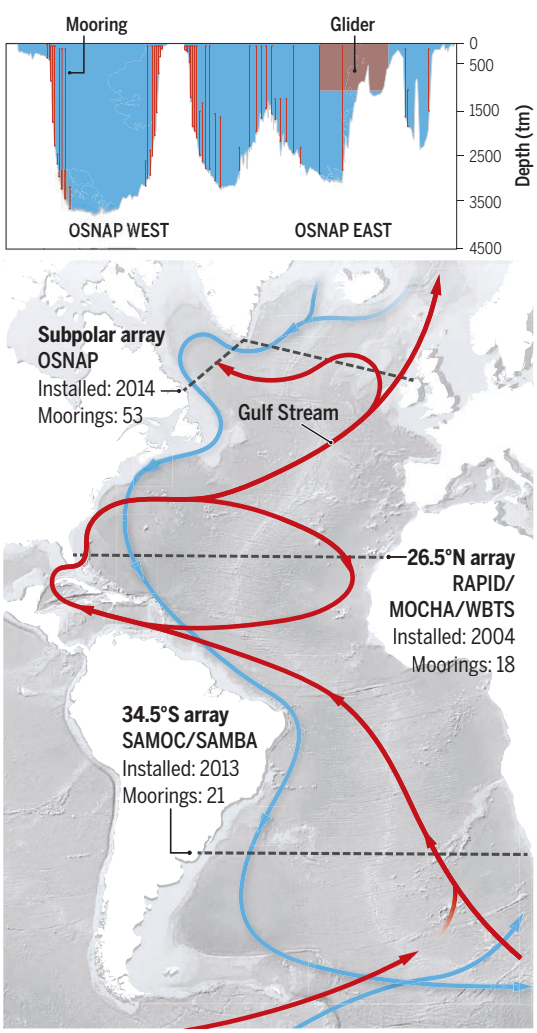


DIAGRAM: ADAPTED BY G. GRULLÓN/*SCIENCE* FROM OSNAP

INFECTIOUS DISEASE

# *Animals show how Zika harms fetuses*

## Mouse and monkey models detail viral attack on the placenta and the brain

*By* **Jon Cohen**

By far the most alarming feature of the Zika virus now marching across South America and the Caribbean is its threat to fetuses. Last month the U.S. Centers for Disease Control and Prevention declared that "a causal relationship" exists between the virus and brain abnormalities in newborns—most noticeably a small head, known as microcephaly. But just how a mother's infection harms the fetus, and how to prevent the damage, is uncertain.

New animal models are now pointing to answers. Pregnant monkeys are showing hints of fetal damage. But the most dramatic results come from mice. Mouse studies published this week in *Cell* and its sister journal *Cell Stem Cell* and in *Nature* show precisely how the virus slows fetal growth, damages the brain, and leads to miscarriage. Two of them also prove for the first time in an animal model that Zika virus can cause microcephaly in fetuses.

Together, the findings indicate that the virus by itself can wreak havoc, says Michael Diamond, a viral immunologist at Washington University in St. Louis in Missouri who led the *Cell* study. "Some people feel there are many cofactors like insecticides," Diamond says. "Our study suggests at least you don't have to invoke other things." And by providing an animal model for the fetal damage, the studies should also ease the path for testing potential vaccines and treatments.

Mice normally cannot sustain a Zika infection because the virus triggers secretion of interferons, molecules that bolster immune responses. Diamond's lab circumvented this problem by creating female mice that had a key interferon gene knocked out; in a second experiment, they treated pregnant animals with an anti-interferon antibody. The team then injected pregnant females with a virus isolated from a person in French Polynesia; the isolate is

Downloaded from http://science.sciencemag.org/ on May 12, 2016



Published by AAAS

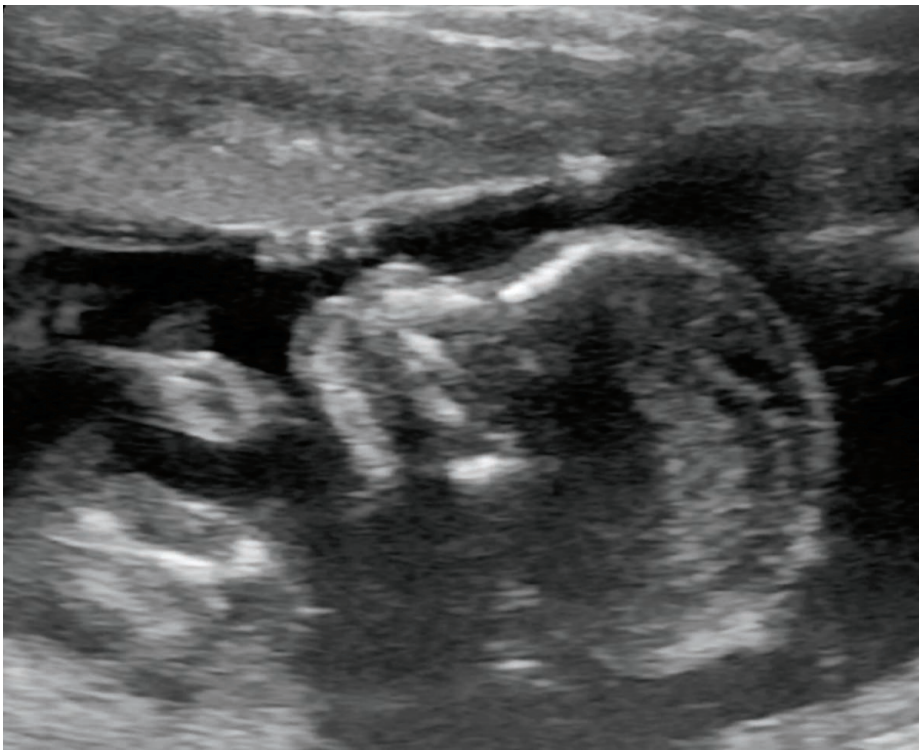

This sonogram shows a rhesus macaque fetus 25 days after being infected.

99% genetically similar to the one now circulating in Latin America.

In the knockout mice, the virus replicated to higher levels than in those treated with the antibody, killing most of the fetuses. The researchers found high levels of Zika virus in the placentas—1000 times more than in the mother's blood—supporting the hypothesis that the virus harms the placenta, which, in turn, cuts the blood supply to the fetus, Diamond says.

Pregnant mice treated with the antibody still made enough interferon to partially control the infection and allow the pups to survive. Mirroring effects seen in humans, they were born small, a condition known as intrauterine growth restriction.

In both sets of mice, the virus also turned up in fetal heads, Diamond says, suggesting that it causes brain damage directly as well as by impairing the placenta. That's consistent with earlier in vitro findings that Zika can infect and damage human neural precursor cells (*Science*, 11 March, p. 1123). Neither set of pups developed microcephaly, which Diamond says could be because the researchers infected the mothers so early during pregnancy that not much brain development had yet occurred.

The two other mouse experiments, published in *Cell Stem Cell* and *Nature*, did document microcephaly. Neither team manipulated their mice to make them more susceptible to the virus. In the *Cell Stem Cell* study, Zhiheng Xu of the Chinese Academy of Sciences in Beijing sidestepped the mice's natural resistance to Zika virus by injecting a Samoan isolate directly into fetal brains. In *Nature*, Fernanda Cugola of the University of São Paulo in Brazil and co-workers injected a Brazilian isolate into the tails of a strain of mice that are naturally immunocompromised. Diamond notes that the Brazilian-led team injected an "astronomical amount of virus" through the intravenous route, which may have sent the virus directly to the placenta and helped dodge the antiviral immune response.

Both studies found malformations associated with microcephaly, including what's known as cortical thinning and smaller brains. The two reports also showed that Zika virus infected and damaged neuronal stem cells harvested from mice and humans. "If you see consistent phenotypes in different models, the things that are happening are probably important," says Guo-li Ming of Johns Hopkins University School of Medicine in Baltimore, Maryland, who led the earlier studies of Zika in human neural progenitor cells.

The researchers who study these various mouse models acknowledge that they differ from humans in many critical ways. "It's very difficult to study humans directly," Diamond notes. Yet he stresses that these mouse models give insights into pathogenesis and will allow for high-throughput screening of drugs and vaccines against the virus.

Monkeys are naturally infected with Zika virus and are far closer to humans in many ways, and at least a half-dozen studies are underway. In an unusual twist for the primate research community, investigators from four U.S. labs have been posting data from their monkey Zika experiments on their websites in near real time, before publication. "We decided that the best thing for the community was that information be made available as widely as possible and freely available," says David O'Connor, whose group at the University of Wisconsin, Madison, is furthest along in studying Zika infection of pregnant monkeys.

One pregnant rhesus macaque that O'Connor's group is following was 50 days postinfection at last report, and a little more than halfway through her pregnancy. Sonograms of the fetus—which are posted online—"sort of" show evidence that the head circumference is small, but O'Connor and colleagues "are not drawing too much attention to it," he says, because it's not that far outside of the normal range. The group will know for sure after they perform a cesarean section on the mother—which will also let them obtain the placenta, normally eaten by rhesus mothers. "I hope we can accelerate the information about what's going on in people," he says.

O'Connor points out that Zika-infected monkeys do not perfectly reflect humans, either, and he sees the various models as complementary. "We can learn a lot from the fact that pregnancies are quick in the mice and you can do much larger experiments, but in monkeys we can do experiments that are much more relevant to human pregnancy," he says. "Clearly, we have a lot of work to do, but these experiments are opening up the possibility that Zika's effects during pregnancy may be much more common than we initially thought." ■

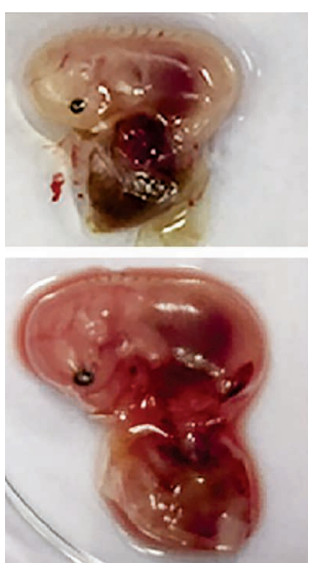

Pregnant mice engineered to have higher levels of Zika virus had smaller fetuses (top) than normal dams (bottom).

PHOTOS: (TOP TO BOTTOM) SARAH KOHN/KATHLEEN ANTONY/SAVERIO CAPUANO/JENNIFER POST; MINER *ET AL.*, *CELL* **165**, (19 MAY 2016)

Downloaded from http://science.sciencemag.org/ on May 12, 2016



Published by AAAS

CLINICAL TRIALS

# Unexpected revelations for study volunteer

## Years after signing up for a cholesterol study, a woman learns she's central to a paper

*By* **Jennifer Couzin-Frankel**

At La Colombe, Rita Woidislawsky's favorite coffee shop steps from Philadelphia's upscale Rittenhouse Square, she is effusive, hugging patrons she knows, waving to baristas, and finding the one table that's about to free up. A Ph.D. psychologist who treats young women with eating disorders, she is athletic and delights in looking younger than her 68 years. Hidden from view is what attracted scientists to Woidislawsky: her remarkably elevated high-density lipoprotein (HDL), or "good" cholesterol, and her decision about 5 years ago to join a research project that's studying people like her.

Like millions of volunteers who give blood and a few hours of their time to scientists, the project had barely registered on her radar recently. And then last month came a startling discovery. After a chance encounter with the lead scientist, she learned that the research group had published a paper in *Science* in which her case figured prominently (although only her age at the time of most recent data collection—67—was listed). The news alarmed her: The researchers suspected that rather than being beneficial, the high HDL Woidislawsky had always been proud of might be deleterious. She had known nothing about the publication plans or her own results.

Rita Woidislawsky has high HDL, and it might have a downside.

Her experience places Woidislawsky at the nexus of two distinct quandaries in clinical research: What health information do researchers owe the volunteers in their studies, especially when it's not clear what it means? And should researchers notify volunteers of publications in which their story appears, even if it's impossible for others to identify them? This incident shows that "the risks of publishing information about people are not just privacy," says Christine Grady, chief of bioethics at the National Institutes of Health Clinical Center in Bethesda, Maryland. "They might learn something about themselves that they didn't know."

The story holds lessons for researchers and for the ethicists who guide them. And after Woidislawsky found a story I wrote about the study and approached me for advice, I came to believe it holds lessons for journalists, too. The tale begins with Woidislawsky's HDL of 152, about triple the norm. It prompted her doctor to suggest she connect with a research group at the nearby University of Pennsylvania. There, Daniel Rader, a well-respected geneticist and lipidologist, was eager to include her in his study of people with naturally high HDL. She signed the necessary forms and gave some blood. DNA sequencing revealed a mutation in a gene called *SCARB1*, but, following the custom of many research groups, the team didn't tell Woidislawsky because no one knew what the mutation meant. (The consent form she had signed said nothing about returning results.) Instead, they reached out to her again and asked whether she ould undergo an ultrasound of her carotid arteries. She readily agreed.

Woidislawsky soon forgot all about the study. Then, sometime around early March, she ran into Rader at her usual haunt, La Colombe. The two chatted amiably, and she mentioned she had recently been diagnosed with high blood pressure. Rader suggested she make an appointment with him. The HDL study didn't come up, she recalls.

But it was about to be published, along with news stories in several outlets. Woidislawsky was the only person whom Rader's team could find with two copies of a mutation in the *SCARB1* gene, one inherited from each parent. (The scientists identified about 300 others with one copy.) The unnamed 67-year-old described in the paper had somewhat more arterial plaque than would be expected for someone her age. The authors attributed her high HDL to the *SCARB1* mutations. Based on additional studies of people and animals, they hypothesized that mutations in this gene could make it more difficult for the liver to siphon the HDL cholesterol out of her circulation.

Rader was uncertain what, if anything, to share with Woidislawsky. On 11 March, weeks before their appointment, he sent her an email. "I wanted to let you know that our manuscript describing the gene variant we found in you was published today in the journal *Science*," he wrote. "It was written up in today's [*Philadelphia*] *Inquirer*! You might want to take a look."

The message didn't make much impression on Woidislawsky. It was the first she'd heard about having a gene variant, but she figured it had been found in thousands of other people, too. She read an account of the work in the *Philadelphia Inquirer* but didn't connect its message—that high HDL in certain cases could be problematic—to herself. She assumed the 67-year-old woman with plaque in her arteries couldn't possibly be her. She shared this with Rader in an email message.

At her appointment late last month Rader confirmed that she was, in fact, the woman in the *Science* paper. He assured her that he felt she had nothing to worry about, but as a precaution he prescribed Crestor, a cholesterol-lowering drug. ■

PHOTO: J. COUZIN-FRANKEL/*SCIENCE*

Downloaded from http://science.sciencemag.org/ on May 12, 2016



Published by AAAS

"I was so startled," she says. She wondered how she had "clogged arteries" when she was so outwardly healthy, a devotee of pilates, yoga, weight-lifting, and aerobics. Her two adult daughters were shocked and are considering getting tested for the same genetic variant, about which almost nothing is known.

She began emailing HDL researchers all over the world to learn more about her unusual biology. She also found my own news story about the paper and read it with mounting alarm. She emailed me a few days after her appointment with Rader, wanting to know whether I could connect her with other researchers. Albeit anonymously, Woidislawsky had been central to my article—and I began to wonder whether I had overplayed her tale, making the condition of her arteries sound worse than it was, in order to more dramatically suggest that HDL might not always be advantageous. "My heart doesn't look so good" was one of the first things she said to me, referring, I realized later, to a generically captioned stock photo of clogged arteries I'd helped select for my news story, which wasn't her heart at all.

Rader is ambivalent about the episode, as he explained last week. "On the one hand, a case can be made" that telling her everything is "kind of the right thing to do. On the other hand, a case can be made that it's reporting research results that the person didn't sign up" to learn. In recent years, many consent forms, including Rader's, have changed: The studies he runs now ask those enrolling whether they want any findings that may be of interest to them.

Grady feels that because Woidislawsky was singled out in the paper, it "seems respectful" to share the publication with her. "In general, we don't do a good job of giving people who have volunteered in research any feedback on the study," Grady says. She wonders whether volunteers even understand that a primary goal of scientists is to publish their results.

While stressing that she likes and respects Rader, Woidislawsky says that the scientists were there when she had something they wanted—but not when the converse was true. "They call you lots of times to get the bloodwork and they're at your doorstep, but when it's time to really say what's it all about, they're gone," she says.

Rader now plans to see Woidislawsky again, recognizing that she needs more reassurance and additional information. She's planning on a cardiac stress test, but hopes that his earlier prediction holds true. "I said to Dr. Rader, 'When am I going to have a heart attack?'" she tells me. "And he said, 'Not before 100.'" ■

PHOTO: JOHN DE DIOS; DATA: NSF

NSF Director France Córdova, center, at a University of Arizona lab that studies tree rings to understand climate.

SCIENCE POLICY

# NSF director unveils big ideas

## Plan is aimed at the next president and Congress

*By* **Jeffrey Mervis**

France Córdova, the director of the National Science Foundation (NSF) in Arlington, Virginia, has unveiled a research agenda intended to shape the agency's next few decades and win over the next U.S. president and Congress.

The nine big ideas illustrate how increased support for the type of basic research that NSF funds could help answer pressing societal problems, she says, ranging from how humans interact with technology to how climate change in the polar regions will impact the global economy, environment, and culture (see box, left). It's unusual for a federal agency to talk publicly about its long-range budget plans, Córdova acknowledges. But she is betting that touting the agency's capabilities during an election year will pay dividends after voters have chosen a successor to President Barack Obama.

"This comes at a time of transition," she told the National Science Board, NSF's oversight body, on 6 May. "So that makes it a great opportunity for NSF to present a menu of the things it can do." And NSF's current budget of $7.46 billion is insufficient to tackle these questions, Córdova told *Science* after the meeting. "We can't do any of these things without future investments. So yes, we need an infusion of money."

But the federal government isn't the only possible source of funding, she added. "We either need to get that investment from new dollars appropriated by Congress, or hope to get on the agenda of one or more of the candidates during the campaign, or spark the imagination of groups in the private sector, including industry and foundations."

Córdova is counting on rank-and-file scientists to help sell the initiative by submitting more grant proposals that don't fit traditional categories or are especially ambitious. "We want people to think about what's missing, and how they would fill those gaps," she says.

The presidentially appointed science board didn't need much convincing after listening to her presentation. "I'm blown away by what I just heard," said Dan Arvizu, the board's outgoing chair and recently retired director of the Department of Energy's National

### A nine-point plan

National Science Foundation Director France Córdova has proposed that six "research frontiers" and three "process" changes shape the agency's future work.

**RESEARCH**

- Harnessing data for 21st century science and engineering
- Shaping the human-technology frontier
- Understanding the rules of life (i.e., predicting phenotypes from genotypes)
- The next quantum revolution (physics)
- Navigating the new Arctic (including a fixed and mobile observing network)
- Windows on the universe: multimessenger astrophysics

**PROCESS**

- More convergent research
- Support for midscale infrastructure (costing tens of millions of dollars)
- NSF 2050 (i.e., a common fund to seed large, ambitious projects)

Downloaded from http://science.sciencemag.org/ on May 12, 2016



Published by AAAS

Renewable Energy Laboratory in Golden, Colorado. "It's an intellectual exercise unparalleled in government, and demonstrates the value of NSF to the nation."

NSF is already drafting its budget request for the 2018 fiscal year, which starts in October 2017. But the next president will ultimately decide what goes to Congress, and may even have a say in NSF's 2017 budget if Congress can't complete its work before Inauguration Day on 20 January 2017.

The list of ideas was finalized last month at a 2-day retreat of Córdova's senior managers. They were asked to come up with two grand challenges facing the scientific disciplines their offices support, and told not to compare notes ahead of time. What eventually emerged both distilled and amalgamated those ideas.

Shaping the human-technology frontier, for example, began as "probably four related proposals," Córdova notes. But some of the ideas weren't grand enough to make the final list. "They weren't things that we were ready to do, or they didn't have broad community appeal." Córdova says she wasn't looking for a particular number of items for the list, but "the nine that came out covered the waterfront of really big ideas."

The six "research" ideas are intended to stimulate cross-disciplinary activity and take on important societal challenges. Exploring the human-technology frontier, for example, reflects NSF's desire "to weave in technology throughout the fabric of society, and study how technology affects learning," says Joan Ferrini-Mundy, who runs NSF's education directorate. She thinks it will also require universities to change how they educate the next generation of scientists and engineers.

Other ideas on the list with no obvious short-term applications are meant to capitalize on newly available research tools. The "windows on the universe" frontier, for example, will build on the recent detection of gravitational waves, explains Fleming Crim, NSF's head of mathematics and physical sciences. "We've thought for a long time about doing electromagnetic, particle, and gravitational-wave observations," Crim says. "And now we have all the pieces."

The three "process" ideas include a new no-strings-attached pot of money to seed all manner of fresh ideas. Córdova compared it to the Common Fund at the National Institutes of Health (NIH), created several years ago within the director's office to encourage scientists to think outside the box.

"It started with money NIH had pooled," she notes, "but Congress really liked it, and [the Common Fund] has grown." Once a new NSF initiative "gets traction," she says, it would likely be handed over to one of the agency's seven directorates. ■

PLANT SCIENCE

# How the Venus flytrap acquired its taste for meat

## Plant turned preexisting defenses against insect pests into tools for catching and eating prey

*By* **Erik Stokstad**

Since the dawn of invertebrates, plants have had to defend themselves against hordes of nibblers. On at least a half-dozen occasions, however, plants turned the tables and became predators: the sundew with its sticky tentacles, pitcher plants with their beckoning pools of enzymes, and the flytrap with its swift clamp of death. These plants' aggressive feeding habits help them survive in poor soil by giving them a new source of nitrogen and other nutrients. Many biologists suspect this predatory behavior evolved when ancestors of today's carnivorous plants turned mechanisms that normally detect and defend against insect pests into offensive weapons.

Genes active in other plants' roots help a flytrap absorb nutrients from its prey.

Now, this hypothesis has gained support from a detailed genetic study of Venus flytraps (*Dionaea muscipula*) as they snared crickets and began to digest them alive. Led by biophysicist Rainer Hedrich and bioinformaticist Jörg Schultz of the Julius Maximilian University of Würzburg in Germany, a team tracked the genes expressed as the plants sensed and then digested their prey. The research, published online before print in *Genome Research*, provides the most detailed view so far of the molecular action during prey capture. "This is a great study," says plant geneticist Victor Albert of the State University of New York at Buffalo. "It's much richer" than previous studies of the process.

To catch an invertebrate that has blundered into its snare, the flytrap relies on an ancient alarm system. It starts ringing when the victim jostles trigger hairs. The hairs in turn generate electrical impulses that somehow stimulate glands in the trap to produce jasmonic acid—the same signal that noncarnivorous plants use to initiate defensive action against herbivores. Patterns of gene expression in the two kinds of plants confirm the similarity, Hedrich says.

The consequences of the alarm, however, are quite different. In noncarnivorous plants, jasmonic acid triggers the synthesis of self-defense toxins and molecules that inhibit hydrolases, enzymes that herbivores secrete to break down the plant's proteins. As part of their counterattack, plants also produce their own hydrolases, which can destroy chitin and other components of insects or microbes. In the flytrap, in contrast, jasmonic acid triggers a voracious response: Tens of thousands of tiny glands make and secrete hydrolases. The trapped invertebrate is drenched in the same digestive enzymes that another plant might use in smaller quantities to ward off an enemy. "It's just a change in emphasis," says Edward Farmer, a plant physiologist at the University of Lausanne in Switzerland.

After a few hours, the glands inside the trap turn on another set of genes that helps the plant absorb nutrients from its meal. Experiments showed that many of these genes are the same ones expressed in the roots of other plants. "We looked at each other and said, 'Yes, it's a root,'" Hedrich says. "It made immediate sense," because the flytrap draws its nutrition not from soil, but from its prey.

"This is the way evolution works," says Andrej Pavlovic, a plant physiologist at Palacký University, Olomouc, in the Czech Republic, who compares the flytrap's innovations to the modification of a bat wing or whale fin from the limb of their terrestrial ancestors. The molecular repurposing that allows carnivorous plants to harvest their nutrients from the air is no less inspiring. ■

PHOTO: © RODNEY_X/ALAMY STOCK PHOTO

Downloaded from http://science.sciencemag.org/ on May 12, 2016



Published by AAAS

Andrew Read, left, has studied how Robert Woods and other doctors decide how and when to use antibiotics.

Downloaded from http://science.sciencemag.org/ on Ma 2016

# RESISTANCE FIGHTERS

## Evolutionary biologists are challenging old dogmas about the way antibiotics should be used

*By* **Kai Kupferschmidt**

PHOTO: BRAD ZIMMER



Published by AAAS

One day in the spring of 2014, Robert Woods, a physician at the University of Michigan Health System in Ann Arbor, stopped by Andrew Read's office. "I've got a patient with an infection that can't be cleared and we have only two drugs left," he told Read. "How should we use them?"

Read, an evolutionary biologist, says his first reaction was: "What do you mean, 'we?'" Read rarely sees patients; based at Pennsylvania State University, University Park, he uses mice and math to study how microbes evolve resistance against therapeutics. He was spending 6 months at the hospital to better understand doctors' decisions about how to use drugs.

Woods's patient was a 56-year-old woman suffering from heart failure. A mechanical pump inside her body helped her blood circulate; it was connected to an external battery by a cable passing through her skin that kept spawning infections. First came methicillin-resistant *Staphylococcus aureus* (MRSA), a notorious hospital dweller, followed by *Enterobacter cloacae*, a species that often infects patients in long-term intensive care. The medical team tried several antibiotics in vain. High doses of ciprofloxacin finally got rid of MRSA, but *Enterobacter* developed resistance to it. They switched to meropenem, with the same result. Next, they tried cefepime—but by then it was too late. As Read and Woods would later write in a case study, "the patient died, in effect, from overwhelming evolution."

Drug resistance has become a huge problem in medicine, which scientists are battling on many fronts, from developing new antibiotics to improving diagnostics that help doctors decide which drug to use. But Read and a handful of other scientists are focused on an issue that gets surprisingly little attention: the evolutionary dynamics that lead to resistance in the first place.

Thinking about resistance in terms of evolution has led these scientists to ideas that fly in the face of conventional medical wisdom. Read's research suggests, for instance, that hitting infections with overwhelming antibiotic firepower, a standard strategy to prevent resistance from evolving, may be counterproductive. Applying a lower dose and letting the immune system do the rest might save countless lives in the long run, he says. Other researchers suggest that combining multiple antimicrobials, another method to avoid resistance, may sometimes backfire as well.

These insights come primarily from lab experiments and computer models; tests in humans are tricky because they might involve giving some patients a suboptimal dose of a life-saving drug. And many researchers and clinicians are skeptical, to say the least. But there's not much evidence for current practices either, says Hinrich Schulenburg, an evolutionary biologist at the University of Kiel in Germany who's also studying fresh strategies to avoid resistance. "We are developing new ideas," Schulenburg says. "I think that is important because we are breaking with dogmas … for which there is little empirical support."

**JUST A FEW YEARS** after his discovery of penicillin in 1928, Alexander Fleming realized that many microbial species were able to develop resistance to the new wonder drug. Since then, bacteria have evolved resistance to every newly discovered antibiotic—sometimes even before the drugs came on the market (see graphic, below).

Drug resistance is taking an ever-larger toll. More than 2 million people become infected with resistant bacteria every year in the United States alone, and at least 23,000 of them die, according to the Centers for Disease Control and Prevention (CDC). (Some would have died even if antibiotics worked, but resistant infections generally lead to disease that is longer, more serious, and more often fatal.) By 2050, the number of deaths worldwide could be 10 million a year, according to a review commissioned by the U.K. government that will soon be published. Scientists have raised the specter of a return to a "preantibiotic era," when a simple thorn prick from a rose could kill you and even minor surgery carried major risks.

There's universal agreement that to avoid this, antibiotics shouldn't be used willy-nilly—for instance, against viral infections. (A CDC report published on 3 May found that one in three antibiotic prescriptions in the United States is inappropriate.) The debate is about what to do when antibiotics are actually useful and needed. Fleming believed he knew the answer: Treat at high doses. In his acceptance speech for the 1945 Nobel Prize, he warned of the dangers of using sublethal levels: "Mr. X. has a sore throat. He buys some penicillin and gives himself not enough to kill the *Streptococci*, but enough to educate them to resist penicillin. He then infects his wife. Mrs. X

## The rise of resistance

Bacteria have developed resistance to every antibiotic discovered so far, sometimes even before the drug reached the market. The appearance of resistance does not mean that a drug has become completely useless.

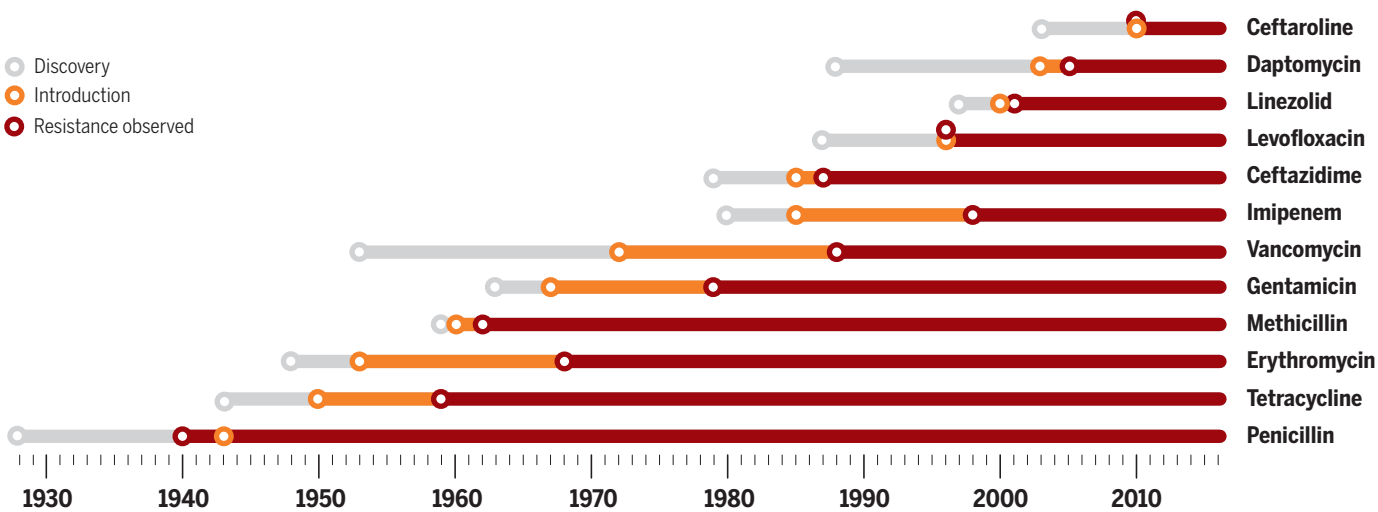


CREDITS: (DATA) CDC; (GRAPHIC) A. CUADRA/*SCIENCE*

Downloaded from http://science.sciencemag.org/ on May 12, 2016



Published by AAAS

gets pneumonia and is treated with penicillin. As the *Streptococci* are now resistant to penicillin, the treatment fails. Mrs. X dies."

That logic still applies, researchers say. High doses kill many bacteria quickly; the fewer that are left to evolve, the less likely one of them is to develop resistance. As some say: "Dead bugs don't mutate." Yet a 2014 review authored by 23 scientists, including Read, noted that "there is surprisingly limited empirical evidence" to support this strategy. "The ignorance is frightening; the ignorance of the ignorance even more so," Read says.

He says the story is more complicated than Fleming realized. Many antibiotics are natural compounds that arose during millions of years of intermicrobial warfare. Antibiotic resistance is a product of natural evolution, too. In 1940, for instance, before penicillin was widely used, scientists found that some bacteria already had an enzyme making them resistant to it. Genes encoding resistance are literally everywhere, even in 30,000-year-old frozen sediments in the Yukon territory in Canada. Combined with the resistant microbes that have emerged more recently in hospitals and the wider community, this means that in many infections, a few resistant bacteria may be present from the start, Read says. The key issue is not keeping resistance from developing—it's stopping its spread.

***"We are developing new ideas. I think that is important because we are breaking with dogmas ... for which there is little empirical support."***

**Hinrich Schulenburg**, University of Kiel

This is why high doses of antibiotics may backfire, Read argues. Resistance usually comes with a "fitness cost" that limits growth: A bacterium may have to expend extra energy to pump out an antibiotic, for instance. High doses of antibiotics will kill susceptible bacteria rapidly, leaving resistant ones without any competition—a phenomenon known as competitive release—and giving them the upper hand.

With lower doses, in contrast, resistant bacteria would have to compete with susceptible bacteria, and would remain a minority. An antibiotic given this way simply holds the bacteria in check: The immune system—which seems able to kill resistant and susceptible bacteria equally well—then mops up the infection.

Read has tested this idea in mice that he infected with *Plasmodium chabaudi* (not a bacterium but a malaria parasite). At the start, one in every million or billion parasites was resistant to pyrimethamine, a malaria drug. When the mice were given an aggressive pyrimethamine treatment—one that mimics the recommended regimens for humans—the resistant parasites quickly became more common. "Once resistance is present in a patient, currently recommended regimens actually maximize its spread," Read says. But with a lower dose and a shorter course, the resistant parasites remained a tiny minority, and the mice didn't suffer more severe disease, Read reported in 2013. Several other studies have shown similar results.

Read acknowledges that high doses may prevent resistance when it isn't present from the start, but emerges during the course of an infection—the scenario Fleming described. But even then, dosing high isn't always the best solution, he has shown in a model developed with mathematician Troy Day of Queen's University in Kingston, Canada.

The model (see graphic, p. 761) has two extremes: When no antibiotics are given, bacteria can replicate freely, and any resistant bacteria that arise are quickly overwhelmed by susceptible ones. At very high doses, any resistant mutants would quickly take over—but because there is much less replication, such resistance is less likely to arise. This means that the likelihood of resistance emerging is equally low at very low and very high doses; it's elevated in between.

The model suggests that antibiotics should be developed and prescribed in a new way, Read says. Drug manufacturers should identify the highest doses patients can still tolerate and the lowest doses at which the medicine is still effective, and doctors should prescribe at one of the two ends of the spectrum. (In some cases, the high dose will turn out to be better, in others the low dose, Read argues.)

Inspired by these ideas, researchers at St. George's Hospital in London recently set up a trial in which children with pneumonia receive either a high or a low dose of amoxicillin, for 3 days or for 7 days. They will compare how often children in the different groups have to undergo another treatment and will take nasal swabs before, during, and after treatment to look for resistant bacteria.

**MANY SCIENTISTS** are unconvinced. Read's ideas may work in the lab, but "his recommendations are potentially dangerous," says Nicholas White, a malaria researcher at Mahidol University in Bangkok. For one, some people break down drugs very fast; if they receive a lower dose, they may not benefit from treatment at all, "and they may die," White says. "Read's argument is fundamentally fallacious because it assumes there is a safe way to undertreat infections. There isn't."

Bruce Levin, a biologist at Emory University in Atlanta, says there are two basic flaws in Read's argument against high doses. Resistance isn't an all-or-nothing phenomenon: Many resistant bacteria can survive lower antibiotic doses but are still susceptible to high doses, contrary to Read's assumption. And the fitness cost of resistance is often not that high, which means competitive release is not a very strong force, says Levin, who published a mathematical model supporting conventional views.

The dispute gets heated sometimes. Levin prefaced a recent talk with a slide that said: "Controversy is great for careers, whether warranted or not, but especially when not." But Read relishes the role of a rebel against what he calls "the curious orthodoxy of aggressive chemotherapy." "Many clinicians don't like my ideas, partly because they have been raised on this 100-year-old idea," he says. "And it's a natural instinct to use everything in your power to get rid of the infection as fast as possible."

Harvard University epidemiologist Marc Lipsitch adds that Read's ideas might saddle doctors with a dilemma. Low-dose treatments could benefit society as a whole but not the individual patient. (Indeed, the best way to prevent resistance is never to use antibiotics at all—obviously not a desirable strategy.) Especially with serious infections, "my guess is that few would be willing to risk the lower dose," Lipsitch says.

But Lipsitch thinks simple conservatism is also at work. "I do think there is a lot of conventional wisdom that prevents novel approaches," he says. "A big contribution of what Andrew has done is to shake up that conventional wisdom."

**EVOLUTIONARY THINKING** is challenging other widely held assumptions as well. Combining two, three, or even four drugs is the norm in treating HIV and tuberculosis, because it's thought to be much harder for a pathogen to develop resistance to all of them at once. Scientists hope combination therapy could thwart resistance in other

PHOTO: CHRISTIAN URBAN/UNIVERSITY OF KIEL

Downloaded from http://science.sciencemag.org/ on May 12, 2016



Published by AAAS

types of infections as well—but research by Schulenburg suggests it could backfire.

In one study, he challenged *Escherichia coli* cells with doxycycline, erythromycin, or both antibiotics together. One day into the experiment, the combination therapy performed better than either antibiotic alone. On day 2, the double whammy still successfully suppressed susceptible cells, but resistant cells had begun to grow. Because the combination therapy was so successful at suppressing susceptible cells, it gave a big competitive advantage to the resistant ones, ultimately producing a higher bacterial burden than either drug alone.

Along with casting doubt on combination therapies, Schulenburg says, the study shows that it's important to give experiments enough time for evolutionary dynamics to play out—many antibiotic studies last only 24 hours. Schulenburg thinks alternating different antibiotics may hold more promise. In lab experiments, he keeps finding that this strategy makes it harder for bacteria to adapt. "I think this is really something that should be tried in the clinic," he says.

Schulenburg is also studying which combinations are best. Doctors, fond of blasting bugs as hard as they can, usually prefer so-called synergistic combinations, in which the effect of two drugs together is greater than the sum of their individual effects. But Schulenburg's studies suggest such combos aren't always best at preventing resistance.

Antibiotic regimens can not only be changed, but also shortened, Read and others argue. Standard treatment courses are often a week or 10 days even though many infections clear within a few days. "People felt that if they treated for a few more days, there was no downside to it," says Ramanan Laxminarayan, who directs the Center for Disease Dynamics, Economics & Policy in Washington, D.C., and New Delhi. But longer treatments are more likely to favor resistant strains. What's more, recent discoveries about the human microbiome have shown that an antibiotic treatment can ravage the microbial ecosystem in the human gut, killing beneficial microbes and potentially giving harmful ones such as *Clostridium difficile* an evolutionary advantage. Gut microbes could also develop resistance and pass those genes on to pathogens later.

For tuberculosis it's critical that patients finish their full course, Laxminarayan says, because hidden pathogen reservoirs in the body take months to smoke out. But in 2012, a Cochrane review concluded that for children with streptococcal throat infections, 3 or 6 days of treatment are just as effective as 10 days. A 2009 review of clinical trials of acute bacterial sinusitis found that long-term treatment is no more effective than short-term. For many other infections, including meningitis and pneumonia, shorter courses still need to be investigated. It's a slow, incremental process; researchers usually err on the side of caution, testing durations well above the theoretical minimum.

Read, Lipsitch, and Schulenburg all say that if they needed antibiotics, they would stop taking the drugs as soon as they had recovered. "But if we are to challenge clinicians, we need much more and better data," Schulenburg says.

**EVEN THOUGH** clinical trials of lower doses or shorter courses of antibiotics could pose ethical challenges, Read says he can envision ways to test these new ideas in humans. Some people at increased risk of an infection—for instance with HIV—take drugs prophylactically; researchers could design studies in which different doses of the drugs are given and watch whether subjects become infected with susceptible or resistant strains, Read says. Lipsitch adds that researchers should find out whether infections include both antibiotic-susceptible and resistant strains from the start, as Read argues.

Perhaps the most important thing evolutionary biology can bring to the table is a change in perspective, says Roy Kishony, who studies antibiotic resistance at the Technion-Israel Institute of Technology in Haifa. Antimicrobial drugs have never wiped a pathogen from the planet, he notes, and probably never will. That means that doctors and researchers need to think about the drugs more as "selecting agents," Kishony says. "What you are doing is not really inhibiting, it's selecting for who is going to be there tomorrow or next year."

One way or another, Read adds, clinical medicine and evolutionary biology should start talking to each other. For him the biggest revelation at the Ann Arbor hospital was the "huge gulf" between the two. Not being able to help that patient was "hugely frustrating," he says. "When she died, [Woods] said it was a failure of our science. He was right." ■

## High or low doses—what's better?

In Andrew Read's model, the risk of resistance emerging is lowest at very low and very high doses of a drug, and elevated in between (red curve). Which dose is best to use depends on the "therapeutic window" (orange), which ranges from the lowest effective dose to the highest dose a patient can tolerate. For some drugs, the risk of resistance emerging is minimal at the lower end of this window (Scenario 1), whereas for others it's at the higher end (Scenario 2).

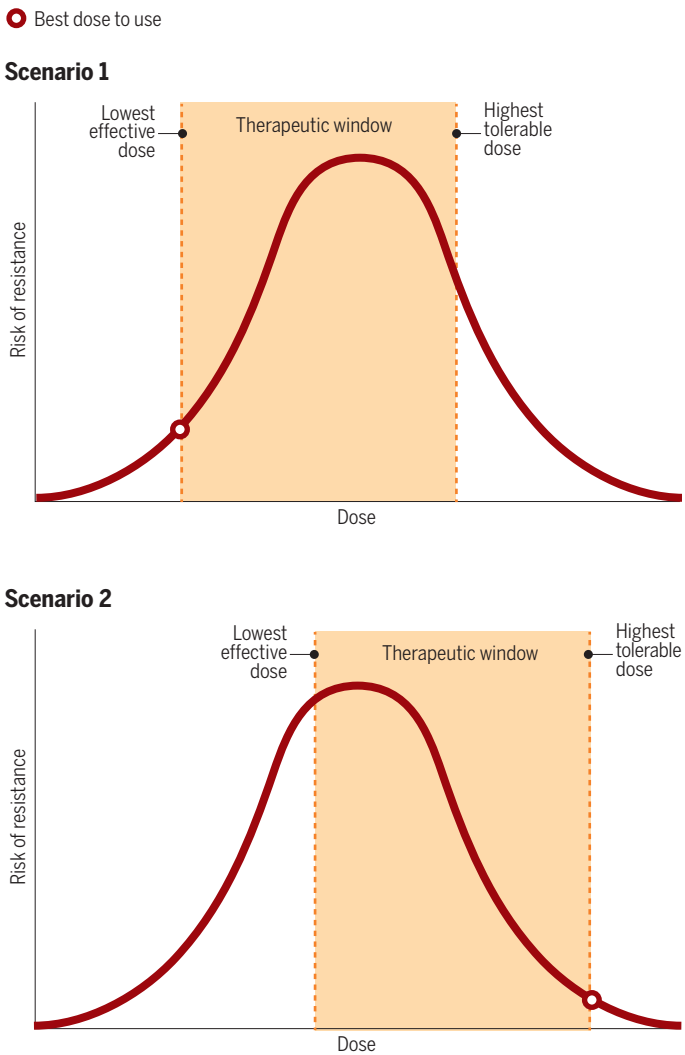


GRAPHIC: C. SMITH/*SCIENCE*

Downloaded from http://science.sciencemag.org/ on May 12, 2016



*Published by AAAS*

# MUSEUM DRAWERS GO DIGITAL

## New technology speeds efforts to display billions of natural history specimens online

*By* **Nala Rogers**, *in Washington, D.C.*

In a back room of the Smithsonian Institution's National Museum of Natural History (NMNH) here, Rochelle Safo handles preserved plant specimens with reverence. The brittle leaves and stems, dried and glued to pieces of paper, hold a wealth of knowledge that spans continents and centuries. Every 4 to 6 seconds, Safo places a new one on the conveyer belt so it can be photographed and digitally shared with the world. "On a good day we can do 3500 specimens," says Safo, a digitization specialist who has been working on the project since it launched in October 2015.

The NMNH conveyer belt system is part of a global effort to open up access to museum collections. No one knows exactly how many natural history specimens exist in museums and other research institutions worldwide, but some calculate it's on the order of 3 billion. In most cases, the displays seen by visitors make up a tiny slice of this treasure; museum curators estimate that more than 99% are stored away from the public gaze.

Researchers have for decades used museum specimens to answer questions about how species diverge, where they move around the globe, and how they respond to changing conditions. "There is more information about biodiversity in natural history collections than in all the other sources of information put together, outside of nature itself," says Larry Page of the Florida Museum of Natural History in Gainesville. "But it's been mostly inaccessible." Researchers wanting to study the specimens have traditionally had to travel from museum to museum in person, or else request that the specimens be mailed to them.

Now, even as they struggle with funding woes that limit their activities, institutions from China to Europe to the United States are working to put specimen photographs and related information online where anyone can view them. Until recently, these efforts were slow and painstaking, barely chipping away at the staggering amount of data in collections. Now, technological advances and innovative workflows are allowing institutions to think bigger, ushering in a new age of mass digitization. With their previous system, the NMNH herbarium staff could digitize 30,000 specimens in a year—photographing them and transcribing label data—at a cost of $5 to $7 per specimen, says Sylvia Orli, a botanist and digitization project leader at NMNH. Now, they expect to finish 650,000 in that time, each one costing just $1.

As digitization grows faster and cheaper, more governments and institutions are investing in it. The NMNH conveyer belt is funded by the Smithsonian's 5-year old Digitization Program Office (DPO) here. And since 2011, the U.S. National Science Foundation (NSF) has devoted $10 million per year to digitization efforts in nonfederal collections across the United States—Page, for example, is project director for iDigBio, an NSF-funded effort to coordinate biological specimen digitization. But even with these new funding opportunities, museum officials and curators stress that there is still far too little money to make all such specimens digital.

Some recent digitization projects have already born scientific fruit, yielding insights into everything from invasive species to climate change. "I can get into a database and bring up one image after another of a

PHOTO: C. CLARK/SMITHSONIAN

Staff at the Smithsonian Institution's National Museum of Natural History manage about 5 million specimens of algae and plants, some dating back centuries.

Downloaded from http://science.sciencemag.org/ on May 13, 2016



Published by AAAS

Downloaded from http://science.sciencemag.org/ on May 12, 2016



Published by AAAS

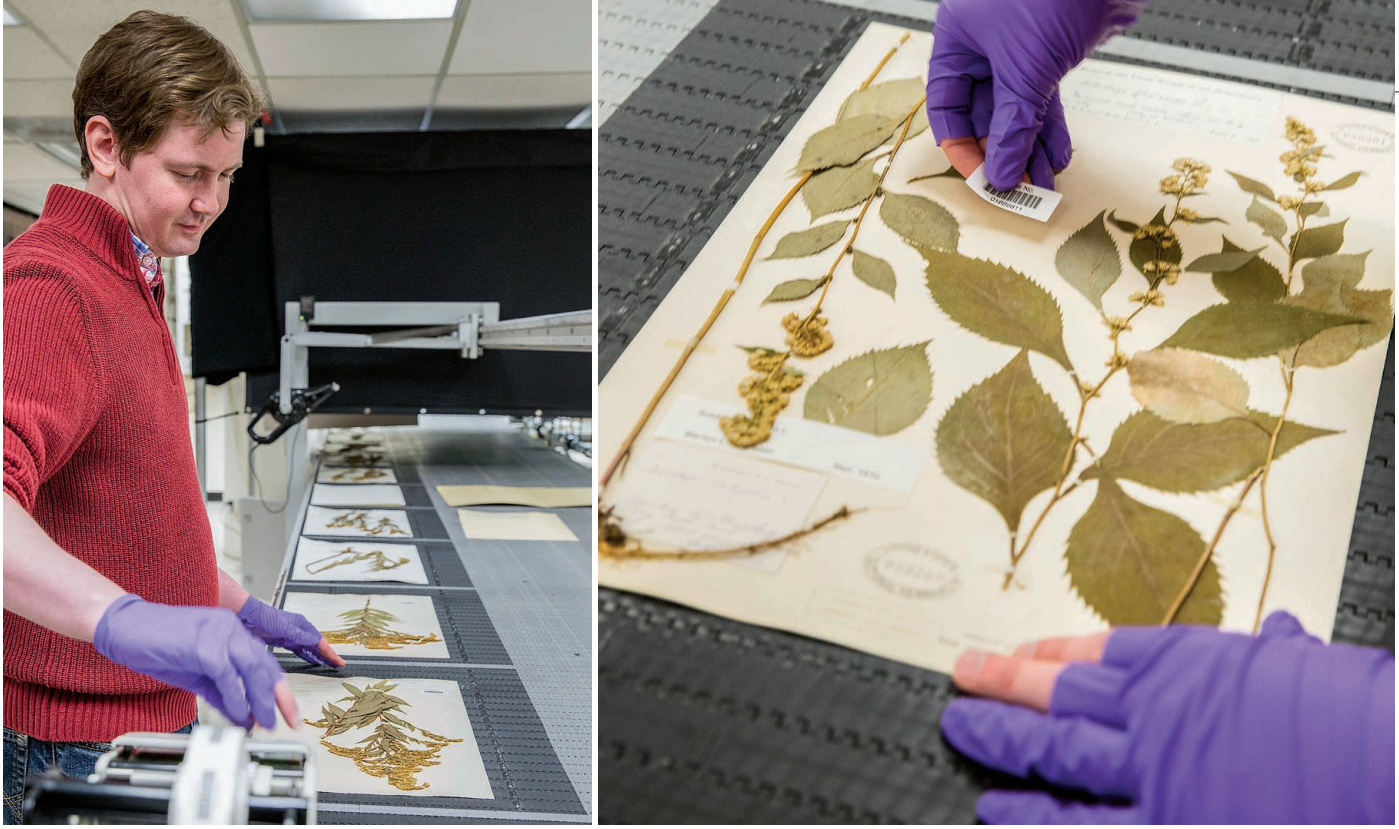

Justin Donaldson places barcode stickers on plant specimen sheets as they travel down a conveyer belt toward a camera at the Smithsonian Institution's National Museum of Natural History in Washington, D.C. The barcodes help software keep track of the images and link them to database records.

plant that I'm interested in," says Michael Donoghue, a phylogenetic biologist at Yale University who co-leads a large digitization project on New England vascular plants. "I can measure the leaves, or measure something about the flowers, and quickly do a scientific study that I never could have done before, because it would have taken me my entire life to go around to every freaking museum."

**EFFORTS TO DIGITIZE** natural history collections aren't new. Curators at NMNH started entering specimen data into computers in the 1960s, when the cutting-edge technology was punch cards, Orli says. The NMNH herbarium began posting records of its most important specimens—the ones used to define species—online in 1992.

Plants and algae lend themselves to digitization because they are usually pressed flat and attached to pieces of paper. A single photograph can capture the label and most of the structural details needed for research. The Paris National Museum of Natural History was one of the first to adopt mass digitization technology with its own conveyor belt system, and it finished off its entire vascular plant collection—about 6 million specimens—in 2012. Other herbaria across the world are working rapidly through their collections with a variety of semiautomated procedures, funded by government grants or the museums themselves.

At NMNH, the new conveyer belt setup has sped up the imaging process by a factor of 10. One person lays herbarium sheets on the 9-meter belt, another attaches barcode stickers so that software can keep track of the images, and a third replaces the sheets in folders when they have finished their journey. Every few seconds, a rumbling chug brings a new specimen beneath the camera.

The images captured are so detailed that researchers can count fern spores less than 50 microns across, says Ken Rahaim of DPO. The plan is to digitize 500,000 specimens, Orli says. After that, unless the Smithsonian can find more funding, the herbarium will have to shut the conveyer belt down and use older techniques to slowly digitize the rest. "It's only a dollar a specimen. You think 'god, that's so cheap.' But we've got 5 million specimens," says Vicki Funk, a botanist at NMNH who uses digitized specimens to study plant systematics.

**2–9 billion**

Total number of natural history specimens, according to several estimates.

Once a picture is taken, custom software automatically reads the barcode and crops and straightens the image. It can't transcribe information from the labels, however, a task some consider to be the toughest remaining problem in mass digitization of museum specimens. Labels include, at a minimum, the name of the collector, the type of organism, and the date and place it was collected, and many bear extra details such as descriptions of the environment. Yet they are often handwritten, some in the archaic scripts of 18th and 19th century naturalists. What's worse, they don't follow standardized formats, so it's hard for a software program to automatically tell which part to put in which database field.

Currently, optical character recognition (OCR) programs do a decent job of turning printed labels into blocks of text, though handwriting still comes out as gibberish. Some institutions are using OCR to sort images of labels so that people can more easily transcribe them into databases, says Barbara Thiers, director of the herbarium at the New York Botanical Garden in New York City. For example, transcribers can search OCR outputs for the names of particular countries or collectors, then work on similar specimens in groups.

Some researchers have tackled the harder problem of automatically transferring OCR outputs to database fields using machine learning and natural language processing algorithms. At the California Academy of Sciences (CAS), which is digitizing its herbarium in San Francisco, such parsing software "helps speed up the entire process," says Anne Barber, a former CAS digitization project manager who helped develop it.

But human users still have to go through the output to correct errors, and many institutions find it cheaper and faster to enter data the old-fashioned way. Some use crowdsourcing initiatives to spread out the labor; NMNH has had a volunteer transcription program for years. But with the new conveyer

PHOTOS: P. FETTERS

Downloaded from http://science.sciencemag.org/ on May 12, 2016



Published by AAAS

belt setup, the NMNH herbarium is producing images too fast for volunteers to keep up. Instead, the pictures are sent to a company called Alembo in Suriname, where professional transcribers type in the label data by hand at a rate of about 60 specimens per hour, according to the company.

The digitization efforts are paying off. When Kellen Calinger, a forest ecologist at Ohio State University, Columbus, wanted to evaluate which native plants are likely to perish and which invasive ones might take over as the climate warms, she turned to 200,000 digitized specimens from the university's herbarium. Using the collection date and location on each label, Calinger assessed changes in the abundance and distribution of more than 200 plant species in Ohio over 115 years, and compared the results with historic temperature records.

Photographs of the specimens showed whether plants were in bloom, allowing her and her colleagues to conclude that the nonnative species most likely to expand their ranges were those that could adapt to rising temperatures by changing when they flowered. That, in turn, can suggest which invasive species are most threatening in a warming world and which natives are at greatest risk from the competition. "Having these predictive metrics can be really useful when selecting which species might be most important to focus our conservation efforts on," says Calinger, whose work was published last year in the journal *Biodiversity and Conservation*. Other researchers have used hundreds of thousands of digitized plants from museums across Australia to study nonnative species, examining when and where they first appeared on the continent to identify likely sources of future invasions.

Pinned insects like these endangered Taylor's checkerspots (*Euphydryas editha taylori*) are difficult to digitize, with fragile bodies often obscuring the labels below.

PHOTO: A. WARREN/MCGUIRE CENTER FOR LEPIDOPTERA AND BIODIVERSITY

**MOST MUSEUM SPECIMENS** are more challenging than plants, and each category presents its own set of problems. There is no automation yet for things stored in jars; to photograph a fish, someone must pluck the dripping specimen and its label out of alcohol and arrange them on a tray. Insects, the most abundant type of specimen worldwide, are a nightmare to digitize. A single drawer can hold hundreds of bugs on pins, sometimes so close their wings overlap. Their fragile bodies often hide the labels below. A careless touch snaps off legs.

Rather than photographing specimens such as insects, fossils, and shells one-by-one, some institutions are capturing images of a whole drawer-full at once. Invertnet, a collaboration that aims to digitize more than 50 million insects and other arthropods in collections across the midwestern United States, is employing a type of robot called BugEye. Developed at the University of Illinois, Urbana-Champaign (UIUC), it looks, appropriately enough, like a giant mechanical spider hanging upside-down over the drawer. BugEye's central camera moves over the drawer in a series of passes, taking hundreds of overlapping images that it stitches together into a high-definition composite. Many of the labels are hidden under the bugs, but human users reveal some of them by tilting the drawers, letting the robot work from different angles.

"With these whole-drawer images I can just sit at my desk and browse through all these collections virtually," says Christopher Dietrich of UIUC, an entomologist and Invertnet project leader. "If I see something that I've never seen before, I can contact the curator of that collection and say 'Hey, the specimen No. 10 in this drawer looks like it might be a new species.'"

Technicians can manually divide a whole-drawer image into images of individual bugs by drawing boxes around them with a cursor. But this is "pretty soul-destroying work," says Lawrence Hudson, a scientific software engineer at the Natural History Museum (NHM) in London. Last November, he and colleagues published a new open-source software package called Inselect that helps automate this process, defining images of individual specimens and streamlining the creation of database records. People still have to adjust the borders of the boxes and transcribe label data, Hudson says, but it speeds up the process; Dietrich says that Invertnet plans to incorporate it into their workflow in the coming months.

Even slower-paced digitization projects can benefit insect researchers. Male silver-spotted skipper butterflies (*Hesperia comma*) tend to grow larger in years that are warm when the caterpillars are feeding, according to a study published last February in the *Journal of Animal Ecology*. To reach that conclusion, Phillip Fenberg, an ecologist and evolutionary biologist at the University of Southampton in the United Kingdom, and colleagues measured the wings of 331 silver-spotted skippers collected over nearly a century. London's NHM recently photographed them one at a time for a digital archive.

The butterflies from Fenberg's study were among nearly half a million butterflies and moths NHM has digitized thus far—a small chunk of its 10-million-specimen Lepidoptera collection, notes Gordon Paterson, chair of the digitization project and a senior researcher in NHM's department of life sciences. As more specimens and more species are added, researchers will be able to assess larger trends, such as the interplay between climate, body size, and reproduction. Certain butterfly species are able to have multiple generations per year, whereas others are limited to one. Fenberg and colleagues suspect the latter butterflies respond to warming climates by increasing body size, whereas other species get smaller and put the saved energy into having generations faster. "I expect to see some amazing things happening with the data," Paterson says. "I think it's really important to have the museums' knowledge released out into the wild."

In the end, these diverse projects will do more than aid individual research projects. The digitizers' ultimate goal is to build an interconnected online library where everyone can see and study specimens stored all over the world. Such a network could allow both professional and citizen scientists to take full advantage of the data their forebears spent centuries collecting. "This is a democratization of knowledge and data," says Mark Lindeman, general director of Picturae, the Dutch digitization company in Heiloo that designed and helps operate the NMNH conveyer belt system. "I really believe that opening up this data will improve the knowledge we have of the world around us."

But the key to doing that may be developing even more innovative digitization solutions that save museums time and money. "The technology is changing so fast," Orli says. "What we're doing now, we'll probably be laughing about in 5 years." ■

Downloaded from http://science.sciencemag.org/ on May 12, 2016



Published by AAAS

**The aftermath of civil war.** Thousands lost limbs during wartime violence in Sierra Leone. Freetown beaches regularly host amputee football matches.

PHOTO: AP PHOTO/GEORGE OSODI

Downloaded from http://science.sciencemag.org/ on May 12, 2016

CONFLICT

# *Reconciliation in Sierra Leone*

## Short, low-cost interventions can help communities to recover from civil war

*By* **Katherine Casey**[1] *and* **Rachel Glennerster**[2]

Since the end of World War II, there have been 259 armed conflicts in 159 locations (*1*). Sierra Leone's civil war began 25 years ago, at a time when roughly 25% of all countries worldwide were experiencing civil war (*2*). How can individuals and groups recover from such violent conflicts? On page 787 of this issue, Cilliers *et al.* (*3*) provide rigorous evidence on the efficacy of one postwar reconciliation strategy that was implemented in 100 communities in Sierra Leone (*4*).

Large-scale efforts are crucial in light of the large numbers of individuals and broad swaths of territory frequently affected by civil war. They are also daunting given the limited resources available in poor countries that are too often hosts to conflict (see the figure). When the Sierra Leone conflict ended in 2002, only one psychiatrist and two trained psychiatric nurses resided in the entire country (*5*).

Community-driven reconstruction/development (CDR/D) is one of the most popular postconflict investments. Communities are given grants to invest in a project of their

[1]*Stanford University Graduate School of Business, Stanford, CA, USA.* [2]*Abdul Latif Jameel Poverty Action Lab, Massachusetts Institute of Technology, Cambridge, MA, USA. Email: kecasey@stanford.edu; rglenner@mit.edu*



*Published by AAAS*

## Trauma versus treatment

Estimates for victims of war violence come from Project Ploughshares cited in UNDP (*16*). Health data show patients receiving any mental health services in 2009, from WHO (*15*).

GRAPHIC: A. CUADRA/*SCIENCE*

choosing but must do so in an open and participatory way in an effort to promote inclusive decision-making, trust, and social capital. Randomized evaluations of this approach in Sierra Leone (*5*), Liberia (*6*), and Democratic Republic of Congo (*7*) have generally found that CDR/D can be effective in improving infrastructure but not in promoting trust, raising contributions to public goods, or changing the way communities interact. These findings raised concerns about whether change in social capital—or the norms and networks undergirding civic engagement (*8*)—was possible over a period of 3 to 4 years (the typical length of these interventions).

In contrast to these previous findings, Cilliers *et al.* show positive effects of 2-day reconciliation ceremonies on measures of community social capital—at a cost of about $200 per location, compared with $5000 for the intensive CDR/D tested in Sierra Leone. During these public ceremonies, which were facilitated by a nongovernmental organization, victims spoke about the war violence that they had experienced, and perpetrators sought forgiveness. Using a randomized control trial, the authors find that these events increased measures of social cohesion, including participation in community groups, the strength of social networks, and contributions to public goods. At the same time, they find negative impacts on individual mental health: Revisiting war atrocities worsened measures of anxiety, posttraumatic stress disorder, and depression. Both positive and negative effects persisted for more than 2 years after the ceremonies.

The positive community-level response to reconciliation ceremonies resonates with broader indicators of the capacity for recovery in Sierra Leone. Gross domestic product doubled in the decade after the restoration of peace (*9*). Multiparty democracy and local government were restored, and the National Electoral Commission oversaw multiple free and fair elections, including the peaceful transfer of presidential power from the incumbent to the main opposition party in 2007. Although conflict can sunder local societal bonds, it can also force communities into self-reliance. Analysis of national survey data suggests that individuals whose households experienced greater war-related violence participate more frequently in community meetings and groups (*10*).

The war in Sierra Leone was not fought along ethnic lines, and levels of civilian abuse were no higher across than within ethnic groups (*11*). This makes it quite distinct from the conflicts in South Africa and Rwanda, which were followed by more intensive national-level truth and reconciliation efforts. Caution is thus warranted in considering whether such "light-touch" ceremonies would be as effective in promoting community reconciliation after ethnic conflict.

Other postconflict research has focused on preventing further violence. Here, relatively short interventions can also change people's behavior in meaningful ways. For example, combinations of cash grants, employment opportunities, and cognitive behavioral therapy (CBT) were successful in reducing violent and illicit behavior among criminally involved men in Liberia (*12*, *13*). The largest effects were found for CBT followed by $200 grants, which reduced engagement in violence up to 50% for a year. Many participants in these studies were involved in Liberia's civil war, which coincided and had many commonalities with that in neighboring Sierra Leone.

The estimated negative effects of reconciliation ceremonies on individual mental health documented by Cilliers *et al.* are cause for alarm and concern. It is unclear what alternative approaches might work better in poor countries. This lack of knowledge is mainly due to the low levels of resources devoted to mental health provision in the developing world: Public expenditure on mental health is less than $2 per capita in low- and middle-income countries, compared with more than $50 in high-income countries (*14*). World Health Organization estimates suggest that less than 1% of the more than 400,000 people suffering mental health disorders in Sierra Leone have received treatment (*15*). Let this be our call to action. ■

### REFERENCES AND NOTES


1. T. Pettersson, P. Wallensteen, *J. Peace Res.* **52**, 536 (2015).
2. J. Fearon, D. Laitin, *Am. Polit. Sci. Rev.* **97**, 75 (2003).
3. J. Cilliers, O. Dube, B. Siddiqi, *Science* **352**, 787 (2016).
4. J. Asare, L. Jones, *Brit. Med. J.* **331**, 720 (2005).
5. K. Casey, R. Glennerster, E. Miguel, *Q. J. Econ.* **127**, 1755 (2012).
6. J. Fearon, M. Humphreys, J. Weinstein, *Am. Polit. Sci. Rev.* **109**, 450 (2015).
7. M. Humphreys, R. Sanchez de la Sierra, P. van der Windt, "Social Engineering in the Tropics: Null Evidence from a Grassroots Democratization Experiment in East Congo," working paper, 2015; see www.columbia.edu/~mh2245/papers1/20150519%20HSW.pdf.
8. R. Putnam, *J. Democr.* **6**, 65 (1995).
9. International Monetary Fund, World Economic Outlook Database, October 2015.
10. J. Bellows, E. Miguel, *J. Public Econ.* **93**, 1144 (2009).
11. M. Humphreys, J. M. Weinstein, *Am. Polit. Sci. Rev.* **100**, 429 (2006).
12. C. Blattman, J. Annan, "Can employment reduce lawlessness and rebellion? A field experiment with high-risk men in a fragile state," World Bank Policy Research Working Paper No. 7648 , 2015.
13. C. Blattman, J. Jamison, M. Sheridan, "Reducing crime and violence: Experimental evidence on adult noncognitive investments in Liberia," working paper, 2015; http://ssrn.com/abstract=2622220.
14. World Health Organization, *Mental Health Atlas* (WHO, Geneva, 2014).
15. WHO, *proMIND: Profiles on Mental Health in Development: Sierra Leone* (WHO, Geneva, 2012).
16. United Nations Development Program, "Evaluation of UNDP support to conflict-affected countries" (UNDP, New York, 2006).


10.1126/science.aaf7874

Downloaded from http://science.sciencemag.org/ on May 12, 2016



*Published by AAAS*

GEOCHEMISTRY

# Identifying remnants of early Earth

## Isotope analysis reveals portions of Earth that have remained the same since accretion

*By* **Tais W. Dahl**

The chemical composition of Earth's mantle can tell us how our planet formed and how subsequent mantle dynamics have since homogenized the mantle through convective processes. Most terrestrial rocks have a similar tungsten (W) isotope composition (*1*), but some rocks that have been dated at 2.8 Ga (billion years old) (*2*), 3.8 Ga (*3*), and 3.96 Ga (*4*) have elevated $^{182}W/^{184}W$ ratios. This is reported as $\mu^{182}W$, in parts per million (ppm) deviation from the bulk silicate Earth. Until now, the outliers have included only these ancient rock samples with a small $\mu^{182}W$ excess (≤15 ppm) that can be attributed to the final ~0.5% of Earth's mass that accreted late in its accretion history. On page 809 of this issue, Rizo *et al.* (*5*) report W isotope data from young mantle-derived rocks with $\mu^{182}W$ excesses of 10 to 48 ppm. This result is spectacular because the range of $\mu^{182}W$ values in mantle-derived rocks is larger than can be accommodated by late accretion; the implication is that remnants of Earth's earliest mantle have been preserved over the entirety of Earth's history.

Two decades ago, geochemists started measuring W isotopes in terrestrial and meteoritic samples to estimate the timing of Earth's core formation (*6*). During core formation, it is presumed that W preferentially partitioned into the metal melt and sank to the core, whereas hafnium (Hf) remained in the silicate mantle. Therefore, the silicate mantle has a higher Hf/W ratio. As $^{182}Hf$ decayed to $^{182}W$ with a half-life of 8.9 million years, the silicate mantle developed $^{182}W$ excesses relative to its source material. Most of the $\mu^{182}W$ variability in the solar system is produced by the separation of metal from silicate during the first 60 million years of solar system history. As a point of reference for calibration, mantle material would have gained a $\mu^{182}W$ excess of >1000 ppm if Earth and its core formed at the very beginning of our solar system. The mantle, however, displays a nearly uniform $\mu^{182}W$ excess of +200 ppm relative to primitive meteorites, which suggests that the last metal-silicate equilibration event occurred ~30 million years into the history of our solar system.

The Moon formed after $^{182}Hf$ went extinct ~4.51 billion years ago. This inference is based on the tiny $\mu^{182}W$ excess in the Moon relative to Earth's mantle, +20 ppm (*7*). The small $^{182}W$ excess may well have developed by disproportionate late accretion on Earth and the Moon (*7*), where the addition of nonradiogenic material had a greater effect on Earth.

The new data from flood basalt lavas that erupted into the North Atlantic Igneous Province (Baffin Bay locale) and the Ontong Java Plateau (western Pacific Ocean) show larger $\mu^{182}W$ variability than between the Moon and Earth's mantle. In fact, the mantle source of the Ontong Java and Baffin Bay lavas prior to late accretion probably had a radiogenic W excess of +70 ppm. This exceeds what can be accomplished by late accretion. By implication, these parts of Earth's mantle predate the Moon and did not chemically equilibrate metal and silicate during the giant impact that formed the Moon.

W isotope heterogeneity in the mantle is likely to arise during the late stages of planet accretion. The planet accreted from dozens of collisions between differentiated bodies with metallic cores and silicate mantles, all with potentially unique W isotope compositions (*8*). The cores contained nonradiogenic W, whereas the radiogenic counterpart was hosted in their mantles. As the planet accreted, Earth's silicate mantle would have lost both radiogenic and nonradiogenic W to its core, assuming that an appreciable portion of each impactor's metal core disintegrated into smaller blobs and mixed down to diffusion-length scales where chemical equilibration occurred.

Several factors may lead to mantle heterogeneity. First, the

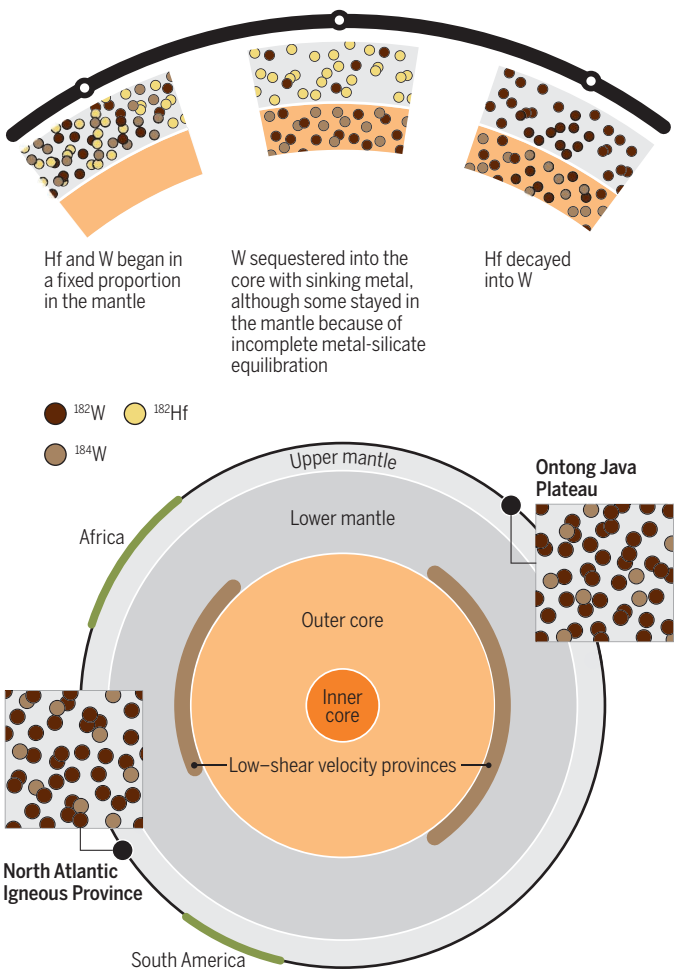


**Equatorial cross section of Earth.** Large low–shear velocity provinces (LLSVPs) occur at the base of the mantle under Africa and the Pacific Ocean. Flood basalts erupted at the North Atlantic Igneous Province and the Ontong Java Plateau show substantial radiogenic W excess relative to rest of the mantle. This compositional heterogeneity may preserve remnants after incomplete metal-silicate equilibration during Earth's core formation in the first 60 million years of solar system history. The chemical heterogeneity may have been preserved in LLSVPs at the base of the mantle for more than 4.5 billion years.

GRAPHIC: V. ALTOUNIAN/*SCIENCE*

*Natural History Museum of Denmark, University of Copenhagen, DK-1350 Copenhagen K, Denmark. Email: tais.dahl@snm.ku.dk*

Downloaded from http://science.sciencemag.org/ on May 12, 2016



Published by AAAS

far-side effect generates heterogeneity on a hemispherical scale, because an impact hits only one side of the planet. Second, portions of the mantle may have been isolated from mixing with the rest of the mantle. Perhaps such a hidden reservoir has existed at the base of the mantle (see the figure). Alternatively, self-gravitating cores may have plunged through the mantle without appreciable emulsification, thus preventing enough metal to mix with the silicate mantle down to small enough length scales for chemical equilibration to occur (*9*).

What is surprising is that such an initial W isotope heterogeneity could be preserved in the mantle today. The mantle source reservoir for the flood basalts is a matter of contention. One candidate is the large low–shear velocity provinces (LLSVPs) at the base of the mantle (see the figure). These regions consist of dense, hot material (*10*) and are thought to be stable at their present antipodal position on the core-mantle boundary close to the equator (*11*). Rizo *et al.* suggest that these regions have existed for essentially all of Earth's history.

Previous analyses of oceanic basalts thought to be derived from deep mantle plumes, including samples from the Ontong Java Plateau, found no $^{182}W$ excesses (±5 ppm) (*2*). If we accept both studies at face value, then the chemical heterogeneity apparently exists within a single source domain, excluding W heterogeneity created by the far-side effect.

Future studies must first rule out the possibility of analytical artifacts, because several processes may obscure high-precision isotope analyses of W poor samples (for example, lavas), including isotope fractionation in the laboratory, contamination, and interferences. In the end, identifying primitive signatures in Earth's mantle today elucidates the style of Earth's core formation and requires certain parts of the mantle to stay sufficiently buoyant to escape convective mixing throughout essentially all of Earth's geodynamical history. ■

## REFERENCES


1. D. C. Lee, A. N. Halliday, *Science* **274**, 1876 (1996).
2. M. Willbold, T. Elliott, S. Moorbath, *Nature* **477**, 195 (2011).
3. M. Touboul, I. S. Puchtel, R. J. Walker, *Science* **335**, 1065 (2012).
4. M. Willbold, S. J. Mojzsis, H. W. Chen, T. Elliott, *Earth Planet. Sci. Lett.* **419**, 168 (2015).
5. H. Rizo *et al.*, *Science* **352**, 809 (2016).
6. A. Halliday, M. Rehkamper, D. C. Lee, W. Yi, *Earth Planet. Sci. Lett.* **142**, 75 (1996).
7. M. Touboul, I. S. Puchtel, R. J. Walker, *Nature* **520**, 530 (2015).
8. J. E. Chambers, *Earth Planet. Sci. Lett.* **223**, 241 (2004).
9. T. W. Dahl, D. J. Stevenson, *Earth Planet. Sci. Lett.* **295**, 177 (2010).
10. R. G. Trønnes, *Mineral. Petrol.* **99**, 243 (2009).
11. K. Burke, *Annu. Rev. Earth Planet. Sci.* **39**, 1 (2011).


10.1126/science.aaf2482

EVOLUTION

# *Toward a prospective molecular evolution*

## Fitness landscapes provide a prospective understanding of chance and necessity in evolution

*By* **Xionglei He** *and* **Li Liu**

The field of molecular evolution is concerned with evolutionary changes in genes and genomes and the underlying driving forces behind those changes. Current studies in molecular evolution are almost entirely retrospective, with a focus on the mutations that were fixed during evolution, and the conclusions are often explanatory, offering no predictive insights. Because only a tiny fraction of all mutations that have ever occurred during evolution have been fixed, the "successes" that we see today provide an incomplete or even biased understanding of the evolutionary process. One way to circumvent this problem is to obtain the whole fitness landscape of a gene to understand, prospectively, chance and necessity in evolution (see the figure). Two studies in this issue, by Li *et al.* on page 837 (*1*) and Puchta *et al.* on page 840 (*2*), each take on this challenge by characterizing the in vivo fitness landscape of two RNA genes.

> ***"One of the most intriguing aspects of a fitness landscape is...the interactions seen between mutations."***

The enormous mutational space of a typical gene poses a considerable challenge to the characterization of fitness landscapes. For example, there are a total of $4^{100}$ (or $10^{60}$) possible variants for an RNA gene of 100 nucleotides, and $20^{100}$ (or $10^{130}$) for a protein of 100 amino acids. The advent of second-generation DNA sequencing goes some way toward addressing this problem. For example, in 2010 a pioneering study used second-generation DNA sequencing to measure the in vitro biochemical activities of millions of variants of a gene (*3*). Li *et al.* and Puchta *et al.* both go one step further than this in vitro study. Li *et al.* generated a library comprising >65,000 mutant alleles of a 72-nucleotide transfer RNA (tRNA) gene of the yeast *Saccharomyces cerevisiae*. They then competed all the yeast strains—each carrying a different allele of the tRNA gene—in a liquid coculture. The frequency of each allele was determined by sequencing the amplicons of the target tRNA gene pool. The increase or decrease in the frequency of a mutant allele relative to the wild-type allele during the competition represents the relative fitness of the allele. In the second study, Puchta *et al.* adopted largely the same strategy and estimated the relative fitness of ~60,000 mutant alleles of a 333-nucleotide small nucleolar RNA (snoRNA) gene, also in yeast. Although the number of mutants they examined is still a small fraction of all possible variants of the genes, most of the possible genotypes that differ from the wild-type by one or two point mutations were characterized. Thus, a high-quality local fitness landscape of a gene has been constructed.

The capability to map large fitness landscapes opens the door to study gene evolution prospectively. Both studies used the landscape constructed to understand the various conservation levels of different sites in the two RNA genes. The same idea could be applied to the study of among-gene differences in evolutionary rate. An outstanding question here is why expression level acts as the most important determinant of sequence conservation (*4*). Mapping fitness landscapes of the same gene expressed at different levels, or different genes expressed at the same level, by manipulating promoter activity would help test many competing hypotheses (*5*).

One of the most intriguing aspects of a fitness landscape is epistasis, or the interactions seen between mutations. Both studies observed widespread epistasis, especially negative epistasis, meaning that the combined deleterious effect of two harmful mutations is greater than that expected from the individual mutations (*6*). Sign epistasis (*7*), where a deleterious mutation becomes beneficial in the presence of another mutation, is of special interest because it can generate fitness peaks that trap an adapting popula-

*The State Key Laboratory of Biocontrol, School of Life Sciences, Sun Yat-sen University, Guangzhou 510275, China. Email: hexiongl@mail.sysu.edu.cn; liul47@mail.sysu.edu.cn*

Downloaded from http://science.sciencemag.org/ on May 12, 2016



*Published by AAAS*

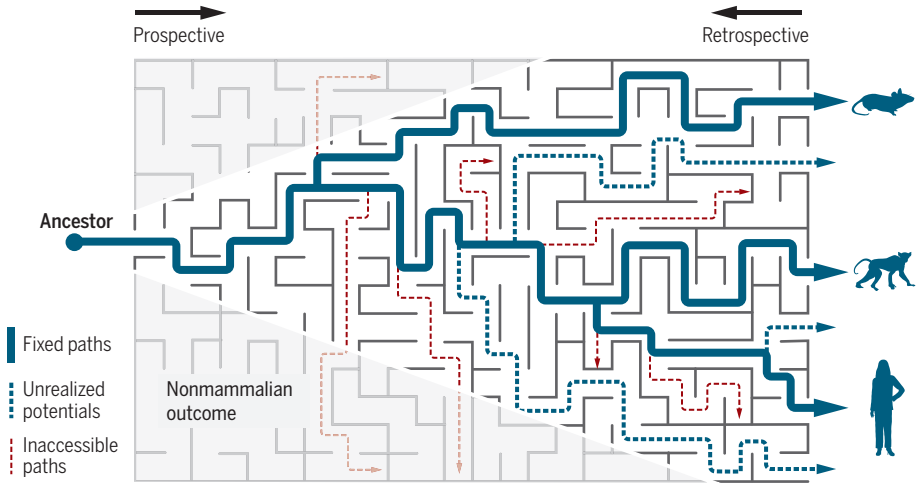


**A prospective versus retrospective view of molecular evolution.** Current retrospective studies of extant genotypes (e.g., human, monkey, and mouse) provide a necessarily biased and limited understanding of the path of evolution (solid blue lines). Mapping the fitness landscape that confronts the ancestor (shown as a maze) reveals possible paths to either "dead end" local fitness peaks (dashed red lines) or routes to new global fitness peaks (dashed blue lines). Knowing the map of the fitness landscape allows for a prospective understanding of the role of chance and necessity as part of an evolutionary process.

tion moving along the path toward the global fitness peak. Li *et al.* observed 160 cases of substantial sign epistasis, as well as a few dozen cases of high-order epistasis involving more than two mutational sites with opposite signs in different genetic backgrounds. For instance, the interaction of two harmful mutations is negative epistasis when the mutations occur in the wild-type strain, but it is sign epistasis when the mutations occur in a mutant strain. It would be interesting to find out how such roadblocks in adaptation are navigated in nature. A recent study (*8*) showed that antagonistic pleiotropy (*9*), where an allele is deleterious in one environment but beneficial in another, can help a population cross fitness valleys between a local fitness peak and the global fitness peak. This idea can be illustrated with a lock-and-key model for a pair of interacting genes that evolve, say, from genotype A-B to genotype A′-B′. Single mutations (A→A′ or B→B′) would destroy the lock-and-key fit and hence are deleterious in the environment where the fit is required. An environmental change making the fit detrimental would drive the fixation of the first mutation, say A→A′. B→B′ could then follow as a compensatory adaptive change should the environment switch back to the first condition. A more recent study (*10*) using the antibiotic resistance gene *TEM-15* β-lactamase provided another example of how environmental changes help genes cross fitness valleys. Specifically, a mutation that is selected for low antibiotic resistance was found to be a prerequisite for evolving variants of the highest antibiotic resistance. Thus, understanding how different environments can shape fitness landscapes and hence evolutionary trajectories will be of great interest.

Determining fitness landscapes empirically, as Li *et al.* and Puchta *et al.* have done, gives us the power to predict evolutionary trajectories and thus is of immediate practical value, for example, in controlling viral epidemics or preventing antibiotic resistance (*11*). Mapping the complete fitness landscape of a typical gene is presently still an unrealistic goal. Instead, in the near future, we will be able to use local fitness landscapes covering most of the possible genotypes within a few mutational steps of the focal genotype. With the evolution of a target gene (e.g., the hemagglutinin gene of influenza virus), a series of local fitness landscapes with updated focal genotypes could be constructed to keep track—in real time—of the target gene's evolution prospectively. ■

## REFERENCES AND NOTES


1. C. Li, W. Qian, C. J. Maclean, J. Zhang, *Science* **352**, 837 (2016).
2. O. Puchta *et al.*, *Science* **352**, 840 (2016).
3. J. N. Pitt, A. R. Ferre-D'Amare, *Science* **330**, 376 (2010).
4. C. Pal, B. Papp, L. D. Hurst, *Genetics* **158**, 927 (2001).
5. J. Zhang, J. R. Yang, *Nat. Rev. Genet.* **16**, 409 (2015).
6. C. Bank, R. T. Hietpas, J. D. Jensen, D. N. Bolon, *Mol. Evol. Biol.* **32**, 229 (2015).
7. D. M. Weinreich, R. A. Watson, L. Chao, *Evolution* **59**, 1165 (2005).
8. M. G. de Vos, A. Dawid, V. Sunderlikova, S. J. Tans, *Proc. Natl. Acad. Sci. U.S.A.* **112**, 14906 (2015).
9. V. S. Cooper, R. E. Lenski, *Nature* **407**, 736 (2000).
10. B. Steinberg, M. Ostermeier, *Sci. Adv.* **2**, e1500921 (2016).
11. J. A. de Visser, J. Krug, *Nat. Rev. Genet.* **15**, 480 (2014).


## ACKNOWLEDGMENTS

We thank J. Zhang and G. Kudla for comments. X.H. is supported by the National Natural Science Foundation of China (grant 91431103).

10.1126/science.aaf7543

NEUROSCIENCE

# REMembering what you learned

## Specific brain activity during REM sleep affects memory consolidation

*By* **Bernat Kocsis**

Which memories are retained, where, and in what form depends on a long afterlife of the acquired information in the brain. Initial steps of consolidation may be completed within a few hours during wakefulness, but other forms of postacquisition processing take longer, extending into sleep (*1*, *2*). The relationship between brain activity during sleep and memory consolidation remains controversial and poorly understood. On page 812 of this issue, Boyce *et al.* (*3*) demonstrate that a distinct form of hippocampal neural activity, called theta oscillation, is critical for memory formation during the rapid eye movement (REM) phase of sleep.

The two-stage process of memory acquisition and "offline" processing is observed in rodents that experience alternating episodes of exploration and quiet waking, and is also linked to distinct patterns of synchronized hippocampal activity (*1*, *4*). Exploration is characterized by regular theta (6 to 10 Hz) and nested gamma (30 to 90 Hz) oscillatory activity in hippocampal neural networks that are open to new information via cortical input. By contrast, synchronized neuronal activity in quiet waking appears as irregular sharp waves and ripple oscillations, during which processed hippocampal content is transferred to distributed cortical circuits to support memory consolidation. The waking theta-gamma versus sharp wave–ripple dichotomy extends to sleep as the dominant pattern of synchronization in the alternating periods of REM sleep and slow-wave (non-REM) sleep. Extensive evidence supports the role of hippocampal sharp wave–ripple events and related cortical oscillations ("spindles") in non-REM sleep in memory consolidation (*1*, *4*), but the relationship between theta rhythm during sleep and

*Harvard Medical School, Department of Psychiatry, Beth Israel Deaconess Medical Center, Boston, MA 02215, USA. Email: bernat_kocsis@hms.harvard.edu*

GRAPHIC: V. ALTOUNIAN/*SCIENCE*

Downloaded from http://science.sciencemag.org/ on May 12, 2016



Published by AAAS

wakefulness appears more difficult to conceptualize. The subregional theta-gamma pattern in REM sleep, compared with waking exploration, suggests enhanced offline processing in the dentate gyrus and CA3 regions of the hippocampus, and short bursts of their synchronization with the output stages in the CA1 region promote communication with neocortical targets (*5*). These short bursts of super-synchronized activity co-occur with pontine waves, previously implicated in memory consolidation (*6*).

Boyce *et al.* used two hippocampus-dependent learning paradigms to test the role of REM sleep theta activity in memory consolidation. The novel object place recognition test is widely used to study rodent models of memory, and is translatable, i.e., similar aspects of recognition memory can be assessed in the human Brief Visuospatial Memory Test (*7*). The task is based on a rodent's natural drive to explore novelty; when a mouse returns to a familiar environment, it pays more attention to novel or misplaced objects compared with prior visits. Boyce *et al.* used selective optogenetic silencing of γ-aminobutyric acid–releasing neurons in the medial septum (MS-GABA) to reduce hippocampal theta power (mice were engineered to express a light-driven ion pump in MS-GABA neurons; pump activation drives hyperpolarization, which inhibits neuron firing). Boyce *et al.* found that suppressing MS-GABA neuron activity in all REM sleep episodes during the critical 4-hour window after learning erased subsequent novel object place recognition (see the figure). Mice receiving light delivery to MS-GABA neurons outside of REM sleep showed normal performance, as did mice in control groups in which either expression of the pump in these neurons or the light stimulus was left out of the treatment.

Another test paradigm was based on fear conditioning to assess the role of REM sleep theta activity in processing the contextual component of emotionally loaded memories (*8*). Mice received mild electrical shocks paired with auditory cue stimuli in a distinct context of the testing chamber, and their task was to remember the circumstances of the negative experience a day later. When returning to the same chamber (hippocampus-dependent context-recall) or when hearing the auditory signal in a new environment (cue-recall, independent of hippocampal processing) on the following day, normal mice and mice in control groups showed robust freezing response without electric shocks. However, if MS-GABA neurons were silenced during REM sleep after learning, mice only reacted to the auditory cue but showed less freezing in the context chamber, indicating impaired hippocampal memory consolidation.

The two most influential current theories—memory consolidation (*1, 2*) and homeostatic synaptic depotentiation in sleep (*9*)—are noncommittal and unenthusiastic with respect to the role of REM sleep in brain function, although REM sleep was historically believed to contribute to memory consolidation, and the first theoretical proposal of depotentiating certain "parasitic associations" was first attributed to REM sleep (*10*). But REM sleep evenutally lost to non-REM sleep on both accounts: homeostatic synaptic depotentiation was associated with non-REM sleep delta rhythm, and consolidation was associated with non-REM sharp wave–ripple oscillations and spindles. However, REM sleep appears to be regaining acceptance in the recent sequential hypotheses, which emphasize linked REM–non-REM–REM sleep mechanisms. REM sleep's role in synaptic consolidation was demonstrated by linking REM sleep to pre-REM spindles (*11*), and its role in homeostatic regulation by linking to post-REM delta rhythm and spindles (*12*). Theta oscillations may have importance for memory consolidation by affecting both mechanisms.

The details of how theta oscillations and MS-GABA neurons are involved in synaptic consolidation and homeostatic regulation were not the focus of Boyce *et al.* Their approach, however, is a radical departure from prior system-level correlational and sleep deprivation studies, offering new opportunities to explore, without disrupting sleep behavior, the role of REM sleep theta activity. Detailed knowledge of wake theta activity—including rhythmic coupling between hippocampus and other structures (prefrontal cortex and amygdala) that are involved in different aspects of memory processing, bidirectional communication between the MS-GABA theta generator and intrinsic intrahippocampal theta synchronization (*13, 14*), and phase segregation for diverse types of neurons enabling spatial and possibly "mental" travel (*15*)—provides a template for future progress. It should be noted, however, that REM sleep is a complex state, and, thus, establishing a causal link between learning and MS-GABA activity does not exclude the roles of REM sleep in other memory- and non-memory–related functions. ■

**Offline processing.** Reducing hippocampal theta oscillations during REM sleep affects what mice remember from learning sessions in the prior waking period.

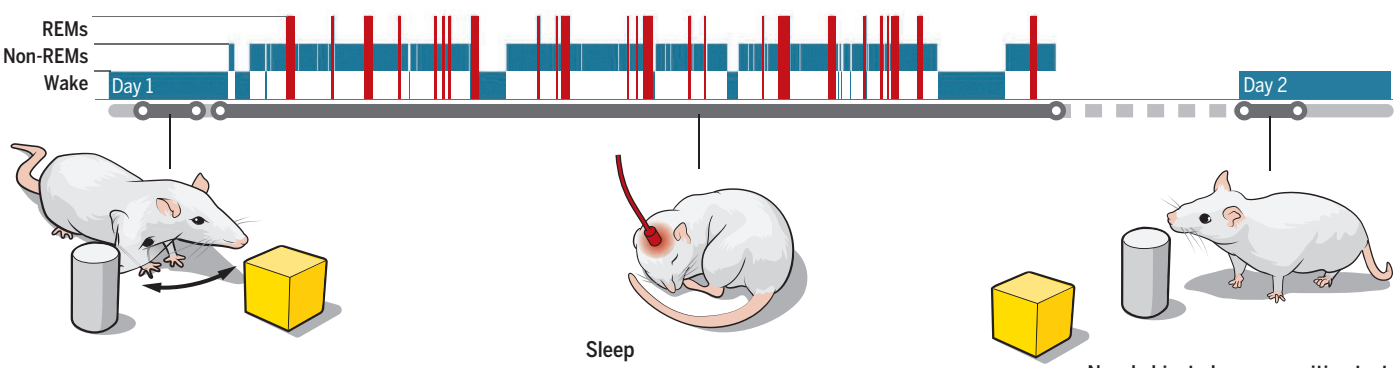


GRAPHIC: V. ALTOUNIAN/*SCIENCE*


## REFERENCES

1. B. Rasch, J. Born, *Physiol. Rev.* **93**, 681 (2012).
2. R. Stickgold, *Curr. Opin. Neurobiol.* **23**, 847 (2013).
3. R. Boyce *et al.*, *Science* **352**, 812 (2016).
4. G. Buzsaki, *Hippocampus* **25**, 1073 (2015).
5. S.M. Montgomery, A. Sirota, G. Buzsaki, *J. Neurosci.* **28**, 6731 (2008).
6. S. Datta, V. Mavanji, J. Ulloor, E. H. Patterson, *J. Neurosci.* **24**, 1416 (2004).
7. J. W. Young, *Pharmacol. Ther.* **122**, 150 (2009).
8. E. F. Pace-Schott, A. Germain, M. R. Milad, *Psychol. Bull.* **141**, 835 (2015).
9. G. Tononi, C. Cirelli, *Sleep Med. Rev.* **10**, 49 (2006).
10. F. Crick, G. Mitchison, *Nature* **304**, 111 (1983).
11. S. Ribeiro, M. A. Nicolelis, *Learn. Mem.* **11**, 686 (2004).
12. A. D. Grosmark *et al.*, *Neuron* **75**, 1001 (2012).
13. F. Manseau *et al.*, *J. Neurosci.* **28**, 4096 (2008).
14. D. Kang, M. Ding, I. Topchiy, L. Schifflett, B. Kocsis, *J. Neurophysiol.* **114**, 2797 (2015).
15. G. Buzsaki, E. I. Moser, *Nat. Neurosci.* **16**, 130 (2013).


10.1126/science.aaf9117

Downloaded from http://science.sciencemag.org/ on May 12, 2016



*Published by AAAS*

**Far from employment.** New settlement for refugees internally displaced by war, some 60 km (37 miles) west of Tbilisi, Georgia, under construction as winter approaches.

PHOTO: REUTERS/DAVID MDZINARISHVILI (GEORGIA)

ESSAY

# Refugee protection and resettlement problems

## Refugees face painful uncertainties that could be ameliorated by aid agency coordination

*By* **Elizabeth Cullen Dunn**

In 2015, more than a million refugees and other migrants entered the European Union. They are just a small part of the world's rapidly burgeoning population of displaced people, which climbed by more than 37% between 2009 and 2015 to reach 59.5 million people. Humanitarian aid to these people has been dramatically insufficient, and many displaced people now lack adequate food, medical care, housing, or transportation. As a geographer, I spent 16 months between 2009 and 2013 conducting participant observation research in camps for displaced people in Georgia (see the photo), where I discovered serious shortfalls in the humanitarian aid system. Increasingly, humanitarian aid is a temporary solution to a permanent problem, a stopgap that not only does not help displaced people resettle but, instead, makes it more difficult for them to move on with their lives.

Since World War II, camps for refugees and internally displaced persons (IDPs) have been the primary feature of the aid system. Meant as spaces of short-term refuge, these camps are now at the center of the current humanitarian crisis. Camps are useful to aid agencies because they provide a central point for delivering food, water, sanitation, and health services to a large number of people. They are also useful to host governments, which often want to keep refugees and IDPs from resettling themselves permanently in major urban labor markets and driving down local wage rates. In theory, keeping refugees and IDPs in camps also makes them more easily deportable. If the war ends and they can return, having them together rather than scattered throughout a city will make it easier for the host government to compel them to depart. Many host governments are so insistent that camps be temporary that they ban the use of permanent building materials, such as concrete or fired brick, so that the camp can be quickly bulldozed (*1*).

Camps are meant to be temporary; but for most refugees, displacement is a permanent state. More than 80% of all refugee crises last more than 10 years, and 40% last 20 years or more (*2*). As a result, displaced people may spend years, decades, or even generations living in flimsy canvas tents or uninsulated metal shelters in camps that lack electricity, sewers, indoor toilets, running water, markets, or schools. This suits host governments, which are reluctant to see camps grow and become permanent settlements. But precisely because camps discourage permanent resettlement, many displaced people see them as holding pens or as traps where they will wait endlessly to return home. Today, more than 60% of refugees and IDPs avoid camps in favor of cities where they may find a more permanent place to live. Jordan's remote Azraq Camp, for example, which was designed for 130,000 residents, had only 13,361 refugees living there at the end of 2015 (*3*), as most Syrian refugees in Jordan sought to join the Jordanian population in cities. For aid agencies, finding these refugees and providing services to them is logistically extremely difficult.

For displaced people both inside and outside camps, unemployment poses a substantial challenge to economic security and mental health that humanitarian aid has done little to resolve. In most of the Georgian settlements where I conducted research, there were few employment opportunities. Because camps were far away from the nearest city (as camps for displaced people usually are), few people could find work. Although several aid agencies offered microcredit loans and business development training, most of the startup businesses financed by the aid agencies quickly failed for lack of capital and clientele. Although the U.S. Agency for International Development cofinanced several large enterprises, these ventures failed to employ many people, and several of them went out of business. This left most of the

*Department of Geography, Indiana University, Bloomington, IN, USA. Email: elcdunn@indiana.edu*

Downloaded from http://science.sciencemag.org/ on May 12, 2016



Published by AAAS

IDPs with little to do as their meager savings drained away. The situation is even more severe in closed camps, like Kakuma Camp in Kenya, where refugees are not only forbidden to work but forbidden to leave the camp at all. Displaced people who live outside the camp system, who have rent to pay, even less aid, and no legal right to work in many of the countries they reside in, face other difficulties. In Turkey, Lebanon, and Jordan, some urban refugees have been forced by the lack of employment and cuts in food aid to choose between risking their lives on the perilous trip across the Aegean so that they can find employment in Europe or returning to Syria and hoping to wait out the war in their homes. Programs to help displaced people reestablish their livelihoods should be at the center of humanitarian aid, but to date, there have been few successful programs for reestablishing economic security.

Uncertainty is another major problem caused by humanitarian aid. The humanitarian system operates in an ad hoc manner, with agencies frequently failing to coordinate their efforts with one another. This is largely due to the enormous number of agencies involved in any one emergency situation. After the 2008 war in Georgia—a 5-day war that displaced only about 100,000 people in the short term and about 28,000 for an indefinite period—98 aid agencies and donor governments provided assistance. In Haiti after the 2010 earthquake, there were more than 1000 aid agencies involved. The work of these independent agencies is supposed to be coordinated by either the United Nations High Commission for Refugees (UNHCR) or the UN's Office for the Coordination of Humanitarian Assistance (OCHA) to avoid duplicating efforts or leaving gaps in coverage.

More often, though, the diverse array of agencies, donors, and government ministries function as a chaotic and improvisational "adhocracy" (*4*). Because aid agencies compete for funding from donors, they are generally unwilling to share planning or information with each other. This leads to enormous inefficiencies: Different agencies will do identical surveys, will deliver the same goods to easy-to-reach camps but will not deliver other urgently needed supplies, and will overlook people who are more distant but equally in need. Adhocracy can also lead to aid that does not meet the needs of the people to whom it is given. For example, the UN Children's Fund (UNICEF) provided a breastfeeding support clinic in Georgia to mothers fleeing the conflict, but because breastfeeding is already widely practiced in Georgia and both infant formula and clean water were available throughout the crisis, only 21 women out of 10,000 mothers of children under age 2 took advantage of the breastfeeding support clinic. We saw an intense interest in providing psychosocial aid to children but almost no interest in helping elderly refugees, who were both more numerous and who had tended to stay in the conflict zone longer than younger people. The aid, which was a standard package offered in conflicts around the world, simply didn't match the social context.

Because aid is largely given ad hoc, neither aid agencies nor donors tell refugees what kind of aid they can expect or when it will be delivered. Nor do they tell them when aid will stop. In this unpredictable and chaotic situation, it is difficult for refugees to plan for the future, much less to leverage their own resources and take action. Without some degree of predictability, refugees are stranded in the present, left in a situation that is forever temporary rather than being able to resettle and craft a stable future.

UN Under-Secretary-General Stephen O'Brien argues that the major problem facing the humanitarian aid is that it is underfunded. It is a system that is "not broken—but it is broke" (*5*). The "Grand Bargain" recently called for by UN Secretary-General Ban Ki-moon, asks donor countries to donate an additional $15 billion (*6*). In exchange, aid agencies promise to focus on longer-term planning, to improve their transparency, and to increase collaborative efficiency. But critics argue that the system is indeed broken, as well as broke, and that the superficial reforms the large aid agencies offer are merely "a rearranging of the deck chairs rather than the construction of a more seaworthy ship…" (*7*). They call for bypassing the large international aid agencies—which currently receive 81% of government funding—and routing more aid dollars directly to small, local aid agencies that provide aid faster, more cheaply, and in culturally appropriate forms (*8*). Another means of bypassing the international aid agencies is cash-based transfer (CBT), which uses new technologies, such as mobile debit card readers and payments via mobile phone, to send money to refugees directly (*9*). CBT allows displaced people to choose the aid they need most, rather than accept the aid that donors want to give. It allows them to leverage their own savings, resources, and skills, whether by buying tools needed to resume their trade, purchasing livestock, or paying for children's education. In my own fieldwork, I saw displaced people use cash aid to purchase everything from piglets to bandsaws to winter coats, all of which improved their economic security and health. But despite the fact that CBT has been successful in diverse sites, such as Turkey and Somalia (*10*), it is still only 6% of the total value of aid to displaced people.

> ***"In this unpredictable and chaotic situation, it is difficult for refugees to plan for the future…"***

The dramatic increase in the world's population of displaced people seems unlikely to slow. Nor is it likely that most people forced to flee today will return home any time soon. Yet, most host governments in Europe, North America, and the Middle East do not want to permit refugees to integrate and to rebuild their own lives, preferring instead to maintain the illusion that refugees are only in their countries temporarily. To stave off misery, political instability, and uncertainty, governments must find the political will to begin dismantling camps and integrating the displaced into local towns and labor markets. Research suggests that with short-term aid and the ability to make choices for their own lives, refugees can resettle and, within a few years, become economic and cultural contributors to their new communities (*11*). ■

## REFERENCES AND NOTES


1. M. Thomson, *Arch. Theory Rev.* **19**, 376 (2014).
2. N. Crawford, J. Cosgrave, S. Haysom, N. Walicki, "Protracted displacement: Uncertain paths to self-reliance in exile" [Humanitarian Policy Group (HPG) commissioned report, Overseas Development Institute (ODI), London, 2015].
3. UNHCR, Jordan Inter-Agency Update (November 2015); www.unhcr.org/cgi-bin/texis/vtx/home/opendocPDFViewer.html?docid=5465c15d9&query=azraq.
4. E. C. Dunn, *Humanity* **3**, 1 (2012).
5. S. O'Brien, "Under-Secretary-General Stephen O'Brien remarks to the high-level discussion on the future of humanitarian financing" (OCHA, Syria, 2015); http://reliefweb.int/report/world/under-secretary-general-stephen-o-brien-remarks-high-level-discussion-future.
6. UN Mission in Liberia [press release] (2016); https://unmil.unmissions.org/humanitarian-finance-gap-%E2%80%9Csolvable-problem%E2%80%9D-says-ban-ki-moon.
7. C. Bennett *et al.*, "Time to let go: Remaking humanitarian action for the modern era" (ODI, London, 2016); www.odi.org/sites/odi.org.uk/files/resource-documents/time_to_let_go_report.pdf.
8. B. Van der Zee, *The Guardian*, 16 October 2015; www.theguardian.com/global-development-professionals-network/2015/oct/16/less-than-2-of-humanitarian-funds-go-directly-to-local-ngos.
9. P. Harvey, "Cash-based responses in emergencies" (HPG, ODI, London, 2007); www.alnap.org/resource/10511.aspx.
10. D. Ali, K. Gelsdorf, *Global Food Secur.* **1**, 57 (2012).
11. R. Capps *et al.*, "The integration outcomes of U.S. refugees" (Migration Policy Institute, Washington, DC, 2015); www.migrationpolicy.org/research/integration-outcomes-us-refugees-successes-and-challenges.


## ACKNOWLEDGMENTS

The author gratefully acknowledges the assistance of A. S.-K. Pang and H. Mintek. Research for this project was funded by the Fulbright Foundation and the International Research and Exchanges Board.

10.1126/science.aaf8962

Downloaded from http://science.sciencemag.org/ on May 12, 2016



Published by AAAS

APPLIED PHYSICS

# Nanophotonics gets twisted

## Simple structures process complex light beams that carry angular momentum

*By* **Gabriel Molina-Terriza**

Nanophotonics investigates the processing of light at the nanoscale, with the promise of transforming the telecommunication, biomedical, and computation industries. Advances in nanophotonics have traditionally been boosted but also limited by our capabilities of fabricating complex structures at the nanoscale. On page 805 of this issue, Ren *et al.* (*1*) try to break free of these limitations with their experimental demonstration of a simple nanostructure that can separate and process complex light modes carrying angular momentum. Thus, instead of processing light fields with complex nanostructures, the idea is to use comparatively simpler structures and push the complexity to the light fields themselves.

The angular momentum of light is a property of electromagnetic fields that endows certain light modes with the capability of rotating material particles (*2*). This property has gained special relevance in the past few years because of its many applications, including enhancement of the channel capacity of fiber and free-space communications, improvements in the security of quantum cryptography, and microscopy (*3*). In nanophotonics, the use of complex or structured light fields to control the properties of nanostructures is not limited to the angular momentum; other techniques include the use of polarization control of ultrashort pulses (*4*) and the deterministic superposition of transversal modes (*5*). Still, the use of angular momentum to control nanoparticles has gained more attention in such areas as control of the scattering of dielectric nanospheres (*6*, *7*) and control of the transmission of light modes through nanoapertures (*8*).

> ***"...these techniques are based on material particles with sizes on the order of the wavelength of the light..."***

Fundamentally, all of these techniques are based on material particles with sizes on the order of the wavelength of the light so that the particle can support different multipolar modes (*9*). One of the problems in intuitively understanding the interaction of light and matter at the nanoscale is that highly focused fields intricately mix their polarization and spatial structure. However, for small particles, the decomposition in multipolar modes provides an optimal way of describing its interaction with electromagnetic fields. Modes of light with angular momentum are particularly suited to controlling this interaction because of their highly symmetric structure.

For all these reasons, the approach of Ren *et al.* is particularly interesting because it provides a simple structure capable of discriminating between modes with different angular momenta. Furthermore, the structure does not make use of resonant properties of the structures, so this effect can be observed over a broad spectrum. Thus, it should be possible to combine angular momentum and wavelength division multiplexing. This kind of light processing has obvious applications in telecommunications, where information can be encoded independently in the frequency and the spatial degrees of freedom. The authors demonstrate this point by multiplexing the information of several images in these degrees of freedom. Other potential applications include the dynamical control of near-field interactions with biomolecules at the nanoscale (see the figure).

These research lines bridge the gap between the use of large arrays of nanoparticles (as in the field of metamaterials) to control the angular momentum (*10*) of light beams or perform other more complex transformations (*11*) and explorations of how we can control the properties of nanostructures with properly engineered light fields. In this respect, the use of the spatial, frequency, and polarization properties of light beams is slowly maturing into a reliable technology, as Ren *et al.* have beautifully shown. The next big step in this direction would be to control the properties of nanostructures with the quantum correlations of electromagnetic fields. This capability would open the path to the quantum processing of light at the nanoscale, with both fundamental and technological implications, thereby finally fulfilling Feynman's visionary predictions of smaller, faster, cleaner, and more powerful devices that can break the limitations of our current systems (*12*). ■

[1]*Department of Physics and Astronomy, Macquarie University, 2109 NSW, Australia, and Centre of Excellence for Engineered Quantum Systems, Macquarie University, 2109 NSW, Australia. Email: gabriel.molina-terriza@mq.edu.au*

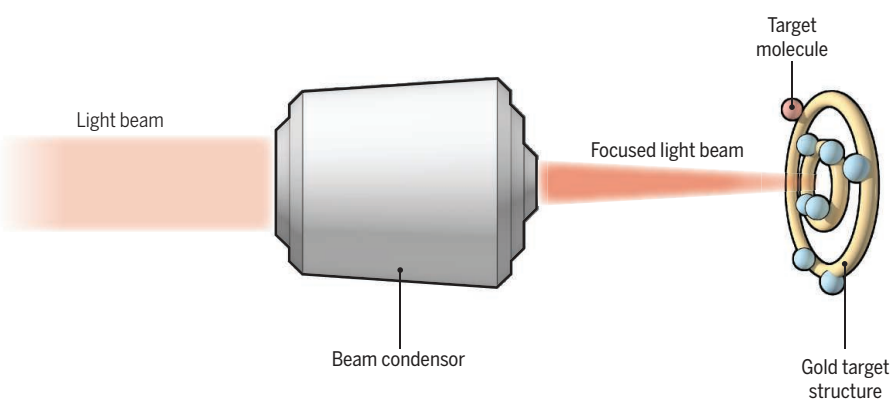


**Complex light modes for spectroscopy.** Artist's impression of an angular momentum beam (coming from the left) being highly focused with a microscope objective onto a gold structure. The structure may have attached several molecules at different positions, which can be independently excited by using different light modes. This schematic represents another application of the system presented by Ren *et al.*, which already shows applications in optical information processing.

GRAPHIC: C. BICKEL/*SCIENCE*


**REFERENCES**

1. H. Ren, X. Li, Q. Zhang, M. Gu, *Science* **352**, 805 (2016).
2. H. He, M. E. J. Friese, N. R. Heckenberg, H. Rubinsztein-Dunlop, *Phys. Rev. Lett.* **75**, 826 (1995).
3. J. P. Torres, L. Torner, Eds., *Twisted Photons: Applications of Light with Orbital Angular Momentum* (Wiley-VCH, 2011).
4. M. Aeschlimann *et al.*, *Nature* **446**, 301 (2007).
5. G. Volpe, G. Molina-Terriza, R. Quidant, *Phys. Rev. Lett.* **105**, 216802 (2010).
6. X. Zambrana-Puyalto, X. Vidal, G. Molina-Terriza, *Opt. Express* **20**, 24536 (2012).
7. P. Woźniak, P. Banzer, G. Leuchs, *Laser Photon. Rev.* **9**, 231 (2015).
8. X. Zambrana-Puyalto, X. Vidal, G. Molina-Terriza, *Nat. Commun.* **5**, 4922 (2014).
9. J. D. Jackson, *Classical Electrodynamics* (Wiley, ed. 3, 1999), chap. 9.
10. E. Karimi *et al.*, *Light Sci. Appl.* **3**, e167 (2014).
11. K. E. Chong *et al.*, *ACS Photonics* **3**, 514 (2016).
12. R. P. Feynman, *Caltech Eng. Sci.* **23**, 22 (1960).


10.1126/science.aaf6388

Downloaded from http://science.sciencemag.org/ on May 12, 2016



Published by AAAS

**Red knots on the move.** Red knots (*Calidris canutus*) are wading birds that use their long bills to probe the mud for invertebrate food. Van Gils *et al.* show that climatic changes in the Arctic habitat of a red knot subspecies affect the birds' physiology in ways that may reduce their survival chances in their tropical habitats.

PHOTO: DAVID TIPLING/NPL/MINDEN PICTURES

Downloaded from http://science.sciencemag.org/ on April 12, 2016

ECOLOGY

# *Living sentinels for climate change effects*

## Migrating birds affected by climate change in the Arctic may have lower survival chances in their tropical habitats

*By* **Martin Wikelski**[1,2,3] *and* **Grigori Tertitski**[4]

Humans have long used animals as sentinels for threats to their own well-being. Canaries in coal mines are a classic example. On a global scale, studies of birds were key to detecting environmental problems caused by the excessive use of pesticides (*1*, *2*). The recent loss of up to 98% of some vulture populations highlights the widespread dangerous effects of diclofenac use in cattle (*3*). Bee populations, sentinels for global insect losses, are also declining owing to the combined stress from pesticides and other environmental changes caused by humans, resulting in a widespread loss of pollination services (*4*). On page 819 of this issue, van Gils *et al.* (*5*) highlight another global ecological warning sign, this time linked to Arctic warming. They show that long-term changes in the body architecture of Arctic wading birds can affect their survival in their tropical wintering range.

The authors study red knots (see the photo), which breed in the high Arctic in the summer and migrate to tropical habitats around the world in the winter. They show that juvenile red knots growing up in warm Arctic habitats have shorter bills, which lower their foraging efficiency in the tropical mudflats and may later decrease their survival chances. Thus, changes in one habitat may have important ecological consequences in habitats halfway around the world. Similar to the early warnings regarding DDT use (*1*), these results show that global warming affects life on our planet in unanticipated ways.

The basic data are ingeniously simple. Van Gils *et al.* measured the body size of red knots over 30 years along one of eight major flyways of Arctic birds (see the figure) and linked the annual and long-term changes in body size to the time of snowmelt. Over this time period, the date of the snowmelt advanced by more than 2 weeks, and the birds produced smaller and smaller offspring—probably because insect populations peaked earlier than in the past, resulting in limited food resources when the parents arrived from their long-distance migration flights.

Many animal species can compensate for periods of slow growth early in life by growing faster at other times (*6*, *7*), but red knots do not. Possible reasons for the lack in catch-up growth are the need to keep adult metabolic rate low (*6*) and cognitive performance high (*7*). Both can be affected by compensatory growth during early development. Overall, van Gils *et al.* nicely show how important early development is for the entire life history of an organism and how subtle many ecological interactions are. These effects only become evident when one considers the mi-

[1]*Department of Migration and Immuno-Ecology, Max Planck Institute for Ornithology, Radolfzell, Germany.* [2]*Department of Biology, University of Konstanz, Konstanz, Germany.* [3]*Smithsonian Tropical Research Institute, Balboa, Republic of Panama.* [4]*Institute of Geography, Russian Academy of Sciences, Moscow, Russia. Email: wikelski@orn.mpg.de*



*Published by AAAS*

gratory connectivity of red knots by following individuals from breeding to wintering (*8*).

The researchers can only determine the "apparent survival" of the birds: Individuals not seen any more are considered dead. This is the accepted standard in field ecology. It is likely that many individuals with short bills die, but some short-billed individuals may identify new foraging grounds and perhaps even establish new, currently unknown migratory populations. Only by tracking the development and morphology of individual birds throughout their life can researchers fully understand the population consequences of environmental change (*8*). One technology that will allow such lifetime tracking of small animals is the satellite-based ICARUS system, which will be installed in early 2017 by the German and Russian space agencies (*9, 10*).

Population-level changes similar to those observed by van Gils *et al.* are currently occurring in many populations of migratory animals throughout the world (*11*). Examples include the loss of more than 400 million songbirds in Europe alone over the past 30 years (*12*). Human societies may soon miss many of the ecosystem services, such as pest control, provided by the masses of migratory species.

The study by van Gils *et al.* beautifully illustrates how simple measures in ecology can alert us to subtle but potentially life-threatening changes in ecosystems around the world. Gaining such understanding requires observing the entire life history of individuals in the wild—a task that can only be achieved if biologists around the world work together to link their data sets (*13*). Over the next 10 years or so, the recently formed International Bio-logging Society (*14*) aims to combine observational and satellite data on hundreds of mobile and migratory species—marine, terrestrial, and aerial—in a global assessment of the health of life on the planet. Once we understand the connectivity and interactions of individual animals, we can capitalize on the superior sensing of the environment that emerges from their collective behavior (*15*). We may then be able to rely on animals to forecast the conditions of life on the planet that we share with them. ■


### REFERENCES AND NOTES

1. T. J. Cade, J. L. Lincer, C. M. White, D. G. Roseneau, L. G. Swartz, *Science* **172**, 955 (1971).
2. M. I. Goldstein *et al.*, *Ecotoxicology* **8**, 201 (1999).
3. F. Proffitt, P. Bagla, *Science* **306**, 223 (2004).
4. D. Goulson, E. Nicholls, C. Botias, E. L. Rotheray, *Science* **347**, 1255957 (2015).
5. J. A. van Gils *et al.*, *Science* **352**, 819 (2016).
6. F. Criscuolo, P. Monaghan, L. Nasir, N. B. Metcalfe, *Proc. Biol. Sci.* **275**, 1565 (2008).
7. M. O. Fisher, R. G. Nager, P. Monaghan, *PLOS Biol.* **4**, e251 (2006).
8. M. S. Webster, P. P. Marra, S. M. Haig, S. Bensch, R. T. Holmes, *Trends Ecol. Evol.* **17**, 76 (2002).
9. E. Pennisi, *Science* **334**, 1042 (2011).
10. M. Wikelski *et al.*, *J. Exp. Biol.* **210**, 181 (2007).
11. D. S. Wilcove, M. Wikelski, *PLOS Biol.* **6**, e188 (2008).
12. R. Inger *et al.*, *Ecol. Lett.* **18**, 28 (2015).
13. R. Kays, M. C. Crofoot, W. Jetz, M. Wikelski, *Science* **348**, aaa2478 (2015).
14. See www.bio-logging.net.
15. A. Berdahl, C. J. Torney, C. C. Ioannou, J. J. Faria, I. D. Couzin, *Science* **339**, 574 (2013).



### ACKNOWLEDGMENTS

We thank the German Aerospace Center (DLR), the Russian Academy of Sciences, and the Max Planck Society for support. M.W. is a member of the International Bio-logging Society and PI of the ICARUS project.

10.1126/science.aaf6544


## East Atlantic flyways of Arctic birds

Long-distance migrating birds such as red knots link their Arctic breeding areas to distant parts of the globe. Van Gils *et al*. studied the *Calidris canutus canutus* subspecies in its East Atlantic flyway. Flyways from www.caff.is.

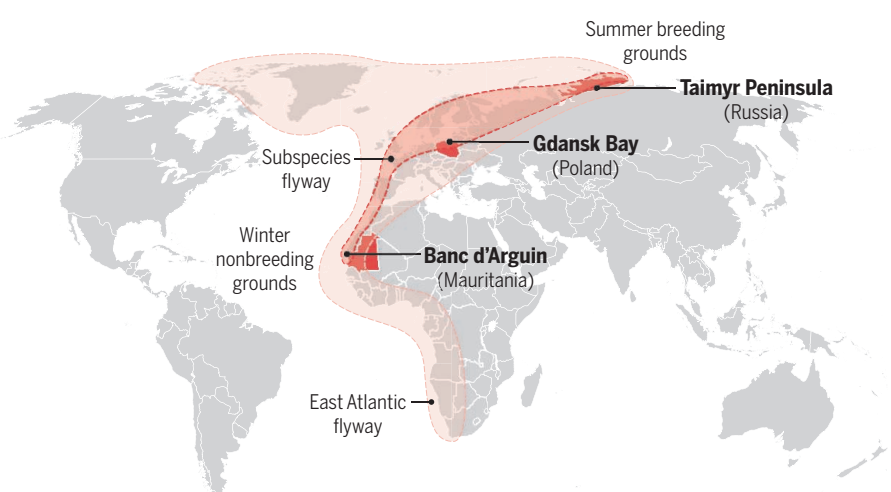


GRAPHIC: C. BICKEL/*SCIENCE*

SCIENTIFIC COMMUNITY

# *Confronting stem cell hype*

## Against hyperbole, distortion, and overselling


*By* **Timothy Caulfield,[1]* Douglas Sipp,[2,3] Charles E. Murry,[4] George Q. Daley,[5] Jonathan Kimmelman[6]**


POLICY

The way science is represented to the public can influence understanding and expectations, frame policy debates, and affect the implementation and use of emerging technologies. Inaccurate representations of research may, for example, lead to public confusion about the readiness of a technology for clinical application. As a result, the issue of science "hype"—in which the state of scientific progress, the degree of certainty in models or bench results, or the potential applications of research are exaggerated—is receiving increased attention from the popular press, the research community, and scientific societies (*1*). In newly issued guidelines on the ethical conduct of human pluripotent stem cell research and clinical translation (*2*), the International Society for Stem Cell Research (ISSCR) explicitly recognizes and confronts the issue of science hype. By placing a clear obligation on researchers, the ISSCR hopes to make balance in public representations of research a norm associated with scientific integrity. The focus on public communication, which is new to this version of the guidelines, is the result of both specific concerns regarding how stem cell research has been portrayed in the public sphere and the growing recognition that researchers play an important role in the science communication process.

Enthusiasm and optimistic speculation are natural parts of research and innovation and can be a constructive force that helps to attract funding and to build research communities. But sustained hype—if defined as scientifically unsupportable exaggeration—cannot, in the aggregate, be viewed as a positive force (*1*). Stem cell research has


[1]*Health Law Institute, University of Alberta, Edmonton, Alberta T6G 2H5, Canada.* [2]*Riken Center for Developmental Biology, Kobe, Japan, 650-0047.* [3]*Keio University School of Medicine, Tokyo, Japan, 160-8582.* [4]*Institute for Stem Cell and Regenerative Medicine, University of Washington, Seattle, WA 98109, USA.* [5]*Boston Children's Hospital, Harvard Medical School, Boston, MA 02115, USA.* [6]*STREAM research group Biomedical Ethics Unit, McGill University, Montreal, Quebec H3A 1X1, Canada.* *Email: caulfield@ualberta.ca


Downloaded from http://science.sciencemag.org/ on May 12, 2016



Published by AAAS

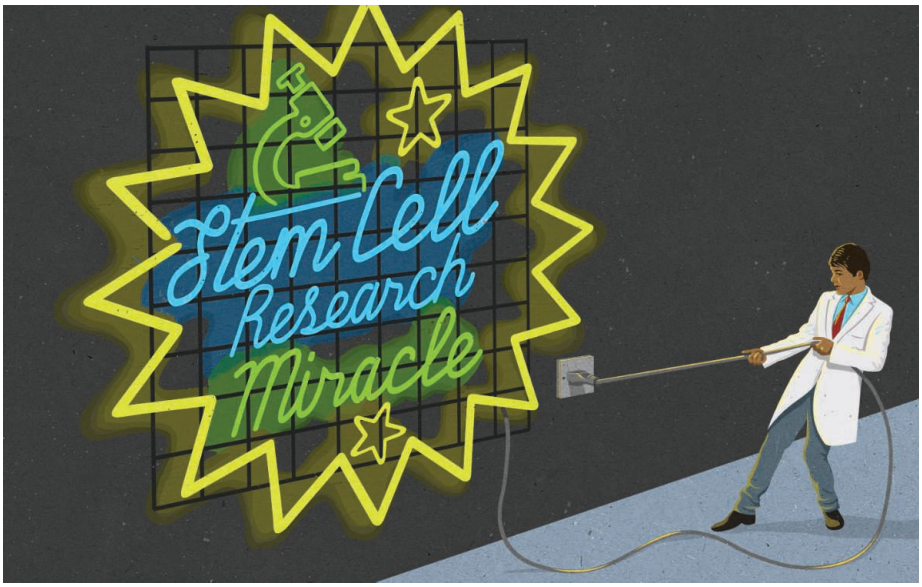


ILLUSTRATION: JOHN HOLCROFT

generated much hyperbolic media attention (*3*), which moves away from discussions of ethical concerns (*4*) and toward positive portrayals of potential therapeutic applications (*5*). This raises the risk of harmful consequences, including misleading the public (*3*), creating unrealistic expectations, misinforming policy debates, devaluing methodical approaches to research (*6*), and driving premature or unwarranted clinical use (*7*). This is particularly important in light of mounting concern about the marketing of unproven stem cell treatments (*8*). This trend may have led to a gap between public expectations and the actual state of stem cell science and clinical development (*9*).

The hyping of science implicates many actors and systemic pressures, including career and publication pressure, overly optimistic press releases, commercialization and translation pressure, and media spin (*10*). Studies have found, for example, widespread use of sensational language in peer-reviewed abstracts, studies, and institutional press releases (*11*–*13*). The popular press privileges benefits over risks and represents stem cells as ready for clinical application (*14*) on overly optimistic timelines (*5*). Social media can further spread distorted accounts of scientific findings and may help to entrench misrepresentations in the public mind (*15*). Social controversies surrounding stem cell research may have also fueled hype by polarizing rhetoric around harms and benefits (*16, 17*).

**GUIDELINES.** The ISSCR guidelines build on norms developed by other scientific organizations in addressing issues in science communication (*18*) and encouraging the scientific community to engage with the public (*19*). Consistent with fundamental principles of scientific integrity, the ISSCR urges stem cell researchers to "promote accurate, balanced, and responsive public representations of stem cell research," including striving to "ensure that benefits, risks and uncertainties of stem cell science are not misrepresented" (*2*). One way of achieving this is for researchers to describe their findings against base rates. For example, if a study reports a new potential treatment for spinal cord injury, researchers should consider how other treatments have fared in previous clinical development programs, as many stakeholders may be unaware of the high attrition rates of investigational products (*20*). Scientists are encouraged to work with institutional communications professionals on press releases, with the understanding that the author of a study should guide the content and tone.

The guidelines call on scientists to avoid offering overly optimistic statements about economic impact and development horizons, such as predicting near-term clinical applications when a finding is preliminary. In reporting on clinical results, the guidelines emphasize the responsibility to describe the primary end points of the study design and to acknowledge whether or not they were met; post hoc shifting of goalposts to give positive spin to negative results violates principles of honest and accurate communication.

The guidelines include recommendations to help clinical researchers avoid confusing the language of research with the language of care. Specifically, research is primarily designed to generate knowledge, which may not lead to improved care for a given patient, e.g., if the patient is in the control group or the intervention is not beneficial. This error is known to facilitate therapeutic misconception and may cause human research subjects to misunderstand the actual objective of experimental interventions (*21*).

The guidelines recommend that researchers should make "timely corrections of inaccurate or misleading public representations of research projects, achievements, or goals" (*2*). The research community's obligation to encourage accuracy does not end when the popular press takes control. Researchers should consider using social media (*22*), which have been shown to be an effective corrective device in other areas of science (*23*).

Because the forces that twist how science is communicated are complex, systemic, and interrelated, correcting for science hype will not be easy and will require the simultaneous use of various policy tools and vigilant self-control. Clarifying appropriate norms of behavior can be a powerful starting point, as it can help to establish a benchmark against which future actions can be measured. By highlighting and cautioning against specific forms of hyperbole and miscommunication, the ISSCR hopes not only to alert its members to the dangers of misinforming stakeholders but also to facilitate accurate and appropriate public exchange. Hype is not inevitable. ■

## REFERENCES AND NOTES


1. A. Rinaldi, *EMBO Rep.* **13**, 303 (2012).
2. ISSCR, "Guidelines for stem cell science and clinical translation" (ISSCR, Skokie, IL, 2016).
3. National Health Service, "Hope and hype: An analysis of stem cells in the media" (National Health Service, London, UK, 2011).
4. R. Shineha, *East Asian Sci. Technol. Soc.* 10.1215/18752160-3326668 (2015).
5. K. Kamenova, T. Caulfield, *Sci. Transl. Med.* **7**, 278ps4 (2015).
6. A. London, J. Kimmelman, *eLife* **4**, e12844 (2015).
7. A. Petersen, I. Krisjansen, *J. Socl.* (Melbourne) **51**, 28 (2015).
8. P. Bianco, D. Sipp, *Nature* **510**, 336 (2014).
9. T. Bubela, M. D. Li, M. Hafez, M. Bieber, H. Atkins, *BMC Med.* **10**, 133 (2012).
10. T. Caulfield, C. Condit, *Public Health Genomics* **15**, 209 (2012).
11. C. H. Vinkers, J. K. Tijdink, W. M. Otte, *Br. Med. J.* **351**, h6467 (2015).
12. S. Woloshin, L. M. Schwartz, S. L. Casella, *Ann. Intern. Med.* **150**, 613 (2009).
13. M. V. Abola, V. Prasad, *JAMA Oncol.* **2**, 139 (2016).
14. K. Sharpe, N. Di Pietro, J. Illes, *Stem Cell Rev. Rep.* **12**, 1 (2016).
15. B. Love, I. Himelboim, A. Holton, K. Stewart, *Am. J. Infect. Control.* **41**, 568 (2013).
16. M. Nisbet, E. M. Markowitz, *PLOS One* **9**, e88473 (2014).
17. A. Caplan, *Scientific Progress*, 18 April 2011.
18. The Royal Society, "Scientists and the media: Guidelines for scientists working with the media and comments on a Press Code of Practice" (The Royal Society, London, 2000).
19. For example, the American Association for the Advancement of Science has created a Center for Public Engagement with Science and Technology (www.aaas.org/pes).
20. M. Hay, D. W. Thomas, J. L. Craighead, C. Economides, J. Rosenthal, *Nat. Biotechnol.* **32**, 40 (2014).
21. J. Kimmelman, *Hastings Center Rep.* **37**, 36 (2007).
22. H. M. Bik, M. C. Goldstein, *PLOS Biol.* **11**, e1001535 (2013).
23. A. D. Thaler, D. Shiffman, *Ocean Coast. Manage.* **115**, 88 (2015).


## ACKNOWLEDGMENTS


The authors thank the ISSCR and the Guidelines Update Taskforce for insight and assistance and B. Murdoch for research help.

10.1126/science.aaf4620



Downloaded from http://science.sciencemag.org/ on May 12, 2016





*Published by AAAS*

BOOKS *et al.*

EXHIBITION

# *Waking dreams*

## Science and art collide in a probing portrait of the boundaries that define consciousness and awareness

*By* **Giovanni Frazzetto**

**States of Mind**
**Tracing the Edges of Consciousness**
*Emily Sargent, curator*
Wellcome Collection, London.
Through 16 October 2016.

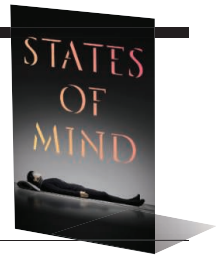


Dead or alive, asleep or awake, focused or drifting. Consciousness switches on, flickers to the wanderings of the mind, rests, and extinguishes. The borders of sentience are the subject of a compact educational exhibition at the Wellcome Collection in London entitled *States of Mind: Tracing the Edges of Consciousness*. Artists, psychologists, neuroscientists, and philosophers contribute artworks, objects, and knowledge to visualize topics that include synesthesia, somnambulism, dream, trauma, language, and memory.

A sizable portion of the show is archival and enriched with images and documents from the history of neuroscience. The millennial mind-body problem is exposed with an 1808 drawing by Luigi Schiavonetti, entitled *The Soul Hovering over the Body Reluctantly Parting with Life*, in which a spirit floats above a human being's lifeless flesh on a deathbed. Settling the same question in favor of materialism are Santiago Ramón y Cajal's notable drawings of ramifying brain cells, there to persuade us that it is in the multiplicity of such branching that consciousness forms and resides. These drawings appear next to original notes from molecular biologist turned neuroscientist Francis Crick.

*Alphabet in Color*, a series of drawings by Jean Holabird, amiably pictures the phenomenon of synesthesia, the involuntary merging of senses that occurs when the stimulation of one sensory pathway leads to the stimulation of another. The Russian-American novelist Vladimir Nabokov, a self-described synesthete, attributed colors to the sound of letters.

A literally resonating piece by Imogen Stidworthy, entitled *The Whisper Heard*, displays the link between consciousness, language, and memory. This installation opposes two voices—a child's and an adult's—that distort the narration of an excerpt from Jules Verne's *Journey to the Center of the Earth*, in which the protagonist hears a voice as he emerges from a state of unconsciousness. The child, who is in the process of acquiring language, listens to the story being told and repeats it, although the meaning of some of the terms is still clearly unknown to him. The adult man is a stroke patient who, unable to utter some of the words he hears from the narrator, relies on their meaning and substitutes synonyms instead.

The tenuousness of an individual's private access to himself or herself and to the external world is further explored in a section dedicated to cases of awareness lost or heavily compromised. Aya Ben Ron's *Shift* is an extremely touching, and at times aching to watch, documentary on vegetative consciousness. Shot against the mechanical sound of medical instruments in the head injury department at the Reuth Medical Center in Tel Aviv, Israel, the film narrates the care provided by hospital staff and family members to men and women who are alive but presumably unaware. Compassionate routines of washing, exercise, feeding, and soothing speech punctuate the fragile existence of patients who are immobile and silent. The film renders their altered state of sentience palpable and strident.

It cannot go unnoticed that only yards away from the premises of the Wellcome Collection are the streets in the Bloomsbury area of London where writers such as Virginia Woolf experimented with the "stream of consciousness" literary technique a century ago.

Given the sizable investment that we have made in attempting to pin down the neural correlates of almost every fragment of perception, the ambition to distill the essence of consciousness into elements that are quantifiable and reproducible will not easily recede. In parallel, complementary artistic explorations will likely continue to expose the elusive inscrutability of the subjective flow of thoughts and feelings with equal motivation.

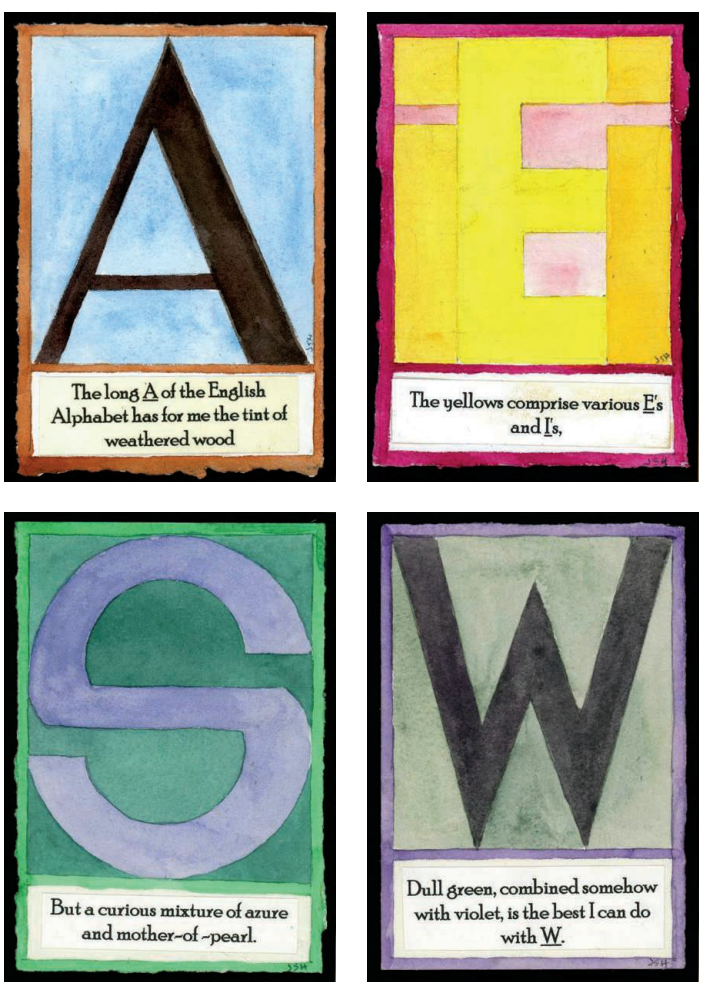


**Individuals with grapheme-color synesthesia perceive color in letters and sounds.**

*The reviewer is the author of* Joy, Guilt, Anger, Love *(Penguin, 2014) and is at Trinity College, Dublin, Ireland. Email: gio@giovannifrazzetto.com*

10.1126/science.aaf6090

PHOTOS: (TOP) GOSHKA MACUGA 'SOMNAMBULIST' 2006, COURTESY OF THE ARTIST AND KATE MACGARRY, LONDON; (BOTTOM) JEAN HOLABIRD

Downloaded from http://science.sciencemag.org/ on May 12, 2016



Published by AAAS

Wisdom hath built her house, she hath hewn out her seven pillars. Proverbs 9:1

PHOTO: RENA SCHILD/ISTOCKPHOTO

DATA ANALYSIS

# The stanchions of statistics

## A new volume explores the origins and history of seven foundational tenets of statistical science

*By* **Howard Wainer**

Statistics, the science of uncertainty, is young as sciences go. Physics, chemistry, geology, botany, and biology were firmly established long before its birth. But despite its late start, modern statistics is as broadly influential as its elders. Too often, however, the field is looked upon as a set of arcane procedures that are implemented, without much thought, by computer algorithms. Such a myopic view of this most modern of the sciences deprives the viewer of the accumulated product of a great deal of beautiful and subtle thinking. Statistician Stephen Stigler's wonderful new book, *The Seven Pillars of Statistical Wisdom*, sets out to remedy this.

Stigler's title echoes that of T. E. Lawrence's iconic 1926 memoir, which in turn was taken from Proverbs 9:1 (see photo caption). Each of the seven pillars that Stigler, in his wisdom, has hewn from the past two centuries of statistical thought provides surprising insights.

The idea that we can gain deeper understanding of a mass of data by summarizing them into a single number—known as "aggregation"—represents Stigler's first pillar. The seemingly contradictory notion that we can learn more about a phenomenon by disregarding information was and is inherently revolutionary.

*The reviewer is the author of* Truth or Truthiness: Distinguishing Fact from Fiction by Learning to Think Like a Data Scientist *(Cambridge University Press, 2016).*
*Email: hwainer@nbme.org*

**The Seven Pillars of Statistical Wisdom**
*Stephen M. Stigler*
Harvard University Press, 2016. 238 pp.

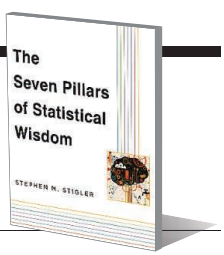


The second of Stigler's pillars is "information" or, more specifically, "information measurement." De Moivre's equation shows that the accuracy of a data summary improves as the square root of the number of observations, meaning that as we gather more information, the value of each additional piece is less than that which preceded it. This, too, is an idea with surprising implications. "Imagine trying to convince an astronomer that if he wished to double the accuracy of an investigation, he needed to quadruple the number of observations, or that the second 20 observations were not nearly so informative as the first 20," writes Stigler.

The third pillar, "likelihood," refers to the calibration of inferences via probability. Stigler illustrates this pillar, as he does with the others, with examples drawn from the past, the plinth of the pillars. In 1748, David Hume, himself a pillar of British empiricism, published the essay "Of Miracles," in which he argued that no credence should be given to reported miracles, since they were, by definition, a violation of natural laws and hence extremely improbable. Hume's courage was manifest when he chose to examine, probabilistically, the resurrection of Christ. His argument rested upon the higher likelihood that an individual who purported to have observed evidence of the resurrection was mistaken or had lied. Thus, he concluded, the probability of a resurrection was vanishingly small. His analysis was challenged in 1767 by the philosopher and mathematician Richard Price. If, in a million binomial trials (deaths), there had not been a single resurrection, Price argued, the probability of a resurrection was small but not zero. The probability of at least one resurrection in the next million deaths, he maintained, was greater than one-half. As Stigler wryly observes, "The possibility of a miracle was much larger than Hume had supposed."

Stigler's fourth pillar, "intercomparison," refers to the arsenal of procedures based on statistical comparisons made, not to some external standard, but to a factor that is interior to the data. An obvious example is analysis of variance, in which we estimate the likelihood of an effect by comparing two different internal estimates of error.

The fifth pillar of statistics is "regression," which is the inevitable outcome of a situation in which one variable is not perfectly predicted from another. In such a case, the predicted outcome inexorably moves (regresses) toward the middle. Thus, tall parents are likely to have tall children, but not as tall as they are, and short parents are likely to have short children, but not as short as they are.

"Design," as in the design of experiments, constitutes the sixth pillar and includes the powerful role played by randomization. The idea of manipulating only one variable at a time can be difficult in practice. For example, in agricultural experiments in which different seeds or fertilizers are to be tested, it is impossible to test each variable in exactly the same location. In 1926, the English statistician R. A. Fisher turned this bug into a feature, carefully showing how an experiment could be designed so that, on average, various factors could be estimated simultaneously. Thus, through careful design, multifactor experiments were born.

Stigler calls the seventh and final pillar of statistical knowledge "residual," which is meant to convey the powerful idea of an analytic magnifying glass that works by subtracting out the effects of obvious phenomena so that we can look carefully at what is left over. In this way, he argues, we can see what was once obscured.

Statistics, Stigler maintains, is a living science, and other pillars may emerge, perhaps in relation to the problems of big data. But with the help of strong allies in other fields, we can be confident that we have the tools necessary to be equal to the challenges we will face moving forward.

10.1126/science.aaf9115

Downloaded from http://science.sciencemag.org/ on May 12, 2016



Published by AAAS

# LETTERS

*Edited by* **Jennifer Sills**

## Reminder to deposit DNA sequences

AS MEMBERS OF the Advisory Committee to the International Nucleotide Sequence Database Collaboration (INSDC), which includes the DNA Data Bank of Japan (DDBJ), ENA, and GenBank databases, we wish to remind the research community of the importance of depositing complete DNA-sequence data in these databases upon publication of their results [see also S. L. Salzberg *et al.*, *Nature*, http://dx.doi.org/10.1038/533179a (2016)]. Indeed, most journals demand a database accession number as a condition of publication.

Access to the INSDC's databases is free and unrestricted (*1*), enabling researchers to plan experiments and to analyze existing data. As original contributions, deposited data form part of the scientific record and are citable in the literature. Authors can also correct and update their data. These amended records may be removed from the next database release but still remain permanently available by accession number.

INSDC has also created major new repositories for large data collections, notably the Sequence Read Archive at the National Center for Biotechnology Information (NCBI) (*2*), the DDBJ Sequence Read Archive (*3*), and the European Nucleotide Archive at the European Molecular Biology Laboratory's European Bioinformatics Institute (EMBL-EBI) (*4*). These archive raw data from sequencing experiments, a crucial facility for reproducibility and reuse.

For papers dependent on sequence data from human subjects, unrestricted data release may not be possible. In these cases, we would encourage journal editors to insist on data sharing through other repositories that are not part of INSDC, such as NCBI's Database of Genotype and Phenotype (*5*), EMBL-EBI's European Genome-phenome Archive (*6*), or DDBJ's Japanese Genotype-phenotype Archive (*7*).

***Mark Blaxter,[1] Antoine Danchin,[2] Babis Savakis,[3] Kaoru Fukami-Kobayashi,[4] Ken Kurokawa,[5] Sumio Sugano,[6] Richard J. Roberts,[7] Steven L. Salzberg,[8]* Chung-I Wu[9,10]***

[1]Edinburgh Genomics Facility and Institute of Evolutionary Biology, University of Edinburgh, Edinburgh, EH8 9YL, UK. [2]Institute of Cardiometabolism and Nutrition, Hôpital de la Pitié-Salpêtrière, Paris, 75013, France. [3]University of Crete and Biomedical Sciences Research Centre "Alexander Fleming", Athens, Greece. [4]Bioresource Information Division, RIKEN BioResource Center, Tsukuba, Ibaraki, 305-0074, Japan. [5]Earth-Life Science Institute, Tokyo Institute of Technology, Tokyo, 152-8550, Japan. [6]Graduate School of Frontier Sciences, The University of Tokyo, Kashiwa, Chiba, 277-8562, Japan. [7]New England Biolabs, Ipswich, MA 01938, USA. [8]McKusick-Nathans Institute of Genetic Medicine, Johns Hopkins University School of Medicine, Baltimore, MD 21205, USA. [9]Department of Ecology and Evolution, University of Chicago, Chicago, IL 60637, USA. [10]Beijing Institute of Genomics, Beijing, 100101, China.

*Corresponding author. Email: salzberg@jhu.edu

**REFERENCES**

1. G. Cochrane, I. Karsch-Mizrachi, T. Takagi, International Nucleotide Sequence Database Collaboration, *Nucleic Acids Res.* **44**, D48 (2016).
2. www.ncbi.nlm.nih.gov/sra.
3. http://trace.ddbj.nig.ac.jp/dra/index_e.html.
4. www.ebi.ac.uk/ena.
5. www.ncbi.nlm.nih.gov/gap.
6. www.ebi.ac.uk/ega/home.
7. http://trace.ddbj.nig.ac.jp/jga/index_e.html.

10.1126/science.aaf7672

## Crimea report leaves readers in the cold

THE NEWS FEATURE "Out in the cold" (R. Stone, 8 April, p. 140) aims to report on the state of science and scientists in the Crimean Peninsula of Ukraine, post-occupation by the Russian Federation. We were dismayed to see it under the heading "Science in Russia." This is in stark disagreement with UN General Resolution 68/262, which calls for no actions interpretable as recognizing the alteration in status of the Autonomous Republic of Crimea (*1*). We call upon *Science* to publish an apology for the article's inappropriate placement and to henceforth refrain from publishing articles that suggest Crimea to be under Russian jurisdiction.

The News story invokes a picture that is very different from the reality in Crimea: Occupation authorities prosecute everyone who dares express an opinion opposing the annexation (*2*, *3*). The story demonstrates the division among Crimean scientists, but it misses the more important point: the unambiguous illegality of the Crimean annexation and the appropriation of Ukrainian state property worth billions of dollars by the Russian Federation (*4*, *5*), including the astronomical observatory, museums, priceless archives, and the institutes mentioned in the story. Moreover, the quotes in the article literally recite slogans of the Russian propaganda (*6*) reminiscent of the Soviet information warfare adopted and perfected by the Kremlin regime (*7*, *8*). Willingly or not, *Science* lends its high reputation to this propaganda.

We call upon the international academic community to show solidarity with Ukrainian scholars and to comply with international law that does not recognize the annexation of Crimea. We firmly believe that the scientific endeavor can be successful only in a free and democratic state, which Ukrainians strive to build. What science in Ukraine needs is assistance in implementing structural reforms and support of its closer integration into the broader international academic community. This is the only strategy that would also help science in Crimea in the long run.

***Alexander Goushcha,[1] Galina Z. Goloverda,[2] Oleh Kotsyuba,[3] Dmitrii F. Perepichka,[4] Oksana Seumenicht,[5] Alexey S. Ladokhin[6]****

[1]Luna Optoelectronics, Camarillo, CA 93012, USA. [2]Xavier University, New Orleans, LA 70125, USA. [3]Harvard University, Cambridge, MA 02138, USA. [4]McGill University, Montreal, QC, H3A 0G4, Canada. [5]Max Delbrück Center for Molecular Medicine, Berlin, 13125, Germany. [6]University of Kansas Medical Center, Kansas City, KS 66160, USA.

*Corresponding author. Email: aladokhin@kumc.edu

The full list of 141 authors is available online.

**REFERENCES**

1. UN General Assembly, "Resolution adopted by the General Assembly on 27 March 2014: 68/262. Territorial integrity of Ukraine" (2014).
2. Amnesty International, "Crimea: One year on from annexation; critics harassed, attacked and silenced" (2015).
3. B. Ovcharuk, "Crimea: Peninsula of fear," Amnesty International (2015).
4. Ukrainian Center for Independent Political Research, "Annexed property in Crimea" (2016); https://drive.google.com/file/d/0B00cox29AXT9QWhkc2x3aGUyLWs/view.
5. Ukrainian Center for Independent Political Research, "'Annexed' Education in Temporary Occupied Crimea," Y. Tyshchenko, O. Smirnov, Eds. (2015); https://drive.google.com/file/d/0B00cox29AXT9TUpUZ0Y3R3BWY1k/view.

IMAGE: BEHOLDINGEYE/ISTOCKPHOTO.COM

Downloaded from http://science.sciencemag.org/ on May 12, 2016



Published by AAAS

6. A. S. Ladokhin, "'Out in the cold' and Kremlin's weaponization of culture" (2016); http://science.sciencemag.org/content/352/6282/140.e-letters.
7. P. Pomerantsev, M. Weiss, "The menace of unreality: How the Kremlin weaponizes information, culture and money," *The Interpreter* (November 2014).
8. T. Snyder, "To understand Putin, read Orwell: Ukraine, Russia and the big lie," *Politico Magazine* (3 September 2014).

**SUPPLEMENTARY MATERIALS**

www.sciencemag.org/content/352/6287/780-b/suppl/DC1
Full author list

10.1126/science.aaf9663

## *Response*

THE PLACEMENT OF this piece under the general heading "Science in Russia" was not meant as an endorsement of Russia's annexation of Crimea, and we apologize for any suggestion otherwise. Our story made it clear that most countries view the annexation as illegal, and we gave a detailed account of the takeover of scientific facilities and the exodus of Ukrainian scientists.

***Tim Appenzeller***
News Editor, *Science*

# *New allies fight for China's environment*

SINCE THE ENACTMENT and formal implementation of China's revised Environmental Protection Law in 2015, a number of serious questions have arisen about its effectiveness, due in part to perceived conflict between the goals of economic development and environmental protection (*1*). However, more progress has been made than expected (*2*), thanks to the positive attitude of the central government and some local governments; nongovernmental organizations (NGOs) that have stepped up as environmental protection advocates; and civic groups, enhanced by proactive citizens, that have promoted and strengthened environmental consciousness and responsibility. These stakeholders have worked together to give effective teeth to the legislation.

To counter the tendency of local governments to focus on economic growth while ignoring excessive resource consumption and environmental damage, the central government commissioned research by highly qualified institutions (*3*) to explore a framework system for a Natural Resource Statement of Assets and Liabilities (NRSAL) (*4*, *5*). As part of a national pilot program that started in November 2015 (*6*), four cities will report resource use according to the NRSAL framework at the end of 2016. In the near future, the NRSAL will hopefully serve as the foundation and provide the basic parameters for the ongoing audits of natural resource assets responsibility at the local government level (*7*).

In 2015, 48 civil public interest suits were filed (*8*). The cases aroused public awareness and encouraged citizen participation in environmental governance, while serving as a warning to potentially polluting domestic and foreign enterprises. This increased awareness and empowerment has prompted stakeholders to seek effective cooperation strategies. For example, the Tengger Desert Pollution Incident (*9*) set the stage for stakeholder involvement. Local residents supported by journalists identified and exposed the contaminated area; the central government responded quickly with appropriate regulations and performance requirements; and the NGO China Biodiversity Conservation and Green Development Foundation (CBCGDF) brought lawsuits against all responsible parties. As a result of this concerted joint effort, the offending companies closed and the sources of pollution were eliminated (*10*).

These developments point to an increase in the number of citizens, civic groups, NGOs, and government agencies actively participating in environmental supervision and protection. This commitment is a step forward as we confront long-term environmental challenges.

***S. Lu,[1,2]* J. Zhou,[2] F. Dubee[2,3]***

[1]State Key Laboratory of Remote Sensing Science, Institute of Remote Sensing and Digital Earth, Chinese Academy of Sciences, Beijing, 100101, China. [2]China Biodiversity Conservation and Green Development Foundation, Beijing, 100089, China. [3]BGI, International Green Economy Association, World Academy of Arts and Sciences, Club of Rome, 18100, Heinola, Finland.

*Corresponding author. Email: lusl@radi.ac.cn

**REFERENCES AND NOTES**

1. H. Yang, X. Huang, J. R. Thompson, R. J. Flower, *Science* **347**, 834 (2015).
2. D. Liu, *Nature* **525**, 321 (2015).
3. The institutions include the Institute of Geographic Sciences and Natural Resources Research, Chinese Academy of Sciences, and the Institute of Industrial Economics, Chinese Academy of Social Sciences.
4. Z. Feng, Y. Yang, P. Li, *Bull. Chin. Acad. Sci.* **29**, 449 (2014) [in Chinese with English abstract].
5. W. Hu, D. Shi, *China Pop. Resources Env.* **25**, 1 (2015) [in Chinese with English abstract].
6. C. Li, *Env. Sustain. Dev.* **6**, 14 (2015) [in Chinese].
7. X. Liu, *Modern Audit Econ.* **2**, 14 (2015) [in Chinese].
8. Court of Environmental Resources, The Supreme People's Court of the People's Republic of China, "National court trial implementation in 2015" (2016); www.court.gov.cn/fabu-xiangqing-18362.html [in Chinese].
9. X. Miao, Y. Tang, C. W. Y. Wong, *Nature* **518**, 483 (2015).
10. Ministry of Environmental Protection of the People's Republic of China, "Notice of termination of the most strict supervision of the Tengger desert area's environmental pollution problems (2015); www.mep.gov.cn/gkml/hbb/bgth/201511/t20151111_316817.htm [in Chinese].

10.1126/science.aaf8345



Published by AAAS

Downloaded from http://science.sciencemag.org/ on May 12, 2016

RESEARCH ARTICLE SUMMARY

MUCOSAL IMMUNOLOGY

# IgA production requires B cell interaction with subepithelial dendritic cells in Peyer's patches

**Andrea Reboldi,* Tal I. Arnon, Lauren B. Rodda, Amha Atakilit, Dean Sheppard, Jason G. Cyster***

**INTRODUCTION:** Secretory immunoglobulin A (IgA) is made by intestinal plasma cells and has roles both in protection from gut pathogens and in maintaining homeostasis of intestinal commensals. Peyer's patches (PPs)—the major organized lymphoid tissues of the small intestine, numbering 100 to 200 in humans and 6 to 12 in mice—are the dominant source of IgA-producing cells. A number of molecular factors have been identified that promote B cell switching from IgM to IgA, the best defined being transforming growth factor–β (TGFβ). TGFβ is made in a latent form and must be activated before it can induce TGFβ receptor (TGFβR) signaling. In this study, we explore the requirements for B cell IgA switching in PPs, concentrating on the location where it takes place and the key cell types involved.

**RATIONALE:** Mice deficient in the chemokine receptor CCR6 had been reported to mount poor IgA responses, but the mechanism responsible was unclear. The CCR6 ligand, CCL20, is abundant in the subepithelial dome (SED) of the PP, and one thought was that CCR6 was required for positioning dendritic cells (DCs) in the SED. However, CCR6 was known to be expressed by B cells and to be up-regulated following B cell activation. In this study, we have pursued the hypothesis that CCR6 is required within B cells to promote migration events and cellular interactions in the SED necessary for PP IgA responses.

**RESULTS:** Using bone marrow (BM) chimera and cell transfer approaches, we find that CCR6 expression in PP B cells is necessary for their efficient switching to IgA and for production of intestinal IgA against cholera toxin and commensal bacteria. Loss- and gain-of-function approaches establish that intrinsic CCR6 expression is necessary and sufficient for B cells to access the SED. CCR6 is up-regulated on pre–germinal center (GC) B cells in a CD40-dependent manner, and a transfer model indicates a more prominent role for CCR6 in T cell–dependent than in T cell–independent IgA responses. PP pre-GC B cells are shown to express IgA germline transcripts and activation-induced cytidine deaminase (AID), consistent with IgA switching initiating in this compartment. Using intravital two-photon microscopy, we find that B cells within the SED undergo prolonged interactions with DCs. Using BM chimera experiments and blocking reagents, we establish that SED DCs are dependent on the cytokine lymphotoxin-α1β2 (LTα1β2). RORγt$^+$ innate lymphoid cells (ILCs) are identified as a necessary source of this cytokine. Deficiency in LTβR-dependent DCs or RORγt-dependent ILCs results in reduced IgA$^+$ B cell frequencies in PPs. Reciprocally, transgenic overexpression of LTα1β2 increases SED DCs and IgA switching. We then examined how the SED DCs augment IgA switching and found that they abundantly expressed αvβ8, an integrin that has an established role in converting TGFβ from its latent to its active state. Experiments with *Itgb8f/f Cd11c-Cre* mice and with an αvβ8 blocking antibody established that DC αvβ8 expression was necessary for PP IgA switching. In vitro experiments provided further evidence that DC αvβ8 could directly activate TGFβ during DC–B cell interactions and showed that LTβR and retinoic acid signaling promote αvβ8 expression on DCs.

ON OUR WEB SITE

Read the full article at http://dx.doi.org/10.1126/science.aaf4822

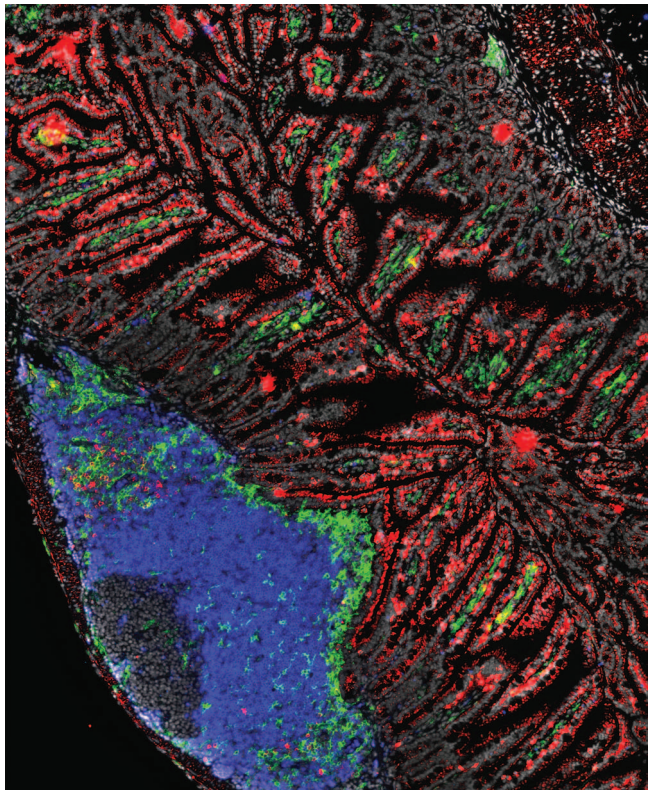

**B cell and dendritic cell distribution in mouse Peyer's patch.** Image is a cross-sectional view of a single PP dome and the neighboring villous epithelium of the small intestine. The 7-μm frozen section was stained to detect naïve and pre-GC B cells (IgD, blue) that occupy the follicle and SED; dendritic cells (CD11c, green) that are abundant in the SED, the interfollicular T zone, and the intestinal lamina propria; T cells (CD8, red) that are present in the interfollicular T zone, the lamina propria, and in the epithelium; and nuclei (DAPI, gray). Red staining also occurred nonspecifically in association with the epithelium, and this was most prominent for the follicle-associated epithelium that overlies the SED. The follicle-associated epithelium is the site of intestinal antigen delivery into the PP. The dark (IgD-negative) oval-shaped structure within the follicle is a GC.

**CONCLUSION:** Our study defines a role for the PP SED as a niche that supports events necessary for IgA switching, in particular the induction of TGFβ activation, and it provides an example of a DC–B cell interaction acting to guide B cell fate. By defining a network of interactions required for IgA switching, this study identifies approaches that could be used to augment IgA responses while also defining sites for defects that could underlie IgA deficiency, the most common immune deficiency syndrome in humans. ■

The list of author affiliations is available in the full article online.
*Corresponding author. Email: andrea.reboldi@ucsf.edu (A.R.); jason.cyster@ucsf.edu (J.G.C.)
Cite this article as A. Reboldi *et al.*, *Science* 352, aaf4822 (2016). DOI: 10.1126/science.aaf4822

Downloaded from http://science.sciencemag.org/ on May 12, 2016

RESEARCH ARTICLE

MUCOSAL IMMUNOLOGY

# IgA production requires B cell interaction with subepithelial dendritic cells in Peyer's patches

Andrea Reboldi,[1]* Tal I. Arnon,[1]† Lauren B. Rodda,[1] Amha Atakilit,[2] Dean Sheppard,[2] Jason G. Cyster[1]*

**Immunoglobulin A (IgA) induction primarily occurs in intestinal Peyer's patches (PPs). However, the cellular interactions necessary for IgA class switching are poorly defined. Here we show that in mice, activated B cells use the chemokine receptor CCR6 to access the subepithelial dome (SED) of PPs. There, B cells undergo prolonged interactions with SED dendritic cells (DCs). PP IgA class switching requires innate lymphoid cells, which promote lymphotoxin-β receptor (LTβR)–dependent maintenance of DCs. PP DCs augment IgA production by integrin αvβ8-mediated activation of transforming growth factor–β (TGFβ). In mice where B cells cannot access the SED, IgA responses against oral antigen and gut commensals are impaired. These studies establish the PP SED as a niche supporting DC–B cell interactions needed for TGFβ activation and induction of mucosal IgA responses.**

Immunoglobulin A (IgA), the most abundantly produced antibody isotype in the body, has the dual roles of maintaining homeostasis with the microbiome and protecting from intestinal infection (*1*, *2*). Plasma cells located in the lamina propria secrete IgA, but the early stages of IgA production take place mainly in Peyer's patches (PPs) (*3*). PPs are lymphoid organs that are organized into B cell–rich follicles, T cell–rich interfollicular zones, and a subepithelial dome (SED) rich in CD11c$^+$ dendritic cells (DCs) that separates the epithelium from the follicles (*4*) (Fig. 1A). Gut-derived antigens delivered across specialized epithelial cells continually stimulate PPs, and PP follicles harbor chronic T cell–dependent germinal centers (GCs) (*1*). PP GCs contain a high frequency of IgA$^+$ cells, and these give rise to IgA plasma cells. Although a number of factors have been implicated in PP B cell switching to IgA, the strongest requirement established in vivo is for transforming growth factor–β receptor (TGFβR) signaling (*5*–*7*). However, the cellular interactions involved in promoting TGFβR signaling in PP B cells have been unclear.

## B cell–intrinsic CCR6 requirement for IgA switching in PPs

Previous studies have shown that CC-chemokine receptor–6 (CCR6)–deficient mice have altered PP organization and reduced antigen-specific IgA levels (*8*, *9*). The CCR6 ligand, CCL20, is made abundantly by PP follicle-associated epithelium, and DC distribution in the SED was affected by CCR6 deficiency (*8*, *9*), though this was not seen in another study (*10*), leaving the mechanism by which CCR6 augments IgA production unclear. An analysis of B cell distribution in wild-type PPs showed that in addition to their dense presence in follicles, IgD$^+$ B cells were detectable more sparsely within the SED, overlapping with the network of CD11c$^+$ Zbtb46$^+$ DCs in this region (Fig. 1A) (*11*). Although CCR6 is widely expressed by B cells (*12*), the dynamics of PP B cell CCR6 expression have not been determined. A fraction of PP IgD$^+$ and IgD$^-$ B cells had high CCR6 surface staining (Fig. 1B), and further phenotypic analysis based on Fas (CD95), CD11c, and IgM expression showed that these B cells were enriched in pre-GC and memory B cells, respectively (fig. S1A). To confirm that PP IgD$^+$CCR6$^+$Fas$^+$CD11c$^+$ cells correspond to pre-GC cells (*13*, *14*), we transferred wild-type follicular B cells to monoclonal MD4 Ig-transgenic mice that have little endogenous PP GC activity. A large fraction of the transferred polyclonal B cells, likely stimulated by intestinal antigen in PPs, acquired an IgD$^-$CCR6$^-$CD38$^-$GL7$^+$ GC phenotype after 1 week (Fig. 1C). Tracking cell differentiation and division at 3 and 4 days after transfer established that CCR6 was up-regulated before the appearance of IgD$^-$ GC B cells (Fig. 1D). Fas and CD11c were up-regulated with a similar time course (fig. S1B). Some cells that had undergone four or more divisions were CCR6$^{hi}$IgD$^{lo/-}$ (Fig. 1D and fig. S1B), indicating that the CCR6$^+$IgD$^-$ gate (Fig. 1B and fig. S1B) may contain some pre-GC cells as well as memory B cells.

In accord with this CCR6 expression pattern, pre-GC and memory B cells, but not follicular or GC B cells, efficiently migrated toward CCL20 in a CCR6-dependent manner (Fig. 1E and fig. S1C). By contrast, PP DCs showed little migration to CCL20 while responding well to CCL21 and CXCL12 (fig. S1D). CCR6 levels and function were up-regulated in follicular B cells shortly after B cell receptor (BCR) engagement in vitro with anti-IgM (fig. S1E), though not after incubation with anti-CD40, consistent with in vitro findings for CCR6 function in activated human B cells (*15*). However, tracking polyclonal B cell activation in PPs with the adoptive transfer system revealed that B cells required CD40 and CD40L for CCR6 up-regulation in vivo (Fig. 1F and fig. S1F). Together, these data provide evidence that CCR6 induction in naïve B cells responding to endogenous PP-associated antigens involves CD40-dependent interactions with T helper ($T_H$) cells. Pre-GC cells also had slightly higher amounts of CXCR4, CXCR5, and CCR7 than naïve B cells, though their response to the corresponding chemokines was not increased compared to naïve B cells (Fig. 1E and fig. S1G).

To determine whether CCR6 up-regulation could be sufficient to control B cell localization to the SED within PPs, we transferred B cells from bone marrow (BM) chimeras transduced with CCR6-encoding retrovirus to wild-type recipients. Three days later, the CCR6-overexpressing B cells, identified by expression of a Thy1.1 reporter, were situated preferentially in the SED (Fig. 1G and fig. S2A). By contrast, B cells transduced with the control retrovirus were distributed uniformly within the follicle and SED (Fig. 1G and fig. S2A). To test whether CCR6 was necessary for B cell localization in the SED, we examined B cell distribution in 50:50 mixed BM chimeras that contained CCR6-deficient or littermate control (Igh$^b$) cells mixed with wild-type (Igh$^a$) cells. Notably, CCR6-deficient and wild-type B cells were equally represented in the follicle, but CCR6-deficient B cells were unable to migrate into the SED (Fig. 1H and fig. S2B). Using the procedure of adoptive cell transfer into MD4 hosts, we found that B cells accessed the SED in a CCR6-dependent manner within 4 days of activation by endogenous antigen (Fig. 1I and fig. S2C).

Because CCR6 up-regulation on follicular B cells is associated with the transitional stage between naive and GC B cell phenotypes, we sought to directly test the importance of CCR6 in PP B cell fate. We used mixed wild-type (Igh$^a$): CCR6-deficient (Igh$^b$) BM chimeras to determine the intrinsic role of CCR6 in B cells and ensure that other CCR6-dependent properties of PPs were intact (*8*–*10*, *16*). CCR6-deficient GC B cells in these chimeras suffered reduced switching to IgA compared to wild-type GC B cells in the same animals and showed instead an increased propensity for switching to IgG1 (Fig. 2A). In accord with most PP IgA$^+$ cells being GC B cells (Fig. 2B), the frequency of IgA$^+$ cells was decreased among total *Ccr6*$^{-/-}$ B cells (Fig. 2C and fig. S3A). Analysis of mesenteric LNs (MLNs) in the same animals showed only a low frequency of IgA$^+$ cells and no impact of CCR6 deficiency (fig. S3B). CCR6 deficiency did not significantly affect the fraction of PP B cells with pre-GC, GC, or memory phenotypes (fig. S3C).

[1]Howard Hughes Medical Institute and Department of Microbiology and Immunology, University of California San Francisco, 513 Parnassus Avenue, San Francisco, CA 94143, USA. [2]Lung Biology Center, Department of Medicine, University of California San Francisco, 1550 4th Street, San Francisco, CA 94158, USA. *Corresponding author. Email: andrea.reboldi@ucsf.edu (A.R.); jason.cyster@ucsf.edu (J.G.C.) †Present address: Kennedy Institute of Rheumatology, University of Oxford, Roosevelt Drive, Headington, Oxford OX3 7FY, UK.

Downloaded from http://science.sciencemag.org/ on May 12, 2016

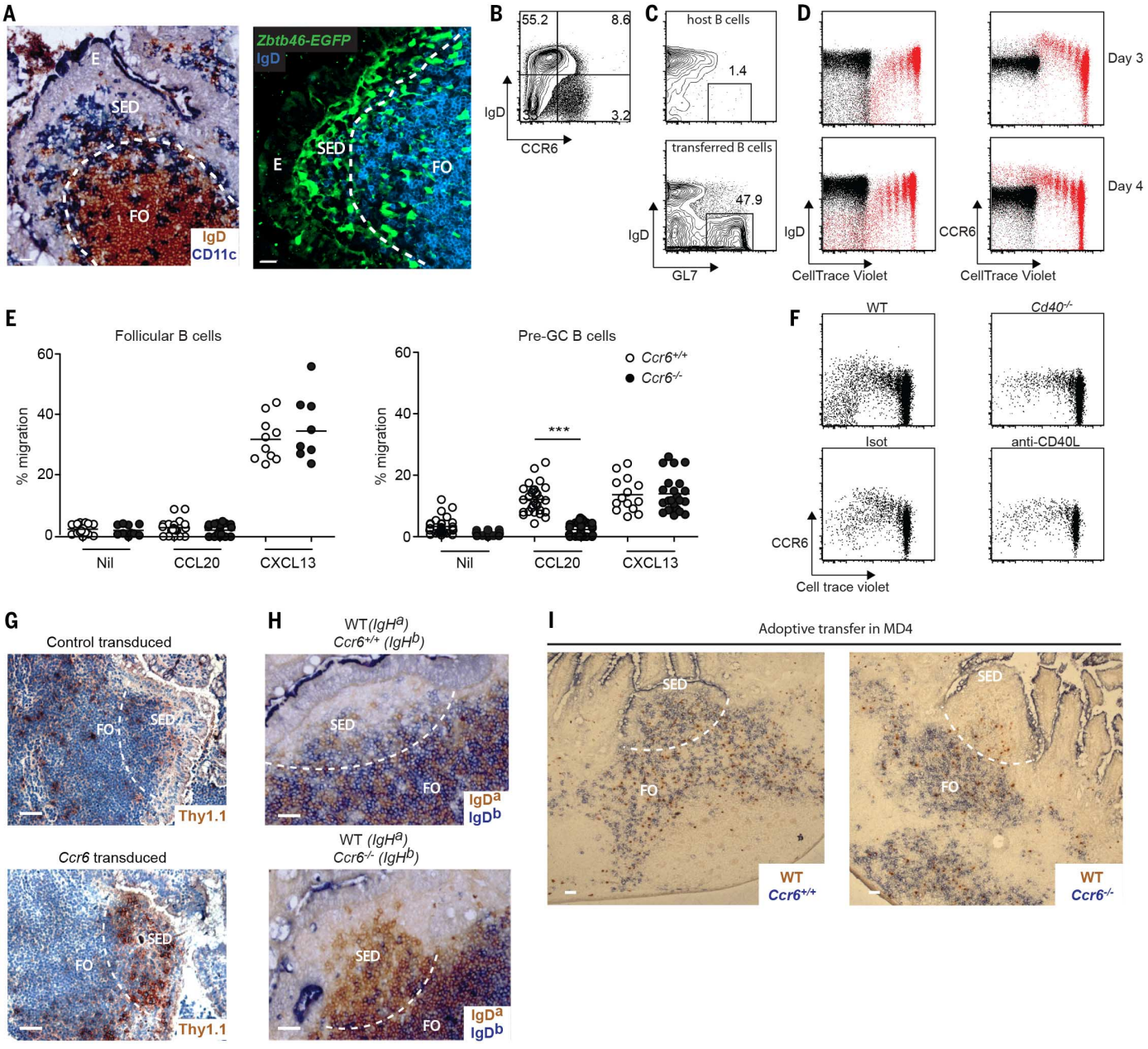


**Fig. 1. B cell access to the PP subepithelial dome (SED) is CCR6-dependent.** (**A**) Representative images of Peyer's patch (PP) dome stained with anti-CD11c (blue) and anti-IgD (brown) (left) or with anti-GFP (green) and anti-IgD (blue) (right). Dashed white line demarcates the follicle-SED boundary. Scale bars, 20 μm. (**B**) Representative flow cytometric analysis of $CD19^+$ B cells in PPs for IgD and CCR6 expression. (**C** and **D**) Representative staining for fluorescence-activated cell sorting (FACS) of transferred CellTrace Violet–labeled polyclonal B cells (red) in MD4 hosts (endogenous B cells, black) for IgD and GL7 at day 7 (C) and IgD and CCR6 at days 3 and 4 after transfer. (**E**) Migration of PP follicular (left) and pre-GC B cells (right) from $Ccr6^{+/+}$ and $Ccr6^{-/-}$ mice to the indicated chemokines. (**F**) Representative CCR6 expression on transferred wild-type (WT) and $Cd40^{-/-}$ B cells in MD4 hosts (upper panels) or wild-type B cells in MD4 hosts treated with either isotype control or anti-CD40L (lower panels) after 7 days. (**G**) Representative images of distribution of transferred B cells (Thy1.1, brown) in sections of PP from mice receiving control vector or CCR6-transduced B cells. Slides were counterstained with hematoxylin. (**H**) Representative images of distribution of B cells in PPs of chimeras reconstituted with 50% $Igh^b$ $Ccr6^{+/+}$ or $Ccr6^{-/-}$ and 50% $Igh^a$ wild-type BM. Sections were stained to detect $Ccr6^{+/+}$ or $Ccr6^{-/-}$ B cells ($IgD^b$, blue) and control B cells ($IgD^a$, brown). (**I**) Distribution of polyclonal $Ccr6^{+/+}$ and $Ccr6^{-/-}$ B cells in PPs of mixed transfer MD4 recipients [75% CD45.2 $Ccr6^{+/+}$ or $Ccr6^{-/-}$ and 25% carboxyfluorescein succinimidyl ester (CFSE) CD45.1 wild-type] 4 days after transfer. Sections were stained to detect $Ccr6^{+/+}$ or $Ccr6^{-/-}$ B cells (CD45.2, blue) and control B cells (CFSE, brown). Each symbol in (E) represents an individual mouse, and data are pooled from at least three independent experiments. Data in (A), (B), (C), (D), (F), (G), (H), and (I) are representative of at least three independent experiments. $^{***}P < 0.005$ (unpaired Student's *t* test).

Analysis of wild-type and CCR6-deficient cells cotransferred to MD4 hosts showed that the early appearance of $IgA^+$ GC cells was CCR6-dependent (Fig. 2D) and, again, CCR6 deficiency did not affect the induction of pre-GC, GC, or memory cells (fig. S3D). IgA class switching in vitro was not affected by CCL20 (fig. S3G), consistent with the CCR6 requirement being to support B cell positioning within the PP. Interestingly, the mixed chimeras also had reduced frequencies of $Ccr6^{-/-}$ $T_H17$ cells in PPs (fig. S3F). However, because the defective IgA response was specific to the allotype marked CCR6-deficient B cells, actions of the receptor in other cell types cannot account for the CCR6 requirement in B cells. The inability to

Downloaded from http://science.sciencemag.org/ on May 12, 2016

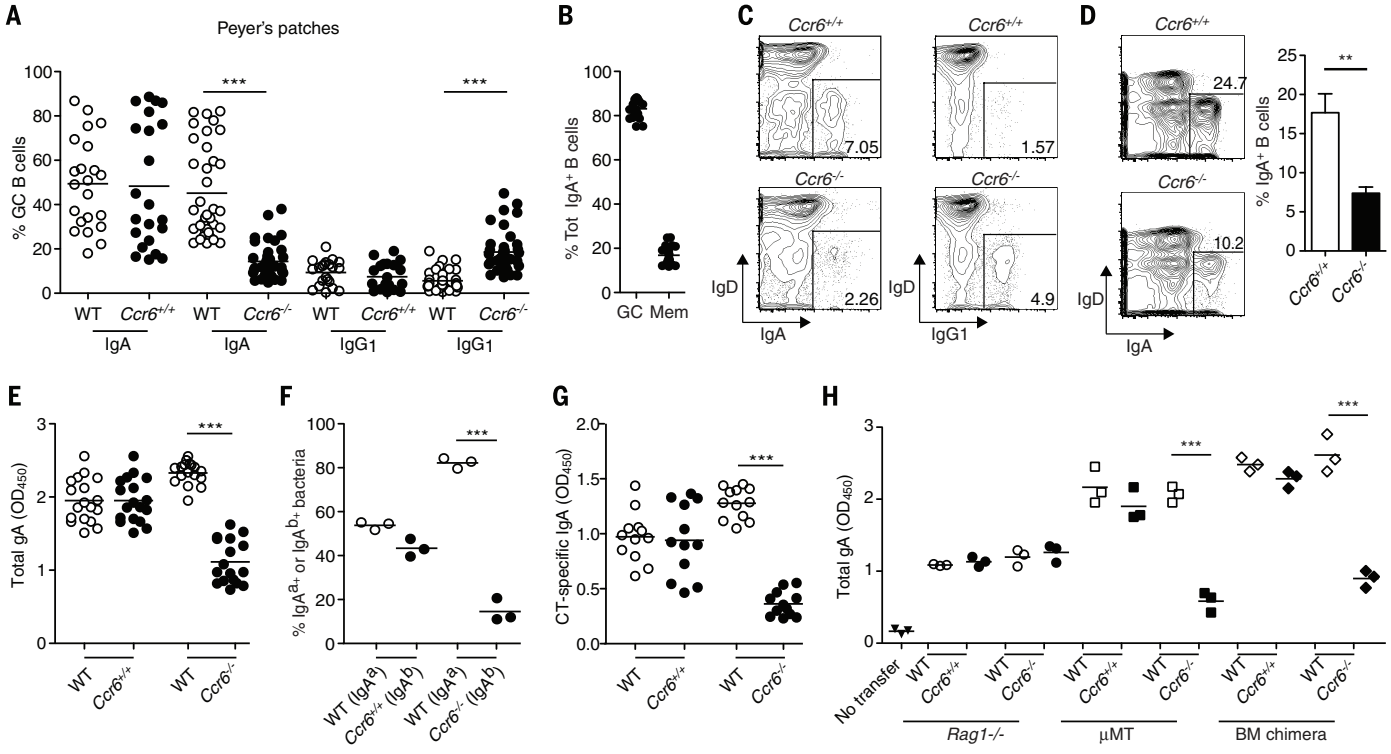


**Fig. 2. B cell isotype switching to IgA is CCR6-dependent.** (**A**) Frequency of WT and *Ccr6*$^{+/+}$ or *Ccr6*$^{-/-}$ GC B cells expressing IgA or IgG1 in PPs from mixed BM chimeras, as determined by FACS. (**B**) GC and memory contribution to IgA$^+$ B cell pool in PPs. (**C**) Representative FACS of frequency of WT and *Ccr6*$^{+/+}$ or *Ccr6*$^{-/-}$ B cells expressing IgA or IgG1 in PPs from mixed BM chimeras. (**D**) Representative FACS staining (left) and frequency (right) of IgA$^+$ B cells among transferred B cells in MD4 recipient PPs after 7 days. (**E**) Fecal IgA from WT (Igh$^a$) and *Ccr6*$^{+/+}$ or *Ccr6*$^{-/-}$ (Igh$^b$) mixed BM chimeras as measured by allotypic ELISA. (**F**) Percentage of fecal bacteria coated with IgA$^a$ or IgA$^b$ measured by FACS from mixed BM chimeras as in (A). (**G**) Fecal CT-specific IgA from WT (Igh$^a$) and *Ccr6*$^{+/+}$ or *Ccr6*$^{-/-}$ (Igh$^b$) mixed BM chimeras orally treated with CT, measured by allotypic ELISA. (**H**) Fecal IgA from WT (Igh$^a$) and *Ccr6*$^{+/+}$ or *Ccr6*$^{-/-}$ (Igh$^b$) B cells cotransferred into either *Rag1*$^{-/-}$ or μMT, or from mixed BM chimeras as in (A), measured by allotypic ELISA. Each symbol in (A), (B), (E), (F), (G), and (H) represents an individual mouse, and data are pooled from at least three independent experiments. Data in (C) and (D) are representative of at least three independent experiments. $^{**}P < 0.01$, $^{***}P < 0.005$ (unpaired Student's *t* test).

undergo productive IgA class switching in PPs had a notable impact on mucosal IgA. In mixed chimeras, free IgA derived from CCR6-deficient B cells was underrepresented in fecal pellets (Fig. 2E), and CCR6-deficient B cells made a diminished contribution to the IgA coating intestinal bacteria (Fig. 2F). The role of CCR6 in controlling B cell class switching to IgA was not restricted to the homeostatic situation because after oral immunization of mixed BM chimeras with cholera toxin (CT), a potent lethal toxin that causes severe diarrhea, the IgA response was dominated by antibody derived from the wild-type B cells (Fig. 2G).

The IgA response against intestinal commensals is thought to involve both T-independent and T-dependent antibody production (*17*, *18*). Because the great majority of IgA$^+$ B cells in wild-type PPs are GC phenotype cells, we anticipated that the role of CCR6 in promoting IgA may be most prominent during T-dependent responses. To test this hypothesis, we transferred mixtures of wild-type Igh$^a$ and *Ccr6*$^{+/+}$ or *Ccr6*$^{-/-}$ Igh$^b$ B cells to mice lacking endogenous B cells and that were either T cell–deficient (*Rag1*$^{-/-}$) or T cell–replete (μMT). Allotype-specific analysis of fecal IgA 1 month later revealed that CCR6 was not required for B cells to mount a T-independent IgA response in the *Rag1*$^{-/-}$ hosts (Fig. 2H), whereas the response in the T cell–replete μMT hosts showed a CCR6 dependence similar to the responses in mixed BM chimeras (Fig. 2H). In accord with the CCR6-dependent secretory IgA responses occurring in PPs, when mixed BM chimeras were generated with lymphotoxin-β-receptor (LTβR)–deficient hosts that are unable to form PPs (*19*), B cell CCR6 expression did not influence total or commensal-bound fecal IgA (fig. S3G).

## IgA class switching is initiated in the subepithelial dome

To determine whether IgA class switch recombination (CSR) was initiating at the pre-GC stage, we examined IgA germline transcript (αGT) expression by semiquantitative and quantitative polymerase chain reaction (PCR) in naïve (IgD$^+$CCR6$^-$), pre-GC (IgD$^+$CCR6$^+$), GC (IgD$^-$CCR6$^-$), and memory (IgD$^-$CCR6$^+$) B cells from wild-type PPs. Pre-GC cells showed a significant increase in αGTs compared to naïve and GC B cells (Fig. 3, A and B). IgA GTs were also abundant in IgD$^-$CCR6$^+$ B cells, perhaps reflecting the presence of both late-stage pre-GC cells and memory-cell–derived pre-GC cells in this gate. Although IgA is the major memory B cell isotype, a fraction of the cells in this gate are unswitched (figs. S1A and S3H). We also detected mature, rearranged, Iμ-Cα transcripts and switch circle transcripts (Iα-Cμ) in the pre-GC cells, though in this case, the levels were higher in IgD$^-$CCR6$^-$ GC B cells, as expected from the high fraction of IgA$^+$ B cells in the GC (Fig. 3A). Consistent with switching initiating in the pre-GC compartment, activation-induced cytidine deaminase (AID) transcripts were elevated in pre-GC compared to naïve B cells (Fig. 3B), and the frequency of AID-GFP$^+$ cells was higher (Fig. 3C). Although AID expression was lower in pre-GC than in GC cells (Fig. 3B), the amounts of AID required for CSR are less than those required for somatic hypermutation of V regions (*20*).

## Lymphotoxin-dependent PP dendritic cells are required for IgA switching

On the basis of the above kinetic and anatomical findings, we reasoned that PP B cells might travel to the SED to receive a stimulus that dictated IgA class switching. The SED is a CD11c$^+$ Zbtb46$^+$ DC–rich area (Fig. 1A), containing mainly CD11b$^+$ and CD11b-CD8-double negative (DN) DCs, with CD8$^+$ DCs localized in the interfollicular region (IFR) (*4*, *9*, *21*, *22*). CD11c$^+$ DCs were minimally detected in PP GCs (fig. S4A). In vitro studies with human and mouse cells have shown that B cell–DC coculturing can augment IgA switching, though a role for such interactions in vivo has not

Downloaded from http://science.sciencemag.org/ on May 12, 2016

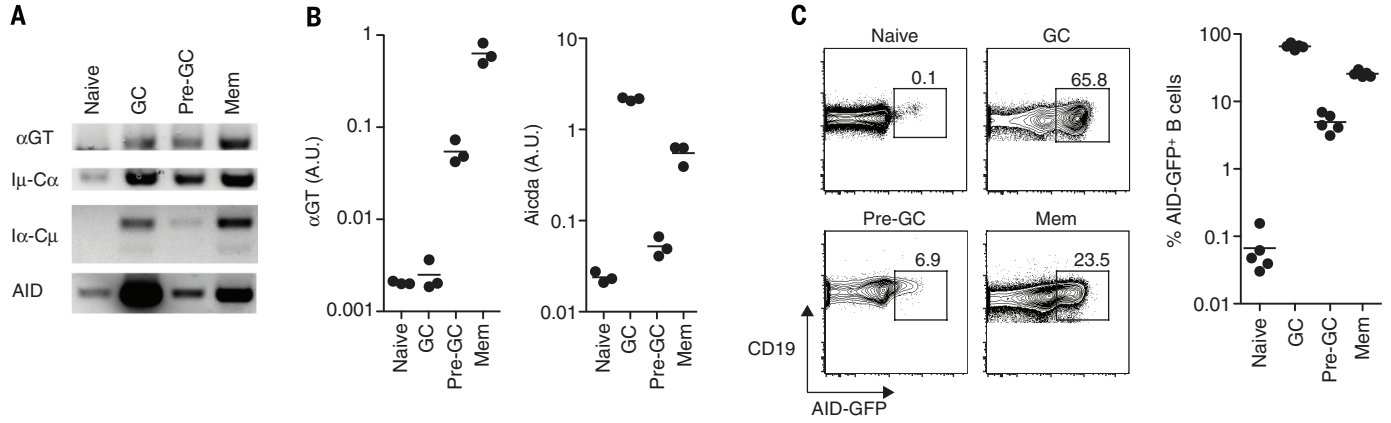


**Fig. 3. Pre-GC B cells in PPs initiate IgA class switching.** (**A** and **B**) Representative semiquantitative (A) or quantitative (B) RT-PCR on B cells from PPs sorted according to IgD and CCR6 expression, for the indicated transcripts. (**C**) Representative FACS staining (left) and frequency (right) of AID-GFP$^+$ PP B cells from reporter mice, according to IgD and CCR6 expression. Each symbol in (B) and (C) represents an individual mouse, and data are pooled from three independent experiments. Data in (A) are representative of three independent experiments. A.U., arbitrary units.

been established (*23*–*29*). To test whether SED DCs were important for B cell IgA switching, we sought to identify perturbations affecting these DCs. LTβR signaling contributes to CD11b$^+$ DC homeostasis in the spleen (*30*), but whether it has a role in maintaining DCs in PPs is unknown. Analysis of *Ltbr* transcripts in sorted DC subsets from PPs showed that CD11b$^+$ and DN DCs had high expression (Fig. 4A), and these cells were positive for surface LTβR by flow cytometry (Fig. 4A and fig. S4B). When wild-type mice were reconstituted with *Ltbr*$^{-/-}$ BM, they had a deficiency in CD11b$^+$ and DN DCs, whereas CD8$^+$ DCs were less affected (Fig. 4B). Notably, in these same chimeras, B cell switching to IgA was reduced, and switching to IgG1 was increased (Fig. 4C). A similar defect in the balance between IgA and IgG1 class switching was observed in *Ltbr*$^{-/-}$: Itgax-diphtheria toxin receptor (CD11c-DTR) mixed BM chimeras that had been treated with diphtheria toxin (DT) such that most DCs remaining in the animals were LTβR-deficient, whereas all hematopoietic CD11c$^-$ cell types were 50% wild-type (Fig. 4D). In a reciprocal experiment, we tested whether increased LTα1β2-LTβR signaling was sufficient to promote SED DC accumulation and IgA class switching by examining PPs from transgenic mice overproducing LTα1β2 (*30*). In these animals, CD11b$^+$ DCs were increased in number, and a greater fraction of GC B cells had switched to IgA compared to littermate controls (Fig. 4, E and F). The transcription factor BATF3 controls the development of CD8a$^+$ DCs (*31*), and mice reconstituted with *Batf3*$^{-/-}$ BM showed a near-absence of CD8a$^+$ DCs in PPs (fig. S4C). In these mice, B cell switching to IgA was normal (fig. S4D), indicating that CD8a$^+$ DCs are dispensable for PP IgA class switching.

A concern with the above studies was that chronic LTβR deficiency in DCs might lead to distant alterations such as changes in the microbiome that have indirect effects on IgA class switching. To address this concern, we used the adoptive transfer approach introduced above (Fig. 1C). Treatment with LTβR-Fc, an LTα1β2 antagonist, during the short period of the transfer decreased the number of CD11b$^+$ DCs (Fig. 4G) and reduced the ability of the transferred B cells to undergo IgA class switching (Fig. 4H), without affecting their participation in the GC reaction (Fig. 4H). Taken together, these findings provide strong evidence that LTβR signaling in DCs is directly required for promoting B cell IgA class switching.

## Innate lymphoid cells maintain PP dendritic cells required for IgA switching

Innate lymphoid cells type 3 (ILC3, also known as lymphoid tissue inducer cells) are an important source of LTα1β2 for LN and PP organogenesis and during mucosal immune responses (*1*, *29*, *32*, *33*). ILC3s in PPs expressed high levels of surface LTα1β2 (Fig. 5A). Although a previous study showed that ILC3-derived LT augmented lamina propria IgA responses, the mice analyzed in that study were PP-deficient, preventing any assessment of the ILC3 role in PP IgA responses (*29*). To test the importance of ILC3s in controlling IgA class switching in PPs, we reconstituted irradiated mice using BM cells deficient for RORγt, a transcription factor essential for ILC3 development (*34*). B cells in chimeras lacking ILC3s showed an impaired ability to undergo IgA class switching and an increased propensity to switch to IgG1 compared to B cells from wild-type chimeras (Fig. 5B). These findings suggested that RORγt$^+$ cells were critical in promoting IgA class switching. However, RORγt (encoded by *Rorc*) is expressed not only in ILC3s, but also in various T cell types (*35*). To further define the ILC contribution to B cell class switching, we reconstituted irradiated mice with wild-type BM, *Rorc*$^{-/-}$ BM, or a mixture of *Rorc*$^{-/-}$ and *Rag1*$^{-/-}$ BM. In the latter mice, the BM mixture could give rise to ILC3s (from the *Rag1*$^{-/-}$ BM) but none of the RORγt-dependent T cell populations. Notable, whereas animals lacking RORγt in all hematopoietic cell types showed decreased IgA and increased IgG1 class switching, the animals reconstituted with a mix of *Rorc*$^{-/-}$ and *Rag1*$^{-/-}$ BM showed IgA and IgG1 class switching similar to that of animals reconstituted with wild-type BM (Fig. 5C). Consistent with ILC3s promoting IgA switching via effects on DCs, the number of CD11b$^+$ and DN DCs was reduced in the chimeras lacking ILC3s (*Rorc*$^{-/-}$ chimeras) but not in those selectively lacking RORγt-dependent T cells (*Rorc*$^{-/-}$: *Rag1*$^{-/-}$ chimeras, fig. S5A). These results provide strong evidence that ILC3s are the only RORγt-dependent population critical in controlling B cell class switching to IgA in PPs.

To evaluate the effect of LT on ILC3s in controlling B cell class switching, we made *Rorc*$^{-/-}$: *Lta*$^{-/-}$ mixed BM chimeras. In such animals, all the RORγt$^+$ cells are LTα-deficient, whereas 50% of the RORγt$^-$ cells are wild-type for LTα. When ILC3s lacked LTα, GC B cells class switched preferentially to IgG1 over IgA (Fig. 5D). These mice also showed a deficiency in CD11b$^+$ and DN DCs, in accord with the dependence of these DCs on LTβR (fig. S5A). The ILC3-deficient mice also had a reduction in CD8$^+$ DCs, suggesting additional influences of these cells on DC maturation. Although B cells are an established source of LTα1β2 within follicles (*19*), they express considerably less of this cytokine than ILC3s (fig. S5B), and in chimeric animals selectively lacking LTα1β2 from B cells, PP GC IgA$^+$ cell frequencies and CD11b$^+$ DC frequencies were normal (fig. S5C). Finally, using RORγt-eGFP reporter mice to track RORγt$^+$ cell distribution in PPs, we found RORγt$^+$ CD3$^-$ ILC3s in the SED making contact with CD11c$^+$ DCs (Fig. 5E and fig. S5D). These results indicate that in PPs, B cell class switching is controlled by the LT-LTβR axis, likely through direct interaction between ILC3s expressing LTα1β2 and SED DCs expressing LTβR.

## B cells undergo prolonged interactions with PP subepithelial dome DCs

To determine whether B cells in the SED were interacting with DCs, we performed intravital imaging using two-photon laser-scanning microscopy (TPLSM). CD11c-YFP (yellow fluorescent protein) mice were injected with CFP$^+$ B cells, and

Downloaded from http://science.sciencemag.org/ on May 12, 2016

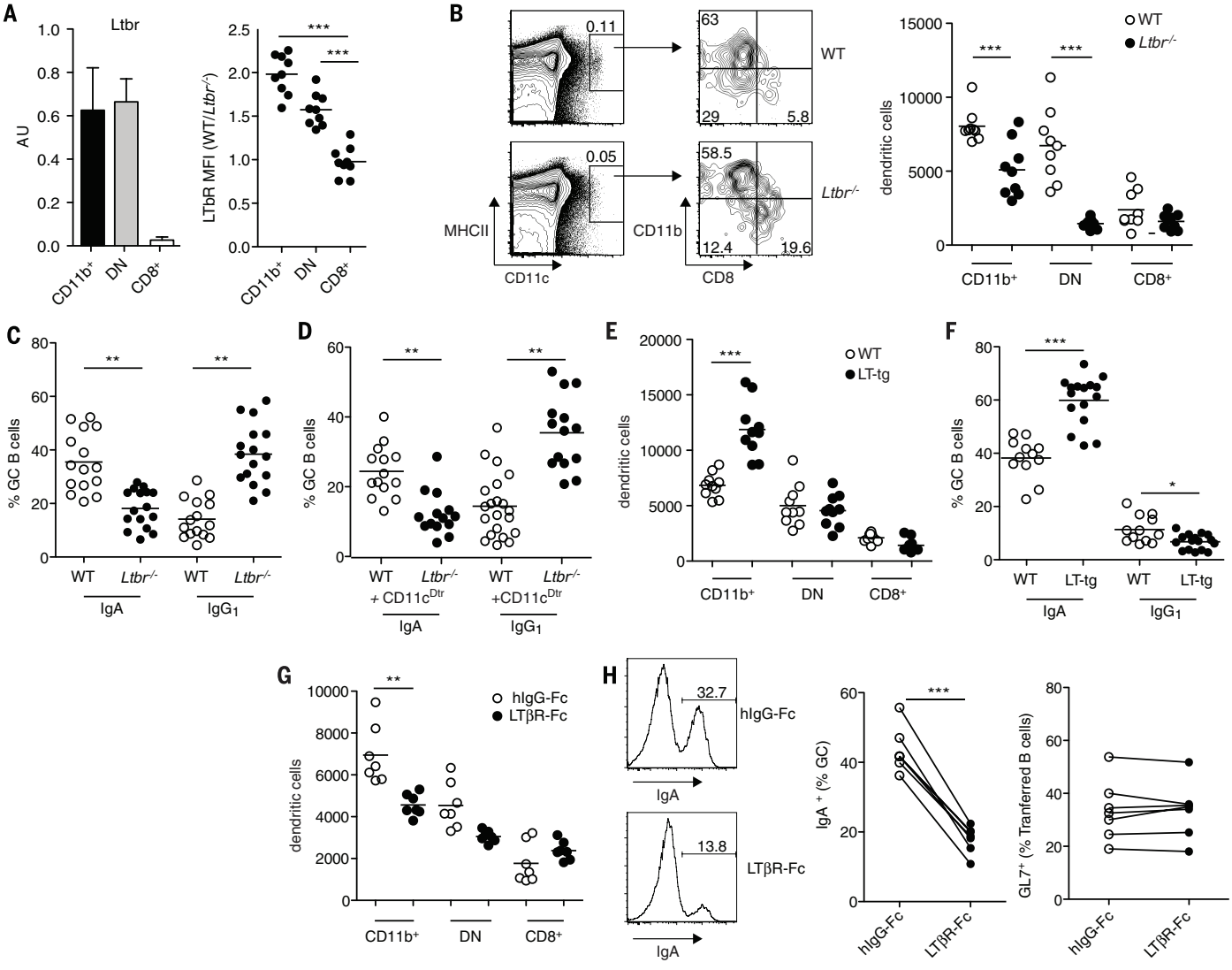


**Fig. 4. LTβR-dependent PP DC support IgA class switching.** (**A**) Quantitative PCR analysis of Ltbr transcript abundance in the indicated DC subsets from PPs (left) and median fluorescence intensity (MFI) ratio for LTβR on the DC subsets from PPs of BM chimeras reconstituted with WT or *Ltbr*$^{-/-}$ BM (right). (**B**) Representative FACS staining (left) and absolute cell number (right) of the indicated DC subset from PPs of BM chimeras reconstituted with WT or *Ltbr*$^{-/-}$ BM. (**C**) Frequency of IgA$^+$ and IgG1$^+$ GC B cells in PPs from BM chimeras as in (B), determined by FACS. (**D**) Frequency of IgA$^+$ and IgG1$^+$ GC B cells in PP from mixed chimeras reconstituted with CD11c-DTR and either *Ltbr*$^{+/+}$ or *Ltbr*$^{-/-}$ BM, treated with DT for 3 weeks. (**E**) Absolute number of the indicated DC subset from PPs of WT or LT-transgenic (tg) mice. (**F**) Frequency of IgA$^+$ and IgG1$^+$ GC B cells in PPs from WT or LT-tg mice, as determined by FACS. (**G**) Absolute number of the indicated DC subset from PPs of mice treated with LTβR-Fc or hIgG-Fc for 7 days. (**H**) Representative FACS staining of polyclonal B cells in PPs 7 days after transfer to MD4 recipients that were treated with LTβR-Fc or hIgG-Fc (left) and frequency of IgA$^+$ B cells and GC B cells in PPs among transferred B cells (right). Each symbol in (A), (B), (C), (D), (E), (F), (G), and (H) represents an individual mouse, and data are pooled from at least three independent experiments. In (B), (C), (D), (E), (F), (G), and (H), **P* < 0.05, ***P* < 0.01, ****P* < 0.005 (unpaired Student's *t* test); in (A), ****P* < 0.005 (one-way ANOVA with Bonferroni's post-hoc test).

10 to 14 days later, individual PPs were surgically exposed and stabilized for imaging by attachment to a platform placed over the mouse abdomen (*36*). Subepithelial dome B cells were identified as being situated in the YFP$^+$ cell-rich area just beneath the epithelial layer. Contours were drawn immediately internal to the YFP$^+$ cells in each *z*-plane and used to generate a three-dimensional surface to separate the SED and follicle (Fig. 6A and movie S1). B cells within the SED or follicle moved with similar velocities (Fig. 6B), but B cells within the SED showed smaller displacement, indicating a greater amount of confinement (Fig. 6C). On average, two-thirds of B cells in the SED engaged in short (Scan) or long (Pause) interactions with DCs during 30-min imaging sessions (Fig. 6, D and E, and movies S2 and S3). To examine B cell migration between follicle and SED, we manually annotated the tracks of cells that crossed between zones. As well as observing B cells migrating from the follicle into the SED, we observed B cells moving in the reverse direction, from the SED into the follicle, in some cases following long, seemingly directed tracks (Fig. 6F and movie S4). When B cells were incubated in vitro with CCL20, CCR6 became down-regulated (fig. S5E), and we suggest that ligand-mediated receptor desensitization over time allows follicular chemoattractant cues to dominate over CCL20 and attract cells away from the SED.

## DC integrin αvβ8 is required for TGFβ activation and induction of IgA switching

Because our findings indicated that interaction between B cells and DCs in the SED was required to achieve a successful IgA class switch, we investigated the factors involved in this interaction. Several molecules have been described as promoting IgA class switching in vivo (*26*, *28*, *37*);

Downloaded from http://science.sciencemag.org/ on May 12, 2016

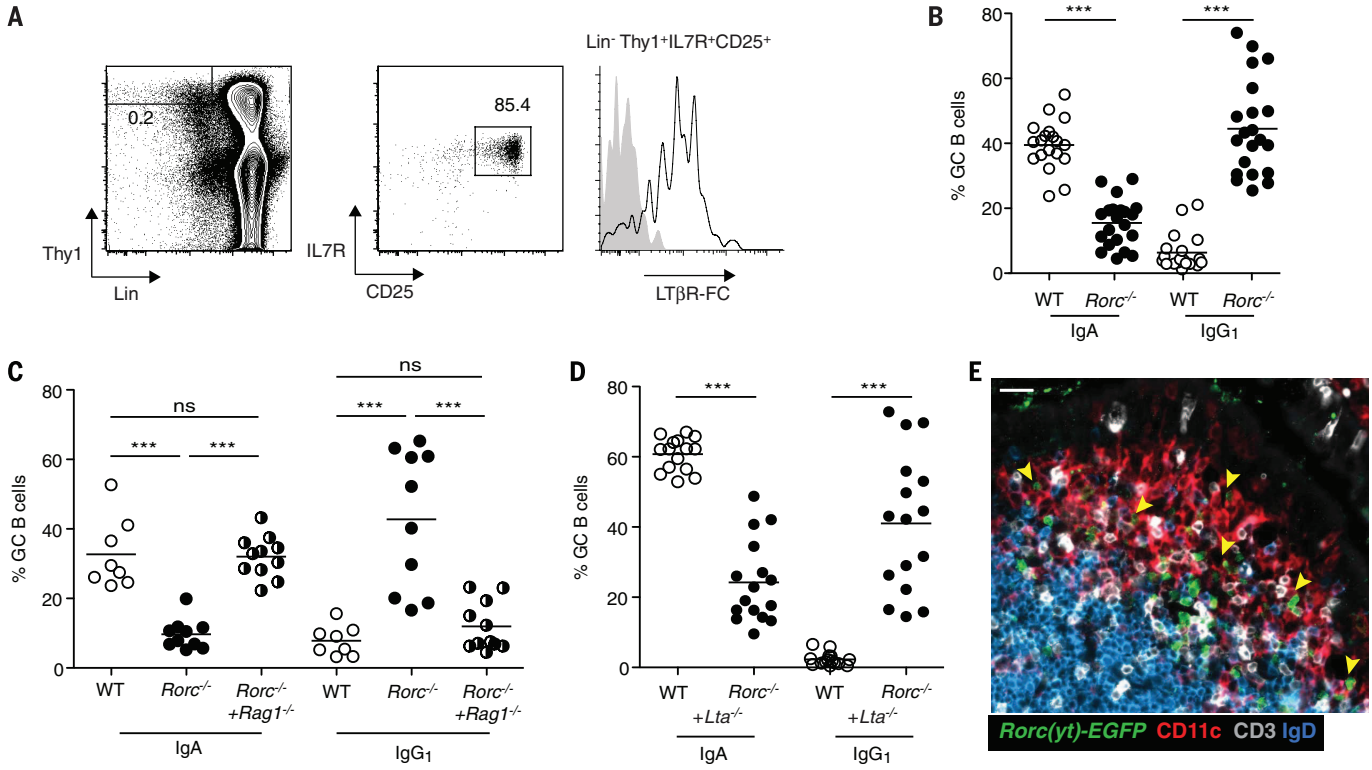


**Fig. 5. LT- and ILC3-dependence of PP IgA response.** (**A**) Representative FACS staining showing gating strategy and LTα1β2 on ILC3s in PP of WT mouse using LTβR-Fc. (**B**) Frequency of IgA$^+$ and IgG1$^+$ GC B cells in PPs from chimeras reconstituted with WT or *Rorc*$^{-/-}$ BM. (**C**) Frequency of IgA$^+$ and IgG1$^+$ GC B cells in PPs as determined by FACS in BM chimeras reconstituted with WT, *Rorc*$^{-/-}$, or a mix of *Rorc*$^{-/-}$ and *Rag1*$^{-/-}$ BM. (**D**) Frequency of IgA$^+$ and IgG1$^+$ GC B cells in PPs as determined by FACS in BM chimeras reconstituted with a mix of *Lta*$^{-/-}$ BM and either WT or *Rorc*$^{-/-}$ BM. (**E**) Representative immunofluorescence of PP SED from Rorc(γt)-EGFP mouse stained for the indicated markers. Yellow arrowheads indicate ILC3s proximal to DCs. Scale bar, 20 μm. Each symbol in (B), (C), and (D) represents an individual mouse, and data are pooled from at least three independent experiments. Data in (A) and (E) are representative of at least three independent experiments. In (B) and (D),***$P < 0.005$ (unpaired Student's *t* test); in (C), ***$P < 0.005$ (one-way ANOVA with Bonferroni's post-hoc test). ns, not significant.

however, the most profound phenotype has been reported in mice where TGF-βRII was specifically deleted in B cells (*6*). Activated B cells abundantly express TGFβ transcripts (*38*), and B cell deficiency in this cytokine leads to a reduction in fecal IgA (*7*). TGFβ activation can be mediated by αvβ6 or αvβ8 integrins binding to latency-associated peptide (LAP) and exerting forces that liberate the active cytokine (*39*). CD11b$^+$ and DN DCs in PPs showed abundant transcripts for the Itgb8 (β8) and Itgav (αv) integrin chains (Fig. 7A), and a subset of these DCs had surface expression of the integrin (Fig. 7B). We therefore tested whether DC expression of integrin β8 was required for IgA switching. Irradiated hosts reconstituted with BM from *Itgb8*$^{flox/flox}$ *Cd11c-Cre* mice showed a defect in IgA class switching in PP GCs and a propensity toward increased IgG1 class switching (Fig. 7C). By contrast, β8 deficiency did not affect the frequency of IgA$^+$ or IgG1$^+$ B cells in MLNs (fig. S5F). Short-term treatment with anti-β8 in vivo reduced the ability of transferred naïve B cells to undergo IgA class switching in PPs (Fig. 7D), making it unlikely that the switching defect was due to indirect effects of DC β8 deficiency. Moreover, when DCs deficient for β8 were sorted from PPs and cocultured in vitro with stimulated B cells, they failed to support IgA class switching, whereas control DCs supported robust IgA switching (Fig. 7E). Blocking TGFβ signaling in these B cell–DC cocultures with anti-TGFβ, anti-LAP, or anti-β8 reduced the ability of B cells to undergo IgA class switching (Fig. 7F). DC subset analysis revealed that CD11b$^+$ DCs could induce IgA class switching in vitro, in accord with their integrin β8 and LTβR expression (Fig. 7G). Finally, using BM-derived DCs, we found that LTβR engagement with an agonistic antibody led to a weak but reproducible induction of β8 integrin expression (Fig. 7H). Retinoic acid (RA) has an established role in augmenting IgA production, possibly through actions on DCs (*40*). RA treatment of the DC cultures led to a slightly greater β8 integrin induction than LTβR agonism, and when the two stimuli were combined, they acted in an additive manner (Fig. 7H).

The increased switching in vivo to IgG1 under conditions of reduced IgA switching may be a consequence of the ready availability of IL4 in PPs because it is highly expressed by PP Tfh cells (fig. S5G). Consistent with this interpretation, in irradiated hosts reconstituted with BM from IL4R-deficient mice, there was an almost complete absence of IgG1$^+$ cells in PPs (fig. S5H). Under normal conditions, TGFβ-mediated IgA switching may dominate, eliminating the intervening Ig constant regions and thereby limiting switching to IgG1.

## Discussion

These studies identify a network of cellular and molecular interactions underpinning the induction of IgA responses in PPs (fig. S6). After activation by foreign or commensal-derived antigen and receipt of CD40-dependent helper signals, PP B cells up-regulate CCR6 and are attracted by CCL20 into the SED, where they undergo extensive interactions with CD11b$^+$ DCs. This DC population is maintained by LTα1β2 provided locally by ILC3s. CD11b$^+$ DCs express integrin αvβ8 and promote TGFβ activation during interactions with B cells. After receipt of TGFβ and likely additional SED-derived signals, B cells return to the follicle by directed migration and participate in the GC response.

Our studies indicate that sustained CCR6 up-regulation in PP B cells occurs in a CD40-, and thus most likely T cell–dependent, manner, and CCR6 deficiency strongly affected T-dependent IgA responses. How CD40 signaling promotes sustained CCR6 expression is not yet clear. Because BCR engagement is sufficient to promote CCR6

Downloaded from http://science.sciencemag.org/ on May 12, 2016

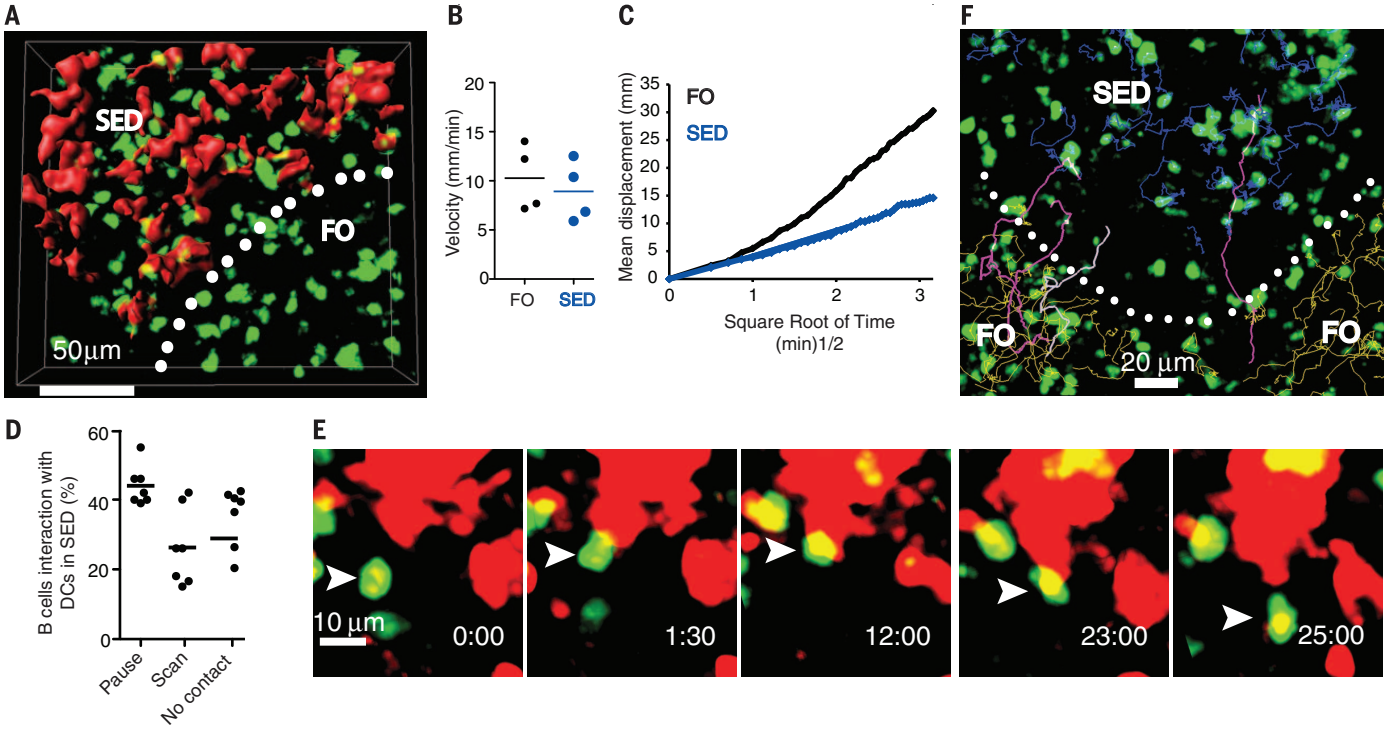


**Fig. 6. PP B cell migration dynamics and interaction with SED DCs.** (**A**) Representative TPLSM of PP for transferred CFP$^+$ B cells (green) in CD11c-YFP mice. YFP$^+$ cells (red) are shown by volume rendering. White dotted line indicates location of the SED. (**B**) Median velocity and (**C**) displacement versus square root of time of B cells in follicle (black) and in the SED (blue). (**D**) Percentage of B cells in the SED pausing (Pause), scanning (Scan), or not contacting (No contact) CD11c-YFP$^+$ cells. (**E**) Representative time-lapse images of CFP$^+$ B cell interaction with CD11c-YFP$^+$ cell in the SED. Arrowheads highlight a single B cell–DC interaction. (Yellow color is due to bleed-through between channels.) Time is shown in minutes:seconds. (**F**) Representative *z*-projection view of PP follicle and SED of the type in (A), showing only the CFP$^+$ B cells. White dotted line, SED–follicle border; yellow lines, tracks of B cells in the follicle; blue lines, tracks of B cells in the SED; pink lines, tracks of B cells moving from the SED to the follicle; white lines, tracks of B cells moving from the follicle to the SED. Each symbol in (B) and (D) represents an individual mouse, and data are pooled from at least three independent experiments. Data in (A), (C), (E), and (F) are representative of at least three independent experiments.

up-regulation in vitro, it remains possible that CCR6 augments certain T-independent IgA responses, with expression perhaps being sustained by other inputs such as from Toll-like receptor ligands. It is notable that memory B cells in PPs have high amounts of CCR6, and we speculate that they have privileged access to the SED, perhaps facilitating more rapid exposure to newly arriving antigens.

A key source of TGFβ1 for intestinal IgA production is the B cells themselves (*7*). However, B cell TGFβ1 deficiency does not cause a complete block in IgA production. Given the widespread expression of TGFβ family members (Immgen.org), we consider it likely that more than one cell type contributes latent TGFβ for DC-mediated activation and triggering of IgA switching. A number of other signals have been implicated in promoting IgA production, including RA, inducible nitric oxide synthase (iNOS), APRIL, and interleukin-6 (IL-6) (*24*, *28*, *37*, *40*), and our studies do not exclude a role for these mediators in directly or indirectly supporting IgA class switching in PPs. In particular, we suggest that RA helps establish an environment where αvβ8$^+$ DCs can develop or be maintained. Although β8-integrin–deficient mice were not reported to have reduced serum IgA (*41*), these mice suffer from inflammatory disease due to regulatory T cell ($T_{reg}$) deficiency, and this likely allows other factors to induce IgA switching or to generate active TGFβ. Consistent with our findings, a recent study of lung DCs noted a correlation between DC *Itgb8* transcript expression and induction of TGFβ-dependent IgA switching (*42*). We speculate that during B cell–DC interactions in PP SEDs, synaptic contacts form where DC αvβ8 exerts force on TGFβ-LAP tethered on the B cell, leading to TGFβ activation (*39*) and engagement of B cell TGFβR to induce isotype switching. By defining a network of interactions required for IgA switching, this study identifies approaches that could be used to augment IgA responses while also defining sites for defects that could underlie IgA deficiency, the most common immune deficiency syndrome in humans (*43*).

## Methods

### Mice

Wild-type and Ly5.2 (CD45.1) congenic C57BL/6 (B6) mice, 6 to 12 weeks old, were from the National Cancer Institute. *Lta*$^{-/-}$, *Ltbr*$^{-/-}$, *Igh*$^a$, *MD4-Ig tg*, and *Lt-tg* [line *Ltb*10 (*44*)] mice were from an internal colony. *Itgax (Cd11c)-cre Itgb8fl/fl* mice (*41*) were backcrossed to C57BL/6J for 10 generations. *Itgax-DTR*, *Ccr6*$^{-/-}$, *Rorc*$^{-/-}$, *Rag1*$^{-/-}$, *Batf3*$^{-/-}$, *Cd40*$^{-/-}$, and AID-GFP mice were from Jackson laboratories. IL4-hCD2 (KN2) and *Il4ra*$^{-/-}$ mice were kindly provided by the Locksley lab. Animals were housed in a specific pathogen-free environment in the Laboratory Animal Research Center at the University of California San Francisco (UCSF), and all experiments conformed to the ethical principles and guidelines approved by the UCSF Institutional and Animal Care and Use Committee.

### Flow cytometry

Spleen, PPs, and mLN cell suspensions were generated by mashing the organs through 70-μm cell strainers. For DC isolation, PPs and mLN were digested with 1.6 mg of type II collagenase (Worthington Biochemical) and deoxyribonuclease I for 10 min at 37°C. Digested PPs were mashed into a single cell suspension through a 70-μm cell strainer in phosphate-buffered saline (PBS) buffers containing 2% fetal calf serum and 2 mM EDTA. Cells were stained with antibodies to CD4 (GK1.5), B220 (RA3-6B2), CD19 (1D3), IgD (11-26c.2a), CD95 (Jo2), GL7, CD38 (90), CCR6 (140706), CD8 (53), MHCII (AF6-120.1), IgA (1040-09), IgG1 (RMA1-1), CD11c (N418), CD11b (M1/70), CD45.1 (A20), CD45.1 (104) (from Biolegend, BD Biosciences, rnBiotech, or eBioscience). Biotin conjugates were detected with streptavidin Qdot605 (Invitrogen). To detect intracellular IgA, cells were stained with fixable viability dye (eFluor780; eBioscience) to

Downloaded from http://science.sciencemag.org/ on May 12, 2016

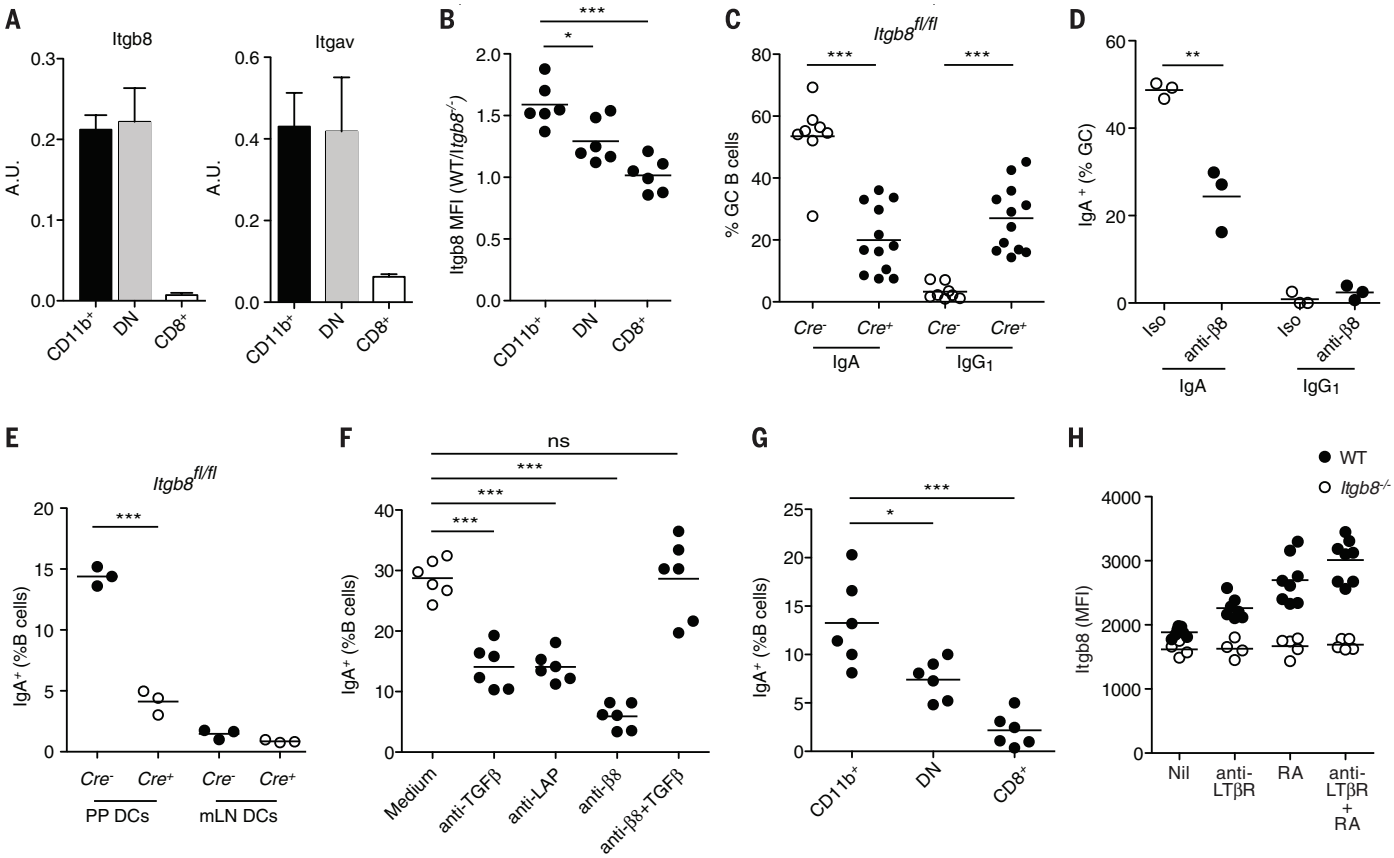


**Fig. 7. DC integrin-β8 promotes TGFβ-dependent IgA switching.** (**A**) Quantitative PCR analysis of Itgb8 (left) and Itgav (right) transcript abundance in the indicated DC subsets from PPs. (**B**) Median fluorescence intensity (MFI) ratio for β8 on the indicated DC subsets from PPs of either CD11c-Cre$^-$ (WT) or CD11c-Cre$^+$ *Itgb8*$^{fl/fl}$ mice. (**C**) Frequency of IgA$^+$ and IgG1$^+$ GC B cells in PPs of either CD11c-Cre$^-$ or CD11c-Cre$^+$ *Itgb8*$^{fl/fl}$ mice as determined by FACS. (**D**) Frequency of IgA$^+$ and IgG1$^+$ GC B cells in PPs 7 days after adoptive transfer in MD4 mice and treatment with either isotype control or anti-β8. (**E**) Frequency of IgA$^+$ splenic B cells upon 5 days of culture with DCs sorted from PPs or mLNs of CD11c-Cre$^-$ or CD11c-Cre$^+$ *Itgb8*$^{fl/fl}$ mice. (**F**) Frequency of IgA$^+$ splenic B cells upon 5 days of culture with DCs sorted from PPs and incubated with the indicated antibodies. (**G**) Frequency of IgA$^+$ splenic B cells upon 5 days of culture with the indicated DC subset sorted from PPs. (**H**) Median fluorescence intensity (MFI) for β8 on the BMDCs generated from CD11c-Cre$^-$ or CD11c-Cre$^+$ *Itgb8*$^{fl/fl}$ BM upon 7 days of culture and incubation with the indicated reagents. Each symbol in (B), (C), (D), (E), (F), (G), and (H) represents an individual mouse, and data are pooled from at least three independent experiments. Data in (A) are pooled from three independent experiments. In (B), (F), and (G), *$P$ < 0.05, **$P$ < 0.01, ***$P$ < 0.005 (one-way ANOVA with Bonferroni's post-hoc test); in (C), (D), and (E), **$P$ < 0.01, ***$P$ < 0.005 (unpaired Student's $t$ test).

exclude dead cells then stained for surface antigens, treated with BD Cytofix Buffer and Perm/Wash reagent (BD Biosciences), and stained with anti-IgA.

### *Immunohistochemistry and immunofluorescence microscopy*

For immunohistochemistry, cryosections of 7 μm were acetone fixed and stained as described (*45*) with combinations of the following antibodies: anti-IgD (11-26c.2a, BD Biosciences), anti-IgD$^a$ (AMS9.1, BD Biosciences), anti-IgD$^b$ (217-170, BD Biosciences), and anti-IgM$^a$ (DS-1, BD Biosciences). In some case, the slides were counterstained with hematoxylin. For immunofluorescence, tissues were fixed in 4% paraformaldehyde in PBS for 2 hours at 4°C, washed three times for 10 min in PBS, then moved to 30% sucrose in PBS overnight. Tissues were flash frozen in Tissue-Tek Cryomold (VWR) the next day, and 7-μm sections were cut and then dried for 1 hour before staining. Sections were rehydrated in PBS with 1% bovine serum albumin (BSA) for 10 min and then stained in primary antibody overnight at 4°C and stained for subsequent steps for 2 hours at room temperature, all in PBS with 1% BSA, 2% mouse serum, and 2% rat serum. Sections were stained with primary antibodies: Rabbit anti-GFP (polyclonal, Life Technologies), goat anti-mouse IgD (goat polyclonal GAM/IGD(FC)/7S, Cedarlane Labs), Alexa647-conjugated anti-CD11c (N418, Biolegend), and PE-conjugated anti-CD3 (17A2, Biolegend). Sections were then stained with the following secondary antibodies: Alexa488-conjugated donkey anti-rabbit (A-21206, Life Technologies) and aminomethylcoumarin (AMCA)–conjugated donkey anti-goat (705-156-147, Jackson Immunoresearch).

### *Cell transfer, immunization, and transwell assays*

For MD4 B cell positioning analysis, (1 to 2) × $10^7$ MD4 wild-type (WT) or MD4 Ccr6$^{-/-}$ B cells were transferred in C57BL/6 recipients for 3 days before immunizing with 5 mg of hen egg lysozyme (HEL) intravenously (i.v.), and PPs were harvested at different time points. For polyclonal B cell transfer, MD4 WT recipients were adoptively transferred with (1 to 2) × $10^7$ splenic B cells from congenic C57BL/6 for the indicated time. In some cases, B cells were stained with CellTrace Violet (Life Technologies) according to the manufacturer's protocol. For LTβR-Fc treatment, mice were treated with LTβR-Fc protein (provided by J. Browning) by i.v. injection of 100 μg of protein every 3.5 days for 7 days. For anti-Itgβ8 treatment, mice were treated with neutralizing antibody by i.v. injection of 10 mg of antibody per kilogram of body weight every 3.5 days for 7 days. For anti-CD40L treatment, mice were treated with neutralizing antibody by i.v. injection of 1 mg of anti-mouse CD40L (clone MR1) every 3.5 days for 7 days. For cholera toxin immunization, mice were injected three times orally with 10 μg of cholera toxin (CT) (EMD Bioscience), oral immunizations were performed 7 days apart, and mice were analyzed 7 days after the final immunization. Transwell migration assays were done with 5-μm transwells using $10^6$ digested PP cells and enumeration of transmigrated cells by flow cytometry as previously described (*46*).

Downloaded from http://science.sciencemag.org/ on May 12, 2016

Chemokines were obtained from PeproTech or R&D Systems.

### Sorting

For DC sorting, PPs and mLNs were digested and stained as described above and sorted on a FACSAira III with a 70-μm nozzle. In same cases, DCs were isolated from PPs of 8- to 10-week-old mice that had been injected subcutaneously in the flank with $5 \times 10^6$ B16 murine Flt3L-secreting tumor cells 7 to 10 days earlier. This treatment led to a ~10-fold expansion in total PP DC numbers.

### Bone marrow chimeras, retroviral transduction, and DT treatment

Ly5.2 congenic B6 mice were lethally irradiated with either 1100 or 1300 rad in split doses and reconstituted with (1 to 3) $\times 10^6$ BM cells from the indicated donors. Mice were analyzed 10 to 14 weeks later. For retroviral transduction, PlatE cells were transfected with murine stem cell virus (MSCV) retroviral constructs encoding full-length mouse Ccr6 with Lipofectamine 2000 (Invitrogen) following the manufacturer's protocol. For transduction of BM-derived cells, BM cells were harvested 4 days after 5-flurouracil (Sigma) injection and cultured in the presence of recombinant IL-3, IL-6, and mouse stem cell factor (SCF) (100 ng/ml, Peprotech). BM cells were spin-infected twice with a retroviral construct expressing Ccr6 and an internal ribosomal entry site (IRES)–Thy1.1 cassette as a reporter. One day after the last spin infection, the cells were injected into lethally irradiated C57BL/6 recipients. Eight to 12 weeks later, splenic B cells were isolated and then injected in C57BL/6 recipients, and their positioning in PP was assessed 3 days later. For DT treatments, BM chimeras received 4 ng of DT (EMD Bioscience) per gram of body weight every 72 hours for 3 weeks.

### Rag1$^{-/-}$ and μMT cells transfer

Splenic B cells were sorted on a FACSAira III with a 70-μm nozzle as CD3, CD43, CD4, CD8, CD11c, Ly6C, Ly6G, CD90 neg, and $10^6$ cells from each genotype were transferred i.v. Recipients were analyzed 4 weeks later.

### Enzyme-linked immunosorbent assay (ELISA)

Ninety-six–well plates (Thermo Fisher Scientific) were coated with purified anti-IgA (RMA-1, BD) or 0.5 nmol/ml monosialotetrahexosylganglioside (GM1) (Sigma-Aldrich) followed by 0.5 μg/ml CT overnight at 4°C (*47*). The plates were washed and clocked with PBS–5% BSA before diluted fecal samples were added and twofold serial dilution was made. Samples were incubated overnight at 4°C, followed by biotinylated anti-mouse antibodies: anti-IgA (C10-1, BD), anti-IgA$^a$, and anti-IgA$^b$ (Hy16 and HISM2, UCSF Hybridoma Core) at 1 μg/ml in PBS–0.1% BSA. Detection antibodies were labeled by streptavidin-conjugated horseradish peroxidase and visualized by the addition of Substrate Reagent Pack (R&D). Color development was stopped with 3 M $H_2SO_4$. Purified mouse IgA (Southern Biotech) served as standard. Absorbances at 450 nm were measured on a tunable microplate reader (VersaMax, Molecular Devices). Antibody titers were calculated by extrapolating absorbance values from standard curves where known concentrations were plotted against absorbance using SoftMax Pro 5 software.

### Flow cytometric analysis of IgA-bound bacteria

Flow cytometric analysis of gut bacteria in feces was done as described (*48*). Briefly, fecal pellets were suspended in filtered PBS (100 μl to 10 mg of feces), homogenized well, and centrifuged at 400*g* for 5 min to remove larger particles from the fecal suspension. Supernatant containing bacteria was centrifuged at 8000*g* for 10 min. The bacterial pellet was blocked on ice in 1 ml of BSA-PBS (1% w/v) for 15 min. Samples were spun at 8000*g* for 10 min. Bacteria were stained with anti-IgA$^a$ and anti-IgA$^b$ on ice for 20 min and washed with PBS. Finally, bacterial pellets were resuspended in SYBR green I [1/10000 (v/v) dilution Life Technologies] and analyzed with an LSRII flow cytometer.

### RNA isolation and real-time reverse transcription–polymerase chain reaction (RT-PCR)

Total RNA was isolated from sorted DCs and B cells from PPs with the TRIzol reagent (Life Technologies) following the manufacturer's protocol. Real-time PCR was performed with SYBR Green PCR Mix (Roche) and an ABI prism 7300 sequence detection system (Applied Biosystems, Foster City, CA).

*Hprt* forward: AGGTTGCAAGCTTGCTGGT; reverse: TGAAGTACTCATTATAGTCAAGGGCA

*Ltbr* forward: CCAGATGTGAGATCCAGGGC; reverse: GACCAGCGACAGCAGGATG

*Itgb8* forward: CTGAAGAAATACCCCGTGGA; reverse: ATGGGGAGGCATACAGTCT

*Itgav* forward: CGCCTATCTTCGGGATGAATC; reverse: CCAACCGATACTCCATGAAAA

*aGT* forward: CCAGGCTAGACAGAGGCAAG; reverse: CGGAAGGGAAGTAATCGTGA

*Aicda* forward: GCCAAGGGACGGCATGAG; reverse: GATGTAGCGTAGGAACAACAA

Semiquantitative RT-PCR on sorted B cells for AID, alpha germline transcripts (αGT), Iμ-Cα, and Iα-Cμ were amplified with primers and conditions described before (*26*).

### In vitro culture

For CCR6 up-regulation, splenic B cells were stimulated with 10 μg/ml anti-IgM [F(ab′)2 goat anti-mouse IgM, Jackson Immunoresearch] for the indicated time. For IgA class switch B-DC coculture experiments, magnetic cell sorter (MACS)–isolated splenic B cells (typically at 50,000 cells per well) were stimulated with 10 μg/ml anti-IgM and 20 μg/ml anti-CD40 (clone FGK4.5, UCSF Hybridoma Core) in the presence or absence of sorted DCs at a ratio of 1:1 for 5 days. The sorted DCs were from PPs of untreated mice in all cases except for the experiment involving sorted DC subsets, where they were from B16-Flt3L–treated mice. For IgA class switching in the absence of DCs, MACS-isolated splenic B cells were stimulated with 10 μg/ml anti-IgM and 20 μg/ml anti-CD40 (clone FGK4.5, UCSF Hybridoma Core) in the presence of TGFβ (2 ng/ml) and RA (100 nM) for 5 days.

For BMDCs, $5 \times 10^6$ BM cells were cultured in 10-cm tissue culture dishes in 10 ml of medium supplemented with supernatants from 3T3 cells transfected with the gene-encoding murine GM-CSF (granulocyte-macrophage colony-stimulating factor) for 7 days. Cells were treated with 1 μg/ml LTβR agonistic antibody (clone 3C8) and 100 nM RA every 3.5 days for 7 days.

### Intravital two-photon laser-scanning microscopy (TPLSM) of PPs

Mice were anesthetized by intraperitoneal injection of 10 ml kg$^{-1}$ saline containing xylazine (1 mg ml$^{-1}$) and ketamine (5 mg ml$^{-1}$). Maintenance doses of intramuscular injections of 4 ml kg$^{-1}$ of xylazine (1 mg ml$^{-1}$) and ketamine (5 mg ml$^{-1}$) were given approximately every 30 min. An incision was made in the abdominal wall, and the small intestine was gently stretched and scanned by eye to identify PP structures. Only small areas (1 to 2 cm long) were exposed at any time. Once a PP was located, the area was embedded in warm saline and stabilized by placing a spring-loaded platform over the mouse and screwed down until the cover glass made contact with the PP. The tissue was placed with the interface between the intestinal lumen and PP facing upwards in an orientation that allowed maximal viewing of the SED. The mouse was placed on a Biotherm stage warmer at 37°C (Biogenics) for the duration of the imaging. Images were acquired with ZEN2009 (Carl Zeiss) with a 7MP two-photon microscope (Carl Zeiss) equipped with a Chameleon laser (Coherent). For video acquisition, a series of planes of 2- or 3-μm *z*-spacing spanning a depth of 30 to 69 μm were collected every 15 to 20 s. Excitation wavelengths were 850 to 890 nm. Because most of the transferred CFP$^+$ B cells occupied the follicular compartment, we used automated tracks (generated by Imaris 7.4.2 ×64, Bitplane) to highlight the follicular region, as previously described (*36*). The SED was identified by the presence of CD11c-YFP DCs and by its typical shape and location above the follicles. The interfollicular regions, which are also rich with CD11c-YFP DCs, were identified on the basis of their distinct positioning and were excluded from analysis. Videos were made and analyzed with Imaris 7.4.2 ×64 (Bitplane). To track cells, surface seed points were created and tracked over time. Tracks were manually examined and verified. Data from cells that could be tracked for at least 15 min were used for analysis. Data presented in Fig. 6 were collected from four independent movies, some of which were split into 2 by 30 min segments and analyzed with Imaris (Bitplane AG), MATLAB (MathWorks), and MetaMorph software. In Fig. 6D, the contact time between B cells and DCs in the SED was measured manually ($n$ = 150 B cells, derived from four independent movies). The behavior of a B cell engaged in prolonged interactions was defined as "Pause" (5 to 25 min of contact time), "Scan" (2 to 5 min of contact time), or "No contact" when

Downloaded from http://science.sciencemag.org/ on May 12, 2016

spending less than 2 min in association with a DC. Statistical analysis was performed with Prism software (GraphPad Software).

## REFERENCES AND NOTES


1. S. Fagarasan, S. Kawamoto, O. Kanagawa, K. Suzuki, Adaptive immune regulation in the gut: T cell-dependent and T cell-independent IgA synthesis. *Annu. Rev. Immunol.* **28**, 243–273 (2010). doi: 10.1146/annurev-immunol-030409-101314; pmid: 20192805
2. E. Slack, M. L. Balmer, A. J. Macpherson, B cells as a critical node in the microbiota-host immune system network. *Immunol. Rev.* **260**, 50–66 (2014). doi: 10.1111/imr.12179; pmid: 24942681
3. S. W. Craig, J. J. Cebra, Peyer's patches: An enriched source of precursors for IgA-producing immunocytes in the rabbit. *J. Exp. Med.* **134**, 188–200 (1971). doi: 10.1084/jem.134.1.188; pmid: 4934147
4. A. Iwasaki, B. L. Kelsall, Localization of distinct Peyer's patch dendritic cell subsets and their recruitment by chemokines macrophage inflammatory protein (MIP)-3alpha, MIP-3beta, and secondary lymphoid organ chemokine. *J. Exp. Med.* **191**, 1381–1394 (2000). doi: 10.1084/jem.191.8.1381; pmid: 10770804
5. F. W. van Ginkel *et al.*, Partial IgA-deficiency with increased Th2-type cytokines in TGF-beta 1 knockout mice. *J. Immunol.* **163**, 1951–1957 (1999). pmid: 10438931
6. B. B. Cazac, J. Roes, TGF-beta receptor controls B cell responsiveness and induction of IgA in vivo. *Immunity* **13**, 443–451 (2000). doi: 10.1016/S1074-7613(00)00044-3; pmid: 11070163
7. M. J. Gros, P. Naquet, R. R. Guinamard, Cell intrinsic TGF-beta 1 regulation of B cells. *J. Immunol.* **180**, 8153–8158 (2008). doi: 10.4049/jimmunol.180.12.8153; pmid: 18523280
8. D. N. Cook *et al.*, CCR6 mediates dendritic cell localization, lymphocyte homeostasis, and immune responses in mucosal tissue. *Immunity* **12**, 495–503 (2000). doi: 10.1016/S1074-7613(00)80201-0; pmid: 10843382
9. R. Varona *et al.*, CCR6-deficient mice have impaired leukocyte homeostasis and altered contact hypersensitivity and delayed-type hypersensitivity responses. *J. Clin. Invest.* **107**, R37–R45 (2001). doi: 10.1172/JCI11297; pmid: 11254677
10. X. Zhao *et al.*, CCL9 is secreted by the follicle-associated epithelium and recruits dome region Peyer's patch CD11b+ dendritic cells. *J. Immunol.* **171**, 2797–2803 (2003). doi: 10.4049/jimmunol.171.6.2797; pmid: 12960300
11. M. Ebisawa *et al.*, CCR6hiCD11c(int) B cells promote M-cell differentiation in Peyer's patch. *Int. Immunol.* **23**, 261–269 (2011). doi: 10.1093/intimm/dxq478; pmid: 21422150
12. T. Kucharzik, J. T. Hudson 3rd, R. L. Waikel, W. D. Martin, I. R. Williams, CCR6 expression distinguishes mouse myeloid and lymphoid dendritic cell subsets: Demonstration using a CCR6 EGFP knock-in mouse. *Eur. J. Immunol.* **32**, 104–112 (2002). doi: 10.1002/1521-4141(200201)32:1<104::AID-IMMU104>3.0.CO;2-C; pmid: 11754009
13. T. A. Schwickert, B. Alabyev, T. Manser, M. C. Nussenzweig, Germinal center reutilization by newly activated B cells. *J. Exp. Med.* **206**, 2907–2914 (2009). doi: 10.1084/jem.20091225; pmid: 19934021
14. J. J. Taylor, K. A. Pape, M. K. Jenkins, A germinal center-independent pathway generates unswitched memory B cells early in the primary response. *J. Exp. Med.* **209**, 597–606 (2012). doi: 10.1084/jem.20111696; pmid: 22370719
15. F. Liao, A. K. Shirakawa, J. F. Foley, R. L. Rabin, J. M. Farber, Human B cells become highly responsive to macrophage-inflammatory protein-3 alpha/CC chemokine ligand-20 after cellular activation without changes in CCR6 expression or ligand binding. *J. Immunol.* **168**, 4871–4880 (2002). doi: 10.4049/jimmunol.168.10.4871; pmid: 11994436
16. K. G. McDonald *et al.*, CC chemokine receptor 6 expression by B lymphocytes is essential for the development of isolated lymphoid follicles. *Am. J. Pathol.* **170**, 1229–1240 (2007). doi: 10.2353/ajpath.2007.060817; pmid: 17392163
17. A. J. Macpherson *et al.*, A primitive T cell-independent mechanism of intestinal mucosal IgA responses to commensal bacteria. *Science* **288**, 2222–2226 (2000). doi: 10.1126/science.288.5474.2222; pmid: 10864873
18. J. J. Bunker *et al.*, Innate and adaptive humoral responses coat distinct commensal bacteria with immunoglobulin A. *Immunity* **43**, 541–553 (2015). doi: 10.1016/j.immuni.2015.08.007; pmid: 26320660
19. J. L. Gommerman, J. L. Browning, Lymphotoxin/light, lymphoid microenvironments and autoimmune disease. *Nat. Rev. Immunol.* **3**, 642–655 (2003). doi: 10.1038/nri1151; pmid: 12974479
20. L. S. Yeap *et al.*, Sequence-intrinsic mechanisms that target AID mutational outcomes on antibody genes. *Cell* **163**, 1124–1137 (2015). doi: 10.1016/j.cell.2015.10.042; pmid: 26582132
21. B. L. Kelsall, W. Strober, Distinct populations of dendritic cells are present in the subepithelial dome and T cell regions of the murine Peyer's patch. *J. Exp. Med.* **183**, 237–247 (1996). doi: 10.1084/jem.183.1.237; pmid: 8551227
22. A. Iwasaki, B. L. Kelsall, Unique functions of CD11b+, CD8 alpha+, and double-negative Peyer's patch dendritic cells. *J. Immunol.* **166**, 4884–4890 (2001). doi: 10.4049/jimmunol.166.8.4884; pmid: 11290765
23. J. Fayette *et al.*, Human dendritic cells skew isotype switching of CD40-activated naive B cells towards IgA1 and IgA2. *J. Exp. Med.* **185**, 1909–1918 (1997). doi: 10.1084/jem.185.11.1909; pmid: 9166420
24. M. B. Litinskiy *et al.*, DCs induce CD40-independent immunoglobulin class switching through BLyS and APRIL. *Nat. Immunol.* **3**, 822–829 (2002). doi: 10.1038/ni829; pmid: 12154359
25. A. J. Macpherson, T. Uhr, Induction of protective IgA by intestinal dendritic cells carrying commensal bacteria. *Science* **303**, 1662–1665 (2004). doi: 10.1126/science.1091334; pmid: 15016999
26. J. R. Mora *et al.*, Generation of gut-homing IgA-secreting B cells by intestinal dendritic cells. *Science* **314**, 1157–1160 (2006). doi: 10.1126/science.1132742; pmid: 17110582
27. M. Tsuji *et al.*, Requirement for lymphoid tissue-inducer cells in isolated follicle formation and T cell-independent immunoglobulin A generation in the gut. *Immunity* **29**, 261–271 (2008). doi: 10.1016/j.immuni.2008.05.014; pmid: 18656387
28. H. Tezuka *et al.*, Regulation of IgA production by naturally occurring TNF/iNOS-producing dendritic cells. *Nature* **448**, 929–933 (2007). doi: 10.1038/nature06033; pmid: 17713535
29. A. A. Kruglov *et al.*, Nonredundant function of soluble LTα3 produced by innate lymphoid cells in intestinal homeostasis. *Science* **342**, 1243–1246 (2013). doi: 10.1126/science.1243364; pmid: 24311691
30. K. Kabashima *et al.*, Intrinsic lymphotoxin-beta receptor requirement for homeostasis of lymphoid tissue dendritic cells. *Immunity* **22**, 439–450 (2005). doi: 10.1016/j.immuni.2005.02.007; pmid: 15845449
31. B. T. Edelson *et al.*, CD8α(+) dendritic cells are an obligate cellular entry point for productive infection by Listeria monocytogenes. *Immunity* **35**, 236–248 (2011). doi: 10.1016/j.immuni.2011.06.012; pmid: 21867927
32. S. A. van de Pavert, R. E. Mebius, New insights into the development of lymphoid tissues. *Nat. Rev. Immunol.* **10**, 664–674 (2010). doi: 10.1038/nri2832; pmid: 20706277
33. S. P. Spencer *et al.*, Adaptation of innate lymphoid cells to a micronutrient deficiency promotes type 2 barrier immunity. *Science* **343**, 432–437 (2014). doi: 10.1126/science.1247606; pmid: 24458645
34. S. Sawa *et al.*, Lineage relationship analysis of RORgammat+ innate lymphoid cells. *Science* **330**, 665–669 (2010). doi: 10.1126/science.1194597; pmid: 20929731
35. I. I. Ivanov *et al.*, The orphan nuclear receptor RORgammat directs the differentiation program of proinflammatory IL-17+ T helper cells. *Cell* **126**, 1121–1133 (2006). doi: 10.1016/j.cell.2006.07.035; pmid: 16990136
36. T. I. Arnon, R. M. Horton, I. L. Grigorova, J. G. Cyster, Visualization of splenic marginal zone B-cell shuttling and follicular B-cell egress. *Nature* **493**, 684–688 (2013). doi: 10.1038/nature11738; pmid: 23263181
37. E. Castigli *et al.*, Impaired IgA class switching in APRIL-deficient mice. *Proc. Natl. Acad. Sci. U.S.A.* **101**, 3903–3908 (2004). doi: 10.1073/pnas.0307348101; pmid: 14988498
38. V. V. Parekh *et al.*, B cells activated by lipopolysaccharide, but not by anti-Ig and anti-CD40 antibody, induce anergy in CD8+ T cells: Role of TGF-beta 1. *J. Immunol.* **170**, 5897–5911 (2003). doi: 10.4049/jimmunol.170.12.5897; pmid: 12794116
39. M. A. Travis, D. Sheppard, TGF-β activation and function in immunity. *Annu. Rev. Immunol.* **32**, 51–82 (2014). doi: 10.1146/annurev-immunol-032713-120257; pmid: 24313777
40. E. J. Villablanca *et al.*, MyD88 and retinoic acid signaling pathways interact to modulate gastrointestinal activities of dendritic cells. *Gastroenterology* **141**, 176–185 (2011). doi: 10.1053/j.gastro.2011.04.010; pmid: 21596042
41. M. A. Travis *et al.*, Loss of integrin alpha(v)beta8 on dendritic cells causes autoimmunity and colitis in mice. *Nature* **449**, 361–365 (2007). doi: 10.1038/nature06110; pmid: 17694047
42. D. Ruane *et al.*, Microbiota regulate the ability of lung dendritic cells to induce IgA class-switch recombination and generate protective gastrointestinal immune responses. *J. Exp. Med.* **213**, 53–73 (2016). doi: 10.1084/jem.20150567; pmid: 26712806
43. L. Hammarström, I. Vorechovsky, D. Webster, Selective IgA deficiency (SIgAD) and common variable immunodeficiency (CVID). *Clin. Exp. Immunol.* **120**, 225–231 (2000). doi: 10.1046/j.1365-2249.2000.01131.x; pmid: 10792368
44. V. N. Ngo, R. J. Cornall, J. G. Cyster, Splenic T zone development is B cell dependent. *J. Exp. Med.* **194**, 1649–1660 (2001). doi: 10.1084/jem.194.11.1649; pmid: 11733579
45. J. P. Pereira, J. An, Y. Xu, Y. Huang, J. G. Cyster, Cannabinoid receptor 2 mediates the retention of immature B cells in bone marrow sinusoids. *Nat. Immunol.* **10**, 403–411 (2009). doi: 10.1038/ni.1710; pmid: 19252491
46. V. N. Ngo, H. L. Tang, J. G. Cyster, Epstein-Barr virus-induced molecule 1 ligand chemokine is expressed by dendritic cells in lymphoid tissues and strongly attracts naive T cells and activated B cells. *J. Exp. Med.* **188**, 181–191 (1998). doi: 10.1084/jem.188.1.181; pmid: 9653094
47. P. Bergqvist *et al.*, Re-utilization of germinal centers in multiple Peyer's patches results in highly synchronized, oligoclonal, and affinity-matured gut IgA responses. *Mucosal Immunol.* **6**, 122–135 (2013). doi: 10.1038/mi.2012.56; pmid: 22785230
48. S. Kawamoto *et al.*, The inhibitory receptor PD-1 regulates IgA selection and bacterial composition in the gut. *Science* **336**, 485–489 (2012). doi: 10.1126/science.1217718; pmid: 22539724


## ACKNOWLEDGMENTS

We thank M. Matloubian for help with the B16-Flt3L, J. Bluestone for RORγt-GFP mice, M. Krummel for Zbtb46-GFP mice, M. Rosenblum for *Baft3*$^{-/-}$ mice, R. Locksley for KN2 mice and *Il4ra*$^{-/-}$ mice, F. Kroese for HISM2 hybridoma, M. Miller for advice regarding intravital microscopy, Y. Xu and J. An for expert technical assistance, and O. Bannard for comments on the manuscript. The data presented in this manuscript are tabulated in the main paper and in the supplementary materials. UCSF has filed a patent (U.S. patent application 14/778,997) describing the αvβ8 blocking antibody used in this manuscript. D.S. and A.A. are listed as inventors. A.R. was a recipient of the Irvington postdoctoral fellowship from the Cancer Research Institute. J.G.C. is an investigator of the Howard Hughes Medical Institute. The work was supported in part by National Institute of Allergy and Infectious Diseases U19 grant AI077439 (to D.S.) and RO1 grants AI045073 and AI074847 (to J.G.C).

## SUPPLEMENTARY MATERIALS

www.sciencemag.org/content/352/6287/aaf4822/suppl/DC1
Figs. S1 to S5
Movies S1 to S4

15 February 2016; accepted 30 March 2016
10.1126/science.aaf4822

Downloaded from http://science.sciencemag.org/ on May 12, 2016

RESEARCH ARTICLE

PSYCHOLOGY

# Reconciling after civil conflict increases social capital but decreases individual well-being

Jacobus Cilliers,[1] Oeindrila Dube,[2]* Bilal Siddiqi[3]

**Civil wars divide nations along social, economic, and political cleavages, often pitting one neighbor against another. To restore social cohesion, many countries undertake truth and reconciliation efforts. We examined the consequences of one such effort in Sierra Leone, designed and implemented by a Sierra Leonean nongovernmental organization called Fambul Tok. As a part of this effort, community-level forums are set up in which victims detail war atrocities, and perpetrators confess to war crimes. We used random assignment to study its impact across 200 villages, drawing on data from 2383 individuals. We found that reconciliation had both positive and negative consequences. It led to greater forgiveness of perpetrators and strengthened social capital: Social networks were larger, and people contributed more to public goods in treated villages. However, these benefits came at a substantial cost: The reconciliation treatment also worsened psychological health, increasing depression, anxiety, and posttraumatic stress disorder in these same villages. For a subset of villages, we measured outcomes both 9 months and 31 months after the intervention. These results show that the effects, both positive and negative, persisted into the longer time horizon. Our findings suggest that policy-makers need to restructure reconciliation processes in ways that reduce their negative psychological costs while retaining their positive societal benefits.**

Most wars today are civil wars (*1*), which divide countries along ethnic, economic, and political cleavages. For example, the Hutus targeted the Tutsis during Rwanda's genocide (in 1994), and illicit diamonds sustained Sierra Leone's civil war (over 1991–2002), pitting one neighbor against another. Because conflicts like this sever social ties among individuals, their prevalence has spurred efforts to promote social cohesion and improve social capital as a part of postconflict recovery (*2*–*7*).

Truth and reconciliation processes are a common approach used around the world to promote this type of rebuilding (*8*). These processes are founded on the idea that airing wartime grievances is the key to restoring social ties. As such, they bring war victims face-to-face with perpetrators through forums in which victims describe war atrocities and perpetrators confess to war crimes without facing prosecution. Proponents of this approach claim that reconciliation processes are highly effective—not just in rebuilding social capital and promoting societal healing but also in providing psychological relief to participants, aiding individual healing (*9*–*15*). Yet, we have little knowledge of whether and how reconciliation processes help communities heal from conflict.

We have some evidence from past work that attitudes toward other groups can improve in the aftermath of nationwide Truth and Reconciliation Commissions (TRCs) (*16*) and with exposure to trauma counseling (*17*). Also, other types of interventions targeted toward individuals have been shown to reduce prejudice (*18*) and improve day-to-day dispute resolution (*19*). But what happens when we induce targeted, person-to-person forgiveness throughout a community? We lack rigorous evidence on how community-wide reconciliation influences either individual or societal healing (*20*, *21*).

Our study seeks to address this gap in the literature. We conducted a randomized control trial of a reconciliation process in Sierra Leone that was designed and implemented by a Sierra Leonean nongovernmental organization (NGO) called Fambul Tok. Fambul Tok's intervention has several features common to truth and reconciliation processes around the world: It initiates forums in which victims describe the violence they experienced and perpetrators seek forgiveness for their crimes. Also, no one receives monetary compensation or is punished for participating. However, Fambul Tok's approach is distinct from nationwide truth and reconciliation because it conducts community-level reconciliation, holding forums at the level of the section, which on average includes 10 villages. We used random assignment to evaluate the impact of its work across 100 sections of Sierra Leone. Our evaluation was independent, and we provided no input into the design of its program.

## War and reconciliation in Sierra Leone

More than 50,000 people were killed during Sierra Leone's civil war. Thousands more were raped and had limbs amputated, and 2.6 million people—more than half the population of ~4 million people (*22*)—were displaced as a part of the Revolutionary United Front (RUF) rebel group's campaign of terror against the population.

Much of the violence was neighbor-on-neighbor and took place among members of the same village. Child soldiers were frequently recruited by the RUF. Sometimes, they willingly rose up against local authorities in their village, and at other times, they were forced to commit atrocities against fellow villagers. The other armed actors in the conflict included the Sierra Leonean Army (SLA) and local militias called the Civil Defense Forces (CDF), which emerged in response to widespread civilian abuses and came to be revered for protecting the population against the rebels. Although all armed actors inflicted civilian casualties, the vast majority of the atrocities were committed by the RUF (*23*, *24*).

After the conflict, the Sierra Leonean government set up a national TRC, but it only had the capacity to cover a small fraction of the war atrocities. Also, many rural Sierra Leoneans were unable to access the district capitals where the forums were held. As a result, a large part of the population was left out of the national reconciliation process.

Fambul Tok ("Family Talk" in Krio) was founded to address this gap in 2007, when it began initiating community-level reconciliation forums. As a part of its program, committees composed of community members were trained in trauma healing and mediation and conducted outreach to encourage victims and perpetrators to participate in the truth-telling process. This culminated in a 2-day bonfire ceremony in which victims described their experiences and perpetrators asked for forgiveness. The ceremonies were relatively cheap, costing between $150 and $200 in total, for all participants. They also incorporated traditional rituals to promote community healing. After the ceremony, Fambul Tok set up a symbolic Peace Tree in each village and, in some areas, communal farms to further sustain community healing. It additionally helped establish a Peace Mothers' group to discuss gender-targeted atrocities perpetrated during the war. As such, this intervention could have some impacts other than reconciliation—for example, on economic activity. Where we discuss alternative accounts, we lay out why effects on psychological health and social capital are likely due to reconciliation rather than these other impacts. (In supplementary text S3, we also discuss how local-level reconciliation processes such as the one implemented by Fambul Tok compare with national-level reconciliation processes.)

## Healing through reconciliation

Reconciliation processes such as this one could theoretically have both positive and negative psychological consequences. On the one hand,

[1]McCourt School of Public Policy, Georgetown University, 3700 O Street, Washington, DC 20057, USA. [2]Department of Politics, New York University, 19 West 4th Street, New York, NY 10012, USA. [3]Development Research Group, World Bank, 1818 H Street NW, Washington, DC 20433, USA.
*Corresponding author. Email: odube@nyu.edu

Downloaded from http://science.sciencemag.org/ on May 12, 2016

they may improve psychological health if sharing war accounts has a cathartic effect (*10*, *11*, *22*) or leads to forgiveness, which has been shown to improve trauma, anxiety, and depression (*25*)—particularly when induced in the context of forgiveness therapies (*26*–*31*).

On the other hand, they may also prove traumatic because they evoke painful war memories without allowing for gradual habituation or desensitization (*32*, *33*). In this regard, reconciliation processes are similar to single-session debriefing (*34*), which seeks to counsel patients by exposing them briefly and intensively to traumatic events but has been shown to have limited therapeutic value (*34*, *35*). In contrast, gradual exposure therapy has been shown to be more effective for mitigating posttraumatic stress disorder (PTSD) (*32*, *36*). Negative psychological effects associated with reconciliation need not be concentrated among those who were directly victimized; for example, other community members may experience vicarious traumatization (*37*–*40*) as they hear about new atrocities committed during the war.

In fact, studies of those who have testified in national TRCs suggest that this participation produces mixed emotional responses (*41*–*43*), may not improve psychological health (*44*), or may even correlate with worse psychological outcomes (*34*, *45*). It is difficult to infer causal effects by comparing those who testified with those who did not because those who chose to testify may have experienced greater violence exposure or had a different psychological makeup. We use a randomized design to mitigate this type of endogeneity concern and better identify the effect of reconciliation on psychological outcomes, including trauma, anxiety, and depression. We also examined whether the effects vary systematically based on the degree to which individuals experienced war violence.

Reconciliation processes may also affect societal healing through their effects on social capital, which is conceptualized as social networks, and norms such as trust and reciprocity that arise from these network ties (*46*). Social capital effects could also arise as a consequence of forgiveness. For example, individuals may stop avoiding places and activities associated with perpetrators and form social ties with them after forgiving them for past actions. They could also arise as a consequence of acknowledgment (*47*): People may be more willing to contribute to communities that have recognized that they were victimized, or that have recognized that they perpetrated crimes without punishing them for these past actions. To determine impacts on social capital, we examined outcomes such as social networks, participation in community groups, and contributions to public goods.

## Evaluation design

In 2011, when Fambul Tok was poised to expand into new sections in its five districts of operation (Kailahun, Kono, Bombali, Moyamba, and Koinadugu), we used random assignment to assign some sections to the Fambul Tok treatment group and other sections to serve as a part of the control group. Geographically, sections are units that lie within districts, whereas villages are even smaller units that lie within sections.

In the supplementary materials (figs. S1 to S3), we show that these five districts are similar to other districts in Sierra Leone along key dimensions such as exposure to war violence and other socioeconomic characteristics. These similarities suggest that the findings of the study are also likely to hold for other areas of Sierra Leone, which helps boost the external validity of the study.

The evaluation occurred in waves so as to allow Fambul Tok to work within its capacity. The first wave included 40 sections, and the second wave included 60 sections. Data collection for a third wave was interrupted by the Ebola crisis in Sierra Leone in 2014. Our field staff had to be evacuated while we were collecting behavioral measures. These 100 sections are also similar in key characteristics to other sections within the districts of study (table S1), which further bolsters potential generalizability to other areas of the country.

Within each section, we sampled two villages: One was the section headquarters, where the reconciliation ceremony was typically held, and the second was randomly chosen among what was on average nine remaining villages. Within each village, we interviewed a random sample of 10 to 12 adults, for a total of 2383 respondents across 200 villages. Almost all of our key outcome variables are individual-level responses from household surveys.

In wave one, we conducted endline surveys both 9 months and 31 months after the ceremonies took place, enabling us to determine both short-run and long-run effects. In wave two, endline surveys were conducted once, ~18 to 19 months after the ceremonies. The evaluation timeline, which spanned the 2011–2014 period, is shown in fig. S4.

For all endline rounds, we sought to resurvey the same respondents interviewed at baseline. We went to great lengths to minimize attrition, with repeat visits and by tracking respondents who had moved to neighboring villages.

The attrition rate of those who appeared in baseline but are missing from either endline round in wave one or the endline in wave two is 13% (315 out of 2382 individuals), and the attrition rate for those missing from both endline rounds in wave one or the endline in wave two is 7% (168 of 2382 individuals). As shown in table S2, neither of these attrition measures—nor the attrition measure of each endline round separately—is predicted by treatment (supplementary text S1).

We also used four village-level variables from a village survey. Because of a mechanical error in the hand-held devices used for data collection, this village-level survey is missing for five villages

**Table 1. The impact of reconciliation on forgiveness and trust.** Each row represents a separate regression of the outcome shown in the first column on treatment assignment. All specifications include section pair fixed effects and the second-round indicator, the baseline outcome variable, and its interaction with both the second-round indicator and the second-wave indicator. SEs are clustered at the section level. *** is significant at the 1% level, ** is significant at the 5% level, and * is significant at the 10% level. The control mean is the mean in the control group at endline.

| Variables | Control mean | Coefficient | SE | Observations | $R^2$ |
|---|---|---|---|---|---|
| *Forgiveness* | | | | | |
| Forgive perpetrators | 2.264 | 0.571** | (0.227) | 2010 | 0.131 |
| Forgive perpetrators (based on questions in both baselines) | 0.951 | 0.277* | (0.145) | 2085 | 0.121 |
| *Trust* | | | | | |
| How much do you trust rebel excombatants? | 1.901 | 0.177** | (0.079) | 900 | 0.222 |
| Indicator: Trust rebel excombatants somewhat or completely | 0.328 | 0.073** | (0.036) | 900 | 0.197 |
| How much do you trust migrants to this community? | 3.161 | 0.123*** | (0.033) | 2203 | 0.172 |
| Indicator: Trust migrants somewhat or completely | 0.861 | 0.058*** | (0.012) | 2203 | 0.094 |
| Index of generalized trust in community | 0 | 0.006 | (0.027) | 2996 | 0.135 |
| Indicators | | | | | |
| People are honest and can be trusted | 2.598 | 0.014 | (0.026) | 2994 | 0.126 |
| People in village are honest and can be trusted | 2.858 | −0.010 | (0.020) | 2976 | 0.167 |
| People in community would not betray fellow community members | 2.550 | 0.003 | (0.028) | 2976 | 0.059 |
| Money left out accidentally will still be there an hour later | 0.365 | 0.010 | (0.020) | 2956 | 0.141 |

Downloaded from http://science.sciencemag.org/ on May 12, 2016

in baseline and a separate six villages in endline. As shown in table S3, whether a village is missing in either baseline or endline is also uncorrelated with treatment. The number of villages and individuals in our sample is shown in table S4, disaggregated by wave and round of data collection. (In supplementary text S1, we discuss additional robustness checks to confirm that missing village-level indicators do not affect our results.)

## Empirical strategy

We used our baseline survey data to match sections into pairs stratified by district and randomly assigned one section in each pair into treatment and the other into control. The balance on key covariates is reported in table S5, and more details on matching and balance statistics are provided in supplementary text S3. To examine treatment effects, our main specification pools together endline surveys from both waves and rounds of the evaluation. For most outcomes, we have baseline data, which enables us to control for the baseline value of the dependent variable (*48*, *49*). This approach reduces noise and increases power and has been commonly used in recent experimental studies in the social sciences [for example, (*50*)].

We estimate regressions that can be represented as

$$y_{rivspw} = \beta_0 + \beta_1 T_s + \rho_p + \beta_2 y_{0ivspw} + \delta_r + \delta_r y_{0ivspw} + \lambda_w y_{0ivspw} + \varepsilon_{rivspw} \quad (1)$$

where $y_{0ivspw}$ and $y_{rivspw}$ denote outcomes at baseline and endline round $r$, respectively, for individual $i$ in village $v$, section $s$, section-pair $p$, and wave $w$. $\rho_p$ denotes section-pair fixed effects, which account for section-level matching in the allocation of treatment (*51*). $\delta_r$ is a round effect that equals 1 for the second-round endline. The interaction term, $\delta_r y_{0ivspw}$, allows the baseline to exert different effects over time. $\lambda_w$ is a wave effect that equals 1 for sections in the second wave. Because each wave includes different sections, wave effects are subsumed by section-pair effects. $\lambda_w y_{0ivspw}$ allows baseline variables to have different effects for the wave-two sections. This control is particularly important because we are only able to include pared-down baseline outcomes collected in the second-wave baseline survey (a point discussed further in the Data section). Last, $T_s$ is assignment to treatment, and $\beta_1$ measures the treatment effect.

If we did not have baseline data for an outcome, we estimated cross-sectional specifications of the form

$$y_{rivspw} = \beta_0 + \beta_1 T_s + \rho_p + \delta_r + \varepsilon_{rivspw} \quad (2)$$

We clustered the standard errors (SEs) at the section level, which is the unit of treatment allocation. This accounts for the potential correlation of errors across individuals within a section (and implicitly, within a village, because a section is larger than a village).

There are three sections in which some responses do not match treatment assignment; these sections were assigned to control, and yet six of the respondents in one village and eight respondents in the other two reported attending a bonfire ceremony. However, we used assignment to treatment in estimating all of our specifications. Thus, ceremony participation among control respondents may lead to an understatement of the effect.

Many of our outcomes are mean effect indices that first standardize and then sum various indicators used to measure similar concepts. We used the methodology of (*52*), which imputes missing values before aggregation. The indicators are standardized by subtracting control group means and dividing by control group standard deviations, so that the control group means for the indices are zero by construction. In supplementary text S3, we provide greater detail on this method, and in table S6, we show robustness to an alternate method that does not first impute missing values (*53*).

To avoid fishing for significant effects (*4*, *6*), we registered a Pre-Analysis Plan (PAP) in the Evidence in Governance and Politics (EGAP) depository before analysis of any endline data from either wave one or wave two. The PAP outlines the indicators comprising each index and all the hypotheses to be tested. A copy can be found at http://egap.org/registration/622. All hypotheses specified in our PAP are listed in table S7. We present results for six of the hypotheses in Tables 1 to 6 and 10 others in the supplementary materials. In supplementary text S2, we discuss the PAP in more detail and also the few circumstances under which we deviated from the prespecified grouping, owing to issues aggregating conditional and unconditional outcomes or to changes in how the social network data were collected over rounds.

In addition, we show in tables S8 and S9 that adjusting for multiple comparisons by controlling for rates of false discovery (*54*–*56*) does not affect any of our main results (supplementary text S3).

## Data

In terms of our dependent variables, we used the Rye Forgiveness Scale to construct an index of forgiveness toward former perpetrators (*57*). This is a sum of 12 questions [and a subset of the 60 questions in the Enright Forgiveness Inventory (*58*)], answered on a four-point Likert scale, which were administered to those who reported being physically or emotionally hurt during the war. These questions are designed to measure affect as well as cognitive and behavioral responses toward former perpetrators.

The questions in this index are listed in table S10. Whereas all three endline surveys and the first-wave baseline included these 12 questions, the second-wave baseline included a subset of seven questions, which serve as a pared-down baseline control for second-wave observations. However, both indices show high internal consistency: Cronbach's $\alpha$ is 0.865 for the full forgiveness index and 0.824 for the pared-down forgiveness index.

To measure trust, we aggregated four questions on perceived trust and honesty of community members into an index of generalized trust. We also asked separate questions on degree of trust toward former RUF rebel combatants (to whom we refer as "rebel ex-combatants," for brevity) as well as migrants, many of whom are former combatants who left their villages after the war. We also measured trust of former members of the SLA and the CDF (supplementary text S2). These trust questions are based on a 4-point Likert scale (with responses "trust completely," "trust somewhat," "distrust somewhat," and "distrust completely"). In order to aid the interpretation of our results, we also constructed a binary variable indicating whether the respondent trusts the relevant subgroup or not.

To gauge impacts on social networks, we asked respondents to identify people from the 9 to 11 other respondents in that village whom they

**Table 2. Reconciliation and social networks.** Each row represents a separate regression of the outcome shown in the first column on treatment assignment. All specifications are cross-sectional because we do not have baseline measures of these dependent variables. All regressions also include section pair fixed effects and the second round indicator. SEs are clustered at the section level. *** is significant at the 1% level, ** is significant at the 5% level, and * is significant at the 10% level. The control mean is the mean in the control group at endline.

| Variables | Control mean | Coefficient | SE | Observations | $R^2$ |
|---|---|---|---|---|---|
| Index of network strength | 0 | 0.099*** | (0.028) | 3008 | 0.061 |
| Indicators | | | | | |
| Number of people respondent would approach for advice / help | 2.894 | 0.148** | (0.069) | 3005 | 0.056 |
| Number of people respondent would ask to collect money for them | 3.144 | 0.155 | (0.142) | 3005 | 0.026 |
| Number of times respondent listed as good friend | 2.123 | 0.232** | (0.091) | 3008 | 0.192 |
| Number of times respondent listed as someone to ask for advice / help | 3.245 | 0.362*** | (0.126) | 3008 | 0.199 |

Downloaded from http://science.sciencemag.org/ on May 12, 2016

would consider a good friend and would ask for advice and help. We used this to construct a measure of how many times a respondent was named by someone else. We also asked the respondent to list all the people in the village they would ask to collect money for them and ask for help. We standardized and summed these four measures into a mean effect index. We were only able to conduct cross-sectional analyses with these questions because they were asked differently in the baseline and endline surveys (supplementary text S2).

We constructed a community group participation index based on whether respondents were members of organizations such as Parent Teacher Associations (PTAs) and religious groups and whether they attended group meetings. We also constructed an index of public goods contributions based on whether individuals contributed money or labor to community groups or to building public facilities (including bridges, schools, wells, and health clinics), gave money to a family in need, or participated in road-brushing (a common form of road maintenance), as well as the number of community projects in their village.

Turning to psychological health, we measured PTSD using 11 questions from the PTSD Symptom Scale that assesses the presence and severity of PTSD symptoms according to the 4th Diagnostic and Statistical Manual of Mental Disorders (DSM-IV). This scale has been validated for research purposes (*59*, *60*) and shown to have good psychometric properties, including high internal consistency and test-retest reliability (*59*). We also drew 7 depression and 10 anxiety questions from the Zung Depression and Zung Anxiety indices (*61*, *62*). The second-wave baseline included a subset of seven and five questions on anxiety and depression, respectively, which again form pared-down baseline-dependent variable controls. The indices for PTSD, anxiety, and depression are sums of questions answered on a four-point Likert scale (all the questions are listed in table S11). We further aggregated these three indices into a mean effect index of psychological health. We inverted the indicators so that a reduction in the index indicates worse psychological health.

The psychometric scales from which we drew our questions have typically been assessed in developed country contexts, which raise questions around whether they are culturally relevant and valid for a developing country such as Sierra Leone. We piloted our survey instruments extensively and adapted the wording of the psychological measures to the Sierra Leonean context so that they better reflect the informality of Krio language. Furthermore, our scales correspond closely to scales used in other recent studies set in postconflict parts of sub-Saharan Africa, where they have demonstrated good psychometric properties. For example, 15 of our 17 questions on anxiety and depression are also a part of the Johns Hopkins 25-Item Checklist for Anxiety and Depression (*63*). An adapted version of this scale shows strong internal consistency among adults who were formerly child soldiers in Sierra Leone (*64*–*66*). Although our PTSD scale has not been applied in Sierra Leone, it uses the same questions as the Child Posttraumatic Stress Disorder Reaction Index (CPTSD-RI) (*67*, *68*), which has been tested on a population of Ugandan and Congolese child soldiers (*69*). Moreover, the psychological wellbeing questions we used also exhibit high internal consistency in our sample, with a Cronbach's α ranging between 0.831 and 0.936 (supplementary text S1).

We also converted the continuous PTSD measure into a dichotomous indicator of whether an individual suffers from clinical PTSD or severe trauma, following guidelines from the Clinician-Administered PTSD Scale (*70*). This is coded as 1 if the individual showed at least one symptom of reexperience, one symptom of avoidance, and at least two symptoms of increased arousal. We did not prespecify that we would look at this indicator in our PAP but do so to better gauge the magnitude of the effects on PTSD.

In terms of our sample, because the 10 to 12 respondents were randomly chosen in each village, some may have been victims during the war and others perpetrators. Our main results examine average impacts on all respondents. However, we also collected data on the ways in which respondents were exposed to violence to determine whether the treatment effect varies based on victimization. In our PAP, we defined a violence-exposed individual as one who was beaten, raped, maimed, abducted, or saw violence during the war. We discuss alternate measures in supplementary text S5. We also define someone as an ex-combatant based on a self-reported measure and whether they indicated that they were abducted and forced to carry a gun after getting abducted. There is likely to be extensive underreporting in both measures, which means the excombatant variable is likely measured with noise.

Descriptive statistics of key variables are presented in table S12. The surveyed respondents reside in impoverished conditions. More than 70% have no formal education, and less than 8% live in a village with a market. They also experienced extensive war violence: 54% had a family member killed, 33% were beaten, 2% report being maimed, and 3% report that they were raped. These latter numbers are also likely to be underestimates, given the sensitivity of these measures.

Respondents in treatment sections were very familiar with Fambul Tok's reconciliation program

**Table 3. Reconciliation and participation in community groups.** Each row represents a separate regression of the outcome shown in the first column on treatment assignment. Variables not shown include section pair fixed effects, the second-round indicator, the baseline outcome variable, and the interaction of the baseline outcome variable with both the second-round indicator and the second-wave indicator. SEs are clustered at the section level. *** is significant at the 1% level, ** is significant at the 5% level, and * is significant at the 10% level. The control mean is the mean in the control group at endline.

| Variables | Control mean | Coefficient | SE | Observations | $R^2$ |
|---|---|---|---|---|---|
| Index of participation in community groups | 0 | 0.058*** | (0.017) | 3004 | 0.160 |
| Index of participation in community groups, without women's membership or meetings | 0 | 0.064*** | (0.017) | 3004 | 0.162 |
| Indicators | | | | | |
| PTA membership | 0.137 | 0.034** | (0.016) | 2732 | 0.223 |
| Village development committee membership | 0.091 | 0.013 | (0.011) | 2737 | 0.141 |
| Youth group membership | 0.101 | 0.015* | (0.008) | 2738 | 0.144 |
| Women's group membership | 0.118 | 0.022 | (0.014) | 2004 | 0.138 |
| Secret society membership | 0.358 | −0.058*** | (0.019) | 2770 | 0.338 |
| Religious group membership | 0.286 | 0.055*** | (0.020) | 2729 | 0.179 |
| PTA meeting attendance | 0.082 | 0.037** | (0.015) | 2739 | 0.138 |
| Village development committee meeting attendance | 0.068 | 0.008 | (0.010) | 2734 | 0.106 |
| Youth group meeting attendance | 0.066 | 0.007 | (0.008) | 2739 | 0.090 |
| Women's group meeting attendance | 0.075 | 0.024* | (0.013) | 2004 | 0.095 |
| Secret society meeting attendance | 0.056 | −0.005 | (0.008) | 2766 | 0.057 |
| Religious group meeting attendance | 0.190 | 0.058*** | (0.016) | 2714 | 0.103 |
| Community meeting attendance | 0.626 | 0.006 | (0.013) | 2983 | 0.077 |

Downloaded from http://science.sciencemag.org/ on May 12, 2016

(table S13), indicating that the intervention was well implemented.

## Results

Our findings on reconciliation and the forgiveness of former perpetrators are presented in Table 1, top. The forgiveness index (of 12 questions) is 0.571 higher in treatment areas (SE = 0.227, $P$ = 0.013), over the control group mean of 2.264. The pared down forgiveness index (of seven questions) is 0.277 higher (SE = 0.145, $P$ = 0.059) than that of its control group mean of 0.951.

Because the forgiveness indices are summed on a Likert scale, the coefficients cannot be interpreted in percent terms by comparing them with control group means. Under these scales, changing the value assigned to responses will not alter the regression coefficients but will alter the control group mean, yielding a different implied percent effect. Moreover, no one valuation is necessarily more appropriate than another because units have no inherent meaning in Likert scales (supplementary text S1) (*77*).

To gauge whether the effects on forgiveness are large, we instead benchmark the treatment effect against how exposure to specific forms of war violence affected feelings toward perpetrators, as reflected in the forgiveness index at baseline. For example, having a family member killed lowered baseline forgiveness by 0.920 (SE = 0.232, $P$ < 0.001) (table S14). Thus, the reconciliation program can be said to offset this effect and increase forgiveness by 30% (0.277/.920 = 0.301). This approach is speculative because we cannot observe the causal effect of violence exposure on forgiveness, and so we are benchmarking our treatment effect against a correlation. As such, the interpretation of magnitudes in this manner should be taken as suggestive.

These forgiveness effects are based on survey responses, which raise potential concerns that respondents may say what they believe surveyors want to hear. But there are four factors that mitigate the concern that the results are driven by social desirability bias. First, our surveyors are completely independent of the implementing NGO, so they would not be associated with messages of reconciliation. Second, we asked these questions 9 to 31 months after the reconciliation ceremonies take place, so talk of forgiveness is not fresh on respondents' minds. Third, respondents are not simply asked whether they have forgiven the perpetrator, but rather asked a series of questions designed to gauge their feeling and behavior toward excombatants (such as avoidance), which are arguably less subject to this type of bias. Last, our respondents experienced traumatic forms of victimization, such as amputations and the killing of family members, so it is not psychologically costless for them to say that they no longer feel anger toward their perpetrator, unless this reflects an underlying change in their perspective. However, to further bolster this interpretation, we also discuss whether these forgiveness effects go hand-in-hand with changes in the community orientation of individuals' behavior.

Next, we examine impacts on trust. As shown in Table 1, bottom, the reconciliation treatment increases trust toward both rebel excombatants and migrants. Looking at the binary indicator, respondents are on average 7.3 percentage points (SE = 0.036, $P$ = 0.046), or 22.2%, more likely to trust a rebel excombatant and 5.8 percentage points (SE = 0.012, $P$ < 0.001), or 6.7%, more likely to trust a migrant. Higher trust of migrants suggests greater inclusion of this marginalized group, whose members are sometimes difficult to distinguish from excombatants. In contrast, there is no discernible impact on trust toward former members of the SLA or CDF (table S8). This indicates that the reconciliation process led to changes in trust toward those who perpetrated atrocities during the war, namely former members of the RUF. Although all of these trust questions are administered to subsets of individuals who know members of each of these groups, our specifications restrict the sample to those who knew group members at both baseline and endline because they include controls for the baseline-dependent variable. In table S15, we further verify that these results are not driven by compositional changes in who knows members of these groups.

Because reconciliation is aimed at forgiving former war perpetrators, it is reassuring to see that the process did increase trust toward former rebel combatants. Yet, at the same time, there is no significant impact on the index of trust toward community members generally (Table 1, bottom). Moreover, the reconciliation process also did not alter individuals' beliefs that former combatants and other community members would fight again in the future (table S16). Both null effects raise questions as to whether the treatment altered individuals' interactions with other community members.

To further investigate this question, we examine impacts on social networks (Table 2). The coefficient on the mean effect index implies that the index of network strength is 0.099 standard deviation (SD) units larger in treatment sections than control sections (SE = 0.028, $P$ = 0.001). Because the index is an aggregation of various indicators, effect sizes have a more intuitive meaning if we look at the individual indicators constituting the index.

For example, the number of individuals whom respondents would ask for advice or help increases by 0.148 above the control group mean of 2.894 (SE = 0.069, $P$ = 0.033), implying a 5% increase. The tendency to be listed as a good friend and as someone to ask for advice or help both also increase by 11% (SE = 0.091, $P$ = 0.013 and SE = 0.126, $P$ = 0.005, respectively). As we discuss in supplementary text S5, we see no significant differential impact of ceremony attendance on the

**Table 4. Reconciliation and contributions to public goods.** Each row represents a separate regression of the outcome shown in the first column on treatment assignment. All specifications include section pair fixed effects and the second-round indicator. All specifications also include the baseline outcome variable and its interaction with both the second-round indicator and the second-wave indicator, except for "Contributed money to someone in need." Because we do not have the second-wave baseline-dependent variable for this outcome, we instead control for the other baseline measures of public goods contributions and their interaction with the second-round indicator and the second-wave indicator in the regression of this outcome. *** is significant at the 1% level, ** is significant at the 5% level, and * is significant at the 10% level. The control mean is the mean in the control group at endline.

| Variables | Control mean | Coefficient | SE | Observations | $R^2$ |
|---|---|---|---|---|---|
| Index of public goods contributions | 0 | 0.042* | (0.022) | 3008 | 0.171 |
| Index of public goods contributions (without contributions to women's group) | 0 | 0.046** | (0.023) | 3008 | 0.184 |
| Index of public goods contributions (indicators in both baselines) | 0 | 0.046** | (0.022) | 3008 | 0.171 |
| Indicators | | | | | |
| Contributed to public facilities | 0.397 | 0.029 | (0.019) | 2911 | 0.078 |
| Brushed roads | 0.290 | 0.005 | (0.014) | 2898 | 0.171 |
| Number of community projects (village-level variable) | 0.539 | −0.060 | (0.057) | 2841 | 0.356 |
| Contributed to PTA | 0.066 | 0.023* | (0.013) | 2732 | 0.105 |
| Contributed to village development committee | 0.062 | 0.002 | (0.009) | 2737 | 0.119 |
| Contributed to youth group | 0.069 | −0.002 | (0.006) | 2738 | 0.081 |
| Contributed to women's group | 0.064 | 0.021** | (0.010) | 2004 | 0.076 |
| Contributed money to someone in need | 0.178 | 0.010 | (0.019) | 2039 | 0.100 |

Downloaded from http://science.sciencemag.org/ on May 12, 2016

social networks index, which suggests that this effect does not arise as a mere consequence of social interactions generated at the ceremony.

We next examine whether the reconciliation process altered the community orientation of individuals' behavior. Estimates on participation in community groups are presented in Table 3. The mean effect index is significantly higher in treatment sections by 0.058 SD units (SE = 0.017, $P$ = 0.001). This overall effect reflects two different types of impacts among individual indicators. Membership and meeting attendance for almost all of the individual community groups increase, with effect sizes ranging from 11% above the control group mean of 0.10 for youth group membership (SE = 0.008, $P$ = 0.066) to 45% above the control group mean of 0.08 for PTA meeting attendance (SE = 0.015, $P$ = 0.017). In contrast, membership and meeting attendance decrease for secret societies by 16% (SE = 0.019, $P$ = 0.004) and 9% (SE = 0.008, $P$ = 0.516), respectively. These effects are interesting because these groups have a closed membership dominated by the elite (72). Thus, these decreases are consistent with substitution toward more broad-based community organizations.

Because the Peace Mothers' Groups are initiated as a part of the intervention, we verify that women's groups do not mechanically drive this result: Dropping women's group membership and attendance from the index does not meaningfully affect the estimate.

The effects on contributions to public goods are gauged in Table 4. The mean effect index is 0.042 SD units larger in treatment villages (SE = 0.022, $P$ = 0.055). Dropping the women's group indicators and the indicator for giving to someone in need (for which we do not have second-wave baseline data) does not substantively alter the estimate. Also, dropping the indicator of the number of community projects in a village from the index does not meaningfully affect the estimate (table S17), suggesting that imputation of missing village-level data does not drive this result.

The coefficient on public goods contributions is the smallest of our significant effects, among the mean effect indices. However, looking within the index again shows that effects on underlying indicators vary in magnitude. The effects are most precisely estimated and largest for contributions to PTAs and women's groups, where implied increases are 32% (SE = 0.013, $P$ = 0.097) and 20% (SE = 0.01, $P$ = 0.045), albeit from relatively small control group means of 6.6 and 6.4%, respectively. The implied effect for contributing to public facilities is 7% (SE = 0.019, $P$ = 0.126), but from a relatively large control group mean of 40%.

These effects on networks, participation, and contribution also support our interpretation that the forgiveness effects are not driven through socially desirable responses regarding anger toward perpetrators because they are coupled with changes in the community orientation of individuals' actions. They also indicate that the reconciliation process boosted social capital as individuals formed more friendships and contributed more to their communities, although these changes were not accompanied by increases in general trust, which increased specifically for migrants and former rebel combatants.

Next, we turn from societal healing to individual healing. The effects on psychological well-being are presented in Table 5. The first row presents the index of complete indicators (with pared baseline controls for wave two). The second row presents the index with just the subset of indicators appearing in the wave two baseline. Both versions show that psychological health was significantly lower in the treatment villages, by 0.147 and 0.138 SD units, respectively (SE = 0.033, $P$ < 0.001 and SE = 0.031, $P$ < 0.001). This overall negative impact stems from a worsening of all three psychological measures.

The dichotomous indicator of clinical PTSD indicates that severe trauma was 36% higher in treatment sections, above the control group mean of 8% (SE = 0.011, $P$ = 0.006). The control group means of the continuous psychometric indicators are again not useful for gauging magnitudes in percent terms because they are also aggregations on a Likert scale. If we instead take the alternate approach of comparing the treatment effect against baseline effects of being maimed (table S14), the treatment is predicted to worsen PTSD by 28%, depression by 47%, and anxiety by 37%. Thus, both the percent effects with the dichotomous PTSD indicator and the more speculative approach of benchmarking against violence exposure are consistent with one another and imply substantial effects.

We found that all of these effects, both positive and negative, are also robust to alternate specifications, as discussed in supplementary texts S3 and S6 and presented in tables S18 and S19.

The negative impacts on psychological well-being suggest that confronting the past through reconciliation processes may be deeply distressing. But are these effects concentrated among victims, specifically? This is important for gauging distributional consequences of the program.

To examine whether the psychological impacts are larger for those who were victimized during

**Table 5. Reconciliation and psychological well-being.** The top portion of the table examines the average treatment effect. Each row represents a separate regression of the outcome shown in the first column on treatment assignment. The control mean is the mean in the control group at endline. The bottom portion examines how the treatment effect varies according to individuals' exposure to violence. All specifications include section pair fixed effects and the second-round indicator, the baseline outcome variable, and its interaction with both the second-round indicator and the second-wave indicator. SEs are clustered at the section level. *** is significant at the 1% level, ** is significant at the 5% level, and * is significant at the 10% level.

| Variables | Control mean | Coefficient | SE | Observations | $R^2$ |
|---|---|---|---|---|---|
| *Average effect* | | | | | |
| Index of psychological well-being (all indicators) | 0 | −0.147*** | (0.033) | 2982 | 0.115 |
| Index of psychological well-being (indicators in both baselines) | 0 | −0.138*** | (0.031) | 2982 | 0.115 |
| Indicators (in both baselines) | | | | | |
| Less PTSD | 28.819 | −0.683*** | (0.197) | 2776 | 0.119 |
| Less anxiety | 14.945 | −0.441*** | (0.117) | 2895 | 0.142 |
| Less depression | 11.677 | −0.289*** | (0.069) | 2913 | 0.092 |
| Clinical PTSD symptoms present | 0.080 | 0.029*** | 0.011 | 2776 | 0.057 |
| *Effect by violence exposure (saw violence, was raped, maimed, beaten, or abducted)* | | | | | |

| | $T$ | | $T$ × violence-exposed | | | |
|---|---|---|---|---|---|---|
| | Coefficient | SE | Coefficient | SE | Observations | $R^2$ |
| Index of psychological well-being | −0.160*** | (0.052) | 0.011 | (0.064) | 2852 | 0.121 |
| Index of psychological well-being (indicators in both baselines) | −0.147*** | (0.052) | 0.005 | (0.064) | 2852 | 0.121 |
| Less PTSD | −0.871*** | (0.309) | 0.298 | (0.391) | 2662 | 0.123 |
| Less anxiety | −0.476** | (0.213) | 0.003 | (0.268) | 2778 | 0.144 |
| Less depression | −0.270** | (0.127) | −0.044 | (0.162) | 2788 | 0.094 |
| Clinical PTSD symptoms present | 0.038** | (0.018) | −0.010 | (0.022) | 2662 | 0.058 |

Downloaded from http://science.sciencemag.org/ on May 12, 2016

the war, we interact treatment with our prespecified measure of violence exposure (Table 5). We have limited power to identify these heterogeneous treatment effects, so we considered the magnitudes of the coefficients instead of focusing solely on statistical significance. However, the coefficients on the interaction terms are not just imprecisely estimated but also differ in sign across indicators. (The coefficient is negative for depression, indicating worse effects for victims, but positive for PTSD and anxiety.)

These results are consistent with the idea that even nonvictims may experience a worsening of psychological health from going through a reconciliation process. For example, other community members may experience vicarious traumatization from hearing about atrocities done to others (*36*–*39*).

Another way of gauging the distributional consequence of the reconciliation treatment is to see whether the impact on social capital is smaller (or larger) for victims. These interaction effects are examined in table S20 with two measures of violence exposure. The coefficients on the interaction term of treatment and victimization are mixed in sign, small in size, and imprecisely estimated for outcomes such as social networks, public goods contributions, and community group participation. Thus, victims do not appear to partake systematically less in social capital improvements.

We examine in table S21 whether effects vary for excombatants. Here, some of the interaction terms are quite large in magnitude; for example, the effect on the psychological well-being index implies that the negative effect on those who are not excombatants is nearly offset for excombatants. These effects are imprecisely estimated in part because the excombatant variable is likely to be underreported and measured with noise. Thus, it is difficult to draw definitive conclusions on the basis of these heterogeneous effects, and future work should probe this further.

A key issue is whether these effects persist over time. We present in Table 6 short-run and long-run effects using the two rounds of wave-one data. Because wave one includes fewer than half the sections in the evaluation, this is a relatively underpowered sample, and some of the effects are individually insignificant. Yet, the broad pattern implied by the coefficients indicates that both the positive and negative effects are sustained.

First, the impacts on all three psychological measures persist up to 31 months. This suggests that the war memories invoked by the reconciliation process are powerful and do not fade quickly.

At the same time, the effects on forgiveness and social capital outcomes also persist. Although the effect on trust of former rebel combatants is individually insignificant in both rounds, the coefficients are not significantly distinguishable from each other at the 5% level, indicating that they do not recede over time. Trust of migrants also persists, and there are even short-run improvements in generalized trust measures, although these effects fall, and significantly so, over the longer horizon. The coefficients on public goods contributions and social networks, if anything, increase in magnitude, suggesting that the effects do not recede. The effect on community group participation is also individually significant in both rounds. As such, reconciliation appears to boost the community orientation of individual behavior in a manner that does not subsequently fade away.

We interpret the results above as indicating that the reconciliation process itself affects both individual and societal healing. We also consider and present evidence against two alternative accounts, drawing on data for additional outcomes.

The first alternative account posits that the reconciliation ceremony may be relatively unimportant, whereas other components of the intervention—such as the Peace Mother's Group, Communal Farms, or Peace Tree—actually drive the estimated effects. We think that this is unlikely because treatment effects on forgiveness, social capital, and psychological health are not statistically distinguishable for men and women (table S22), nor if we include a control for communal farms (table S23). The effect on economic outcomes is even negative in sign (table S24), further suggesting limited impacts of communal farms. The coefficient capturing effects on the resolution of day-to-day disputes, which was the focus of the Peace Tree, is also negative and imprecise (table S25). Moreover, it is difficult to see how the negative effects on psychological well-being could emerge as a response to these other components. Together, these results suggest that the reconciliation component of the intervention is an important driver of the estimated effects.

A second alternative account posits that the reconciliation component may be driving the psychological effects, but the social capital outcomes arise from simply getting community members together in a gathering. We think that this is unlikely because it has proven incredibly difficult to move social capital outcomes in Sierra Leone. For example, a large-scale Community-Driven Restoration (CDR) program was implemented in Sierra Leone in 2008 in one of the same districts as in our study. This program spent $100 per household and fostered ongoing gatherings of the community in village-wide meetings in order to promote inclusive governance and collective action. A randomized evaluation found it successfully delivered economic benefits but had no effects on social capital outcomes such as community group participation, as measured with indicators similar to those used in our study (*4*). Given that social capital outcomes did not move in response to a well-implemented and well-resourced intervention, it is hard to see how a 2-day gathering initiated by Fambul Tok could deliver persistent effects on similar outcomes for up to nearly 3 years after the intervention, unless it entailed a deeper transformation of person-to-person interactions.

Second, if simply getting people together improved person-to-person interactions, then we should also have observed reductions in societal tensions and the incidence of other day-to-day disputes. But again, little support for this idea is provided in table S25. For example, the coefficient on the number of conflicts is only 0.002 (relative to a mean of 0.16) (SE = 0.019, $P$ = 0.894). Rather, we observe improvements in

Downloaded from http://science.sciencemag.org/ on May 12, 2016

**Table 6. Persistence of effects.** These results present separate estimates for the two endline rounds in wave one. Each row represents a separate regression of the outcome shown in the first column on treatment assignment. Variables not shown include section pair fixed effects and the second-round indicator. The final column indicates whether the specification also includes the baseline outcome variable, and its interaction with both the second-round indicator and the second-wave indicator. SEs are clustered at the section level. *** is significant at the 1% level, ** is significant at the 5% level, and * is significant at the 10% level. The control mean is the mean in the control group at endline.

| | Round 1 | | | Round 2 | | | |
|---|---|---|---|---|---|---|---|
| **Variables** | **Coefficient** | **SE** | **Observations** | **Coefficient** | **SE** | **Observations** | **Baseline-dependent variable controls?** |
| Forgive perpetrators | 0.986*** | (0.272) | 550 | 1.231*** | (0.361) | 521 | Y |
| Trust rebel excombatants | 0.100 | (0.073) | 241 | 0.048 | (0.198) | 203 | Y |
| Trust migrants | 0.140** | (0.053) | 653 | 0.119* | (0.069) | 564 | Y |
| Index of generalized trust in community | 0.119** | (0.050) | 878 | −0.009 | (0.038) | 845 | Y |
| Index of network strength | 0.015 | (0.027) | 885 | 0.119 | (0.085) | 850 | N |
| Index of community group participation | 0.038* | (0.022) | 884 | 0.084** | (0.040) | 847 | Y |
| Index of contributions to public goods | 0.024 | (0.033) | 885 | 0.035 | (0.046) | 850 | Y |
| Index of psychological well-being | −0.166*** | (0.052) | 873 | −0.170*** | (0.058) | 837 | Y |

outcomes that are specific to the war, such as forgiveness of war perpetrators and trust of former rebel combatants. This reiterates the idea that talking about the war is important in giving rise to the observed effects. In the supplementary materials, we examine these additional outcomes further by gauging their long-run impacts (table S19) and discussing them in greater detail.

## Conclusion

Our findings highlight the long shadow of war along two dimensions. The reconciliation forums we analyzed were held nearly a decade after the end of Sierra Leone's civil war. Yet, the positive effects on forgiveness and social capital suggest that the need for reconciliation persists long after the violence ends. At the same time, the negative psychological impacts indicate that truth-telling opened up psychological wounds, pointing to the potency of these war memories when they are evoked suddenly (*32*–*34*).

These psychological effects do not preclude the possibility that individuals who forgave in response to reconciliation gained a psychological benefit—but they do suggest that these gains were offset by other negative impacts, such as the difficulty of coping with negative memories. In that regard, they corroborate the idea that forgiving is not the same as forgetting (*73*). They also suggest that forgiveness stemming from an intense, one-time event that evokes negative memories may differ in its psychological impact relative to forgiveness stemming from ongoing therapy (*74*).

Overall, our results indicate that the gains in societal healing associated with reconciliation came at a substantial cost in individual psychological healing. As such, they imply that policymakers need to find ways of holding reconciliation processes that reduce these psychological costs, while retaining the societal benefits. For example, it is possible that the negative psychological impacts may be smaller or even reversed if reconciliation efforts are held in the direct aftermath of the war, when trauma symptoms are high and people have yet to move on in their own way (*75*). A second possibility lies in combining reconciliation with other types of complementary interventions. For example, coupling these programs with sustained counseling—as used by forgiveness therapies (*26*–*31*), exposure therapy (*32*, *36*), or trauma healing interventions (*17*)—may help mitigate the detrimental impacts. Given the global prevalence of conflict and postconflict reconciliation, future research should explore alternate designs for efforts aimed at unifying societies in the aftermath of war.

### REFERENCES AND NOTES


1. T. Pettersson, P. Wallensteen, *J. Peace Res.* **52**, 536–550 (2015).
2. J. Fearon, M. Humphreys, J. Weinstein, *Am. Econ. Rev.* **99**, 287–291 (2009).
3. J. Fearon, M. Humphreys, J. Weinstein, *Am. Polit. Sci. Rev.* **109**, 450–469 (2015).
4. K. Casey, R. Glennerster, E. Miguel, *Q. J. Econ.* **127**, 1755–1812 (2012).
5. A. Beath, F. Christia, R. Enikolopov, *Am. Polit. Sci. Rev.* **107**, 540–557 (2013).
6. M. Humphreys, R. Sanchez de la Sierra, P. van der Windt, *Polit. Anal.* **21**, 1–20 (2013).
7. G. Mansuri, V. Rao, *Localizing Development: Does Participation Work?* (The World Bank, 2013).
8. E. Brahm, "Patterns of truth: Examining truth commission impact in cross-national context," paper presented at the annual meeting of the International Studies Association, Honolulu, HI (2005).
9. N. Kritz, *War Crimes: The Legacy of Nuremberg*, B. Cooper, Ed. (TV Books, 1999).
10. H. Cobban, *Boston Review* **27**, 2 (2003).
11. B. Hamber, *Reconciliation After Violent Conflict: A Handbook* (International Institute for Democracy and Electoral Assistance, 2003).
12. N. Biggar, *Burying the Past: Making Peace and Doing Justice After Civil Conflict* (Georgetown Univ. Press, 2003).
13. J. Lederarch, *The Journey Towards Reconciliation* (Herald Press, 1999).
14. K. Asmal, L. Asmal, R. Roberts, *Reconciliation Through Truth: A Reckoning of Apartheid's Criminal Governance* (Cambridge Univ. Press, 1994).
15. Truth and Reconciliation Commission, *Truth and Reconciliation Commission of South Africa Report* (South African Government, 1998).
16. J. Gibson, *Am. J. Pol. Sci.* **48**, 201–217 (2004).
17. E. L. Staub, A. Pearlman, A. Gubin, A. Hagengimana, *J. Soc. Clin. Psychol.* **24**, 297–334 (2005).
18. E. L. Paluck, *J. Pers. Soc. Psychol.* **96**, 574–587 (2009).
19. C. Blattman, A. C. Hartman, R. A. Blair, *Am. Polit. Sci. Rev.* **108**, 100–120 (2014).
20. D. Mendeloff, *Int. Stud. Rev.* **6**, 355–380 (2004).
21. D. Mendeloff, *Hum. Rights Q.* **31**, 592–623 (2009).
22. M. Kaldor, J. Vincent, *Evaluation of UNDP assistance to conflict-affected countries: Case study Sierra Leone* (United Nations Development Programme Evaluation Office, 2006).
23. R. Conibere *et al.*, *Statistical Appendix to the Report of the Truth and Reconciliation Commission of Sierra Leone* (Benetech Human Rights Data Analysis Group, 2004), pp. 1–38.
24. L. A. Smith, C. Gambette, T. Longley, *Conflict Mapping in Sierra Leone: Violations of International Humanitarian Law from 1991 to 2002: Executive Summary* (No Peace Without Justice, 2004).
25. R. D. Enright, R. Fitzgibbons, *Helping Clients Forgive: An Empirical Guide for Resolving Anger and Restoring Hope* (American Psychological Association, 2000).
26. R. H. Al-Mabuk, R. D. Enright, P. A. Cardis, *J. Moral Educ.* **24**, 427–444 (1995).
27. C. T. Coyle, R. D. Enright, *J. Consult. Clin. Psychol.* **65**, 1042–1046 (1997).
28. S. R. Freedman, R. D. Enright, *J. Consult. Clin. Psychol.* **64**, 983–992 (1996).
29. W. F. Lin, D. Mack, R. D. Enright, D. Krahn, T. W. Baskin, *J. Consult. Clin. Psychol.* **72**, 1114–1121 (2004).
30. M. S. Rye *et al.*, *J. Consult. Clin. Psychol.* **73**, 880–892 (2005).
31. G. L. Reed, R. D. Enright, *J. Consult. Clin. Psychol.* **74**, 920–929 (2006).
32. J. Joseph, M. Gray, *J. Behav. Anal. Offend. Victim Treat. Prevent.* **1**, 69–79 (2008).
33. A. A. van Emmerik, J. H. Kamphuis, A. M. Hulsbosch, P. M. G. Emmelkamp, *Lancet* **360**, 766–771 (2002).
34. K. Brounéus, *J. Conflict Resolut.* **54**, 408–437 (2010).
35. S. Rose, J. Bisson, R. Churchill, S. Wessely, *Cochrane Database Syst. Rev.* **2**, CD000560 (2002).
36. J. Bisson, M. Andrew, *Cochrane Libr.* **2009**, 1 (2009).
37. I. L. McCann, L. Pearlman, *J. Trauma. Stress* **3**, 131–149 (1990).
38. L. A. Pearlman, W. Karen, Saakvitne, *Trauma and the Therapist: Countertransference and Vicarious Traumatization in Psychotherapy with Incest Survivors* (Norton, 1995).
39. M. J. Arvay, *Int. J. Adv. Couns.* **23**, 283–293 (2001).
40. M. Cunningham, *Soc. Work* **48**, 451–459 (2003).
41. R. Shaw, "Rethinking Truth and Reconciliation Commissions: Lessons from Sierra Leone," United States Institute of Peace Special Report 130 (USIP Press, 2005).
42. D. Backer, "The human face of justice: Victims' responses to South Africa's truth and reconciliation commission process," thesis, University of Michigan (2004).
43. D. Backer, *Security, Reconstruction, and Reconciliation: When the Wars End*, M. Ndulo, Ed. (University College London, 2007) p. 165–196.
44. D. Kaminer, D. J. Stein, I. Mbanga, N. Zungu-Dirwayi, *Br. J. Psychiatry* **178**, 373–377 (2001).
45. K. Brounéus, *Secur. Dialogue* **39**, 55–76 (2008).
46. R. D. Putnam, *J. Democracy* **6**, 65–78 (1995).
47. J. Quinn, *The Politics of Acknowledgement: Truth Commissions in Uganda and Haiti* (UBC Press, 2010).
48. L. Frison, S. J. Pocock, *Stat. Med.* **11**, 1685–1704 (1992).
49. D. McKenzie, *J. Dev. Econ.* **99**, 210–221 (2012).
50. A. Banerjee *et al.*, *Science* **348**, 1260799 (2015).
51. M. Bruhn, D. McKenzie, *Am. Econ. J. Appl. Econ.* **1**, 200–*232* (2009).
52. J. R. Kling, J. B. Liebman, L. F. Katz, *Econometrica* **75**, 83–119 (2007).
53. M. L. Anderson, *J. Am. Stat. Assoc.* **103**, 1481–1495 (2008).
54. Y. Benjamini, Y. Hochberg, *J. R. Stat. Soc., B* **57**, 289–300 (1995).
55. D. Curran-Everett, D. J. Benos, *Am. J. Physiol. Lung Cell. Mol. Physiol.* **287**, L259–L261 (2004).
56. D. Curran-Everett, *Am. J. Physiol. Regul. Integr. Comp. Physiol.* **279**, R1–R8 (2000).
57. M. S. Rye, "Evaluation of a secular and a religiously integrated forgiveness group therapy program for college students who have been wronged by a romantic partner," thesis, Bowling Green State University, Bowling Green, OH (1998).
58. M. J. Subkoviak *et al.*, *J. Adolesc.* **18**, 641–655 (1995).
59. E. Foa, D. Riggs, C. Dancu, B. Rothbaum, *J. Trauma. Stress* **6**, 459–473 (1993).
60. E. B. Foa, D. F. Tolin, *J. Trauma. Stress* **13**, 181–191 (2000).
61. W. W. Zung, C. B. Richards, M. J. Short, *Arch. Gen. Psychiatry* **13**, 508–515 (1965).
62. W. W. Zung, *Psychosomatics* **12**, 371–379 (1971).
63. L. R. Derogatis, R. S. Lipman, K. Rickels, E. H. Uhlenhuth, L. Covi, *Behav. Sci.* **19**, 1–15 (1974).
64. S. Theresa, *Integr. Psychiatry* **7**, 60–62 (2010).
65. T. S. Betancourt *et al.*, *Child Dev.* **81**, 1077–1095 (2010).
66. T. S. Betancourt, I. I. Borisova, M. de la Soudière, J. Williamson, *J. Adolesc. Health* **49**, 21–28 (2011).
67. A. M. Steinberg, M. J. Brymer, K. B. Decker, R. S. Pynoos, *Curr. Psychiatry Rep.* **6**, 96–100 (2004).
68. S. S. Hawkins, J. Radcliffe, *J. Pediatr. Psychol.* **31**, 420–430 (2006).
69. C. P. Bayer, F. Klasen, H. Adam, *JAMA* **298**, 555–559 (2007).
70. F. W. Weathers, J. A. Huska, T. M. Keane, *PCL-M for DSM-IV* (National Center for PTSD—Behavioral Science Division, 1991).
71. G. M. Sullivan, A. R. Artino Jr., *J. Grad. Med. Educ.* **5**, 541–542 (2013).
72. W. P. Murphy, *Africa J. Int. Afr. Inst.* **50**, 193–207 (1980).
73. T. W. Baskin, R. D. Enright, *J. Couns. Dev.* **82**, 79–90 (2004).
74. R. D. Enright, A. Holter, T. Baskin, C. Knutson, *J. Res. Ed.* **17**, 63–78 (2007).
75. E. B. Foa, *J. Clin. Psychiatry* **67** (suppl. 2), 40–45 (2006).


### ACKNOWLEDGMENTS

We thank J. Caulker from Fambul Tok and L. Hoffman from Catalyst for Peace for enabling us to study Fambul Tok's initiative. We are grateful to E. Dixon, Q.-A. Do, M. Gilligan, S. Mullainathan, and D. Stasavage for providing detailed comments and suggestions on the manuscript and to T. Betancourt for providing valuable input on the psychometric survey measures used in the study. We additionally thank A. Mansaray, A. Ahmed, J. Creighton, and N. Hasham (in chronological order of involvement) for outstanding research assistance in the field. This project was funded by 3ie (grant code OW2.253) and the J-PAL Governance Initiative (subaward 5710003563) and received extensive implementation support from Innovations for Poverty Action. We thank them, without implicating them, for making this project possible. This research also received institutional review board (IRB) approval from Oxford University (ref. SSD/CUREC1/11-028), New York University (HS# 11-8528; IRB#: 14-9936), and Innovations for Poverty Action (Protocol 534.11February002). All errors and omissions are our own. Upon publication, the replication data and code from this study will be made publicly available through the Interuniversity Consortium for Political and Social Research (ICPSR) data depository. The Pre-Analysis Plan, which is already posted publicly in the EGAP depository, will also be made available as a part of the ICPSR replication package.

### SUPPLEMENTARY MATERIALS

www.sciencemag.org/content/352/6287/787/suppl/DC1
Supplementary Texts S1 to S6
Figs. S1 to S4
Tables S1 to S26
References (*76*–*98*)

30 November 2015; accepted 29 March 2016
10.1126/science.aad9682

Downloaded from http://science.sciencemag.org/ on May 12, 2016

REPORTS

NONLINEAR OPTICS

# Large optical nonlinearity of indium tin oxide in its epsilon-near-zero region

M. Zahirul Alam,[1] Israel De Leon,[1,3]* Robert W. Boyd[1,2]

**Nonlinear optical phenomena are crucial for a broad range of applications, such as microscopy, all-optical data processing, and quantum information. However, materials usually exhibit a weak optical nonlinearity even under intense coherent illumination. We report that indium tin oxide can acquire an ultrafast and large intensity-dependent refractive index in the region of the spectrum where the real part of its permittivity vanishes. We observe a change in the real part of the refractive index of 0.72 ± 0.025, corresponding to 170% of the linear refractive index. This change in refractive index is reversible with a recovery time of about 360 femtoseconds. Our results offer the possibility of designing material structures with large ultrafast nonlinearity for applications in nanophotonics.**

A long-standing goal in nonlinear optics has been the development of materials whose refractive index can be drastically changed using a low-power optical field. Ideally, these materials should possess sub-picosecond time response and be compatible with existing complementary metal-oxide semiconductor (CMOS) fabrication technologies (*1*–*2*). Simple calculus shows that, for a given change ($\Delta\varepsilon$) in the permittivity $\varepsilon$, the resulting change ($\Delta n$) in the refractive index $n$ is given for a lossless material by $\Delta n = \Delta\varepsilon/(2\sqrt{\varepsilon})$. We see that this change becomes large as the permittivity becomes small, suggesting that the epsilon-near-zero (ENZ) frequencies of a material system should give rise to strong nonlinear optical properties.

Materials possessing free charges, such as metals and highly doped semiconductors, have zero real permittivity at the bulk plasmon wavelength. A number of authors have reported on the unusual properties of matter under ENZ conditions (*3*–*5*) and on their promise for applications in nonlinear optics (*6*–*10*).

We used commercially available indium tin oxide (ITO), a CMOS-compatible degenerate semiconductor, as the ENZ medium (Fig. 1). The zero-permittivity wavelength of ITO occurs at near-infrared wavelengths and can be tuned by controlling the doping density or by applying a static electric field (*11*, *12*). The *z*-scan technique was used to characterize the intensity-dependent refractive index of ITO for transverse magnetic (TM) polarized light (Fig. 2A) (*13*, *14*). The wavelength-dependent effective nonlinear refractive index coefficient $n_{2(\text{eff})} = \Delta n/I$ ($I$ is the intensity of the laser beam) and effective nonlinear attenuation constant $\beta_{(\text{eff})} = \Delta\alpha/I$ extracted from our measurements are plotted for angles of incidence varying from $\theta$ = 0° to $\theta$ = 60° (Fig. 2, A and B). The results indicate that ITO exhibits positive $n_{2(\text{eff})}$ and negative $\beta_{(\text{eff})}$, corresponding to self-focusing and saturable absorption, respectively. Our results reveal a substantial wavelength- and angle-dependent enhancement of the material's nonlinear response at ENZ wavelengths. The measured value of $n_{2(\text{eff})}$ ($6 \times 10^{-5}$ cm$^2$/GW) at the shortest wavelength (970 nm) agrees well with the value reported by Elim *et al.* (*15*). At a wavelength of 1240 nm for normal incidence, $n_{2(\text{eff})}$ and $\beta_{(\text{eff})}$ are ~43 and ~53 times larger than the corresponding values at 970 nm, respectively. For TM-polarized light at oblique incident, the nonlinear response is further enhanced. The enhancement factors, defined relative to the values far from the ENZ spectral region (at $\lambda$ = 970 nm) at normal incidence, are plotted as functions of $\theta$ in Fig. 2C. The enhancement tends to increase with $\theta$ for 0° < $\theta$ < 60° and decreases sharply for $\theta$ > 60°. The maximum enhancement factors, measured at $\theta$ = 60°, are 1837 and 2377 for $n_{2(\text{eff})}$ and $\beta_{(\text{eff})}$, respectively. Thus, at $\lambda_0$ = 1240 nm, the $n_{2(\text{eff})}$ and $\beta_{(\text{eff})}$ values for $\theta$ = 60° are ~43 and ~45 times larger than for normal incidence, respectively.

The temporal dynamics of the optical nonlinear response was studied using a degenerate pump-probe transmission measurement. Here, an intense pump pulse and a weak probe pulse at the same wavelength interact with the sample, and the induced change in probe transmittance $\Delta T$ is measured as a function to the time delay $\tau$ between the two pulses. The measured temporal response is proportional to the convolution of the probe's temporal envelope with the material's temporal response function. (Fig. 2D). The transient nonlinear response has a rise time no longer than 200 fs (this estimate is limited by our laser pulse duration) and a recovery time of 360 fs. Such ultrafast response would allow all-optical modulation speeds of at least 1.5 THz.

The nonlinear coefficients shown in Fig. 2, A and B, may be slightly overestimated because the *z*-scan method neglects the change in reflectivity caused by $\Delta n$ (*16*), but this overestimation is no larger than by a factor of ~1.8. In any case, the measured values are extremely large. In particular, the value of $n_{2(\text{eff})}$ = 0.11 cm$^2$/GW measured at $\theta$ = 60° is more than two orders of magnitude larger than that of $As_2Se_3$ chalcogenide glass (*17*) and ~5 times larger in magnitude than that of a recently proposed highly nonlinear metamaterial (*6*). The optical losses of ITO at ENZ wavelengths can be quite large, although in (*16*) we describe some realistic applications that can tolerate this much loss.

We attribute the observed nonlinearity primarily to a modification of the energy distribution of conduction-band electrons as a consequence of the laser-induced electron heating. We describe the nonlinear optical response by means of a phenomenological two-temperature model (*16*, *18*–*20*). Figure 3A shows the calculated temporal evolution of the free-electron temperature ($T_e$) and lattice temperature ($T_l$) of ITO after irradiation by the laser pulse (denoted by the dashed curve). The free-electron temperature exhibits an ultrafast transient and is limited by the electron-phonon relaxation time of the material (*21*). The normalized transient nonlinear response measured via the degenerate pump-probe technique is well described by the temporal profiles of $T_e$ convolved with the probe's intensity envelope, which is plotted as the solid curve in Fig. 2D.

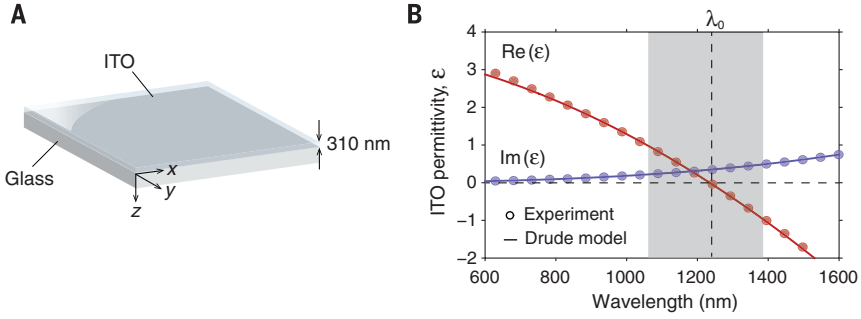


**Fig. 1. The ITO sample under investigation and its linear optical response.** (**A**) Structure under investigation. (**B**) Linear relative permittivity of the ITO film measured via spectroscopic ellipsometry (symbols) and estimated by the Drude model (lines). The condition Re($\varepsilon$) = 0 occurs at $\lambda_0$ = 1240 nm. The shaded region shows the spectral range investigated in our nonlinear optical characterization.

[1]Department of Physics and Max Planck Centre for Extreme and Quantum Photonics, University of Ottawa, 25 Templeton Street, Ottawa, ON, K1N 6N5, Canada. [2]Institute of Optics and Department of Physics and Astronomy, University of Rochester, Rochester, NY 14627, USA. [3]School of Engineering and Sciences, Tecnológico de Monterrey, Monterrey, Nuevo León 64849, Mexico.
*Corresponding author. Email: ideleon@itesm.mx

Downloaded from http://science.sciencemag.org/ on May 12, 2016

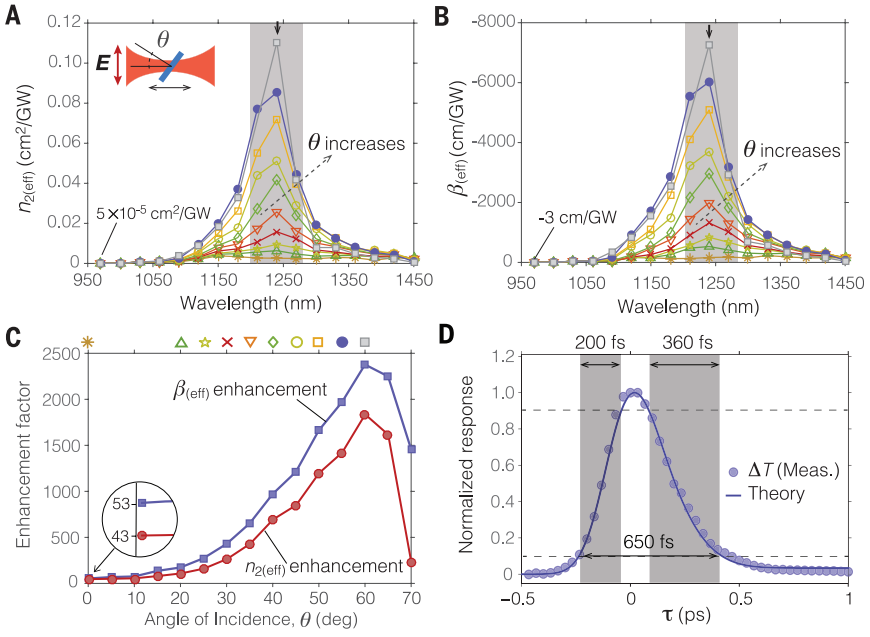


**Fig. 2. Nonlinear optical response of the ITO sample.** Wavelength dependence of (**A**) the nonlinear effective refractive index, $n_{2(eff)}$, and (**B**) the effective nonlinear attenuation constant, $\beta_{(eff)}$. The nonlinear response is enhanced in the ENZ region of the spectrum (shaded). The vertical arrows indicate the wavelength $\lambda_0$ = 1240 nm. (**C**) The corresponding enhancement for $n_{2(eff)}$ and $\beta_{(eff)}$ at $\lambda_0$, compared with values at 970 nm, are plotted as functions of θ. The values of θ corresponding to the different symbols in (A) and (B) are indicated at the top. (**D**) Time dependence of the normalized transient change of transmittance ($\Delta T$) obtained via a degenerate pump-probe measurement.

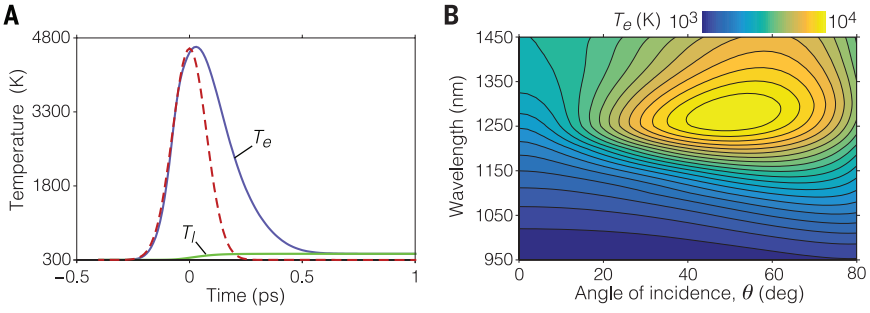


**Fig. 3. Numerical modeling of the hot-electron dynamics of ITO.** (**A**) Transient response of $T_e$ and $T_l$ obtained using the two-temperature model. The dashed curve denotes the pulse intensity profile (in arbitrary units). (**B**) Map of the peak free-electron temperature in ITO calculated as a function of θ and λ. Both calculations assume a normally incident laser with an intensity of 66 GW/cm$^2$.

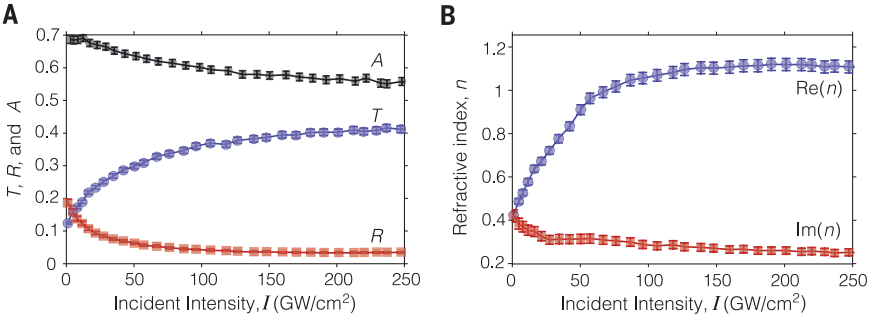


**Fig. 4. Nonlinear optical response of ITO for laser fields sufficiently intense to produce saturation.** (**A**) Intensity-dependent transmittance ($T$), reflectance ($R$), and absorptance ($A$) of the ITO-glass structure at $\lambda_0$ for θ = 30°. (**B**) Complex effective refractive index of ITO extracted from the measured values in (A) using a transfer-matrix method.

The peak values of $T_e$ obtained with our model are plotted in Fig. 3B as functions of the wavelength and the angle of incidence. The temperature profile exhibits the main features present in our experimental results, namely a pronounced enhancement of the response at ENZ wavelengths that reaches a maximum for an angle of incidence close to θ = 60°. The general behavior observed in this result can be understood in terms of two contributions. The increasing values of $T_e$ for longer wavelengths result from the increase in free carrier absorption, and the peak that develops around θ ≈ 60° results from an enhancement of the electric field within the ITO film. This enhancement occurs only for obliquely incident TM polarized light at wavelengths within the ENZ region and follows from the continuity of the normal electric displacement field across an ITO-air interface (*16*, *22*). As discussed in (*16*), Δε results from an effective red shift in the material's plasma frequency caused by an increase in the free-electron temperature ($\Delta T_e$). It is important to note that Δε does not scale linearly with $\Delta T_e$ for a large $\Delta T_e$ and that $\Delta n$ is a nonlinear function of Δε at ENZ. Consequently, a modest field intensity enhancement in the ITO film can lead to a large enhancement of $n_{2(eff)}$ at ENZ wavelengths. This is confirmed by our model presented in (*16*), which accounts for such nonlinear relationships between $\Delta n$, Δε, and $\Delta T_e$.

The hot-electron–induced optical nonlinearity of ITO at ENZ wavelengths differs from that of noble metals under infrared irradiation in two ways. First, as argued above, for a given change in permittivity, the nonlinear change in refractive index is always larger in the ENZ region than in non-ENZ regions. Second, the free-electron heat capacity of ITO (4.53 Jm$^{-3}$K$^{-1}$) is more than an order of magnitude smaller than that of a noble metal such as gold. Thus, the increase in the free-electron temperature compared with the Fermi temperature and the consequent change in refractive index in ITO is much larger.

For sufficiently large optical intensities, the nonlinear response of ITO at ENZ wavelengths can lead to changes in its refractive index that are larger than the linear refractive index. As a result, the Fresnel reflection and transmission coefficients undergo a large change as a function of the incident optical intensity. To demonstrate this phenomenon, we measured the intensity-dependent transmittance ($T$), reflectance ($R$), and absorptance ($A$) of the sample at 1240 nm for θ = 30° (Fig. 4A). At the lowest intensity, these measurements agree well with the predictions of a simple linear Fresnel analysis. As the intensity is increased, we observe a large monotonic increase (reduction) in transmittance (reflectance). The maximum reduction in absorptance is ~30%, which is consistent with the saturable absorption observed in our $z$-scan measurements. The real part of the refractive index of ITO undergoes a dramatic change from its linear value of 0.42 to a value of 1.14 ± 0.025 for an intensity of 150 GW/cm$^2$ (Fig. 4B). Similarly, the imaginary part of the index is substantially reduced from

Downloaded from http://science.sciencemag.org/ on May 12, 2016

its linear value of 0.42 to a value of 0.27 ± 0.015 at this intensity. Both the real and the imaginary parts of the refractive index saturate for even higher input power. We found that these measurements are highly repeatable and that the material does not exhibit a permanent change of its optical properties.

The magnitude of the optically induced ultrafast change of the real part of the refractive index ($\Delta n$ = 0.72 ± 0.025) and the relative change of 170% in comparison to the linear value are unprecedented. The change in the refractive index corresponds to a change of the permittivity from $\varepsilon = 0 + 0.352i$ to $\varepsilon = 1.22 + 0.61i$ where i is the square root of −1. This result shows that ITO can exhibit a reversible transition from metallic to a lossy dielectric state with a subpicosecond time response at wavelengths slightly longer than the bulk plasmon wavelength. Moreover, the usual perturbation expansion description of nonlinear optical effects is not applicable for this material at high intensities.

We have shown that a thin ITO film exhibits an extremely large ultrafast third-order nonlinearity at ENZ wavelengths. Moreover, it can acquire an optically induced change in the refractive index that is unprecedentedly large. Our results challenge the notion that the nonlinear optical response is only a perturbation to the linear response. Materials with such a large nonlinear response are expected to enable exotic nonlinear dynamics (*22*) and allow all-optical control of metasurface and active plasmonics devices. Thus, our results introduce a completely new paradigm in nonlinear optics and open new avenues for developing optical nanostructures with large nonlinearity for applications in nanophotonics, plasmonics, and nonlinear nano-optics.

## REFERENCES AND NOTES


1. M. Kauranen, A. V. Zayats, *Nat. Photonics* **6**, 737–748 (2012).
2. M. Abb, P. Albella, J. Aizpurua, O. L. Muskens, *Nano Lett.* **11**, 2457–2463 (2011).
3. M. Silveirinha, N. Engheta, *Phys. Rev. Lett.* **97**, 157403 (2006).
4. A. Alù, M. Silveirinha, A. Salandrino, N. Engheta, *Phys. Rev. B* **75**, 155410 (2007).
5. A. R. Davoyan, A. M. Mahmoud, N. Engheta, *Opt. Express* **21**, 3279–3286 (2013).
6. A. D. Neira *et al.*, *Nat. Commun.* **6**, 7757 (2015).
7. H. Suchowski *et al.*, *Science* **342**, 1223–1226 (2013).
8. A. Capretti, Y. Wang, N. Engheta, L. Dal Negro, *Opt. Lett.* **40**, 1500–1503 (2015).
9. T. S. Luk *et al.*, *Appl. Phys. Lett.* **106**, 151103 (2015).
10. N. Kinsey *et al.*, *Optica* **2**, 616 (2015).
11. G. V. Naik, V. M. Shalaev, A. Boltasseva, *Adv. Mater.* **25**, 3264–3294 (2013).
12. E. Feigenbaum, K. Diest, H. A. Atwater, *Nano Lett.* **10**, 2111–2116 (2010).
13. M. Sheik-Bahae, A. A. Said, T.-H. Wei, D. J. Hagan, E. W. Van Stryland, *IEEE J. Quantum Electron.* **26**, 760–769 (1990).
14. B. K. Rhee, J. S. Byun, E. W. Van Stryland, *J. Opt. Soc. Am. B* **13**, 2720 (1996).
15. H. I. Elim, W. Ji, F. Zhu, *Appl. Phys. B* **82**, 439–442 (2006).
16. See supplementary materials on *Science* Online.
17. R. W. Boyd, *Nonlinear Optics* (Elsevier, 2008).
18. C. Sun, F. Vallée, L. Acioli, E. P. Ippen, J. G. Fujimoto, *Phys. Rev. B Condens. Matter* **48**, 12365–12368 (1993).
19. S. D. Brorson, J. G. Fujimoto, E. P. Ippen, *Phys. Rev. Lett.* **59**, 1962–1965 (1987).
20. E. Carpene, *Phys. Rev. B* **74**, 024301 (2006).
21. B. Rethfeld, A. Kaiser, M. Vicanek, G. Simon, *Phys. Rev. B* **65**, 214303 (2002).
22. D. de Ceglia, S. Campione, M. A. Vincenti, F. Capolino, M. Scalora, *Phys. Rev. B* **87**, 155140 (2013).



## ACKNOWLEDGMENTS

The authors gratefully acknowledge the support of the Canada Excellence Research Chairs Program. R.W.B. is the cofounder and Chief Technology Officer of KBN Optics, Pittsford, NY.


## SUPPLEMENTARY MATERIALS

www.sciencemag.org/content/352/6287/795/suppl/DC1
Materials and Methods
Supplementary Text
Figs. S1 to S4
References (*23*–*32*)


7 December 2015; accepted 12 April 2016
Published online 28 April 2016
10.1126/science.aae0330


CATALYSIS

# Photochemical route for synthesizing atomically dispersed palladium catalysts


**Pengxin Liu,[1] Yun Zhao,[1] Ruixuan Qin,[1] Shiguang Mo,[1] Guangxu Chen,[1] Lin Gu,[2] Daniel M. Chevrier,[3] Peng Zhang,[3] Qing Guo,[1] Dandan Zang,[1] Binghui Wu,[1] Gang Fu,[1]* Nanfeng Zheng[1]***



**Atomically dispersed noble metal catalysts often exhibit high catalytic performances, but the metal loading density must be kept low (usually below 0.5%) to avoid the formation of metal nanoparticles through sintering. We report a photochemical strategy to fabricate a stable atomically dispersed palladium–titanium oxide catalyst ($Pd_1/TiO_2$) on ethylene glycolate (EG)–stabilized ultrathin $TiO_2$ nanosheets containing Pd up to 1.5%. The $Pd_1/TiO_2$ catalyst exhibited high catalytic activity in hydrogenation of C=C bonds, exceeding that of surface Pd atoms on commercial Pd catalysts by a factor of 9. No decay in the activity was observed for 20 cycles. More important, the $Pd_1/TiO_2$-EG system could activate $H_2$ in a heterolytic pathway, leading to a catalytic enhancement in hydrogenation of aldehydes by a factor of more than 55.**


Atomically dispersed catalysts with mononuclear metal complexes or single metal atoms anchored on supports have recently attracted increasing research attention (*1*–*15*). With 100% metal dispersity, atomically dispersed catalysts offer the maximum atom efficiency, providing the most ideal strategy to create cost-effective catalysts, particularly those based on Earth-scarce metals such as Pt (*1*–*5*), Au (*5*–*8*), Pd (*9*–*12*), and Ir (*13*, *14*). Moreover, the uniform active sites of atomically dispersed catalysts make them a model system to understand heterogeneous catalysis at the molecular level (*4*, *6*, *10*, *12*–*14*, *16*–*21*), bridging the gap between heterogeneous and homogeneous catalysis.

During the past decade, several strategies for atomically dispersing metal sites on catalyst supports have emerged; these include lowering the loading amount of metal components (*1*, *8*–*10*, *12*, *20*), enhancing the metal-support interactions (*4*, *6*, *9*, *19*), and using voids in supports or vacancy defects on supports (*3*, *11*, *14*, *22*). In most cases, the supports for atomically dispersed catalysts are deliberately chosen. Zeolites provide effective voids to anchor individual metal atoms therein and prevent them from sintering during catalysis (*23*, *24*). Defects on reducible oxides (e.g., $TiO_2$ and $CeO_2$) (*25*, *26*) and on graphene or $C_3N_4$ (*9*, *11*, *22*) help to stabilize atomically dispersed metal atoms on supports. Coordinatively unsaturated $Al^{3+}$ ions on $\gamma$-$Al_2O_3$ act as binding centers to maintain the high dispersion of Pt atoms, but Pt rafts form as the loading amount of Pt increases (*3*). Currently, two major challenges remain in the field of atomically dispersed catalysts: (i) to ensure a loading content high enough for practical applications while maintaining the metal centers as individual sites under catalytic conditions (*27*, *28*), and (ii) to address whether atomically dispersed catalysts offer distinct active sites and/or undergo catalytic pathways different from those of conventional metal catalysts (*1*, *4*–*6*, *8*–*10*, *12*, *16*–*21*).

We report a room-temperature photochemical strategy to fabricate a highly stable, atomically dispersed Pd catalyst ($Pd_1/TiO_2$) on ultrathin $TiO_2$ nanosheets with Pd loading up to 1.5%.


[1]State Key Laboratory for Physical Chemistry of Solid Surfaces, Collaborative Innovation Center of Chemistry for Energy Materials, Engineering Research Center for Nano-Preparation Technology of Fujian Province, National Engineering Laboratory for Green Chemical Productions of Alcohols, Ethers, and Esters, and Department of Chemistry, College of Chemistry and Chemical Engineering, Xiamen University, Xiamen 361005, China. [2]Institute of Physics, Chinese Academy of Sciences, Beijing 100190, China. [3]Department of Chemistry, Dalhousie University, Halifax, Nova Scotia B3H 4R2, Canada.
***Corresponding author. Email: nfzheng@xmu.edu.cn (N.Z.);**


Downloaded from http://science.sciencemag.org/ on May 12, 2016

Ultraviolet (UV) light–induced formation of ethylene glycolate (EG) radicals on $TiO_2$ nanosheets was shown to be critical for preparing $Pd_1/TiO_2$. With abundant Pd-O interfaces, $Pd_1/TiO_2$ activates $H_2$ in a heterolytic pathway distinct from the homolytic pathway on conventional Pd heterogeneous catalysts. The $Pd_1/TiO_2$ catalyst exhibits extremely high catalytic activities and stabilities in hydrogenation of C=C and C=O. A turnover frequency (TOF) greater than that of surface Pd atoms on commercial Pd catalysts by a factor of >55 was demonstrated on $Pd_1/TiO_2$ in the hydrogenation of aldehyde at room temperature, and no decay in the catalytic activity was observed during catalysis.

Two-atom-thick $TiO_2$(B) nanosheets [figs. S1 to S4 (*29*)] were prepared by reacting $TiCl_4$ with EG and were used as the support (*30*). $H_2PdCl_4$ was introduced into a water dispersion of $TiO_2$(B) to allow the adsorption of Pd species (figs. S5 and S6). The mixture was then irradiated by low-density UV provided by a Xe lamp (fig. S7). After 10 min of irradiation, the $Pd_1/TiO_2$ catalyst was collected and washed thoroughly with water. No formation of Pd nanoparticles (NPs) was observed in transmission electron microscopy (TEM) images (Fig. 1A and fig. S8) or in the x-ray diffraction pattern (fig. S9) of the obtained $Pd_1/TiO_2$ catalyst, even with the loading content of Pd as high as 1.5 weight percent (wt %) as analyzed by inductively coupled plasma mass spectrometry (ICP-MS). Energy-dispersive x-ray spectroscopy (EDS) analysis in a scanning transmission electron microscope (STEM) revealed that atomic Pd was evenly dispersed in $Pd_1/TiO_2$ (Fig. 1B), unlike in supported Pd NPs prepared by a conventional impregnation method followed by calcination in air at 350°C (fig. S10). To verify that Pd atoms were dispersed in $Pd_1/TiO_2$, we performed x-ray absorption near-edge structure (XANES) and extended x-ray absorption fine structure (EXAFS) spectrometry (Fig. 1C and figs. S11 and S12). There was only one notable peak in the region 1 to 2 Å from the Pd-O contribution, and no peak in the region 2 to 3 Å from the Pd-Pd contribution, confirming the sole presence of dispersed Pd atoms in $Pd_1/TiO_2$ (table S1). The calcination of the as-prepared $Pd_1/TiO_2$ in air at 350°C removed the organic residues on the surface of $Pd_1/TiO_2$ and thus allowed direct observation of the atomic dispersion of Pd by aberration-corrected STEM (Fig. 1D and fig. S13).

After calcination, there were still a large number of dispersed Pd atoms on the $TiO_2$ support, even with the Pd loading up to 1.5 wt%. We also investigated the CO adsorption behavior of $Pd_1/TiO_2$ (fig. S14) to confirm the atomic dispersion of Pd on the catalyst. There was only a weak band at 2100 $cm^{-1}$ ascribed to CO adsorbed on $Pd^{\delta+}$ in a top configuration (*31*). No signals attributed to CO adsorbed on bridge or hollow sites were observed, quite unlike supported Pd nanoparticulate catalysts (fig. S15).

Styrene hydrogenation was chosen as a model reaction to evaluate the catalytic activity of $Pd_1/TiO_2$. The $Pd_1/TiO_2$ catalyst displayed an extremely high activity and stability (Fig. 2, A and B) relative to commercial Pd/C (fig. S16), $TiO_2$(B)-supported Pd NPs (fig. S17), and unsupported homogeneous $H_2PdCl_4$ catalysts. We achieved 100% styrene conversion in 1 hour at a molar ratio of $1:10^4$ (Pd:styrene). The calculated TOF value of $Pd_1/TiO_2$, 8973 $hours^{-1}$, was greater than that of surface Pd atoms on the Pd/C catalyst (972 $hours^{-1}$) by a factor of 9. The reaction rate of $Pd_1/TiO_2$ was maintained even after 20 cycles with the same catalyst (fig. S18), which suggests that the atomically dispersed structure of $Pd_1/TiO_2$ was robust under the catalytic conditions. There was no detectable change in the EXAFS fitting profiles after 20 catalytic cycles (fig. S19 and table S2). In contrast, an obvious decreased activity was observed on unsupported $H_2PdCl_4$ in the second cycle and even at the end of the first run (fig. S20). Because styrene hydrogenation is a zero-order reaction whose reaction rate is independent of the styrene's concentration (*32*, *33*), the decline in the reaction rate of $H_2PdCl_4$ (Fig. 2B) was caused by the changing status of the catalyst. After reaction, small Pd NPs were detected in the reaction mixture (figs. S21 and S22).

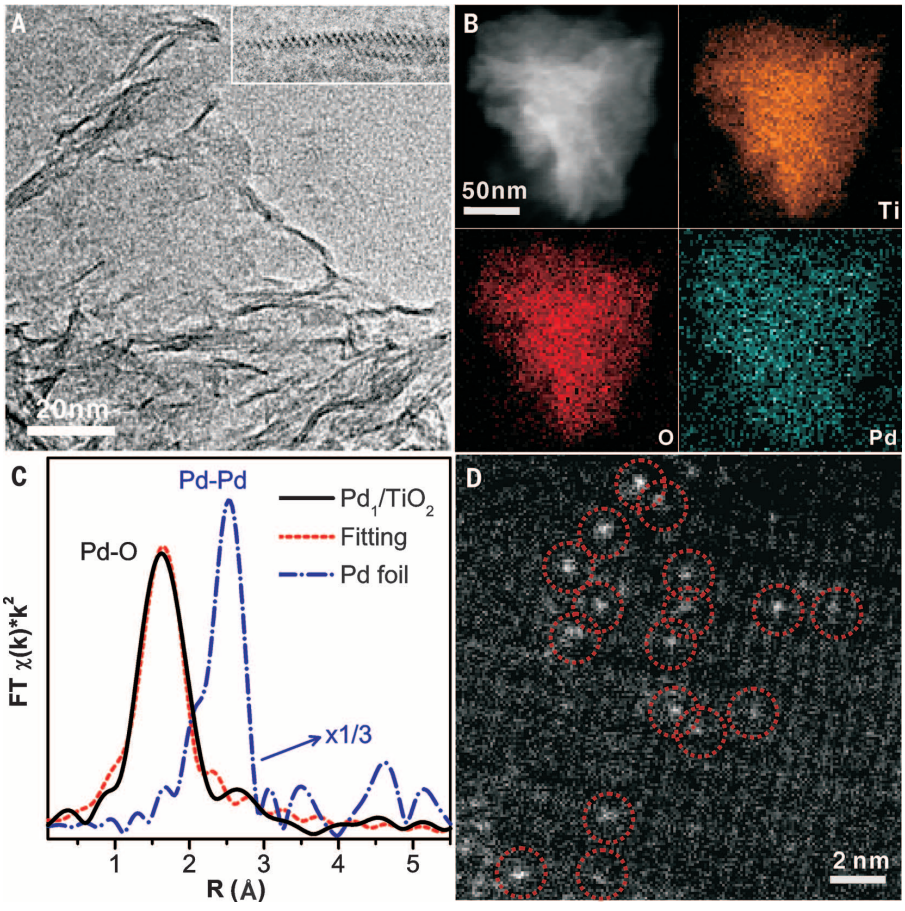


**Fig. 1. Structural characterizations of $Pd_1/TiO_2$.** (**A**) Representative TEM image of $Pd_1/TiO_2$. The inset is an aberration-corrected STEM image for cross sections of ultrathin $TiO_2$(B), showing that it is composed of only two layers of Ti atoms. (**B**) STEM-EDS elemental mapping of a single $Pd_1/TiO_2$ nanosheet. (**C**) FT-EXAFS spectra of $Pd_1/TiO_2$ and bulk palladium foil at the Pd K-edge, showing the surrounding atoms adjacent to Pd atoms. (**D**) High-resolution high-angle annular dark-field (HAADF) STEM image of $Pd_1/TiO_2$. The sample was calcined in air at 350°C for better contrast.

To better understand why the $Pd_1/TiO_2$ catalyst possessed such a high catalytic activity and stability, we prepared a catalyst (denoted $PdCl_2/TiO_2$) by the same method as for $Pd_1/TiO_2$ but without the UV treatment (fig. S23). No Pd-Pd bonds in $PdCl_2/TiO_2$ were detected by EXAFS (Fig. 2C and fig. S24), similar to $Pd_1/TiO_2$. The coordination numbers of Pd-O and Pd-Cl in the obtained $PdCl_2/TiO_2$ were 2.2 and 1.7, respectively (table S3). The Pd:Cl molar ratio of ~1:2 in the catalyst was confirmed by the elemental analysis (fig. S25). All of these data indicated that Pd atoms in $PdCl_2/TiO_2$ were in the form of individual $PdCl_2$ species bound on $TiO_2$(B). The presence of two $Cl^-$ ligands on each Pd atom made the catalytic performance of $PdCl_2/TiO_2$ much poorer than that of $Pd_1/TiO_2$ (Fig. 2D). The reaction rate already declined during the first run and kept decreasing after every recycle, suggesting a deleterious effect of Pd-Cl bonds on the catalysis. Similar to $H_2PdCl_4$, the decreased activity of $PdCl_2/TiO_2$ was attributed to the sintering of Pd atoms into NPs during catalysis. EXAFS studies revealed that a peak in the region 2 to 3 Å from the Pd-Pd contribution emerged for the $PdCl_2/TiO_2$ catalyst after catalysis (Fig. 2C and table S4).

Downloaded from http://science.sciencemag.org/ on May 12, 2016

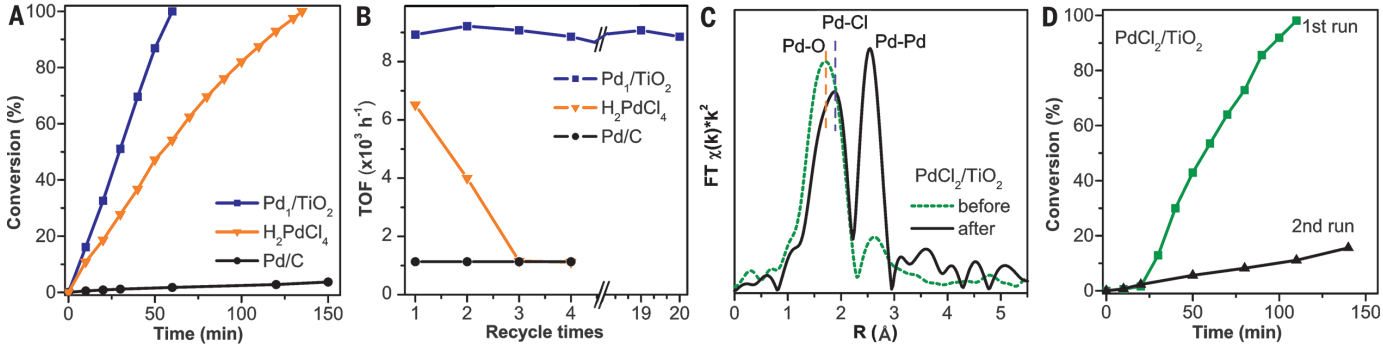


**Fig. 2. Catalytic performances of $Pd_1/TiO_2$ and reference materials in styrene hydrogenation.** (**A** and **B**) Catalytic performances for the first run (A) and TOF (B) of several recycles of repeated reactions for $Pd_1/TiO_2$, $H_2PdCl_4$, and commercial Pd/C. The same portion of $Pd_1/TiO_2$ catalyst was recycled and used for 20 runs without loss of activity. (**C**) FT-EXAFS spectra at the Pd K-edge of $PdCl_2/TiO_2$ before and after catalysis reaction. (**D**) First- and second-run catalytic performances of $PdCl_2/TiO_2$. Reaction conditions: ethanol, 10 ml; Pd, 0.005 μmol; styrene, 50 μmol; $T$ = 303 K; pressure = 0.1 MPa.

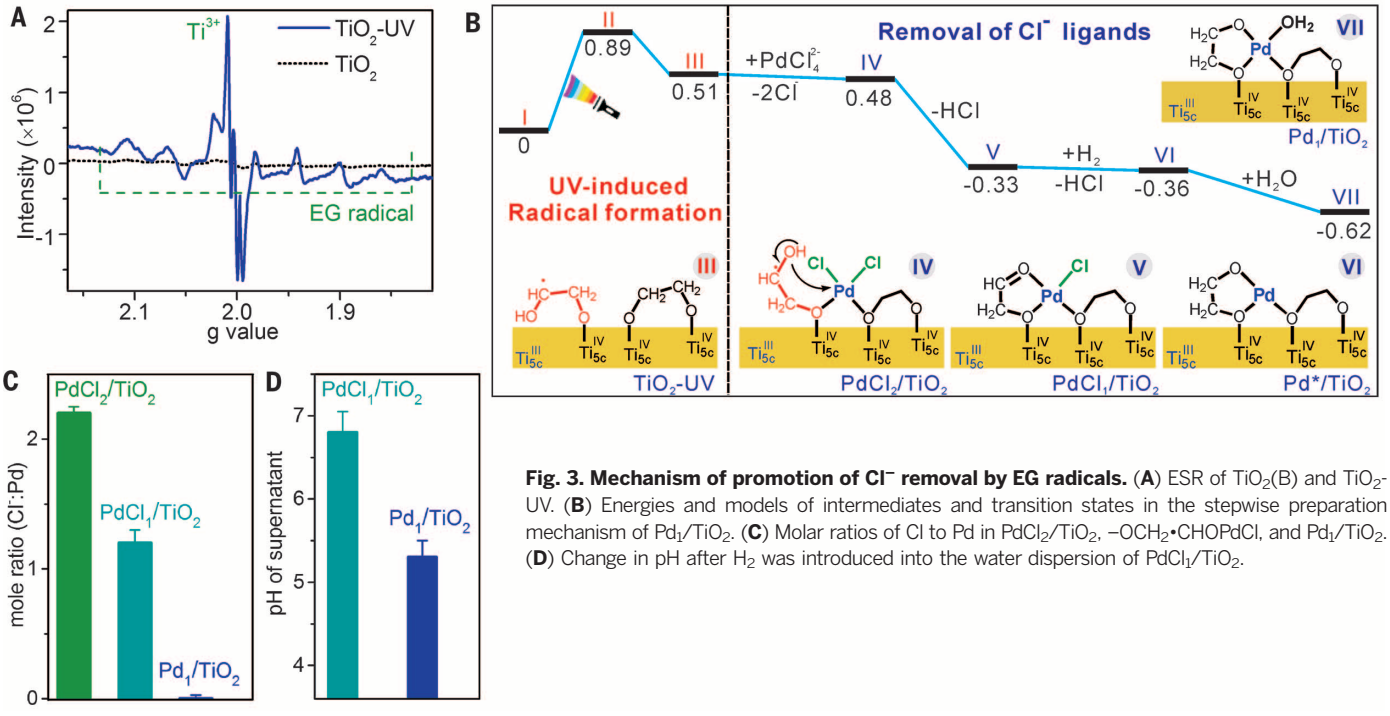


**Fig. 3. Mechanism of promotion of $Cl^-$ removal by EG radicals.** (**A**) ESR of $TiO_2$(B) and $TiO_2$-UV. (**B**) Energies and models of intermediates and transition states in the stepwise preparation mechanism of $Pd_1/TiO_2$. (**C**) Molar ratios of Cl to Pd in $PdCl_2/TiO_2$, $-OCH_2$•CHOPdCl, and $Pd_1/TiO_2$. (**D**) Change in pH after $H_2$ was introduced into the water dispersion of $PdCl_1/TiO_2$.

Pd NPs were observed in TEM images for the used $PdCl_2/TiO_2$ catalyst (fig. S26), indicating that the presence of Pd-Cl bonds would destabilize atomically dispersed Pd on $TiO_2$ and induce their sintering into NP during catalysis.

The removal of $Cl^-$ ligands on Pd under mild UV conditions appears vital for preparing highly stable and active Pd catalysts. To confirm this, we thoroughly washed $PdCl_2/TiO_2$ with water until no $Cl^-$ was detected in the supernatant. The water dispersion of $PdCl_2/TiO_2$ was then exposed to UV for 10 min. As expected, all $Cl^-$ ligands on $PdCl_2/TiO_2$ were released into the supernatant (figs. S25 and S27). The molar ratio of the released $Cl^-$ to the anchored Pd was measured to be ~2, confirming the formation of the $Cl^-$-free $Pd_1/TiO_2$ catalyst after the UV treatment.

The UV-induced elimination of $Cl^-$ from $PdCl_2/TiO_2$ was attributed to the photoreactivity of $TiO_2$(B) nanosheets. As shown in Fig. 3A, $TiO_2$(B) nanosheets treated by UV alone (denoted as $TiO_2$-UV) already displayed an electron spin resonance (ESR) spectrum with an intense peak corresponding to a $Ti^{3+}$ species and a set of six peaks that matched perfectly with EG radicals ($HOCH_2$•CHOH) (*34*). Similar signals were observed for the as-prepared $Pd_1/TiO_2$ catalyst (fig. S28). However, no obvious ESR peaks were found on the original $TiO_2$(B) nanosheets without UV treatment (Fig. 3A).

Together with selected-area electron diffraction (SAED) (fig. S1) and the aberration-corrected STEM (fig. S2), thermogravimetric analysis (fig. S29) and infrared (IR) spectroscopy (fig. S30) suggested that two-atom-thick $TiO_2$ nanosheets used in this work had $TiO_2$(B)(010) as their major exposed facets, and these exposed facets were highly covered by deprotonated EG (~19 wt %) (fig. S31). Once exposed to UV, electron-hole pairs were generated on $TiO_2$(B) nanosheets. Electrons were trapped in Ti-3d orbitals to form $Ti^{3+}$ sites (*35*), and holes broke Ti-O bonds between glycolate and $TiO_2$, leading to the formation of $-OCH_2CH_2O$• radicals (from I to II in Fig. 3B) (figs. S32 and S33). Because of the presence of α-H, $-OCH_2CH_2O$• was not stable and would thus undergo hydrogen transfer to give $-OCH_2$•CHOH. According to density functional theory (DFT) calculations, such a process (from II to III in Fig. 3B) was predicted to be exothermic by 0.38 eV. Such UV-generated surface organic radicals are not unusual, as the oxidation potentials of most organic compounds lie below that of the holes in the valence band of $TiO_2$ (*36*–*38*). The ESR signals from the samples after washing and drying processes suggest that, once formed upon UV irradiation, the EG radicals on the surface of $TiO_2$ nanosheets were quite stable.

To understand how EG radicals promoted the release of $Cl^-$ from Pd sites, we also designed a

Downloaded from http://science.sciencemag.org/ on May 12, 2016

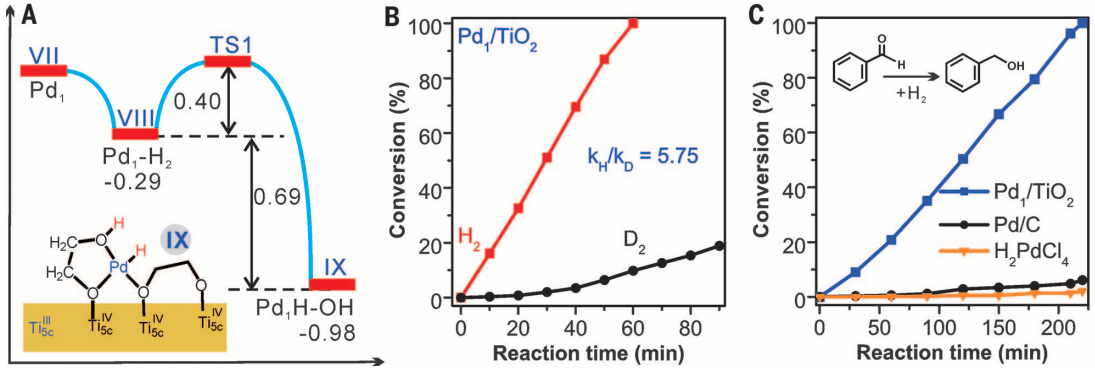


**Fig. 4. Catalytic mechanism of $Pd_1/TiO_2$ in hydrogenation reactions.** (**A**) Energies and model of intermediates and transition states in the heterolytic $H_2$ activation process for $Pd_1/TiO_2$. (**B**) Primary isotope effect observed for $Pd_1/TiO_2$ in styrene hydrogenation. (**C**) First-run reaction performances for $Pd_1/TiO_2$, Pd/C, and $H_2PdCl_4$ in benzaldehyde hydrogenation.

stepwise route (fig. S34) to prepare the $Pd_1/TiO_2$ catalyst. UV treatment was first used to obtain $TiO_2$-UV nanosheets containing EG radicals on their surfaces. $H_2PdCl_4$ was then introduced into the water dispersion of $TiO_2$-UV. Our calculations showed that once adsorbed onto $TiO_2$, each $PdCl_4^{2-}$ liberated two $Cl^-$ ligands, yielding an intermediate with individual $PdCl_2$ units adsorbed on $TiO_2$ (IV in Fig. 3B) (fig. S35). Such a process was predicted to be slightly exothermic by 0.03 eV. Subsequently, the OH group in $-OCH_2$•CHOH attacked its nearby Pd site by replacing one $Cl^-$, leading to the formation of $PdCl_1/TiO_2$ intermediate (V in Fig. 3B) with an exothermicity of 0.81 eV. As shown in fig. S35, $PdCl_1/TiO_2$ has three Ti-O bonds and one Pd-Cl bond. Experimentally, both EXAFS data and elemental analysis showed a Cl:Pd molar ratio of ~1:1 for $PdCl_1/TiO_2$ (Fig. 3C, figs. S36 and S37, and table S4), lower than the 2:1 molar ratio in $PdCl_2/TiO_2$ made from untreated $TiO_2$. Moreover, mixing $TiO_2$(B)-UV with $H_2PdCl_4$ solution decreased the amount of EG radicals, as evidenced by the reduced intensity of each ESR peak (fig. S38).

All of these results strongly confirmed that the UV-generated EG radicals facilitated the removal of $Cl^-$ on Pd and stabilized individual Pd atoms by forming more Pd-O bonds. The remaining $Cl^-$ on $PdCl_1/TiO_2$ could be easily removed by using $H_2$ treatment, giving rise to $H^+$ and $Cl^-$ (from V to VII in Fig. 3B) (table S5). This result explained why treating the water dispersion of $PdCl_1/TiO_2$ resulted in a pH drop from 6.8 to 5.3 (Fig. 3D). Alternatively, further UV treatment completely removed $Cl^-$ from $PdCl_1/TiO_2$ (fig. S39), also leading to the formation of $Pd_1/TiO_2$. The catalyst prepared in the stepwise procedure showed the same catalytic properties as that prepared by the one-pot method in which the aqueous mixture of $TiO_2$ and $H_2PdCl_4$ was directly treated with UV (fig. S40). More important, the insight into the formation mechanism of $Pd_1/TiO_2$ allowed us to prepare the catalyst in large scale by using a continuous UV-flow reactor (fig. S41).

To evaluate the importance of EG radicals in the preparation of the atomically dispersed $Pd_1/TiO_2$ catalyst, we also synthesized EG-free $TiO_2$ by calcination of $TiO_2$(B) nanosheets at 350°C in air and used it as the support for the catalyst preparation. A photochemical strategy similar to that used in the one-step preparation of $Pd_1/TiO_2$ was applied to load Pd onto EG-free $TiO_2$, but Pd NPs were formed (fig. S42); this result shows that surface EG helps to stabilize atomically dispersed Pd catalysts during their preparation. When surface EG was removed by calcination, the obtained $Pd_1/TiO_2$-cal catalyst displayed a substantially decreased activity with a TOF of only 1930 $hours^{-1}$ (fig. S43).

It is generally accepted that $H_2$ would undergo homolytic dissociation on conventional Pd particulate catalysts into H atoms with partially negative charge ($H^{\delta-}$) (*39*). In this case, the presence of more than two Pd atoms in the vicinity is required. However, all Pd atoms in $Pd_1/TiO_2$ are individually dispersed, with no Pd-Pd pairs available for homolytic dissociation of $H_2$, so the dissociation of $H_2$ must go via an alternative pathway on $Pd_1/TiO_2$. According to our DFT calculations (Fig. 4A and figs. S44 to S46), $H_2$ adsorbed on Pd was readily split into two H atoms. One of the H atoms moved to a nearby oxygen on EG to yield O-$H^{\delta+}$, leaving the other H atom on Pd as $H^{\delta-}$ (Fig. 4A). This step was calculated to be exothermic by 0.69 eV and exhibited a barrier of 0.40 eV. We expected that both Pd-$H^{\delta-}$ and O-$H^{\delta+}$ should then be involved in the hydrogenation catalysis. DFT calculations revealed that the hydrogenation of styrene using $Pd_1/TiO_2$ followed a stepwise process. Computationally, we considered two possible pathways (figs. S44 to S46), one beginning with $H^{\delta-}$ transfer from Pd to C=C and the other beginning with $H^{\delta+}$ transfer. The first of these is energetically favorable, with a barrier of only 0.47 eV required for the $H^{\delta-}$ transfer from Pd to the terminal $CH_2$ to make the half-hydrogenated intermediate, which in turn adds $H^{\delta+}$ from a nearby O-H group by overcoming a barrier of 0.73 eV. This pathway leads to the formation of ethylbenzene and simultaneously recovers the Pd-EG interfaces.

To test the proposed mechanism, we explored the kinetic isotope effect (KIE) with the use of $D_2$ in styrene hydrogenation. For Pd/C, the reaction was slowed down by a factor of 1.43 (fig. S47) as a result of the zero-point energy difference between isotopic isomers. However, on $Pd_1/TiO_2$, a larger KIE was observed (ratio of reaction rates using $H_2$ and $D_2$, $k_H/k_D$ = 5.75) (Fig. 4B) because the bond cleavage was O-D rather than Pd-D in the rate-determining step. Both our IR spectroscopy and nuclear magnetic resonance measurements, which were performed with deuterium-labeled reagents, confirmed the proposed mechanism (figs. S48 and S49). Such a large KIE in hydrogenation caused by the participation of both $H^{\delta-}$ and $H^{\delta+}$ has usually been observed on homogeneous catalysts (e.g., Au, Pd, and Ru complexes) (*7*, *40*, *41*) but has not been reported on heterogeneous Pd catalysts. In this regard, atomically dispersed metal catalysts can share the same hydrogenation mechanism as homogeneous catalysts.

Because the heterolytic activation of $H_2$ yielded both $H^{\delta-}$ and $H^{\delta+}$ at the Pd-O interface, $Pd_1/TiO_2$ should allow better hydrogenation of polar unsaturated bonds. As expected, in the hydrogenation of benzaldehyde, we observed a much superior catalytic performance by $Pd_1/TiO_2$ (Fig. 4C and fig. S50). $Pd_1/TiO_2$ readily converted all of the benzaldehyde into benzyl alcohol in 3.5 hours at room temperature with a TOF of 1002 $hours^{-1}$. No decay in the catalysis was observed after the catalyst was used for five cycles. In comparison, both Pd/C and $H_2PdCl_4$ showed negligible activity under the same catalytic condition, with TOF less than 18 $hours^{-1}$. This work demonstrates that upgrading catalytically active components from nanoparticles to single atoms not only boosts the catalytic reaction because of the high atom efficiency, but also endows atomically dispersed catalysts with catalytic capability that conventional nanocatalysts do not possess.

## REFERENCES AND NOTES


1. B. Qiao *et al.*, *Nat. Chem.* **3**, 634–641 (2011).
2. K. Ding *et al.*, *Science* **350**, 189–192 (2015).
3. J. H. Kwak *et al.*, *Science* **325**, 1670–1673 (2009).
4. Y. Zhai *et al.*, *Science* **329**, 1633–1636 (2010).
5. Q. Fu, H. Saltsburg, M. Flytzani-Stephanopoulos, *Science* **301**, 935–938 (2003).
6. M. Yang *et al.*, *Science* **346**, 1498–1501 (2014).
7. A. Comas-Vives *et al.*, *J. Am. Chem. Soc.* **128**, 4756–4765 (2006).
8. X. Zhang, H. Shi, B. Q. Xu, *Angew. Chem. Int. Ed.* **44**, 7132–7135 (2005).
9. G. Vilé *et al.*, *Angew. Chem. Int. Ed.* **54**, 11265–11269 (2015).
10. S. Abbet *et al.*, *J. Am. Chem. Soc.* **122**, 3453–3457 (2000).
11. H. Yan *et al.*, *J. Am. Chem. Soc.* **137**, 10484–10487 (2015).
12. E. J. Peterson *et al.*, *Nat. Commun.* **5**, 4885 (2014).
13. J. Lin *et al.*, *J. Am. Chem. Soc.* **135**, 15314–15317 (2013).


Downloaded from http://science.sciencemag.org/ on May 12, 2016

14. V. Ortalan, A. Uzun, B. C. Gates, N. D. Browning, *Nat. Nanotechnol.* **5**, 506–510 (2010).
15. J. M. Thomas, *Nature* **525**, 325–326 (2015).
16. W. E. Kaden, T. Wu, W. A. Kunkel, S. L. Anderson, *Science* **326**, 826–829 (2009).
17. J. M. Thomas, Z. Saghi, P. L. Gai, *Top. Catal.* **54**, 588–594 (2011).
18. G. Kyriakou *et al.*, *Science* **335**, 1209–1212 (2012).
19. M. Yang, L. F. Allard, M. Flytzani-Stephanopoulos, *J. Am. Chem. Soc.* **135**, 3768–3771 (2013).
20. H. Wei *et al.*, *Nat. Commun.* **5**, 5634 (2014).
21. M. Yang *et al.*, *J. Am. Chem. Soc.* **137**, 3470–3473 (2015).
22. S. Sun *et al.*, *Sci. Rep.* **3**, 1775 (2013).
23. J. O. Ehresmann *et al.*, *Angew. Chem. Int. Ed.* **45**, 574–576 (2006).
24. A. Uzun, B. C. Gates, *J. Am. Chem. Soc.* **131**, 15887–15894 (2009).
25. X.-Q. Gong, A. Selloni, O. Dulub, P. Jacobson, U. Diebold, *J. Am. Chem. Soc.* **130**, 370–381 (2008).
26. D. Matthey *et al.*, *Science* **315**, 1692–1696 (2007).
27. M. Flytzani-Stephanopoulos, B. C. Gates, *Annu. Rev. Chem. Biomol. Eng.* **3**, 545–574 (2012).
28. J. M. Thomas, R. Raja, *Top. Catal.* **40**, 3–17 (2006).
29. See supplementary materials on *Science* Online.
30. G. Xiang, T. Li, J. Zhuang, X. Wang, *Chem. Commun. (Camb.)* **46**, 6801–6803 (2010).
31. V. V. Kaichev *et al.*, *J. Phys. Chem. B* **107**, 3522–3527 (2003).
32. Z. Király, B. Veisz, Á. Mastalir, *Catal. Lett.* **95**, 57–59 (2004).
33. B. Veisz, Z. Király, L. Tóth, B. Pécz, *Chem. Mater.* **14**, 2882–2888 (2002).
34. T. Shiga, *J. Phys. Chem.* **69**, 3805–3814 (1965).
35. R. F. Howe, M. Gratzel, *J. Phys. Chem.* **89**, 4495–4499 (1985).
36. M. R. Hoffmann, S. T. Martin, W. Choi, D. W. Bahnemann, *Chem. Rev.* **95**, 69–96 (1995).
37. Y. Chen, S. Yang, K. Wang, L. Lou, *J. Photochem. Photobiol. Chem.* **172**, 47–54 (2005).
38. L. Yu *et al.*, *Phys. Chem. Chem. Phys.* **14**, 3589–3595 (2012).
39. S. Syrenova *et al.*, *Nat. Mater.* **14**, 1236–1244 (2015).
40. A. M. Kluwer, T. S. Koblenz, T. Jonischkeit, K. Woelk, C. J. Elsevier, *J. Am. Chem. Soc.* **127**, 15470–15480 (2005).
41. A. Dedieu, S. Humbel, C. Elsevier, C. Grauffel, *Theor. Chem. Acc.* **112**, 305–312 (2004).

**ACKNOWLEDGMENTS**

Supported by Ministry of Science and Technology of China grant 2015CB932303; National Natural Science Foundation of China grants 21420102001, 21131005, 21390390, 21133004, 21373167, 21573178, and 21333008; a NSERC CGS Alexander Graham Bell scholarship (D.M.C.); and a NSERC Discovery grant (P.Z.). We thank the XAFS station (BL14W1) of the Shanghai Synchrotron Radiation Facility.

**SUPPLEMENTARY MATERIALS**

www.sciencemag.org/content/352/6287/797/suppl/DC1
Materials and Methods
Supplementary Text
Figs. S1 to S50
Tables S1 to S5
References (*42*–*55*)

22 February 2016; accepted 5 April 2016
10.1126/science.aaf5251

ORGANIC CHEMISTRY

# A general alkyl-alkyl cross-coupling enabled by redox-active esters and alkylzinc reagents

**Tian Qin,[1]* Josep Cornella,[1]* Chao Li,[1]* Lara R. Malins,[1] Jacob T. Edwards,[1] Shuhei Kawamura,[1] Brad D. Maxwell,[2] Martin D. Eastgate,[3] Phil S. Baran[1]†**

**Alkyl carboxylic acids are ubiquitous in all facets of chemical science, from natural products to polymers, and represent an ideal starting material with which to forge new connections. This study demonstrates how the same activating principles used for decades to make simple C–N (amide) bonds from carboxylic acids with loss of water can be used to make C–C bonds through coupling with dialkylzinc reagents and loss of carbon dioxide. This disconnection strategy benefits from the use of a simple, inexpensive nickel catalyst and exhibits a remarkably broad scope across a range of substrates (>70 examples).**

The heart of chemical synthesis relies on forging new C–C bonds, with the evolution and advancement of the field being easily correlated to new developments on this front. For example, pioneering work on the cross-coupling of halogenated aromatic or vinylic ($sp^2$) systems (Heck, Suzuki, Negishi, and Stille) has transformed the practice of organic synthesis (*1*). Similarly, a general and practical approach to $C(sp^3)$–$C(sp^3)$ variants would have the potential to open up new vistas in retrosynthetic analysis. Indeed, such transformations have been on organic chemists' wish list for well over a century (*2*, *3*). Historically, alkyl-alkyl transition metal–catalyzed cross-coupling reactions have been difficult to accomplish, but examples can be traced to the early work of Kharasch in the 1950s (*4*), followed by Noller (*5*, *6*) and Kochi and Tamura (*7*, *8*) in the 1960s to more recent work from the groups of Suzuki (*9*), Fu (*10*), Knochel (*11*), Kambe (*12*), Oshima (*13*), and many others (*14*). Thus far, the vast majority of approaches to this problem have involved the coupling of alkyl halides (or related species) to organometallic reagents (*15*–*18*). However, the limited availability, perceived instability, and frequent toxicity of alkyl halides has perhaps prevented the area of alkyl cross-coupling from blossoming. If one only considers convenience, stability, and availability as desired attributes in a functional group for such a coupling, the carboxylic acid reigns supreme (Fig. 1A). Alkyl carboxylic acids are ubiquitous in every aspect of chemistry and can be readily found in medicines, materials, and natural products and in the pages of commercial chemical supplier catalogs. They are a stable functional group, nontoxic, and eminently diversifiable owing to the field of combinatorial chemistry, in which they are the "workhorse" building block. Although certain carboxylic acids have already been demonstrated to engage in cross-coupling reactions (*19*), the use of alkyl carboxylic acids in alkyl-alkyl cross-coupling remains elusive.

Carboxylic acids can be primed for reaction through a process known as activation (such as formation of an active ester, –OA*), dating back to the classic work of Sheehan in the synthesis of penicillin (*20*). Once activated, a gateway opens to access a myriad of related functional groups such as amides, ketones, esters, or alcohols via addition of a nucleophile or alternative oxidation states by the formal addition of hydrogen. In this Report, we present a broadly useful transform that is able to forge $C(sp^3)$–$C(sp^3)$ bonds via this age-old activation process.

We recently reported a Ni-catalyzed decarboxylative cross-coupling of alkyl carboxylic acids with arylzinc reagents to forge $C(sp^3)$–$C(sp^2)$ bonds by repurposing activating methods more typically associated with amide-bond formation (*21*, *22*). Certain active esters [such as HOAt (*N*-hydroxy-7-azabenzotriazole), HOBt (*N*-hydroxybenzotriazole), NHPI (*N*-hydroxyphthalimide), and TCNHPI (*N*-hydroxytetrachlorophthalimide)] can accept an electron to trigger an ensuing cascade of events that liberates $CO_2$ from the parent alkyl group ($Alk_1$); such esters (*23*) are termed redox-active (*21*, *22*). The application of this chemistry to $sp^3$–$sp^3$ C–C bond formation poses a number of substantial challenges, with potentially unproductive pathways far outnumbering the desired reaction (Fig. 1B) (*15*–*18*). For example, β-hydride elimination from the alkyl metal intermediates, dimerization of the organometallic reagent, reduction of the electrophile, and proto-demetallation are problems that also historically plague traditional $C(sp^3)$–$C(sp^3)$ cross-coupling reactions. With a redox-active ester as an electrophile, oxidative addition of low-valent Ni into the activated C–O bond could result in the formation of an acyl-Ni complex, which could reductively eliminate and ultimately result in undesired ketone by-products. These fundamental challenges notwithstanding, we describe a straightforward solution to this problem.

Dialkylzinc reagents were chosen for the organometallic coupling partner because of their

[1]Department of Chemistry, Scripps Research Institute, 10550 North Torrey Pines Road, La Jolla, CA 92037, USA. [2]Discovery Chemistry Platforms–Radiochemistry, Bristol-Myers Squibb, Post Office Box 4000, Princeton, NJ, USA. [3]Chemical Development, Bristol-Myers Squibb, One Squibb Drive, New Brunswick, NJ 08903, USA.
*These authors contributed equally to this work. †Corresponding author. Email: pbaran@scripps.edu

Downloaded from http://science.sciencemag.org/ on May 12, 2016

ease of preparation from the parent alkyl halide, high functional group tolerance, and their propensity for facile transmetallation. Over the years, mono and dialkylzinc reagents have been shown to be viable cross-coupling partners in Negishi cross-coupling through use of alkyl halides, and related species with Ni-based catalysts (*16*, *18*). Thus, an exploration of the coupling of redox-active esters **1a** and **1b** (Fig. 1C) with diethylzinc (**2**) was undertaken. An exhaustive screen of ligands, including bipy (**L1**, entries 1 and 2) and di-*t*Bubipy (**L2**, entries 3 and 4) showed that the electron-deficient TCNHPI ester **1b** with **L2** afforded the desired product in 84% isolated yield (entry 4). TCNHPI can be easily prepared from tetrachlorophthalic anhydride, an industrial nontoxic flame retardant [~$48/kg from VWR (Radnor, PA)] (*24*), and it has recently been commercialized by Aldrich (catalog no. ALD00564). Additional screening of ligands based on phenanthroline (**L3** to **L5**, entries 5 to 7) and terpyridine (**L6** and **L7**, entries 8 and 9) did not improve the yield and were in many cases detrimental. When the reaction was performed in the absence of $NiCl_2$·glyme, the desired product was not formed (entry 10).

With an optimized set of conditions in hand, we explored the scope of this new reaction and found it to be remarkably broad. First, we explored a range of 16 dialkylzinc reagents (Fig. 2A) with piperidine esters **1a** and **1b**. With the exception of dibenzylzinc reagents, all primary dialkylzinc reagents explored were viable in the cross-coupling. From dimethylzinc (**4**) and simple alkyl chains (**3**, **5**, **6**, **9**, and **10**) to derivatives harboring olefins (**7** and **8**), alkynes (**11** and **12**), acetals (**16**), ethers (**14** and **15**), and even alkyl halides (**13**) were tolerated. The reaction was easily run on a gram scale (as exemplified by **3**) and could even be used to produce isotopically labeled piperidine **4**-$^{13}$**C**. In addition to **3**, this example highlights that a lower loading of dialkylzinc reagent (0.5 equivalent) could be used when a highly valuable alkyl group is involved. Secondary alkylzinc reagents such as cyclopropylzinc could also be accommodated, as exemplified by **17**.

Next, we explored 15 secondary alkyl carboxylic acids (Fig. 2B). Cyclic (**18**, **19**, and **21**), heterocyclic (**20**, **22**, **26** to **28**, and **31**), bridging (**25**), indane (**24**), acyclic (**29**), and even fluorinated (**23** and **30**) alkyl carboxylic acids were all viable coupling partners. Substrates **30** through **32** are particularly striking and open the door to access a vast array of fluorinated building blocks and optically pure tartrate-derived materials. Many of these products would be either inconvenient or chemically intractable to access from the corresponding alkyl halide starting materials (**27**, **28**, **30**, **31**, and **32**).

Primary alkyl carboxylic acids, representing some of the most inexpensive organic materials available, could also be readily used. Of the eight examples depicted in Fig. 2C, most notable are the use of mono-methyladipic acid (**34**; 2.5 billion kg of adipic acid are produced per year) (*25*), a pyridine-containing substrate (**36**), and a polyfluorinated acid (**40**). Tertiary alkyl carboxylic acids (Fig. 2D) could also be used to generate quaternary centers. Although limited in scope, bridgehead systems such as adamantane (**41** and **42**) or bicyclo[2.2.2]octane (**43**) smoothly participated in the cross-coupling. The preparation of such bridged systems is traditionally performed via a three-step Wittig/hydrogenation sequence from the parent aldehyde (*26*). Although pivalic acid (**44**) did not couple in this context, its failure led to a distinct type of coupling (vide infra).

Simple primary and secondary α-oxyacids could also be used (Fig. 2E, **45** to **49**), representing a practical route to form ethers that would not be possible by using alkyl halides. The classic Williamson ether synthesis is still the staple transform for constructing ethers, but in many cases, the $S_N2$ reaction is either sluggish or unworkable because of steric hindrance. This cross-coupling opens a distinct disconnection strategy for ether synthesis by using easily obtained α-oxyacids (either commercial or derived via alkylation with bromoacetic acid) as progenitors for a virtually limitless array of new ethers.

Redox-active esters enable the cross-coupling of alkylzinc reagents with high chemoselectivity (Fig. 2F) even in complex contexts, reminiscent of that exhibited in classic amide-bond formation. For example, a variety of sensitive fatty acids reacted smoothly to give the corresponding alkyl chains (**50**, **57**, and **58**) without olefin isomerization or epoxide opening. Naturally occurring carboxylic acids such as biotin, cholic acid, and dehydrocholic acid were also amenable to alkylation (**54** to **56**). Pharmaceuticals and agrochemicals such as pregabalin, 2,4-D, cetirizine, and atorvastatin smoothly reacted with alkylzinc reagents to afford good yields of the alkyl coupling products (**51** to **53** and **59**).

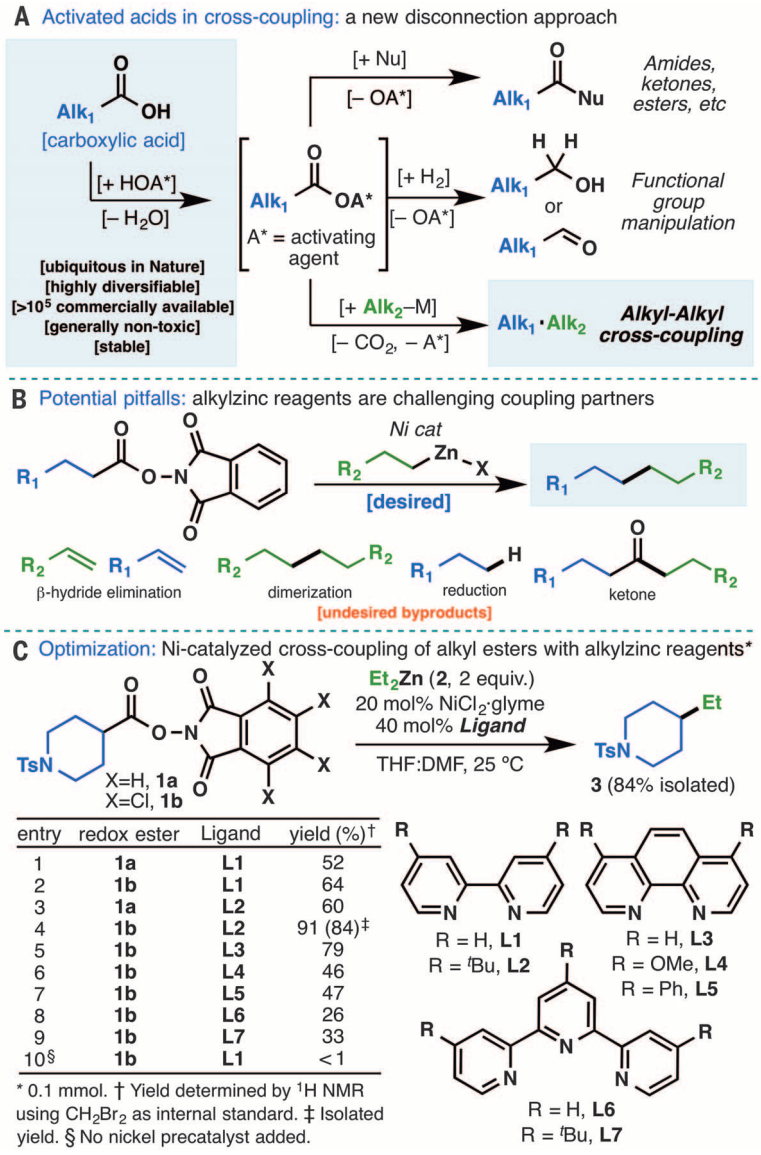


| entry | redox ester | Ligand | yield (%)† |
|---|---|---|---|
| 1 | **1a** | **L1** | 52 |
| 2 | **1b** | **L1** | 64 |
| 3 | **1a** | **L2** | 60 |
| 4 | **1b** | **L2** | 91 (84)‡ |
| 5 | **1b** | **L3** | 79 |
| 6 | **1b** | **L4** | 46 |
| 7 | **1b** | **L5** | 47 |
| 8 | **1b** | **L6** | 26 |
| 9 | **1b** | **L7** | 33 |
| 10§ | **1b** | **L1** | <1 |

* 0.1 mmol. † Yield determined by $^1$H NMR using $CH_2Br_2$ as internal standard. ‡ Isolated yield. § No nickel precatalyst added.

**Fig. 1. Development of a Ni-catalyzed decarboxylative alkyl-alkyl cross-coupling.** (**A**) Activation of carboxylic acids in organic synthesis. (**B**) Potential side products. (**C**) Ni-catalyzed cross-coupling of redox-active esters and alkylzinc reagents.

Downloaded from http://science.sciencemag.org/ on May 12, 2016

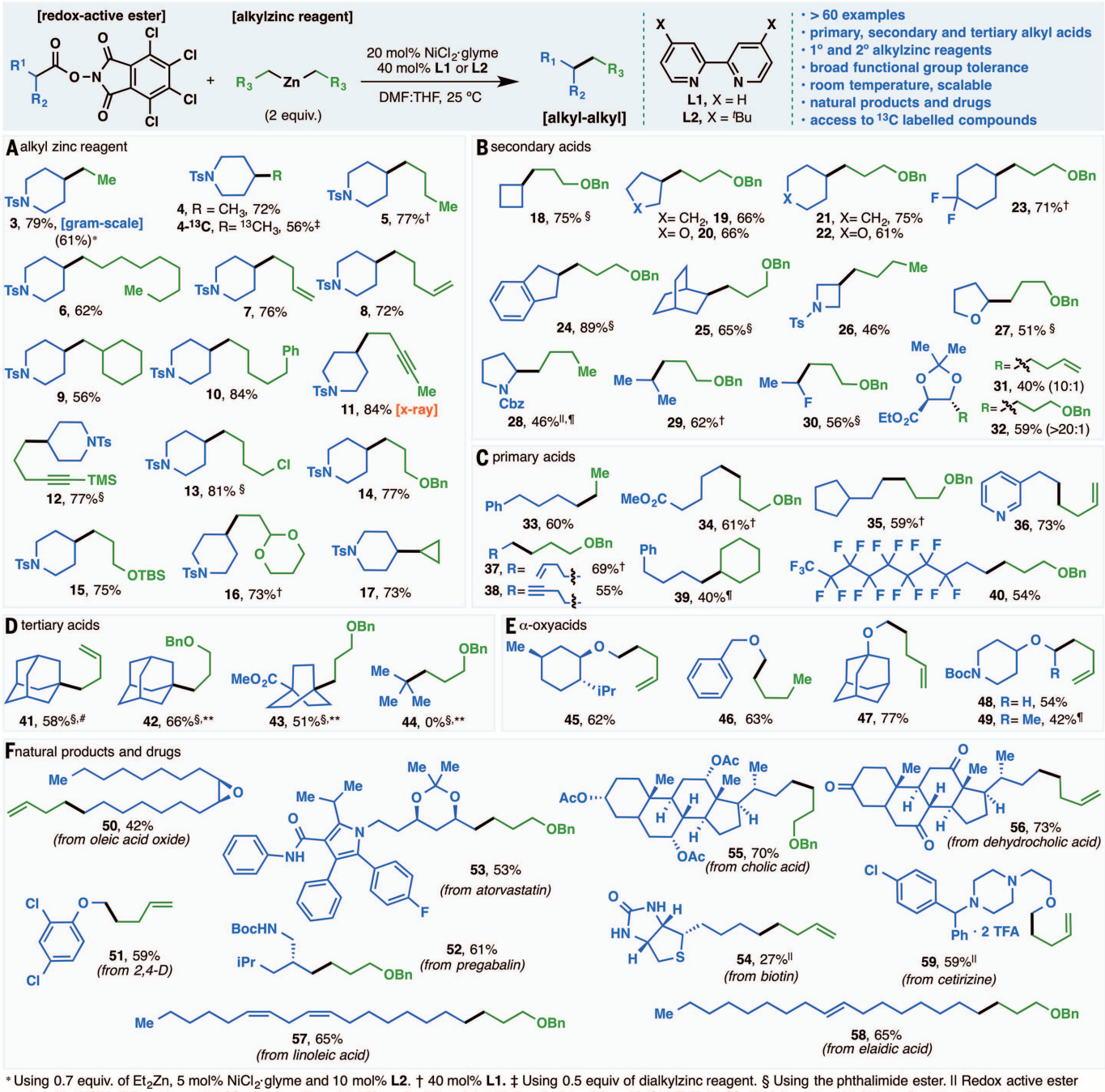


*Using 0.7 equiv. of $Et_2Zn$, 5 mol% $NiCl_2$·glyme and 10 mol% **L2**. † 40 mol% **L1**. ‡ Using 0.5 equiv of dialkylzinc reagent. § Using the phthalimide ester. || Redox active ester made with HATU. ¶ Reaction at 60 °C. # Using 20 mol% $Ni(acac)_2$, 20 mol% 6,6'-dimethylbipyridine, MeCN:THF, 80 °C. ** Using 40 mol% $Ni(acac)_2$, 40 mol% 6,6'-dimethylbipyridine, MeCN: THF, 80 °C.

**Fig. 2. Scope of the Ni-catalyzed decarboxylative alkyl-alkyl cross-coupling.** (**A**) Alkyl zinc reagent. (**B**) Secondary acids. (**C**) Primary acids. (**D**) Tertiary acids. (**E**) α-oxyacids. (**F**) Natural products and drugs. Standard conditions were redox-active ester (1 eq), dialkylzinc reagent (2 eq), $NiCl_2$·glyme (20 mol %), **L2** (40 mol %), THF:DMF, 25°C, 8–14 hours. THF, tetrahydrofuran; DMF, dimethylformamide.

In perhaps the most impressive feat of chemoselectivity for this methodology, the cross-coupling could be conducted on solid phase in the context of peptide synthesis. On-resin coupling of dialkylzinc reagents to proteinogenic amino acids (both side-chain and α-carboxylic acids) facilitates the late-stage introduction of designer amino acids, which would otherwise require de novo synthesis. Valuable synthetic handles including alkenes (**60** and **62**) and alkyl ethers (**63**) could be readily incorporated into resin-bound substrates (Fig. 3), and the installation of an aliphatic side chain (**61**) provides a facile approach to the modulation of peptide lipophilicity (*27*). Double activation of a peptide substrate bearing both Asp and Glu residues also enables the simultaneous introduction of multiple nonproteinogenic side chains (**64** and **65**). This convenient approach to diversely functionalized peptides provides a tool for the construction of therapeutic peptide leads and stapled peptides (*28*, *29*) and for applications in bioconjugation (*30*).

Returning to the limitations posed by tertiary systems, mechanistic studies involving *5-exo-trig* cyclization, racemization, and ring-strain opening experiments clearly point to the radical nature of this reaction (figs. S1 to S3). We reasoned that the steric limitations encountered could be overcome by engaging these reactive species with a radical trap that could subsequently combine

Downloaded from http://science.sciencemag.org/ on May 12, 2016

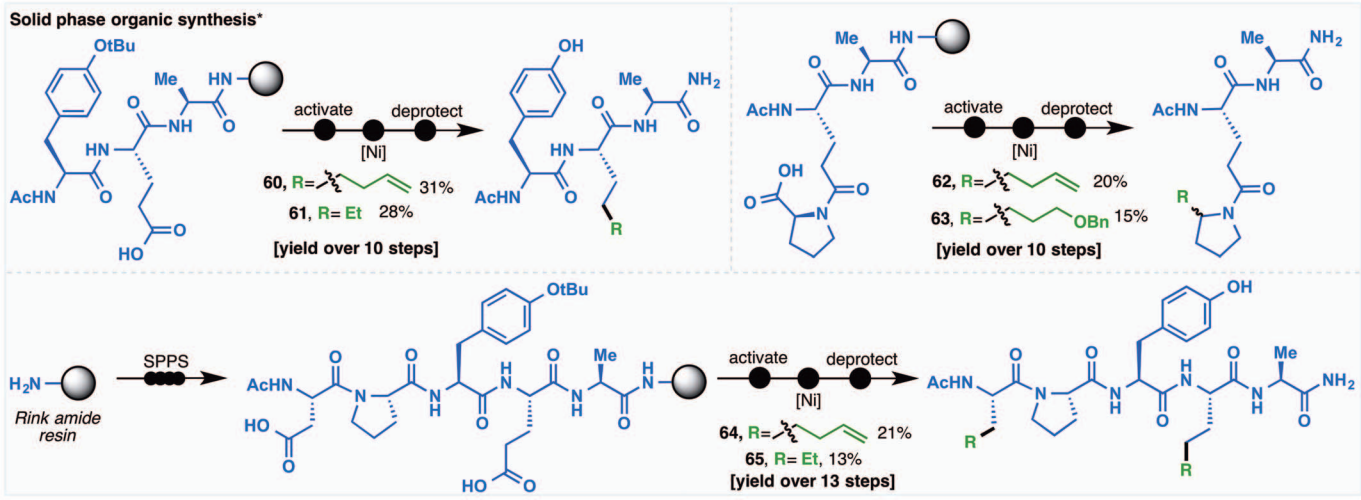


**Fig. 3. Ni-catalyzed decarboxylative alkyl-alkyl coupling in solid-phase synthesis.** Experimental details are provided in the supplementary materials.

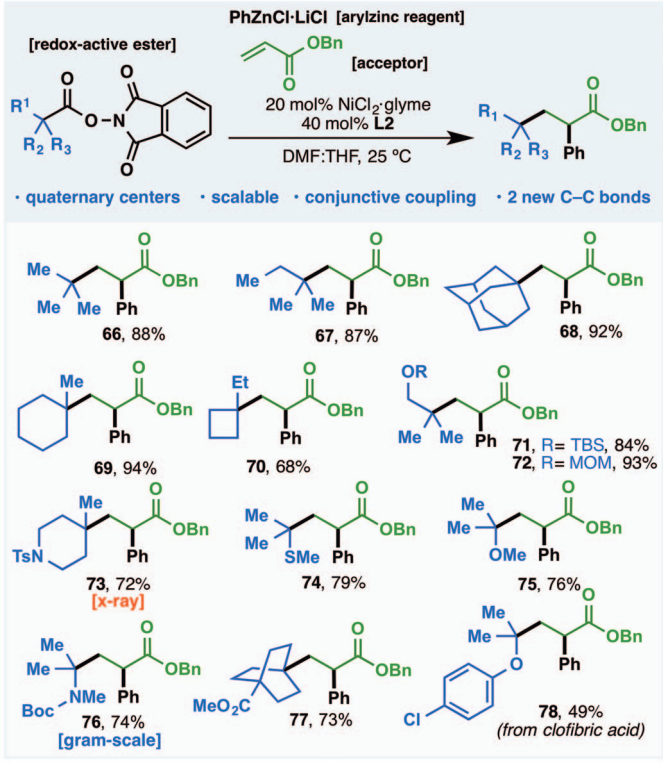


**Fig. 4. Scope of the Ni-catalyzed three-component conjunctive cross-coupling.** Standard conditions were redox-active ester (1 eq), acceptor (2.5 eq), PhZnCl·LiCl complex (3 eq), $NiCl_2$·glyme (20 mol %), **L2** (40 mol %), THF:DMF, 25°C, 8 hours. All the products shown were obtained in racemic form.

with an organozinc reagent. Remarkably, such a conjunctive cross-coupling could be realized, as shown in Fig. 4 (*31*). By using benzylacrylate as a radical trap and phenylzinc as a coupling partner, 13 different tertiary alkyl carboxylic acids could be smoothly engaged in a three-component cross-coupling to generate useful building blocks that would be extremely difficult to access in any other way (**66** to **78**). This reaction is scalable (as exemplified by **76**), generates two new C–C bonds, and is a rare example of a multicomponent cross-coupling reaction that forms quaternary centers in high yield. In addition to the broad functional group tolerance [heteroatom containing substrates, Boc (*tert*-butoxycarbonyl), TBS (*tert*-butyldimethylsilyl), and MOM (methoxymethyl) groups], this reaction features the use of electronically different radical precursors, such as α-heteroatom acids or electronically unbiased and neutral alkyl acids such as pivalic acid.

As with any methodology, there are obvious drawbacks. For example, the atom-economy is low because of the use of an activating group. We do note, however, that such considerations are ignored in the enormous field of peptide chemistry, in which expensive coupling agents are regularly used to make a simple amide bond (*32*). The activating agents used here, NHPI ($19.5/mol) and TCNHPI, are both commercially available and derived from cheap, readily available materials and open a gateway of reactivity heretofore inaccessible. The use of two equivalents of the dialkylzinc reagent is another disadvantage in cases in which the zinc-derived fragment is valuable. However, as shown in **3** and **4**-$^{13}$**C**, the reaction proceeds with workable yields when simply equimolar amounts of alkylzinc reagents and 5 mole percent (mol %) catalyst were used.

The data presented here suggests that the advantages associated with this method far outweigh its limitations. Without exception, the carboxylic acids used represent the most inexpensive sources of these carbon frameworks; all of these were commercially available. In contrast, in the cases in which an alkyl halide would be chemically stable, only a handful are commercially available. Conceptually, carboxylic acids can perhaps be considered nature's version of a boronic acid. For the past seven decades, these ubiquitous functional groups have usually been dehydrated with incorporation of a nucleophile (such as an amine to make an amide). This method extends the native diversification of this functional group (*33*) to allow for the addition of a new carbon framework via extrusion of $CO_2$. As such, it is anticipated that this technique will greatly expand planning options in retrosynthetic analysis.

## REFERENCES AND NOTES

1. F. Diederich, P. J. Stang, *Metal-catalyzed Cross-coupling Reactions* (Wiley-VCH, 1998).
2. P. Jolibois, *Compt. Rend. Acad. Sciences* **155**, 213 (1912).
3. E. Späth, *Monatsh. Chem.* **34**, 1965–2014 (1913).
4. M. S. Kharasch, J. K. Hambling, T. P. Rudy, *J. Org. Chem.* **24**, 303–305 (1959).
5. V. D. Parker, L. H. Piette, R. M. Salinger, C. R. Noller, *J. Am. Chem. Soc.* **86**, 1110–1112 (1964).
6. V. D. Parker, C. R. Noller, *J. Am. Chem. Soc.* **86**, 1112–1116 (1964).

Downloaded from http://science.sciencemag.org/ on May 12, 2016

7. M. Tamura, J. Kochi, *J. Am. Chem. Soc.* **93**, 1483 (1970).
8. M. Tamura, J. Kochi, *J. Am. Chem. Soc.* **93**, 1485 (1970).
9. T. Ishiyama, S. Abe, N. Miyaura, A. Suzuki, *Chem. Lett.* **21**, 691–694 (1992).
10. M. R. Netherton, C. Dai, K. Neuschütz, G. C. Fu, *J. Am. Chem. Soc.* **123**, 10099–10100 (2001).
11. A. Devasagayaraj, T. Stüdemann, P. Knochel, *Angew. Chem. Int. Ed. Engl.* **34**, 2723–2725 (1995).
12. J. Terao, H. Watanabe, A. Ikumi, H. Kuniyasu, N. Kambe, *J. Am. Chem. Soc.* **124**, 4222–4223 (2002).
13. T. Tsuji, H. Yorimitsu, K. Oshima, *Angew. Chem. Int. Ed.* **41**, 4137–4139 (2002).
14. K. B. Urkalan, M. S. Sigman, *J. Am. Chem. Soc.* **131**, 18042–18043 (2009).
15. M. R. Netherton, G. C. Fu, *Adv. Synth. Catal.* **346**, 1525–1532 (2004).
16. A. C. Frisch, M. Beller, *Angew. Chem. Int. Ed.* **44**, 674–688 (2005).
17. A. Rudolph, M. Lautens, *Angew. Chem. Int. Ed.* **48**, 2656–2670 (2009).
18. R. Jana, T. P. Pathak, M. S. Sigman, *Chem. Rev.* **111**, 1417–1492 (2011).
19. N. Rodríguez, L. J. Goossen, *Chem. Soc. Rev.* **40**, 5030–5048 (2011).
20. J. C. Sheehan, *The Enchanted Ring. The Untold Story of Penicillin* (MIT Press, 1982)
21. J. Cornella *et al.*, *J. Am. Chem. Soc.* **138**, 2174–2177 (2016).
22. K. M. M. Huihui *et al.*, *J. Am. Chem. Soc.* **138**, 5016–5019 (2016).
23. K. Okada, K. Okamoto, M. Oda, *J. Am. Chem. Soc.* **110**, 8736–8738 (1988).
24. Data retrieved from https://us.vwr.com/store on 6 April 2016.
25. M. T. Musser, *Adipic Acid. Ullmann's Encyclopedia of Industrial Chemistry* (Wiley-VCH, 2000).
26. S. T. Waddell *et al.*, PCT international patent application US 20040133011 (2004).
27. J. A. Arnott, S. L. Planey, *Expert Opin. Drug Discov.* **7**, 863–875 (2012).
28. J. A. Kritzer, *Nat. Chem. Biol.* **6**, 566–567 (2010).
29. Y. H. Lau, P. de Andrade, Y. Wu, D. R. Spring, *Chem. Soc. Rev.* **44**, 91–102 (2015).
30. O. Boutureira, G. J. L. Bernardes, *Chem. Rev.* **115**, 2174–2195 (2015).
31. L. Zhang *et al.*, *Science* **351**, 70–74 (2016).
32. Y. Ishihara, A. Montero, P. S. Baran, *The Portable Chemist's Consultant* (Apple Publishing Group, 2013).
33. M. A. Ogliaruso, J. F. Wolfe, *Synthesis of Carboxylic Acids, Esters and their Derivatives* (John Wiley, 1991).



## ACKNOWLEDGMENTS

Financial support for this work was provided by Bristol-Myers Squibb, the Catalan Government (postdoctoral fellowship to J.C.), the U.S. Department of Defense (National Defense Science and Engineering Graduate fellowship to J.T.E.), NIH (F32GM117816 postdoctoral fellowship to L.R.M.), the China Scholarship Council (postdoctoral fellowship to C.L.), and the National Institute of General Medical Sciences (GM106210). We thank D.-H. Huang and L. Pasternack for assistance with nuclear magnetic resonance spectroscopy; M. Collins for providing samples of atorvastatin, cetirizine, and pregabalin; R. Mills for experimental assistance; A. Rheingold, C. E. Moore, and M. A. Galella for x-ray crystallographic analysis; M. R. Ghadiri for providing access to preparative HPLC equipment; and K. Chen for helpful discussions. Metrical parameters for the structures of **11** and **73** are available free of charge from the Cambridge Crystallographic Data Center under reference nos. CCDC-1457710 and CCDC-1457711, respectively.


## SUPPLEMENTARY MATERIALS

www.sciencemag.org/content/352/6287/801/suppl/DC1
Materials and Methods
Supplementary Text
Figs. S1 to S3
Tables S1 to S6
References (*34*–*60*)


4 March 2016; accepted 11 April 2016
Published online 21 April 2016
10.1126/science.aaf6123


APPLIED PHYSICS

# On-chip noninterference angular momentum multiplexing of broadband light


**Haoran Ren,[1] Xiangping Li,[1,2] Qiming Zhang,[1,3] Min Gu[1,3]***



**Angular momentum division has emerged as a physically orthogonal multiplexing method in high-capacity optical information technologies. However, the typical bulky elements used for information retrieval from the overall diffracted field, based on the interference method, impose a fundamental limit toward realizing on-chip multiplexing. We demonstrate noninterference angular momentum multiplexing by using a mode-sorting nanoring aperture with a chip-scale footprint as small as 4.2 micrometers by 4.2 micrometers, where nanoring slits exhibit a distinctive outcoupling efficiency on tightly confined plasmonic modes. The nonresonant mode-sorting sensitivity and scalability of our approach enable on-chip parallel multiplexing over a bandwidth of 150 nanometers in the visible wavelength range. The results offer the possibility of ultrahigh-capacity and miniaturized nanophotonic devices harnessing angular momentum division.**


In the age of information technology, optical multiplexing using physical dimensions of light, including space (*1*), frequency (*2*), brightness (*3*), color (*1*, *4*), polarization (*1*, *5*, *6*), mode (*7*), and lifetime (*8*), has played a crucial role in high-definition displaying (*3*–*5*), high-capacity data storage (*1*, *6*), high-speed communications (*7*), and highly sensitive biological sensing (*8*). As one of the most fundamental physical properties in both classical and quantum optics, angular momentum (AM) of light—including spin angular momentum (SAM) possessed by circularly polarized light and orbital angular momentum (OAM) manifested by the helical wavefront of light—has emerged as a physically orthogonal multiplexing approach to high-capacity optical communications ranging from free-space (*9*) to compact optical fibers (*10*). However, macroscale interference-based detection methods through hologram-coding (*9*, *10*) or phase-shifting (*11*, *12*) of AM-carrying beams have imposed a fundamental physical limit for realizing such a principle at a chip-scale footprint.

The advance of strong light-confinement nanophotonic approaches has been a major propellant of miniaturized optical circuits to harness AM of light. The chip-scale generation and transmission of AM-carrying beams on silicon-integrated circuits have been realized through whispering gallery mode resonators (*13*) and resonant microring fibers (*10*). However, these approaches are resonant in nature, leading to a narrow bandwidth down to several nanometers. Surface plasmon polaritons (SPPs) capable of strong light confinements have long been pursued to overcome the size limitation of nanophotonic devices and, hence, potentially facilitate the chip-scale multiplexing of SAM through the SAM-distinguishing nanostructures (*14*–*18*). Even though the OAM generators mediated by SPPs have been demonstrated either through digitalized metasurfaces with a helical phase (*19*) or geometric metasurfaces based on spin-orbit interaction (*20*), the extrinsic nature of OAM (*21*) with helical wavefronts restricts its detection to a phase-sensitive interference-based method through a holographic metasurface (*22*), which inevitably degrades the perceptive devices for on-chip applications.

The concept of our on-chip noninterference AM multiplexing of broadband light is illustrated in Fig. 1. Without losing the generality, coaxially superposed AM-carrying beams with four selected AM modes [$l_0 = -4$, $s = -1$ ($AM_1$); $l_0 = -2$, $s = -1$ ($AM_2$); $l_0 = +2$, $s = +1$ ($AM_3$); and $l_0 = +4$, $s = +1$ ($AM_4$); where $l_0$ and $s$ are the modal indices for OAM and SAM, respectively (Fig. 1A)] propagate through a nanoring aperture (NRA) multiplexing unit that consists of shallow nanogrooves and the spatially shifted mode-sorting nanoring slits of different sizes (Fig. 1B and fig. S1A). The nanogroove structures act as the metal-dielectric interfaces to convert the AM modes carried by photons into SPPs and to spatially route the excited plasmonic AM modes to the locations of the nanoring slits. A set of AM-carrying beams of $l_0 = \pm1, \pm2, \pm3, \pm4$ and $s = \pm1$ (fig. S2) can be adopted to excite a range of plasmonic AM modes (determined by total AM $L = l_0 + s + l_s$, where $l_s$ is the geometrical topological charge arising from the nanogrooves), with a distinguished spatial separability from


[1]Centre for Micro-Photonics and Centre for Ultrahigh Bandwidth Devices for Optical Systems (CUDOS), Faculty of Science, Engineering and Technology, Swinburne University of Technology, Hawthorn, Victoria 3122, Australia. [2]Institute of Photonics Technology, Jinan University, Guangzhou, China. [3]Artificial Intelligence Nanophotonics Laboratory, School of Science, RMIT University, Melbourne, Victoria 3001, Australia.
***Corresponding author. Email: min.gu@rmit.edu.au**


Downloaded from http://science.sciencemag.org/ on May 12, 2016

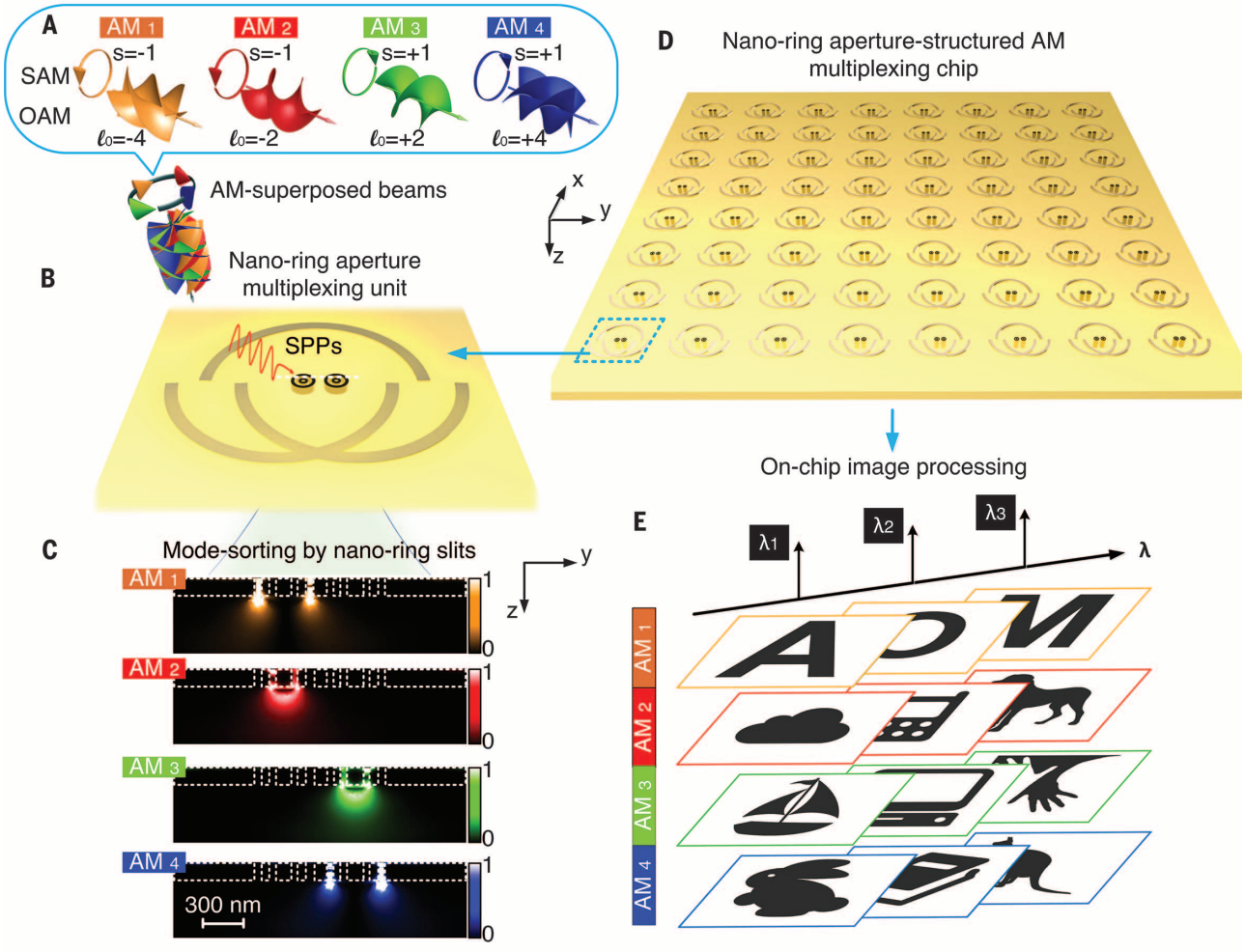


**Fig. 1. The principle of on-chip noninterference AM multiplexing of broadband light.** (**A**) Four selected AM beams [$l_0$ = −4, $s$ = −1 ($AM_1$); $l_0$ = −2, $s$ = −1 ($AM_2$); $l_0$ = +2, $s$ = +1 ($AM_3$); and $l_0$ = +4, $s$ = +1 ($AM_4$)] are coaxially overlapped as the AM-superposed beams. (**B**) Schematic of a NRA multiplexing unit consisting of nanogroove structures and the mode-sorting nanoring slits. (**C**) Mechanism for AM mode-sorting by nanoring slits that have different sizes and lateral shifts. (**D**) NAMMC integrated by an array of 8 NRA units by 8 NRA units. (**E**) Concept of on-chip processing of AM-multiplexed images over a broadband by the NAMMC. λ, wavelength.

the structure depicted in fig. S1A. The formation of the spatial separability by nanogrooves provides a physical ground for AM mode sorting. As a result of the distinctive AM mode-sorting sensitivity by nanoring slits, the plasmonic AM modes can be selectively coupled out through the slits that have different sizes and spatial shifts (Fig. 1C). Furthermore, the nonresonant AM mode-sorting sensitivity by the nanoring slits enables the AM multiplexing over a broad bandwidth. As such, a large-scale NRA-structured AM multiplexing chip (NAMMC) (Fig. 1D) consisting of an array of individually addressable NRAs, wherein NRA units are separated by a spacing larger than the diffraction-limit distance, allows for on-chip processing of an AM-multiplexed image in parallel through a multibeam approach (Fig. 1E).

In terms of the operation mechanism, we considered a nanoring slit enclosed by a concentric nanogroove ($l_s$ = 0) in a gold film. Throughout this paper, the width of the nanoring slit is fixed as 50 nm. We carried out a full vectorial approach for the analysis of the AM mode in the nanoring slit (*23*). With respect to the cut-off AM mode (fig. S3) of the nanoring slit, the calculated effective indices of the eigen-AM modes of $L$ = ±1 and ±3 indicate that the lower AM mode of $L$ = ±1 can be supported by both slits, with inner radii of 75 nm ($R_{in1}$) and 200 nm ($R_{in2}$), but the higher AM mode of $L$ = ±3 can only be maintained by the slit with $R_{in2}$ (Fig. 2A). Moreover, the effective index differences almost remain flat in visible wavelengths, which indicates the nonresonant nature of AM modes supported by nanoring slits and lays the foundation for multiplexing broadband light.

The outcoupling (transmittance) efficiency of nanoring slits can be determined by the mode matching between the eigen-AM mode supported by nanoring slits (fig. S4, A to C) and the plasmonic AM mode excited from nanogrooves (fig. S4, D to F). A mode-matching factor (MF) can be defined (*23*) so that we intuitively understand the distinctive AM mode-sorting selectivity by the nanoring slits. The MF can be selectively maximized from its dependence on the illumination wavelength and the slit radius (fig. S4, G to I). As an example, the black curves in Fig. 2A reveal that plasmonic modes with total AM of $L$ = ±1 and ±3 can be distinctively coupled out through nanoring slits with $R_{in1}$ and $R_{in2}$, respectively. In addition, theoretical analysis of the fundamental symmetries in nanophotonics (*24*, *25*) provides physical insight into the NRA exhibiting the distinctive sensitivity on the total AM of SPPs, which yields additional flexibility in the subsequent chip design operating by different SAM and OAM combinations with the given total AM.

The distinctive AM mode-sorting selectivity, as defined in (*23*), can be experimentally verified for AM modes of $L$ = ±1 and ±3 over a

Downloaded from http://science.sciencemag.org/ on May 12, 2016

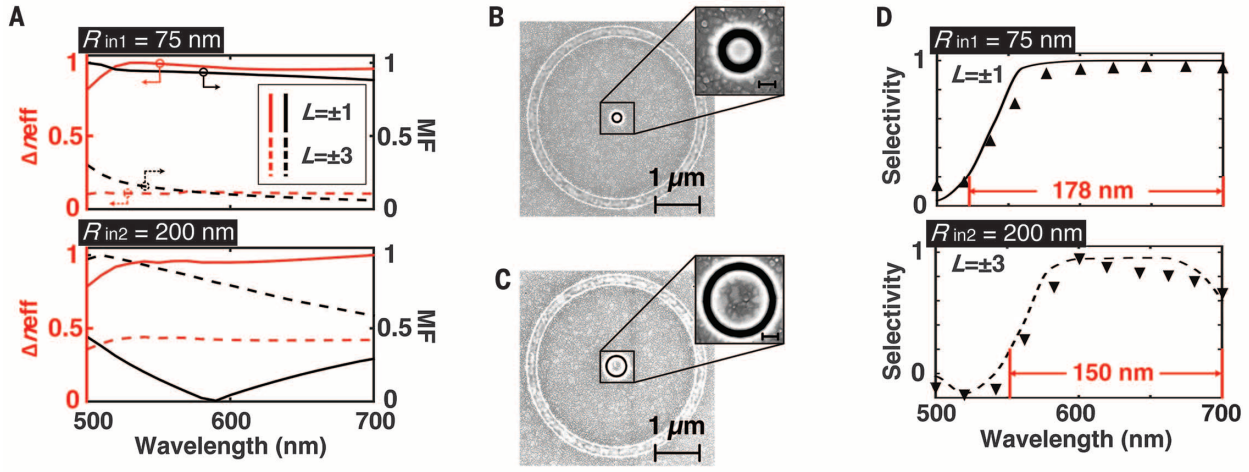


**Fig. 2. Distinctive AM mode-sorting selectivity by a nanoring slit of varying size.** (**A**) Theoretically calculated effective index differences (Δneff) (red curves) and MFs (black curves) for the plasmonic modes with total AM of $L = \pm 1$ (solid lines) and $L = \pm 3$ (dashed lines) for a nanoring slit with $R_{in1} = 75$ nm (top) and $R_{in2} = 200$ nm (bottom), respectively. (**B** and **C**) Scanning electron microscopy (SEM) images of the fabricated NRAs consisting of concentric nanogrooves and nanoring slits with inner radii of $R_{in1}$ (see fig. S1B for 45° view) and $R_{in2}$ (see fig. S1C for 45° view), respectively. The insets show enlarged views of the nanoring slits (scale bars, 100 nm). (**D**) Numerically calculated (curves) and experimentally confirmed (triangles) AM mode-sorting selectivity spectra of the AM beams of $l_0 = -2, s = +1$ ($L = -1$) and $l_0 = +2, s = +1$ ($L = +3$) for nanoring slits with inner radii of $R_{in1}$ (top) and $R_{in2}$ (bottom), respectively. The red color indicates the bandwidths (defined as the selectivity ≥ 0.1) of AM mode-sorting selectivity by nanoring slits.

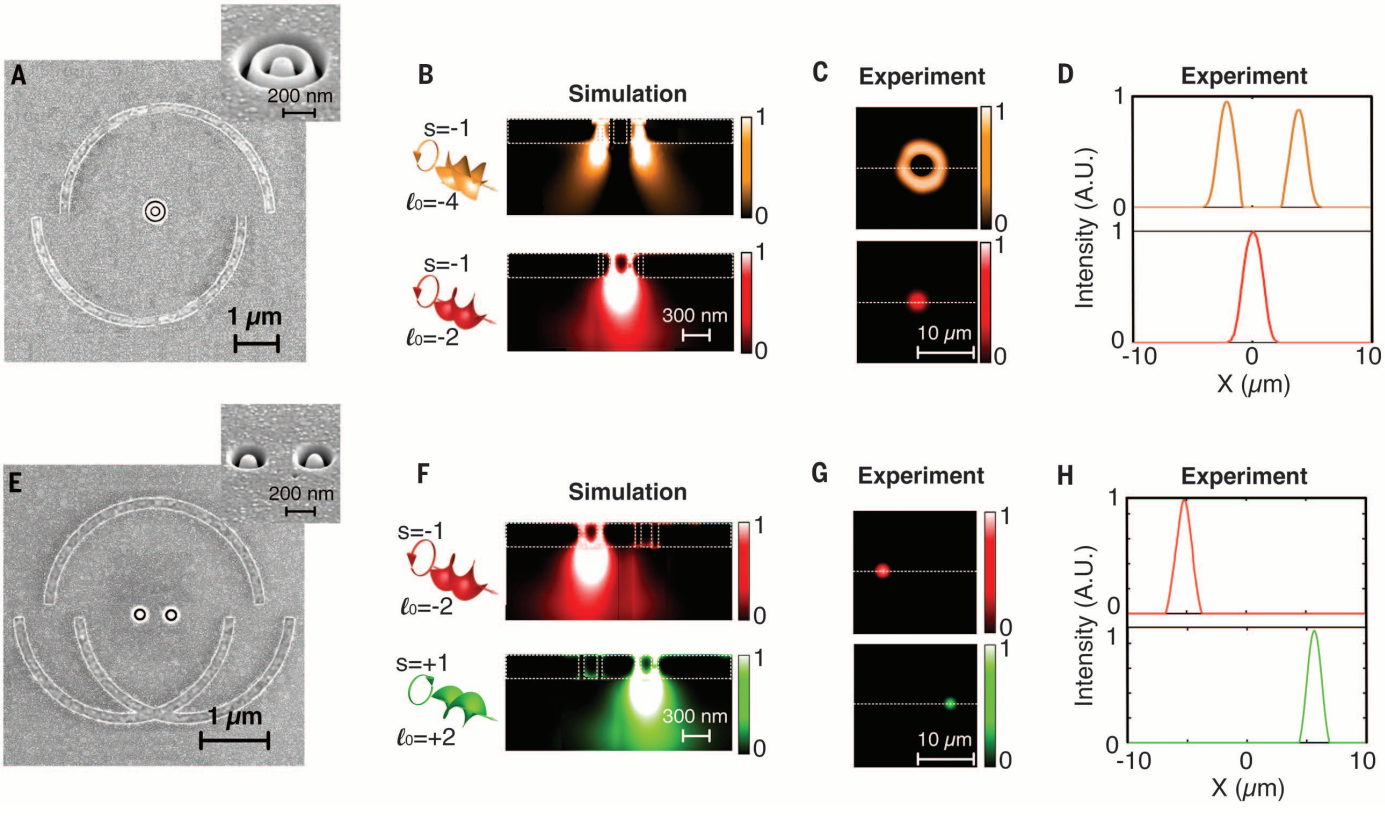


**Fig. 3. Experimental characterization of chip-scale AM multiplexing based on double concentric and spatially shifted nanoring slits enclosed by sections of spatially shifted nanogrooves.** (**A**) SEM image of the double nanoring slits (inset), with $R_{in1}$ and $R_{in2}$ enclosed by the two sections of shifted grooves with $l_s = +2$. (**B**) Simulated total intensity distributions of the AM beams of $AM_1$ (top) and $AM_2$ (bottom) in the longitudinal planes of the nanoring slits. (**C**) Experimental far-field intensity distributions of the AM beams of $AM_1$ and $AM_2$ in the transverse planes. (**D**) Experimental cross-section plots of the far-field intensity distributions in (C), as labeled by the dashed white lines. A.U., arbitrary units. (**E** to **H**) Counterparts of (A) to (D), based on the spatially shifted nanoring slits with $R_{in1}$ and nanogrooves with $l_s = +2$ (left) and $l_s = -2$ (right). In (F) to (H), top images correspond to $AM_2$ (top); bottom images correspond to $AM_3$.

Downloaded from http://science.sciencemag.org/ on May 12, 2016

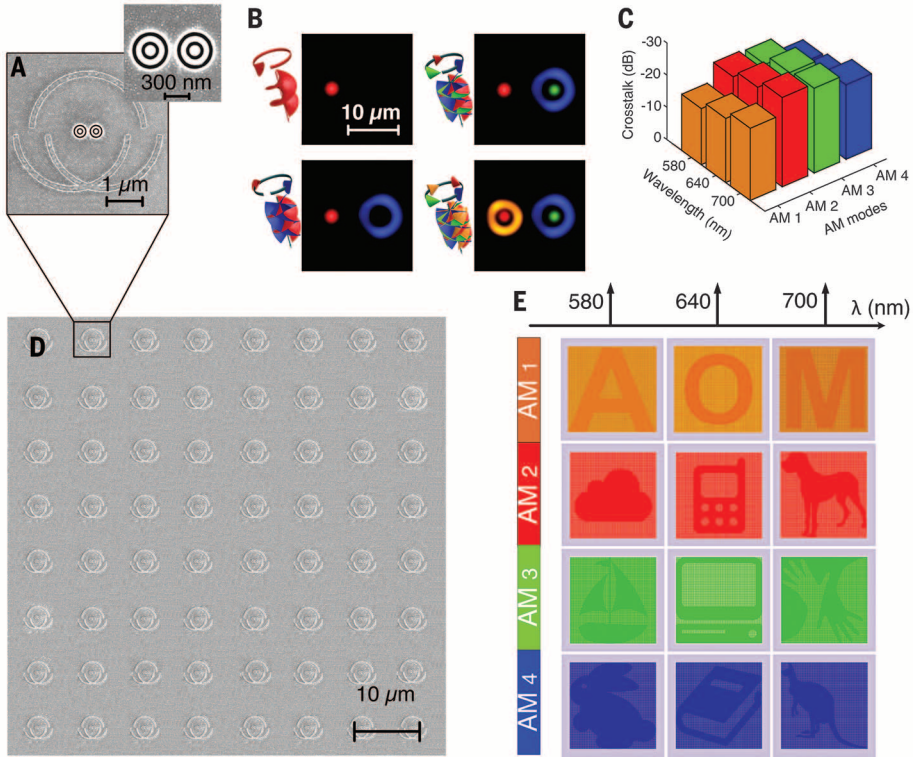


**Fig. 4. Four-state AM multiplexing through a NRA unit and parallel AM- and wavelength-division multiplexing through the large-scale NAMMC.** (**A**) SEM image of the single NRA (see fig. S1D for 45° view) in the NAMMC and the two concentric double nanoring slits (inset). (**B**) Experimental characterization of the four-state AM multiplexing by dynamically switching on the AM-superposed beams. The images are presented in pseudo-colors. (**C**) Measured modal cross-talk of the four AM modes at different wavelengths. (**D**) SEM image of the NAMMC. (**E**) Experimentally reconstructed AM- and wavelength-coded images retrieved from the four AM modes ($AM_1$, $AM_2$, $AM_3$, and $AM_4$) (Fig. 1A) at the three different wavelengths.

broad bandwidth of 150 nm in visible wavelengths (Fig. 2D). As an illustration, fig. S5 shows transmissive patterns of the AM beams at a wavelength of 640 nm. The physical principle of the distinctive AM mode-sorting selectivity can be extended to other wavelengths, such as telecommunication bands ranging from 1.45 to 1.65 μm (fig. S6).

The principle of the AM mode-sorting selectivity by nanoring slits of different sizes can be adopted for chip-scale multiplexing of AM-superposed beams if two nanoring slits with $R_{in1}$ and $R_{in2}$ are used concentrically. As shown in Fig. 3, A to D, two sections of the circular nanogrooves were spatially shifted in opposite directions, yielding $l_s$ = +2. Additionally, AM beams of $AM_1$ and $AM_2$ can excite plasmonic AM modes corresponding to $L$ = −3 and −1, respectively, leading to the distinctive transmittance from the concentrically aligned nanoring slits. The capacity of the AM mode-sorting multiplexing can be increased by laterally shifting one of the circular nanogroove sections and the enclosed nanoring slit in opposite directions (Fig. 3, E to H). Using this nanogroove-shifting principle, AM beams with OAM modes ranging from $l_0$ = −4 to +4 and SAM modes of $s$ = −1 and +1 can be coupled out by the two spatially shifted nanoring slits that have different locations and sizes, with the smallest footprint of 4.2 μm by 4.2 μm (fig. S7).

Based on the AM mode-sorting principle, we can achieve on-chip multiplexing of multiple AM modes (Fig. 4). We used two concentric double nanoring slits (Fig. 4A and fig. S1D) to selectively couple out the AM beams of $AM_1$, $AM_2$, $AM_3$, and $AM_4$, which can easily be evidenced by their distinctive transmissive patterns in the far-field region (fig. S8). As such, chip-scale AM multiplexing by dynamically switching on individual AM beams can be directly observed at different wavelengths (Fig. 4B and fig. S9), with a modal cross-talk as low as −17 dB (Fig. 4C).

The broadband feature of the noninterference AM multiplexing by the chip-scale NRA can enable a multiplexing chip constructed by an array of NRAs (i.e., the NAMMC) to carry out both AM- and wavelength-division multiplexing in parallel. The NAMMC, which consists of an array of 8 NRA units by 8 NRA units, was fabricated (Fig. 4D) and illuminated by an array of 8 by 8 multibeams carrying well-defined SAM and OAM (*23*) (figs. S10 and S11). Consequently, Fig. 4E shows the experimentally reconstructed AM- and wavelength-coded images (100 pixels by 100 pixels), which were constructed one piece at a time through the dynamic area-by-area coding method (*23*). In addition, we show that the NAMMC is also capable of displaying the AM-coded image by simultaneously addressing the four AM information channels (fig. S12).

In bulky optics, OAM multiplexing is outperformed by conventional multiplexing techniques, in terms of multiplexing capacity. However, OAM multiplexing outperforms other techniques in nanoscale systems with a small space-bandwidth product (*26*). In general, the AM mode-sorting sensitivity of the NRAs can be extended to spiral nanogroove systems with different $l_s$ (figs. S13 and S14) and to multiple concentric nanoring slits. This generalization can be advantageous for further reduction of the NRA footprint while multiplexing optical beams with a greater number of AM modes. The noninterference operating principle in NRAs removes the requirement of bulky interference-based optics, and the associated nonresonance nature can largely increase the multiplexing capacity in conjunction with the wavelength-division multiplexing in a broad band. The large-scale NAMMC can be further integrated with chip-scale AM generators and could thereby offer compact on-chip AM applications in optical communications, information display, data storage, and data encryption.

## REFERENCES AND NOTES


1. P. Zijlstra, J. W. M. Chon, M. Gu, *Nature* **459**, 410–413 (2009).
2. N. J. Karl, R. W. Mckinney, Y. Monnai, R. Mendis, D. M. Mittleman, *Nat. Photonics* **9**, 717–720 (2015).
3. H. Yun, S. Y. Lee, K. Hong, J. Yeom, B. Lee, *Nat. Commun.* **6**, 7133 (2015).
4. R. Deng *et al.*, *Nat. Nanotechnol.* **10**, 237–242 (2015).
5. X. Li *et al.*, *Nat. Commun.* **6**, 6984 (2015).
6. X. Li, T. H. Lan, C. H. Tien, M. Gu, *Nat. Commun.* **3**, 998 (2012).
7. L. W. Luo *et al.*, *Nat. Commun.* **5**, 3069 (2014).
8. Y. Lu *et al.*, *Nat. Photonics* **8**, 32–36 (2014).
9. J. Wang *et al.*, *Nat. Photonics* **6**, 488–496 (2012).
10. N. Bozinovic *et al.*, *Science* **340**, 1545–1548 (2013).
11. G. C. G. Berkhout, M. P. J. Lavery, J. Courtial, M. W. Beijersbergen, M. J. Padgett, *Phys. Rev. Lett.* **105**, 153601 (2010).
12. M. Mirhosseini, M. Malik, Z. Shi, R. W. Boyd, *Nat. Commun.* **4**, 2781 (2013).
13. X. Cai *et al.*, *Science* **338**, 363–366 (2012).
14. J. K. Gansel *et al.*, *Science* **325**, 1513–1515 (2009).
15. Y. Gorodetski, N. Shitrit, I. Bretner, V. Kleiner, E. Hasman, *Nano Lett.* **9**, 3016–3019 (2009).


Downloaded from http://science.sciencemag.org/ on May 12, 2016

16. X. Yin, Z. Ye, J. Rho, Y. Wang, X. Zhang, *Science* **339**, 1405–1407 (2013).
17. J. Lin *et al.*, *Science* **340**, 331–334 (2013).
18. X. Zambrana-Puyalto, X. Vidal, G. Molina-Terriza, *Nat. Commun.* **5**, 4922 (2014).
19. N. Yu *et al.*, *Science* **334**, 333–337 (2011).
20. M. Pu *et al.*, *Sci. Adv.* **1**, e1500396 (2015).
21. A. T. O'Neil, I. MacVicar, L. Allen, M. J. Padgett, *Phys. Rev. Lett.* **88**, 053601 (2002).
22. P. Genevet, J. Lin, M. A. Kats, F. Capasso, *Nat. Commun.* **3**, 1278 (2012).
23. Materials and methods and supplementary text are available as supplementary materials on *Science* Online.
24. I. Fernandez-Corbaton, X. Zambrana-Puyalto, G. Molina-Terriza, *Phys. Rev. A* **86**, 042103 (2012).
25. I. Fernandez-Corbaton *et al.*, *Phys. Rev. Lett.* **111**, 060401 (2013).
26. N. Zhao, X. Li, G. Li, J. M. Kahn, *Nat. Photonics* **9**, 822–826 (2015).

**ACKNOWLEDGMENTS**

We thank X. Li for help with the ion beam lithography, G. Gervinskas and F. Eftekhari from the Melbourne Centre for Nanofabrication for their fabrication efforts, H. Lu for technical assistance with the waveguide calculation, and J. Storteboom for assistance with using the Spectra-Physics Inspire laser system. This work was supported under the Australian Research Council Laureate Fellowship program (grant FL100100099). M.G. acknowledges support from the Australian Research Council Centre for Ultrahigh Bandwidth Devices for Optical Systems (CUDOS) (project CE110001018). X.L. acknowledges support from the Australian Research Council (grant DE150101665). All data related to the experiments described in this manuscript are archived on a lab computer at Swinburne University of Technology.

**SUPPLEMENTARY MATERIALS**

www.sciencemag.org/content/352/6287/805/suppl/DC1
Materials and Methods
Supplementary Text
Figs. S1 to S14
References (*27–30*)

18 December 2015; accepted 9 March 2016
Published online 7 April 2016
10.1126/science.aaf1112

GEOCHEMISTRY

# Preservation of Earth-forming events in the tungsten isotopic composition of modern flood basalts

**Hanika Rizo,[1]* Richard J. Walker,[2] Richard W. Carlson,[3] Mary F. Horan,[3] Sujoy Mukhopadhyay,[4] Vicky Manthos,[4] Don Francis,[5] Matthew G. Jackson[6]**

**How much of Earth's compositional variation dates to processes that occurred during planet formation remains an unanswered question. High-precision tungsten isotopic data from rocks from two large igneous provinces, the North Atlantic Igneous Province and the Ontong Java Plateau, reveal preservation to the Phanerozoic of tungsten isotopic heterogeneities in the mantle. These heterogeneities, caused by the decay of hafnium-182 in mantle domains with high hafnium/tungsten ratios, were created during the first ~50 million years of solar system history, indicating that portions of the mantle that formed during Earth's primary accretionary period have survived to the present.**

Four and a half billion years of geologic activity have overprinted much of the evidence for the processes involved in Earth's formation and initial chemical differentiation. High-precision isotopic measurements of the decay products of short-lived radionuclides that were present when Earth formed can provide a view of events that occurred during the first tens to hundreds of million years of Earth history. Data from both the $^{146}$Sm-$^{142}$Nd (half-life, $t_{1/2}$ = 103 million years) and $^{129}$I-$^{129}$Xe ($t_{1/2}$ = 15.7 million years) systems show the importance of early mantle differentiation and outgassing events but provide conflicting evidence about the preservation of early-formed mantle reservoirs to the present day (*1–4*). Of the short-lived systems, the $^{182}$Hf-$^{182}$W ($t_{1/2}$ = 8.9 million years) system is distinctively sensitive to metal-silicate separation and has been used effectively to trace the timing and processes of core formation (*5*), which is arguably the most important chemical differentiation event to occur on a rocky planet. Only recently, however, have measurement techniques improved to the point of resolving $^{182}$W/$^{184}$W variability in ancient (>2.7 billion years old) terrestrial rocks; such variability reflects the preservation of compositionally distinct domains in Earth's interior that were probably created during Earth's formation (*6–10*). Young mantle-derived rocks examined to date have shown neither $^{142}$Nd nor $^{182}$W isotopic heterogeneity, suggesting that the early-formed compositional domains in Earth's interior were largely destroyed by mantle-mixing processes during the first half of Earth history (*1–4*, *6–10*). Here we report $^{182}$W/$^{184}$W ratios in Phanerozoic flood basalts from Baffin Bay and the Ontong Java Plateau, some of which are among the highest ever measured in terrestrial rocks. These results document the preservation of regions within Earth's interior whose compositions were established by events that occurred within the first ~50 million years of solar system history. This study, consequently, provides new insights into the processes at work during planet formation, the chemical structure of Earth's interior, and the interior dynamics that allowed the preservation of chemical heterogeneities for 4.5 billion years.

Flood basalts are the largest volcanic eruptions identified in the geological record. These types of eruptions created both the North Atlantic

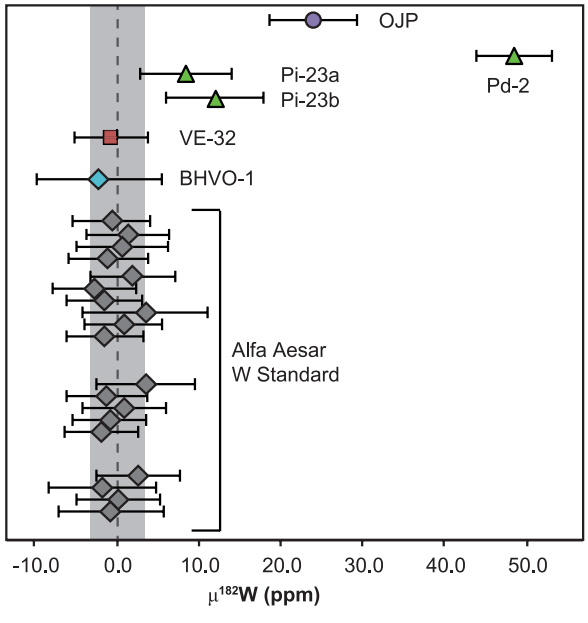


**Fig. 1. μ$^{182}$W values measured for the Baffin Bay and Ontong Java Plateau samples, the geological reference materials VE-32 and BHVO-1, and the Alfa Aesar W standard.** The values are expressed as deviations, in parts per million (ppm), from the average value measured for the W standard. The gray shaded area represents 2σ for the average W standard value. Errors for each data point are 2σ.

[1]Geotop, Département des Sciences de la Terre et de l'Atmosphère, Université du Québec à Montréal, Montreal, Canada. [2]Department of Geology, University of Maryland, College Park, MD, USA. [3]Carnegie Institution for Science, Washington, DC, USA. [4]Department of Earth and Planetary Sciences, University of California–Davis, Davis, CA, USA. [5]Department of Earth and Planetary Sciences, McGill University, Montreal, Canada. [6]Department of Earth Science, University of California–Santa Barbara, Santa Barbara, CA, USA.
***Corresponding author. Email: rizo.hanika@uqam.ca**

Downloaded from http://science.sciencemag.org/ on May 12, 2016

Igneous Province, which hosts the Baffin Bay locale (*11*), and the Ontong Java Plateau in the western Pacific Ocean (*12*). We studied pillow lavas with high-MgO picritic compositions (table S1) from Padloping Island, Baffin Bay (samples Pi-23 and Pd-2). We targeted these rocks because some Baffin Bay lavas contain the highest $^{3}He/^{4}He$ ratios ever measured (*13*), along with Pb isotopic compositions (*14*) and D/H ratios (*15*) that indicate that their mantle source was relatively primitive and undegassed, consistent with it being isolated since shortly after Earth's formation. Ontong Java is Earth's largest known volcanic province and shares chemical and isotopic similarities with the Baffin Bay lavas, consistent with a primitive mantle source (*16*). The Ontong Java sample (192-1187A-009R-04R) is a basalt (table S1) collected from the plateau's eastern flank by Ocean Drilling Project Leg 192.

We present data from the short-lived $^{182}Hf$-$^{182}W$ and $^{146}Sm$-$^{142}Nd$ systems, because these two systems are variably sensitive to the core formation and mantle differentiation processes that occurred early in Earth history. We compare these data with data from the long-lived U-Th-He, $^{147}Sm$-$^{143}Nd$, and $^{187}Re$-$^{187}Os$ isotope systems, together with W and highly siderophile element (HSE; Re, Os, Ir, Ru, Pt, and Pd) concentrations, to better distinguish early differentiation events from those occurring over all of Earth history.

Glassy rim and core pieces of sample Pi-23 (Pi-23a and Pi-23b, respectively), a bulk sample of Pd-2, and a bulk sample of 192-1187A-009R-04R are characterized by high $^{182}W/^{184}W$ ratios that are well resolved from standards, with $\mu^{182}W$ values ranging from +10 to +48 {where $\mu^{182}W = [(^{182}W/^{184}W)_{sample}/(^{182}W/^{184}W)_{standard} - 1] \times 10^{6}$} (Fig. 1 and Table 1) (*17*). The $\mu^{182}W$ values for samples Pi-23a and Pi-23b are in good agreement. This rules out the influence of stable W isotope fractionation through interaction of seawater with the pillow rim in creating the measured $^{182}W$ values (*17*). Samples 192-1187A-009R-04R and Pd-2 had the lowest W concentrations and the highest $\mu^{182}W$ values (Table 1). The W concentrations of these two samples [23 and 26 parts per billion (ppb), respectively] are broadly consistent with those of magmas derived by 15-to-20% partial melting of a mantle source with ~5 ppb W, indicating a primitive source free of W-rich recycled crust (fig. S2) (*17*). The geological reference materials VE-32 (mid-ocean ridge glass) and BHVO-1 (Hawaiian basalt) were measured at the same time as the Baffin Bay and Ontong Java samples and yielded $\mu^{182}W$ values of −0.8 ± 4.5 and −2.3 ± 7.7, respectively (Table 1). These $\mu^{182}W$ values are indistinguishable from the terrestrial Alfa Aesar W standard ($\mu^{182}W = 0$) and other modern rocks (*6*–*10*). The $^{3}He/^{4}He$ ratios measured in olivines from the Baffin Bay samples (table S3) (*17*) yielded values up to 48.4 times higher than the $^{3}He/^{4}He$ ratio of the atmosphere ($1.39 \times 10^{-6}$), in agreement with previous findings (*13*), indicating that the source of these lavas is relatively undegassed and possibly has been isolated since Earth's formation. The HSE abundances and initial $^{187}Os/^{188}Os$ ratios (which provide a record of the long-term Re/Os ratio) from the Baffin Bay and Ontong Java Plateau samples are indistinguishable from other modern mantle-derived lavas with similar MgO abundances that do not show elevated $\mu^{182}W$ (Fig. 2 and table S4) (*18*).

Variability in $^{182}W/^{184}W$ ratios reflects Hf/W fractionation while $^{182}Hf$ was extant. Hf/W fractionation has been observed in early solar system materials (*5*), so variable W isotopic compositions in terrestrial samples can reflect the imperfect mixing of late additions of such materials (*6*, *9*). The $\mu^{182}W$ value of +48 for Baffin Bay sample Pd-2, however, is larger than can be accounted for by this process, and so this possibility is discounted (supplementary text). Hf/W fractionation can also occur as the result of endogenous Earth differentiation processes, such as magma ocean crystallization (*7*) and core formation (*9*). However, silicate fractionation processes cannot be responsible for the generation of the anomalous $^{182}W$ in the sources of the Baffin Bay and Ontong Java lavas. If the high $\mu^{182}W$ was due to silicate fractionation in a magma ocean while $^{182}Hf$ was extant, then $\mu^{182}W$ should positively correlate with $\mu^{142}Nd$, the decay product of the short-lived $^{146}Sm$ ($t_{1/2}$ = 103 million years) isotope system. Instead, the $\mu^{142}Nd$ values of the samples are indistinguishable from all other

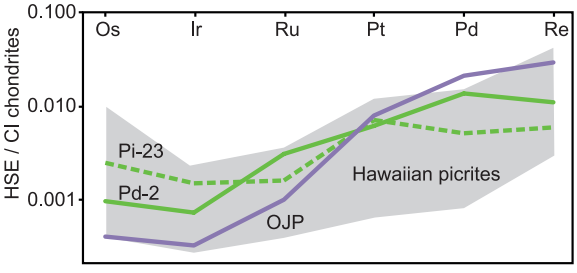


**Fig. 2. HSE abundances for the Baffin Bay and Ontong Java Plateau (OJP) samples.** Abundances are normalized to the HSEs of carbonaceous chondrites (CI group) from (*25*). The gray shaded area shows the range of HSE abundances for type-2 Hawaiian picrites (*26*).

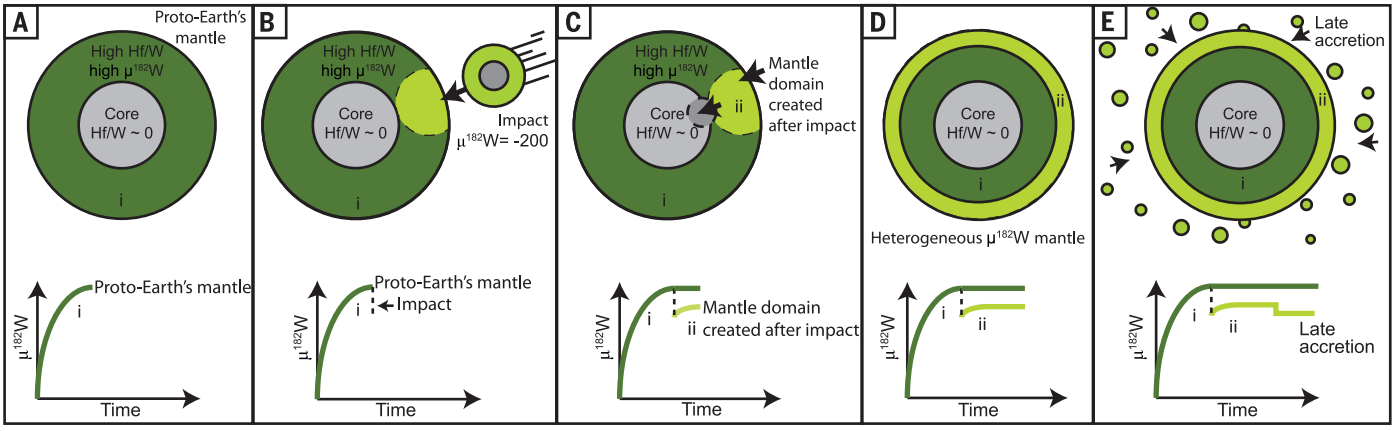


**Fig. 3. Model for the creation of mantle reservoirs with distinct W isotopic compositions.** (**A**) Early core formation leaves the proto-Earth's mantle with a high Hf/W ratio that, with time, evolves to a high $\mu^{182}W$ value (i). (**B**) The impact of a large body affects the Hf/W ratio and W isotopic composition of a portion of the proto-Earth's mantle. (**C**) Evolution of the portion of the mantle (ii) affected by the impact of a large body, involving some degree of isotopic equilibration between the impactor materials and the mantle. The core of the impactor subsequently merges with the core of the proto-Earth. (**D**) Possible scenario after isostatic adjustment (*27*) and creation of a mantle with heterogeneous $\mu^{182}W$ through impacts of large bodies. Mantle domains affected by impacts that occur after the extinction of $^{182}Hf$ no longer generate radiogenic $^{182}W$, so their $^{182}W/^{184}W$ ratios can change only by mixing with other terrestrial reservoirs or with late-accreted chondritic material. (**E**) Late accretion, representing ~0.5% of Earth's mass, decreases the $^{182}W/^{184}W$ ratio of all the earlier-formed reservoirs by ~15 ppm. This last accretion is responsible for endowing the modern mantle with chondritic relative abundances of the HSEs.

Downloaded from http://science.sciencemag.org/ on May 12, 2016

**Table 1. Tungsten concentrations and isotopic compositions.** Included are data from the Baffin Bay samples Pi-23a, Pi-23b, and Pd-2; the Ontong Java Plateau sample 192-1187A-009R-04R; the mid-ocean ridge glass sample VE-32; and the BHVO-1 basalt standard. Uncertainties are ±2σ. More details are given in (*17*) and table S2.

| Locality | Geodynamic context | Sample | $\mu^{182}W$ (ppm) | ±2σ (ppm) | W (ppb) |
|---|---|---|---|---|---|
| Baffin Bay | Flood basalt | Pi-23a | 11.9 | 5.9 | 62 |
| Baffin Bay | Flood basalt | Pi-23b | 8.3 | 5.6 | 62 |
| Baffin Bay | Flood basalt | Pd-2 | 48.4 | 4.6 | 26 |
| Ontong Java Plateau | Flood basalt | 192-1187A-009R-04R | 23.9 | 5.3 | 23 |
| East Pacific Rise | Mid-ocean ridge basalt | VE-32 | −0.8 | 4.5 | 54 |
| Hawaii | Ocean island basalt | BHVO-1 | −2.3 | 7.7 | 274 |

modern basalts measured so far (fig. S3 and table S5) (*17*).

This leaves Hf/W fractionation resulting from metal-silicate segregation accompanying core formation as the probable cause of the observed anomalies in the Phanerozoic samples. Metal-silicate segregation is the process that can fractionate Hf/W most effectively, because Hf is a strongly lithophile trace element, whereas W is moderately siderophile. The low W concentrations estimated for the mantle source of the flood basalts described here are consistent with mantle domains that experienced metal-silicate segregation (Table 1 and supplementary text). Repeated metal-silicate segregation events during planet formation (*19*) could create one or more mantle domains with distinct $\mu^{182}W$, without affecting the Sm-Nd system. Such events would result in variable $\mu^{182}W$, due to metal-silicate segregation events occurring at different times (Fig. 3), or, alternatively, different Hf/W ratios in the resulting mantle reservoirs that reflect different oxidation states and, hence, different partitioning of W into metal (supplementary text).

The key observation to consider, which is supported by the results reported here, is that terrestrial samples with $^{182}W$ excesses do not seem to derive from sources depleted in HSEs (Fig. 2) (*6*–*10*). HSEs have partition coefficients between metal and silicate of $>10^4$ (*20*); thus, their concentrations in metal-depleted mantle domains are expected to be very low. Evolving oxidation states during Earth accretion might explain the decoupling of $^{182}W$ and HSEs, because although W becomes less siderophile under oxidizing conditions, the HSEs, even at high oxidation states, are not soluble in silicates (*20*). This model, however, would require subsequent late-accreted HSEs to have been mixed into different mantle domains without the mixing away of W isotopic heterogeneity. Alternatively, the observed decoupling could be explained if some metal from the core of the Moon-forming giant impactor was retained in the mantle, followed by a minor amount of late accretion (*9*). This model would require a substantial mass of high-density metal to have been retained in Earth's mantle after the impact, when the mantle was partially or wholly molten, and this retained metal would have to have contained chondritic relative abundances of the HSEs. These models are summarized in the supplementary text, along with a few additional potential explanations for the apparent decoupling of W isotopic compositions and HSE abundance variations.

Regardless of the origin of the $^{182}W$ variability, what is arguably more unexpected than the fact that Earth experienced such early differentiation events is that reservoirs formed by these early processes remain in the mantle today. This conclusion is now supported by isotopic variability in both W and Xe (*1*, *21*), but not in $^{142}Nd$, which suggests that the observed heterogeneity in $^{142}Nd/^{144}Nd$ ratios was reduced to an unobservable level by the end of the Archean, probably through the mixing caused by mantle convection. Perhaps the key to reconciling these observations is that the $^{129}I$-$^{129}Xe$ system primarily reflects mantle outgassing, and the $^{182}Hf$-$^{182}W$ system reflects metal-silicate separation, whereas the $^{146}Sm$-$^{142}Nd$ system is controlled by internal mantle differentiation. For both W and Xe, one component of the complementary chemical differentiation (the core for W and the atmosphere for Xe) may not be available for effective recycling and mixing in the mantle (*22*). In contrast, for Nd, the main reservoirs created during early Earth differentiation may have been in a portion of the mantle that has since been effectively mixed by mantle circulation. Estimates for how much of the mantle can remain unmixed depend on the rheological properties assigned to the various materials involved. Some models (*23*) show that as much as 20% of the mantle may remain isolated as distributed masses. An important aspect of the results presented here is that both $^{182}W$ anomalies and elevated $^3He/^4He$ ratios (table S3) appear in at least two major flood basalts. Flood basalt eruptions require the melting of large volumes of mantle during unusual thermal events in the history of mantle circulation. The large size and sporadic nature of flood basalt eruptions are perhaps indicative of a layer in the mantle whose density or rheological properties keep it from effectively mixing with the rest of the mantle. The large low–shear velocity provinces (LLSVPs) that have been imaged at the base of the mantle (*24*) may constitute such a reservoir. These regions appear to be warmer and compositionally different from the surrounding mantle. Estimates of their volume range to as high as 7% of the mantle, or on the order of $6 \times 10^{10}$ km$^3$. If the LLSVPs are remnants of early differentiation events on Earth, they must have a delicately balanced density contrast relative to the surrounding mantle to allow their survival through 4.5 billion years of dynamic Earth history.

## REFERENCES AND NOTES


1. S. Mukhopadhyay, *Nature* **486**, 101–104 (2012).
2. M. Boyet, M. O. Garcia, R. Pik, F. Albarede, *Geophys. Res. Lett.* **32**, L04306 (2005).
3. V. C. Bennett, A. D. Brandon, A. P. Nutman, *Science* **318**, 1907–1910 (2007).
4. H. Rizo, M. Boyet, J. Blichert-Toft, M. T. Rosing, *Earth Planet. Sci. Lett.* **377–378**, 324–335 (2013).
5. T. Kleine *et al.*, *Geochim. Cosmochim. Acta* **73**, 5150–5188 (2009).
6. M. Willbold, T. Elliott, S. Moorbath, *Nature* **477**, 195–198 (2011).
7. M. Touboul, I. S. Puchtel, R. J. Walker, *Science* **335**, 1065–1069 (2012).
8. M. Touboul, J. Liu, J. O'Neil, I. S. Puchtel, R. J. Walker, *Chem. Geol.* **383**, 63–75 (2014).
9. M. Willbold, S. J. Mojzsis, H.-W. Chen, T. Elliot, *Earth Planet. Sci. Lett.* **419**, 168–177 (2015).
10. H. Rizo *et al.*, *Geochim. Cosmochim. Acta* **175**, 319–336 (2016).
11. A. D. Saunders, J. G. Fitton, A. C. Kerr, M. J. Norry, R. W. Kent, *Geophys. Monogr. Ser.* **100**, 45–94 (1997).
12. C. R. Neal, J. J. Mahoney, L. W. Kroenke, R. A. Duncan, M. G. Petterson, *Geophys. Monogr. Ser.* **100**, 183–216 (1997).
13. N. A. Starkey *et al.*, *Earth Planet. Sci. Lett.* **277**, 91–100 (2009).
14. M. G. Jackson *et al.*, *Nature* **466**, 853–856 (2010).
15. L. J. Hallis *et al.*, *Science* **350**, 795–797 (2015).
16. M. G. Jackson, R. W. Carlson, *Nature* **476**, 316–319 (2011).
17. Materials and methods are available as supplementary materials on *Science* Online.
18. C. W. Dale *et al.*, *Earth Planet. Sci. Lett.* **278**, 267–277 (2009).
19. D. Rubie, F. Nimmo, H. J. Melosh, "Formation of Earth's core," in *Treatise on Geophysics*, G. Schubert, Ed. (Elsevier, ed. 2, 2015), pp. 51–90.
20. H. St. C. O'Neill, D. B. Dingwell, A. Borisov, B. Spettel, H. Palme, *Chem. Geol.* **120**, 255–273 (1995).


Downloaded from http://science.sciencemag.org/ on May 12, 2016

21. M. K. Pető, S. Mukhopadhyay, K. A. Kelley, *Earth Planet. Sci. Lett.* **369–370**, 13–23 (2013).
22. M. G. Jackson, S. B. Shirey, E. H. Hauri, M. D. Kurz, H. Rizo, *Geochim. Cosmochim. Acta* 10.1016/j.gca.2016.02.011 (2016).
23. J. P. Brandenburg, E. H. Hauri, P. E. van Keken, C. J. Ballentine, *Earth Planet. Sci. Lett.* **276**, 1–13 (2008).
24. E. J. Garnero, A. K. McNamara, *Science* **320**, 626–628 (2008).
25. M. Horan, R. J. Walker, J. W. Morgan, J. N. Grossman, A. E. Rubin, *Chem. Geol.* **196**, 27–42 (2003).
26. T. J. Ireland, R. J. Walker, M. O. Garcia, *Chem. Geol.* **260**, 112–128 (2009).
27. W. B. Tonks, H. J. Melosh, *J. Geophys. Res. Planets* **98**, 5319–5333 (1993).

**ACKNOWLEDGMENTS**

We thank T. Mock for assistance with mass spectrometry. This work was improved by helpful discussions with J. O'Neil, S. Shirey, and B. Wood. We thank S. Shirey, who provided sample VE-32. We also appreciate the helpful comments and suggestions from three anonymous reviewers. We thank M. Garçon, who developed the four-step $^{142}$Nd acquisition method. This work was supported by NSF grant EAR-1265169 (Cooperative Studies of the Earth's Deep Interior program) to R.J.W. and grant EAR-1250419 to S.M. All data are available in the main manuscript and supplementary materials.

**SUPPLEMENTARY MATERIALS**

www.sciencemag.org/content/352/6287/809/suppl/DC1
Materials and Methods
Figs. S1 to S6
Tables S1 to S5
References (*28*–*56*)

12 November 2015; accepted 5 April 2016
10.1126/science.aad8563

SLEEP RESEARCH

# Causal evidence for the role of REM sleep theta rhythm in contextual memory consolidation

**Richard Boyce,[1] Stephen D. Glasgow,[2] Sylvain Williams,[2]*† Antoine Adamantidis[2,3]*†**

**Rapid eye movement sleep (REMS) has been linked with spatial and emotional memory consolidation. However, establishing direct causality between neural activity during REMS and memory consolidation has proven difficult because of the transient nature of REMS and significant caveats associated with REMS deprivation techniques. In mice, we optogenetically silenced medial septum γ-aminobutyric acid–releasing (MS$^{GABA}$) neurons, allowing for temporally precise attenuation of the memory-associated theta rhythm during REMS without disturbing sleeping behavior. REMS-specific optogenetic silencing of MS$^{GABA}$ neurons selectively during a REMS critical window after learning erased subsequent novel object place recognition and impaired fear-conditioned contextual memory. Silencing MS$^{GABA}$ neurons for similar durations outside REMS episodes had no effect on memory. These results demonstrate that MS$^{GABA}$ neuronal activity specifically during REMS is required for normal memory consolidation.**

The physiological function of rapid eye movement sleep (REMS) is unclear (*1*). Evidence linking REMS to aspects of memory consolidation in mammals has been obtained using techniques such as statistical correlation, pharmacology, and REMS deprivation (*2*, *3*). However, whether REMS has a direct role in learning and memory remains controversial; correlative studies are not definitive, REMS has a transient pattern of occurrence that prevents REMS-selective pharmacological manipulation, and REMS deprivation has critical caveats that are difficult to fully control for (*4*, *5*).

During REMS in mice and rats, a prominent ~7-Hz theta oscillation is observed in local field potential (LFP) recordings from cortical structures, including the hippocampus (*6*, *7*). Hippocampal theta rhythms during REMS may contribute to memory consolidation by providing a mechanism for strengthening place cells formed during prior wakefulness (*8*, *9*). Theta rhythm generation requires an intact medial septum (MS) (*10*, *11*), although the MS is not involved in REMS generation itself (*12*, *13*). MS γ-aminobutyric acid–releasing (MS$^{GABA}$) neurons project to the hippocampus, probably pacing the hippocampal theta rhythm during REMS (*14*–*16*). In mice, we therefore used optogenetics to silence MS$^{GABA}$ neurons and reduce theta activity selectively during REMS, without disturbing sleeping behavior, to determine whether intact MS$^{GABA}$ neural activity during REMS is important for memory consolidation.

Adeno-associated virus (AAVdj) encoding Archaerhodopsin fused to an enhanced yellow fluorescent protein (eYFP) reporter (ArchT-eYFP) was injected into the MS of VGAT::Cre mice (Fig. 1A, top). The resulting ArchT-eYFP expression was ~95% specific for MS$^{GABA}$ neurons (Fig. 1A, bottom, and fig. S1A), stable, and localized to the MS and the diagonal band of Broca (DBB) region for at least 3 months after injection. MS$^{GABA}$ neural projections were observed throughout the hippocampus (Fig. 1B).

Whole-cell voltage and current clamp recordings of ArchT-eYFP–expressing MS neurons in acute brain slices (fig. S1B) revealed hyperpolarization (−39.9 ± 6.6 mV) and outward current (293.9 ± 69.2 pA) upon 594-nm light exposure (fig. S1B). Single-unit recordings in behaving transfected mice (fig. S1C) confirmed that photoinhibition during REMS, non-REM sleep (NREMS), and wakefulness rapidly produced a potent and reversible reduction in spiking of putative MS$^{GABA}$ neurons (fig. S1D).

We next tested the effect of silencing MS$^{GABA}$ neurons during REMS in freely behaving mice. Photoinhibition with constant light pulses delivered to the MS in ArchT-eYFP–expressing mice (ArchT mice) resulted in significantly (65.3 ± 5.6%) reduced theta power measured from dorsal hippocampal area CA1 LFP (CA1LFP) recording (Fig. 1D, top). No other frequency bands were affected, and the spectral profile of the CA1LFP returned to baseline levels almost immediately upon release of MS$^{GABA}$ neurons from photoinhibition (Fig. 1D, top, and Fig. 2A). Current source density (CSD) analysis revealed that reduced theta power was present in all layers of dorsal hippocampal CA1 (Fig. 2B). Light pulses delivered to the MS of mice only expressing eYFP in MS$^{GABA}$ neurons (YFP control mice) did not affect CA1LFP power (Fig. 1D, bottom), ruling out light as a potential confounding factor in these results. Inhibition of MS$^{GABA}$ neurons did not perturb sleeping behavior (Fig. 1D, top), and the probability of state transition during REMS in ArchT mice was unaltered relative to YFP control mice ($n$ = 30 ArchT mice, $n$ = 19 YFP control mice; $P$ = 0.63, unpaired Student's $t$ test).

We optogenetically silenced MS$^{GABA}$ neurons selectively during each REMS episode after acquisition of a novel object place recognition (NOPR) task (Fig. 3A). Mice showed no preference for either object during initial object habituation [day 1 (D1), task acquisition] (Fig. 3A, right). After acquisition, EEG/CA1LFP/EMG (EEG, electroencephalogram; EMG, electromyogram) activity was monitored for 4 hours. Upon entry into REMS, mice in the ArchT or YFP control group had light continuously delivered to the MS until transition to another state occurred, at which time light delivery ceased until subsequent REMS was detected (Fig. 3B). A group of ArchT-eYFP expressing mice that never received light (ArchT control) served as a baseline control for ArchT-eYFP transfection. To determine whether REMS was a critical factor in our results, a final group

[1]Integrated Program in Neuroscience, McGill University, Montreal, Quebec, Canada. [2]Department of Psychiatry, McGill University, Montreal, Quebec, Canada. [3]Department of Neurology and Department of Clinical Research, Inselspital University Hospital, University of Bern, Bern, Switzerland.
*Corresponding author. Email: sylvain.williams@douglas.mcgill.ca (S.W.); antoine.adamantidis@dkf.unibe.ch (A.A.) †These authors contributed equally to this work.

Downloaded from http://science.sciencemag.org/ on May 12, 2016

of mice expressing ArchT-eYFP (ArchT REM control) underwent the same protocol as mice in the ArchT group, with the exception that light delivery to the MS was delayed upon detection of REMS by ~5 min (supplementary methods). After the delay, light was delivered continuously to the MS for a duration equaling that of the preceding REMS episode. The result was a pattern of inhibition that, whereas statistically similar to the REMS-specific pattern that ArchT mice received, occurred primarily when mice were not engaged in REMS. $MS^{GABA}$ neurons were inhibited during 91.6 ± 1.3% of the cumulative REMS duration occurring during the post-test period in ArchT mice (Fig. 3C, top, and fig. S3A), with little inhibition during other states (Fig. 3C, top; laser on 0.2 ± 0.0% of NREMS; 1.5 ± 0.2% of wakefulness). Sleep architecture was unaffected by REMS-selective $MS^{GABA}$ neural photoinhibition during the 4-hour post-test period (fig. S3, A and B), and the only significant effect on the CA1LFP spectral profile (Fig. 3C, bottom, and figs. S4, A to C, and S5C) was reduced (60.2 ± 2.4%) REMS theta power. Basic firing activity during wakefulness, NREMS, and REMS of isolated single neurons recorded at the dorsal CA1 cell layer in a subset of mice during the 4-hour post-test period (supplementary methods) was unaffected by REMS-specific $MS^{GABA}$ neural inhibition (fig. S6, A and B). Analysis of REMS immediately after the 4-hour post-test period when optogenetic silencing of $MS^{GABA}$ neurons during REMS had ceased (4- to 5-hour post-test/recovery period) revealed an immediate return of REMS CA1LFP spectral power to baseline levels (fig. S4, B and C) and no alteration in cumulative and average episode durations in ArchT mice relative to controls (fig. S3C). EEG spindles (tables S1 to S3) and hippocampal ripples (tables S6 to S9) measured during NREMS throughout the course of the NOPR protocol were also unaltered.

On day 2 (D2), object 2 was moved to a new location while object 1 remained stationary (Fig. 3D, left). Because mice preferentially investigate novel stimuli, if object orientation memory is intact, mice should intrinsically investigate object 2 more than object 1 (*17*). Preference for object 2 [object 2 discrimination index (DI), supplementary methods] was not different relative to D1 testing in ArchT mice (Fig. 3D, right, and 3E). This result is not due to the MS light delivery method, because YFP control mice that underwent the same light delivery protocol (Fig. 3C, top; laser on 86.8 ± 4.6% of REMS; 0.2 ± 0.1% of NREMS; 2.7 ± 0.3% of wakefulness) had higher D2 object 2 DI relative to neutral D1 discrimination (Fig. 3D, right, and 3E). ArchT control mice also had increased object 2 DI during D2 testing from neutrality observed on D1 (Fig. 3D, right, and 3E). The co-occurrence of $MS^{GABA}$ neural inhibition with REMS was a critical factor in the deficit observed in ArchT mice, because ArchT REM control mice demonstrated intact object recognition memory comparable to that of YFP control and ArchT control mice (Fig. 3D, right, and 3E). No evidence for differences in locomotion or motivation during testing were found between groups (fig. S5, A and B).

We next investigated whether normal contextual and emotional memory consolidation requires $MS^{GABA}$ neural activity (Fig. 4). ArchT, YFP control, ArchT control, and ArchT REM control mice were fear-conditioned in a distinct context (context A) with three tone-shock events spanning a 9.5-min session. Freezing behavior between groups was not different during conditioning (Fig. 4A). For the subsequent 4 hours, a protocol similar to that used after D1 NOPR testing was again used

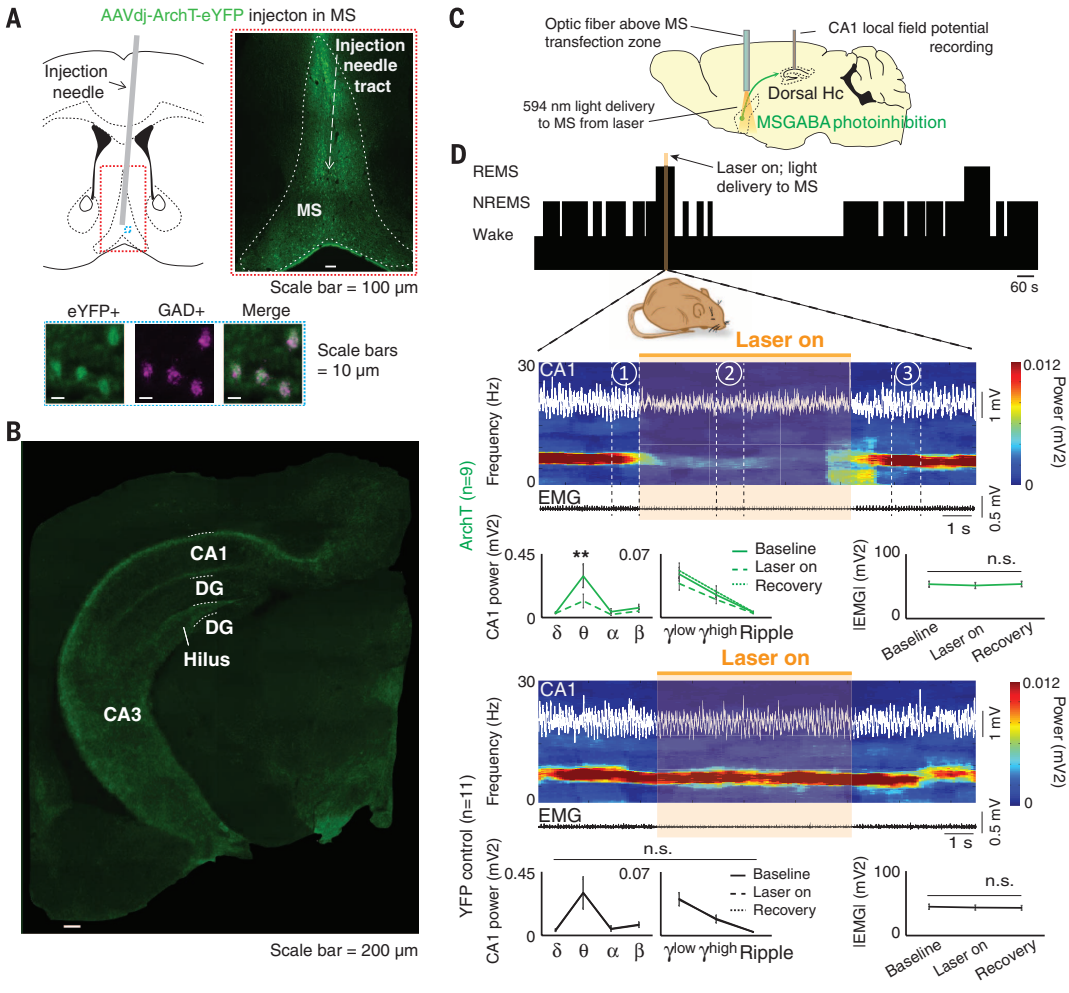


**Fig. 1. ArchT-mediated inhibition of $MS^{GABA}$ neurons during REMS reduces theta rhythm.** (**A**) Schematic (top left) showing the MS injection site of Cre-dependent AAV in VGAT::Cre mice. After virus delivery, ArchT-eYFP is inverted in $MS^{GABA}$ neurons, allowing transcription from the EF-1α promoter and subsequent expression of ArchT-eYFP to occur in the MS (top right). (Bottom) Cell-specific expression of ArchT-eYFP (green) in $MS^{GABA}$ [glutamic acid decarboxylase ($GAD^{+}$)] neurons (magenta) (quantified in fig. S1A). (**B**) Dense projections in the hippocampus originating from $MS^{GABA}$ neurons (green). DG, dentate gyrus. (**C**) Schematic of the in vivo recording configuration; an optic fiber delivered orange laser light to the MS, allowing for optogenetic inhibition of $MS^{GABA}$ neurons while recording the LFP signal from electrodes implanted in dorsal CA1. (**D**) Effect of $MS^{GABA}$ neural inhibition during REMS on CA1LFP and EMG activity. Mice injected with a control virus resulting in expression of only eYFP in $MS^{GABA}$ neurons controlled for the use of orange light (YFP control) [$n$ = 9 for ArchT mice, $n$ = 11 for YFP control mice; n.s. = not significant, $^{**}P < 0.01$, two-way analysis of variance (ANOVA) with Tukey post-hoc test].

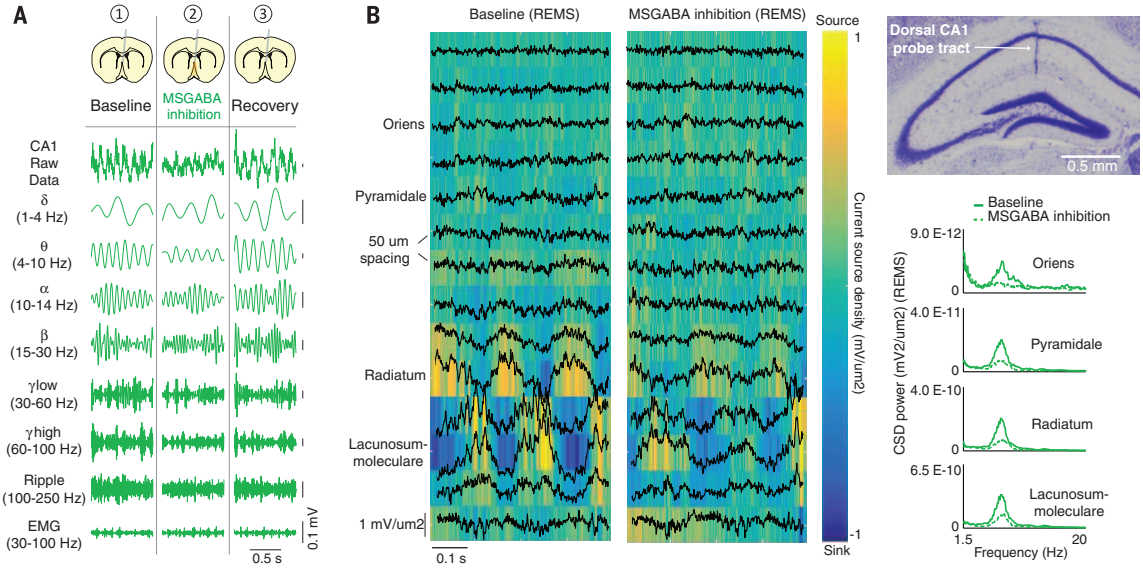


**Fig. 2. MS$^{GABA}$ neural silencing during REMS reduces theta power in all layers of dorsal hippocampal CA1.** (**A**) Sample raw and filtered traces from ArchT example trace in Fig. 1D, as indicated. Recordings were from the stratum radiatum of dorsal hippocampal CA1. (**B**) (Left) CSD analysis completed on recordings obtained from dorsal hippocampal CA1 (top right) using a chronically implanted linear 16-channel probe (50 μm spacing between successive channels) during REMS under baseline and MS$^{GABA}$ neural inhibition conditions. Graphs at right show layer-specific spectral analysis of CSDs for the baseline versus the MS$^{GABA}$ neural inhibition condition ($n$ = 1 AAVdj-ArchT–injected mouse).

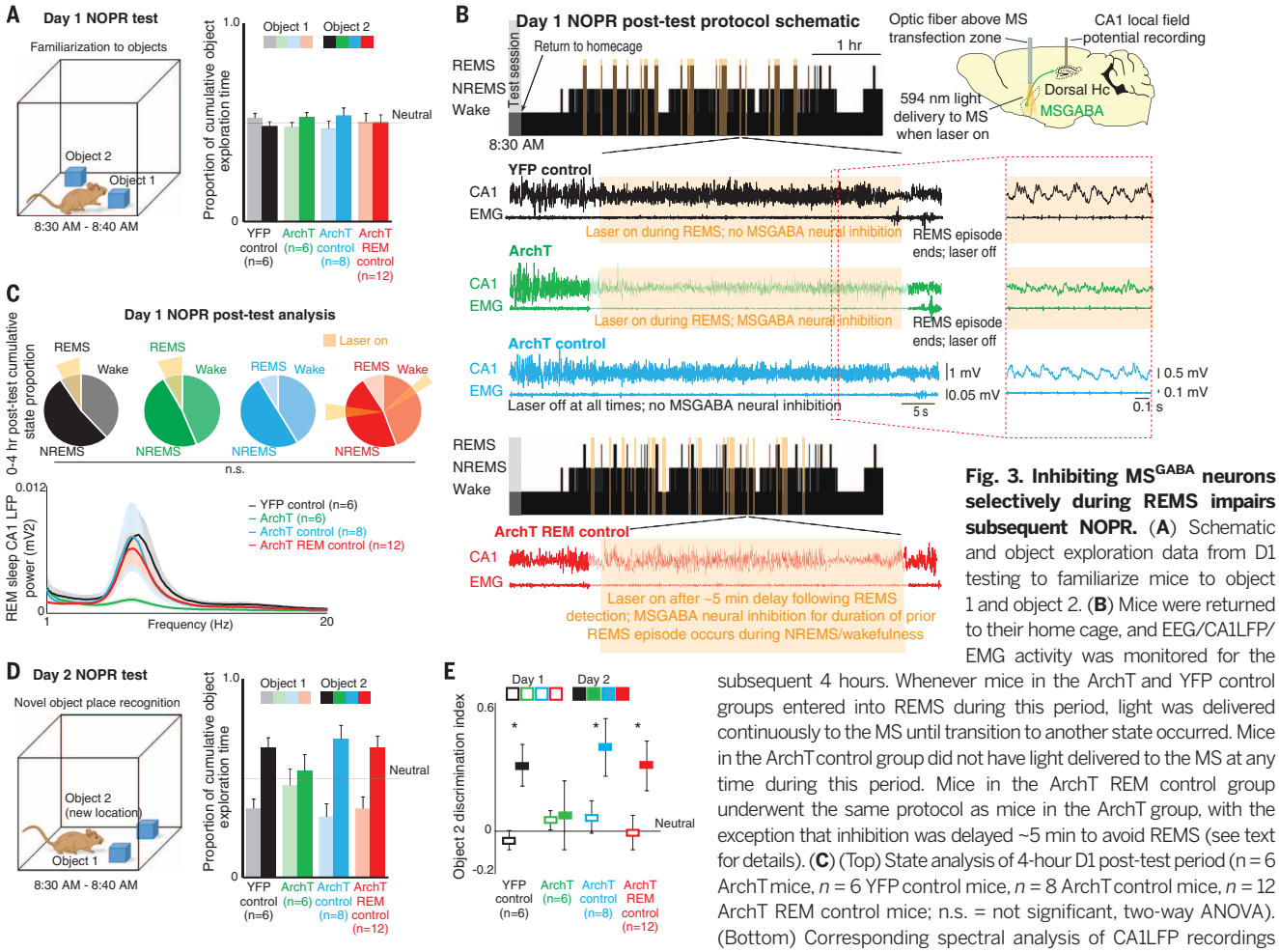


**Fig. 3. Inhibiting MS$^{GABA}$ neurons selectively during REMS impairs subsequent NOPR.** (**A**) Schematic and object exploration data from D1 testing to familiarize mice to object 1 and object 2. (**B**) Mice were returned to their home cage, and EEG/CA1LFP/EMG activity was monitored for the subsequent 4 hours. Whenever mice in the ArchT and YFP control groups entered into REMS during this period, light was delivered continuously to the MS until transition to another state occurred. Mice in the ArchT control group did not have light delivered to the MS at any time during this period. Mice in the ArchT REM control group underwent the same protocol as mice in the ArchT group, with the exception that inhibition was delayed ~5 min to avoid REMS (see text for details). (**C**) (Top) State analysis of 4-hour D1 post-test period (n = 6 ArchT mice, $n$ = 6 YFP control mice, $n$ = 8 ArchT control mice, $n$ = 12 ArchT REM control mice; n.s. = not significant, two-way ANOVA). (Bottom) Corresponding spectral analysis of CA1LFP recordings during REMS. (**D**) Schematic and object exploration data from D2 testing; only object 2 placement differed relative to D1. (**E**) Analysis of object 2 preference between D1 and D2 ($n$ = 6 ArchT mice, $n$ = 6 YFP control mice, $n$ = 8 ArchT control mice, $n$ = 12 ArchT REM control mice; *$P$ < 0.05, paired Student's $t$ test).

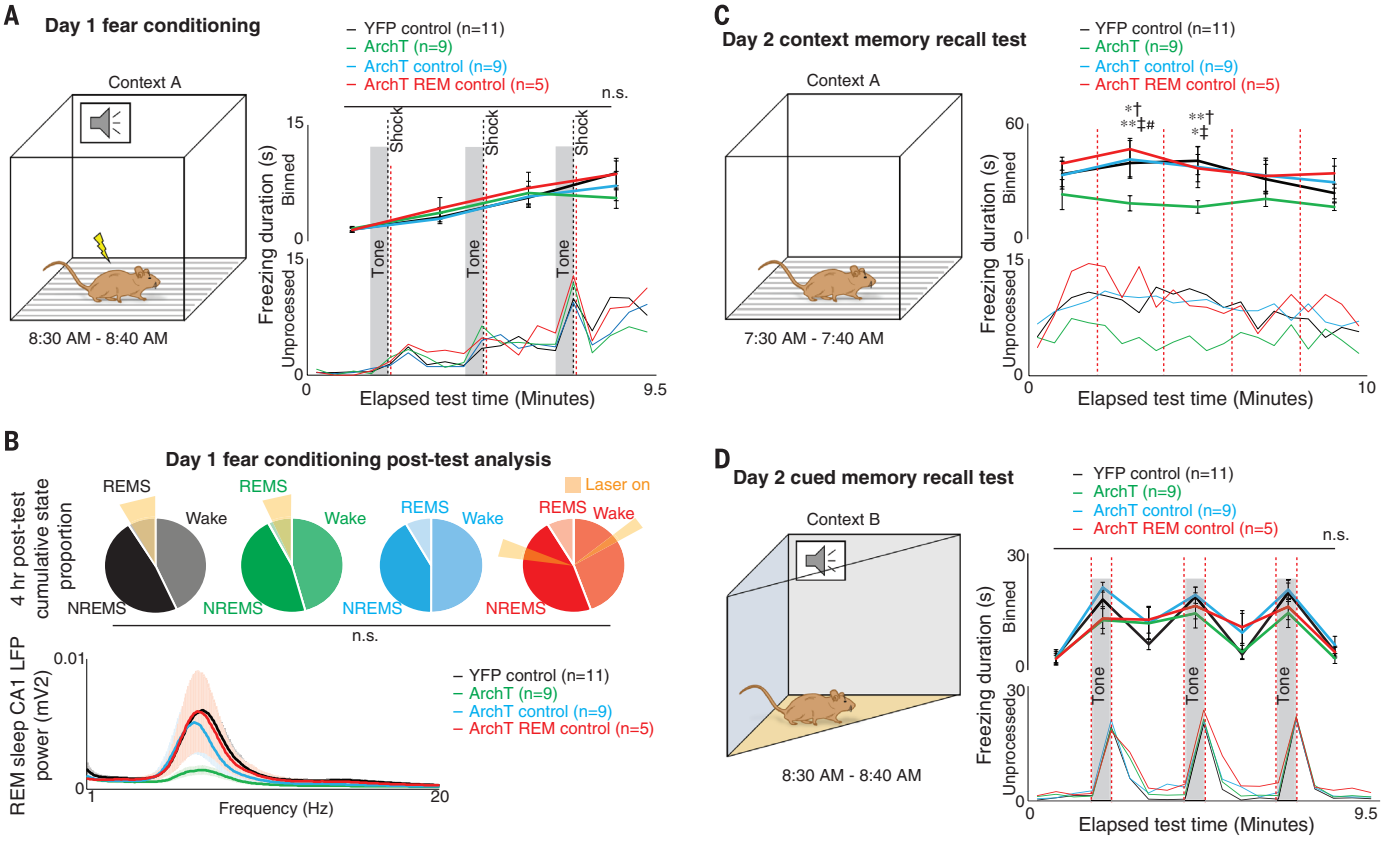


**Fig. 4. Inhibiting MS$^{GABA}$ neurons selectively during REMS after fear conditioning impairs contextual memory.** (**A**) Fear conditioning schematic and freezing data. (**B**) Immediately after conditioning, mice were returned to their home cage, where they underwent the same procedure as that described after D1 NOPR testing (a full schematic is in Fig. 3B). (Top) State analysis of 4-hour post-conditioning period ($n$ = 9 ArchT mice, $n$ = 11 YFP control mice, $n$ = 9 ArchT control mice, $n$ = 5 ArchT REM control mice; n.s. = not significant, two-way ANOVA). (Bottom) Corresponding spectral analysis of CA1LFP recordings during REMS. (**C**) D2 contextual recall memory test schematic and freezing analysis. (**D**) D2 cued recall memory test schematic and freezing analysis. (A), (C), and (D) Freezing versus time graphs ($n$ = 9 ArchT mice, $n$ = 11 YFP control mice, $n$ = 9 ArchT control mice, $n$ = 5 ArchT REM control mice; n.s. = not significant, *$P$ < 0.05, **$P$ < 0.01, two-way repeated-measures ANOVA with Tukey post-hoc test; †YFP control versus ArchT mice, ‡ArchT control versus ArchT mice, #ArchT REM control versus ArchT mice). (A) and (D) Statistical results confirmed with Kruskal-Wallis test. Red lines indicate unprocessed data bin boundaries used for statistics (top right plot).

(see Fig. 3B for a detailed schematic). ArchT mice received selective MS$^{GABA}$ neural inhibition during REMS (laser on 92.2 ± 2.2% of REMS; 0.2 ± 0.0% of NREMS; 1.6 ± 0.2% of wakefulness) during the 4-hour post–fear conditioning period (Fig. 4B). No difference in sleep-wake architecture (Fig. 4B, top, and fig. S7, A to C) or NREMS EEG spindle activity (tables S4 and S5) was found between groups, and the only significant effect on the CA1LFP spectral profile was a 57.8 ± 5.7% reduction in theta power in ArchT mice (Fig. 4B, bottom, and fig. S8, A to C).

The next day mice were first tested for contextual recall memory (Fig. 4C) followed by cued recall memory (Fig. 4D). Mice were placed in context A for 10 min, where conditioning had occurred the prior day, and allowed to move freely without any tone or shock. ArchT mice froze less than YFP control, ArchT control, and ArchT REM control mice (Fig. 4C, right). One hour later, mice were placed in a novel context (context B) for 9.5 min for cued recall testing, and a sequence of tones identical to those from prior fear conditioning was played. Freezing behavior was not different between the ArchT, YFP control, ArchT control, or ArchT REM control groups, with each group showing a robust freezing response selectively to the cue (tone) (Fig. 4D, right).

NOPR and fear-conditioned contextual memory in these experiments were probably hippocampus-dependent (*18*, *19*). Considering the potential importance of hippocampal REMS theta oscillations in processing place cell information (*8*, *9*), the impairments reported here could result from disrupted theta-dependent plasticity in hippocampal neurons during REMS after initial memory consolidation. REMS may also contribute to the homeostasis of network excitability (*20*, *21*). Disruption of hippocampal homeostasis could have contributed to the memory impairment we observed, although analysis of CA1 unit data did not reveal any clear indication of altered activity resulting from MS$^{GABA}$ neural inhibition during REMS. Extrahippocampal inputs also must be considered, given known MS projection patterns (*22*). Indeed, current source density analysis from CA1 during REMS indicated a reduction in theta rhythm power at all layers upon MS$^{GABA}$ neural inhibition. Thus, in addition to disrupted input from the Schaffer-collaterals, input from the entorhinal cortex via the perforant path was also disrupted. Given the importance of these inputs in spatial memory and hippocampal place cell activity (*18*, *23*), their disruption may be a mechanism involved in the blockade of consolidation we observed. In summary, our data provide experimental proof in a mouse model that MS$^{GABA}$ neural activity occurring specifically during REMS after acquisition of a NOPR task or fear conditioning is critical for normal spatial and contextual memory consolidation.

## REFERENCES AND NOTES

1. J. M. Siegel, *Nature* **437**, 1264–1271 (2005).
2. S. Diekelmann, J. Born, *Sleep* **11**, 114–126 (2010).
3. R. Stickgold, M. P. Walker, *Sleep* **28**, 1225–1227 (2005).
4. J. M. Siegel, *Science* **294**, 1058–1063 (2001).

5. R. P. Vertes, *Neuron* **44**, 135–148 (2004).
6. T. E. Robinson, R. C. Kramis, C. H. Vanderwolf, *Brain Res.* **124**, 544–549 (1977).
7. G. Buzsáki, *Neuron* **33**, 325–340 (2002).
8. G. R. Poe, D. A. Nitz, B. L. McNaughton, C. A. Barnes, *Brain Res.* **855**, 176–180 (2000).
9. K. Louie, M. A. Wilson, *Neuron* **29**, 145–156 (2001).
10. J. D. Green, A. A. Arduini, *J. Neurophysiol.* **17**, 533–557 (1954).
11. S. J. Mitchell, J. N. Rawlins, O. Steward, D. S. Olton, *J. Neurosci.* **2**, 292–302 (1982).
12. B. E. Jones, *Neuroscience* **40**, 637–656 (1991).
13. R. E. Brown, R. Basheer, J. T. McKenna, R. E. Strecker, R. W. McCarley, *Physiol. Rev.* **92**, 1087–1187 (2012).
14. H. Petsche, C. Stumpf, G. Gogolak, *Electroencephalogr. Clin. Neurophysiol.* **14**, 202–211 (1962).
15. A. P. Simon, F. Poindessous-Jazat, P. Dutar, J. Epelbaum, M. H. Bassant, *J. Neurosci.* **26**, 9038–9046 (2006).
16. K. Tóth, T. F. Freund, R. Miles, *J. Physiol.* **500**, 463–474 (1997).
17. M. Antunes, G. Biala, *Cogn. Process.* **13**, 93–110 (2012).
18. M. B. Moser, D. C. Rowland, E. I. Moser, *Cold Spring Harbor Perspect. Biol.* **7**, 1–15 (2016).
19. J. J. Kim, M. S. Fanselow, *Science* **256**, 675–677 (1992).
20. A. A. Borbély, *Hum. Neurobiol.* **1**, 195–204 (1982).
21. A. D. Grosmark, K. Mizuseki, E. Pastalkova, K. Diba, G. Buzsáki, *Neuron* **75**, 1001–1007 (2012).
22. R. C. Meibach, A. Siegel, *Brain Res.* **119**, 1–20 (1977).
23. M. E. Hasselmo, *Eur. J. Neurosci.* **28**, 1301–1315 (2008).

**ACKNOWLEDGMENTS**

We thank all members of the Williams and Tidis labs for their helpful comments on the manuscript, E. Boyden for viral constructs, and B. Lowell and L. Vong for mice. R.B. was supported by an Alexander Graham Bell Canada Graduate Scholarship [Natural Sciences and Engineering Research Council of Canada (NSERC)] while completing this research. S.D.G. was supported by a postdoctoral fellowship from Fonds de la Recherche en Santé du Québec. S.W. is supported by the Canadian Institutes of Health Research (CIHR) and NSERC. A.A. is supported by the Human Frontier Science Program (RGY0076/2012), the Douglas Foundation, McGill University, the Canadian Fund for Innovation (CFI), the Canadian Research Chair (CRC Tier 2), CIHR, NSERC, the Swiss National Science Foundation, the Inselspital, and the University of Bern. All data are available in the supplementary materials. We declare no conflicts of interest.

**SUPPLEMENTARY MATERIALS**

www.sciencemag.org/content/352/6287/812/suppl/DC1
Materials and Methods
Figs. S1 to S8
Tables S1 to S9
References (*24*–*27*)

9 October 2015; accepted 24 March 2016
10.1126/science.aad5252

ZIKA VIRUS

# Zika virus impairs growth in human neurospheres and brain organoids

**Patricia P. Garcez,[2,1]* Erick Correia Loiola,[1]† Rodrigo Madeiro da Costa,[1]† Luiza M. Higa,[3]† Pablo Trindade,[1]† Rodrigo Delvecchio,[3] Juliana Minardi Nascimento,[1,4] Rodrigo Brindeiro,[3] Amilcar Tanuri,[3] Stevens K. Rehen[1,2]***

**Since the emergence of Zika virus (ZIKV), reports of microcephaly have increased considerably in Brazil; however, causality between the viral epidemic and malformations in fetal brains needs further confirmation. We examined the effects of ZIKV infection in human neural stem cells growing as neurospheres and brain organoids. Using immunocytochemistry and electron microscopy, we showed that ZIKV targets human brain cells, reducing their viability and growth as neurospheres and brain organoids. These results suggest that ZIKV abrogates neurogenesis during human brain development.**

Primary microcephaly is a severe brain malformation characterized by the reduction of the head circumference. Patients display a heterogeneous range of brain impairments that compromise motor, visual, hearing, and cognitive functions (*1*).

Microcephaly is associated with decreased neuronal production as a consequence of proliferative defects and death of cortical progenitor cells (*2*). During pregnancy, the primary etiology of microcephaly varies from genetic mutations to external insults. The so-called TORCHS factors (toxoplasmosis, rubella, cytomegalovirus, herpes virus, and syphilis) are the main congenital infections that compromise brain development in utero (*3*).

[1]D'Or Institute for Research and Education (IDOR), Rio de Janeiro, Brazil. [2]Institute of Biomedical Sciences, Federal University of Rio de Janeiro, Rio de Janeiro, Brazil. [3]Institute of Biology, Federal University of Rio de Janeiro, Rio de Janeiro, Brazil. [4]Institute of Biology, State University of Campinas, Campinas, Brazil.
***Corresponding author. Email: ppgarcez@icb.ufrj.br (P.P.G.); srehen@lance-ufrj.org (S.K.R.)** †These authors contributed equally to this work.

An increase in the rate of microcephaly in Brazil has been associated with the recent outbreak of Zika virus (ZIKV) (*4*, *5*), a flavivirus that is transmitted by mosquitoes (*6*) and sexually (*7*–*9*). So far, ZIKV has been described in the placenta and amniotic fluid of microcephalic fetuses (*10*–*13*) and in the blood of microcephalic newborns (*11*, *14*). ZIKV had also been detected within the brain of a microcephalic fetus (*13*, *14*), and recently, direct evidence has emerged that ZIKV is able to infect and cause the death of neural stem cells (*15*).

We used human induced pluripotent stem (iPS) cells cultured as neural stem cells (NSCs), neurospheres, and brain organoids to explore the consequences of ZIKV infection during neurogenesis and growth with three-dimensional culture models. Human iPS-derived NSCs were exposed to ZIKV [multiplicity of infection (MOI), 0.25 to 0.0025]. After 24 hours, ZIKV was detected in NSCs (Fig. 1, A to D); viral envelope protein was evident in 10.10% (MOI, 0.025) and 21.7% (MOI, 0.25) of cells exposed to ZIKV (Fig. 1E). Viral RNA was also detected in the supernatant of infected NSCs (MOI, 0.0025) by quantitative reverse transcriptase polymerase chain reaction (qRT-PCR) (Fig. 1F), providing evidence of productive infection.

To investigate the effects of ZIKV during neural differentiation, mock- and ZIKV-infected NSCs were cultured as neurospheres. After 3 days in vitro (DIV), mock-infected NSCs generated round neurospheres. However, ZIKV-infected NSCs generated neurospheres with morphological abnormalities and cell detachment (Fig. 2B). After 6 DIV, hundreds of neurospheres grew under mock conditions (Fig. 2, C and E). In ZIKV-infected NSCs (MOI, 2.5 to 0.025), only a few neurospheres survived (Fig. 2, D and E).

Mock-infected neurospheres presented the expected ultrastructural morphology of the nucleus and mitochondria (Fig. 3A). Viral particles were present in ZIKV-infected neurospheres, similar to those observed in murine glial and neuronal cells (*16*). ZIKV was bound to the membranes and observed in mitochondria and vesicles of cells within infected neurospheres (arrows in Fig. 3, B and F). Apoptotic nuclei, a hallmark of cell death, were observed in all ZIKV-infected neurospheres that we analyzed (Fig. 3B). ZIKV-infected cells in neurospheres presented smooth membrane structures (Fig. 3, B and F), similar to other cell types infected with dengue virus (*17*). These results suggest that ZIKV induces cell death in human neural stem cells and thus impairs the formation of neurospheres.

To further investigate the impact of ZIKV infection during neurogenesis, human iPS-derived brain organoids (*18*) were exposed to ZIKV and observed for 11 DIV (Fig. 4). The growth rates of 12 individual organoids (six mock- and six ZIKV-infected) were measured during this period (Fig. 4, A to D). As a result of ZIKV infection, the average growth area of ZIKV-exposed organoids was reduced by 40% compared with brain organoids under mock conditions [$0.624 \pm 0.064$ mm$^2$ for ZIKV-exposed organoids versus $1.051 \pm 0.1084$ mm$^2$ for mock-infected organoids (normalized); Fig. 4E].

Downloaded from http://science.sciencemag.org/ on May 12, 2016

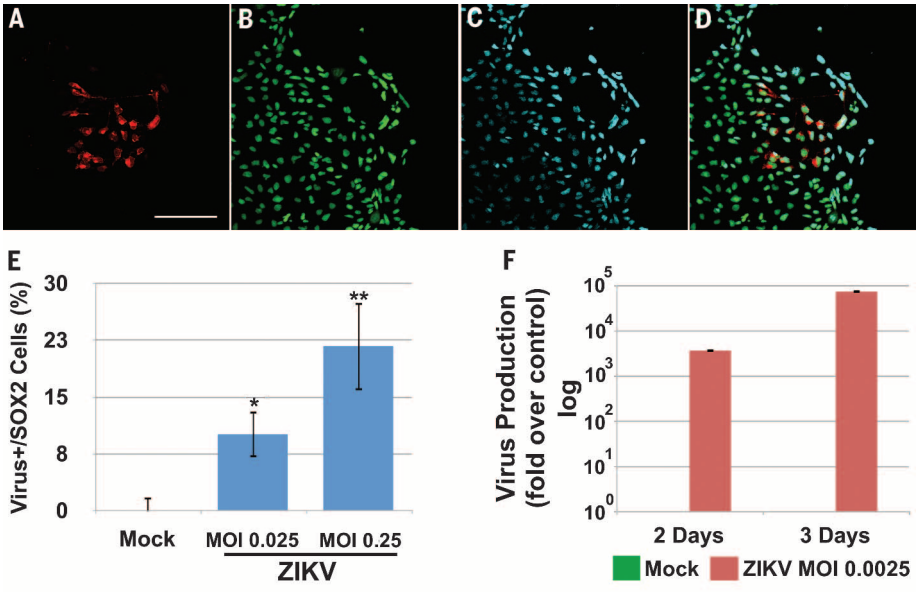


**Fig. 1. ZIKV infects human NSCs.** Shown are confocal microscopy images of iPS-derived NSCs double-stained for (**A**) ZIKV in the cytoplasm and (**B**) SOX2 in the nuclei, 1 day after virus infection. (**C**) DAPI (4′,6-diamidino-2-phenylindole) nuclear staining. (**D**) Merged channels show perinuclear localization of ZIKV (red). Scale bar, 100 μm. (**E**) Percentage of ZIKV-infected SOX2-positive cells (MOI, 0.25 and 0.025). (**F**) qRT-PCR analysis of ZIKV RNA extracted from supernatants of mock- and ZIKV-infected neurospheres (MOI, 0.0025) after 3 DIV, showing amplification only in infected cells. Virus production was normalized to 12-hour postinfection controls. Data are presented as means ± SEM ($n = 5$). *$P < 0.05$; **$P < 0.01$; Student's $t$ test.

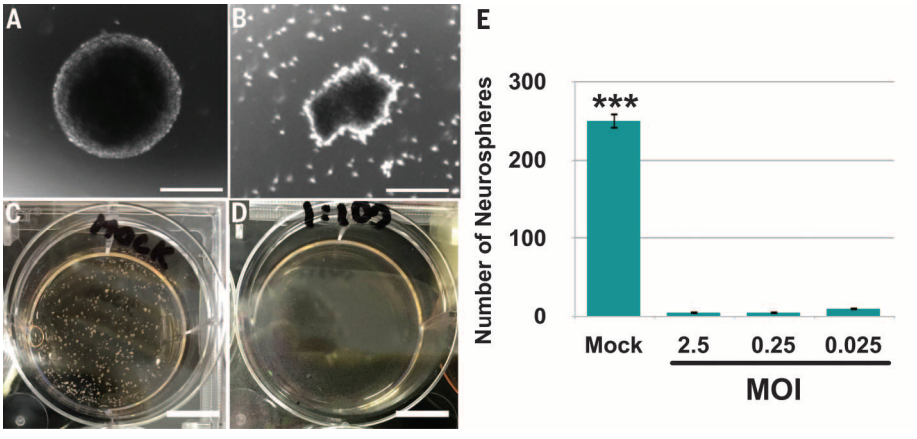


**Fig. 2. ZIKV alters morphology and halts the growth of human neurospheres.** (**A**) A control neurosphere displays spherical morphology after 3 DIV. (**B**) An infected neurosphere shows morphological abnormalities and cell detachment after 3 DIV. (**C**) A culture well plate containing hundreds of mock-infected neurospheres after 6 DIV. (**D**) A well plate containing few ZIKV-infected neurospheres (MOI, 2.5 to 0.025) after 6 DIV. Scale bars, 250 μm in (A) and (B) and 1 cm in (C) and (D). (**E**) The number of neurospheres at different MOI. Data are presented as means ± SEM ($n = 3$). ***$P < 0.01$; Student's $t$ test.

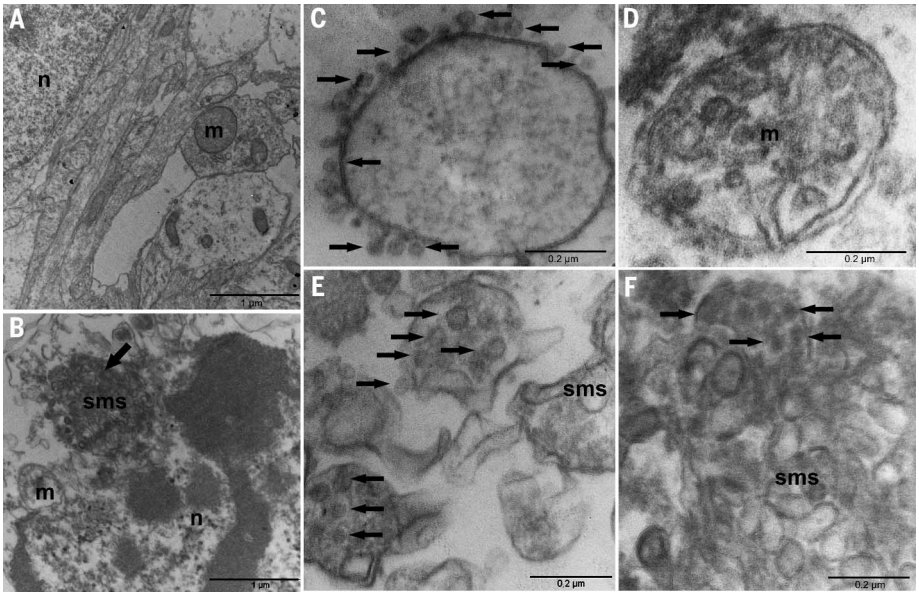


**Fig. 3. ZIKV induces death in human neurospheres.** These micrographs show the ultrastructure of mock- and ZIKV-infected neurospheres after 6 DIV. (**A**) Mock-infected neurosphere showing cell processes and organelles. (**B**) ZIKV-infected neurosphere showing a pyknotic nucleus, swollen mitochondria, smooth membrane structures, and viral envelopes (arrow). (**C**) Viral envelopes on the cell surface (arrows). (**D**) Swollen mitochondria. (**E**) Viral envelopes inside the endoplasmic reticulum (arrows). (**F**) Viral envelopes close to smooth membrane structures (arrows). Scale bars, 1 μm in (A) and (B) and 0.2 μm in (C) to (F). m, mitochondria; n, nucleus; sms, smooth membrane structures.

Downloaded from http://science.sciencemag.org/ on May 12, 2016

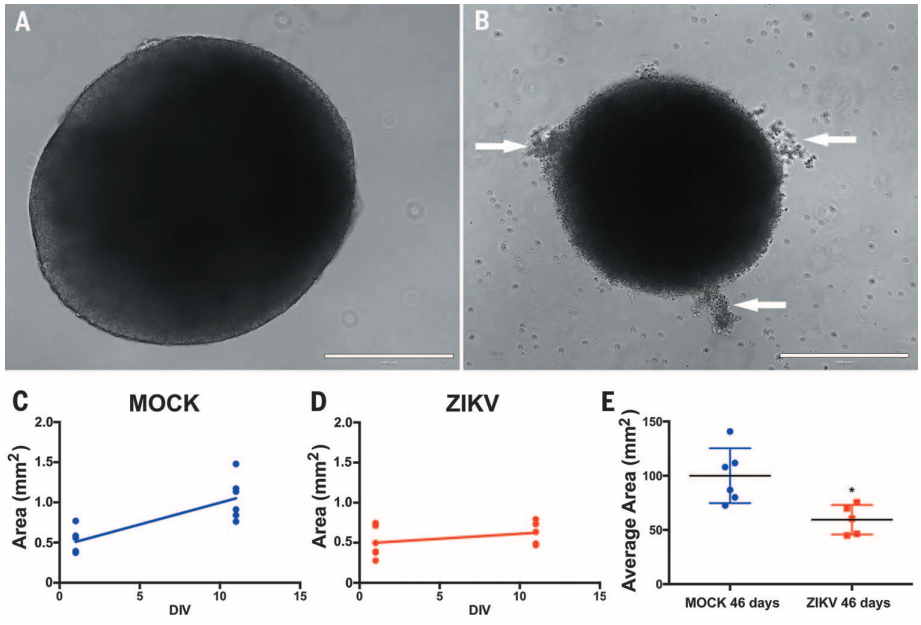


**Fig. 4. ZIKV reduces the growth rate of human brain organoids.** Brain organoids 35 days old were exposed to (**A**) mock conditions or (**B**) ZIKV for 11 DIV. ZIKV-infected brain organoids show reduced growth compared with the mock-infected controls. Arrows point to detached cells. Organoid area was measured before and after 11 DIV of exposure to (**C**) mock conditions or (**D**) ZIKV. Plotted lines represent the growth rate. (**E**) The average area of 46-DIV brain organoids, 11 DIV after mock or ZIKV infection. Data are presented as means (black bars) ± SEM ($n$ = 6). *$P$ < 0.05; Student's $t$ test.

We used cells infected with dengue virus 2 (DENV2), a flavivirus with genetic similarities to ZIKV (*11*, *19*), as a second control group in addition to the mock infection group. One day after viral exposure, DENV2 infected human NSCs at a similar rate as that of ZIKV (fig. S1, A and B). However, after 3 DIV, there was no increase in caspase 3/7–mediated cell death induced by DENV2 at the same MOI of 0.025 that was used for ZIKV infection (fig. S1, C and D). In contrast, ZIKV induced caspase 3/7–mediated cell death in NSCs, consistent with the results described by Tang and colleagues (*15*). After 6 DIV, cell viability significantly differed between ZIKV-exposed NSCs and DENV2-exposed NSCs (fig. S1, E and F). In addition, neurospheres exposed to DENV2 displayed a round morphology similar to that of uninfected neurospheres after 6 DIV (fig. S1G). Last, there was no reduction of growth in brain organoids that were exposed to DENV2 for 11 days, relative to those grown under mock conditions [1.023 ± 0.1308 $mm^2$ for DENV2-infected organoids versus 1.011 ± 0.2471 $mm^2$ for mock-infected organoids (normalized); fig. S1, H and I]. These results suggest that the deleterious consequences of ZIKV infection in human NSCs, neurospheres, and brain organoids are not a general feature of the flavivirus family. Neurospheres and brain organoids are complementary models for studying embryonic brain development in vitro (*20*, *21*). Whereas neurospheres present the very early characteristics of neurogenesis, brain organoids recapitulate the orchestrated cellular and molecular early events comparably to the first-trimester fetal neocortex, including gene expression and cortical layering (*18*, *22*). Our results demonstrate that ZIKV induces cell death in human iPS-derived NSCs, disrupts the formation of neurospheres, and reduces the growth of organoids (fig. S2). These models mimic the first trimester of brain development, indicating that ZIKV infection during this developmental time window may result in severe damage. Other studies are necessary to further characterize the consequences of ZIKV infection during different stages of fetal development.

Cell death that impairs brain enlargement, calcification, and microcephaly are well described in congenital infections with TORCHS factors (*3*, *23*, *24*). Our results, together with recent studies showing brain calcification in microcephalic fetuses and newborns infected with ZIKV (*10*, *14*), reinforce the growing body of evidence connecting the ZIKV outbreak to the increased reports of congenital brain malformations in Brazil.

## REFERENCES AND NOTES


1. E. C. Gilmore, C. A. Walsh, *WIREs Dev. Biol.* **2**, 461–478 (2013).
2. C. G. Woods, J. Bond, W. Enard, *Am. J. Hum. Genet.* **76**, 717–728 (2005).
3. N. Neu, J. Duchon, P. Zachariah, *Clin. Perinatol.* **42**, 77–103 (2015).
4. C. Zanluca *et al.*, *Mem. Inst. Oswaldo Cruz* **110**, 569–572 (2015).
5. G. S. Campos, A. C. Bandeira, S. I. Sardi, *Emerg. Infect. Dis.* **21**, 1885–1886 (2015).
6. E. B. Hayes, *Emerg. Infect. Dis.* **15**, 1347–1350 (2009).
7. G. W. A. Dick, *Trans. R. Soc. Trop. Med. Hyg.* **46**, 521–534 (1952).
8. D. Musso *et al.*, *Emerg. Infect. Dis.* **21**, 359–361 (2015).
9. B. D. Foy *et al.*, *Emerg. Infect. Dis.* **17**, 880–882 (2011).
10. M. Sarno *et al.*, *PLOS Negl. Trop. Dis.* **10**, e0004517 (2016).
11. G. Calvet *et al.*, *Lancet Infect. Dis.* 10.1016/S1473-3099(16)00095-5 (2016).
12. A. S. Oliveira Melo *et al.*, *Ultrasound Obstet. Gynecol.* **47**, 6–7 (2016).
13. R. B. Martines *et al.*, *MMWR Morb. Mortal. Wkly. Rep.* **65**, 159–160 (2016).
14. J. Mlakar *et al.*, *N. Engl. J. Med.* **374**, 951–958 (2016).
15. H. Tang *et al.*, *Cell Stem Cell* **18**, 1–4 (2016).
16. T. M. Bell, E. J. Field, H. K. Narang, *Arch. Gesamte Virusforsch.* **35**, 183–193 (1971).
17. C. Grief, R. Galler, L. M. C. Côrtes, O. M. Barth, *Arch. Virol.* **142**, 2347–2357 (1997).
18. M. A. Lancaster *et al.*, *Nature* **501**, 373–379 (2013).
19. R. S. Lanciotti *et al.*, *Emerg. Infect. Dis.* **14**, 1232–1239 (2008).
20. B. A. Reynolds, S. Weiss, *Science* **255**, 1707–1710 (1992).
21. M. A. Lancaster, J. A. Knoblich, *Nat. Protoc.* **9**, 2329–2340 (2014).
22. J. G. Camp *et al.*, *Proc. Natl. Acad. Sci. U.S.A.* **112**, 15672–15677 (2015).
23. Z. W. Naing *et al.*, *Aust. N.Z. J. Obstet. Gynaecol.* **56**, 9–18 (2016).
24. D. V. Vasconcelos-Santos *et al.*, *Ophthalmology* **116**, 2199–205. e1 (2009).


## ACKNOWLEDGMENTS


The authors thank the laboratory crew members M. Costa, I. Gomes, G. Vitória, J. Sochacki, R. Maciel, and M. Alloati for providing technical support and cultures of human iPS cells and brain organoids. We acknowledge O. M. Barth for comments on the electron micrographs. We also thank F. Pamplona for assistance with the Mind the Graph science infographic maker and Centro Nacional de Biologia Estrutural e Bioimagem for the use of their electron microscopy facility. Funds (not specifically for Zika virus studies) were provided by the Brazilian Development Bank; the Funding Authority for Studies and Projects; the National Council of Scientific and Technological Development; the Foundation for Research Support in the State of Rio de Janeiro; and fellowships from the São Paulo Research Foundation (grant 2014/21035-0) and Coordination for the Improvement of Higher Education Personnel. All protocols and procedures were approved by the institutional research ethics committee of Hospital Copa D'Or under approved protocol no. 727.269. The authors declare no competing financial interests.


## SUPPLEMENTARY MATERIALS

www.sciencemag.org/content/352/6287/816/suppl/DC1
Materials and Methods
Figs. S1 and S2
References (*25*–*27*)


2 March 2016; accepted 4 April 2016
Published online 14 April 2016
10.1126/science.aaf6116


Downloaded from http://science.sciencemag.org/ on May 12, 2016

CLIMATE CHANGE

# Body shrinkage due to Arctic warming reduces red knot fitness in tropical wintering range

Jan A. van Gils,[1]* Simeon Lisovski,[2] Tamar Lok,[3,4] Włodzimierz Meissner,[5] Agnieszka Ożarowska,[5] Jimmy de Fouw,[1] Eldar Rakhimberdiev,[1,6] Mikhail Y. Soloviev,[6] Theunis Piersma,[1,3] Marcel Klaassen[2]

**Reductions in body size are increasingly being identified as a response to climate warming. Here we present evidence for a case of such body shrinkage, potentially due to malnutrition in early life. We show that an avian long-distance migrant (red knot, *Calidris canutus canutus*), which is experiencing globally unrivaled warming rates at its high-Arctic breeding grounds, produces smaller offspring with shorter bills during summers with early snowmelt. This has consequences half a world away at their tropical wintering grounds, where shorter-billed individuals have reduced survival rates. This is associated with these molluscivores eating fewer deeply buried bivalve prey and more shallowly buried seagrass rhizomes. We suggest that seasonal migrants can experience reduced fitness at one end of their range as a result of a changing climate at the other end.**

Phenological changes and geographical range shifts are well-known responses to climate change (*1*). A third broadly observed response to global warming appears to be shrinkage of bodies (*2*–*5*). It has been hypothesized that body shrinkage is a genetic microevolutionary response to warming, due to smaller individuals being better able to dissipate body heat because of the larger surface/volume ratio of their bodies [e.g., Bergmann's rule (*2*)]. Alternatively, it has been put forward that climate change may disrupt trophic interactions, potentially leading to malnutrition during an organism's juvenile life stage (*6*, *7*). Because poor growth may not be compensated for later in life (*8*), this would lead to smaller bodies (i.e., shrinkage as a phenotypically plastic response).

Under climate change, some regions are warming faster than others. Especially in the Arctic, warming has been observed at unprecedented rates (*9*, *10*). Hence, body-size reductions would be expected to be most pronounced in the world's most northerly region (*6*). Many Arctic-breeding avian species, however, are long-distance migrants that spend the northern winter at lower latitudes (*11*), where the impacts of climate change are less obvious.

Based on analysis of satellite data, we show here that over the past 33 years, snowmelt has occurred progressively earlier in the high-Arctic breeding grounds of the red knot (*Calidris canutus canutus*) at Taimyr Peninsula (76° to 78°N; Fig. 1), changing at a rate of about half a day per year [coefficient of determination ($R^2$) = 0.32, $F_{1,31}$ = 14.77, $P$ < 0.001; Fig. 2A, table S1, and figs. S1 to S3]. Over these three decades, 1990 juvenile red knots were caught and their body sizes measured in Gdańsk Bay, Poland, during their first southward migration to their West African nonbreeding grounds (Fig. 1). These measurements show that juvenile birds were smaller after Arctic summers with early snowmelts, particularly with respect to body mass [corrected Akaike information criterion ($AIC_c$) = 14775.24, $P$ < 0.0005; Fig. 2B and table S2], bill length ($AIC_c$ = 7610.48, $P$ < 0.005; Fig. 2C and table S3), and overall body size [first principal component (PC1) on bill, tarsus, and wing; $AIC_c$ = 5925.22, $P$ < 0.05; table S4]. The models that best explained the variation in bill length and overall body size additionally included the Normalized Difference Vegetation Index [NDVI, a proxy for total primary biomass production (*12*)] of the breeding ground; longer-billed, bigger birds were captured after summers with high NDVI values (Fig. 2C). These size variations were still apparent when juveniles arrived at their main wintering ground on the Banc d'Arguin, Mauritania (annual average juvenile bill lengths in Poland and Mauritania correlated strongly: Pearson's $r$ = 0.73), where red knots showed no signs of compensatory growth (measurements of body size dimensions, including bill length, were highly consistent within individuals; fig. S4B).

In this tropical nonbreeding area, red knots use their tapered bills to detect and retrieve mollusk prey buried in intertidal sediments (*13*). Stable isotope analysis of 2340 birds caught at Banc d'Arguin between 2002 and 2013 shows that longer-billed birds relied mostly on the abundant bivalve prey species *Loripes lucinalis* (hereafter, *Loripes*), whereas shorter-billed individuals did not ($R^2$ = 0.18, $F_{3,2336}$ =170.70, $P$ < 0.00001; Fig. 3A). This may be due to most *Loripes* being buried out of reach for shorter-billed knots: An individual with a 40-mm bill has access to about two-thirds of all *Loripes*, whereas a bird with a 30-mm bill is able to access only one-third (Fig. 3B). Shorter-billed red knots consumed relatively more of the shallowly buried bivalve *Dosinia isocardia* (hereafter, *Dosinia*) and rhizomes of the seagrass *Zostera noltii* (hereafter, *Zostera*; Fig. 3B and fig. S5). Juvenile red knots consumed fewer *Loripes* compared with older birds ($P$ < 0.00001 for the age-bill interaction; Fig. 3A). This is probably due to the fact that *Loripes* is mildly toxic; the sulphide metabolism of endosymbiotic bacteria living inside its gill causes diarrhea (*14*). In spite of its toxic effects, red knots depend on *Loripes*, especially in years with few alternatives (*15*). Juveniles may need physiological adjustments before they can digest this special type of prey efficiently (*16*). Only birds with longer bills can make this switch to eating the deeply buried *Loripes*; the shorter-billed birds are restricted to a "juvenile diet" of relatively rare *Dosinia (15)* and poor-quality rhizomes (*17*). Hence, for the shorter-billed birds, the inability to access the high-quality and abundant *Loripes* after the first winter may come at a cost.

Individual color-ringing of 2381 red knots during annual expeditions to Banc d'Arguin from 2002 to 2013, and subsequent resightings of these individuals (*12*), indicate that birds with shorter bills had lower apparent survival rates, primarily in the case of juveniles between their first and second winters [Fig. 4A, fig. S6, and tables S5 to S8; we use the term "apparent survival" because mortality is confounded with permanent emigration (*18*)]. The much weaker bill-length effect in adults may be attributable to the advantages of a short bill when feeding on arthropods on the tundra (*19*); juveniles do not benefit from these advantages because they stay at the Mauritanian nonbreeding grounds year-round (*20*). Because early-snowmelt years produced shorter-billed juveniles (Fig. 2C), and because shorter-billed juveniles experienced hampered survival in the tropics (Fig. 4A), overwintering juveniles thus had poor survival rates after Arctic summers with early snowmelt [proportion of variation explained by date of snowmelt ($R^2_{dev}$) = 0.32 (*12*); Fig. 4B]. However, with snowmelt occurring progressively earlier over the years (Pearson's $r$ = –0.58 for 2002–2012), the temporal variation in juvenile survival was similarly well explained by a linear time trend (model 13 versus 14, $\Delta AIC_c$=1.01; table S7). Strictly speaking, we therefore cannot distinguish an effect of snowmelt date on survival from any other potential covariate changing over time. We see this problem as inherent to any descriptive study of climate change effects.

[1]Department of Coastal Systems, NIOZ Royal Netherlands Institute for Sea Research, and Utrecht University, Post Office Box 59, 1790 AB Den Burg (Texel), Netherlands. [2]Centre for Integrative Ecology, School of Life and Environmental Sciences, Deakin University, Waurn Ponds Campus, Victoria 3217, Australia. [3]Conservation Ecology Group, Groningen Institute for Evolutionary Life Sciences (GELIFES), University of Groningen, Post Office Box 11103, 9700 CC Groningen, Netherlands. [4]Centre d'Ecologie Fonctionnelle et Evolutive, Unité Mixte de Recherche 5175, Campus Centre National de la Recherche Scientifique, 1919 Route de Mende, 34293 Montpellier Cedex 5, France. [5]Avian Ecophysiology Unit, Department of Vertebrate Ecology and Zoology, University of Gdańsk, Wita Stwosza 59, 80-308 Gdańsk, Poland. [6]Department of Vertebrate Zoology, Lomonosov Moscow State University, Moscow, 119991, Russia.
***Corresponding author. Email: jan.van.gils@nioz.nl**

Downloaded from http://science.sciencemag.org/ on May 12, 2016

In the face of climate change–induced body shrinkage and the strong selection pressure against shorter-billed juveniles at the nonbreeding grounds, one would expect the adult population to maintain a relatively constant bill length or at least to show less shrinkage of the bill compared with other structural body-size components. This was the case (fig. S7): Although overall body size (PC1 on bill, tarsus, and wing) in adults decreased at a rate of 0.020 SDs per year ($R^2$ = 0.26, $F_{2,1727}$ = 299.20, $P$ < 0.001), their bill length decreased at a rate of only 0.010 SDs per year ($R^2$ = 0.21, $F_{2,1727}$ = 223.57, $P$ = 0.097), suggesting a climate change–induced directional selection on body shape.

The body shrinkage observed in juvenile red knots may be a phenotypically plastic response to an altered environment. Neonatal red knots feed on arthropods (*21*) that emerge from a defrosting tundra soil (*22*). With the rapid advancement in the seasonal appearance of high-Arctic arthropods (*23*), red knot chicks may face a trophic mismatch by hatching too late relative to the peak food abundance (*23*)—in spite of evidence for earlier nesting in high-Arctic shorebirds (*24*), and in spite of the observation that red knot spring migration through France is advancing [although at only 0.25 days/year, which is half the rate at which the timing of snowmelt is advancing) (*25*)]. In addition to advancing the timing of the arthropod peak, earlier snowmelts are also known to depress the peak's amplitude. This is because earlier snowmelts produce smaller-bodied insects (*26*) and cause greater soil temperature fluctuations, thereby enhancing mortality among larvae (*27*). Our finding that bills and bodies are smaller in years with low breeding-ground NDVI values (Fig. 2C) hints at the importance of the food peak's amplitude, because low NDVI values are considered to reflect low insect abundances (*28*).

The negative effects of climate change on the growth of red knots may thus be due to a trophic mismatch. The fitness-related consequences of this growth inhibition are that smaller, shorter-billed individuals have, on average, reduced apparent survival rates at their tropical wintering grounds. This mechanism may be one of the drivers of the steep and ongoing population decline of the *C. c. canutus* red knots (*15*, *29*). The discovery of rapid body shrinkage and its downstream effects on population size may extend to other Arctic migrants.

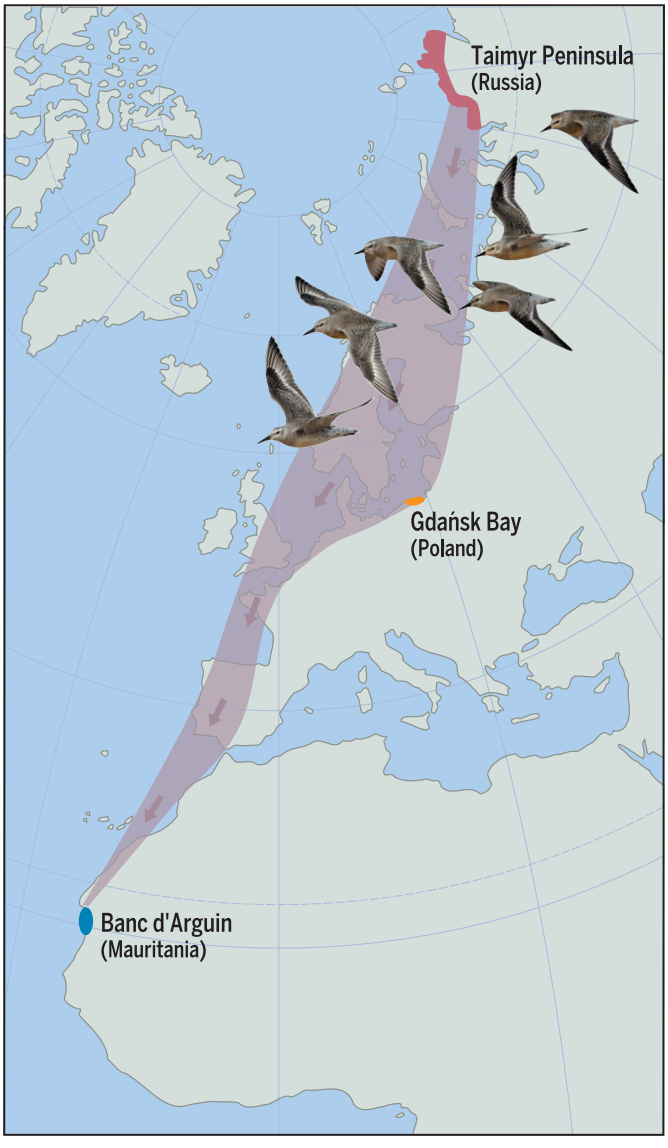


**Fig. 1. Red knots breed during summer in the high Arctic at Taimyr Peninsula and spend the long nonbreeding season at Banc d'Arguin, Mauritania, West Africa.** On their first southward migration to West Africa, many juvenile red knots make a stopover on the Baltic coast of Poland.

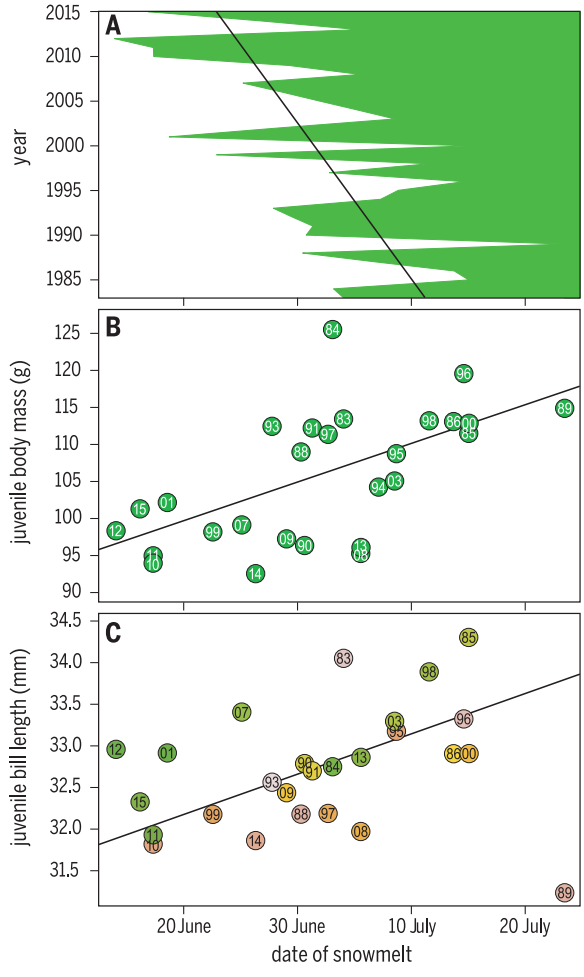


**Fig. 2. Changes in Arctic climate and red knot body size over the past three decades.** (**A**) Snow at the red knots' breeding ground at Taimyr Peninsula has been melting progressively earlier at an average rate of 0.5 days/year. (**B**) Juvenile red knots, captured during brief stopovers in Poland on their first southward migration from the Arctic, had lower body masses after breeding seasons in which snow had disappeared early (each circle denotes the annual mean, with number inside the circle giving the year). (**C**) They also had shorter bills after breeding seasons in which the Arctic snow melted earlier [circles denote annual means as in (B)], especially in years when breeding-ground NDVI [as a proxy for total primary biomass production (*12*)] was low [NDVI is indicated by the color range of the circles (green, high; pink, low)].

Downloaded from http://science.sciencemag.org/ on May 12, 2016

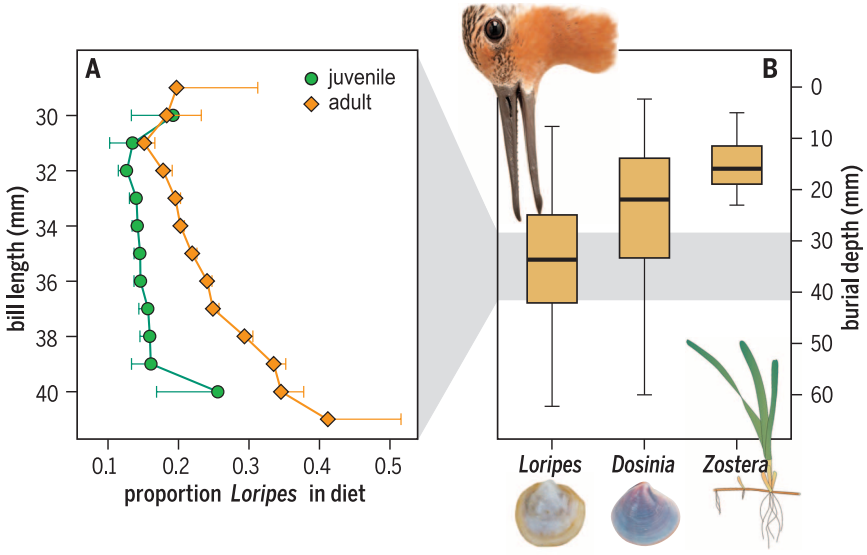


**Fig. 3. Prey choice and prey availability at the Mauritanian wintering grounds.** (**A**) Analysis of stable isotopes of blood samples shows that juvenile red knots ($n$ = 676 birds) largely ignored the most abundant but mildly toxic prey, *Loripes*. However, with an increase in age, adult red knots ($n$ = 1664) added substantial amounts of *Loripes* to their diet, but only if they had long bills. Plotted are means ± SE. (**B**) This bill length–dependent diet shift may be explained by the depth distribution of *Loripes*. The majority of these bivalves live between 30 and 40 mm below the seafloor, which is precisely the range of the bill lengths. The other two food sources, *Dosinia* bivalves and *Zostera* rhizomes, are found at shallower depths and are accessible to all red knots. Bars indicate medians, boxes indicate 25th to 75th percentiles, and whiskers indicate ranges.

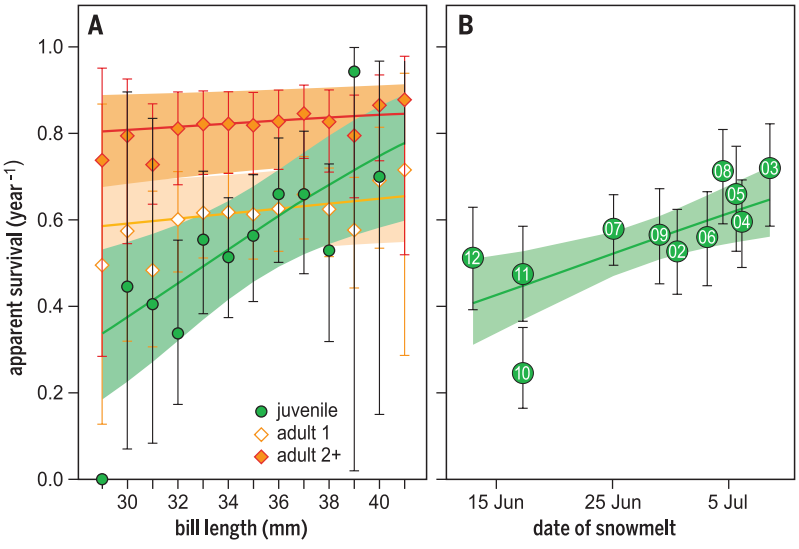


**Fig. 4. Annual survival rates of individually marked red knots.** (**A**) Annual apparent survival rates [± 95% confidence intervals (CIs)] increase significantly as a function of bill length in juveniles (the slope β of the relationship of logit-transformed values = 0.30; 95% CI, 0.08 to 0.51; $n$ = 690 birds), whereas this relation is not significant for adults [β = 0.05; 95% CI, −0.02 to 0.11; $n$ = 1691 birds; distinguishing between survival in the first year after capture (adult 1) and later (adult 2+)]. Symbols show apparent survival rates of juveniles born in 2009 (a year with average survival; model 11, table S7); lines show these data as a linear function of bill length [model 1 (the best-supported model), table S7]. Shaded areas are 95% CIs of the linear functions. Bill-length effect is assumed to be the same in all years. (**B**) Annual apparent survival rates (± 95% CIs) of juveniles increase with the date of snowmelt in their year of birth (the year is indicated inside the circle). Symbols show juvenile apparent survival rates estimated per year (model 8, table S7); lines show these data as a linear function of the date of snowmelt (model 14, table S7). Time dependence in both the apparent survival and resighting makes the survival estimate for the final year (i.e., for juveniles born in 2013) unreliable; hence, this estimate was excluded.

## REFERENCES AND NOTES


1. C. Parmesan, G. Yohe, *Nature* **421**, 37–42 (2003).
2. C. Teplitsky, V. Millien, *Evol. Appl.* **7**, 156–168 (2014).
3. A. R. Baudron, C. L. Needle, A. D. Rijnsdorp, C. T. Marshall, *Glob. Change Biol.* **20**, 1023–1031 (2014).
4. J. A. Sheridan, D. Bickford, *Nat. Clim. Change* **1**, 401–406 (2011).
5. J. L. Gardner, A. Peters, M. R. Kearney, L. Joseph, R. Heinsohn, *Trends Ecol. Evol.* **26**, 285–291 (2011).
6. K. D. Rode, S. C. Amstrup, E. V. Regehr, *Ecol. Appl.* **20**, 768–782 (2010).
7. C. Teplitsky, J. A. Mills, J. S. Alho, J. W. Yarrall, J. Merilä, *Proc. Natl. Acad. Sci. U.S.A.* **105**, 13492–13496 (2008).
8. N. B. Metcalfe, P. Monaghan, *Trends Ecol. Evol.* **16**, 254–260 (2001).
9. M. P. Tingley, P. Huybers, *Nature* **496**, 201–205 (2013).
10. J. A. Screen, I. Simmonds, *Nature* **464**, 1334–1337 (2010).
11. T. Piersma, *Oikos* **80**, 623–631 (1997).
12. Materials and methods are available as supplementary materials on *Science* Online.
13. T. Piersma, R. van Aelst, K. Kurk, H. Berkhoudt, L. R. M. Maas, *Proc. Biol. Sci.* **265**, 1377–1383 (1998).
14. T. Oudman *et al.*, *Am. Nat.* **183**, 650–659 (2014).
15. J. A. van Gils *et al.*, *Proc. Biol. Sci.* **280**, 20130861 (2013).
16. R. W. Stein, A. R. Place, T. Lacourse, C. G. Guglielmo, T. D. Williams, *Physiol. Biochem. Zool.* **78**, 434–446 (2005).
17. J. L. Pérez-Lloréns, M. Muchtar, F. X. Niell, P. H. Nienhuis, *Bot. Mar.* **34**, 319–322 (1991).
18. J. D. Lebreton, K. P. Burnham, J. Clobert, D. R. Anderson, *Ecol. Monogr.* **62**, 67–118 (1992).
19. P. E. Jönsson, T. Alerstam, *Biol. J. Linn. Soc. Lond.* **41**, 301–314 (1990).
20. A. J. van Dijk, F. E. de Roder, E. C. L. Marteijn, H. Spiekman, *Ardea* **78**, 145–156 (1990).
21. H. Schekkerman, I. Tulp, T. Piersma, G. H. Visser, *Oecologia* **134**, 332–342 (2003).
22. H. V. Danks, *Eur. J. Entomol.* **96**, 83–102 (1999).
23. T. T. Høye, E. Post, H. Meltofte, N. M. Schmidt, M. C. Forchhammer, *Curr. Biol.* **17**, R449–R451 (2007).
24. J. R. Liebezeit, K. E. B. Gurney, M. Budde, S. Zack, D. Ward, *Polar Biol.* **37**, 1309–1320 (2014).
25. J. Leyrer *et al.*, *Wader Study Group Bull.* **116**, 145–151 (2009).
26. J. J. Bowden *et al.*, *Biol. Lett.* **11**, 20150574 (2015).
27. J. S. Bale, S. A. L. Hayward, *J. Exp. Biol.* **213**, 980–994 (2010).
28. M. P. Grilli, D. E. Gorla, *Bull. Entomol. Res.* **87**, 45–53 (1997).
29. M. van Roomen, S. Nagy, R. Foppen, T. Dodman, G. Citegetse, A. Ndiaye, *Status of Coastal Waterbird Populations in the East Atlantic Flyway* (Programme Rich Wadden Sea, Sovon, Wetlands International, Birdlife International, Common Wadden Sea Secretariat, 2015).


## ACKNOWLEDGMENTS


This paper was conceptualized during J.A.v.G.'s sabbatical at the Centre for Integrative Ecology at Deakin University and benefited greatly from discussions with Y. Aharon-Rotman and B. J. Hoye at Deakin University; discussions with A. I. Bijleveld, S. Duijns, E. M. A. Kok, and T. Oudman at NIOZ; and comments by three anonymous referees. We thank W. Bouma and F. Sanders for wordsmithing and D. Visser for graphical support. Field support was provided by Waterbird Research Group KULING in the Polish Baltic and the Banc d'Arguin teams led by B. Spaans, J. Leyrer, M. Brugge, A. Dekinga, and J. ten Horn; we were hosted at Iwik by Parc National du Banc d'Arguin (PNBA) staff (notably M. Camara). We thank the directors of the PNBA for access to the study area. Stable isotope analyses were conducted by T. Leerink, J. Ossebaar, and K. Donkers. Financial support was provided by a NWO (Netherlands Organisation for Scientific Research) Vidi grant (864.09.002) to J.A.v.G., NWO-Rubicon funding to T.L., a suite of grants to T.P. [Waddenfonds project Metawad (WF209925), BirdLife Netherlands, World Wildlife Fund–Netherlands, the Prins Bernhard Cultuurfondsprijs voor Natuurbehoud, NWO-WOTRO (Science for Global Development) Integrated Programme (W.01.65.221.00), and MAVA (Switzerland)], and a grant from the Australian Research Council (DP130101935) to M.K. Data and R codes are available at Dryad at http://dx.doi.org/10.5061/dryad.n1m8d.


## SUPPLEMENTARY MATERIALS

www.sciencemag.org/content/352/6287/819/suppl/DC1
Materials and Methods
Figs. S1 to S7
Tables S1 to S8
References (*30*–*54*)


14 October 2015; accepted 5 April 2016
10.1126/science.aad6351


Downloaded from http://science.sciencemag.org/ on May 12, 2016

METALLOPROTEINS

# Radical SAM catalysis via an organometallic intermediate with an Fe–[5′-C]-deoxyadenosyl bond

Masaki Horitani,[1] Krista Shisler,[2] William E. Broderick,[2] Rachel U. Hutcheson,[2] Kaitlin S. Duschene,[2] Amy R. Marts,[1] Brian M. Hoffman,[1]* Joan B. Broderick[2]*

**Radical *S*-adenosylmethionine (SAM) enzymes use a [4Fe-4S] cluster to cleave SAM to initiate diverse radical reactions. These reactions are thought to involve the 5′-deoxyadenosyl radical intermediate, which has not yet been detected. We used rapid freeze-quenching to trap a catalytically competent intermediate in the reaction catalyzed by the radical SAM enzyme pyruvate formate-lyase activating enzyme. Characterization of the intermediate by electron paramagnetic resonance and $^{13}C$, $^{57}Fe$ electron nuclear double-resonance spectroscopies reveals that it contains an organometallic center in which the 5′ carbon of a SAM-derived deoxyadenosyl moiety forms a bond with the unique iron site of the [4Fe-4S] cluster. Discovery of this intermediate extends the list of enzymatic bioorganometallic centers to the radical SAM enzymes, the largest enzyme superfamily known, and reveals intriguing parallels to $B_{12}$ radical enzymes.**

The radical SAM superfamily is the largest known superfamily of enzymes, with more than 100,000 functional domains found throughout all kingdoms of life (*1*). These enzymes use a $[4Fe\text{-}4S]^+$ cluster and *S*-adenosylmethionine (SAM) to catalyze a diverse array of finely tuned (*2*) radical reactions that are central to key pathways, such as heme and chlorophyll biosynthesis, vitamin biosynthesis, DNA repair, and metal cluster assembly (*1*). Spectroscopic studies of the radical SAM enzymes pyruvate formate-lyase activating enzyme (PFL-AE) and lysine 2,3-aminomutase (LAM) demonstrated that these enzymes bind SAM as a classical coordination complex in which the amino and carboxyl moieties of SAM chelate the unique iron site of a [4Fe-4S] cluster, as confirmed by x-ray structure determinations (*3*–*6*). One-electron reduction of SAM by the $[4Fe\text{-}4S]^+$ cluster initiates SAM cleavage, generating the 5′-deoxyadenosyl radical intermediate (5′-dAdo•), which carries out subsequent radical chemistry. To date, neither the 5′-dAdo• radical nor any SAM- or 5′-dAdo-–derived intermediate has been detected for any radical SAM enzyme. However, the use of the enzymatically active SAM analog 3′,4′-anhydro-*S*-adenosylmethionine has allowed characterization of the allylically stabilized anhydroadenosyl radical, a functional analog of the 5′-dAdo• radical, generated within the active site of LAM during the LAM-catalyzed reaction (*7*–*9*).

Pyruvate formate-lyase activating enzyme is a radical SAM enzyme that catalyzes the formation of a catalytically essential glycyl (G•) radical on $Gly^{734}$ (G734) of PFL, a central enzyme in anaerobic glucose metabolism (Fig. 1) (*10*). We used rapid freeze-quench (rfq) electron paramagnetic resonance (EPR) and electron nuclear double-resonance (ENDOR) spectroscopies to trap and characterize a catalytically competent intermediate species formed during the reaction catalyzed by PFL-AE. We hoped that this approach would allow us to capture the elusive 5′-dAdo• radical intermediate that is implicated as the central species in radical SAM mechanisms, but instead our work yielded a state with unanticipated properties.

When reduced PFL-AE is rapidly mixed with PFL and SAM, followed by rfq of the reaction at times ranging from 25 ms to 1.0 s after mixing, the characteristic $[4Fe\text{-}4S]^+$ EPR signal of reduced PFL-AE/SAM ($g$ values: $g$ = 2.01, 1.88, 1.87) (*11*) is diminished in intensity, concomitant with the appearance of a new EPR signal, denoted Ω ($g_{||}$ = 2.035, $g_{\perp}$ = 2.004), whose intensity reaches a maximum at 500-ms quench times (fig. S1). At longer quench times, the Ω signal is lost in parallel with the appearance of the G• radical signal that is characteristic of activated PFL, which indicates that Ω is an intermediate in the formation of the G• radical.

To explore the reactivity of Ω, we cryo-annealed a frozen 500-ms quench sample for 1 or 3 min at progressively higher temperatures, up to 220 K. During cryo-annealing of the frozen solid, the Ω signal is lost in parallel with quantitative generation of the PFL G• $g$-2 radical signal, with its characteristic doublet from hyperfine coupling, $A$ ~ 15 Gauss (G), to the α proton (Fig. 2A) (*12*). This annealing progression confirms that Ω is a catalytically competent reaction intermediate that can generate the G• radical product by H atom extraction from G734 of PFL and can even do so in the frozen solid. As a control, the rfq reaction was carried out using PFL $Gly^{734}$→$Ala^{734}$ (G734A), where the G• radical site was substituted with alanine. The rfq EPR spectrum at 12 K is identical to the one for the PFL wild type, which indicates that Ω is formed by cleavage of SAM in these reactions (Fig. 2B). However, the EPR spectrum at 40 K shows that Ω does not proceed to produce a G• radical, at a quench time ≥500 ms or during cryo-annealing.

We conclude from these observations that (i) Ω is associated with PFL-AE and SAM or 5′-dAdo; (ii) Ω is a precursor in the formation of the G• radical of the substrate protein PFL; and (iii) in Ω, the target G734 has been positioned so precisely that H atom abstraction to generate the G• radical can take place without major conformational changes, which are quenched in the frozen solid.

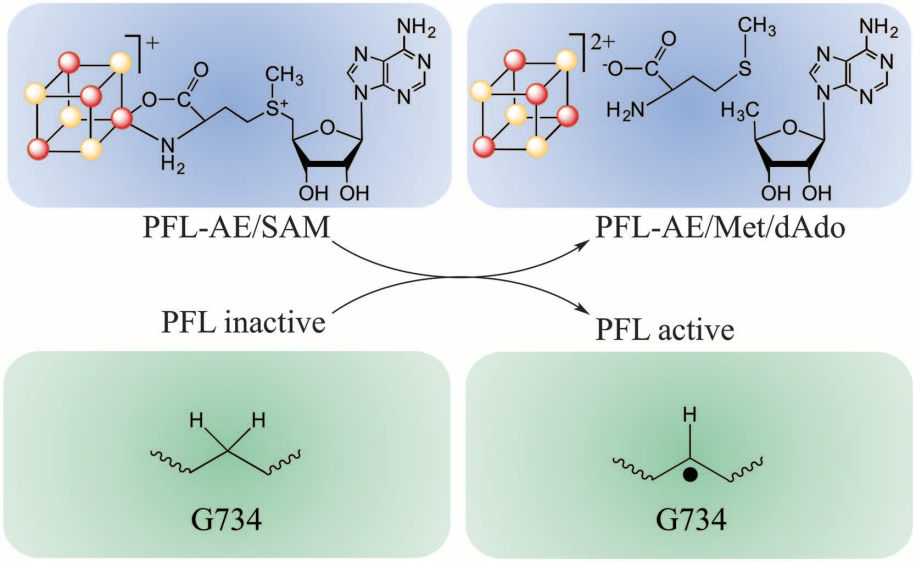


**Fig. 1. Activation of PFL by PFL-AE, with concomitant cleavage of SAM to methionine and 5′-deoxyadenosine.**

[1]Department of Chemistry, Northwestern University, Evanston, IL 60208, USA. [2]Department of Chemistry and Biochemistry, Montana State University, Bozeman, MT 59717, USA.
*Corresponding author. Email: bmh@northwestern.edu (B.M.H.); jbroderick@chemistry.montana.edu (J.B.B.).

Downloaded from http://science.sciencemag.org/ on May 12, 2016

The $g$ values for Ω are not compatible with assignment to a "free" organic radical, such as the elusive 5′-dAdo• radical, which would exhibit a near-isotropic $g$ ~ 2.0 signal. Moreover, the EPR spectrum for the primary-carbon 5′-dAdo• radical would necessarily exhibit well-resolved splittings arising from the hyperfine coupling between the odd electron in the 2p π orbital of C(5′) and the two equivalent protons of $^1H_2C(5')$ (fig. S3), but these are absent in the spectrum of Ω. The $g$ values are similar to those of compound ES of cytochrome $c$ peroxidase, where they reflect a weak exchange coupling between an organic radical and an integer-spin metal-ion center (*13*–*15*). In our work, the analogous situation would involve the 5′-dAdo• radical spin-coupled to an integer-spin $[4Fe\text{-}4S]^{2+}$ cluster. However, for multiple reasons, this model is also unambiguously incapable of describing Ω, not least because the EPR spectrum for such a spin-coupled center would necessarily exhibit the same $^1H$ hyperfine couplings to the $^1H_2C(5')$ of the 5′-dAdo• radical that are required for the free radical, unchanged by the exchange interaction (*13*–*15*) (fig. S3), but absent in the spectrum of Ω.

To determine whether Ω nonetheless involves the 5′-dAdo• radical in some fashion, we carried out rfq experiments, using $^{13}C$-labeled SAM and 35-GHz continuous wave (CW) and pulsed ENDOR spectroscopies to examine Ω. When Ω was formed with SAM—in which all adenosyl carbons, both of the base and ribose, are $^{13}C$ ([adenosyl-$^{13}C_{10}$]-SAM)—CW ENDOR spectra collected at $g_\perp$ = 2.004 disclosed a strong coupling to $^{13}C$ (Fig. 3A, top). This signal can be simulated by a hyperfine interaction with a single $^{13}C$ with a large isotropic coupling, $a_{iso}$ = 9.4 MHz, and an axial dipolar coupling, $2T \gtrsim 5.3$ MHz, depending on the extent to which the dipolar direction deviates from the $g_\perp$ plane. A second, more weakly coupled $^{13}C$ signal arising from $^{13}C$ at other positions ($A$ ~ 0.7 MHz) is revealed by the Mims pulse technique (Fig. 3A, inset).

The strong isotropic coupling to one $^{13}C$ of SAM reveals that this carbon is covalently integrated into the paramagnetic center of Ω. However, in addition to the absence of a large $^1H_2C(5')$ hyperfine coupling (see above), the magnitude of $a_{iso}$ is ~10-fold too low (*16*, *17*) to be attributed to the sought-after 5′-dAdo• primary-carbon radical, either free or weakly coupled to the cluster spin. As alternative possibilities, ω might be a precursor to SAM cleavage with enhanced bonding between the sulfonium sulfur and the unique Fe of the $[4Fe\text{-}4S]^{1+}$ cluster, or a product of electron transfer in which the unpaired electron of Ω is on the sulfur of an intact SAM neutral radical. However, in either case we would expect that each of the three carbons bound to the sulfur would exhibit similarly strong hyperfine couplings. Instead, experiments using [methyl-$^{13}C$]-SAM revealed that the coupling of the methyl $^{13}C$ ($A$ ~ 0.5 MHz) (Fig. 3B) is roughly 20 times weaker than that of the strongly coupled adenosyl $^{13}C$, ruling out these alternatives.

These considerations lead to the idea that Ω involves a SAM fragment associated with a spin $S$ = 1/2 form of the [4Fe-4S] cluster. To test this

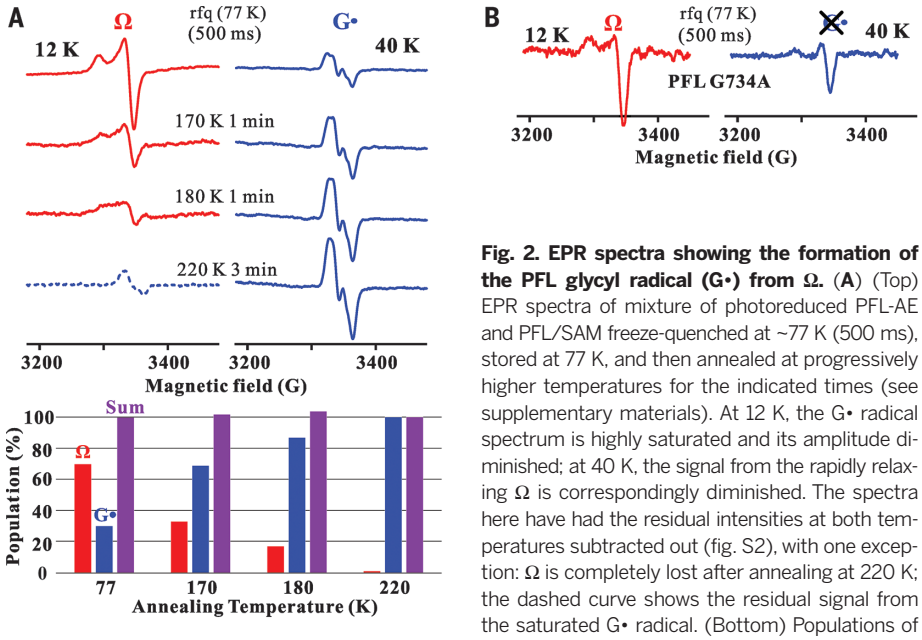


**Fig. 2. EPR spectra showing the formation of the PFL glycyl radical (G•) from Ω.** (**A**) (Top) EPR spectra of mixture of photoreduced PFL-AE and PFL/SAM freeze-quenched at ~77 K (500 ms), stored at 77 K, and then annealed at progressively higher temperatures for the indicated times (see supplementary materials). At 12 K, the G• radical spectrum is highly saturated and its amplitude diminished; at 40 K, the signal from the rapidly relaxing Ω is correspondingly diminished. The spectra here have had the residual intensities at both temperatures subtracted out (fig. S2), with one exception: Ω is completely lost after annealing at 220 K; the dashed curve shows the residual signal from the saturated G• radical. (Bottom) Populations of Ω and the G• radical, relative to the final (220 K) G• radical concentration taken as 100% (Sum), as derived from EPR spectra (see supplementary materials). (**B**) X-band EPR spectra for photoreduced PFL-AE freeze-quenched (77 K) 500 ms after mixing with PFL G734A/SAM, with spectra collected at 12 and 40 K. Conditions: microwave frequency = 9.23 GHz, microwave power = 1 mW, 100-kHz modulation amplitude = 8 G, and $T$, as indicated. The gain at a given $T$ is fixed.

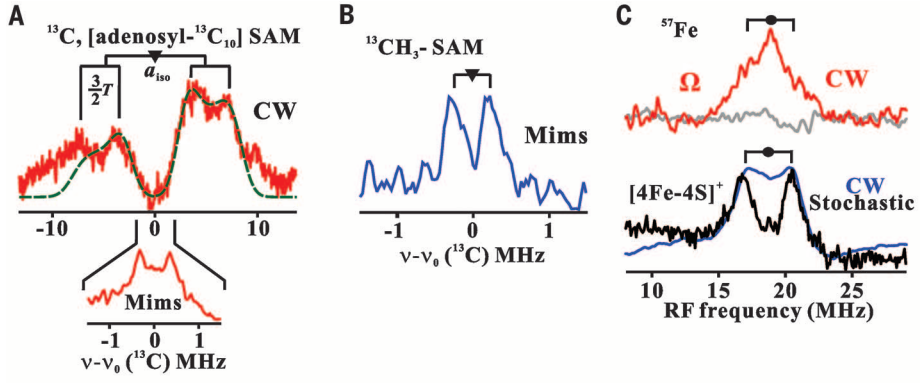


**Fig. 3. 35-GHz ENDOR spectra at $g_\perp$ for photoreduced PFL-AE freeze-quenched with PFL/SAM.** To first order, an ENDOR spectrum of a spin $I$ = 1/2 nucleus (N) in a frozen solution comprises a superposition of signals from different orientations, each signal a doublet at frequencies $\nu_\pm = |\nu(N) \pm A/2|$, where ν(N) is the nuclear larmor frequency and $A$ is the orientation-dependent hyperfine coupling (*23*). For $^{13}C$, $A/2 << \nu(^{13}C)$, and it is convenient to plot spectra versus $\nu - \nu(^{13}C)$. For $^{57}Fe$, $\nu(^{57}Fe) << A/2$, and spectra are plotted versus ν. (**A**) $^{13}C$ CW ENDOR for [adenosyl-$^{13}C_{10}$] SAM. The green dashed lines denotes the best-match simulation to the axial hyperfine tensor (see supplementary materials). Simulation parameters: $a_{iso}$ = 9.4 MHz, $2T$ = 5.3 MHz, and β = 90°. Conditions: microwave frequency = 35.39 GHz, microwave power = 1 mW, 100-kHz modulation amplitude = 1.3 G, rf sweep rate = 1 MHz/s, and $T$ = 2 K. (Inset) Mims ENDOR spectrum. Conditions: microwave frequency = 35.20 GHz; MW pulse length, (π/2) = 50 ns; τ = 500 ns; and $T$ = 2 K. (**B**) Mims ENDOR spectrum from [methyl-$^{13}C$] SAM. Conditions: microwave frequency = 35.08 GHz; MW pulse length, (π/2) = 50 ns; τ = 500 ns; and $T$ = 2 K. (**C**) $^{57}Fe$ CW ENDOR for $^{57}Fe$-enriched Ω and photoreduced PFL-AE. (Top) CW ENDOR spectra for $^{57}Fe$-enriched (red) and natural-abundance (gray) rfq samples. (Bottom) Frequency sweep and randomly hopped stochastic CW ENDOR spectra (*23*) for $^{57}Fe$-enriched reduced PFL-AE. Conditions: microwave frequency = 35.45 GHz and 35.07 GHz for rfq and $^{57}Fe$-enriched reduced PFL-AE, respectively; microwave power = 1 mW; 100-kHz modulation amplitude = 1.3 G; rf sweep rate = 1 MHz/s; stochastic CW ENDOR cycle, rf-on = 3 ms, rf-off = 1 ms; sample collection time = 3 ms; and $T$ = 2 K. See supplementary materials for details.

Downloaded from http://science.sciencemag.org/ on May 12, 2016

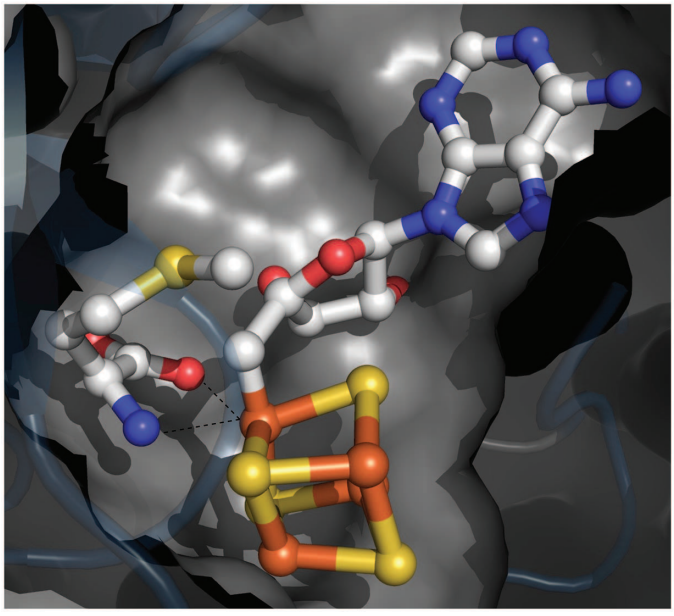

**Fig. 4. Model for bio-organometallic intermediate Ω.** Whether methionine remains coordinated to the unique iron site is not currently known. Blue, nitrogen; white, carbon; red, oxygen; yellow, sulfur; orange, iron.

idea, we used $^{57}$Fe-enriched PFL-AE to prepare Ω. ENDOR spectroscopy of this sample revealed an $^{57}$Fe signal centered at $A/2$ = ~17 MHz, essentially the same as the much-better-resolved signal for the $^{57}$Fe-labeled protein in its paramagnetic [4Fe-4S]$^{+}$ state (Fig. 3C). This establishes that the electron spin giving rise to the Ω EPR signal resides on the iron-sulfur cluster, whereas the isotropic coupling to a single carbon of dAdo requires a carbon of the 5′-dAdo fragment to be covalently bound to the paramagnetic cluster. Although all carbons of the adenosyl moiety of SAM were $^{13}$C in this sample, the only reasonable interpretation is that the 5′ C of the 5′-dAdo• radical created by reductive cleavage of SAM has formed an Fe–C bond with the unique cluster iron and gives rise to the stronger coupling observed in the $^{13}$C ENDOR spectrum of Ω (Fig. 4). The weakly coupled carbon observed in the Mims ENDOR spectrum (Fig. 3B) would then be assigned to the 4′ C of dAdo.

In the commonly proposed mechanism of radical SAM enzymes, an electron from a [4Fe-4S]$^{+}$ cluster is transferred to the sulfonium of SAM, thereby promoting S-[5′-C] bond cleavage to generate the 5′-dAdo• radical intermediate (*1*). If this is indeed the initial step in catalysis, then our current results would indicate that in PFL-AE, the 5′-dAdo• radical thus formed by SAM reduction adds to the [4Fe-4S]$^{2+}$ cluster product of the electron transfer to generate Ω, an organometallic intermediate in which the $S$ = 1/2 cluster, formally [4Fe-4S]$^{3+}$, is covalently linked to 5′-dAdo through an Fe–C bond between [5′-C] and the unique iron of the cluster. As a plausible alternative mechanism, nucleophilic attack of the unique iron of the [4Fe-4S]$^{+}$ cluster on the 5′ C of SAM initiates SAM cleavage, to release methionine and generate the [4Fe-4S]$^{3+}$-adenosyl intermediate, Ω. In this case, the 5′-dAdo• radical is truly "never free" (*9*).

Regardless of the mechanism for its formation, the organometallic intermediate Ω proposed here for PFL-AE provides intriguing parallels to the adenosylcobalamin cofactor, which is used by $B_{12}$ radical enzymes to initiate radical catalysis by homolytic cleavage of the Co(III)-[5′-C]-deoxyadenosyl bond to generate a 5′-dAdo• radical and Co(II) cobalamin (*18*, *19*). Analogously, the H atom abstraction from G734 by Ω would begin with homolytic cleavage of the [4Fe-4S]$^{3+}$ Fe-[5′-C]-adenosyl bond to generate [4Fe-4S]$^{2+}$ and a 5′-dAdo• radical, which then abstracts a precisely positioned hydrogen atom from G734 of PFL.

The results reported here provide evidence that, contrary to expectation, cleavage of SAM by PFL-AE generates a catalytically competent bio-organometallic intermediate (Ω) in which the 5′-dAdo moiety derived from SAM is covalently bound through the 5′ C to the [4Fe-4S] cluster (Fig. 4). This intermediate generates the G• product radical on PFL during annealing of the activated protein-protein complex in the frozen solid at temperatures at or below 170 K (Fig. 2). This confirms that, in the ternary complex, the structures of both PFL and PFL-AE have rearranged so that the target G734 of PFL is proximate to the [4Fe-4S]/SAM radical-generating construct of PFL-AE. This proximity, which was predicted on the basis of structural studies of PFL-AE in complex with a heptamer peptide of PFL (*5*), requires that formation of the PFL-AE/PFL complex involves substantial conformational changes in PFL, whose G734 residue is normally buried 8 Å from the protein surface (*20*, *21*).

If Ω is truly formed through nucleophilic attack of the unique Fe on the 5′ C of SAM as a means to cleave the S-[5′-C] bond of SAM and generate a radical initiator Fe-[5′-C] bond, then such an intermediate may well be common to many, or even all, radical-SAM enzymes. In particular, it is interesting to consider whether the formation of Ω might represent a mechanistic difference between those radical SAM enzymes that, like PFL-AE, use SAM as a cosubstrate and those that use SAM as a cofactor; further studies will be required to address this possibility. The mechanistic importance of such an intermediate may lie in providing a means to control and store the reactive 5′-dAdo• radical intermediate until the target hydrogen atom of the substrate is bound appropriately for abstraction. Given the complexity of the 170-kDa substrate PFL and the requirement for large protein conformational changes during its activation by PFL-AE (*5*, *21*), the need for such storage and control seems plausible. In either case, the discovery of this organometallic radical initiator moiety in a radical-SAM enzyme provides an additional parallel to the $B_{12}$ radical enzymes: Not only do both classes use a 5′-dAdo• radical in catalytic H atom abstraction, but both also employ a precursor complex with a direct metal-[5′-C] bond.

The work presented here reveals a catalytically competent [4Fe-4S]-cluster–bound 5′-deoxyadenosyl species in PFL-AE. This radical initiator Fe-[5′-C]-adenosyl complex expands the growing list of enzymatic bioorganometallic centers, whose first entry was coenzyme $B_{12}$ (*18*, *19*) but now includes the active-site metal clusters of hydrogenases (*22*), nitrogenase (*23*, *24*), and a catalytic intermediate of IspH (*25*, *26*). Our study shows that radical SAM enzymes, the largest known superfamily of enzymes, can also function through an organometallic center.

## REFERENCES AND NOTES


1. J. B. Broderick, B. R. Duffus, K. S. Duschene, E. M. Shepard, *Chem. Rev.* **114**, 4229–4317 (2014).
2. G. Sicoli *et al.*, *Science* **351**, 1320–1323 (2016).
3. C. J. Walsby, D. Ortillo, W. E. Broderick, J. B. Broderick, B. M. Hoffman, *J. Am. Chem. Soc.* **124**, 11270–11271 (2002).
4. D. Chen, C. Walsby, B. M. Hoffman, P. A. Frey, *J. Am. Chem. Soc.* **125**, 11788–11789 (2003).
5. J. L. Vey *et al.*, *Proc. Natl. Acad. Sci. U.S.A.* **105**, 16137–16141 (2008).
6. B. W. Lepore, F. J. Ruzicka, P. A. Frey, D. Ringe, *Proc. Natl. Acad. Sci. U.S.A.* **102**, 13819–13824 (2005).
7. O. T. Magnusson, G. H. Reed, P. A. Frey, *J. Am. Chem. Soc.* **121**, 9764–9765 (1999).
8. O. T. Magnusson, G. H. Reed, P. A. Frey, *Biochemistry* **40**, 7773–7782 (2001).
9. M. Horitani *et al.*, *J. Am. Chem. Soc.* **137**, 7111–7121 (2015).
10. K. A. Shisler, J. B. Broderick, *Arch. Biochem. Biophys.* **546**, 64–71 (2014).
11. C. J. Walsby *et al.*, *J. Am. Chem. Soc.* **124**, 3143–3151 (2002).
12. A. F. V. Wagner, M. Frey, F. A. Neugebauer, W. Schäfer, J. Knappe, *Proc. Natl. Acad. Sci. U.S.A.* **89**, 996–1000 (1992).
13. M. Sivaraja, D. B. Goodin, M. Smith, B. M. Hoffman, *Science* **245**, 738–740 (1989).
14. A. L. P. Houseman, P. E. Doan, D. B. Goodwin, B. M. Hoffman, *Biochemistry* **32**, 4430–4443 (1993).
15. J. E. Huyett *et al.*, *J. Am. Chem. Soc.* **117**, 9033–9041 (1995).
16. H. M. McConnell, R. W. Fessenden, *J. Chem. Phys.* **31**, 1688 (1959).
17. T. Cole, C. Heller, *J. Chem. Phys.* **34**, 1085 (1961).
18. R. Banerjee, *Chem. Rev.* **103**, 2083–2094 (2003).
19. K. L. Brown, *Chem. Rev.* **105**, 2075–2150 (2005).


Downloaded from http://science.sciencemag.org/ on May 12, 2016

20. A. Becker *et al.*, *Nat. Struct. Mol. Biol.* **6**, 969–975 (1999).
21. Y. Peng, S. E. Veneziano, G. D. Gillispie, J. B. Broderick, *J. Biol. Chem.* **285**, 27224–27231 (2010).
22. W. Lubitz, H. Ogata, O. Rüdiger, E. Reijerse, *Chem. Rev.* **114**, 4081–4148 (2014).
23. G. E. Cutsail III, J. Telser, B. M. Hoffman, *Biochim. Biophys. Acta* **1853**, 1370–1394 (2015).
24. H.-I. Lee *et al.*, *J. Am. Chem. Soc.* **126**, 9563–9569 (2004).
25. W. Xu *et al.*, *Biochemistry* **51**, 4835–4849 (2012).
26. I. Span *et al.*, *J. Am. Chem. Soc.* **136**, 7926–7932 (2014).

**ACKNOWLEDGMENTS**

This work was funded by the NIH (grant GM 111097 to B.M.H. and grant GM 54608 to J.B.B.). We thank B.-H. Huynh and C. Krebs for contributions in the early stages of this study.

**SUPPLEMENTARY MATERIALS**

www.sciencemag.org/content/352/6287/822/suppl/DC1
Materials and Methods
Supplementary Text
Figs. S1 to S3
References (*27*–*39*)

29 February 2016; accepted 29 March 2016
10.1126/science.aaf5327

ATMOSPHERIC SCIENCE

# Empirical evidence of contrasting soil moisture–precipitation feedbacks across the United States

**Samuel Tuttle* and Guido Salvucci**

**Soil moisture influences fluxes of heat and moisture originating at the land surface, thus altering atmospheric humidity and temperature profiles. However, empirical and modeling studies disagree on how this affects the propensity for precipitation, mainly owing to the difficulty in establishing causality. We use Granger causality to estimate the relationship between soil moisture and occurrence of subsequent precipitation over the contiguous United States using remotely sensed soil moisture and gauge-based precipitation observations. After removing potential confounding effects of daily persistence, and seasonal and interannual variability in precipitation, we find that soil moisture anomalies significantly influence rainfall probabilities over 38% of the area with a median factor of 13%. The feedback is generally positive in the west and negative in the east, suggesting dependence on regional aridity.**

Land-surface moisture content affects the partitioning of radiative energy into latent and sensible heat fluxes (*1*) and therefore can affect the state of the overlying atmosphere by supplying water vapor, inducing moist convection and lateral convergence, and growing the planetary boundary layer (*2*). Previous studies have recognized that soil water content can modify atmospheric processes on a range of spatial and temporal scales (*1*, *3*), potentially leading to cloud formation (*4*) and precipitation (*2*, *5*). In extreme cases, soil moisture may indirectly influence atmospheric circulation (*6*). It is important that the soil moisture–precipitation relationship is characterized, as it has implications for adaptations to future climate change and our ability to forecast weather and make climate projections. For instance, a positive feedback between soil moisture and precipitation could increase the duration of severe dry and wet periods (i.e., droughts and floods), as drier soils would lead to lower precipitation likelihood, and vice versa.

However, the nature of the soil moisture–precipitation relationship is still debated. Past observational and reanalysis studies have indicated that it varies by location, but some analyses have led to disagreements on feedback sign, strength, and statistical significance over the same regions (*5*, *7*–*12*), even using the same data (*13*, *14*). These discrepancies are partly due to the sparse record of soil moisture observations, the different techniques used to identify feedbacks (e.g., temporal versus spatial analyses) (*15*), and the difficulty of distinguishing a causal soil moisture–precipitation effect from lagged correlations that arise from the autocorrelation, seasonality, and interannual variability of each signal (*1*, *14*, *16*, *17*). Modeling studies have been used to circumvent these challenges, with most finding a positive soil moisture–precipitation feedback (*3*, *18*, *19*). However, a wide range of coupling has been found in different models (*18*, *20*), and it has been suggested that land-atmosphere feedbacks are not yet accurately represented (*5*), as convective parameterization and spatial scale may determine not only the feedback strength, but the sign as well (*21*). A review on soil moisture–climate interactions noted the ambiguity in past studies and highlighted the need to identify the causal link between soil moisture and precipitation using observational data (*1*). We believe our results satisfy this need, for the given temporal and spatial scales used here.

Much of the difficulty in determining the nature of soil moisture–precipitation feedback is due to the direct, positive relationship between precipitation and soil moisture in conjunction with the relatively long memory (i.e., autocorrelation) of soil moisture (*1*, *14*–*17*). Precipitation events elevate soil moisture content and may be reflected in the soil moisture record for weeks (*22*) as soil water slowly percolates, evaporates, and is taken up by vegetation. This confounds the observed soil moisture–precipitation relationship by making it difficult to determine whether an increase in precipitation occurrence after a large soil moisture anomaly is a direct effect (i.e., causal), or simply a result of temporal autocorrelation in precipitation, which is then imprinted on soil moisture. To our knowledge, only one previous study (*14*) has sought to directly account for precipitation autocorrelation using statistical causal identification methods (*23*). Others have attempted to address it by incorporating additional information on atmospheric stability (*8*, *10*, *11*); by relating convective triggering to spatial, as opposed to temporal, anomalies in soil moisture (*5*, *15*); by examining covariance with possible confounding variables (*20*); or by stratifying results according to past precipitation (*8*).

We resolve the issue of precipitation autocorrelation by explicitly including both lagged soil moisture and lagged precipitation in a generalized linear model (GLM) of precipitation occurrence (specifically, a probit model), constructed to diagnose the relationship between soil moisture and the probability of next-day precipitation (*24*). We include both continuous and indicator variables in the regression, which represent a set of climatic, atmospheric, and land-surface processes that could influence precipitation occurrence. These consist of sinusoids that vary on interannual and seasonal time scales (to account for external atmospheric and climatic influences on precipitation; e.g., sea surface temperature, seasonality), binary indicator variables that represent the prior occurrence of precipitation [up to 4 days into the past (*24*)], lagged atmospheric pressure (4 days into the past), and previous-day soil moisture (for simple example models, see Fig. 1). The indicator variables account for precipitation persistence from synoptic weather systems (where precipitation events may span multiple days), plus any other source of short-term precipitation persistence, by allowing the regression to predict higher probability of precipitation on days following precipitation. Because this increased probability is statistically accounted for by the indicator variables, it is not attributed to soil moisture, eliminating the influence of precipitation autocorrelation on the soil moisture–precipitation feedback signal. Similarly, including lagged pressure accounts for atmospheric persistence such as drying during lingering high-pressure systems, and seasonal and interannual sinusoids in the regression eliminate the confounding effect of low-frequency correlations of soil moisture and precipitation (caused simply by water balance) on the potential short-term feedback signal.

Boston University, Boston, MA 02215, USA.
*Corresponding author. Email: stuttle@bu.edu

Downloaded from http://science.sciencemag.org/ on May 12, 2016

The soil moisture data used in this study are 0.25° resolution satellite observations from the Advanced Microwave Scanning Radiometer for the Earth Observing System (AMSR-E) (*25*, *26*). The precipitation data are gridded gauge observations from the North American Land Data Assimilation System, Phase 2 (NLDAS-2) (*27*).

Because we do not know a priori which factors will influence the probability of precipitation at any given location, we run a large suite of regressions with all permutations of the variables listed above, other than soil moisture (and pressure). This so-called all possible regressions (APR) method is computationally intensive but superior to stepwise methods. We determine which variables are important for predicting precipitation probability and soil moisture for each 0.25° pixel by selecting the regression model that yields the minimum Akaike information criterion (AIC), which penalizes against the model fit by the number of free parameters included in the model (*24*) (for the number of variables selected at each location, see fig. S1). These models yield predictions of precipitation occurrence and soil moisture derived from climatic factors and precipitation persistence (but not soil moisture). Then, employing Granger causality (*23*), we fit the residual precipitation probability to the residual soil moisture and lagged pressure (*24*), focusing only on days where precipitation did not occur on the previous day to further eliminate precipitation persistence. We also use a block bootstrapping method to correct for bias in the regression coefficients introduced by the endogeneity of soil moisture and precipitation occurrence and to test for statistically significant improvement in prediction capability due to soil moisture (*24*). The difference in predictions between the two models estimates the impact of soil moisture on precipitation probability.

By including terms in the regression that account for interannual and seasonal variations, and atmospheric and precipitation persistence, we expect that we have isolated the causal relationship between soil moisture state and the probability of precipitation [although it is always possible in studies employing Granger causality that the inclusion of some neglected common factor could cause the soil moisture coefficient to lose statistical significance (*20*)]. Accounting for lagged precipitation and low-frequency (i.e., seasonal and interannual) variability frames the analysis as a test of rejecting the null, where the null hypothesis is that soil moisture has no influence on future precipitation, and no precipitation persistence is due to soil moisture–precipitation feedback. It is only rejected if, after removing the confounding effects of precipitation autocorrelation, low-frequency variability, and atmospheric persistence, soil moisture still improves the prediction of future precipitation occurrence. Null testing indicated that the model is not vulnerable to false-positive identification of soil moisture–precipitation feedback (fig. S2). This Granger causality (*23*) framework is capable of detecting (*14*) the presence of a feedback provided that soil moisture dynamics are not entirely determined by precipitation (i.e., they are also influenced by other aspects of weather, such as evapotranspiration).

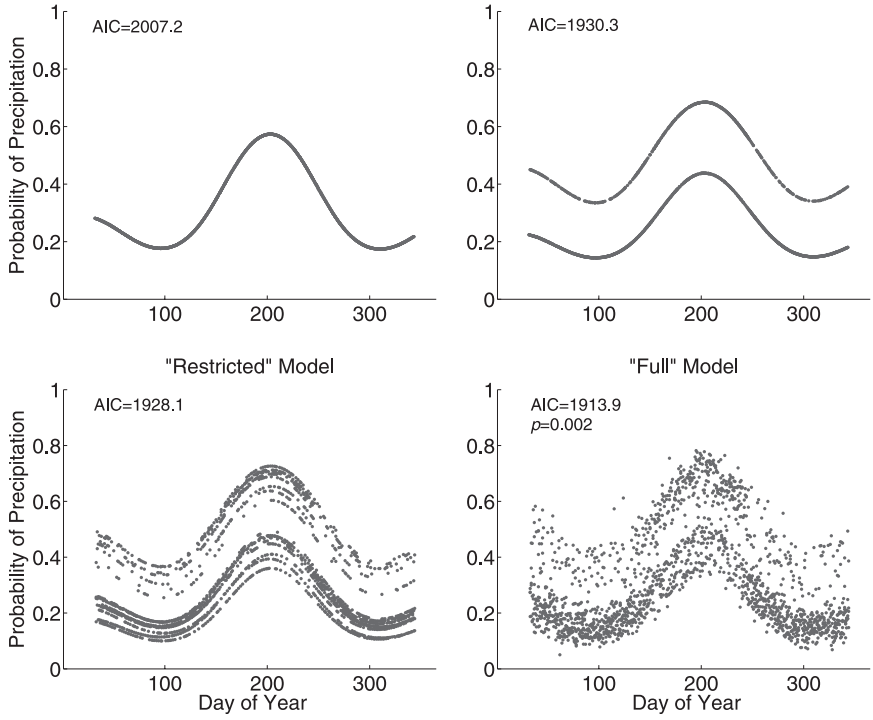


**Fig. 1. Example plots illustrating precipitation models of increasing complexity.** The plots show probit models of precipitation probability that were fit to observed precipitation occurrence at one location. In each, 9 years of model-estimated precipitation probability are plotted against day of year. In the top left panel, only seasonal terms and a constant were included in the model. In the top right panel, lagged precipitation occurrence was added to the seasonal model. The bottom curve in this panel shows the predicted precipitation probability when precipitation did not occur on the previous day, while the top curve reflects the increased probability predicted by the model when precipitation occurred on the previous day. In the bottom left panel, interannual terms were added to the seasonal-and-persistence model (top right). This is the minimum Akaike information criterion (AIC) (*24*) model for this location, which was determined by regressing all possible combinations of the seasonal, interannual, and lagged precipitation terms on precipitation occurrence [i.e., all possible regressions (APR)]. The model was not required to contain each of these components, but for this location, it contained a constant, two seasonal and two interannual terms, and 1-day lagged precipitation. In the bottom right panel, soil moisture and lagged atmospheric pressure were included, forming the "full" model.

Figure 2 displays the mean soil moisture impact on precipitation probability, for both high and low soil moisture (defined as the mean impact above or below the median seasonally detrended soil moisture anomaly, respectively; see fig. S3) across the United States, for each of two AMSR-E soil moisture products used here (*25*, *26*). The impact is presented as a relative probability factor, reflecting the precipitation probability predicted by the full regression model (i.e., including soil moisture) divided by the precipitation probability predicted without soil moisture. This illustrates the mean degree to which the soil moisture causes the precipitation probability to deviate from its climatological average value, after accounting for persistence and low-frequency variability.

Figure 2 shows a positive feedback of soil moisture on next-day precipitation probability in the western United States and a negative feedback in the east. In general, the areas of positive feedback correspond to more arid regions, whereas more humid, vegetated areas exhibit a negative feedback. Approximately 38% of the United States displays significant feedback (at the 5% significance level), and we find that soil moisture anomalies modify rainfall probabilities by a median factor of 13% (i.e., median absolute impact across all significant pixels in the four panels of Fig. 2). The impact magnitudes differ somewhat between the two AMSR-E soil moisture products, but the sign of the feedback (i.e., positive, negative, or insignificant) agrees over 58% of the study area, and both display an obvious east-negative, west-positive pattern. This same general pattern arises when the analysis period is restricted to individual seasons (fig. S4), or when the data are averaged to larger spatial scales (fig. S5), and is observed in land-surface models (LSMs) forced by the same precipitation data (fig. S6).

Soil moisture–precipitation feedback is not significant over much of the study area, including the Great Plains (a transitional zone between arid and humid regions), where previous modeling studies indicated a "hot spot" of strong land-atmosphere coupling (*18*, *19*, *28*). Our results indicate that weak soil moisture–precipitation feedback

Downloaded from http://science.sciencemag.org/ on May 12, 2016

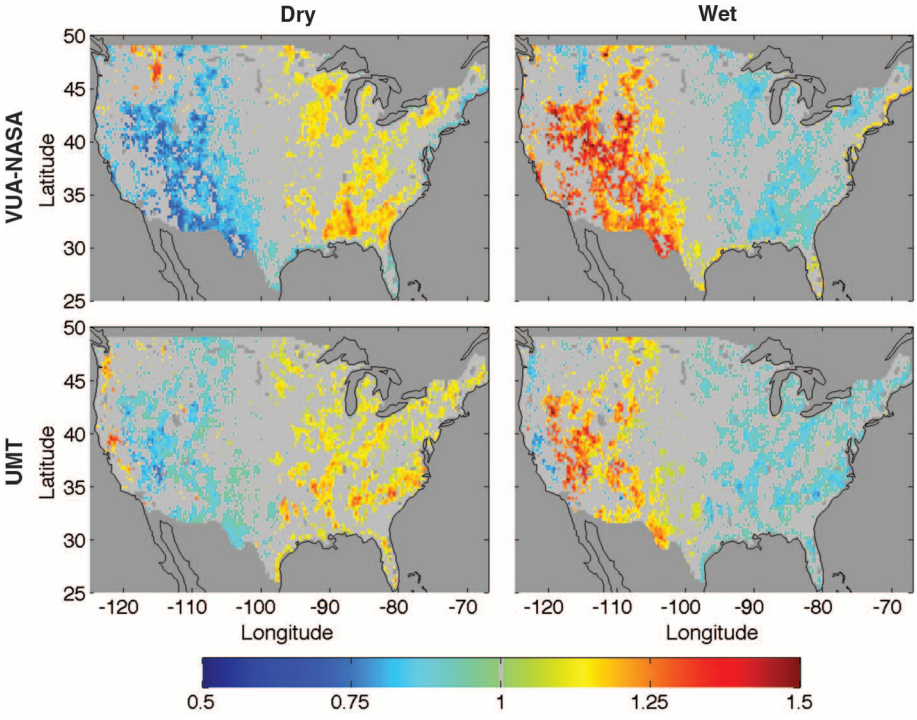


**Fig. 2. Maps of the impact of soil moisture on the probability of next-day precipitation.** Relative probability factors that represent the mean impact of soil moisture on precipitation probability, calculated as the predicted precipitation probability when soil moisture was included in the regression model divided by the predicted precipitation probability when soil moisture was removed, are shown. Blue colors indicate that the inclusion of soil moisture in the model reduced the predicted precipitation probability, while red colors indicate that the probability increased. Light gray areas denote the absence of a statistically significant relationship ($\alpha$ = 0.05), and dark gray areas were not tested. The values shown are for VUA-NASA (*25*) (top row) and UMT (*26*) (bottom row) soil moisture. The left column shows mean relative impact below median soil moisture anomaly (i.e., drier than seasonal median conditions), and mean relative impact above median soil moisture anomaly (i.e., wetter than seasonal median conditions) is presented in the right column. Negative feedback (i.e., impact higher than 1 in dry soil moisture conditions and lower than 1 in wet conditions) dominates the eastern portion of the study area, while positive feedback (i.e., impact higher than 1 in wet conditions and lower than 1 in dry conditions) is more prominent in western areas.

exists in these areas, after accounting for climatic factors and removing the effects of persistence. We do not find evidence of a strong feedback that varies between positive and negative in sign on a seasonal basis (fig. S4), which could have resulted in temporal cancellation (*9*). Although soil moisture is both highly variable and limits evapotranspiration in this transition zone (*19*), the absence of a feedback indicates that evapotranspiration may not strongly influence precipitation (*11*). Much of the precipitation in the Great Plains occurs during the night (fig. S7) as a result of remotely triggered, eastward-propagating convective systems (*29*), so it is possible that local land-atmosphere interaction is not important for predicting precipitation in this region.

Nevertheless, our results are consistent with a recent observational study (*5*) that found convective initiation over drier soils (i.e., a negative feedback) in limited areas of the eastern United States, and no clear signal in the Great Plains, as well as another study (*10*) that found mostly insignificant feedbacks in the Upper Midwest using atmospheric profiles to filter the relationship between observed precipitation and modeled soil moisture. The east-negative, west-positive pattern in Fig. 2 is quite similar to those found using a feedback strength parameter in monthly evapotranspiration and precipitation reanalysis data (*12*). Another study (*9*) found rank correlations between soil moisture and the lifting condensation level in observations and some models, which spatially agree with our findings of strong positive impact in the west and an abrupt decrease in impact east across the Midwest.

However, the pattern detected here is opposite of that found in studies that used a boundary layer model and sounding data to diagnose areas likely to display positive and negative feedbacks (*7*), and in a study relating morning evaporative fraction and afternoon precipitation from reanalysis data (*11*). When the latter technique is expanded to observational data, the agreement is marginally better, but lack of adequate control for precipitation persistence may still be an issue (*8*).

We emphasize that the results of this analysis only reflect soil moisture–precipitation feedback at a daily timestep and 0.25° spatial scale (and larger, fig. S5) and are dependent on satellite and gridded precipitation data quality. Our conclusions include a number of qualifications. First, this study identifies local feedbacks using a temporal analysis, but does not consider spatial effects [e.g., (*5*, *15*)]. Second, in areas of dense vegetation [e.g., east of the Mississippi River (*9*)], the soil moisture signal detected by AMSR-E may be contaminated and obscured by vegetation (supplementary text and fig. S8). Third, the applied method (*24*) is an effective way to ensure against false positives (e.g., fig. S2), but like any conservative-null approach, it reduces statistical power, thereby increasing the possibility of not identifying a soil moisture–precipitation feedback where one exists.

Fourth, this analysis investigates the probability of precipitation occurrence independent of time of day, which differs from some other studies [e.g., (*5*, *8*, *11*, *15*)] that focused on afternoon precipitation. An assessment of feedback as a function of time of day would be a valuable follow-up investigation, but would require longer data records.

Finally, because the model allows for up to five sinusoidal frequencies to represent the seasonal cycle of precipitation occurrence, the model can adequately represent complex climatological mean patterns. However, other procedures such as window averages could potentially capture sharper transitions.

This analysis does not identify specific mechanisms for soil moisture–precipitation feedback, which are likely a complex interplay between atmospheric and land-surface moisture sources (*8*), boundary layer processes, atmospheric stability (*4*), and possibly nonlocal effects or wind (*30*). However, the opposing results in humid versus arid areas could indicate that the feedback may be different in different climates. The results shown here are consistent with the hypothesis that a lack of atmospheric moisture may be the limiting factor for precipitation in more arid areas [i.e., moisture recycling (*31*)], whereas in humid areas, where atmospheric moisture is abundant, the feedback may be controlled by more dynamic mechanisms [e.g., dampened instability (*32*), or convection triggered by thermal buoyancy over relatively drier soils, or mesoscale convergence (*2*, *3*, *5*)].

This study supports the concept of soil moisture–atmosphere feedback and indicates that knowledge of soil moisture can help to constrain the probability of next-day precipitation in many areas, independently of any precipitation persistence. Further study on boundary layer processes is needed to tease out the physical pathways behind the results shown here, so that these hydrologic relationships may be better represented in weather and climate models.

## REFERENCES AND NOTES

1. S. I. Seneviratne *et al.*, *Earth Sci. Rev.* **99**, 125–161 (2010).
2. R. A. Pielke Sr., *Rev. Geophys.* **39**, 151–177 (2001).
3. C. M. Taylor *et al.*, *Nat. Geosci.* **4**, 430–433 (2011).

Downloaded from http://science.sciencemag.org/ on May 12, 2016

4. M. B. Ek, A. A. M. Holtslag, *J. Hydrometeorol.* **5**, 86–99 (2004).
5. C. M. Taylor, R. A. M. de Jeu, F. Guichard, P. P. Harris, W. A. Dorigo, *Nature* **489**, 423–426 (2012).
6. E. M. Fischer, S. I. Seneviratne, P. L. Vidale, D. Lüthi, C. Schär, *J. Clim.* **20**, 5081–5099 (2007).
7. K. L. Findell, E. A. B. Eltahir, *J. Hydrometeorol.* **4**, 570–583 (2003).
8. B. P. Guillod *et al*., *Atmos. Chem. Phys.* **14**, 8343–8367 (2014).
9. C. R. Ferguson, E. F. Wood, R. K. Vinukollu, *J. Hydrometeorol.* **13**, 749–784 (2012).
10. L. Alfieri, P. Claps, P. D'Odorico, F. Laio, T. M. Over, *J. Hydrometeorol.* **9**, 280–291 (2008).
11. K. L. Findell, P. Gentine, B. R. Lintner, C. Kerr, *Nat. Geosci.* **4**, 434–439 (2011).
12. X. Zeng, M. Barlage, C. Castro, K. Fling, *J. Hydrometeorol.* **11**, 979–994 (2010).
13. K. L. Findell, E. A. B. Eltahir, *Water Resour. Res.* **33**, 725–735 (1997).
14. G. D. Salvucci, J. A. Saleem, R. Kaufmann, *Adv. Water Resour.* **25**, 1305–1312 (2002).
15. B. P. Guillod, B. Orlowsky, D. G. Miralles, A. J. Teuling, S. I. Seneviratne, *Nat. Commun.* **6**, 6443 (2015).
16. J. Wei, R. E. Dickinson, H. Chen, *J. Hydrometeorol.* **9**, 1364–1376 (2008).
17. S. I. Seneviratne, R. D. Koster, *J. Hydrometeorol.* **13**, 404–412 (2012).
18. R. D. Koster *et al*., *J. Hydrometeorol.* **7**, 590–610 (2006).
19. R. D. Koster *et al*., *Science* **305**, 1138–1140 (2004).
20. B. Orlowsky, S. I. Seneviratne, *J. Clim.* **23**, 3918–3932 (2010).
21. C. Hohenegger, P. Brockhaus, C. S. Bretherton, C. Schär, *J. Clim.* **22**, 5003–5020 (2009).
22. P. A. Dirmeyer, C. A. Schlosser, K. L. Brubaker, *J. Hydrometeorol.* **10**, 278–288 (2009).
23. C. W. J. Granger, *Econometrica* **37**, 424–438 (1969).
24. Materials and methods are available as supplementary materials on *Science* Online.
25. M. Owe, R. A. M. de Jeu, J. Walker, *IEEE Trans. Geosci. Rem. Sens.* **39**, 1643–1654 (2001).
26. L. A. Jones *et al*., A method for deriving land surface soil moisture, vegetation optical depth, and open water fraction from AMSR-E. *Proc. IEEE Geosci. Remote Sens. Symp. (IGARSS 2009), Cape Town, South Africa*. **3**, III-916-III-919 (2009).
27. K. E. Mitchell *et al*., *J. Geophys. Res.* **109**, D07S90 (2004).
28. R. Mei, G. Wang, *J. Hydrometeorol.* **13**, 1010–1022 (2012).
29. R. E. Carbone, J. D. Tuttle, *J. Clim.* **21**, 4132–4146 (2008).
30. P. Froidevaux, L. Schlemmer, J. Schmidli, W. Langhans, C. Schär, *J. Atmos. Sci.* **71**, 782–799 (2014).
31. J. A. Eddy, C. K. Stidd, W. B. Fowler, J. D. Helvey, *Science* **188**, 279–281 (1975).
32. F. Giorgi, L. O. Mearns, C. Shields, L. Mayer, *J. Clim.* **9**, 1150–1162 (1996).



## ACKNOWLEDGMENTS

Thanks to P. Dirmeyer and two anonymous reviewers for constructive comments that helped to strengthen this analysis. The data used in this study are freely available online from the NASA Goddard Earth Sciences (GES) Data and Information Services Center (DISC) (http://disc.sci.gsfc.nasa.gov/hydrology), the National Snow and Ice Data Center (NSIDC) Distributed Active Archive Center (DAAC) (http://nsidc.org/data/nsidc-0451), and the Oak Ridge National Laboratory (ORNL) DAAC for biogeochemical dynamics (https://daac.ornl.gov/NACP/guides/NBCD_2000_V2.html). This research was funded by NASA under grant NNX12AP78G (to G.S.).


## SUPPLEMENTARY MATERIALS

www.sciencemag.org/content/352/6287/825/suppl/DC1
Materials and Methods
Supplementary Text
Figs. S1 to S8
References (*33*–*51*)

18 January 2015; accepted 4 April 2016
10.1126/science.aaa7185

HIV-1 ANTIBODIES

# Fusion peptide of HIV-1 as a site of vulnerability to neutralizing antibody

**Rui Kong,[1]* Kai Xu,[1]* Tongqing Zhou,[1]* Priyamvada Acharya,[1] Thomas Lemmin,[2] Kevin Liu,[1] Gabriel Ozorowski,[3,4,5] Cinque Soto,[1] Justin D. Taft,[1] Robert T. Bailer,[1] Evan M. Cale,[1] Lei Chen,[1] Chang W. Choi,[1] Gwo-Yu Chuang,[1] Nicole A. Doria-Rose,[1] Aliaksandr Druz,[1] Ivelin S. Georgiev,[1] Jason Gorman,[1] Jinghe Huang,[6] M. Gordon Joyce,[1] Mark K. Louder,[1] Xiaochu Ma,[7] Krisha McKee,[1] Sijy O'Dell,[1] Marie Pancera,[1] Yongping Yang,[1] Scott C. Blanchard,[8] Walther Mothes,[7] Dennis R. Burton,[9,10] Wayne C. Koff,[11] Mark Connors,[6] Andrew B. Ward,[3,4,5] Peter D. Kwong,[1]† John R. Mascola[1]†**

**The HIV-1 fusion peptide, comprising 15 to 20 hydrophobic residues at the N terminus of the Env-gp41 subunit, is a critical component of the virus-cell entry machinery. Here, we report the identification of a neutralizing antibody, N123-VRC34.01, which targets the fusion peptide and blocks viral entry by inhibiting conformational changes in gp120 and gp41 subunits of Env required for entry. Crystal structures of N123-VRC34.01 liganded to the fusion peptide, and to the full Env trimer, revealed an epitope consisting of the N-terminal eight residues of the gp41 fusion peptide and glycan N88 of gp120, and molecular dynamics showed that the N-terminal portion of the fusion peptide can be solvent-exposed. These results reveal the fusion peptide to be a neutralizing antibody epitope and thus a target for vaccine design.**

Type 1 viral fusion machines, including HIV-1 envelope glycoprotein (Env), mediate virus entry through structural rearrangements that drive virus-cell membrane fusion (*1*–*3*). The hydrophobic N-terminal region of the gp41 transmembrane subunit (the fusion peptide), which is liberated by cleavage of the envelope precursor, is a critical element in this process because it directly interacts with the target-cell membrane in both intermediate and postfusion states (*1*–*3*). In the prefusion state, sequestration of the HIV-1 Env fusion peptide has been thought essential to avoid its being snared by the viral membrane or forming a hydrophobic aggregate with other fusion peptides. Published structures of trimeric HIV-1 Env in its prefusion closed state indicated a surface-exposed fusion peptide located in the membrane-proximal quartile of the viral spike (*4*–*6*); however, substantial disorder of the N-terminal portion of the fusion peptide in both antibody-bound and ligand-free crystal structures (*6*, *7*) made exposure of the fusion peptide unclear.

A chronically HIV-1–infected individual, donor N123 (*8*, *9*), displayed potent serum neutralization (fig. S1A); however, the epitope specificity of the serum-neutralizing antibodies could not be clearly categorized (fig. S1, B and C). We performed antigen-specific single memory B cell sorting with the BG505 SOSIP.664 trimer (*6*, *10*, *11*); among 92 antigen-specific B cells were 7 members of the clonal lineage N123-VRC34 (named for donor "N123" and antibody lineage "VRC34," with specific clone "x" referred to as VRC34."x") (Fig. 1A and fig. S2). The most potent member of the clonal family (VRC34.01) neutralized 16 out of 22 HIV-1 Env-pseudoviruses, including BG505 (fig. S3), and further neutralized 49% of 208 HIV-1 strains (fig. S4 and database S1). VRC34.01 and clonal members bound to BG505 SOSIP.664, but not BG505 gp120 monomer in enzyme-linked immunosorbent assay (ELISA) (Fig. 1B and fig. S5A), and VRC34.01-04, but not VRC34.05-07, bound to cell-surface BG505 trimer (fig. S5, B and C). In competition ELISA, VRC34.01 was partially inhibited by antibody PGT151 (*12*) (fig. S6), and on a panel of 28 glycan mutants of strain BG505, VRC34.01 displayed a profile distinct from PGT151 (fig. S7). VRC34.01 neutralization was reduced by elimination of the N88 glycan and was enhanced by glycan mutations N611Q and N611D. There was minimal effect on VRC34.01 neutralization when viruses were grown in the presence of glycosylation inhibitors kifunensine, swainsonine, or in GnTI$^{-/-}$ cells (fig. S8), suggesting that VRC34.01

[1]Vaccine Research Center, National Institute of Allergy and Infectious Diseases, National Institutes of Health, Bethesda, MD 20892, USA. [2]Department of Pharmaceutical Chemistry, University of California San Francisco, San Francisco, CA, USA. [3]Department of Integrative Structural and Computational Biology, The Scripps Research Institute, La Jolla, CA 92037, USA. [4]Center for HIV/AIDS Vaccine Immunology and Immunogen Discovery, The Scripps Research Institute, La Jolla, CA 92037, USA. [5]International AIDS Vaccine Initiative, Neutralizing Antibody Center, The Scripps Research Institute, La Jolla, CA 92037, USA. [6]HIV-Specific Immunity Section, Laboratory of Immunoregulation, National Institute of Allergy and Infectious Diseases, National Institutes of Health, Bethesda, MD 20892, USA. [7]Department of Microbial Pathogenesis, Yale University School of Medicine, New Haven, CT 06536, USA. [8]Department of Physiology and Biophysics, Weill Cornell Medical College of Cornell University, New York, NY 10021, USA. [9]Department of Immunology and Microbial Science, International AIDS Vaccine Initiative Neutralizing Antibody Center, Center for HIV/AIDS Vaccine Immunology and Immunogen Discovery, The Scripps Research Institute, La Jolla, CA 92037, USA. [10]Ragon Institute of Massachusetts General Hospital, Massachusetts Institute of Technology and Harvard University, Boston, MA 02142, USA. [11]International AIDS Vaccine Initiative, New York, NY 10038, USA.
*These authors contributed equally to this work. †Corresponding author. Email: pdkwong@nih.gov (P.D.K); jmascola@nih.gov (J.R.M)

Downloaded from http://science.sciencemag.org/ on May 12, 2016

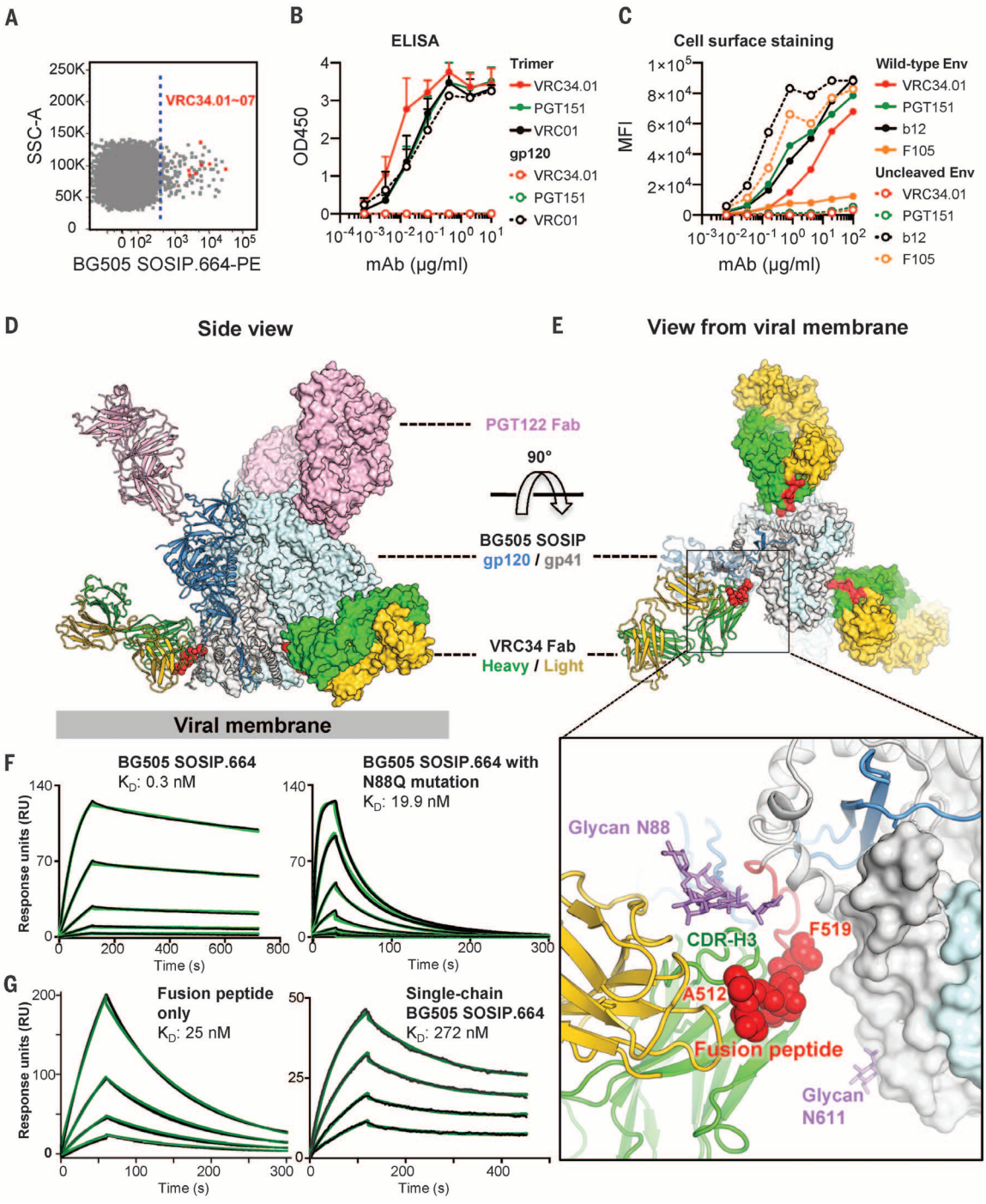


**Fig. 1. HIV-1-Env fusion peptide is targeted by antibody N123-VRC34.01.** (**A**) Flow cytometric sorting of $CD19^+/IgG^+/IgM^-$ B cells from donor N123 that bind the BG505 SOSIP.664-PE probe. Cells are shown in dot plot format, with events to the right of the dotted line sorted. Red dots indicate VRC34 lineage B cells; SSC, side scatter. (**B**) Antibody binding to BG505 SOSIP.664 trimer and gp120 monomer. Mean and SD of three independent experiments shown. (**C**) Antibody staining of 293T cells with surface expression of wild-type or uncleaved JR-FL Env trimer. MFI, median fluorescence intensity. Data are from one of three independent experiments. (**D** and **E**) Ternary complex crystal structure comprising Env trimer (BG505 SOSIP.664) and Fabs PGT122 and VRC34.01. One Env protomer and interacting Fabs is shown in ribbon representation; the rest of the complex is shown in surface representation, with the fusion peptide highlighted in red. (D) Side view. (E) View from the viral membrane. (Inset) An expanded view of the Env-VRC34.01 interface. The fusion peptide (red) and glycan N88 (purple) comprise the VRC34.01 epitope. N-terminal residues recognized by VRC34.01 depicted as red spheres and glycan N88 as purple sticks. (**F**) Fab VRC34.01 binding to BG505 SOSIP.664 trimer (left panel) and to a glycan N88 knock-out mutant (N88Q, right panel) measured by SPR. Three-fold serial dilutions from 200 nM Fab injected onto the captured trimers. (**G**) VRC34.01 binding to fusion peptide (left panel) and to single-chain BG505 SOSIP.664 trimer (right panel), as measured by SPR. Fab VRC34.01 Fab injected in two-fold serial dilutions starting from 128 nM (left panel) and 3200 nM (right panel). For (F) and (G), three independent experiments were performed, with data from one representative experiment shown. Black lines indicate experimental data and green lines global fit to a Langmuir 1:1 binding model.

Downloaded from http://science.sciencemag.org/ on May 12, 2016

recognition does not require complex glycosylation. Similar to PGT151 (*13*), VRC34.01 stained 293T cells expressing wild-type JR-FL Env, but not its uncleaved mutant (Fig. 1C). Overall, these results indicated that VRC34.01 targets a unique trimer-specific, cleavage-dependent epitope that involved glycan N88.

To define further VRC34 recognition, we crystallized a ternary complex formed by antigen-binding fragment (Fab) VRC34.01, BG505 SOSIP.664, and Fab PGT122, a glycan-V3–directed antibody (*4*, *6*, *14*). Diffraction data extended to 4.3 Å resolution, and we determined (*15*) and refined the ternary complex structure (Fig. 1D and table S1). Each gp120-gp41 protomer bound a single VRC34.01 Fab and a single PGT122 Fab (Fig. 1, D and E). VRC34.01 recognized an epitope in the gp120-gp41 interface consisting primarily of the fusion peptide on gp41 (residues 512 to 519, 55% interactive surface area) and glycan N88 on gp120 (26% interactive surface area) (Fig. 1E and table S2) (*16*).

The fusion peptide and glycan N88 formed a contiguous surface on HIV-1 Env, with the heavy and light chains of VRC34.01 oriented perpendicular to this surface, so that both heavy and light chains were involved in binding both fusion peptide and glycan N88 (Fig. 1E). The first eight residues of fusion peptide (*17*) were embedded in a hydrophobic groove formed by complementarity-determining regions (CDRs) H1, H2, H3, L1, and L3, consistent with VRC34.01 neutralization of strain BG505 being knocked out by site-directed mutations in this region (fig. S9) (*18*). Glycan N88 was recognized by a pocket formed by CDRs L1, L2, and H3 of VRC34.01 (fig. S10) (*19*). Surface plasma resonance (SPR) studies of the N88Q variant of BG505 SOSIP.664 indicated removal of glycan N88 to decrease VRC34.01 affinity from 0.3 nM to 19.9 nM (Fig. 1F). The ability of VRC34.01 to recognize the N88Q mutant with nM affinity indicated its interaction with fusion peptide to dominate the energetics of interaction; a more substantial decrease in affinity (to 272 nM) was observed with a single-chain version of BG505, indicating the charged N terminus to be critical in VRC34.01 recognition (Fig. 1G). Consistent with the ternary complex crystal structure, negative-stain electron microscopy (EM) of Fab VRC34.01 and BG505 SOSIP.664 trimer revealed a three-antibody to one-trimer stoichiometry (fig. S11).

We next cocrystallized Fab VRC34.01 with the N-terminal portion of the fusion peptide (residues 512 to 520). Diffraction data extended to 1.5 Å resolution, and we determined and refined the peptide-Fab structure (Fig. 2A and table S1). Well-defined electron density extended from 512 to 518, with the side chain of F519 partially ordered and residue L520 completely disordered (fig. S12). A shallow groove spanning all of the CDRs except L2 held the fusion peptide in extended conformation, with residues A512, V513, I515, and V518 fitting snugly into four hydrophobic pockets spanning the VRC34.01 paratope (Fig. 2A) (*20*). We also determined the ligand-free structure of VRC34.01 (table S1); no significant change in VRC34.01 paratope occurred upon fusion-peptide engagement (fig. S13).

About 50% of HIV-1 isolates tested were resistant to VRC34.01 (fig. S4 and database S1). This resistance could arise from structural or sequence variation. Because glycan N88 is conserved in 98.6% of HIV-1 sequences (*21*), we analyzed the fusion-peptide sequence of 3943 HIV-1 sequences (*22*), which identified variation at several residues (Fig. 2B). We individually introduced less prevalent residues into the fusion peptide of the BG505-Env pseudovirus and assessed VRC34.01 neutralization. Several mutants displayed diminished neutralization, and a Thr insertion at position 514b led to complete resistance to VRC34.01 (Fig. 2C). Notably, most mutations led to incomplete neutralization, which could be potentially explained by the inability of VRC34.01 to remain tightly bound to the fusion peptide throughout the HIV-1 entry process (*23*, *24*). We also analyzed the sequences and neutralization sensitivity of 208 Env-pseudoviruses. Two sequences lacked the glycosylation site at N88 and were resistant to VRC34.01 (database S2). The remaining 206 sequences, divided into three groups based on their fusion-peptide sequence (*25*), showed distinct VRC34.01 sensitivity (Fig. 2D and database S2). These results indicate that a dominant component of neutralization resistance to VRC34.01 stems from sequence variation of the fusion peptide, a corollary being that a majority of HIV-1 strains appear to be capable of assuming the solvent-exposed conformation of the fusion peptide observed in the VRC34.01-Env complex.

To delineate further the conformation of HIV-1 Env recognized by VRC34.01, we evaluated the interaction of VRC34.01 with cell-free virus and the contribution of this interaction to neutralization (Fig. 3A). These data indicated neutralization to be mediated primarily by binding to cell-free

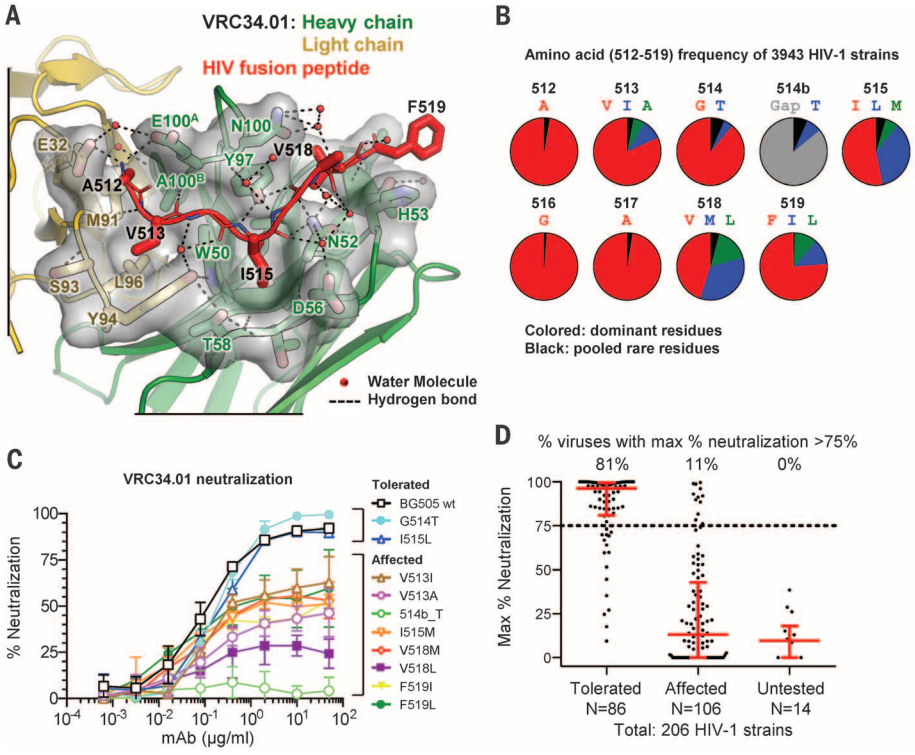


**Fig. 2. Fusion-peptide sequence variation is a dominant determinant of neutralization resistance to VRC34.01.** (**A**) Crystal structure of complex between Fab VRC34.01 and a synthetic fusion peptide (comprising residues 512 through 520, red) is shown in ribbon representation with interface residues as sticks and the molecular surface of VRC34.01-peptide interactive residues in gray. Hydrogen bonds are indicated by dotted lines. The side chains of $N52_{CDR\ H2}$ and $Y97_{CDR\ H3}$ were hydrogen-bonded with fusion peptide residue 515 to 517, and side chains of $E32_{CDR\ L1}$, $E100^{A}_{CDR\ H3}$ formed electrostatic interactions with the free amine group of residue A512, anchoring the N terminus of fusion peptide. The last residue of the synthetic fusion peptide with ordered electron density, F519, stacked with the side chain of $H53_{CDR\ H2}$. (**B**) Frequency of N-terminal amino acids of the fusion peptide. Red, most prevalent; blue, second-most prevalent; green, third-most prevalent; black, pooled rare residues; gray, sequence gap. (**C**) VRC34.01 neutralization of BG505 Env pseudoviruses containing fusion-peptide mutations. Variants displaying more than 75% neutralization at highest antibody concentration were termed "tolerated"; variants showing less than 75% neutralization were termed "affected." Mean and SD of three independent experiments are shown. (**D**) Maximum percentage neutralization by VRC34.01 against 206 HIV-1 Env pseudoviruses grouped according to their fusion-peptide sequences (*25*). Each dot represented one Env pseudovirus. Results were based on serial dilutions, starting at 50 µg/ml of VRC34.01. For each group, the percentage of viruses with a maximum neutralization greater than 75% is indicated on top, with the bar showing the median and interquartile range in red.

Downloaded from http://science.sciencemag.org/ on May 12, 2016

virus before cell surface attachment. Next we performed SPR assays to quantify VRC34.01 binding to soluble BG505 SOSIP.664 trimers (*10*), as well as a 201C-433C variant (DS-SOSIP.664), which had been disulfide-stabilized to prefer the prefusion closed Env conformation (*7*). VRC34.01 bound tightly to 2G12-captured SOSIP.664 and DS-SOSIP.664 trimers, as well as to CD4-Ig-captured DS-SOSIP.664 trimers (Fig. 3B and fig. S14). In contrast, VRC34.01 binding to CD4-captured SOSIP.664, which undergoes CD4-induced conformational opening, was substantially reduced. VRC34.01 thus appears to recognize a prefusion Env conformation before CD4-induced rearrangement.

We tested the ability of VRC34.01-bound BG505 SOSIP.664 to engage CD4 by preincubating the Env trimer with an excess of VRC34.01 and analyzed interactions with CD4-Ig or 2G12 by SPR. Preincubation with VRC34.01 showed little effect on CD4 engagement (Fig. 3C and fig. S15). Although VRC34.01 neutralized Env-pseudotyped JR-FL virions (Fig. 3A and fig. S16), incubation with these virions showed little effect on attachment to TZM-bl cells expressing surface CD4 (Fig. 3D). Single-molecule fluorescence resonance energy transfer (smFRET) of JR-FL Env molecules on native virions revealed VRC34.01 to increase the population of a partially open conformation (*24*), which is a required entry intermediate (Fig. 3E). This is in contrast to other broadly neutralizing antibodies that stabilize the prefusion closed conformation (*6*, *24*). We also tested the effect of VRC34.01 on the CD4-induced formation of

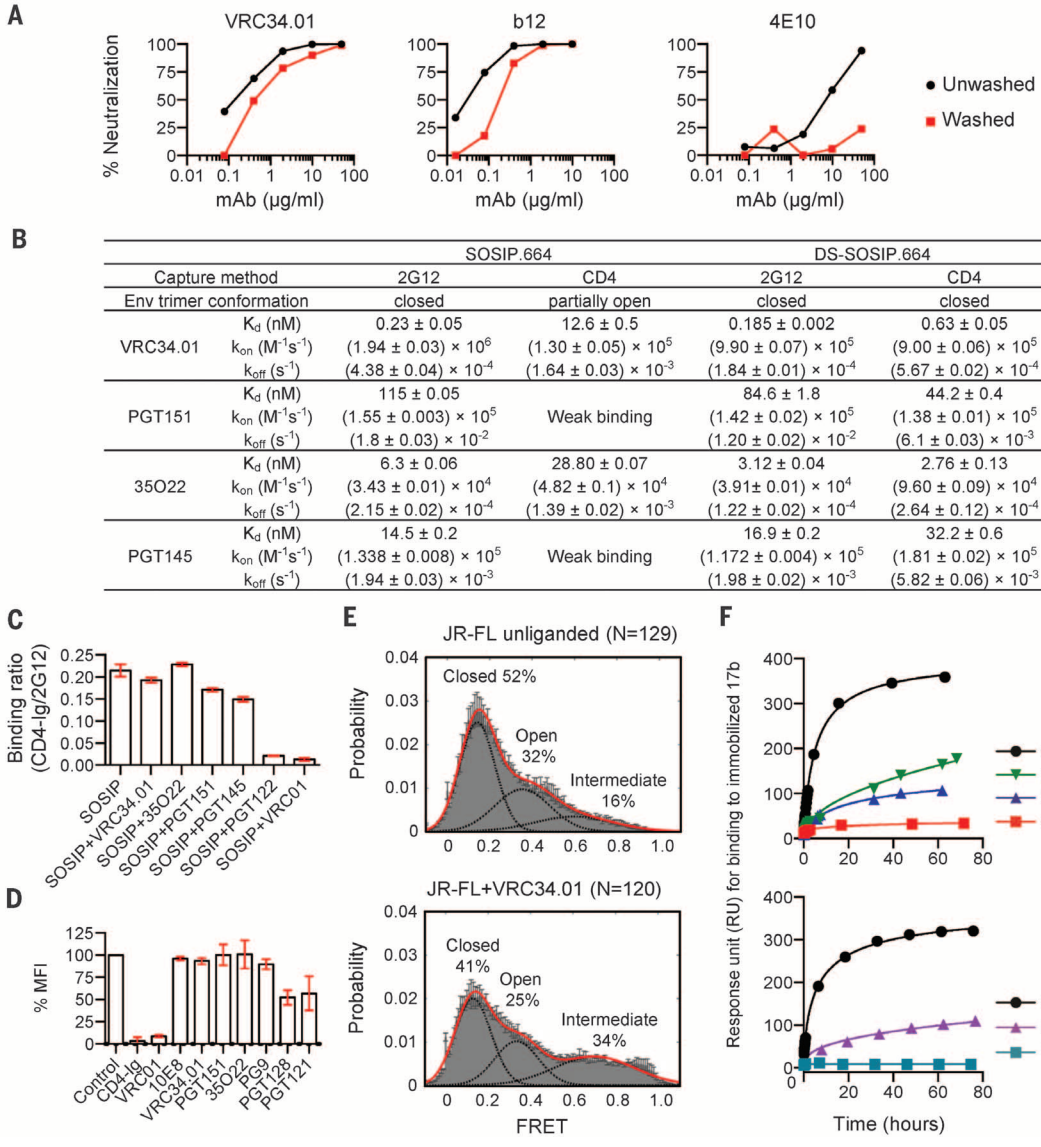


| | | SOSIP.664 | | DS-SOSIP.664 | |
|---|---|---|---|---|---|
| Capture method | | 2G12 | CD4 | 2G12 | CD4 |
| Env trimer conformation | | closed | partially open | closed | closed |
| VRC34.01 | $K_d$ (nM) | 0.23 ± 0.05 | 12.6 ± 0.5 | 0.185 ± 0.002 | 0.63 ± 0.05 |
| | $k_{on}$ ($M^{-1}s^{-1}$) | (1.94 ± 0.03) × $10^6$ | (1.30 ± 0.05) × $10^5$ | (9.90 ± 0.07) × $10^5$ | (9.00 ± 0.06) × $10^5$ |
| | $k_{off}$ ($s^{-1}$) | (4.38 ± 0.04) × $10^{-4}$ | (1.64 ± 0.03) × $10^{-3}$ | (1.84 ± 0.01) × $10^{-4}$ | (5.67 ± 0.02) × $10^{-4}$ |
| PGT151 | $K_d$ (nM) | 115 ± 0.05 | | 84.6 ± 1.8 | 44.2 ± 0.4 |
| | $k_{on}$ ($M^{-1}s^{-1}$) | (1.55 ± 0.003) × $10^5$ | Weak binding | (1.42 ± 0.02) × $10^5$ | (1.38 ± 0.01) × $10^5$ |
| | $k_{off}$ ($s^{-1}$) | (1.8 ± 0.03) × $10^{-2}$ | | (1.20 ± 0.02) × $10^{-2}$ | (6.1 ± 0.03) × $10^{-3}$ |
| 35O22 | $K_d$ (nM) | 6.3 ± 0.06 | 28.80 ± 0.07 | 3.12 ± 0.04 | 2.76 ± 0.13 |
| | $k_{on}$ ($M^{-1}s^{-1}$) | (3.43 ± 0.01) × $10^4$ | (4.82 ± 0.1) × $10^4$ | (3.91± 0.01) × $10^4$ | (9.60 ± 0.09) × $10^4$ |
| | $k_{off}$ ($s^{-1}$) | (2.15 ± 0.02) × $10^{-4}$ | (1.39 ± 0.02) × $10^{-3}$ | (1.22 ± 0.02) × $10^{-4}$ | (2.64 ± 0.12) × $10^{-4}$ |
| PGT145 | $K_d$ (nM) | 14.5 ± 0.2 | | 16.9 ± 0.2 | 32.2 ± 0.6 |
| | $k_{on}$ ($M^{-1}s^{-1}$) | (1.338 ± 0.008) × $10^5$ | Weak binding | (1.172 ± 0.004) × $10^5$ | (1.81 ± 0.02) × $10^5$ |
| | $k_{off}$ ($s^{-1}$) | (1.94 ± 0.03) × $10^{-3}$ | | (1.98 ± 0.02) × $10^{-3}$ | (5.82 ± 0.06) × $10^{-3}$ |

**Fig. 3. VRC34.01 engages prefusion closed HIV-1 Env and inhibits CD4-induced rearrangements.** (**A**) Neutralization of JR-FL by indicated antibodies in which parallel virus-antibody mixtures were either pelleted and unbound antibody removed (washed, red lines) or not pelleted and antibody not removed (unwashed, black lines) before infection of TZM-bl cells. Representative data from one of three independent experiments are shown. The mean and SD inhibitory concentration ($IC_{50}$ and $IC_{80}$) values are shown in table S3. (**B**) Affinity of interaction of indicated antibodies with BG505 SOSIP.664 (*10*) or stabilized DS-SOSIP.664 (*7*). Standard errors from global fit of sensorgrams, obtained from independent injections of different concentrations of analyte, to a 1:1 Langmuir binding model are reported. Data sets are representative of at least two independent experiments. (**C**) Binding of BG505 SOSIP.664 to CD4, either alone or in the presence of antibodies (*36*). Mean and SD of three independent experiments are shown. (**D**) Influence of antibody on virus-cell attachment (*37*). Mean % MFI and SD of four independent experiments are shown. (**E**) smFRET analysis of VRC34.01 incubation with JR-FL Env on native virions shows an increase in the high-FRET state, which is associated mechanistically with a required intermediate in the HIV-1 entry pathway (*24*, *38*). *N* is the number of FRET traces analyzed. (**F**) Influence of antibody on the CD4-induced activation of BG505 SOSIP.664. Activation of SOSIP was monitored by assessing binding to the CD4-induced antibody, 17b, at different time points (*39*). Representative data of three independent experiments are shown.

Downloaded from http://science.sciencemag.org/ on May 12, 2016

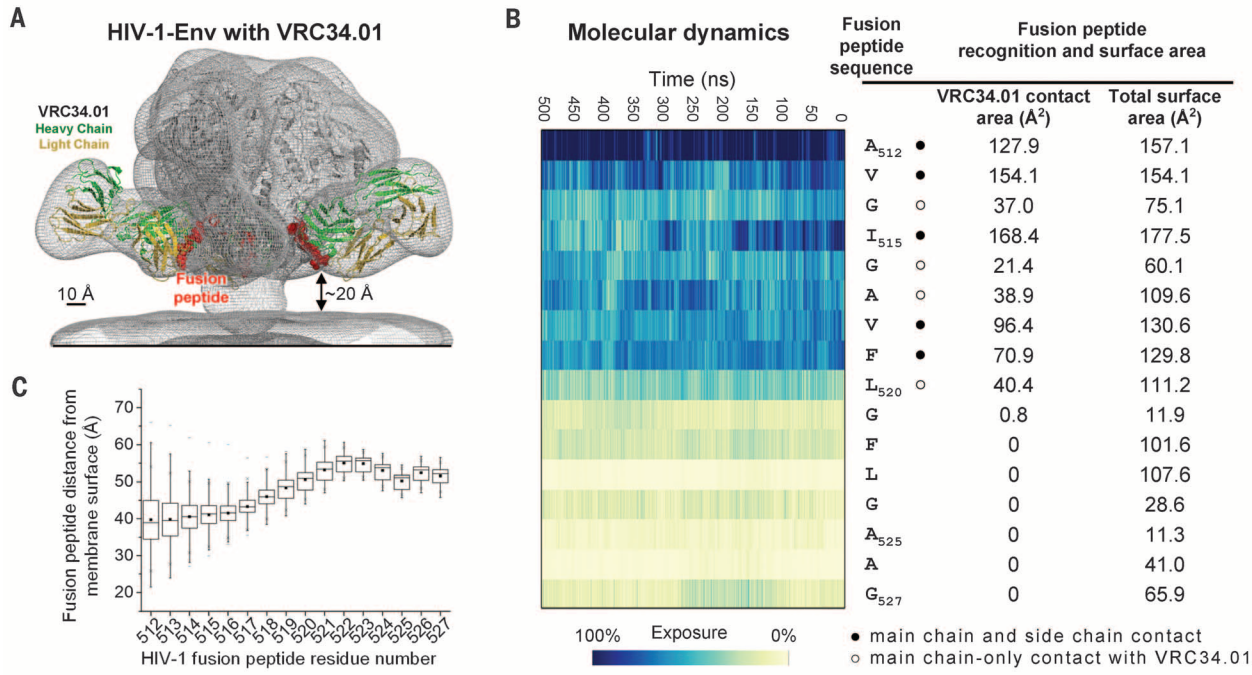


**Fig. 4. Fusion peptide accessibility and position relative to viral membrane.** (**A**) Superposed EM map of the BG505 SOSIP.664-VRC34.01 complex and that of HIV-1 Env trimers reconstructed from their membrane-bound context (EMDB 5019 and 5022) (gray meshes). Fab VRC34.01 bound to BG505 SOSIP.664, as extracted from the ternary complex crystal structure, was docked and shown in ribbon representation with VRC34.01-contacting fusion peptide (512 to 519) in red spheres. (**B**) Fusion peptide in the context of a molecular dynamic simulation of fully glycosylated HIV-1 Env trimer. The degree of solvent exposure of each residue in the fusion peptide is depicted on a blue-to-yellow color scale, with antibody-contact surface and total surface area shown for context. (**C**) Range of distance to the viral membrane for each residue of the HIV-1 fusion peptide over the course of the molecular dynamics simulation. The median distance for each residue is represented as a horizontal line in each box. The mean value is represented as a small filled box. The height of each box is set by the 25th and 75th interquartile range, and the whiskers are determined by the 5th and 95th percentiles. The minimum and maximum distances for each residue over the length of the simulation is represented as "x." See fig. S23 for an analysis of immune recognition of fusion peptide in other type 1 viral fusion machines.

bridging sheet, which is required for co-receptor binding and virus entry (*26*, *27*). We observed the CD4-induced formation of the bridging sheet formation—as detected by binding to antibody 17b—to be substantially inhibited by VRC34.01 (Fig. 3F and fig. S17). These results indicate that VRC34.01 recognizes cell-free virus and is able to engage the prefusion closed state while stabilizing Env in an intermediate state; VRC34.01 thus appears not to interfere with virus attachment to cell surface CD4 but to inhibit CD4-induced formation of the bridging sheet (*26*), which is required for co-receptor engagement and viral entry.

We docked the VRC34.01-SOSIP.664 complex into EM-observed electron density (*28*), which positioned the N terminus of the fusion peptide ~20 Å from the membrane (Fig. 4A). We carried out molecular dynamics simulations (*29*) over 500 ns on fully glycosylated BG505 SOSIP.664 with fusion peptide initially in the VRC34.01-bound conformation (Fig. 4B and fig. S18) (*30*); this analysis indicated residues 512 to 520 of the fusion peptide to be solvent-exposed, with the exposed residue range coinciding closely with the epitope recognized by VRC34.01 (Fig. 4B and fig. S18). Despite this flexibility, a 20 Å approach to the viral membrane (Fig. 4C), and intrinsic prefusion motion of HIV-1 Env (*24*), there did not seem to be an issue with the fusion peptide being trapped by the viral membrane or inducing trimer aggregation (*31*).

VRC34.01 antibody recognition of the fusion peptide is shared to a limited degree by antibody PGT151, which binds in the vicinity of VRC34.01 (figs. S9 and S11). To provide further insight into the antibody-specific recognition of the fusion peptide during HIV-1 infection, we designed a VRC34-epitope scaffold (*32*, *33*) (fig. S19 and database S3). This scaffold was used to assess 24 sera from a cohort of HIV-1–infected subjects. Ten sera displayed specific recognition of the fusion peptide (figs. S20 and S21), with four sera showing reduced neutralization when a fusion peptide–specific mutation G516A was introduced (fig. S22).

In summary, the N terminus of the fusion peptide on HIV-1 is antibody-accessible, binding and neutralizing antibodies against it are elicited during natural infection, and broadly neutralizing antibodies recognize it either partially (antibody PGT151) (*34*, *35*) or more completely (antibody VRC34.01). Taken together, our results indicate the fusion peptide of the Env trimer to be a region of interest for vaccine design against HIV-1.

## REFERENCES AND NOTES


1. P. M. Colman, M. C. Lawrence, *Nat. Rev. Mol. Cell Biol.* **4**, 309–319 (2003).
2. D. M. Eckert, P. S. Kim, *Annu. Rev. Biochem.* **70**, 777–810 (2001).
3. S. C. Harrison, *Nat. Struct. Mol. Biol.* **15**, 690–698 (2008).
4. J. P. Julien *et al.*, *Science* **342**, 1477–1483 (2013).
5. D. Lyumkis *et al.*, *Science* **342**, 1484–1490 (2013).
6. M. Pancera *et al.*, *Nature* **514**, 455–461 (2014).
7. Y. D. Kwon *et al.*, *Nat. Struct. Mol. Biol.* **22**, 522–531 (2015).
8. N. A. Doria-Rose *et al.*, *J. Virol.* **84**, 1631–1636 (2010).
9. N. A. Doria-Rose *et al.*, *J. Virol.* **83**, 188–199 (2009).
10. R. W. Sanders *et al.*, *PLOS Pathog.* **9**, e1003618 (2013).
11. D. Sok *et al.*, *Proc. Natl. Acad. Sci. U.S.A.* **111**, 17624–17629 (2014).
12. C. Blattner *et al.*, *Immunity* **40**, 669–680 (2014).
13. E. Falkowska *et al.*, *Immunity* **40**, 657–668 (2014).
14. L. M. Walker *et al.*, *Nature* **477**, 466–470 (2011).
15. A. J. McCoy *et al.*, *J. Appl. Crystallogr.* **40**, 658–674 (2007).
16. Residue number for HIV-1 Env follows the standard HXB2 convention (www.hiv.lanl.gov/content/sequence/HIV/REVIEWS/HXB2.html).
17. VRC34.01-bound portions of fusion peptide (residues 512 to 517) were disordered in previous HIV-1 Env structures, whereas residues 518 to 530 were ordered in the PGT122-35O22–bound HIV-1 structure (PDB ID 4TVP) and assumed the same conformation as in the VRC34.01-bound structure (0.19 Å root mean square deviation).
18. Residues 512 to 519 (which correspond to the N terminus of the fusion peptide and are recognized by VRC34.01) do not interact with other portions of the HIV-1 Env. Residues 520 to 530 of the fusion peptide are embedded in a groove defined by gp41 residues 533 to 543 and 627 and by gp120 residues 45, 84 to 89, 492, and glycan N88.
19. Antibody residue numbers follow Kabat convention, and, for clarity, heavy-chain residues are followed by an "HC" subscript and light-chain residues by an "LC" subscript. In some cases, the CDR loops are specified to provide further clarity.
20. The pocket for A512 is defined by $E32_{CDR\ L1}$, $M91_{CDR\ L3}$, $E100^{A}_{CDR\ H3}$, and $A100^{B}_{CDR\ H3}$; the pocket for V513 is defined by $S93_{CDR\ L3}$, $Y94_{CDR\ L3}$, $W50_{CDR\ H2}$, and $A100^{B}_{CDR\ H3}$; the pocket for I515 is defined by $A33_{CDR\ H1}$, $W50_{CDR\ H2}$, $I51_{CDR\ H2}$,


Downloaded from http://science.sciencemag.org/ on May 12, 2016

$N52_{CDR\ H2}$, and $Y97_{CDR\ H3}$; and the pocket for V518 is defined by $G31_{CDR\ H1}$, $N52_{CDR\ H2}$, and $Y97_{CDR\ H3}$.
21. J. Huang *et al.*, *Nature* **515**, 138–142 (2014).
22. Sequences of 3943 HIV-1 strains were downloaded from the HIV database (www.hiv.lanl.gov/content/index).
23. P. D. Kwong *et al.*, *Nature* **420**, 678–682 (2002).
24. J. B. Munro *et al.*, *Science* **346**, 759–763 (2014).
25. The following nomenclature is used: "Tolerated" Env sequences contained one or more mutations within the eight residue fusion-peptide sequence, which individually showed little effect on VRC34.01 neutralization. "Affected" sequences contained one or more residues (513I, 513A, 514b_T, 515M, 518M, 518L, 519I, or 519L) that diminished VRC34.01 neutralization. "Untested" sequences contained one or more untested residues plus tolerated residues.
26. P. D. Kwong *et al.*, *Nature* **393**, 648–659 (1998).
27. A. Trkola *et al.*, *Nature* **384**, 184–187 (1996).
28. J. Liu, A. Bartesaghi, M. J. Borgnia, G. Sapiro, S. Subramaniam, *Nature* **455**, 109–113 (2008).
29. M. J. Harvey, G. Giupponi, G. D. Fabritiis, *J. Chem. Theory Comput.* **5**, 1632–1639 (2009).
30. While 500 ns is not enough time to sample large-scale conformational transitions associated with the prefusion HIV-1 Env trimer, it should be sufficient to assess local motions of the fusion peptide.
31. When trimers are positioned into nearest-neighbor contact, only the N-terminal three residues of the fusion peptide can extend to contact a fusion peptide on a neighboring trimer. The N-terminal three residues of the fusion peptide are Ala-Val-Gly. Although the Ala-Val are somewhat hydrophobic, the positive charges of two N termini likely repel, preventing aggregation. In terms of close-by glycans, these may help to prevent aggregation, especially glycans N88, N611, and N618. However, it appears to be primarily the recessed nature of the fusion peptide, coupled to the fact that only eight residues of the fusion peptide are flexible (Fig. 4), that prevents aggregation.
32. Materials and methods are available as supplementary materials on *Science* Online.
33. M. Pancera *et al.*, *Nat. Struct. Mol. Biol.* **20**, 804–813 (2013).
34. J. H. Lee, G. Ozorowski, A. B. Ward, *Science* **351**, 1043–1048 (2016).
35. The structure of PGT151 in complex with HIV-1 Env was recently reported (*34*). This structure shows PGT151 to recognize the fusion peptide in an exposed, extended conformation.
36. Trimer (or trimer-antibody complex) was injected for 60 s onto CD4-IgG (immunoglobulin G) captured on a Biacore CM5 chip coated with a monoclonal mouse anti-human IgG (Fc) antibody (GE Healthcare), and binding responses were measured 60 s after the injection ended. Binding to CD4-Ig normalized with binding to antibody 2G12, which was measured similarly on a parallel-flow cell.
37. TZM-bl cells were incubated with JR-FL Env pseudovirus in the presence of antibodies at 50 μg/ml or medium control and then stained with biotinylated 2G12 followed by phycoerythrin (PE)-conjugated streptavidin. MFI was obtained from at least 10,000 cell events and normalized to the medium control.
38. The HIV Env trimer is conformationally dynamic. Binding and smFRET experiments show that VRC34 do not bind to the open co-receptor binding-competent conformation. Thus, any molecule spontaneously in that conformation would not be neutralized. The conformation specificity of VRC34.01 for the closed and intermediate conformation may explain the observed incomplete neutralization.
39. Specifically, soluble SOSIP.664 trimers were incubated with soluble, two-domain CD4, either alone or following preincubation with Fab, and the incubated trimer samples were injected over a 17b-coupled surface for 30 s, with response units reported 10 s after the injection ended.

### ACKNOWLEDGMENTS

We thank the members of the Flow Cytometry Core, Vaccine Research Center, and especially R. Nguyen for his assistance in cell sorting. We thank members of the Structural Biology Section, Structural Bioinformatics Core Section, and Human Immunology Section, Vaccine Research Center, for discussions and comments on the manuscript. We thank J. Baalwa, D. Ellenberger, F. Gao, B. Hahn, K. Hong, J. Kim, F. McCutchan, D. Montefiori, L. Morris, J. Overbaugh, E. Sanders-Buell, G. Shaw, R. Swanstrom, M. Thomson, S. Tovanabutra, C. Williamson, and L. Zhang for contributing the HIV-1 Envelope plasmids used in our neutralization panel. The data presented in this manuscript are tabulated in the main paper and in the supplementary materials. Nucleotide sequences of VRC34.01-VRC34.07 variable regions are available under GenBank accession numbers KU711816 to KU711829. Atomic coordinates and structure factors of the reported crystal structures have been deposited with the Protein Data Bank (PDB) under accession codes 5I8C, 5I8E, and 5I8H. EM data have been deposited with the Electron Microscopy Data Bank under accession code EMD-8125. Support for this work was provided by the Intramural Research Programs of the Vaccine Research Center and Division of Intramural Research, National Institute of Allergy and Infectious Diseases (NIAID), National Institutes of Health, and from the International AIDS Vaccine Initiative's (IAVI's) Neutralizing Antibody Consortium. IAVI's work is made possible by support from many donors, including the Bill & Melinda Gates Foundation, the Ministry of Foreign Affairs of Denmark, Irish Aid, the Ministry of Finance of Japan, the Ministry of Foreign Affairs of the Netherlands, the Norwegian Agency for Development Cooperation (NORAD), the UK Department for International Development (DFID), and the U.S. Agency for International Development (USAID). The full list of IAVI donors is available at www.iavi.org. S.C.B. was supported by NIH grants R01GM079238 and P01GM56550. W.M. was supported by NIH grants R01GM116654 and P01GM56550. Use of sector 22 (Southeast Region Collaborative Access team) at the Advanced Photon Source was supported by the U.S. Department of Energy, Basic Energy Sciences, Office of Science, under contract number W-31-109-Eng-38. The following patent applications are pending: U.S. Patent Application 13/202,351, Methods and Compositions for Altering Photopysical Properties of Fluorophores via Proximal Quenching (S.C.B.); U.S. Patent Application 14/373,402 Dye Compositions, Methods of Preparation, Conjugates Thereof, and Methods of Use (S.C.B.); and International and U.S. Patent Application PCT/US13/42249 Reagents and Methods for Identifying Anti-HIV Compounds (S.C.B. and W.M.). S.C.B. holds an equity interest in Lumidyne Technologies Corporation.

### SUPPLEMENTARY MATERIALS

www.sciencemag.org/content/352/6287/828/suppl/DC1
Materials and Methods
Figs. S1 to S23
Tables S1 to S3
Databases S1 to S3
References (*40*–*68*)

10 December 2015; accepted 30 March 2016
10.1126/science.aae0474

ORIGIN OF LIFE

# A high-yielding, strictly regioselective prebiotic purine nucleoside formation pathway

**Sidney Becker,* Ines Thoma,* Amrei Deutsch, Tim Gehrke, Peter Mayer, Hendrik Zipse, Thomas Carell†**

**The origin of life is believed to have started with prebiotic molecules reacting along unidentified pathways to produce key molecules such as nucleosides. To date, a single prebiotic pathway to purine nucleosides had been proposed. It is considered to be inefficient due to missing regioselectivity and low yields. We report that the condensation of formamidopyrimidines (FaPys) with sugars provides the natural *N*-9 nucleosides with extreme regioselectivity and in good yields (60%). The FaPys are available from formic acid and aminopyrimidines, which are in turn available from prebiotic molecules that were also detected during the Rosetta comet mission. This nucleoside formation pathway can be fused to sugar-forming reactions to produce pentosides, providing a plausible scenario of how purine nucleosides may have formed under prebiotic conditions.**

It is assumed that life originated from a simple set of small molecules. These prebiotic molecules can be found on comets and as components of Earth's early atmosphere (*1*, *2*). The RNA-world hypothesis (*3*, *4*) posits that these molecules assembled to produce nucleosides, and later informational polymers, which are able to replicate themselves. A prebiotically plausible route to pyrimidine nucleosides provides these key building blocks in a stepwise reaction sequence in high yields (*5*). The situation is less clear for the purine nucleosides, which are not only central components of DNA and RNA but also constituents of adenosine triphosphate and guanosine triphosphate and substructures in many coenzymes (*6*).

Presently, the only prebiotic route to purine nucleosides proposes the condensation of the complete nucleobase, such as adenine (**1**, $R^1$ = $NH_2$, $R^2$ = H), with ribose **2** in the molten state (Fig. 1A) (*7*). This reaction provides complex mixtures of purine ribosides with yields of about 4% for adenosine (β-fA). The reaction needs adenine **1** as its hydrochloride salt and subsequent equilibration of the mixture under basic ($NH_4OH$) conditions (*8*). Because many of the N atoms of the purine skeleton can react, a regioselectivity problem is encountered, which is responsible for the low yields. In addition, the *N*-9 atoms of the purine heterocycles, which connect the nucleobase with the sugar in canonical purine ribosides, are particularly unreactive. This, together with the fact that the purine heterocycles themselves are available only in low yields under prebiotic

Ludwig-Maximilians-Universität München, Department für Chemie, D-81377 Munich, Germany.
*These authors contributed equally to this work.
†Corresponding author. Email: thomas.carell@cup.uni-muenchen.de

Downloaded from http://science.sciencemag.org/ on May 12, 2016

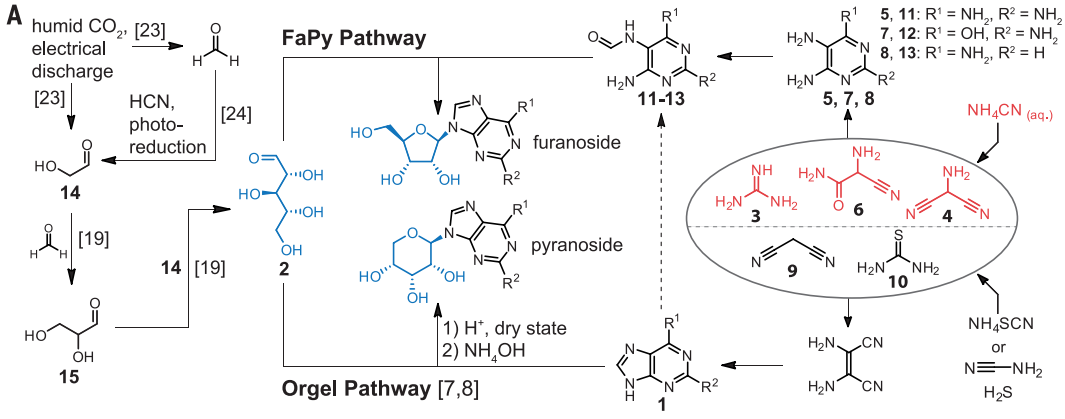


**Fig. 1. Prebiotic pathways to purine ribosides.** (**A**) The FaPy pathway starts with the formamidopyrimidines **11** to **13**, which are prebiotically available from simple starting materials (encircled) via multi-aminopyrimidines. The molecules in red are derived directly from $NH_4CN$. For comparison, Orgel's pathway is shown involving coupling of the full nucleobases. Ribose is generated from glycolaldehyde and formaldehyde, formed from an early atmosphere containing humid $CO_2$ (left). (**B**) Nitrogen reactivity analysis of the multi-aminopyrimidines and crystal structure of the monoprotonated 4,5,6-triaminopyrimidine **8** with bond length and the bond angles of the critical amino groups.

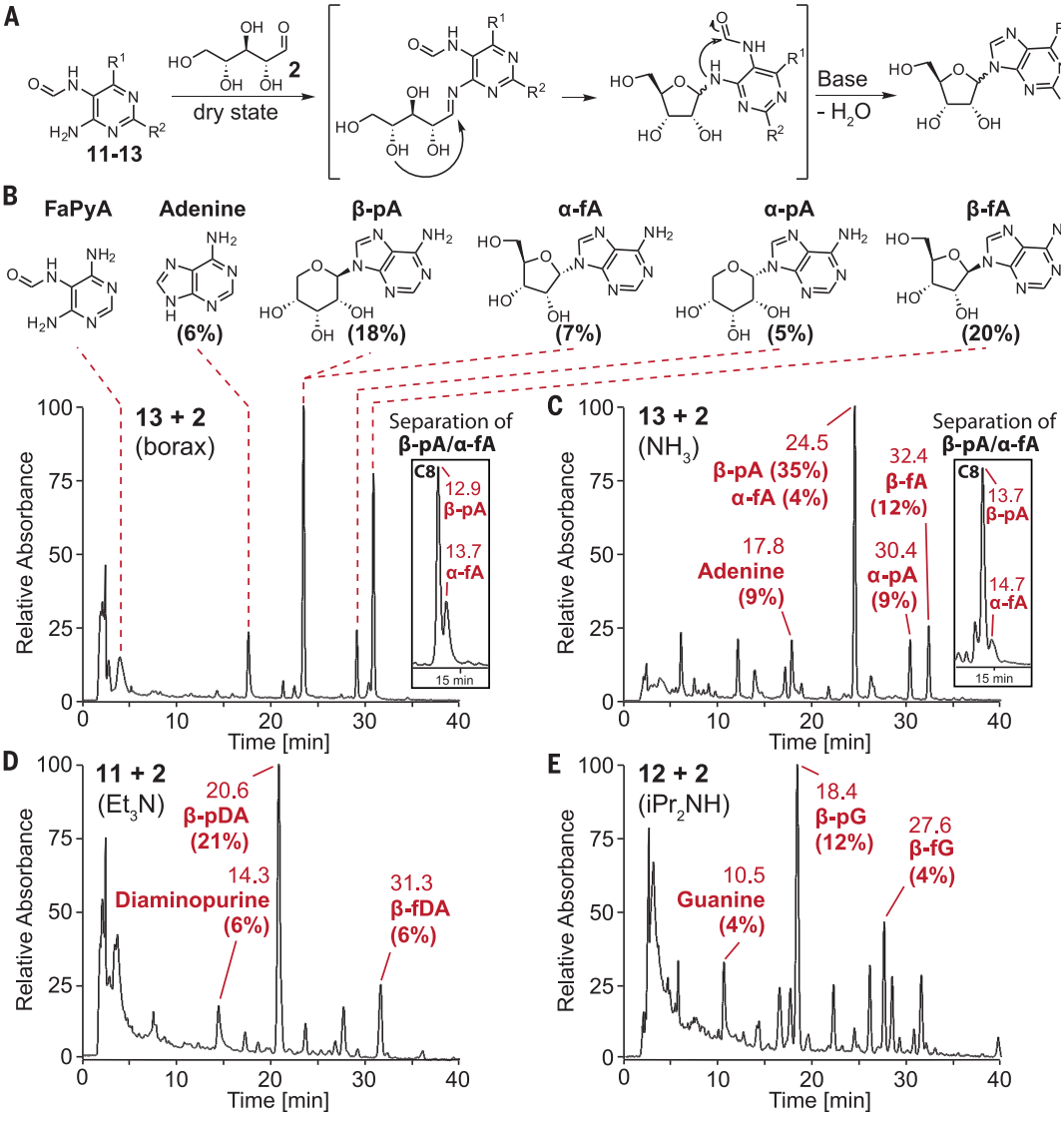


**Fig. 2. Formation of the purine ribosides.** The FaPy pathway provides pyranosides (p) and furanosides (f) as α- and β-isomers (A, adenine; DA, diaminopurine; G, guanine). (**A**) Mechanism of the FaPy pathway. (**B**) Depiction of the formed products analyzed by HPLC [ultraviolet (UV) detection] of the reaction of **13** ($R^1$, $NH_2$; $R^2$, H) with ribose **2**, followed by treatment with either borax (0.125 M at 100°C for 2 days) or (**C**) $NH_3$ (0.5 M for 7 days). (**D**) Reaction of **11** ($R^1$, $NH_2$; $R^2$, $NH_2$) with ribose **2**, followed by heating in $Et_3N$ (0.5 M for 14 days). (**E**) Reaction of **12** ($R^1$, OH; $R^2$, $NH_2$) with ribose **2** and subsequent heating in $iPr_2NH$ (0.5 M for 12 days).

Downloaded from http://science.sciencemag.org/ on May 12, 2016

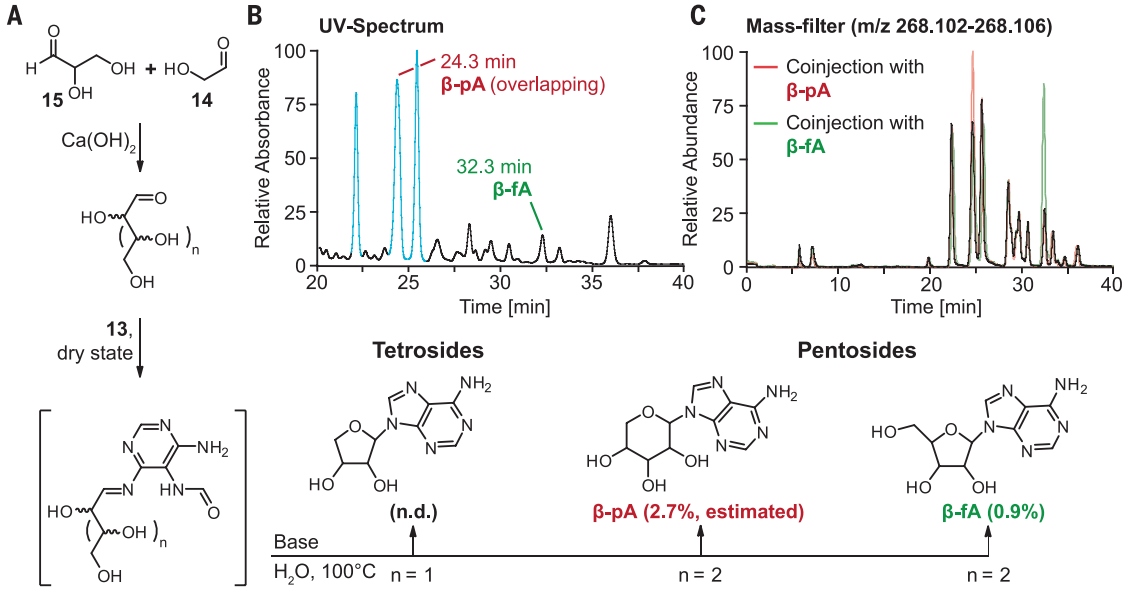


**Fig. 3. Prebiotic formation of purine ribosides from sugar precursors.** (**A**) Glycolaldehyde **14** and glyceraldehyde **15** react in the presence of $Ca(OH)_2$ and formamidopyrimidine **13** to tetrosides and pentosides. (**B**) HPLC analysis (UV detection) of the reaction. The four main peaks (light blue, peak at 24.30 min, two peaks overlapping) are the α- or β-pyranosyl isomers of the aldopentoses (arabinose, lyxose, ribose, and xylose). (**C**) Detection of the purine pentosides by HPLC-MS with a specific mass filter and coinjection of synthetic material.

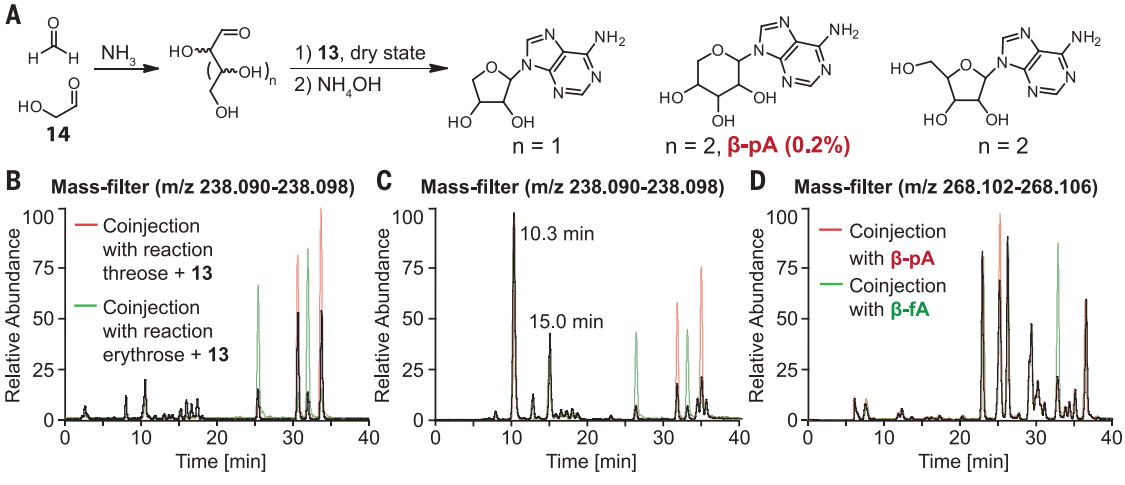


**Fig. 4. Prebiotic formation of purine nucleosides in a formose-type reaction.** (**A**) Reaction scheme. (**B**) Detection of the α/β-purine tetroside from HCHO (0.21 M) and glycolaldehyde (0.4 M) by HPLC-MS and coinjection (red, threoside; green, erythroside). (**C**) Increased concentrations of HCHO (2.1 M) and glycolaldehyde (4 M) results in increased formation of two unidentified side products at 10.26 and 14.99 min with decreasing tetroside yields. (**D**) Same reaction conditions as (C) produced more pentosides ($n$ = 2) compared with tetrosides ($n$ = 1). The β-pA (0.2%) and β-fA were identified by coinjection.

conditions (0.5%) (*9*, *10*), prompted us to search for an alternative prebiotic pathway (Fig. 1A, FaPy pathway).

The FaPy pathway starts from aminopyrimidines, which are accessible from simple molecules such as $NH_4CN$ under prebiotically plausible conditions. Guanidine **3** (available from cyanamide and $NH_3$), for example reacts, with the HCN trimer aminomalononitrile **4** to produce tetraaminopyrimidine **5** (72%) (*11*). Despite the high nitrogen content of such molecules, they are very robust. The aminopyrimidines are often electron rich and hence readily oxidized in an oxygen-containing atmosphere but stable in the absence of oxygen (*2*). Other amino-substituted pyrimidines may have been formed when the HCN trimer **4** is hydrolyzed in the presence of formaldehyde, to produce aminocyanoacetamide **6** (*12*), which reacts with guanidine **3** to produce triaminopyrimidinone **7** (53%) (*12*). Finally, triaminopyrimidine **8** is available by condensation of malononitrile **9** with thiourea **10** (84%) (*13*), followed by nitrosation in water and desulfuration (Ni and $H_2$ or HCOOH) (see the supplementary materials) (*14*). Thiourea **10** is prebiotically available via addition of $H_2S$ to cyanamide or directly from ammonium thiocyanate (*15*). The so-formed aminopyrimidines (**5**, **7**, **8**) feature, in contrast to the purines, high solubility in water.

Although the aminopyrimidines **5**, **7**, and **8** feature multiple nucleophilic positions, a deeper reactivity analysis and symmetry relations uncover a proton-assisted reactivity guidance (red, green, and blue N atoms in Fig. 1B) that eliminates the regioselectivity problem. The two in-ring N atoms (red, Fig. 1B) are due to the present exocyclic amino groups unusually basic ($pK_a$ ~ 7.5), which leads to monoprotonation already under slightly acidic conditions. Due to the symmetry of the molecules, protonation of either one of the two-ring N atoms blocks the reactivity of the exocyclic amino groups (2, 4, and 6, in blue, Fig. 1B) in ortho- and para-position. As such, the proton serves as a protecting group for most amines on the ring structure, leaving only the *N*-5 amino group (green, Fig. 1B) nucleophilic. To support this analysis, we crystallized monoprotonated triaminopyrimidine **8**. Structural analysis shows short C–N bonds (1.33 Å) and planar geometry for amino groups 4 and 6, allowing full conjugation with the electron-deficient pyrimidine ring. In contrast, the *N*-5 amino group (green, Fig. 1B) has a longer C–N bond (1.41 Å) and pyramidal geometry (109°), hence showing increased $sp^3$ character, which results in a nucleophilic lone pair oriented at an angle of 65° to the ring plane.

When we heated aminopyrimidines **5**, **7**, and **8** with formic acid or formamide, we obtained—in agreement with this analysis—in all cases

Downloaded from http://science.sciencemag.org/ on May 12, 2016

regioselectively just the *N*-5 formylated FaPy product (**11** to **13**, Fig. 1A) in excellent yields (70 to 90%). Formylation provides the C1 unit needed for later purine formation. It also acts as a protecting group for the 5-$NH_2$ group. The amino groups 2, 4, and 6 are now, under neutral conditions, available for a condensation reaction with a sugar. The amino groups in ortho position to the formamide are symmetry-related by a C2 axis (in **11** and **13**), which eliminates the second regioselectivity problem. Reaction of either one with ribose provides the same product. Indeed, when we reacted the formamides **11** to **13** with ribose **2**, followed by stirring of the mixture under slightly basic conditions, we obtained in all cases regioselectively only the *N*-9–reacted α/β-furanosides and α/β-pyranosides (Fig. 2). To assign the high-performance liquid chromatography and mass spectrometry (HPLC-MS)–detected compounds, we synthesized all expected α- and β-pyranosides and furanosides (Fig. 2 and supplementary materials) and performed coinjection studies. To further support the data regarding adenosine, we also isolated this compound (β-fA) by HPLC and confirmed the correct structure by nuclear magnetic resonance (fig. S1). The β- and not the α-anomers are observed as the main products in all experiments. The reaction mechanism involves condensation of FaPy compounds **11** to **13** with ribose to produce an imine intermediate, followed by sugar-ring closure to produce the FaPy ribosides. The following second-cyclization reaction under mild basic conditions provides the purine skeleton (Fig. 2A). This cyclization can occur even without previous reaction with the sugar, which generates the corresponding (sugar-free) nucleobase as a side product. The formed heterocycles can, however, be prebiotically recycled. Formamide in the presence of $TiO_2$ or, alternatively, riboflavin in the presence of light was shown to allow degradation of the purines back into the corresponding FaPy compounds (Fig. 1A and fig. S2) (*16*, *17*).

We studied purine nucleoside synthesis in detail and found that slightly basic conditions gave the highest yields. Reaction of **13** with **2** in pure ammonia solutions (0.5 M) provided the main purine nucleosides β-pyranosyladenosine (β-pA) (35%) and β-fA (12%) in good yields, although ammonia will certainly react with ribose as well (Fig. 2C). We found that the presence of basic amino acids (0.5 M) (fig. S3, A and B) instead of ammonia, such as lysine (β-pA, 13% and β-fA, 4%) and arginine (β-pA, 22% and β-fA, 6%), gave satisfactory yields as well. Good yields were also obtained when we used borax. In this case, the FaPy building block **13** reacted with ribose **2** (Fig. 2B) to produce mainly furanosides (*18*) with the canonical β-adenosine (β-fA) formed as the main product (20%). Similar results were obtained with a carbonate/borate buffer (*19*). Under these conditions, the yields for β-pA and β-fA were 15% and 18%, respectively (fig. S3C). Silicate buffers, reported to stabilize pentoses, however, failed in our hands (*20*). The FaPy pathway also provides direct access to diaminopurine and guanine ribosides upon reaction of FaPy building block **11** (Fig. 2D) and **12** (Fig. 2E) with ribose **2**. Although we did not optimize the reaction conditions for these nucleosides, the purine β-furanosides are obtained in yields between 4 and 6% when the reaction is equilibrated with alkylamines. The reaction of **11** with **2** directly provides some guanosine via hydrolysis of the diaminopurine moiety. Formation of the alternative hydrolysis product isoguanosine was not observed (*21*, *22*). Importantly, the FaPy pathway provides canonical β-adenosine in yields of up to 20%. The highest total yields for *N*-9 ribosides of up to 60% was achieved using simple amines as bases that were also discovered on comet 67P/Churyumov-Gerasimenko (Fig. 2, B to E) (*1*).

We next asked whether the FaPy pathway can be linked to potential prebiotic sugar syntheses (Fig. 3). An attractive route involves the formaldehyde and glycolaldehyde **14**–based formose reaction, e.g., as a mineral-guided version (*19*). Formaldehyde and small amounts of **14** are both formed by electrical discharge of humid $CO_2$ (*23*). The formed formaldehyde can further react with HCN by photoreduction to produce **14** (*24*). A central reaction in the mineral-guided sugar formation is an aldol addition of **14** with formaldehyde, which produces glyceraldehyde **15**. This can react with a second molecule of **14** to pentose sugars (Fig. 1A) (*19*). When we reacted **14** and **15** (both 16.7 mM) in the presence of $Ca(OH)_2$ (23 mM) (*25*) with FaPy **13**, we indeed found purine pentosides as the main products (estimated yield, 21%). Quantification of D/L β-adenosine (D/L-β-fA, Fig. 3) gave 0.9% (based on **13**). Despite overlapping signals, we were also able to estimate a yield of 2.7% for the D/L-β-pA. When we performed the reaction in the presence of borax, the D/L-β-fA yield increased among all other aldopentoses to 1.3% ultimately (*18*). Product identification was achieved by HPLC-MS and coinjection studies (Fig. 3C). Small amounts of purine threosides and erythrosides were also found (fig. S4).

The FaPy route delivers ribosides even directly from formaldehyde and glycolaldehyde **14** (Fig. 4). We mixed formaldehyde (0.21 M) and glycolaldehyde (0.40 M) with $Ca(OH)_2$ (0.5 M), borax (0.125 M), or $NH_3$ (0.5 M) in water and heated the mixture for 1 hour at 65°C. The FaPy compound **13** (0.12 M) was added and the mixture was heated in an open vessel for another 8 hours at 100°C. Water (or 0.5 M $NH_3$) was added to the obtained solid, and the mixture was heated for another 2 to 3 days at 100°C. Reactions containing borax or $Ca(OH)_2$ gave complex spectra with only small signals for nucleosides. In the experiments with $NH_3$, however, purine threosides and erythrosides were formed as the main nucleoside components, with the threose nucleosides slightly favored (*19*). To identify the tetrosides, we again performed coinjection studies (Fig. 4, B and C). Besides the purine tetrosides, we were able to identify D/L-β-pA and D/L-β-fA (D/L-adenosine) in this one-pot reaction (Fig. 4D), with a preference for the β-pyranosyl compound (D/L-β-pA, 0.2% based on **13**).

Overall, we show that the reported FaPy pathway with the corresponding aminopyrimidine (*11*, *12*) precursor molecules provides a feasible pathway to purine nucleosides that is compatible with early Earth conditions and that provides adenosine under a variety of conditions in yields of up to 20%. The starting materials are small organic molecules such as HCN, $NH_3$, and particularly formic acid derivatives that were all discovered on comets like 67P/Churyumov-Gerasimenko (*1*).

## REFERENCES AND NOTES


1. F. Goesmann *et al*., *Science* **349**, aab0689 (2015).
2. J. F. Kasting, *Science* **259**, 920–926 (1993).
3. F. H. C. Crick, *J. Mol. Biol.* **38**, 367–379 (1968).
4. L. E. Orgel, *Crit. Rev. Biochem. Mol. Biol.* **39**, 99–123 (2004).
5. M. W. Powner, B. Gerland, J. D. Sutherland, *Nature* **459**, 239–242 (2009).
6. H. B. White 3rd, *J. Mol. Evol.* **7**, 101–104 (1976).
7. W. D. Fuller, R. A. Sanchez, L. E. Orgel, *J. Mol. Biol.* **67**, 25–33 (1972).
8. W. D. Fuller, R. A. Sanchez, L. E. Orgel, *J. Mol. Evol.* **1**, 249–257 (1972).
9. J. Oró, *Biochem. Biophys. Res. Commun.* **2**, 407–412 (1960).
10. J. Oró, A. P. Kimball, *Arch. Biochem. Biophys.* **94**, 217–227 (1961).
11. U. P. Trinks, A. Eschenmoser, thesis, ETH Zurich (1987), ETH 2-collection; http://dx.doi.org/10.3929/ethz-a-000413538.
12. K. E. Koch, A. Eschenmoser, thesis, ETH Zurich (1992), ETH e-collection; http://dx.doi.org/10.3929/ethz-a-000694124.
13. W. Traube, *Liebigs Ann. Chem.* **331**, 64–88 (1904).
14. J. Clark, R. K. Grantham, J. Lydiate, *J. Chem. Soc. C. Org.* **1968**, 1122 (1968).
15. M. P. Robertson, M. Levy, S. L. Miller, *J. Mol. Evol.* **43**, 543–550 (1996).
16. R. Saladino *et al*., *Chem. Bio. Chem.* **4**, 514–521 (2003).
17. T. Mori, K. Tano, K. Takimoto, H. Utsumi, *Biochem. Biophys. Res. Commun.* **242**, 98–101 (1998).
18. A. Ricardo, M. A. Carrigan, A. N. Olcott, S. A. Benner, *Science* **303**, 196 (2004).
19. H. J. Kim *et al*., *J. Am. Chem. Soc.* **133**, 9457–9468 (2011).
20. J. B. Lambert, S. A. Gurusamy-Thangavelu, K. Ma, *Science* **327**, 984–986 (2010).
21. R. B. Trattner, G. B. Elion, G. H. Hitchings, D. M. Sharefkin, *J. Org. Chem.* **29**, 2674–2677 (1964).
22. M. D. Kirnos, I. Y. Khudyakov, N. I. Alexandrushkina, B. F. Vanyushin, *Nature* **270**, 369–370 (1977).
23. W. Löb, *Berichte der Dtsch. Chem. Gesellschaft* **46**, 684–697 (1913).
24. D. J. Ritson, J. D. Sutherland, *Angew. Chem. Int. Ed.* **52**, 5845–5847 (2013).
25. G. Harsch, H. Bauer, W. Voelter, *Liebigs Ann. Chem.* **1984**, 623–635 (1984).


## ACKNOWLEDGMENTS


We thank the Deutsche Forschungsgemeinschaft (SFB749, SFB646, and SFB1032) and the Excellence cluster EXC114 (Center for Integrated Protein Science) for financial support. Additional figures and synthetic procedures can be found in the supplementary materials. The crystallographic data (CCDC 1416691) can be obtained from The Cambridge Crystallographic Data Centre via www.ccdc.cam.ac.uk.


## SUPPLEMENTARY MATERIALS

www.sciencemag.org/content/352/6287/833/suppl/DC1
Materials and Methods
Supplementary Text
Figs. S1 to S6
Table S1 to S3
References (*26*–*36*)


20 August 2015; accepted 15 March 2016
10.1126/science.aad2808


Downloaded from http://science.sciencemag.org/ on May 12, 2016

MOLECULAR EVOLUTION

# The fitness landscape of a tRNA gene

Chuan Li, Wenfeng Qian,* Calum J. Maclean, Jianzhi Zhang†

**Fitness landscapes describe the genotype-fitness relationship and represent major determinants of evolutionary trajectories. However, the vast genotype space, coupled with the difficulty of measuring fitness, has hindered the empirical determination of fitness landscapes. Combining precise gene replacement and next-generation sequencing, we quantified Darwinian fitness under a high-temperature challenge for more than 65,000 yeast strains, each carrying a unique variant of the single-copy $tRNA^{Arg}_{CCU}$ gene at its native genomic location. Approximately 1% of single point mutations in the gene were beneficial and 42% were deleterious. Almost half of all mutation pairs exhibited statistically significant epistasis, which had a strong negative bias, except when the mutations occurred at Watson-Crick paired sites. Fitness was broadly correlated with the predicted fraction of correctly folded transfer RNA (tRNA) molecules, thereby revealing a biophysical basis of the fitness landscape.**

Fitness landscapes can provide information about the direction and magnitude of natural selection and can elucidate evolutionary trajectories (*1*), but their empirical determination requires quantifying the fitness of an astronomically large number of possible genotypes. Past studies were limited to relatively few genotypes (*2*, *3*). Next-generation DNA sequencing (NGS) has permitted the analysis of many more genotypes (*4*–*11*), but research has focused on biochemical functions (*4*, *6*, *8*–*12*) rather than fitness. In the few fitness landscapes reported, only a small fraction of sites or combinations of mutations per gene were examined (*5*–*7*, *9*).

Here, we combined gene replacement in *Saccharomyces cerevisiae* with an NGS-based fitness assay to determine the fitness landscape of a tRNA gene. tRNAs carry amino acids to ribosomes for protein synthesis, and mutations can cause diseases such as cardiomyopathy and deafness (*13*). tRNA genes are typically shorter than 90 nucleotides, allowing coverage by a single Illumina sequencing read. We focused on $tRNA^{Arg}_{CCU}$, which recognizes the arginine codon AGG via its anticodon 5′-CCU-3′. Because AGG is also recognizable by $tRNA^{Arg}_{UCU}$ via wobble pairing, $tRNA^{Arg}_{CCU}$ is known to be encoded by a single-copy nonessential gene in *S. cerevisiae* (*14*). Deleting the $tRNA^{Arg}_{CCU}$ gene (fig. S1 and table S1) reduces growth rates in both fermentable (YPD) and nonfermentable (YPG) yeast growth media, a problem exacerbated by high temperature (fig. S2).

We chemically synthesized the 72-nucleotide $tRNA^{Arg}_{CCU}$ gene with a mutation rate of 3% per site (1% per alternate nucleotide) at 69 sites; for technical reasons, we kept the remaining three sites invariant (*15*). Using these variants, we constructed a pool of $>10^5$ strains, each carrying a $tRNA^{Arg}_{CCU}$ gene variant at its native genomic location (Fig. 1 and fig. S1). Six parallel competitions of this strain pool were performed in YPD medium at 37°C for 24 hours. The $tRNA^{Arg}_{CCU}$ gene amplicons from the common starting population ($T_0$) and those from six replicate competitions ($T_{24}$) were sequenced with 100-nucleotide paired-end NGS (Fig. 1 and table S2). Genotype frequencies were highly correlated between two $T_0$ technical repeats (Pearson's correlation $r$ = 0.99997; fig. S3A) and among six $T_{24}$ biological replicates (average $r$ = 0.9987; fig. S3B) (*15*). Changes in genotype frequencies between $T_0$ and $T_{24}$ were used to determine the Darwinian fitness of each genotype relative to the wild type (*15*). For our fitness estimation, we considered 65,537 genotypes with read counts of ≥100 at $T_0$. In theory, a cell that does not divide has a fitness of 0.5 (*16*). Because $tRNA^{Arg}_{CCU}$ mutations are unlikely to be fatal, we set genotype fitness at 0.5 when the estimated fitness is <0.5 (due to stochasticity) (*15*). Fitness values from these en masse competitions agreed with those obtained from growth curve and pairwise competition (fig. S4), as reported previously (*16*). We observed strong fitness correlations across diverse environments for a subset of genotypes examined (fig. S5), which suggests that our fitness landscape is broadly relevant (*15*).

We estimated the fitness ($f$) of all 207 possible mutants that differ from the wild type by one point mutation (N1 mutants) and calculated the average mutant fitness at each site (Fig. 2A). Average fitness decreased to <0.75 by mutation at nine key sites, including all three anticodon positions (table S3), three TΨC loop sites, one D stem site, and two paired TΨC stem sites (Fig. 2A). The TΨC loop and stem sites are components of the B-box region of the internal promoter, with C55 essential for both TFIIIC transcription factor binding and polymerase III (Pol III) transcription (*17*). In addition, some sites such as T54 are ubiquitously posttranscriptionally modified (*18*). By contrast, the average mutant fitness is ≥0.95 at 30 sites (Fig. 2A). Overall, mutations in loops are more deleterious than in stems ($P$ = 0.01, Mann-Whitney $U$ test), although this difference becomes insignificant after excluding the anticodon ($P$ = 0.09). Unsurprisingly, different mutations at a site have different fitness effects (fig. S6). For example, mutation C11T in the D stem is tolerated ($f_{C11T}$ ± SE = 1.006 ± 0.036), but C11A and C11G are not ($f_{C11A}$ = 0.676 ± 0.030 and $f_{C11G}$ = 0.661 ± 0.035), likely because of G:U paring in RNA.

The fitness distribution of N1 mutants shows a mean of 0.89 and a peak at 1 (Fig. 2B). Only 1% of mutations are significantly beneficial (nominal $P$ < 0.05; $t$ test based on the six replicates), whereas 42% are significantly deleterious. We estimated the fitness of 61% of all possible genotypes carrying two mutations (N2 mutants) and observed a left-shifted distribution peaking at 0.50 and 0.67 (Fig. 2C). We also estimated the fitness of 1.6% of genotypes with three mutations (N3 mutants); they exhibited a distribution with only one dominant peak at 0.5, indicating that many triple mutations completely suppress yeast growth in the en masse competition (Fig. 2D).

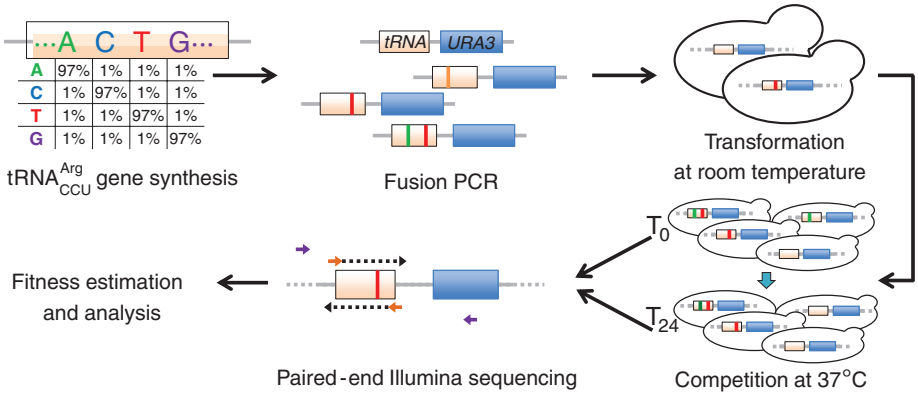


**Fig. 1. Determining the fitness landscape of the yeast $tRNA^{Arg}_{CCU}$ gene.** Chemically synthesized $tRNA^{Arg}_{CCU}$ gene variants are fused with the marker gene *URA3* before placement at the native $tRNA^{Arg}_{CCU}$ locus. The tRNA variant–carrying cells are competed with one another. The fitness of each $tRNA^{Arg}_{CCU}$ genotype relative to the wild type is calculated from the relative frequency change of paired-end sequencing reads covering the tRNA gene variant during competition (fig. S1) (*15*).

Department of Ecology and Evolutionary Biology, University of Michigan, Ann Arbor, MI 48109, USA.
*Present address: Key Laboratory of Genetic Network Biology, Institute of Genetics and Developmental Biology, Chinese Academy of Sciences, Beijing, China. †Corresponding author. Email: jianzhi@umich.edu

Downloaded from http://science.sciencemag.org/ on May 12, 2016

The fitness distribution narrows and shifts further toward 0.5 in strains carrying more than three mutations (Fig. 2E).

Fitness landscapes allow prediction of evolution, because sites where mutations are on average more harmful should be evolutionarily more conserved. We aligned 200 nonredundant $tRNA^{Arg}_{CCU}$ gene sequences across the eukaryotic phylogeny (*15*). The percentage of sequences having the same nucleotide as yeast at a given site is negatively correlated with the average fitness upon mutation at the site (Spearman's $\rho = -0.61$, $P = 2 \times 10^{-8}$; Fig. 2F). Among N1 mutants, the number of times that a mutant nucleotide appears in the 200 sequences is positively correlated with the fitness of the mutant ($\rho = 0.51$, $P = 2 \times 10^{-15}$; Fig. 2G). Furthermore, mutations observed in other eukaryotes have smaller fitness costs in yeast than those unobserved in other eukaryotes ($P = 9 \times 10^{-6}$, Mann-Whitney *U* test).

Two mutations may interact with each other, creating epistasis (ε) with functional and evolutionary implications (*19*). We estimated ε within the tRNA gene from the fitness of 12,985 N2 mutants and 207 N1 mutants (Fig. 3A) (*15*). ε is negatively biased, with only 34% positive values ($P < 10^{-300}$, binomial test; Fig. 3B and figs. S7A and S8). Among the 45% of ε values that differ significantly from 0 (nominal $P < 0.05$, *t* test based on the six replicates), 86% are negative ($P < 10^{-300}$, binomial test; Fig. 3B and figs. S7A and S8). Consistent with the overall negative ε, the mean fitness of N2 mutants (0.75) is lower than that predicted from N1 mutants under the assumption of no epistasis (0.81) (Fig. 2E). Note that as the first mutation becomes more deleterious, the mean epistasis between this mutation and the next mutation becomes less negative and, in some cases, even positive (Fig. 3C and fig. S9), similar to between-gene epistasis involving an essential gene (*20*). Consequently, the larger the fitness cost of the first mutation, the smaller the mean fitness cost of the second mutation (Fig. 3D and fig. S10). Pairwise epistasis involving three or four mutations is also negatively biased (fig. S11). Consistently, N3 to N8 mutants all show lower average fitness than expected under the assumption of no epistasis (Fig. 2E).

The distribution of epistasis between mutations at paired sites is expected to differ from the above general pattern, because different Watson-Crick (WC) pairs may be functionally similar (*21*). We estimated the fitness of 71% of all possible N2 mutants at WC paired sites. Among the 41 cases that switched from one WC pair to another, 23 (56%) have positive ε (Fig. 3E). Among the 80 N2 mutants that destroyed WC pairing, 39 (49%) showed positive ε (Fig. 3F). The ε values are more positive for each of these two groups than for N2 mutants where the two mutations do not occur at paired sites ($P = 7 \times 10^{-6}$ and $2.6 \times 10^{-3}$, respectively; Mann-Whitney *U* test). Furthermore, ε is significantly more positive in the 41 cases with restored WC pairing than in the 80 cases with destroyed pairing ($P = 0.04$). These two trends also apply to cases with significant epistasis (corresponding to $P = 3 \times 10^{-5}$, 0.01, and 0.01, respectively; Fig. 3, E and F, and fig. S7, B and C). However, epistasis is not always positive between paired sites, likely because base pairing is not the sole function of the nucleotides at paired sites. We observed 160 cases of significant sign epistasis (*15*), which is of special interest because it may block potential paths for adaptation (*2*). We also detected ε with opposite signs in different genetic backgrounds, indicating a high-order epistasis (table S4).

A tRNA can fold into multiple secondary structures. We computationally predicted the proportion of $tRNA^{Arg}_{CCU}$ molecules that are potentially functional (i.e., correctly folded with no anticodon mutation) for each genotype ($P_{func}$). Raising $P_{func}$ increases fitness ($\rho = 0.40$, $P < 10^{-300}$), albeit with diminishing returns (Fig. 4A), and this correlation holds after controlling for mutation number ($\rho = 0.26$, 0.37, and 0.24 for N1, N2, and N3 mutants, respectively). Because computational prediction of RNA secondary structures is only moderately accurate, the $P_{func}$-fitness correlation demonstrates an important role of $P_{func}$ in shaping the tRNA fitness landscape. Nonetheless, after controlling for $P_{func}$, mutant fitness still correlates with mutation

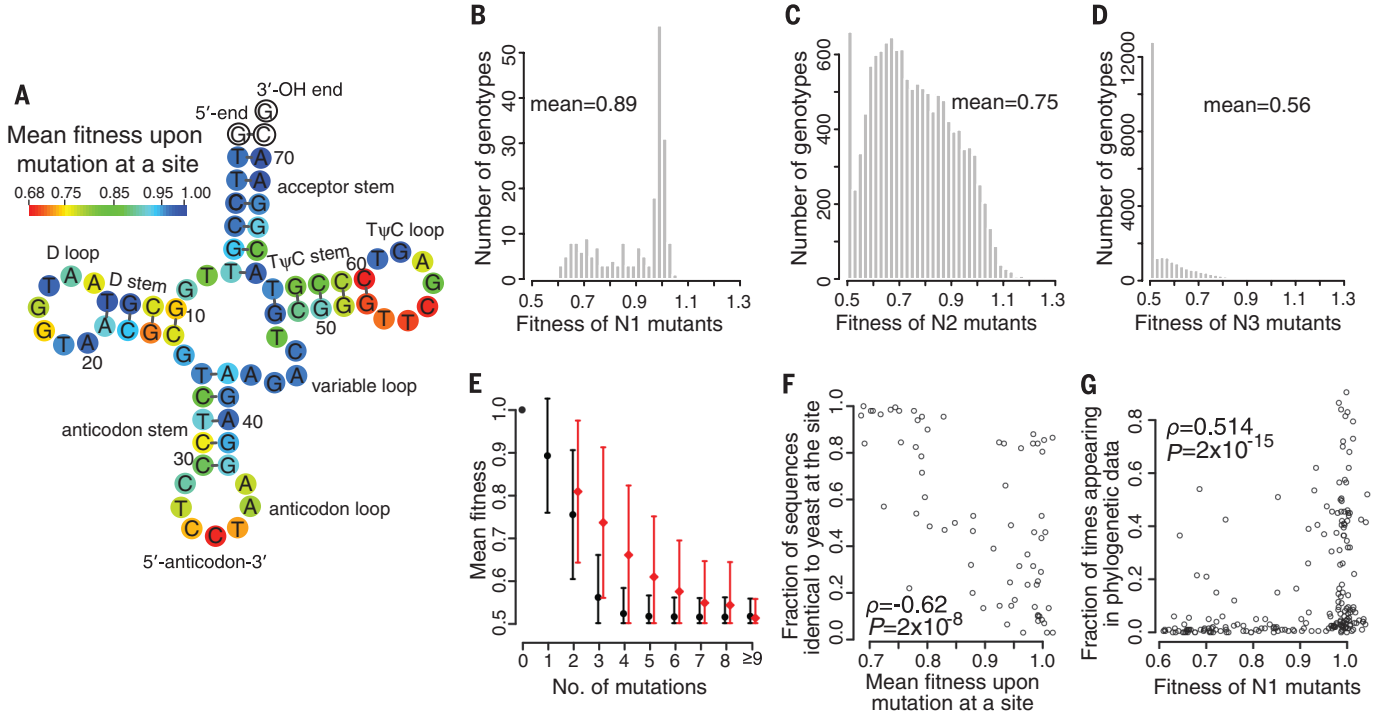


**Fig. 2. Yeast $tRNA^{Arg}_{CCU}$ gene fitness landscape.** (**A**) Average fitness upon a mutation at each site. White circles indicate invariant sites. (**B** to **D**) Fitness distributions of N1 (B), N2 (C), and N3 (D) mutants. (**E**) Mean observed fitness (black circles) decreases with mutation number. Red circles show mean expected fitness without epistasis (right-shifted for viewing). Error bars denote SD. (**F**) Fraction of the 200 eukaryotic $tRNA^{Arg}_{CCU}$ genes with the same nucleotide as yeast at a given site decreases with the average fitness upon mutation at the site in yeast. Each dot represents one of the 69 examined tRNA sites. (**G**) Fraction of times that a mutant nucleotide appears in the 200 sequences increases with the fitness of the mutant in yeast. Each dot represents a N1 mutant. In (F) and (G), ρ is the rank correlation coefficient; *P* values are from *t* tests.

Downloaded from http://science.sciencemag.org/ on May 12, 2016

number [ρ = −0.51, $P < 10^{-300}$; see also locally weighted polynomial regressions (LOESS) for N1, N2, and N3 mutants in Fig. 4B], which suggests that other factors also have an impact on fitness.

To investigate whether $P_{func}$ explains epistasis, we computed epistasis using the fitness of N1 and N2 mutants predicted from their respective $P_{func}$-fitness regression curves (Fig. 4B) and observed a significant correlation between the predicted and observed epistasis (ρ = 0.04, $P = 2.7 \times 10^{-5}$). The weakness of this correlation is at least partly because epistasis is computed from three fitness measurements (or predictions) and is therefore associated with a considerable error. There is a similar bias in predicted epistasis toward negative values (Fig. 4C), but further analyses suggest that it probably arises from factors other than tRNA folding (*15*). These results regarding $P_{func}$ and epistasis are not unexpected, given that a tRNA site can be involved in multiple molecular functions (*17*, *18*).

Our results clarify the in vivo fitness landscape of a yeast tRNA gene under a high-temperature

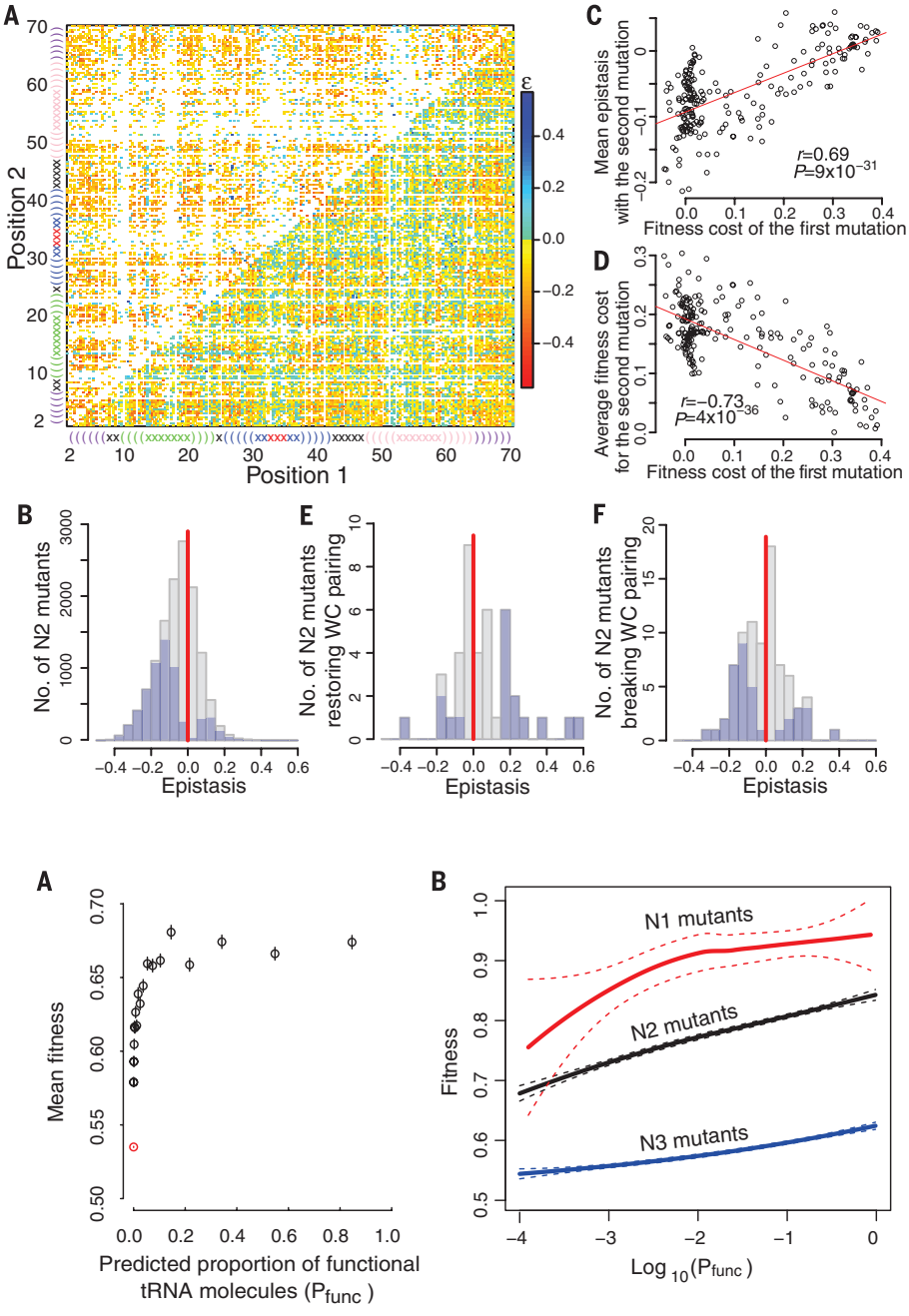


**Fig. 3. Epistasis (ε) in fitness between point mutations in the $tRNA^{Arg}_{CCU}$ gene is negatively biased.** (**A**) Epistasis between point mutations. Lower right triangle shows all pairwise epistasis (white = not estimated); upper left triangle shows statistically significant epistasis (white = no estimation or insignificant). $tRNA^{Arg}_{CCU}$ secondary structure is plotted linearly. Parentheses and crosses show stem and loop sites, respectively. Same color indicates sites in the same loop or stem. Each site has three mutations. (**B**) Distributions of pairwise epistasis (gray) and statistically significant pairwise epistasis (blue) among 12,985 mutation pairs. (**C**) Mean epistasis between first and second mutations increases with the fitness cost of the first mutation. (**D**) Mean fitness cost of the second mutation decreases with the fitness cost of the first mutation. In (C) and (D), the Pearson's correlation (*r*), associated *P* value, and linear regression (red) are shown. (**E** and **F**) Distributions of epistasis (gray) and statistically significant epistasis (blue) between pairs of mutations that convert a Watson-Crick (WC) base pair to another WC pair (E) or break a WC pair in stems (F). In (B), (E), and (F), the vertical red line shows zero epistasis.

**Fig. 4. $tRNA^{Arg}_{CCU}$ folding offers a mechanistic explanation of the fitness landscape.** (**A**) Relationship between the predicted proportion of tRNA molecules that are functional ($P_{func}$) for a genotype and its fitness. Genotypes (with $P_{func} \geq 10^{-4}$) are ranked by $P_{func}$ and grouped into 20 equal-size bins; mean $P_{func}$ and mean fitness ± SE of each bin are shown. The red dot represents all variants with $P_{func} < 10^{-4}$. (**B**) LOESS regression curves between $P_{func}$ and fitness for N1, N2, and N3 mutants, respectively, with dashed lines indicating 95% confidence intervals. (**C**) Quantile-quantile plot between epistasis predicted from $P_{func}$ values using N1 and N2 LOESS curves and observed epistasis. The *i*th dot from the left shows the *i*th smallest predicted epistasis value (*y* axis) and *i*th smallest observed epistasis value (*x* axis). Red diagonal line shows the ideal situation of *y* = *x*. Above and left of the plot are frequency distributions of observed and predicted epistasis, respectively. Red horizontal and vertical lines indicate zero epistasis.

Downloaded from http://science.sciencemag.org/ on May 12, 2016

challenge. Broadly consistent with the neutral theory, beneficial mutations are rare (1%), relative to deleterious (42%) and (nearly) neutral mutations (57%). We found widespread intragenic epistasis between mutations, consistent with studies at smaller scales (*1*). Intriguingly, 86% of significant epistasis is negative, indicating that the fitness cost of the second mutation is on average greater than that of the first. A bias toward negative epistasis was also observed in protein genes (*7*, *10*, *11*, *22*); hence, this may be a general trend. Variation in fitness is partially explained by the predicted fraction of correctly folded tRNA molecules; this implies the existence of general principles underlying complex fitness landscapes. Our tRNA variant library provides a resource in which various mechanisms contributing to the tRNA's fitness landscape can be evaluated, and the methodology developed here is applicable to the study of fitness landscapes of longer genomic segments, including protein genes.

## REFERENCES AND NOTES


1. J. A. de Visser, J. Krug, *Nat. Rev. Genet.* **15**, 480–490 (2014).
2. D. M. Weinreich, N. F. Delaney, M. A. Depristo, D. L. Hartl, *Science* **312**, 111–114 (2006).
3. P. A. Lind, O. G. Berg, D. I. Andersson, *Science* **330**, 825–827 (2010).
4. J. N. Pitt, A. R. Ferré-D'Amaré, *Science* **330**, 376–379 (2010).
5. R. T. Hietpas, J. D. Jensen, D. N. Bolon, *Proc. Natl. Acad. Sci. U.S.A.* **108**, 7896–7901 (2011).
6. G. M. Findlay, E. A. Boyle, R. J. Hause, J. C. Klein, J. Shendure, *Nature* **513**, 120–123 (2014).
7. C. Bank, R. T. Hietpas, J. D. Jensen, D. N. Bolon, *Mol. Biol. Evol.* **32**, 229–238 (2015).
8. M. P. Guy *et al.*, *Genes Dev.* **28**, 1721–1732 (2014).
9. A. Melnikov, P. Rogov, L. Wang, A. Gnirke, T. S. Mikkelsen, *Nucleic Acids Res.* **42**, e112 (2014).
10. D. Melamed, D. L. Young, C. E. Gamble, C. R. Miller, S. Fields, *RNA* **19**, 1537–1551 (2013).
11. C. A. Olson, N. C. Wu, R. Sun, *Curr. Biol.* **24**, 2643–2651 (2014).
12. T. Hinkley *et al.*, *Nat. Genet.* **43**, 487–489 (2011).
13. J. A. Abbott, C. S. Francklyn, S. M. Robey-Bond, *Front. Genet.* **5**, 158 (2014).
14. Z. Bloom-Ackermann *et al.*, *PLOS Genet.* **10**, e1004084 (2014).
15. See supplementary materials on *Science* Online.
16. W. Qian, D. Ma, C. Xiao, Z. Wang, J. Zhang, *Cell Rep.* **2**, 1399–1410 (2012).
17. S. Hiraga, S. Botsios, D. Donze, A. D. Donaldson, *Mol. Biol. Cell* **23**, 2741–2754 (2012).
18. E. M. Phizicky, A. K. Hopper, *Genes Dev.* **24**, 1832–1860 (2010).
19. P. C. Phillips, *Nat. Rev. Genet.* **9**, 855–867 (2008).
20. X. He, W. Qian, Z. Wang, Y. Li, J. Zhang, *Nat. Genet.* **42**, 272–276 (2010).
21. M. V. Meer, A. S. Kondrashov, Y. Artzy-Randrup, F. A. Kondrashov, *Nature* **464**, 279–282 (2010).
22. S. Bershtein, M. Segal, R. Bekerman, N. Tokuriki, D. S. Tawfik, *Nature* **444**, 929–932 (2006).


## ACKNOWLEDGMENTS

We thank S. Cho, W.-C. Ho, G. Kudla, and J.-R. Yang for valuable comments. Supported by NSF DDIG grant DEB-1501788 (J.Z. and C.L.) and NIH grant R01GM103232 (J.Z.). The NCBI accession number for the sequencing data is PRJNA311172.

## SUPPLEMENTARY MATERIALS

www.sciencemag.org/content/352/6287/837/suppl/DC1
Materials and Methods
Figs. S1 to S11
Tables S1 to S4
References (*23*–*27*)

11 December 2015; accepted 23 March 2016
Published online 14 April 2016
10.1126/science.aae0568

MOLECULAR EVOLUTION

# Network of epistatic interactions within a yeast snoRNA

**Olga Puchta,[1] Botond Cseke,[2]* Hubert Czaja,[3] David Tollervey,[4,5] Guido Sanguinetti,[2,4] Grzegorz Kudla[1]†**

**Epistatic interactions play a fundamental role in molecular evolution, but little is known about the spatial distribution of these interactions within genes. To systematically survey a model landscape of intragenic epistasis, we quantified the fitness of ~60,000 *Saccharomyces cerevisiae* strains expressing randomly mutated variants of the 333-nucleotide-long U3 small nucleolar RNA (snoRNA). The fitness effects of individual mutations were correlated with evolutionary conservation and structural stability. Many mutations had small individual effects but had large effects in the context of additional mutations, which indicated negative epistasis. Clusters of negative interactions were explained by local thermodynamic threshold effects, whereas positive interactions were enriched among large-effect sites and between base-paired nucleotides. We conclude that high-throughput mapping of intragenic epistasis can identify key structural and functional features of macromolecules.**

The effect of a mutation on phenotype may depend on the presence of additional mutations. This phenomenon, known as epistasis, explains synthetic lethal interactions, in which a combination of two individually viable mutations causes death, and compensatory interactions, in which the fitness cost of a mutation is reduced by a second mutation (*1*, *2*). Epistasis plays a major role in evolution; it determines the accessibility of mutational pathways (*3*) and thereby influences the rate of adaptation and the diversity and robustness of genetic variants (*4*, *5*). Although genome-wide studies have revealed a network of intergenic epistasis (*6*), it has been suggested that interactions within genes may be even more common (*7*–*11*). However, previous studies focused on relatively small networks of interactions, and the comprehensive pattern of epistasis has not yet been determined for any gene.

We used "doped" oligonucleotides to synthesize ~130,000 randomly mutated variants of the 333-nucleotide *Saccharomyces cerevisiae* gene *SNR17A*, which encodes the U3 small nucleolar RNA. U3 forms base pairs with the primary ribosomal RNA (rRNA) transcript (pre-rRNA), and this interaction is required for pre-rRNA cleavage and 18*S* rRNA biogenesis. Our mutagenesis approach ensures uniform coverage of mutations among positions 7 to 333, which encompass 98% of the gene, and prevents bias toward specific types of mutations (Fig. 1A and fig. S1). We generated two independent mutant libraries, which contained, on average, 3 and 10 single-nucleotide polymorphisms (SNPs) per allele, respectively. In addition to the SNPs, 43.6% of variants also contained short deletions [median length, 1 nucleotide (nt)] or insertions (median length, 1 nt). All 981 (3 × 327) possible point mutations were represented in the library, and 99.4% of the 53,301 (327 × 326/2) possible pairs of sites were jointly mutated, most of them in alleles that contained additional mutations. To facilitate unambiguous identification of variants by high-throughput sequencing, we tagged each variant with a unique 20-nt barcode (Fig. 1A) placed in a nontranscribed region downstream of the U3 gene to minimize interference with function.

To measure fitness, we used the D343 yeast strain, which contains a single copy of the wild-type U3 gene under the control of a galactose-inducible promoter (*12*). D343 cells can grow in galactose-containing medium, but shifting to glucose results in down-regulation of U3 and growth arrest. Transformation of wild-type U3 on a plasmid allows the cells to survive on glucose, but nonfunctional U3 mutants do not support growth (fig. S2). We transformed D343 cells with centromeric plasmids carrying the U3 mutant libraries and measured the frequency of each mutant during competitive growth on glucose (Fig. 1B). As expected, nonfunctional variants decreased in frequency during the competition, whereas the wild-type gene increased (Fig. 1C). Growth patterns were reproducible between four replicate experiments and across replicate U3 variants within an experiment (Fig. 1D and fig. S3).

We measured the logarithm of relative fitness (log fitness) of ~60,000 variants that passed quality filters by fitting exponential decay curves to the barcode count data (*13*). Log fitness of wild-type U3 was set to 0. We first focused on the effects of single mutations in an otherwise wild-type gene (*13*). In most positions, mutations were tolerated with minimal effect on fitness (Fig. 2A). The exceptions were the conserved protein binding sites known as boxes B, C, C′, and D, in which mutations are lethal or highly deleterious. In addition, a moderate fitness decrease

[1]MRC Human Genetics Unit, Institute of Genetics and Molecular Medicine, University of Edinburgh, Edinburgh EH4 2XU, Scotland, UK. [2]School of Informatics, University of Edinburgh, Edinburgh, Scotland, UK. [3]Scott Tiger SA, Warsaw, Poland. [4]SynthSys, Centre for Synthetic and Systems Biology, University of Edinburgh, Edinburgh, Scotland, UK. [5]Wellcome Trust Centre for Cell Biology, University of Edinburgh, Edinburgh, Scotland, UK.
*Present address: Microsoft Research Cambridge, Cambridge, UK.
†Corresponding author. Email: gkudla@gmail.com

Downloaded from http://science.sciencemag.org/ on May 12, 2016

was observed for mutations within stems I, II, III, and V, particularly in G-C base pairs located at the base of stems, which suggests a role in structural stability. Folding predictions confirmed that destabilizing mutations in individual stems reduced fitness (fig. S4). The 5-nt 3′-terminal stem of U3 confers protection from degradation by 3′-5′ exonucleases (*12*). Mutations in this stem reduced fitness proportionally to their predicted effect on RNA folding strength (figs. S4 and S5). U→C mutations in positions 178 and 191 were highly deleterious (fig. S5), possibly because they created consensus binding motifs (UCUUG) for the RNA degradation factor Nab3 (*14*). The fitness effects of mutations were slightly larger at 37°C than at 30°C, consistent with the destabilizing effect of temperature on U3 structure (fig. S6). We found no mutations that consistently increased fitness, which suggested that wild-type U3 is optimally adapted for function. In conditions where the genomic copy of U3 was coexpressed with the mutant library, the mutations had no effect, which indicated a lack of dominant-negative or gain-of-function effects (Fig. 1D). Overall, these results show the expected pattern of single-site fitness effects and support the reliability of the measurements.

We then calculated $p_i$, the aggregate log fitness effect of position $i$ across all genetic backgrounds represented in the library (*13*). In contrast to the single mutants (Fig. 2A), most positions showed substantial effects on fitness in combination with other mutations (Fig. 2B). The variation in $p_i$ across the gene was reproducible between replicate experiments, was observed in both mutant libraries, was robust to the exclusion of outlier variants, and did not reflect the co-occurrence of mutations with large-effect mutations in other sites (figs. S6 and S7). Most positions with very negative $p_i$ map to the conserved core of the U3 gene (stems I to III, 5′ hinge, 3′ hinge, see Fig. 2B). In contrast, sites with near-zero $p_i$ were located in the fungal- or yeast-specific regions of the molecule (stems IV to VI, see Fig. 2B). The $p_i$ values were correlated with fitness effects in wild-type background (Spearman rho = 0.57, $P < 2 \times 10^{-16}$) (Fig. 2C). However, the relation was markedly nonlinear, which indicated that many mutations had small effects in an otherwise wild-type U3 but large effects in the context of additional mutations.

This pattern suggests a high prevalence of negative epistatic interactions within U3. To confirm this, we analyzed the distribution of fitness effects as a function of the number of mutations in each allele (Fig. 2D). As expected, the average fitness of variants decreased with increasing numbers of mutations. Notably, measured fitness was consistently lower than we expected under an additive model (Fig. 2E). This indicates overall enrichment of negative epistatic interactions relative to positive interactions.

We estimated the strength of all pairwise interactions from measurements of single, double, and multiple mutants (*13*) with a regression model (*15*–*17*) that explained ~86% of variance in measured fitness and produced similar patterns of

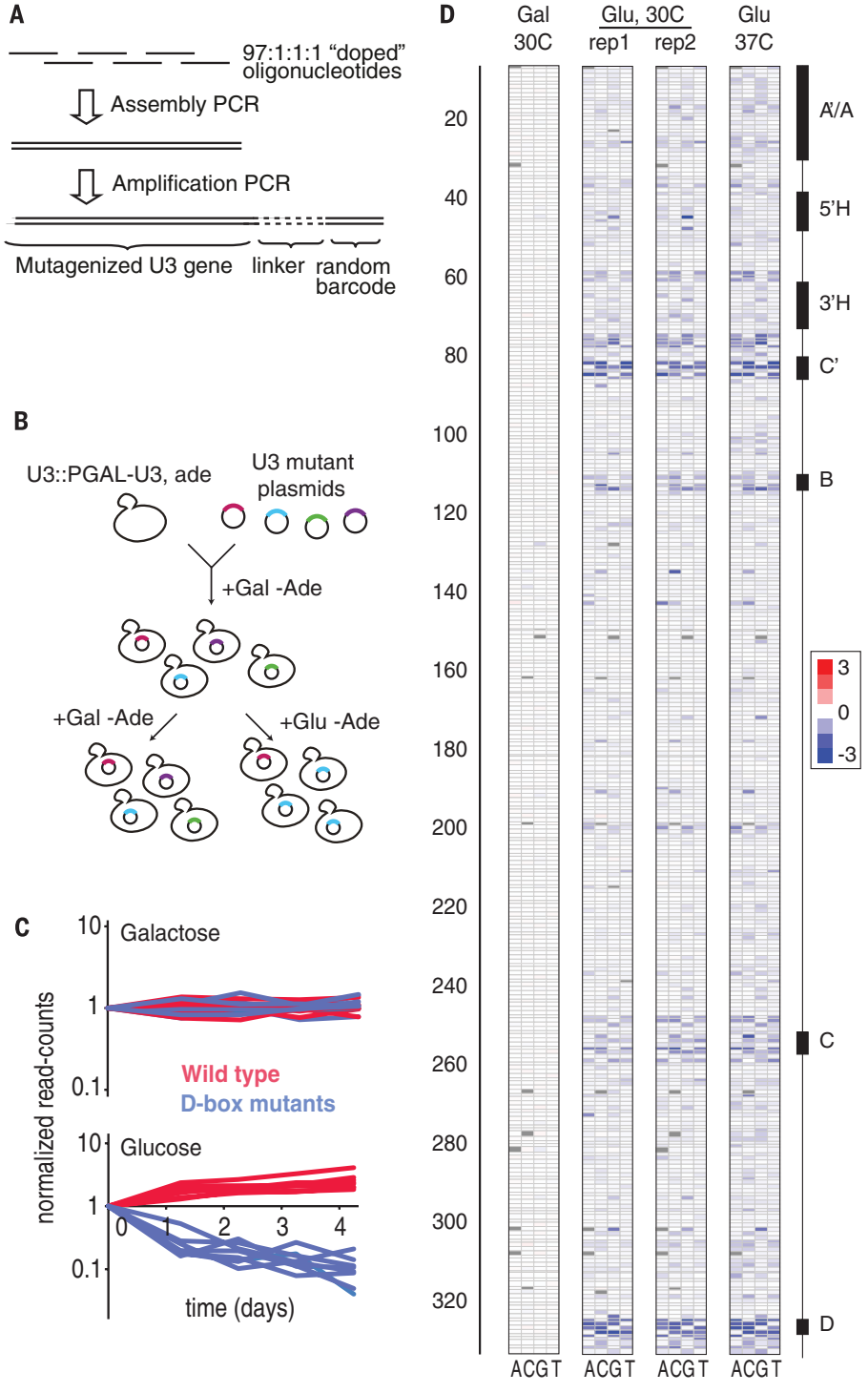


**Fig. 1. Experimental mapping of the U3 fitness landscape.** (**A**) To perform saturation mutagenesis of U3, we used the polymerase chain reaction (PCR) to assemble overlapping "97:1:1:1-doped" and nondoped oligonucleotides covering the whole length of the gene (*13*) and attached a unique 20-nt barcode to each variant. (**B**) We cloned the U3 mutant library into centromeric plasmids and transformed the plasmids into the D343 yeast strain. PGAL, galactose-inducible promoter; –Ade, without adenine. (**C**) Normalized read-counts from barcode sequencing for seven randomly chosen wild-type U3 variants (red) and seven variants carrying a single mutation in box D (blue), under control (galactose) and competitive (glucose) conditions. Fitness was approximated by fitting exponential decay curves to the barcode count data. (**D**) Rows indicate positions along U3, and columns indicate substitution to one of four bases: A, C, G, and T. Log fitness effects are shown in blue for deleterious effects, red for positive effects, and white for no effect on galactose at 30°C (Gal) and glucose (Glu) at 30°C and 37°C. Genetic variants with one or two mutations were included in the analysis (*13*). Positions for which no data were obtained are shown in gray.

Downloaded from http://science.sciencemag.org/ on May 12, 2016

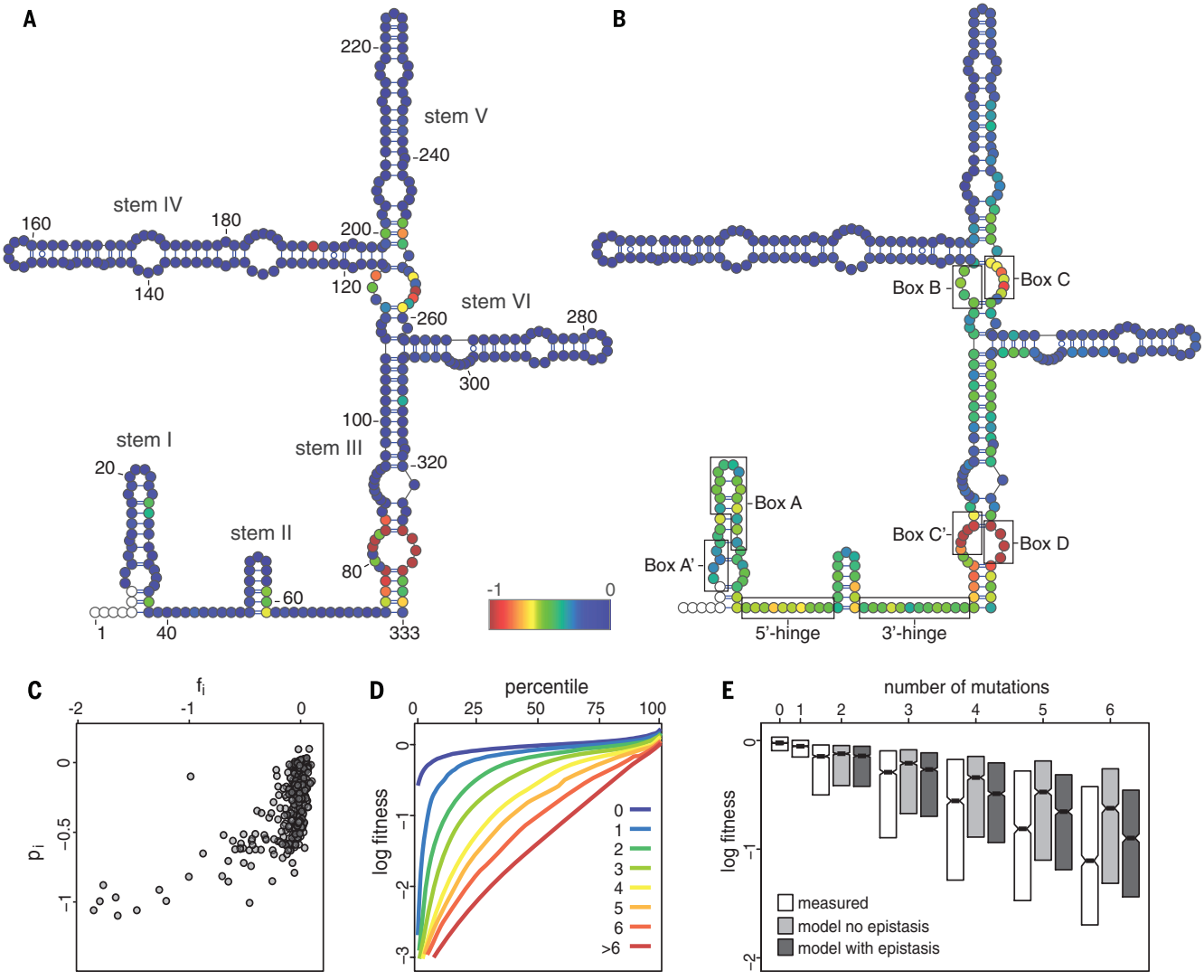


**Fig. 2. Distribution of fitness effects mapped to secondary structure.** (**A**) The log fitness of single mutants at each position of U3 ($f_i$) is represented according to the color scale, from blue for no effect to red for effects –1 and stronger; nonmutagenized positions are white. (**B**) The population-average log fitness effect for each position in the background of multiple mutations ($p_i$) (*13*). Evolutionarily conserved motifs are indicated on the secondary structure. (**C**) Nonlinear relation between the fitness effects of single mutations in wild-type background ($f_i$) and in mutated backgrounds ($p_i$). (**D**) Cumulative distributions of log fitness for mutants grouped by the number of mutations per variant. (**E**) Mean measured log fitness (white boxes) is always lower than expected in the absence of epistasis (gray boxes). Inclusion of epistasis improves the fit between the model and the data (dark gray boxes). The boxes show the median and interquartile ranges.

interactions when applied to our replicate experiments (fig. S9). We obtained a consensus set of epistatic interactions by averaging the interaction estimates from all four glucose competition experiments. Plotting these interactions resulted in a characteristic tartan pattern (Fig. 3A), in which several positions in the gene showed strong positive interactions with most other sites. These hubs of positive epistasis correspond to the C′, C, and D boxes, which are highly conserved in evolution and show the largest individual effects on fitness. This observation indicates a saturation effect, whereby large-effect mutations inactivate the gene to such an extent that additional mutations become irrelevant, which results in positive epistasis. Consistently, sites with large individual effects showed a strong bias toward positive epistasis (Wilcoxon test, $P < 2 \times 10^{-16}$) (Fig. 3, B and C), and the fitness of C′, C, and D box mutants did not depend strongly on the presence of additional mutations in the gene. The saturation effect is the within-gene equivalent of positive epistasis between pairs of mutations that independently inactivate the same metabolic pathway (*18*, *19*).

We also expected positive interactions between base-paired positions, because of the presence of compensatory mutations, which are common in RNA evolution (*5*). Indeed, base-paired positions showed an enrichment of positive epistasis relative to all pairs of positions (Wilcoxon test, $P = 2 \times 10^{-7}$) (Fig. 3D). In particular, all positions within the essential terminal stem formed strong positive interactions with their corresponding base-paired residues (Fig. 3E). To test whether positive epistasis can be used to predict RNA folding, we intersected the set of positive interactions with a list of all potentially interacting triplets of nucleotides (*13*). In this analysis, five out of six of the strongest positive interactions corresponded to known base pairs. When we used these interactions as constraints in RNA folding prediction, the accuracy of predicted secondary structure was improved (fig. S10).

Despite the enrichment of positive interactions among large-effect or base-paired sites, negative interactions were more common overall (Fig. 3, A and B). Whereas the strongest positive interactions typically involved at least one large-effect position (Fig. 4A), negative interactions were common among low- and intermediate-effect sites and were distributed throughout the molecule,

Downloaded from http://science.sciencemag.org/ on May 12, 2016

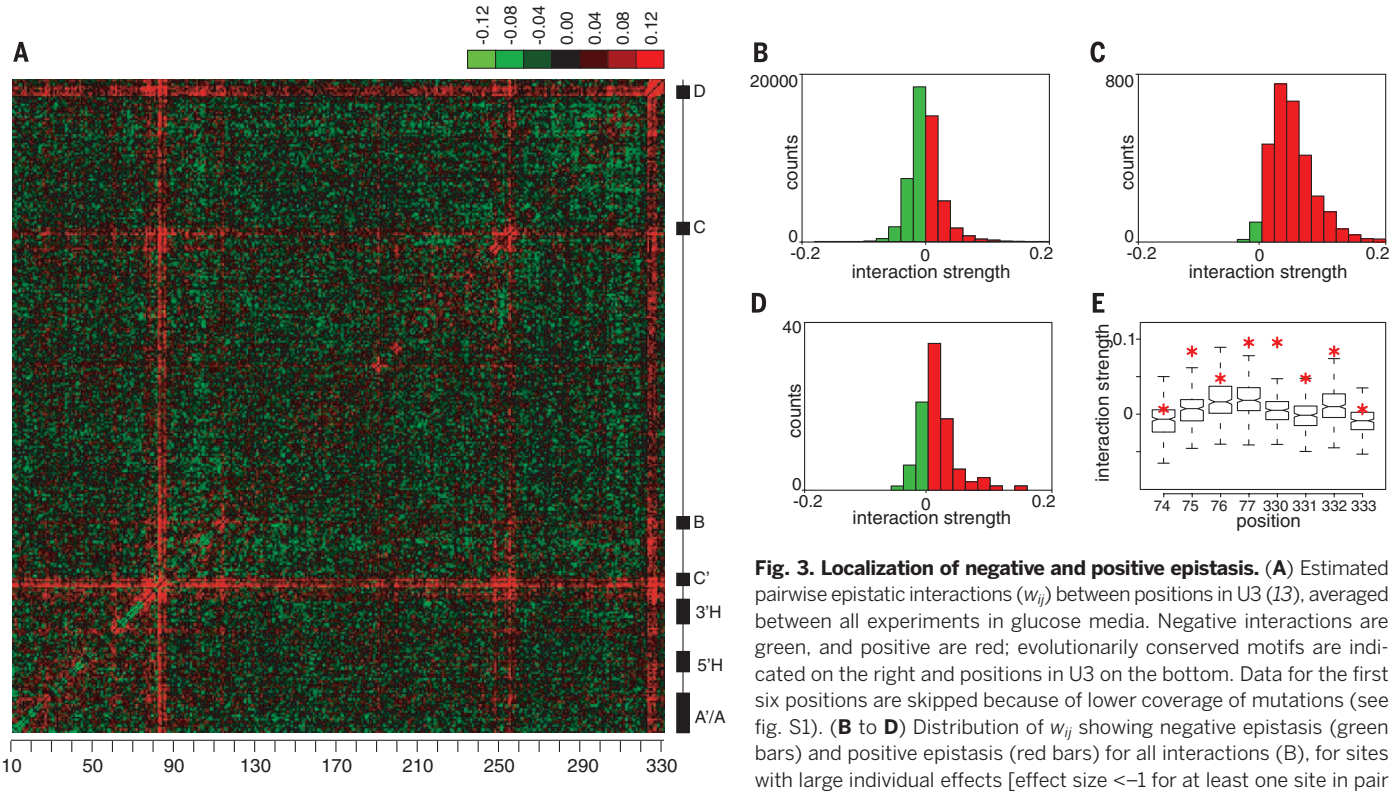


**Fig. 3. Localization of negative and positive epistasis.** (**A**) Estimated pairwise epistatic interactions ($w_{ij}$) between positions in U3 (*13*), averaged between all experiments in glucose media. Negative interactions are green, and positive are red; evolutionarily conserved motifs are indicated on the right and positions in U3 on the bottom. Data for the first six positions are skipped because of lower coverage of mutations (see fig. S1). (**B** to **D**) Distribution of $w_{ij}$ showing negative epistasis (green bars) and positive epistasis (red bars) for all interactions (B), for sites with large individual effects [effect size <–1 for at least one site in pair (C)], and among pairs of base-paired positions (D). (**E**) Distributions of $w_{ij}$ for individual positions in the terminal stem (74 to 77, 330 to 333). Red asterisks indicate interactions between known base pairs.

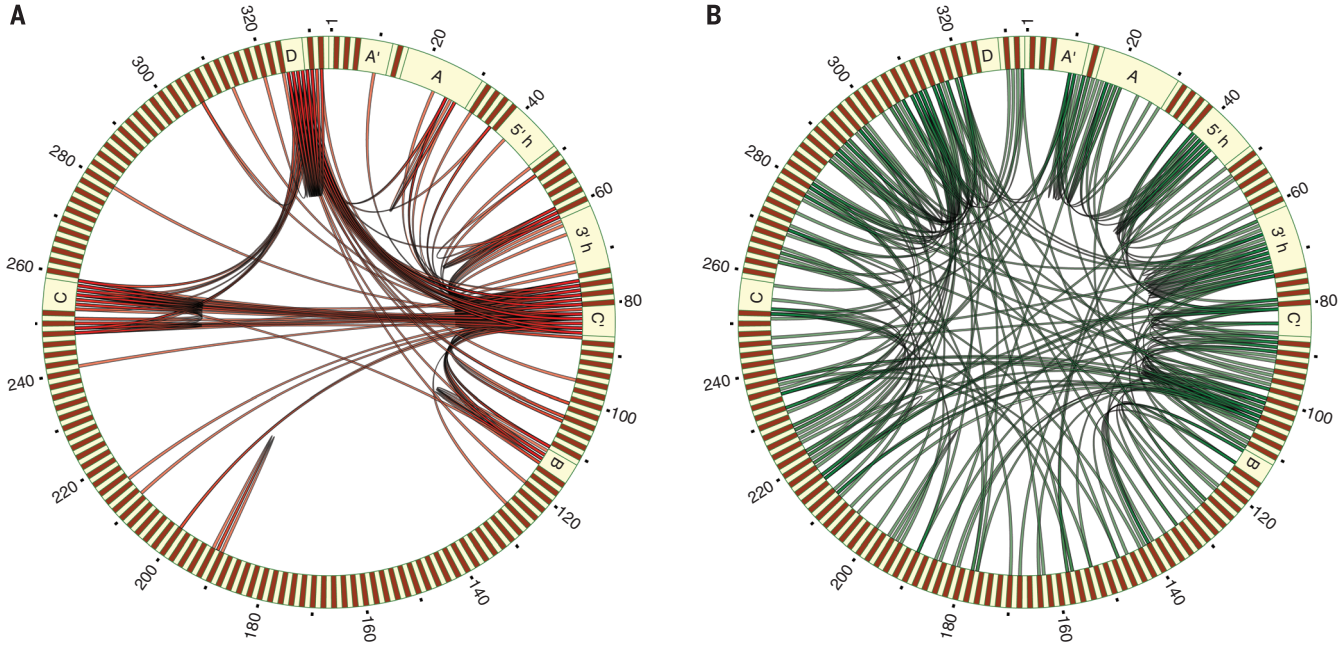


**Fig. 4. Network of epistatic interactions.** Circos plots showing patterns of the 200 strongest positive (**A**) and negative (**B**) interactions within U3. Evolutionarily conserved motifs are indicated.

with enrichment in the conserved core (Fig. 4B). The strength of negative epistasis was inversely correlated with the distance along the primary sequence: 8 out of the 10 strongest negative interactions were between pairs of adjacent nucleotides, and the median distance between the 100 most strongly interacting pairs was 18 nt. We thus focused on a hotspot of interactions encompassing the 3′ hinge (fig. S11A) that mediates base-pairing between U3 and the pre-rRNA and is necessary for the pre-rRNA cleavage step of ribosome biogenesis (*20*). Our results suggest

Downloaded from http://science.sciencemag.org/ on May 12, 2016

that the 3′ hinge can tolerate a single SNP but that multiple mutations within this region reduce fitness, probably because they disrupt U3-rRNA binding. A similar, but less pronounced, pattern was found in the 5′ hinge area. Our analysis shows that the thermodynamic threshold model, wherein fitness decreases abruptly when molecule stability falls below a certain level (*9*), also operates at the level of interactions between distinct molecules (fig. S11B).

In genome-wide studies, epistatic interactions between genes correlate with physical contacts, coevolution, and co-occurrence within biochemical pathways (*6*). Mapping genetic interaction networks therefore provides information about cellular organization. We postulate that intragenic interaction maps will similarly illuminate patterns of molecular organization. This and other studies (*8*, *17*, *21*, *22*) suggest that within-gene epistatic interactions are enriched among residues in physical proximity. Were this correlation sufficiently strong, intragene epistasis would identify secondary and tertiary structures of macromolecules. Notably, recent studies have successfully predicted the 3D structures of proteins and complexes by measuring coevolution between residues within protein alignments, a phenomenon intimately linked to epistasis (*23*, *24*). Improved methods to extract structurally relevant interactions from the dense network of intramolecular epistasis should allow macromolecular structures to be derived from maps of within-gene epistasis.

## REFERENCES AND NOTES


1. P. C. Phillips, *Nat. Rev. Genet.* **9**, 855–867 (2008).
2. J. A. de Visser, J. Krug, *Nat. Rev. Genet.* **15**, 480–490 (2014).
3. D. M. Weinreich, N. F. Delaney, M. A. Depristo, D. L. Hartl, *Science* **312**, 111–114 (2006).
4. J. I. Jiménez, R. Xulvi-Brunet, G. W. Campbell, R. Turk-MacLeod, I. A. Chen, *Proc. Natl. Acad. Sci. U.S.A.* **110**, 14984–14989 (2013).
5. M. V. Meer, A. S. Kondrashov, Y. Artzy-Randrup, F. A. Kondrashov, *Nature* **464**, 279–282 (2010).
6. M. Costanzo *et al.*, *Science* **327**, 425–431 (2010).
7. B. Lehner, *Trends Genet.* **27**, 323–331 (2011).
8. B. H. Davis, A. F. Poon, M. C. Whitlock, *Proc. Biol. Sci.* **276**, 1823–1827 (2009).
9. S. Bershtein, M. Segal, R. Bekerman, N. Tokuriki, D. S. Tawfik, *Nature* **444**, 929–932 (2006).
10. C. Bank, R. T. Hietpas, J. D. Jensen, D. N. Bolon, *Mol. Biol. Evol.* **32**, 229–238 (2015).
11. A. I. Podgornaia, M. T. Laub, *Science* **347**, 673–677 (2015).
12. D. A. Samarsky, M. J. Fournier, *Mol. Cell. Biol.* **18**, 3431–3444 (1998).
13. Materials and methods are available as supporting material on *Science* Online.
14. W. Wlotzka, G. Kudla, S. Granneman, D. Tollervey, *EMBO J.* **30**, 1790–1803 (2011).
15. J. Otwinowski, I. Nemenman, *PLOS One* **8**, e61570 (2013).
16. J. Otwinowski, J. B. Plotkin, *Proc. Natl. Acad. Sci. U.S.A.* **111**, E2301–E2309 (2014).
17. T. Hinkley *et al.*, *Nat. Genet.* **43**, 487–489 (2011).
18. R. P. St Onge *et al.*, *Nat. Genet.* **39**, 199–206 (2007).
19. X. He, W. Qian, Z. Wang, Y. Li, J. Zhang, *Nat. Genet.* **42**, 272–276 (2010).
20. L. M. Dutca, J. E. Gallagher, S. J. Baserga, *Nucleic Acids Res.* **39**, 5164–5180 (2011).
21. H. Braberg *et al.*, *Cell* **154**, 775–788 (2013).
22. C. Li *et al.*, *Science* **352**, 837–840 (2016).
23. T. A. Hopf *et al.*, *eLife* **3**, (2014).
24. D. S. Marks *et al.*, *PLOS One* **6**, e28766 (2011).



## ACKNOWLEDGMENTS

We thank B. Charlesworth, A. DeLuna, J. Plotkin, C. Schneider, and J. Zhang for discussions; E. Wacker and A. Gallacher for technical assistance; M. Bartosovic for computational help; and Edinburgh Genomics, Edinburgh Clinical Research Facility, and Institute of Genetics and Molecular Medicine technical support for next-generation sequencing. The sequencing and barcode count data were deposited in GEO (accession number GSE77709), and the data modeling pipeline can be found on https://github.com/terembura/EpistaticInteractionsYeastU3. G.K. and O.P. designed the project; O.P. performed experiments; O.P., B.C., H.C., D.T., G.S., and G.K. analyzed the data; B.C. and G.S. designed and B.C. implemented the data modeling pipeline; and G.K. wrote the manuscript with input from other coauthors. O.P. and G.K. were supported by Wellcome Trust grant 097383 and by the U.K. Medical Research Council, D.T. was supported by Wellcome Trust grant 077248, G.S. was supported by the European Research Council grant MLCS306999.

## SUPPLEMENTARY MATERIALS

www.sciencemag.org/content/352/6287/840/suppl/DC1
Materials and Methods
Figs. S1 to S11
Tables S1 and S2
References (*25*–*41*)

16 December 2015; accepted 23 March 2016
Published online 14 April 2016
10.1126/science.aaf0965


CANCER

# Histone H3K36 mutations promote sarcomagenesis through altered histone methylation landscape


**Chao Lu,[1] Siddhant U. Jain,[2,3] Dominik Hoelper,[2,3] Denise Bechet,[4] Rosalynn C. Molden,[5,6]* Leili Ran,[7] Devan Murphy,[7] Sriram Venneti,[8] Meera Hameed,[9] Bruce R. Pawel,[10] Jay S. Wunder,[11,12] Brendan C. Dickson,[13,14] Stefan M. Lundgren,[2,3] Krupa S. Jani,[6] Nicolas De Jay,[4] Simon Papillon-Cavanagh,[4] Irene L. Andrulis,[13,14,15,16] Sarah L. Sawyer,[17] David Grynspan,[18] Robert E. Turcotte,[19] Javad Nadaf,[4] Somayyeh Fahiminiyah,[4] Tom W. Muir,[6] Jacek Majewski,[4] Craig B. Thompson,[20] Ping Chi,[7,21] Benjamin A. Garcia,[5] C. David Allis,[1]† Nada Jabado,[4,22]† Peter W. Lewis[2,3]†**



**Several types of pediatric cancers reportedly contain high-frequency missense mutations in histone H3, yet the underlying oncogenic mechanism remains poorly characterized. Here we report that the H3 lysine 36–to–methionine (H3K36M) mutation impairs the differentiation of mesenchymal progenitor cells and generates undifferentiated sarcoma in vivo. H3K36M mutant nucleosomes inhibit the enzymatic activities of several H3K36 methyltransferases. Depleting H3K36 methyltransferases, or expressing an H3K36I mutant that similarly inhibits H3K36 methylation, is sufficient to phenocopy the H3K36M mutation. After the loss of H3K36 methylation, a genome-wide gain in H3K27 methylation leads to a redistribution of polycomb repressive complex 1 and de-repression of its target genes known to block mesenchymal differentiation. Our findings are mirrored in human undifferentiated sarcomas in which novel K36M/I mutations in H3.1 are identified.**


Somatic missense mutations in histone H3 genes were recently identified in pediatric brain and bone malignancies (*1*–*3*). These include lysine 27–to–methionine (K27M) and glycine 34–to–arginine/valine (G34R/V) mutations found in pediatric gliomas, glycine 34–to–tryptophan/leucine (G34W/L) mutations found in giant cell tumors of the bone, and lysine 36–to–methionine (K36M) mutations reported in ~95% of chondroblastomas. These cancer-associated H3 mutations (so-called "oncohistones") map to, or close to, well-known sites of histone posttranslational modifications such as methylation of H3K27 and H3K36. The highly clustered mutational patterns and only 1 of the 30 alleles encoding human histone H3 being mutated in tumors imply that the mutations are dominant or neomorphic. Moreover, the high degree of tumor type specificity suggests that oncohistones derived from different tissues of origin are likely to be functionally and mechanistically distinct. Although progress has been made in understanding the oncogenic effect of glioma-associated histone mutations (*4*–*8*), their role in bone and cartilage neoplasms remains unclear.

We focused on the chondroblastoma-derived H3K36M mutation. Chondroblastoma is characterized by the accumulation of immature chondroblasts (*9*), suggesting that the neoplasm may arise from uncontrolled proliferation and/or incomplete differentiation of mesenchymal progenitor cells (MPCs). We created isogenic C3H10T1/2 murine MPCs that stably express either wild-type or K36M mutant H3.3 at pathologically relevant levels (hereafter referred to as H3.3WT or H3.3K36M cells, respectively) (fig. S1, A and B).

Downloaded from http://science.sciencemag.org/ on May 12, 2016

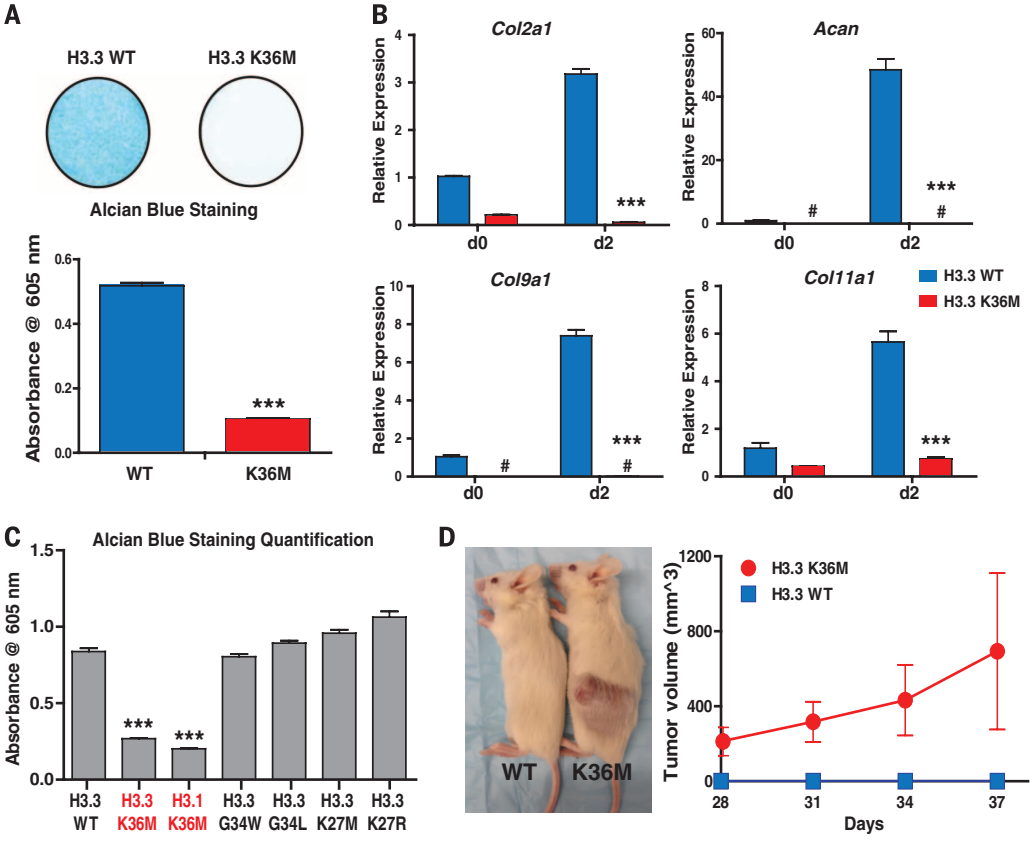


**Fig. 1. H3K36M mutation impairs mesenchymal differentiation and generates undifferentiated sarcoma.** (**A**) Representative Alcian blue–stained images of cell culture wells after 9 days of chondrocyte differentiation. The bar graph shows the quantification of staining in cell extract. (**B**) The mRNA expression of *Acan*, *Col2a1*, *Col9a1*, and *Col11a1* in cells before (d0) and two days after (d2) chondrocyte differentiation induction. (**C**) Quantification of Alcian blue staining in cell extract after 9 days of chondrocyte differentiation. (**D**) Measurement of subcutaneous tumor growth of H3.3WT or H3.3K36M cells. A representative image of mice implanted with cells is shown at the time when they were killed. In (D), error bars indicate standard deviation (SD) ($n$ = 10 mice in each group). In other experiments, error bars indicate SD from three biological replicates. #undetectable, ***$P$ < 0.001.

Differentially expressed genes between H3.3WT and H3.3K36M cells were highly enriched in pathways involved in cellular and developmental processes (fig. S1, C and D, and table S1), suggesting that H3.3K36M mutation induces aberrant expression of genes involved in cell differentiation. Although H3.3WT and H3.3K36M cells displayed comparable proliferation rates (fig. S1E), H3.3K36M cells exhibited significantly diminished chondrocytic differentiation capacity (Fig. 1A). H3.3K36M cells also showed a decrease in mRNA expression of mature chondrocyte markers (*Col2a1*, *Col9a1*, *Col11a1*, and *Acan*) before and after differentiation induction (Fig. 1B). Expressing the H3.3K36M mutation in murine prechondrocytic ATDC5 cells (*10*) also substantially inhibited chondrocyte differentiation (fig. S1F).

Oncohistones found in other cancer types (H3.3K27M or H3.3G34W/L) had little impact on chondrocyte differentiation of MPCs (Fig. 1C and fig. S2A). These results are consistent with the tissue specificity of histone mutations identified in human cancers. Expression of H3.1K36M in MPCs altered the transcriptome and inhibited chondrocyte differentiation to a similar extent as H3.3K36M (Fig. 1C and fig. S2, A and B). The presence of the K36M mutation did not affect the genome-wide deposition profiles of H3.1 and H3.3 (fig. S2, C to E) (*11*).

Whole-genome sequencing of chondroblastomas revealed H3.3K36M as the only recurrent mutation (*3*). We sought to determine whether the differentiation arrest induced by the H3K36M mutation is sufficient to facilitate tumor development in vivo. Subcutaneous injection of MPCs stably expressing H3.3 or H3.1 K36M, but not WT H3, generated tumors in severe combined immunodeficiency (SCID) mice (Fig. 1D and fig. S3A). These tumors resembled human undifferentiated sarcomas (fig. S3B), retained the expression of mutant histones, and shared a similar gene expression profile with cells cultured in vitro (figs. S2B and S3C).

Although H3K36M mutations are uncommon in bone and cartilage tumors other than chondroblastomas (*3*), our in vivo modeling results suggest that K36M mutations in H3.3 or H3.1 may exist in poorly differentiated soft tissue tumors. Pediatric undifferentiated soft tissue sarcomas are rare but aggressive tumors with poor prognosis and an undefined mutational landscape (*12*). By screening a panel of 10 pediatric undifferentiated soft tissue sarcomas, we identified one tumor carrying an H3.1K36M mutation and confirmed its protein expression (fig. S4).

The development of undifferentiated sarcomas by H3K36M mutant MPCs prompted us to determine whether the mutation interferes with the differentiation of these cells toward other

[1]Laboratory of Chromatin Biology and Epigenetics, The Rockefeller University, New York, NY 10065, USA. [2]Epigenetics Theme, Wisconsin Institute for Discovery, University of Wisconsin, Madison, WI 53715, USA. [3]Department of Biomolecular Chemistry, School of Medicine and Public Health, University of Wisconsin, Madison, WI 53715, USA. [4]Department of Human Genetics, McGill University, Montreal, Quebec H3Z 2Z3, Canada. [5]Epigenetics Program and Department of Biochemistry and Biophysics, Perelman School of Medicine at the University of Pennsylvania, Philadelphia, PA 19104, USA. [6]Department of Chemistry, Princeton University, Princeton, NJ 08544, USA. [7]Human Oncology and Pathogenesis Program and Department of Medicine, Memorial Sloan Kettering Cancer Center, New York, NY 10065, USA. [8]Department of Pathology, University of Michigan Medical School, Ann Arbor, MI 48109, USA. [9]Department of Pathology, Memorial Sloan Kettering Cancer Center, New York, NY 10065, USA. [10]Department of Pathology and Laboratory Medicine, The Children's Hospital of Philadelphia and Perelman School of Medicine at the University of Pennsylvania, Philadelphia, PA 19104, USA. [11]University Musculoskeletal Oncology Unit, Mount Sinai Hospital, Toronto, Ontario M5G 1X5, Canada. [12]Department of Surgical Oncology and Division of Orthopedic Surgery, Princess Margaret Hospital, University of Toronto, Toronto, Ontario M5T 2M9, Canada. [13]Department of Laboratory Medicine and Pathobiology, University of Toronto, Toronto, Ontario M5S 1A8, Canada. [14]Department of Pathology and Laboratory Medicine, Mount Sinai Hospital, Toronto, Ontario M5G 1X5, Canada. [15]Department of Molecular Genetics, University of Toronto, Toronto, Ontario M5S 1A8, Canada. [16]The Lunenfeld-Tanenbaum Research Institute, Sinai Health System, Toronto, Ontario M5G 1X5, Canada. [17]Department of Medical Genetics and Children's Hospital of Eastern Ontario Research Institute, University of Ottawa, Ottawa, Ontario K1H 8L1, Canada. [18]Department of Pathology and Laboratory Medicine and Children's Hospital of Eastern Ontario Research Institute, University of Ottawa, Ottawa, Ontario K1H 8L1, Canada. [19]Division of Orthopaedic Surgery, Montreal General Hospital, McGill University Health Centre, Montreal, Quebec H3G 1A4, Canada. [20]Cancer Biology and Genetics Program, Memorial Sloan Kettering Cancer Center, New York, NY 10065, USA. [21]Department of Medicine, Weill Cornell Medical College, New York, NY 10065, USA. [22]Department of Pediatrics, McGill University, Montreal, Quebec H3Z 2Z3, Canada.
*Present address: Regeneron Pharmaceuticals, Tarrytown, NY 10591, USA. †Corresponding author. Email: plewis@discovery.wisc.edu (P.W.L.); nada.jabado@mcgill.ca (N.J.); alliscd@rockefeller.edu (C.D.A.)

Downloaded from http://science.sciencemag.org/ on May 12, 2016

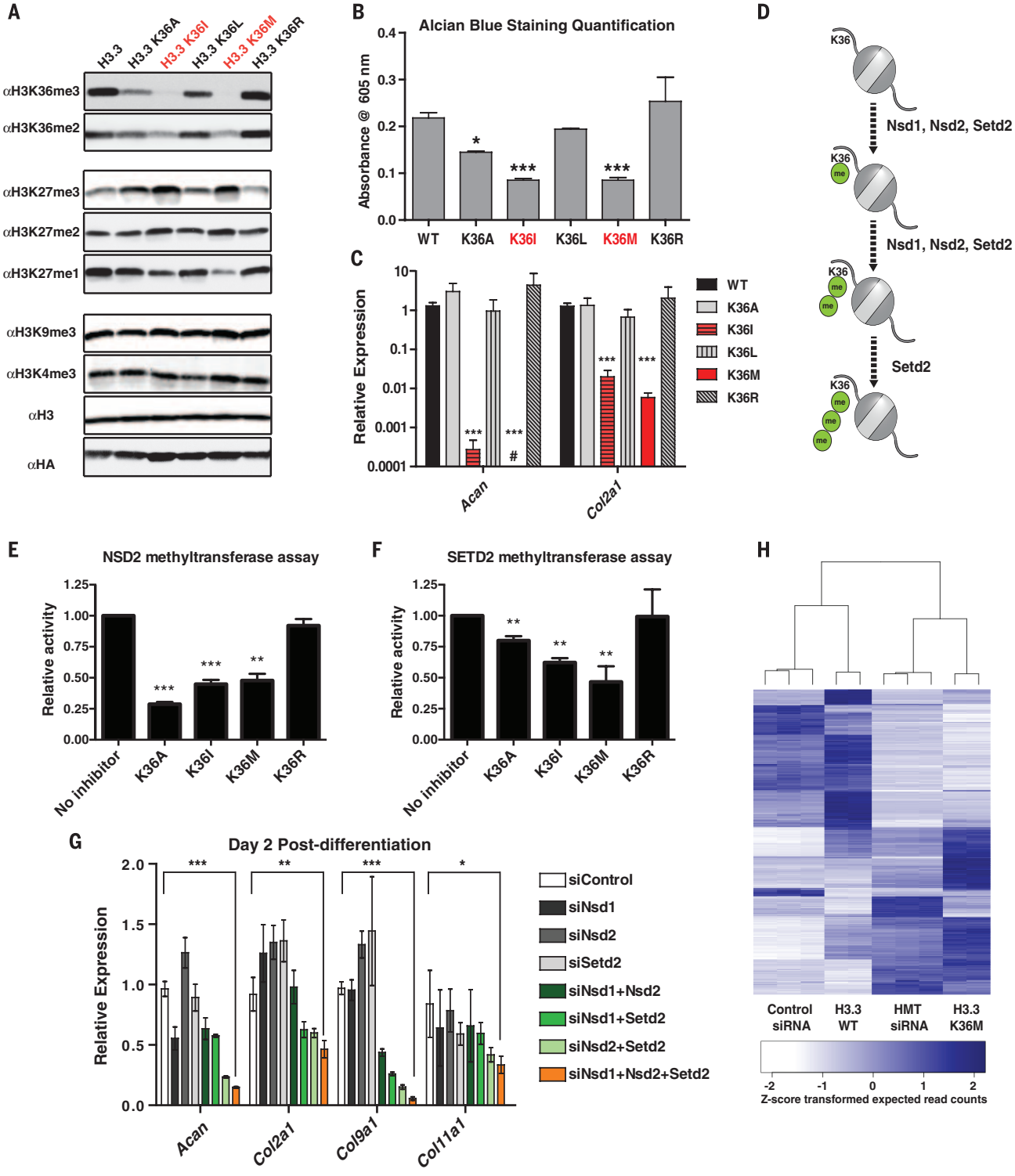


**Fig. 2. H3K36 mutations dominantly inhibit H3K36 methyltransferases.** (**A**) Immunoblots of lysates generated from 293T cells expressing FLAG- and hemagglutinin (HA)–tagged WT or K36A/I/L/M/R mutant H3.3. (**B**) Quantification of Alcian blue staining in cell extract after 9 days of chondrocyte differentiation. (**C**) The mRNA expression of *Acan* and *Col2a1* in cells after 2 days of chondrocyte differentiation. (**D**) Schematic introduction of mammalian H3K36 methyltransferases. (**E** and **F**) In vitro methyltransferase assays with recombinant human full-length NSD2 (E) or SET domain of SETD2 (F), recombinant substrate nucleosomes, and tritiated S-adenosyl methionine. Various K36 mutant H3(27-47) peptides were added to the reaction mixture. For NSD2 assays, the final concentration of inhibitor peptides was 30 μM; for SETD2 assays, it was 50 μM. Methyltransferase activity was quantified via scintillation and normalized. (**G**) MPCs were transfected with siRNA for 3 days, followed by chondrocyte differentiation induction for 2 days. The mRNA expression of *Acan*, *Col2a1*, *Col9a1*, and *Col11a1* was measured. (**H**) Heat map showing the expression pattern of greater than fourfold differentially expressed genes between cells treated with siRNAs against Nsd1/2 and Setd2 (HMT siRNA) or control siRNA. For all experiments, error bars indicate SD from three biological replicates. #undetectable; **P* < 0.05, ***P* < 0.01, ****P* < 0.001.

Downloaded from http://science.sciencemag.org/ on May 12, 2016

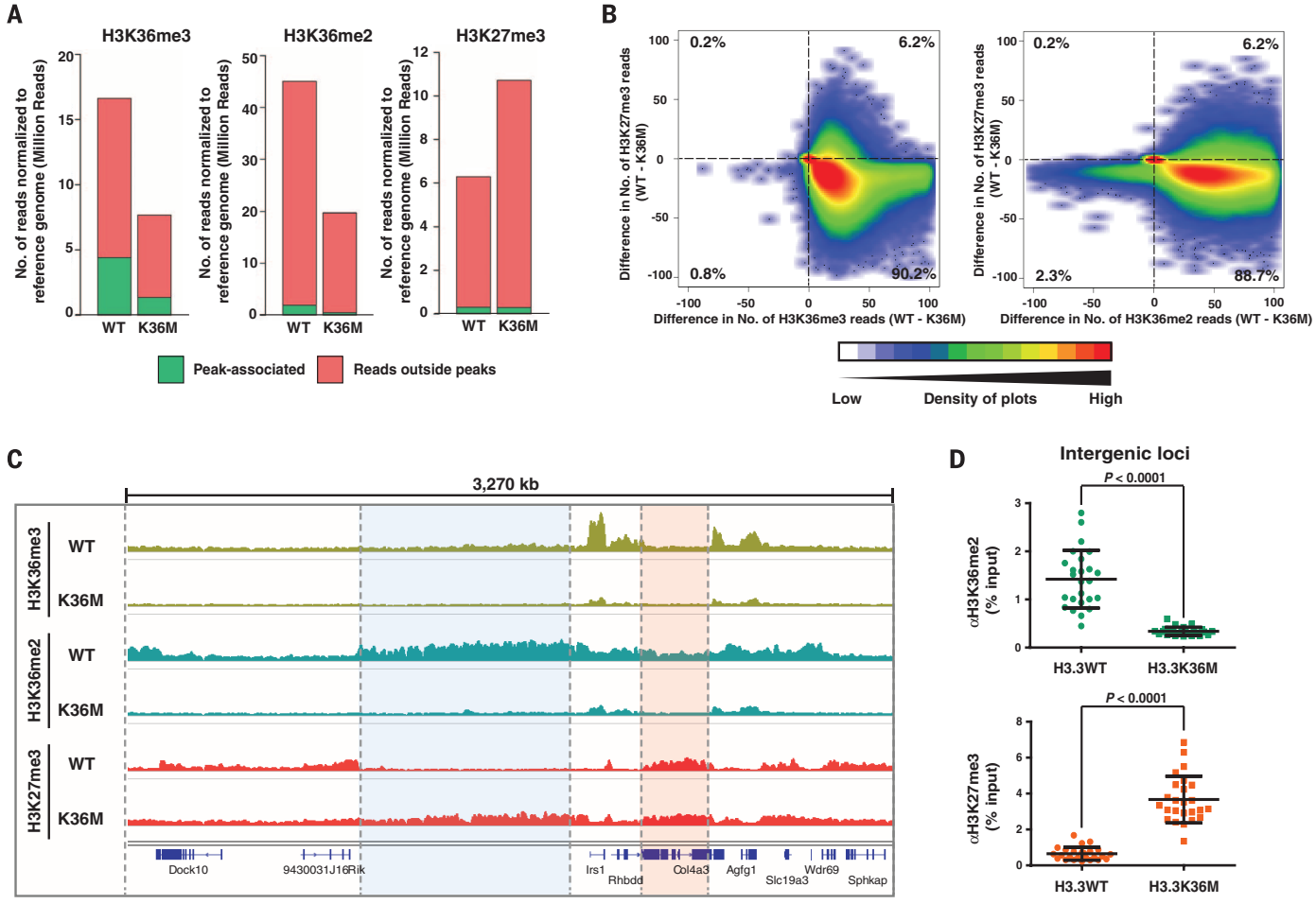


**Fig. 3. Genome-wide profiling of H3K36me2/3 and H3K27me3 in H3.3WT and H3.3K36M cells.** (**A**) After normalization, the number of H3K36me2/3 and H3K27me3 reads that are peak-associated or outside peaks are shown. (**B**) Scatter plot showing the correlation between genome-wide changes in H3K27me3 and H3K36me2/3. The genome was divided into 10,000 base pair bins, and the difference in the number of normalized ChIP-seq reads of H3K36me2/3 or H3K27me3 between H3.3WT and H3.3K36M cells was plotted. The percentage of bins found in each quadrant is shown. (**C**) Genome viewer representations of normalized ChIP-seq reads for H3K36me2/3 and H3K27me3 at a 3270-kb region. Refseq genes are annotated at the bottom. (**D**) The enrichment (% input) of H3K36me2 and H3K27me3 at various intergenic regions was measured with ChIP–quantitative polymerase chain reaction. Each data point represents a genomic locus.

lineages. H3.3K36M cells exhibited a significant block of differentiation to adipocytes and osteocytes (fig. S5, A and B). Moreover, the expression of master regulators of adipogenesis and osteogenesis was decreased in H3.3K36M cells, in addition to regulators of chondrocyte differentiation. H3.3K36M cells also displayed enhanced expression of transcription factors involved in the maintenance of mesenchymal multipotency (fig. S5C).

We found that the H3K36M transgene caused a marked reduction in H3K36me2/3 and a concomitant increase in H3K27me2/3 in various cell types (Fig. 2A and fig. S6, A to C). Immunoblots of purified heterotypic mononucleosomes containing epitope-tagged H3.3 and endogenous H3 revealed that K36M-containing nucleosomes displayed decreased H3K36me2/3 and increased H3K27me3 on the endogenous WT H3 (fig. S6D). Coimmunostaining of murine H3.3K36M tumors demonstrated an inverse correlation between H3.3K36M expression and levels of H3K36me3 (fig. S6E). Chondroblastoma samples carrying the H3.3K36M mutation exhibited decreased H3K36me2/3 and increased H3K27me3 as compared to H3 WT chondroblastoma or chondrosarcomas (fig. S7, A and B). Immunohistochemistry staining revealed that H3.3K36M-expressing chondroblastoma cells, but not concomitant nonneoplastic multinuclear osteoclasts (*3*) or H3 WT chondroblastomas or chondrosarcomas, were negative for H3K36me3 (fig. S7, C and D).

The capacity of various H3K36 mutants to impair chondrocyte differentiation of MPCs was correlated to the magnitude of changes in H3K36 and H3K27 methylation (Fig. 2, A to C, and fig. S8A). In particular, the H3K36I mutation recapitulated H3K36M's impact on histone methylation and gene expression (Fig. 2A and fig. S8, A to C). Furthermore, an H3.1K36I mutation was identified in a pediatric undifferentiated soft tissue sarcoma from the same patient cohort where we found the H3.1K36M mutation (fig. S4 and table S2). Therefore, H3K36 hypomethylation and H3K27 hypermethylation appear to be characteristic features shared by the oncogenic H3K36M/I mutations.

Gliomas containing the H3K27M mutation exhibit low levels of H3K27 methylation, and we demonstrated that this loss of methylation occurred primarily through inhibition of the polycomb repressive complex 2 (PRC2) histone methyltransferase (*6*). Because the catalytic mechanism is highly conserved among SET domain–containing histone methyltransferases, we hypothesized that H3K36M/I mutations inhibit their cognate methyltransferases. Unlike H3K27, methylation of H3K36 is catalyzed by several methyltransferases, including Nsd1 and Nsd2, which catalyze H3K36me1/2, and Setd2, which catalyzes H3K36me1/2/3 (*13*) (Fig. 2D). Methyltransferase assays with peptides or purified nucleosomes demonstrated that H3K36M/I, but not H3K36R, were potent inhibitors of SETD2 and NSD2 activity (Fig. 2, E and F, and fig. S9, A to C). H3K36A substantially inhibited NSD2 activity while modestly inhibiting

Downloaded from http://science.sciencemag.org/ on May 12, 2016

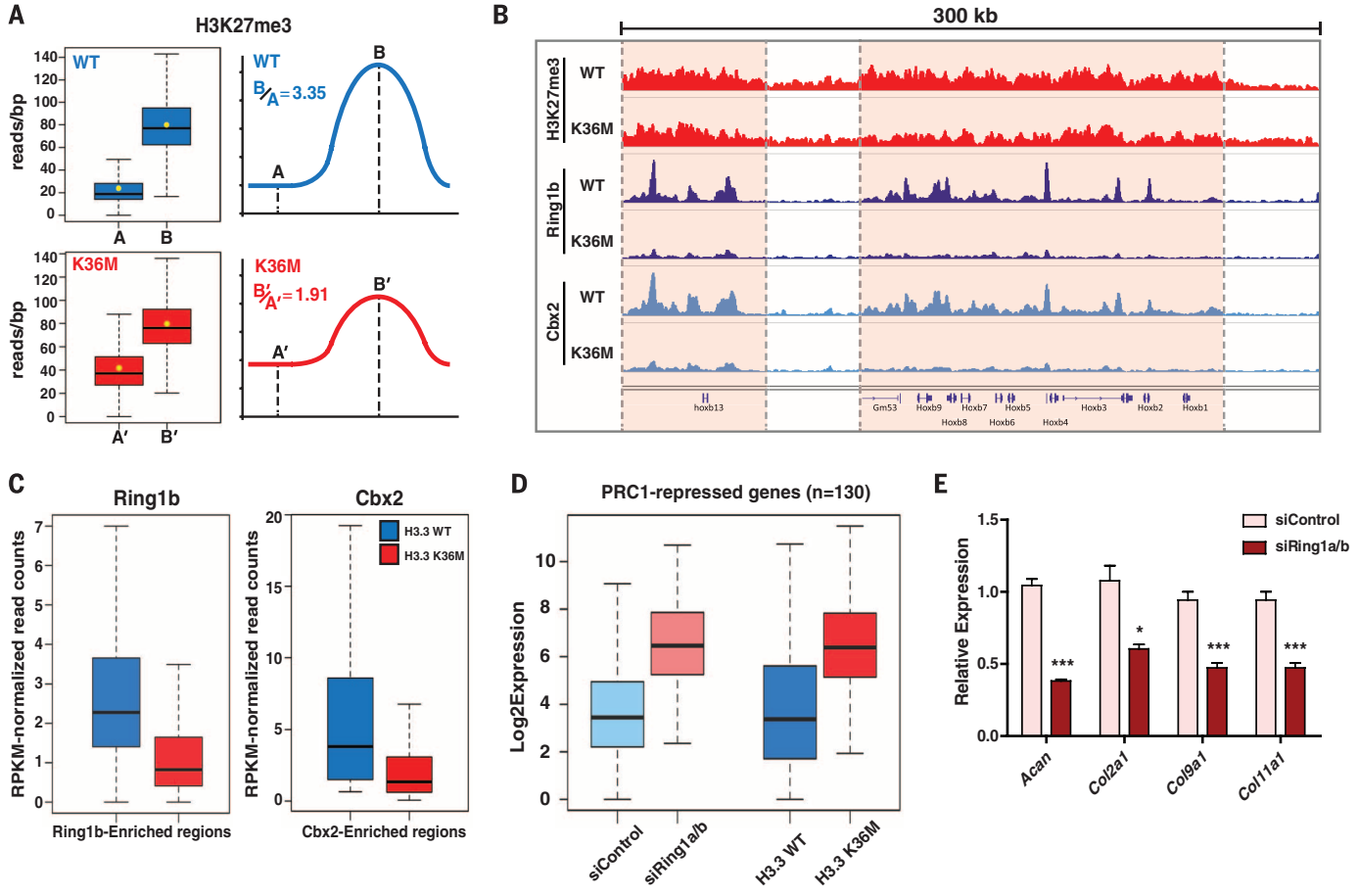


**Fig. 4. Intergenic gain of H3K27me3 leads to redistribution of PRC1 and aberrant gene activation.** (**A**) Box plots (left) and schematics (right) displaying the ratio of average H3K27me3 reads per base pair between gene-associated peaks (B or B') and intergenic regions (A or A'). (**B**) Genome viewer representations of normalized ChIP-seq reads for H3K27me3, Ring1b, and Cbx2 at A *Hoxb* gene cluster. Refseq genes are annotated at the bottom. (**C**) Box plots of normalized Ring1b and Cbx2 ChIP-seq peak reads. *P* value < $2.2 \times 10^{-16}$ was determined by Wilcoxon's rank sum test. RPKM, reads per kilobase per million. (**D**) Box plots of expression levels of PRC1-repressed genes are shown for control or Ring1a/b siRNA knockdown cells and for H3.3WT and H3.3K36M cells. *P* value < $2.2 \times 10^{-16}$ was determined by Wilcoxon's rank sum test. (**E**) MPCs were transfected with siRNA for 3 days, followed by chondrocyte differentiation induction for 2 days. The mRNA expression of *Acan*, *Col2a1*, *Col9a1*, and *Col11a1* was measured. Error bars indicate SD from three biological replicates. *$P < 0.05$, ***$P < 0.001$.

SETD2 (Fig. 2, E and F, and fig. S9D), which is consistent with its observed effects on cellular H3K36me2/3 (Fig. 2A and fig. S8A). Although expression of the H3K36 methyltransferases was not reduced in H3.3K36M cells, we found that immunoprecipitates from H3K36M-containing mononucleosomes were markedly enriched in these proteins (fig. S10, A and B), suggesting that the global H3K36 hypomethylation in H3.3K36M cells results from the dominant sequestration and inhibition of methyltransferases by mutant nucleosomes.

To assess the contribution of methyltransferase inhibition to the H3K36M-induced differentiation arrest, Nsd1, Nsd2, and Setd2 were depleted separately or in combination in MPCs by the use of small interfering RNA (siRNA). Depletion of Nsd1, Nsd2, and Setd2 in combination, but not individually, impaired the chondrocyte differentiation of MPCs, with the most dramatic effect being observed in cells treated with siRNAs against all three methyltransferases (Fig. 2G and fig. S10C). In addition, clustering analysis revealed that transcriptome changes induced by H3.3K36M could be largely recapitulated via the combined knockdown of Nsd1/2 and Setd2 (Fig. 2H). As anticipated, the individual knockdown of Nsd1/2 and Setd2 led to specific decreases in H3K36me2 and H3K36me3, respectively (fig. S10C). Cells depleted in all H3K36-directed methyltransferases not only displayed reduced H3K36me2/3 but also showed elevated levels of H3K27me3 comparable to that in H3.3K36M cells, indicating that the gain of H3K27me3 in H3.3K36M cells only occurs upon global loss of both H3K36me2 and H3K36me3. Nucleosomes containing H3K36me2/3 are poor substrates for PRC2 in vitro (*14*, *15*). Our data are consistent with a model whereby K36M-mediated loss of H3K36 methylation provides new nucleosomal substrates for PRC2, which results in increased H3K27me3 levels.

We next used chromatin immunoprecipitation followed by DNA sequencing (ChIP-seq) to profile the chromatin landscape in H3.3K36M cells. Because traditional ChIP-seq methods preclude direct comparison of amplitudinal signals between samples, we adopted a strategy that uses exogenous reference chromatin (ChIP-Rx) as an internal normalization control to achieve quantitative analysis of H3K27me3 and H3K36me2/3 (fig. S11A) (*16*). We observed a genome-wide loss of H3K36me2/3 and a concomitant increase in H3K27me3 in H3.3K36M cells (Fig. 3, A and B). Although the levels of gene-associated H3K27me3 remained unchanged, we observed a specific gain of H3K27me3 at intergenic regions previously devoid of H3K27me3 and marked by H3K36me2/3 (Fig. 3, C and D, and fig. S11B). Highly similar genome-wide changes in H3K36me2 and H3K27me3 were observed in H3.1K36M cells (fig. S11, C and D), which were independent of the mutant nucleosome localization (fig. S12A). Depletion of Nsd1/2 and Setd2 was sufficient to mimic K36M's effects on the intergenic loss of H3K36me2 and gain of H3K27me3 (fig. S12B).

Downloaded from http://science.sciencemag.org/ on May 12, 2016

As a consequence of increased nucleosomal substrate availability, levels of chromatin-bound Ezh2 and Suz12 were elevated in H3.3K36M cells (fig. S12, C and D).

The increase in H3K27me3 at intergenic regions led to a decreased ratio of gene-associated–to–intergenic H3K27me3 (Fig. 4A). Genes marked by high H3K27me3 enrichment showed loss of H3K27me3 relative to the genome-wide average and increased expression (fig. S13). We hypothesized that recruitment of the H3K27me3 "readers" may be altered in H3.3K36M cells due to the gain of intergenic H3K27me3 and the relative loss of H3K27me3 enrichment at genes. The localization of Ring1b and Cbx2, integral components of the canonical PRC1 complex that binds to H3K27me3 and suppresses gene expression, was markedly decreased at their bound genes in H3.3K36M cells or after knockdown of H3K36 methyltransferases (Fig. 4, B and C, and fig. S14, A and B), even though protein levels and chromatin association of the PRC1 complex remained unchanged (fig. S12C). Increased enrichment of H2AK119ub1 was found at intergenic loci that gained H3K27me3 in H3.3K36M cells, suggesting a spreading of PRC1 activity to these regions (fig. S14C).

We postulate a model in which "dilution" of the PRC1 complex away from repressed genic loci leads to ectopic gene expression contributing to the differentiation blockade by H3.3K36M (fig. S14D). We found that the majority of PRC1-dependent gene expression changes (93 of 130 up-regulated and 60 of 72 down-regulated genes upon Ring1a/b knockdown) were recapitulated by H3.3K36M expression (Fig. 4D; fig. S15, A to C; and table S3). A specific upregulation of PRC1-repressed genes was observed in H3.3K36M cells (fig. S15D). Many of these genes (such as *Wnt6* and *Sox6*) are implicated in the self-renewal and lineage specification of mesenchymal stem cells (fig. S15E) (*17*, *18*). Consistently, Ring1a/b knockdown was sufficient to impair the chondrocyte differentiation of MPCs (Fig. 4E and fig. S15F). Transcriptome analyses of human chondroblastoma samples revealed a similar de-repression of polycomb-bound genes associated with H3.3K36M mutation (fig. S16).

We have presented evidence that the H3K36M mutation plays a driver role in the development of mesenchymal neoplasms through impaired differentiation of MPCs. Although H3.1 and H3.3 K36M are found at different genomic locations, they result in the same genome-wide changes in chromatin landscape, gene expression profile, and tumorigenic capacity. These data imply that the specific genomic locations of H3K36M-containing nucleosomes are relatively unimportant for K36M's function. Although other non–mutually exclusive mechanisms may be involved (*19*), the dominant inhibition of H3K36 methyltransferases is a critical downstream event mediating H3K36M's differentiation-arresting potential. The concurrent inactivation of multiple methyltransferases via a single missense mutation in histone H3 provides an efficient means to "lock" cells into an aberrant chromatin state that, in the context of mesenchymal progenitors, promotes neoplastic transformation. Our study highlights an underappreciated role of intergenic H3K36 methylation in polycomb complex recruitment through the antagonization of H3K27me3 propagation (*20*, *21*) and demonstrates that modest alterations to the intergenic–to–gene-associated H3K27me3 ratio can have profound outcomes on polycomb-mediated gene silencing. We speculate that similar mechanisms may underlie other human cancers in which histone H3K27 and K36-directed enzymes are frequently dysregulated.

## REFERENCES AND NOTES


1. J. Schwartzentruber *et al.*, *Nature* **482**, 226–231 (2012).
2. G. Wu *et al.*, *Nat. Genet.* **44**, 251–253 (2012).
3. S. Behjati *et al.*, *Nat. Genet.* **45**, 1479–1482 (2013).
4. L. Bjerke *et al.*, *Cancer Discov.* **3**, 512–519 (2013).
5. K.-M. Chan *et al.*, *Genes Dev.* **27**, 985–990 (2013).
6. P. W. Lewis *et al.*, *Science* **340**, 857–861 (2013).
7. S. Bender *et al.*, *Cancer Cell* **24**, 660–672 (2013).
8. K. Funato, T. Major, P. W. Lewis, C. D. Allis, V. Tabar, *Science* **346**, 1529–1533 (2014).
9. C. D. M. Fletcher, World Health Organization, International Agency for Research on Cancer, Eds, *WHO Classification of Tumours of Soft Tissue and Bone* (IARC Press, Lyon, France, ed. 4, 2013).
10. Y. Yao, Y. Wang, *J. Cell. Biochem.* **114**, 1223–1229 (2013).
11. L. A. Banaszynski, C. D. Allis, P. W. Lewis, *Dev. Cell* **19**, 662–674 (2010).
12. G. R. Somers *et al.*, *Pediatr. Dev. Pathol.* **9**, 132–142 (2006).
13. E. J. Wagner, P. B. Carpenter, *Nat. Rev. Mol. Cell Biol.* **13**, 115–126 (2012).
14. W. Yuan *et al.*, *J. Biol. Chem.* **286**, 7983–7989 (2011).
15. F. W. Schmitges *et al.*, *Mol. Cell* **42**, 330–341 (2011).
16. D. A. Orlando *et al.*, *Cell Rep.* **9**, 1163–1170 (2014).
17. T. F. Day, X. Guo, L. Garrett-Beal, Y. Yang, *Dev. Cell* **8**, 739–750 (2005).
18. P. Smits, P. Dy, S. Mitra, V. Lefebvre, *J. Cell Biol.* **164**, 747–758 (2004).
19. H.-M. Herz *et al.*, *Science* **345**, 1065–1070 (2014).
20. L. J. Gaydos, A. Rechtsteiner, T. A. Egelhofer, C. R. Carroll, S. Strome, *Cell Rep.* **2**, 1169–1177 (2012).
21. R. Popovic *et al.*, *PLOS Genet.* **10**, e1004566 (2014).


## ACKNOWLEDGMENTS

We thank D. Weinberg, B. Carey, B. Sabari, and R. Phillips for help in manuscript preparation. This research was supported by funding from Rockefeller University (to C.D.A.), a startup provided by the Wisconsin Institute for Discovery (to P.W.L.), the Greater Milwaukee Foundation (to P.W.L), the Starr Cancer Consortium (grant SCC I6-A614 to C.D.A.), the Sidney Kimmel Foundation (Kimmel Scholar Award to P.C. and P.W.L.), and NIH grants (P01CA196539 to P.W.L., C.D.A., T.W.M., N.J., J.M., and B.A.G.; Innovator grant DP2OD007447 and R01GM110174 to B.A.G.; DP2CA174499 and K08CA151660 to P.C.; K08CA181475 to S.V.; and Cancer Center Support grant P30CA008748 to C.B.T.). This work was performed within the context of the I-CHANGE consortium and supported by funding from Genome Canada, Genome Quebec, The Institute for Cancer Research of the Canadian Institutes for Health Research (CIHR), McGill University, and the Montreal Children's Hospital Foundation. C.L. is the Kandarian Family Fellow supported by the Damon Runyon Cancer Research Foundation (grant DRG-2195-14). N.J. is a member of the Penny Cole lab and the recipient of a Chercheur Clinician Senior Award. J.M. holds a Canada Research Chair (tier 2). D.H. is supported by a Boehringer Ingelheim Fonds Predoctoral fellowship. D.B. is supported by a studentship from the T.D Trust/Montreal Children's Hospital Foundation. C.B.T. is a founder of Agios Pharmaceuticals and a member of its scientific advisory board and also serves on the board of directors of Merck and Charles River Laboratories. R.E.T. is the president of the Quebec Orthopaedic Association. We thank the molecular cytology core facility of Memorial Sloan Kettering Cancer Center for technical help and EMD Millipore for H3.3K36M antibody generation. The sequencing data reported in this paper are deposited at the Gene Expression Omnibus database (accession number GSE69291).

## SUPPLEMENTARY MATERIALS

www.sciencemag.org/content/352/6287/844/suppl/DC1
Materials and Methods
Figs. S1 to S16
Tables S1 to S4
References (*22*–*26*)

3 June 2015; accepted 11 March 2016
10.1126/science.aac7272

Downloaded from http://science.sciencemag.org/ on May 12, 2016

NEW ENGLAND BioLabs® Inc.

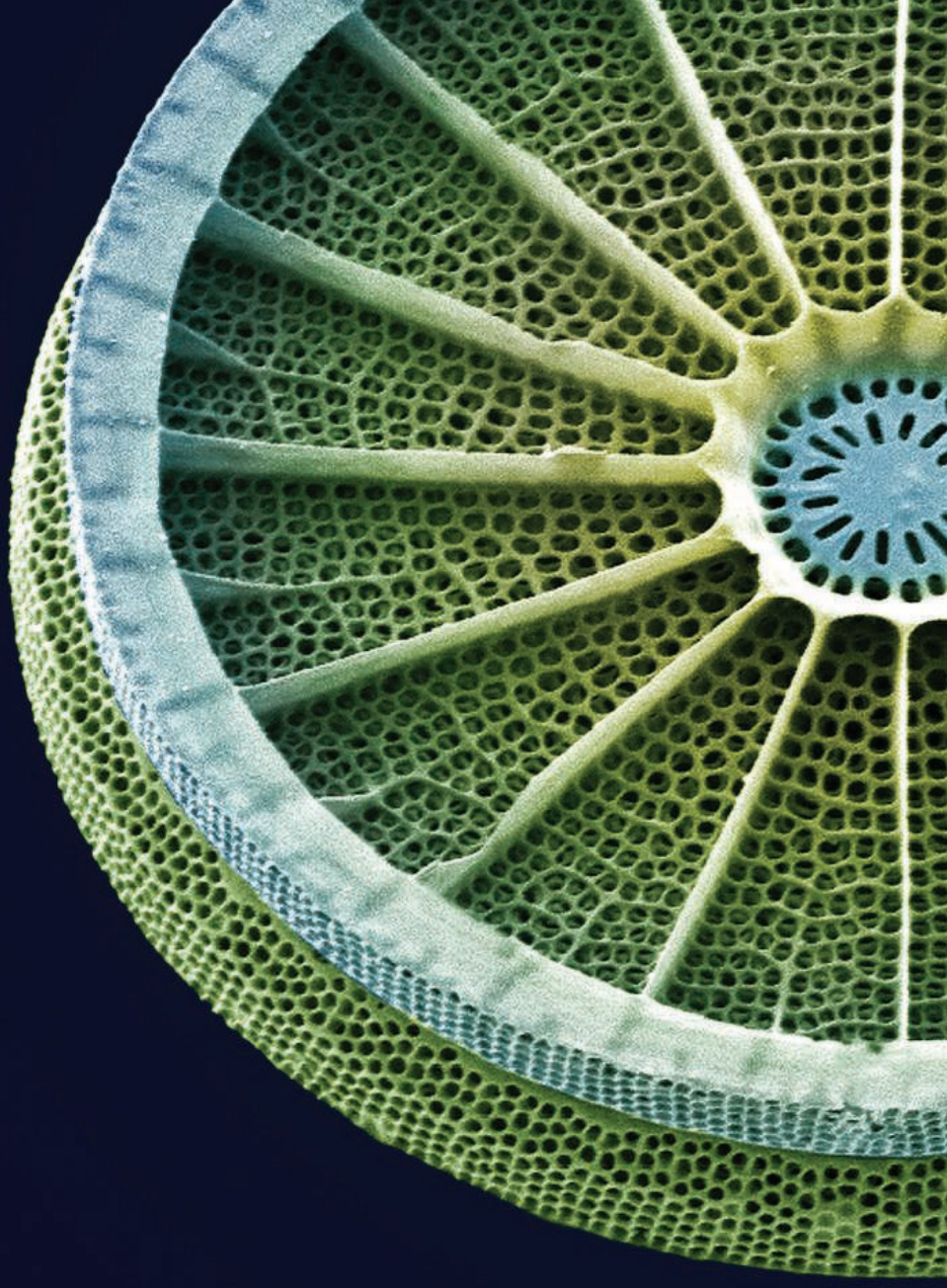

# Target with precision.

## Introducing the NEBNext Direct™ Cancer HotSpot Panel

Using a unique approach, the NEBNext Direct Cancer HotSpot Panel enriches for 190 common cancer targets from 50 genes prior to next generation sequencing. Combining a novel method for hybridization-based target enrichment with library preparation, the NEBNext Direct technology reduces processing time and minimizes sample loss. Ideal for automation, NEBNext Direct enables highly-specific deep sequencing of genomic regions of interest for the discovery and identification of low frequency variants from challenging sample types.

Visit **NEBNextDirect.com** to learn more and to inquire about sampling this product.

**TARGETS INCLUDE REGIONS FROM THE FOLLOWING CANCER-RELATED GENES, INCLUDING >18,000 COSMIC FEATURES:**

| | | | | |
|---|---|---|---|---|
| ABL1 | EGFR | GNAQ | KRAS | PTPN11 |
| AKT1 | ERBB2 | GNAS | MET | RB1 |
| ALK | ERBB4 | HNF1A | MLH1 | RET |
| APC | EZH2 | HRAS | MPL | SMAD4 |
| ATM | FBXW7 | IDH1 | NOTCH1 | SMARCB1 |
| BRAF | FGFR1 | IDH2 | NPM1 | SMO |
| CDH1 | FGFR2 | JAK2 | NRAS | SRC |
| CDKN2A | FGFR3 | JAK3 | PDGFRA | STK11 |
| CSF1R | FLT3 | KDR | PIK3CA | TP53 |
| CTNNB1 | GNA11 | KIT | PTEN | VHL |

*For research use only; not intended for diagnostic use.*

NEW ENGLAND BIOLABS® and NEB® are registered trademarks of New England Biolabs, Inc.
NEBNEXT DIRECT™ is a trademark of New England Biolabs, Inc.

# Don't miss the debut of *Science Immunology*.

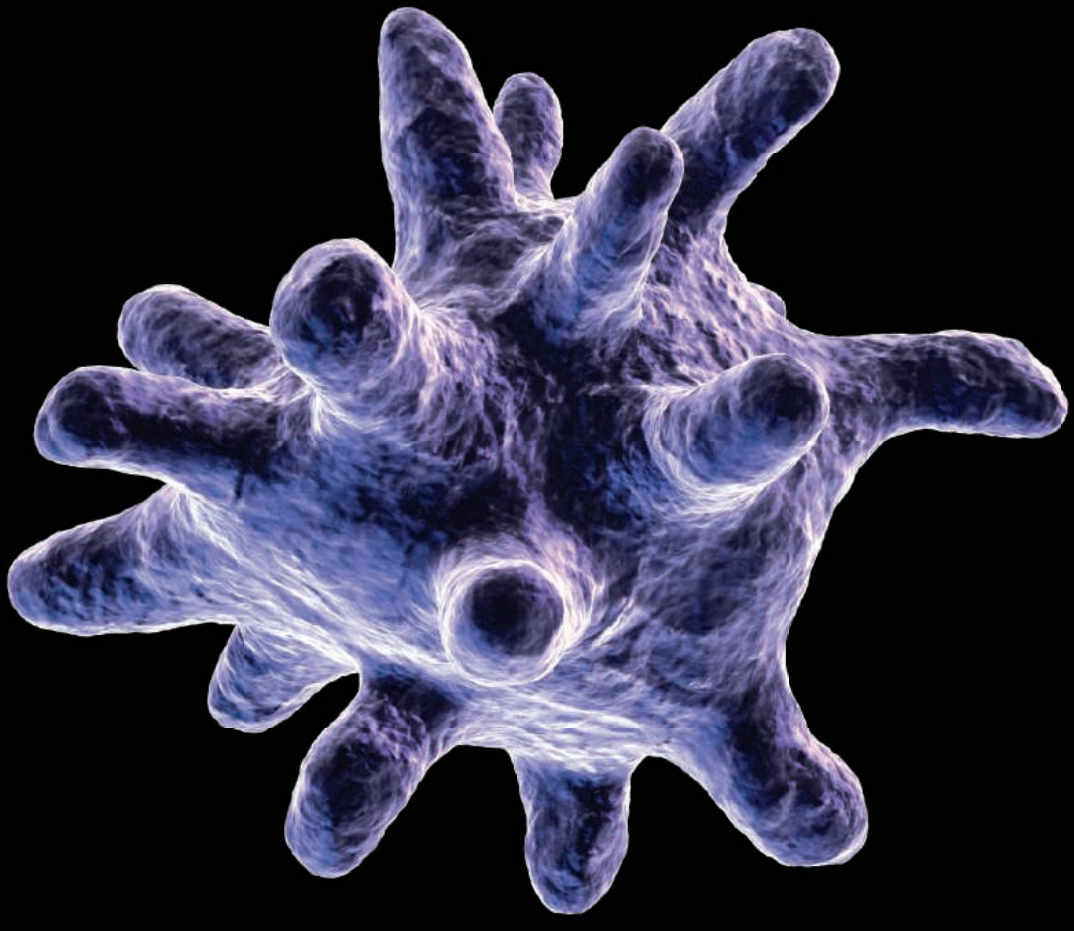

Image: Eraxion / iStockPhoto

NOW ACCEPTING PAPERS

*Science* is expanding its reach into immunology—now offering the newest online-only, weekly journal in the *Science* family of publications. *Science Immunology* will provide original, peer-reviewed research articles that report critical advances in all areas of immunological research, including studies that provide insight into the human immune response in health and disease.

Be a part of the *Science Immunology* debut issue publishing Summer 2016!

Submit your manuscript today at **ScienceImmunology.org.**

Science Immunology

AAAS

eppendorf & Science

# PRIZE FOR NEURO BIOLOGY

2015 Winner
Shigeki Watanabe, Ph.D.
Johns Hopkins University
For research on synaptic vesicle endocytosis

# Call for Entries

**Application Deadline**
**June 15, 2016**

**Eppendorf & Science Prize for Neurobiology**
The annual Eppendorf & Science Prize for Neurobiology is an international award which honors young scientists for their outstanding contributions to neurobiological research based on methods of molecular and cell biology. The winner and finalists are selected by a committee of independent scientists, chaired by Science's Senior Editor, Dr. Peter Stern. Researchers who are not older than 35 years are invited to apply.

**You could be next to win this prize and to receive**
> Prize money of US$25,000
> Publication of your work in Science
> Full support to attend the Prize Ceremony held in conjunction with the Annual Meeting of the Society for Neuroscience in the USA
> An invitation to visit Eppendorf in Hamburg, Germany

It's easy to apply!
Learn more about the Prize and its past winners at:

www.eppendorf.com/prize

eppendorf Science AAAS

AAAS® and Science® are registered trademarks of the American Association for the Advancement of Science, USA. Eppendorf® and the Eppendorf logo are registered trademarks of Eppendorf AG, Germany. U.S. Design Patents are listed on www.eppendorf.com/ip. All rights reserved, including graphics and images. Copyright © 2016 by Eppendorf AG. Kurstin Roe Photography.

# X
# Y
# ZOOM

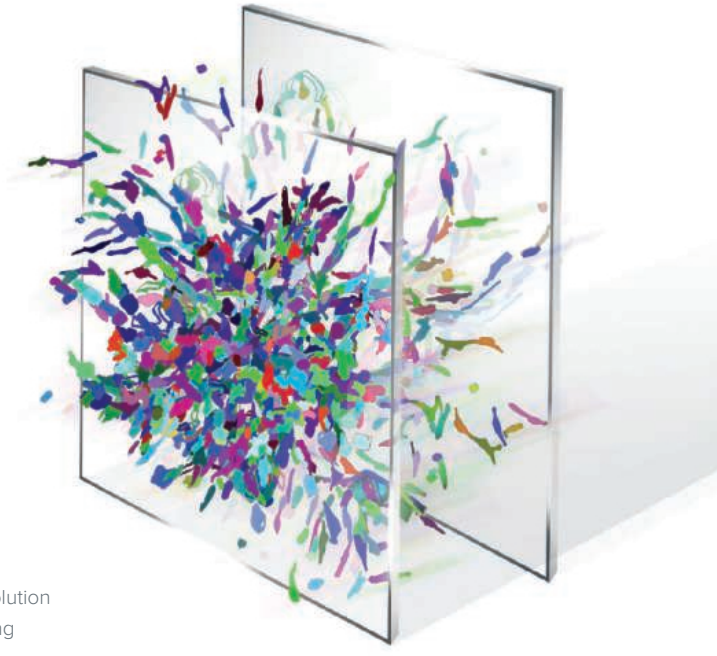

**Position your research with our new ImageXpress® Micro 4 High-Content Imaging System**

- Tackle your toughest assays with an imaging platform that adapts to your needs
- Image over 15 million cells per hour in a 3-color cell scoring assay
- Acquire and analyze in both 2D and 3D using our seamless, integrated end-to-end solution
- Drive your research with a system that builds on over 30 years of innovation in imaging

moleculardevices.com/ixm4

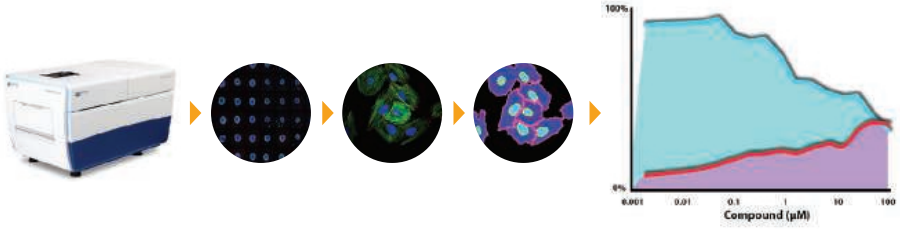


MOLECULAR DEVICES

www.moleculardevices.com | 800.635.5577

For Research Use Only. Not for use in diagnostic procedures.
© 2016 Molecular Devices, LLC. All Rights Reserved. The trademarks mentioned herein are the property of Molecular Devices, LLC or their respective owners.

# VF-1 EDGE™

NEW

Tunable Filter Technology

**FEATURES**

- Separate tunable high-pass and low-pass filters let user define the bandpass in nanometer steps.
- User selectable band-with and center wavelength.
- Blocking filter ensures best blocking outside bandpass.
- Based on Semrock™ VersaChrome™ edge filter technology.

SUTTER INSTRUMENT®

PHONE: 415.883.0128 | FAX: 415.883.0572
EMAIL: INFO@SUTTER.COM | WWW.SUTTER.COM

# AAAS *Travels*

## Discover SICILY

**October 11-23, 2016**

***Archaeology • Landscapes • Heritage!***

Explore the cultural heritage and landscapes of this fascinating land of myth and legend! Sicily offers an intoxicating blend of archaeology, history, and nature which is the envy of the Mediterranean. Sicily was home to philosophers and mathematicians. Syracuse was one of the most powerful cities in the Greek world. See ancient temples and theatres, discover a Roman palace, and marvel at the rich heritage of this land of volcanic Mt. Etna! $3,995 + air.

***For a detailed brochure, call (800) 252-4910***
All prices are per person twin share + air

BETCHART EXPEDITIONS Inc.
17050 Montebello Rd, Cupertino, CA 95014
*Email:* AAASInfo@betchartexpeditions.com
www.betchartexpeditions.com

**The Serengeti Rules**

**The Quest to Discover How Life Works and Why It Matters**

Sean B. Carroll

Cloth $24.95

"A compelling read filled with big, bold ideas."
—Brian J. Enquist, *Nature*

"Sean Carroll is one of our great science writers. . . . This is a visionary book."
—Peter Forbes, *The Guardian*

**Strange Glow**

**The Story of Radiation**

Timothy J. Jorgensen

Cloth $35.00

"Unbiased, comprehensible information on radiation risk is hard to come by. Timothy J. Jorgensen's book *Strange Glow* fills this gap, using history to explain how we encounter radiation and how it affects us. . . . Jorgensen is a good storyteller, with an eye for compelling details."
—Angela Creager, *Science*

**Silent Sparks**

**The Wondrous World of Fireflies**

Sara Lewis

Cloth $29.95

"With stunning illustrations and accessible text, *Silent Sparks* takes readers on a guided tour into the hidden world of fireflies. This book explores the wonders of their coded light messages and reveals what has been learned about these beloved beetles through the sleuthing of researchers."
—Bernd Heinrich, author of *The Homing Instinct*

PRINCETON UNIVERSITY PRESS

See our E-Books at press.princeton.edu



LIFE SCIENCE TECHNOLOGIES
SUPERRESOLUTION MICROSCOPY

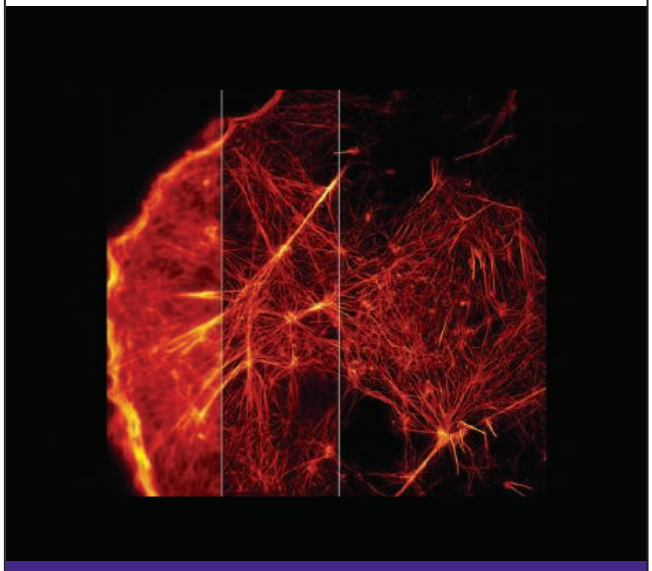

# Superresolution microscopy

The latest superresolution microscopes (GSDIM, PALM, SIM, STED, STORM) bend a centuries-old rule in the field as well as researchers' minds on cellular structures they thought they knew.


**See the full story on page 850.**


**Upcoming Features**

Exosomes/Microvesicles—June 10

Proteomics—July 15

Genomics—October 7

Produced by the *Science*/AAAS Custom Publishing Office

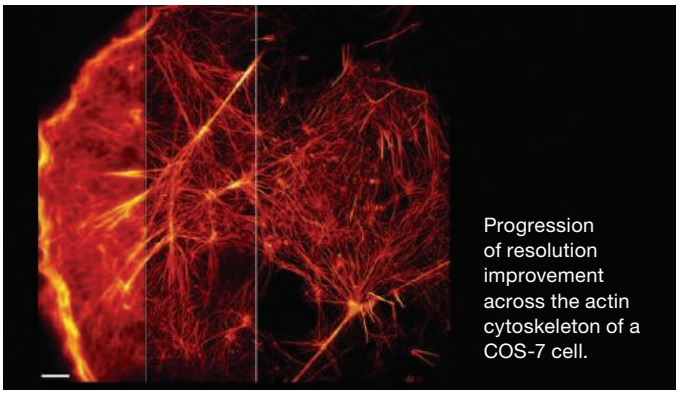

Progression of resolution improvement across the actin cytoskeleton of a COS-7 cell.

# Superresolution microscopy

From van Leeuwenhoek to the new millennium, microscopy was governed by one seemingly unbreakable principle: The ability to resolve two objects is constrained by the wavelength of the light used to view them. But in 2000, researchers showed this so-called diffraction limit could be broken, unveiling over the next decade an alphabet soup of superresolution techniques from GSDIM and PALM to SIM, STED, and STORM. The resulting images are both beautiful and revealing, documenting biological phenomena and structures that researchers never even knew they were missing. **By Jeffrey M. Perkel**

No, there hasn't been a breakdown in copy editing, this sentence really does end with two periods.. Your brain caught that apparent mistake because the lenses in your eyes have sufficient resolving power to distinguish objects spaced that close together. Microscopes, of course, can resolve much finer details, but not infinitely fine. The so-called Abbe (or diffraction) limit constrains the microscope's power, and at some point, two objects will appear as one.

In 2006, Xiaowei Zhuang's team at **Harvard University** first described the superresolution technique known as stochastic optical reconstruction microscopy (STORM), a single-molecule localization method whose 20-nm lateral (*xy*) resolution beats the diffraction limit by a full order of magnitude.

Over the following decade, Zhuang's team steadily refined the technique to make it multicolor, higher resolution, and 3D.

"Almost all biological structures are three-dimensional," says Zhuang, a Howard Hughes Medical Institute Investigator and the David B. Arnold Jr. Professor of Science at Harvard. "So if you break your diffraction limit in only [the] *xy* [plane] and not in *z*, you're quite limited."

To overcome that limitation, Zhuang's team inserted a cylindrical lens in the microscope's optical path. In that configuration, light arising from a single molecule produces not a circle but an ellipse, which indicates the molecule's axial position with 50-nm resolution. Later, the lab boosted resolution still further by positioning objectives above and below the sample, which when combined with the cylindrical lens yielded axial positions with better than 20-nm resolution.

When her team applied that technique to fixed rat hippocampal neurons, they discovered something completely unexpected, Zhuang says. Under conventional fluorescence microscopy, actin in the axons of these neurons appears as a uniform, featureless green. But when they used STORM to zoom in, just beneath the plasma membrane of the axonal shaft they discovered a literal cytoskeleton: periodic rings of green actin 180 nm apart, separated by magenta spectrin spacers (see page 851).

"It's a beautiful structure," Zhuang says, providing both mechanical flexibility and organizational scaffolding. With it, the cell can precisely position key membrane proteins, such as ion channels, to ensure the efficient propagation of neural impulses. "Having these very important signaling molecules being anchored on the structure gives you the possibility that this is the case," she says, adding, "It was really one of those STORM images that I'm most proud of."

Published in 2013, Zhuang's study is "a seminal contribution," agrees Joerg Bewersdorf, Associate Professor of Cell Biology and Biomedical Engineering at the **Yale University School of Medicine**, who builds superresolution microscopes (including one now commercialized by **Bruker**) in his lab. "Nobody had seen these actin rings before, even though people had looked with the electron microscope for 20 years to understand the actin organization in axons."

## Superresolution explained

According to Professor Stefan Hell of the **Max Planck Institute for Biophysical Chemistry**, who was the first to break the diffraction barrier in 2000, all superresolution methods rely on the same fundamental principle.

"If you have freely propagating light, that light will always be diffracted. You can't focus it more sharply than to an area that is about half the wavelength of light across. Full stop," Hell explains. As a result, objects that are closer together than about 200 nm will be illuminated simultaneously and fluoresce in concert. Long story short: multiple objects bleed together into a single, indistinguishable blur. "The solution to that problem was to make sure that not all objects that are flooded with excitation light are in the end capable of emitting fluorescence."

STORM, photoactivated localization microscopy (PALM), and ground state depletion microscopy with individual molecule return (GSDIM)—commercialized by **Nikon**, **Zeiss**, and **Leica**, respectively—are stochastic, localization-based methods, using photoactivatable or photoswitchable fluorescent proteins or dyes to switch on a few fluorophores at random while the majority remain dark. Under those conditions, researchers can be relatively certain that each fluorescent point corresponds to only a single active molecule, thus making it possible to assign their positions with nanometer precision. Those fluorophores then turn off, another handful turns on, and the cycle repeats until a complete dataset has been collected.

"Basically we take advantage of what I typically call the 'fourth dimension,'" explains Zhuang. If multiple, otherwise

IMAGE: L. DONG *ET AL.*, *SCIENCE* **349**, 944 (2015).

*Upcoming Features*

*Exosomes/Microvesicles—June 10* ■ *Proteomics—July 15* ■ *Genomics—October 7*

indistinguishable objects are closely positioned in space, she says, "we don't allow them to overlap in time."

Stimulated emission depletion (STED), reversible saturable optical fluorescence transitions (RESOLFT), and structured illumination microscopy (SIM), conversely, use "patterns of light … that determine where the molecules are active and where the molecules are off," says Hell, who developed both STED and RESOLFT and cofounded a company called **Abberior** to commercialize fluorophores for those and other superresolution methods. STED, for instance, is usually implemented as a point-scanning approach that uses a "donut" of light, superimposed on the excitation beam, to force fluorophores at the periphery of the illumination volume to stay dark via a process called "stimulated emission," thereby shrinking the emitting region to the donut's center. (RESOLFT uses photoswitchable fluorophores to achieve the same effect.)

According to Jochen Sieber, STED and GSDIM microscopy product manager at Leica Microsystems, localization systems typically offer sharper resolution than STED or RESOLFT, but take far longer as they require the acquisition and merging of thousands of frames to build a single image. (Indeed, **National Institutes of Health** Distinguished Investigator Jennifer Lippincott-Schwartz, in whose lab PALM was invented, notes that those first images took hours to collect; today the typical frame rate is about 5 minutes.)

SIM—commercialized by Nikon, **GE Healthcare Life Sciences**, and Zeiss—is generally regarded as the fastest approach available and also the easiest, as it requires no special sample preparation. But at 100 nm, it also yields the poorest resolution.

Recently, **Janelia Research Campus** Investigator Eric Betzig, who with Hell and William E. Moerner of Stanford University won the 2014 Nobel Prize in Chemistry for his work on superresolution, demonstrated that even that limit is not insurmountable. In late 2015, Betzig and his team documented two strategies, including "nonlinear SIM with patterned activation," to increase the method's resolution to about 45 nm. "My personal feeling is that SIM is the superresolution method that is likely to answer the most biological questions in the next decade," Betzig says, laughing. "And yet it's the one that wasn't involved in the Nobel Prize."

Raman Das, Medical Research Council (MRC) Career Development Fellow at the **University of Manchester**, United Kingdom, answered one such question in 2014 when he used SIM (among other methods) to document a new form of cell subdivision called "apical abscission." Das was interested in how progenitor cells in the embryonic spinal cord differentiate into neurons and exit the tissue. By using time-lapse diffraction-limited fluorescence microscopy and SIM, Das's team discovered that the cells actually prune off the cellular "tip," removing those proteins in one shot—a process that Das likens to closing a draw-string purse. "This results in an acute loss of cell polarity in these cells," he explains, leading to the formation of functional neuronal architecture.

Perhaps the simplest, and certainly least expensive, superresolution option is expansion microscopy. Developed by Ed Boyden of the **Massachusetts Institute of Technology**, the technique improves imaging resolution by encasing samples in a "swellable polymer" gel that causes the sample to grow isotropically about fivefold larger. Functionally, that's the same as increasing resolution from 200 nm down to 40 nm. "It's kind of like an optical zoom," explains Silvio Rizzoli, a professor at the **University of Göttingen**, Germany, who uses this technique (as well as STED and STORM) in his neural synapse research.

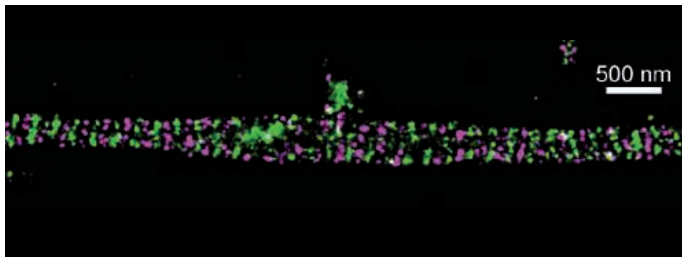


**When [Zhuang's team] used STORM to zoom in, just beneath the plasma membrane of the axonal shaft they discovered a literal cytoskeleton: periodic rings of green actin 180 nm apart, separated by magenta spectrin spacers.**

IMAGE: XU *ET AL.*, *SCIENCE* **339**, 452 (2013).

## Fluorophore on, fluorophore off

Stefan Jakobs, head of the Mitochondrial Structure and Dynamics Research Group at the Max Planck Institute for Biophysical Chemistry, uses superresolution methodologies to study the role mitochondria play in cell death or apoptosis. One protein, called Bax, was known to induce mitochondrial membrane disruption in response to apoptotic signals. What wasn't clear was how the protein does that.

Using fixed-cell STED, Jakobs's team showed that multiple Bax molecules assemble into rings in the mitochondrial outer membrane, like diaphanous green halos crowning the red membrane. That structure explains how Bax translocation during apoptosis can cause the mitochondrial contents to spill, Jakobs says. "It appears that these rings represent pores," he explains. Yet they were impossible to discern via conventional microscopy, in which the rings appear as "a smear."

To see those rings, Jakobs used anti-Bax antibodies labeled with a fluorescent dye. Yet good fluorescent probes for superresolution microscopy can be hard to come by. "You want to have fast image acquisition and high resolution; you want to have many colors and low phototoxicity. None of the techniques is currently at the point where all of these parameters are entirely fulfilled," he says.

Jakobs has developed reversibly switchable fluorescent proteins (RSFPs)—variants of green fluorescent proteins (GFPs), such as rsEGFP2—that can be pushed repeatedly from a fluorescent to nonfluorescent state and back again using specific wavelengths of light. Such proteins are amenable to RESOLFT and STED live-cell applications, he notes, as they require no external antibody for labeling. But it is critical not to overexpress these proteins, he says, as that can lead to artifacts. So, Jakobs's team has used the gene-editing system known as CRISPR/Cas9 to couple rsEGFP2 to protein-coding genes in order to ensure endogenous expression levels. Such work is "challenging," he admits, "but I think it is very important for the field that we do that."

Another genetic labeling option involves tagging genes with self-labeling protein tags, such as the SNAP-tag and CLIP-tag (available from **New England BioLabs**) or **Promega**'s cont.>

## Featured Participants

Abberior
www.abberior.com

3i—Intelligent Imaging Innovations
www.intelligent-imaging.com

Bruker
www.bruker.com

École Polytechnique Fédérale de Lausanne
www.epfl.ch

GE Healthcare Life Sciences
www.gelifesciences.com

Harvard University
www.harvard.edu

Institute of Photonic Sciences, Barcelona
www.icfo.eu

Janelia Research Campus
www.janelia.org

King's College London
www.kcl.ac.uk

Leica
www.leica-microsystems.com

Massachusetts Institute of Technology
www.mit.edu

Max Planck Institute for Biophysical Chemistry
www.mpibpc.mpg.de/en

New England BioLabs
www.neb.com

National Institutes of Health
www.nih.gov

Nikon
www.nikoninstruments.com

Promega
www.promega.com

Spirochrome
spirochrome.com

University of Göttingen
www.uni-goettingen.de/en

University of Manchester
www.manchester.ac.uk

Yale University School of Medicine
medicine.yale.edu

Zeiss
www.zeiss.com

HaloTag, which allow researchers to specifically label proteins of interest in live cells by adding cell-permeable dyes linked to the appropriate substrate. The trick, of course, is that such dyes must be both bright and cell-permeable, and few current fluorophores meet that standard, says Kai Johnsson, professor at the Institute of Chemical Sciences and Engineering at **École Polytechnique Fédérale de Lausanne** in Switzerland.

Janelia Research Campus researcher Luke Lavis recently reported a collection of cell-permeable, high-quantum-efficiency rhodamine variants, which are compatible with HaloTag chemistry. Johnsson has likewise developed rhodamine variants that he calls "SiR dyes" (carboxylated silicon-rhodamine) that are commercialized by **Spirochrome**.

By coupling these dyes to targeting ligands such as the DNA fluorescent stain Hoechst or the cancer drug taxol, Johnsson created probes capable of specifically lighting up genetic material and microtubules respectively, in live-cell STED and SIM (but not PALM or STORM).

### In living color

Because of the extended time required to compile images in localization superresolution microscopy, the method can be largely incompatible with live cells.

One solution is replacing traditional charge-coupled devices (CCDs) with high-speed scientific complementary metal-oxide semiconductor (sCMOS) cameras, which can capture thousands of frames per second. In 2013, Bewersdorf and colleagues demonstrated noise-handling algorithms that allowed an sCMOS camera to record superresolved images at up to 32 frames per second, for instance. Today, Leica's GSDIM instrument includes an sCMOS camera that reduces data acquisition times to "well below a minute," says product manager Peter Laskey, thus putting live-cell applications "within reach." So too does Nikon's new N-STORM 4.0, which also boasts a brighter laser to "get the blinking on-off rates extremely high," according to general manager Stephen Ross.

Researchers also have devised alternative strategies to circumvent the speed problem. Melike Lakadamyali, a group leader at the **Institute of Photonic Sciences** in Barcelona, Spain, for instance, studies microtubule vesicle trafficking, specifically how the motor proteins transporting these vesicles can "evade roadblocks and traffic jams in the crowded environment of a living cell."

To answer that question, Lakadamyali plays to her system's strengths. By recording a live-cell movie of the vesicles at high temporal (but low spatial) resolution, her team can track vesicle motion, overlaying those trajectories on a STORM image of microtubule positions.

The researchers found that vesicles tend to pause at microtubule intersections; the pausing "correlates with tight intersections in which the separation of the two microtubules is small," says Lakadamyali. But they also found that motors can eventually navigate through the intersection. The group is now using 3D particle tracking to focus on microtubule-associated protofilaments that may provide a kind of highway shoulder for skirting roadblocks.

Susan Cox, Royal Society University Research Fellow at **King's College London**, is similarly interested in live-cell localization microscopy. Working with Lippincott-Schwartz, Cox has developed an algorithm, called "Bayesian analysis of blinking and bleaching (3B)," that allows researchers to image more fluorophores simultaneously, even some that are actually spatially overlapping, thereby reducing the number of images required per experiment by about an order of magnitude. "We've looked at systems like cardiac myocytes, [and] been able to image them between the 'beats' of the cells," Cox says.

Still, for all that high resolution can teach, microscopy is about trade-offs. In talks, Betzig says he typically displays a tetrahedron whose axes represent different goals: resolution, speed, low phototoxicity, and imaging depth. "You can't have it all," he tells the audience. For Betzig, speed is paramount, and he focuses his efforts on squeezing every last photon from his samples. That's why he has edged away from pure superresolution toward ultrahigh-speed imaging with a new (albeit superresolution-compatible) design called "lattice light-sheet microscopy," soon to be commercialized by Zeiss and **3i**.

Others may interpret the tetrahedron differently, of course. But the bottom line is this: When it comes to microscopy, the future has never looked brighter—or sharper.

*Jeffrey M. Perkel is a freelance science writer based in Pocatello, Idaho.*

DOI: 10.1126/science.opms.p1600105

### Confocal Microscope

The new Smartproof 5 widefield confocal microscope is designed for a wide range of industrial applications in quality assurance and quality control departments, production environments, and R&D labs. The Smartproof system provides 3D reconstructions and roughness measurements for a wide range of workpiece surfaces. Users benefit from an integrated design, repeatable results, and high throughput. The Smartproof 5's integrated, robust design offers the option of installing and running it in different working environments without additional antivibration equipment. The optics, electronics, and camera are all embedded in the microscope, and the number of cables is minimized to eliminate clutter. The Smartproof 5 software provides the user with easy-to-operate workflow routines. In addition to geometrical measurements, the user can carry out roughness analyses in 2D (profile) and 3D (area)—both based on International Organization for Standardization (ISO) standards. The workflows can be saved, ready to perform the same 3D analysis again.

**Zeiss**
For info: +49-(0)-3641-64-3949
www.zeiss.com

### Adjustable Microscope Platform

The ZDeck Quick Adjust Platform range is a high-quality, height-adjustable platform designed specifically for upright microscopes. The ZDeck is compatible with most commercially available vibration isolation tables and offers an exceptionally stable platform, ensuring that your experimental area is as smooth and vibration-free as possible. The ZDeck's large top plate provides an extensive surface area, enabling users to undertake a comprehensive range of tasks and allowing enough space to set up even the most complex experiments, which may involve environmentally controlled chambers, micromanipulators, and other instruments. The ZDeck's top surface breadboard design (6-mm holes on 25-mm centers) is ideal for quickly and accurately mounting equipment. Offering the ability to switch between imaging heights within seconds, the ZDeck is well suited for observation of both thin-sample and whole-animal imaging. In applications where electrical noise might be an issue, the power to the ZDeck's motors can be switched off after movement.

**Prior Scientific**
For info: 800-877-2234
www.prior.com

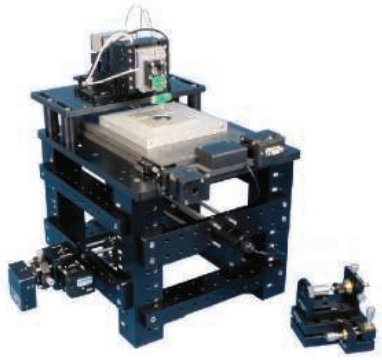

### Scanning Optical Microscope

The Mad City Labs near-field scanning optical microscope (MCL-NSOM) leverages MCL expertise with high-resolution scanning probe microscopy instrumentation and closed-loop nanopositioning systems to design an NSOM that meets the performance criteria and versatility demanded by leading researchers. The MCL-NSOM is an aperture NSOM built on a Mad City Labs RM2 inverted optical microscope, which allows users to convert to apertureless NSOM, atomic force microscopy (AFM), and fluorescence optical microscopy. The MCL-NSOM includes XYZ closed-loop nanopositioning for sample and fiber scanning, providing subnanometer precision and exceptional low-noise performance. Six axes of automated positioning are provided, including independent automation for fiber alignment to the optical axis, and are controlled with LabVIEW-based software. The MCL-NSOM includes a fiber launch with excitation source, alignment camera, and detection avalanche photodiode (APD), but can also easily accommodate user ancillary excitation and detection optics, further enhancing the versatility of this microscope.

**Mad City Labs**
For info: 608-298-0855
www.madcitylabs.com/nsom.html

### Histology Slide Scanning

The new slide scanner from Eikonix brings high-quality slide scanning to a much wider market. This compact device utilizes a host of the latest automated imaging technologies along with a proven scanning engine to create an effective, reliable tool for the rapid acquisition of whole-slide images from standard glass microscope slides. The easy-to-use system can be operated by anyone and requires no specialist training. The intuitive software effortlessly guides the user through each step to produce images of exceptional quality. Designed to scan up to two standard slides or one double-sized slide, the system can produce high-resolution images in just a few minutes. Automatic tissue detection and focusing eliminate complicated setup procedures and guarantee outstanding results for every scan. The integrated computer ensures that the system is ready to go right out of the box, and the preloaded control software requires minimal setup to begin scanning.

**Eikonix**
For info: +44-(0)-1223-515440
www.eikonix.com

### Raman Microscopes

The DXR2 line of Raman microscopes is ideal for scientists working in advanced materials research, pharmaceuticals, polymers, and the developing life science research market. They provide improved workflows that are designed to deliver unparalleled ease of use and accessibility for nonexperts without compromising robustness or reliable performance. Scientists can benefit from rapid, easy setup and a design that facilitates obtaining visually informative, submicron-resolution images. The new DXR2 line, which includes the DXR2 and the DXR2xi, provides both spectrographic and spatial imaging for regulated environments. New polarization techniques provide continuously variable angle polarization analysis, and software automation, coupled with equivalent optical performance, provides a more complete understanding yet is still easy to use. Kinetic imaging allows for real-time studies of dynamic processes such as battery cycling or biological activities in cells. The new DXR2xi Raman imaging microscope is image-centric and works much like the scanning microscopes already used by many scientists.

**Thermo Fisher Scientific**
For info: 800-556-2323
www.thermofisher.com/dxr2

Electronically submit your new product description or product literature information! Go to www.sciencemag.org/about/new-products-section for more information.

Newly offered instrumentation, apparatus, and laboratory materials of interest to researchers in all disciplines in academic, industrial, and governmental organizations are featured in this space. Emphasis is given to purpose, chief characteristics, and availability of products and materials. Endorsement by *Science* or AAAS of any products or materials mentioned is not implied. Additional information may be obtained from the manufacturer or supplier.

# want new technologies?

antibodies
apoptosis
biomarkers
cancer
cytometry
data
diseases
DNA
epigenetics
genomics
immunotherapies
medicine
microbiomics
microfluidics
microscopy
neuroscience
proteomics
sequencing
toxicology
transcriptomics

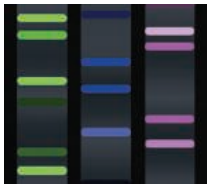

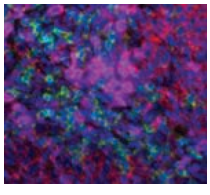

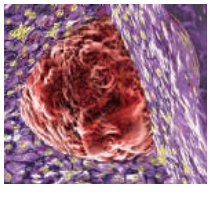

## watch our webinars

Learn about the latest breakthroughs, new technologies, and ground-breaking research in a variety of fields. Our expert speakers explain their quality research to you and answer questions submitted by live viewers.

**VIEW NOW!**
**webinar.sciencemag.org**

Science
AAAS

Brought to you by the *Science*/AAAS Custom Publishing Office

@SciMagWebinars

# WHO WILL WIN THE PRIZE

**The result will be unveiled in May.**
**The winners will receive:**

★A Grand Prize of $25,000 and a Runner-Up Prize of $5,000 will be awarded.
★The Grand Prize Winning Essay will be published in *Science*;
a brief abstract of the Runner-Up Essay will be published in *Science*.

**The 2016 award ceremony will be held in San Francisco, on 23rd June, 2016.**

Stem cells and regenerative medicine is the new frontier in life sciences. Boyalife, *Science*, and *Science Translational Medicine* jointly establish a global award to recognize and reward scientists in the fields of stem cells and regenerative medicine with a focus on developing cell-based treatments for cancer, degenerative disorders, immunotherapy and stem cells transplantation.

BOYALIFE Science & Science Translational Medicine
Award | in Stem Cells and Regenerative Medicine

Learn more about the Prize, visit :
http://www.sciencemag.org/prizes/boyalife

BOYALIFE® For Better Health
Science AAAS
Science Translational Medicine AAAS

There's only one Science

# *Science* Careers Advertising

For full advertising details, go to ScienceCareers.org and click For Employers, or call one of our representatives.

**Tracy Holmes**
Worldwide Associate Director
*Science* Careers
Phone: +44 (0) 1223 326525

THE AMERICAS

E-mail: advertise@sciencecareers.org
Fax: +1 (202) 289 6742

**Tina Burks**
Phone: +1 (202) 326 6577

**Nancy Toema**
Phone: +1 (202) 326 6578

**Online Job Posting Questions**
Phone: +1 (202) 312 6375

EUROPE / INDIA / AUSTRALIA / NEW ZEALAND / REST OF WORLD

E-mail: ads@science-int.co.uk
Fax: +44 (0) 1223 326532

**Sarah Lelarge**
Phone: +44 (0) 1223 326527

**Kelly Grace**
Phone: +44 (0) 1223 326528

**Online Job Posting Questions**
Phone: +44 (0) 1223 326528

JAPAN

**Katsuyoshi Fukamizu** (Tokyo)
E-mail: kfukamizu@aaas.org
Phone: +81 3 3219 5777

**Hiroyuki Mashiki** (Kyoto)
E-mail: hmashiki@aaas.org
Phone: +81 75 823 1109

CHINA / KOREA / SINGAPORE / TAIWAN / THAILAND

**Ruolei Wu**
E-mail: rwu@aaas.org
Phone: +86 186 0082 9345

All ads submitted for publication must comply with applicable U.S. and non-U.S. laws. *Science* reserves the right to refuse any advertisement at its sole discretion for any reason, including without limitation for offensive language or inappropriate content, and all advertising is subject to publisher approval. *Science* encourages our readers to alert us to any ads that they feel may be discriminatory or offensive.

ScienceCareers
FROM THE JOURNAL SCIENCE AAAS

ScienceCcareers.org

There's only one *Science*.

Special Job Focus:

# Microbiology

Issue date: June 10

Book ad by May 24 to guarantee space

Ads accepted until June 3 if space allows

## What makes *Science* the best choice?

- Read and respected by 400,00 readers around the globe
- 75% of readers read *Science* more often than any other journal
- Your ad dollars support AAAS and its programs, which strengthens the global scientific community.

## Why choose this Microbiology Focus for your advertisement?

- Relevant ads lead off the career section with special microbiology banner
- Bonus distribution to American Society for Microbiology, June 16–20, Boston, MA.

## Expand your exposure. Post your print ad online to benefit from:

- Link on the job board homepage directly to microbiology jobs
- Dedicated landing page for jobs in microbiology
- Additional marketing driving relevant job seekers to the job board.

Produced by the *Science*/AAAS Custom Publishing Office.

SCIENCECAREERS.ORG

Science Careers
AAAS

To book your ad: **advertise@sciencecareers.org**

**The Americas**
202 326 6582

**Europe/RoW**
+44(0)1223 326500

**Japan**
+81 3 32195777

**China/Korea/Singapore/Taiwan**
+86 186 00829345

hhmi | Howard Hughes Medical Institute

# INTERNATIONAL RESEARCH SCHOLARS PROGRAM

## Grants for Biomedical Research

**The Howard Hughes Medical institute (HHMI) and philanthropic partners, the Bill & Melinda Gates Foundation, the Wellcome Trust, and the Calouste Gulbenkian Foundation, have created a new grant program to help develop scientific talent worldwide.**

**Application Deadline:**
**June 30, 2016, 3 p.m.**
**U.S. Eastern Time**

Application information:
hhmi.org/IRS2017

hhmi | Howard Hughes Medical Institute

BILL & MELINDA GATES foundation

wellcome trust

CALOUSTE GULBENKIAN FOUNDATION

The International Research Scholars Program will select and support up to 50 outstanding early career scientists working in selected countries.

**Grant Term and Award Amount**
$250,000 in year 1; $100,000 each subsequent year

**Application Deadline**
June 30, 2016, **3 p.m.** U.S. Eastern Time

**Application Information**
hhmi.org/IRS2017

Successful applicants will have trained through the postdoctoral level in a vigorous basic research environment. Eligible candidates must have trained in the United States or United Kingdom at the doctoral, medical, or postdoctoral level. Applicants are expected to have outstanding scientific training records and exceptional potential for significant productivity and originality in their independent careers.

HHMI and its partners recognize that a supportive research environment is crucial to launching a successful research program, so awards will be made only to institutions that can clearly support the research activities of the grant recipient.

**Eligibility Criteria**
*Applicants must:*

- Hold a doctoral degree or medical degree and have completed postdoctoral research training
- Hold a full-time appointment as an independent scientist at a research-oriented university, medical school, or nonprofit institution in any eligible country
- Have received training at the doctoral, medical, or postdoctoral level in the US or UK for at least one year
- Have been the first or senior author on at least two peer-reviewed, English-language, original research publications
- Started their first independent research position on or after April 1, 2009
- Control their own research direction, laboratory space, and funding and devote most of their professional time to research, mentoring, and teaching; applicants must have no major administrative duties

**Eligible Countries**
This program is open to scientists working in all countries except G7 countries (Canada, France, Germany, Italy, Japan, United Kingdom and United States) and *countries identified by the US Department of Treasury, Office of Foreign Assets Control (OFAC) as being subject to comprehensive country or territory-wide sanctions or where current OFAC regulations prohibit U.S. persons or entities from engaging in the funding arrangements contemplated by this grant program. For this program, such sanctioned countries or territories currently include Iran, North Korea, Sudan, Syria, and the Crimea region of Ukraine*

Science Careers online @sciencecareers.org

## State Key Lab of Respiratory Disease, China: seeking talents to lead respiratory research

**Employer**

State Key Lab of Respiratory Disease, Guangzhou Medical University, Guangzhou, China

**Location**

Guangzhou, China

**Research Discipline**

Focus on respiratory Diseases, including but not limited to: respiratory infections and immunology, lung stem cell and regeneration, lung injury, COPD, asthma, lung cancer, bioinformatics with a focus on respiratory diseases.

**Job Type**

Professor, Associate Professor, Assistant Professor.

**Salary**

Highly competitive salary and benefits that is comparable to the best packages (including housing subsidy) in Guangzhou and Pearl Delta region will be provided depending on the candidate's qualifications.

**Further information**

The State Key Laboratory of Respiratory Disease (SKLRD), led by Director and Academician Prof. Nanshan ZHONG, and Executive Director Prof. Ling CHEN, is a leading research Centre for Respiratory Diseases in China. SKLRD was jointly established by Guangzhou Institute of Respiratory Disease (GIRD)/Guangzhou Medical University, and Guangzhou Institute of Biomedicine and Health (GIBH)/Chinese Academy of Sciences. SKLRD aims to improve the quality of life by advancing the medical sciences in prevention and treatment of respiratory diseases. Current research areas include studying epidemiology and influencing factors, identifying disease mechanisms, exploring new treatment and prevention modalities of respiratory diseases. SKLRD is committed to focus on translational research with a focus on unmet medical needs and to take the discovery in basic research into more effective treatment and prevention of respiratory diseases. SKLRD published 175 SCI papers in 2015. Some of the research work represented the leading advancement in the field of respiratory diseases, such as the new etiology and management of COPD, the new mechanism and treatment for asthma, the visualization of influenza virus infection in living mice, the new diagnostics for respiratory diseases. In 2016, SKLRD will expand its laboratory space into a newly renovated building in the center city. A new Guangzhou respiratory Center that integrated clinical research and basic research is under construction. SKLRD is striving to become a world leading research center in the field of respiratory diseases.

SKLRD is seeking highly qualified scientists to fill leading scientist positions. The candidates will be supported to apply for "1000 Talent Program" or "Young 1000 Talent Program", "NSF Distinguished Scholar" or "NSF Young Distinguished Scholar", and "Pearl River Scholar".

Successful candidates must possess a Ph.D or MD degree from top universities, have publications in internationally peer-reviewed journals in recent 5 years. Preference will be given to those with a strong background and successful experiences in both clinical and basic research.

Applicants should send curriculum vitae, one-page future research proposal, PDF reprints of 5 representative publications, and your inquires to: sldrddirector@gird.cn and taochen@gird.cn

---

## Faculty Positions Available in the Third Military Medical University, Chongqing, China

The Third Military Medical University (TMMU) is seeking high-level medical talents from home and abroad. Applicants must have a nationality of China and a Ph.D. and/or M.D. degree. Competitive remuneration packages will be provided to successful applicants.

Located in Chongqing, the TMMU is a national key university, one of the military "2110 Project" key universities , and one of the first universities allowed to grant doctor's degree and to offer eight-year medical education program in China. Currently, the university has 3 academicians of Chinese Academy of Sciences and Chinese Academy of Engineering, over 200 high-level talents including distinguished professors entitled "Changjiang Scholar" and winners of "National Outstanding Youth Foundation," and over 900 staff members with senior professional titles. The TMMU has 25 national key disciplines, key state laboratories and national engineering centers, and three grade-A affiliated hospitals. It has harvested over 1700 scientific and technological achievements, including 7 first prizes of the National Science and Technology Progress Award.

Further information is available at

www.edu.cn/tmmu

Please forward your CV and any other proof materials reflecting your teaching and research background to sydrcb@sina.com. Please call at +86-23-68752105 for any queries.

---

## Southwest Jiaotong University, Chengdu, China Invites Applications for the Academic Positions

Southwest Jiaotong University (SWJTU), founded in 1896 and located in Chengdu, the capital of Sichuan province--China's dynamically growing West. SWJTU is an elite university with national key multidisciplinary "211" and "985 Feature" projects directly managed by the Ministry of Education.SWJTU is currently on the strategic "Developing and Strengthening the University by Introducing and Cultivating talents" campaign.

Thus, you are cordially invited to apply for the following academic positions. More information is available at http://www.swjtu.edu.cn/

**Positions and Requirements**

A. High-level Talented Leaders: Candidates should be qualified to be listed in national top talents programs such as Program of Global Experts, Top Talents of National Special Support Program, "Chang Jiang Scholars", China National Funds for Distinguished Young Scientists and National Award for Distinguished Teacher.

B. Young Leading Scholars: Candidates are preferable to be listed or qualified for the following programs: National Thousand Young Talents Program,The Top Young Talents of National Special Support Program (Program for Supporting Top Young Talents), Science Foundation for the Excellent Youth Scholars.

C. Excellent Young Academic Backbones

D. Excellent Doctors and Post Doctoral Fellows

Please contact Mr. Yu Wang, Ms. Ye Zeng,Ms.Qing Ya Wang

Telephone number: +86-28-66367238/ 66366202

Email: talent@swjtu.edu.cn

Address: Human Resources Department, SWJTU, Western Park of High-Tech Zone, Chengdu, Sichuan, China, 611756

# 1000 TALENTS GLOBAL RECRUITMENT PROGRAM

## SOUTHERN UNIVERSITY OF SCIENCE AND TECHNOLOGY

南方科技大学
SOUTHERN UNIVERSITY OF SCIENCE AND TECHNOLOGY

Southern University of Science and Technology (SUSTech) in Shenzhen, China, is seeking outstanding candidates for the "1000 Talents Global Recruitment Program" sponsored by the Central Government of China. Applications are invited for all major science and engineering disciplines. Successful applicants will be appointed to the faculty of SUSTech at a level commensurate with each applicant's background and experience, from tenure-track assistant professor to chair professor.

SUSTech offers a generous salary and startup package for "1000 Talents Global Recruitment Program" recipients, including:

a) world-wide competitive starting salary;
b) a living subsidy of 2.75 million RMB for "1000 Young Talents" and 4.5 million RMB for "1000 Talents" over 3-5 years;
c) a start-up fund of up to 10 million RMB;
d) PI system and tenure-track system;
e) housing accommodation in an on-campus apartment of 100-150 $m^2$;
f) health and welfares insurance.

Applicants should have a Ph.D. degree in a relevant science and engineering field. Applicants for "1000 Talents Global Recruitment Program" should be a professor or a senior researcher. Applicants for "1000 Young Talents Global Recruitment Program" should have three years or more of post-doctoral research or work experience. Applicants must have a proven track record of high-quality peer-reviewed academic publications. They must also have excellent communication skills and the capacity to teach in English.

If interested, please apply through the website at http://talent.sustc.edu.cn/en/enindex.aspx.

**Contact person:** Ms. Jing Long
**Phone:** +86-755-88010968
**Email:** talents@sustc.edu.cn.
http://www.sustc.edu.cn

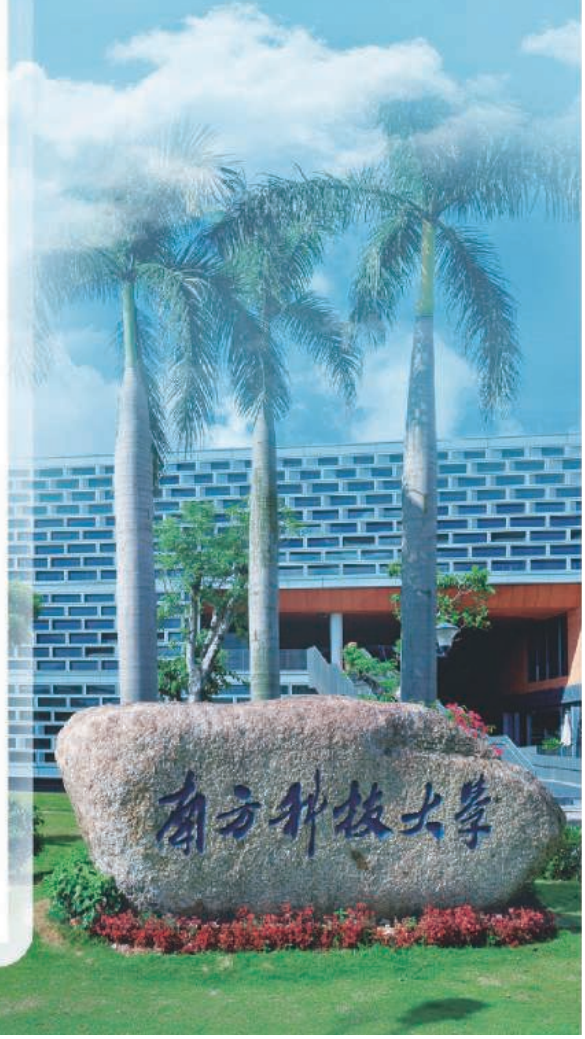


Science Careers online @sciencecareers.org
OPPORTUNITIES IN CHINA

ScienceCareers online @sciencecareers.org

# FUNDING OPPORTUNITIES — U.S. Department of Defense

## Defense Health Program

## Peer Reviewed Medical Research Program

The Peer Reviewed Medical Research Program (PRMRP) funds exceptional research with the goal to improve the health and well-being of all military Service Members, Veterans, and their beneficiaries. The PRMRP received ***$278.7 million*** in fiscal year 2016 (FY16) and seeks grant applications in the following ***topic areas:***

*Acute Lung Injury*
*Antimicrobial Resistance*
*Chronic Migraine and Post-Traumatic Headache*
*Congenital Heart Disease*
*Constrictive Bronchiolitis*
*Diabetes*
*Dystonia*
*Emerging Infectious Diseases*
*Focal Segmental Glomerulosclerosis*
*Fragile X Syndrome*
*Hepatitis B*
*Hereditary Angioedema*
*Hydrocephalus*
*Inflammatory Bowel Disease*
*Influenza*
*Integrative Medicine*
*Interstitial Cystitis*
*Lupus*
*Malaria*
*Metals Toxicology*
*Mitochondrial Disease*
*Nanomaterials for Bone Regeneration*
*Nonopioid Pain Management*
*Pancreatitis*
*Pathogen-Inactivated Dried Plasma*
*Polycystic Kidney Disease*
*Post-Traumatic Osteoarthritis*
*Psychotropic Medications*
*Pulmonary Fibrosis*
*Respiratory Health*
*Rett Syndrome*
*Rheumatoid Arthritis*
*Scleroderma*
*Sleep Disorders*
*Tinnitus*
*Tuberculosis*
*Vaccine Development for Infectious Disease*
*Vascular Malformations*
*Women's Heart Disease*

Descriptions of the FY16 PRMRP Program Announcements and General Application Instructions are anticipated to be posted on Grants.gov by ***mid-March 2016:***

- Clinical Trial Award
- Discovery Award
- Focused Program Award
- Investigator-Initiated Research Award
- Technology/Therapeutic Development Award

*All applications must conform to the Program Announcements and General Application Instructions that will be available for electronic downloading from the Grants.gov website (all viewable under CFDA number 12.420). Execution management support will be provided by the Congressionally Directed Medical Research Programs.*

**For more information, please visit: http://cdmrp.army.mil/funding/prmrp.shtml**
**http://cdmrp.army.mil**

## PRIZES

# 2017 Vetlesen Prize

## Achievement in the Earth Sciences

# Call for Nominations

**Nominations should be sent prior to 1 August 2016 to:**

Sean C. Solomon, Director
Lamont-Doherty Earth Observatory
PO Box 1000
61 Route 9W, Palisades, NY 10964
Tel: 845/365-8729

or via electronic submission to:
vetlesenprize@ldeo.columbia.edu

Lamont-Doherty Earth Observatory
Columbia University | Earth Institute

The Vetlesen Prize, established in 1959 by the G. Unger Vetlesen Foundation, is awarded for scientific achievement that has resulted in a clearer understanding of the Earth, its history, or its relations to the universe. The prize consists of a medal and a cash award of $250,000. Nominations are now open for the next prize, which will be awarded in 2017.

The prize is awarded to a single individual, who can reside and work anywhere in the world. The prize is administered by Columbia University's Lamont-Doherty Earth Observatory.

Nomination packages should include at least two letters that describe the nominee's contributions to a fuller understanding of the workings of our planet, along with a one-paragraph biographical sketch and the full curriculum vitae of the candidate.

**For more information about the Vetlesen Prize:**
http://www.ldeo.columbia.edu/vetlesen-prize

### Past Vetlesen Laureates

2015 Stephen Sparks
2012 Susan Solomon, Jean Jouzel
2008 Walter Alvarez
2004 W. Richard Peltier, Sir Nicholas J. Shackleton
2000 W. Jason Morgan, Walter C. Pitman III, Lynn R. Sykes
1996 Robert E. Dickinson, John Imbrie
1993 Walter H. Munk
1987 Wallace S. Broecker, Harmon Craig
1981 M. King Hubbert
1978 J. Tuzo Wilson
1974 Chaim L. Pekeris
1973 William A. Fowler
1970 Allan V. Cox, Richard R. Doell, S. Keith Runcorn
1968 Francis Birch, Sir Edward Bullard
1966 Jan Hendrik Oort
1964 Pentti E. Eskola, Arthur Holmes
1962 Sir Harold Jeffreys, Felix Andries Vening Meinesz
1960 W. Maurice Ewing

MEDICAL SCHOOL
UNIVERSITY OF MICHIGAN

## Chief Scientific Officer and Executive Vice Dean for Research

**The University of Michigan Health System (UMHS) seeks an internationally renowned biomedical researcher and academic leader to serve as the Chief Scientific Officer and Executive Vice Dean for Research (CSO) of the University of Michigan Medical School (UMMS) and UMHS**. UMHS is a premier academic medical center made up of three hospitals and more than 40 health centers and clinics; the University of Michigan Medical School; and a physician faculty group practice.

The CSO reports to the Executive Vice President for Medical Affairs and Dean (EVPMA/Dean) and will work collaboratively with the EVPMA/Dean and Executive Vice Deans to recruit outstanding leaders to chair the basic science departments and direct the centers and institutes that are primarily focused on research. He or she will work closely with the U-M Vice President for Research in setting the ongoing vision and leadership for the medical school research mission and strategies.

Candidates must have a PhD or a doctoral degree in medicine, have an active research program and qualify for tenure as a full professor in the medical school. The successful candidate will be a proven visionary leader who has developed or grown an innovative program in cutting-edge biomedical research, has been recognized internationally as a scholar and/or academic leader, and has a strong record of scientific accomplishment and administrative, managerial and operational experience in oversight of research programs.

Inquiries, nominations and applications are invited and should be sent electronically to **MichiganMed.CSO@russellreynolds.com**. All applications and nominations will be held in the strictest confidence. Applications should include a CV and a bullet point summary of one's leadership roles and major accomplishments. Review will begin immediately and continue until the position is filled.

The search committee composition and an expanded version of the position description can be found at **http://umhealth.me/CSO_search**.

Additional information about the University Michigan Health System and Medical School can be found at http://www.med.umich.edu/ and https://medicine.umich.edu/medschool/.

*The University of Michigan is an Equal Opportunity/Affirmative Action Employer.*

TEXAS BIOMEDICAL
RESEARCH INSTITUTE
Enhancing Lives Through Discovery℠

## FACULTY POSITION
## VIROLOGY AND IMMUNOLOGY

The Department of Virology and Immunology at Texas Biomedical Research Institute, located in San Antonio, Texas, invites applications for a faculty-level position at the Assistant through full Scientist level (equivalent to an Assistant, Associate, and Full Professor). The successful candidate will show strong potential (Assistant level) or have an established research program (Associate or full Scientist) with emphasis on infectious disease, molecular biology, pathogenesis and/or immune responses. Candidates that demonstrate ability to take advantage of the extensive resources of the Department and Institute are preferred. Departmental resources include the capacity to work with animal models at all levels of containment laboratories (BSL2, BSL3, BSL4), and extensive expertise in nonhuman primate models, for development of vaccines, therapeutics and diagnostics and the study of the immune responses against viral and bacterial infections including several select agents. Collaborations with Texas Biomed's Department of Genetics and the Southwest National Primate Research Center are encouraged. Strong associations with the University of Texas Health Science Center at San Antonio and the University of Texas at San Antonio allow participation in teaching and graduate student programs.

Qualified applicants must have as a minimum a doctoral degree in the biological sciences and/or an M.D. or D.V.M. degree, with a strong research-based publication record.

**Apply online at http://www.txbiomed.org/about/employment. Application packets are accepted electronically or in hard copy. A completed application packet is a requirement for all positions. Incomplete applications will not be accepted.**

*EOE*

## Kuwait University
## Faculty of Science
## Department of
## Biological Sciences

The College of Sciences at Kuwait University invites applications for faculty positions at the academic rank (Associate Professor or Professor) in the Department of Biological Sciences in the field of **Zoology**.

**The following minimum qualifications are required:**

- All Degrees must be from Kuwait University of an accredited university in a traditional residential and on-campus format.
- PhD in one of the following fields: Chordates, Invertebrate, Immunology, Cell Biology
- M.Sc. Zoology from a reputable university
- B.Sc. in Biological Sciences with a GPA not less than 3.00 out of 4 points scale, or equivalent
- The applicant is expected to have research experience and publications in the specified field
- The applicant is expected to have teaching experience of related course in the English language
- Excellent command of the English language

Kuwait University offers an internationally competitive salary and benefits package, salary, rank and benefits will be determined in accordance with the university rules and regulations. The university provides strong support for research. **For consideration, applications should be submitted two months within the announcement date.**

Qualified applications should apply online for open faculty positions using the following web address **http://vpaa.kuniv.edu.kw/en/index.php**.

**For inquiries use: biology@ku.edu.kw**
**Fax: 00965-24836127**

ScienceCareers online @sciencecareers.org

# 10 ways that *Science* Careers can help advance your career

1. Register for a free online account on **ScienceCareers.org**.
2. Search thousands of job postings and find your perfect job.
3. Sign up to receive e-mail alerts about job postings that match your criteria.
4. Upload your resume into our database and connect with employers.
5. Watch one of our many webinars on different career topics such as job searching, networking, and more.
6. Download our career booklets, including Career Basics, Careers Beyond the Bench, and Developing Your Skills.
7. Complete an interactive, personalized career plan at "my IDP."
8. Visit our Career Forum and get advice from career experts and your peers.
9. Research graduate program information and find a program right for you.
10. Read relevant career advice articles from our library of thousands.

Visit **ScienceCareers.org** today — all resources are free

ScienceCareers

FROM THE JOURNAL SCIENCE AAAS

SCIENCECAREERS.ORG

Universität Konstanz

The University of Konstanz, with its "Institutional Strategy to promote Top-Level Research", has been receiving continuous funding since 2007 within the framework of the Excellence Initiative by the German Federal and State Governments.

The Faculty of Sciences of the University of Konstanz, Department of Computer and Information Science, has an immediate opening for a definite-term

## Junior Professorship in "Modelling of Complex Self-organizing Systems" (salary scale W1)

The appointment is initially for 3 years and can be extended to 6 years. We are looking for a renowned expert in data-driven modelling and analysis of spatial and dynamic aspects of complex systems with a clear focus on computer science with applications in the natural sciences.

For further information please visit our website:
http://www.uni-konstanz.de/stellenangebote/?cont=stellausw&id=3

Zertifikat seit 2006 audit familiengerechte hochschule

Please send your digital application (including a CV, letter of motivation etc.) *as a single pdf-file attachment* by e-mail to Prof-2016-105@uni-konstanz.de **until 6 June 2016**. If you have questions about the procedure please contact Hanns Fahlbusch, phone +49 (0)7531 / 88-2413.

## NEUROINFLAMMATION AND NEURODEGENERATION FACULTY POSITION

The Department of Anatomy and Neurobiology (http://www.uthsc.edu/anatomy-neurobiology/) at the University of Tennessee Health Science Center seeks an outstanding researcher in the area of neuroinflammation and neurodegeneration to fill an open rank tenure track position (Assistant, Associate, Full Professor). We seek candidates to complement and extend departmental and campus-wide research on the role of microglia/neuroinflammation in neurodegenerative diseases, especially, but not limited to, traumatic brain injury, chronic traumatic encephalopathy, stroke, Alzheimer's disease, Parkinson's disease, and amyotrophic lateral sclerosis. Successful candidates are expected to have and maintain an independent, extramurally funded research program, and contribute to the department's teaching mission. The department and campus have state-of-the-art laboratories, core facilities, and unique populations of inbred mouse strains for elucidating the pathogenesis and treatment of neurodegenerative diseases (http://cgb.uthsc.edu).

We offer competitive salary and start-up packages, and membership in our vibrant interdepartmental Neuroscience Institute (http://www.uthsc.edu/neuroscience/). Candidates must have a Ph.D. or M.D., with preference given to those with funding. For best consideration applications should be submitted by **July 1, 2016**. Submit curriculum vitae, summary of research interests, and contact information for three references, in a single Word or PDF file to **bjsmith@uthsc.edu**.

*The University of Tennessee is an EEO/AA/Title VI/Title IX, Section 504/ADA/ADEA institution in the provision of its education and employment programs and services.*

UNIVERSITY OF CAMBRIDGE

**www.jobs.cam.ac.uk**

## University Lecturer (2 Posts)

### Department of Physiology, Development and Neuroscience • £38,896-£49,230

Applications are invited for two research-oriented, tenure-track University Lectureships in Physiology, Development and Neuroscience available from 1 January 2017 or as soon as possible thereafter. Based in central Cambridge, we are searching for two outstanding scientists, with excellent publication records, undertaking fundable work with synergies with our research programme (http://www.pdn.cam.ac.uk/research/). The research field is open for one post but, for the other post, we are looking to recruit a Neuroscientist and are particularly interested in candidates working in systems or circuitry.

The successful applicants will have PhDs in relevant subject areas, will have aptitude and enthusiasm for teaching, and be willing to contribute effectively to our undergraduate programmes in preclinical medicine, preclinical veterinary science, and natural sciences (http://www.pdn.cam.ac.uk/teaching). They will be expected to contribute to the design and delivery of undergraduate and graduate lecture courses and to perform other academic duties including administration, examining and assessment.

We welcome applications from all qualified candidates and we strongly encourage women to apply. Appointment will be based on merit alone.

Informal enquiries may be made to Professor Bill Harris, Head of Department (wah20@cam.ac.uk; +44 (0) 1223 766137/333772).

Appointment will be made at University Lecturer level with a probationary period of five years, with appointment to the retirement age thereafter. The pensionable salary scale starts at £38,896 to £49,230 per annum. Once an offer of employment has been accepted, the successful candidates will be required to undergo a health assessment, with a satisfactory outcome determined by the University.

**To apply online for this vacancy and to view further information about the role, please visit: http://www.jobs.cam.ac.uk/job/10262.**

**The closing date for applications is midnight on Sunday 10 July 2016.**

**Please quote reference PM09036 on your application and in any correspondence about this vacancy.**

The University values diversity and is committed to equality of opportunity.

The University has a responsibility to ensure that all employees are eligible to live and work in the UK.

Science Careers online @sciencecareers.org

There's only one Science

# *Science* Careers Advertising

For full advertising details, go to ScienceCareers.org and click For Employers, or call one of our representatives.

**Tracy Holmes**
Worldwide Associate Director
*Science* Careers
Phone: +44 (0) 1223 326525

THE AMERICAS

E-mail: advertise@sciencecareers.org
Fax: +1 (202) 289 6742

**Tina Burks**
Phone: +1 (202) 326 6577

**Nancy Toema**
Phone: +1 (202) 326 6578

**Online Job Posting Questions**
Phone: +1 (202) 312 6375

EUROPE / INDIA / AUSTRALIA / NEW ZEALAND / REST OF WORLD

E-mail: ads@science-int.co.uk
Fax: +44 (0) 1223 326532

**Sarah Lelarge**
Phone: +44 (0) 1223 326527

**Kelly Grace**
Phone: +44 (0) 1223 326528

**Online Job Posting Questions**
Phone: +44 (0) 1223 326528

JAPAN

**Katsuyoshi Fukamizu** (Tokyo)
E-mail: kfukamizu@aaas.org
Phone: +81 3 3219 5777

**Hiroyuki Mashiki** (Kyoto)
E-mail: hmashiki@aaas.org
Phone: +81 75 823 1109

CHINA / KOREA / SINGAPORE / TAIWAN / THAILAND

**Ruolei Wu**
E-mail: rwu@aaas.org
Phone: +86 186 0082 9345

All ads submitted for publication must comply with applicable U.S. and non-U.S. laws. *Science* reserves the right to refuse any advertisement at its sole discretion for any reason, including without limitation for offensive language or inappropriate content, and all advertising is subject to publisher approval. *Science* encourages our readers to alert us to any ads that they feel may be discriminatory or offensive.

ScienceCareers
FROM THE JOURNAL SCIENCE AAAS

ScienceCcareers.org

There's only one *Science*.

Special Job Focus:

# Microbiology

Issue date: June 10

Book ad by May 24 to guarantee space

Ads accepted until June 3 if space allows

## What makes *Science* the best choice?

- Read and respected by 400,00 readers around the globe
- 75% of readers read *Science* more often than any other journal
- Your ad dollars support AAAS and its programs, which strengthens the global scientific community.

## Why choose this Microbiology Focus for your advertisement?

- Relevant ads lead off the career section with special microbiology banner
- Bonus distribution to American Society for Microbiology, June 16–20, Boston, MA.

## Expand your exposure. Post your print ad online to benefit from:

- Link on the job board homepage directly to microbiology jobs
- Dedicated landing page for jobs in microbiology
- Additional marketing driving relevant job seekers to the job board.

Produced by the *Science*/AAAS Custom Publishing Office.

SCIENCECAREERS.ORG

Science Careers
AAAS

To book your ad: **advertise@sciencecareers.org**

**The Americas**
202 326 6582

**Europe/RoW**
+44(0)1223 326500

**Japan**
+81 3 32195777

**China/Korea/Singapore/Taiwan**
+86 186 00829345

hhmi | Howard Hughes Medical Institute

# INTERNATIONAL RESEARCH SCHOLARS PROGRAM

## Grants for Biomedical Research

**The Howard Hughes Medical institute (HHMI) and philanthropic partners, the Bill & Melinda Gates Foundation, the Wellcome Trust, and the Calouste Gulbenkian Foundation, have created a new grant program to help develop scientific talent worldwide.**

**Application Deadline:**
**June 30, 2016, 3 p.m.**
**U.S. Eastern Time**

Application information:
hhmi.org/IRS2017

hhmi | Howard Hughes Medical Institute

BILL & MELINDA GATES foundation

wellcome trust

CALOUSTE GULBENKIAN FOUNDATION

The International Research Scholars Program will select and support up to 50 outstanding early career scientists working in selected countries.

**Grant Term and Award Amount**
$250,000 in year 1; $100,000 each subsequent year

**Application Deadline**
June 30, 2016, **3 p.m.** U.S. Eastern Time

**Application Information**
hhmi.org/IRS2017

Successful applicants will have trained through the postdoctoral level in a vigorous basic research environment. Eligible candidates must have trained in the United States or United Kingdom at the doctoral, medical, or postdoctoral level. Applicants are expected to have outstanding scientific training records and exceptional potential for significant productivity and originality in their independent careers.

HHMI and its partners recognize that a supportive research environment is crucial to launching a successful research program, so awards will be made only to institutions that can clearly support the research activities of the grant recipient.

**Eligibility Criteria**
*Applicants must:*

- Hold a doctoral degree or medical degree and have completed postdoctoral research training
- Hold a full-time appointment as an independent scientist at a research-oriented university, medical school, or nonprofit institution in any eligible country
- Have received training at the doctoral, medical, or postdoctoral level in the US or UK for at least one year
- Have been the first or senior author on at least two peer-reviewed, English-language, original research publications
- Started their first independent research position on or after April 1, 2009
- Control their own research direction, laboratory space, and funding and devote most of their professional time to research, mentoring, and teaching; applicants must have no major administrative duties

**Eligible Countries**
This program is open to scientists working in all countries except G7 countries (Canada, France, Germany, Italy, Japan, United Kingdom and United States) and *countries identified by the US Department of Treasury, Office of Foreign Assets Control (OFAC) as being subject to comprehensive country or territory-wide sanctions or where current OFAC regulations prohibit U.S. persons or entities from engaging in the funding arrangements contemplated by this grant program. For this program, such sanctioned countries or territories currently include Iran, North Korea, Sudan, Syria, and the Crimea region of Ukraine*

Science Careers online @sciencecareers.org

## State Key Lab of Respiratory Disease, China: seeking talents to lead respiratory research

**Employer**

State Key Lab of Respiratory Disease, Guangzhou Medical University, Guangzhou, China

**Location**

Guangzhou, China

**Research Discipline**

Focus on respiratory Diseases, including but not limited to: respiratory infections and immunology, lung stem cell and regeneration, lung injury, COPD, asthma, lung cancer, bioinformatics with a focus on respiratory diseases.

**Job Type**

Professor, Associate Professor, Assistant Professor.

**Salary**

Highly competitive salary and benefits that is comparable to the best packages (including housing subsidy) in Guangzhou and Pearl Delta region will be provided depending on the candidate's qualifications.

**Further information**

The State Key Laboratory of Respiratory Disease (SKLRD), led by Director and Academician Prof. Nanshan ZHONG, and Executive Director Prof. Ling CHEN, is a leading research Centre for Respiratory Diseases in China. SKLRD was jointly established by Guangzhou Institute of Respiratory Disease (GIRD)/Guangzhou Medical University, and Guangzhou Institute of Biomedicine and Health (GIBH)/Chinese Academy of Sciences. SKLRD aims to improve the quality of life by advancing the medical sciences in prevention and treatment of respiratory diseases. Current research areas include studying epidemiology and influencing factors, identifying disease mechanisms, exploring new treatment and prevention modalities of respiratory diseases. SKLRD is committed to focus on translational research with a focus on unmet medical needs and to take the discovery in basic research into more effective treatment and prevention of respiratory diseases. SKLRD published 175 SCI papers in 2015. Some of the research work represented the leading advancement in the field of respiratory diseases, such as the new etiology and management of COPD, the new mechanism and treatment for asthma, the visualization of influenza virus infection in living mice, the new diagnostics for respiratory diseases. In 2016, SKLRD will expand its laboratory space into a newly renovated building in the center city. A new Guangzhou respiratory Center that integrated clinical research and basic research is under construction. SKLRD is striving to become a world leading research center in the field of respiratory diseases.

SKLRD is seeking highly qualified scientists to fill leading scientist positions. The candidates will be supported to apply for "1000 Talent Program" or "Young 1000 Talent Program", "NSF Distinguished Scholar" or "NSF Young Distinguished Scholar", and "Pearl River Scholar".

Successful candidates must possess a Ph.D or MD degree from top universities, have publications in internationally peer-reviewed journals in recent 5 years. Preference will be given to those with a strong background and successful experiences in both clinical and basic research.

Applicants should send curriculum vitae, one-page future research proposal, PDF reprints of 5 representative publications, and your inquires to: sldrddirector@gird.cn and taochen@gird.cn

---

## Faculty Positions Available in the Third Military Medical University, Chongqing, China

The Third Military Medical University (TMMU) is seeking high-level medical talents from home and abroad. Applicants must have a nationality of China and a Ph.D. and/or M.D. degree. Competitive remuneration packages will be provided to successful applicants.

Located in Chongqing, the TMMU is a national key university, one of the military "2110 Project" key universities , and one of the first universities allowed to grant doctor's degree and to offer eight-year medical education program in China. Currently, the university has 3 academicians of Chinese Academy of Sciences and Chinese Academy of Engineering, over 200 high-level talents including distinguished professors entitled "Changjiang Scholar" and winners of "National Outstanding Youth Foundation," and over 900 staff members with senior professional titles. The TMMU has 25 national key disciplines, key state laboratories and national engineering centers, and three grade-A affiliated hospitals. It has harvested over 1700 scientific and technological achievements, including 7 first prizes of the National Science and Technology Progress Award.

Further information is available at

www.edu.cn/tmmu

Please forward your CV and any other proof materials reflecting your teaching and research background to sydrcb@sina.com. Please call at +86-23-68752105 for any queries.

---

## Southwest Jiaotong University, Chengdu, China Invites Applications for the Academic Positions

Southwest Jiaotong University (SWJTU), founded in 1896 and located in Chengdu, the capital of Sichuan province--China's dynamically growing West. SWJTU is an elite university with national key multidisciplinary "211" and "985 Feature" projects directly managed by the Ministry of Education.SWJTU is currently on the strategic "Developing and Strengthening the University by Introducing and Cultivating talents" campaign.

Thus, you are cordially invited to apply for the following academic positions. More information is available at http://www.swjtu.edu.cn/

**Positions and Requirements**

A. High-level Talented Leaders: Candidates should be qualified to be listed in national top talents programs such as Program of Global Experts, Top Talents of National Special Support Program, "Chang Jiang Scholars", China National Funds for Distinguished Young Scientists and National Award for Distinguished Teacher.

B. Young Leading Scholars: Candidates are preferable to be listed or qualified for the following programs: National Thousand Young Talents Program,The Top Young Talents of National Special Support Program (Program for Supporting Top Young Talents), Science Foundation for the Excellent Youth Scholars.

C. Excellent Young Academic Backbones

D. Excellent Doctors and Post Doctoral Fellows

Please contact Mr. Yu Wang, Ms. Ye Zeng,Ms.Qing Ya Wang

Telephone number: +86-28-66367238/ 66366202

Email: talent@swjtu.edu.cn

Address: Human Resources Department, SWJTU, Western Park of High-Tech Zone, Chengdu, Sichuan, China, 611756

# 1000 TALENTS GLOBAL RECRUITMENT PROGRAM

## SOUTHERN UNIVERSITY OF SCIENCE AND TECHNOLOGY

南方科技大学
SOUTHERN UNIVERSITY OF SCIENCE AND TECHNOLOGY

Southern University of Science and Technology (SUSTech) in Shenzhen, China, is seeking outstanding candidates for the "1000 Talents Global Recruitment Program" sponsored by the Central Government of China. Applications are invited for all major science and engineering disciplines. Successful applicants will be appointed to the faculty of SUSTech at a level commensurate with each applicant's background and experience, from tenure-track assistant professor to chair professor.

SUSTech offers a generous salary and startup package for "1000 Talents Global Recruitment Program" recipients, including:

a) world-wide competitive starting salary;
b) a living subsidy of 2.75 million RMB for "1000 Young Talents" and 4.5 million RMB for "1000 Talents" over 3-5 years;
c) a start-up fund of up to 10 million RMB;
d) PI system and tenure-track system;
e) housing accommodation in an on-campus apartment of 100-150 $m^2$;
f) health and welfares insurance.

Applicants should have a Ph.D. degree in a relevant science and engineering field. Applicants for "1000 Talents Global Recruitment Program" should be a professor or a senior researcher. Applicants for "1000 Young Talents Global Recruitment Program" should have three years or more of post-doctoral research or work experience. Applicants must have a proven track record of high-quality peer-reviewed academic publications. They must also have excellent communication skills and the capacity to teach in English.

If interested, please apply through the website at http://talent.sustc.edu.cn/en/enindex.aspx.

**Contact person:** Ms. Jing Long
**Phone:** +86-755-88010968
**Email:** talents@sustc.edu.cn.
http://www.sustc.edu.cn

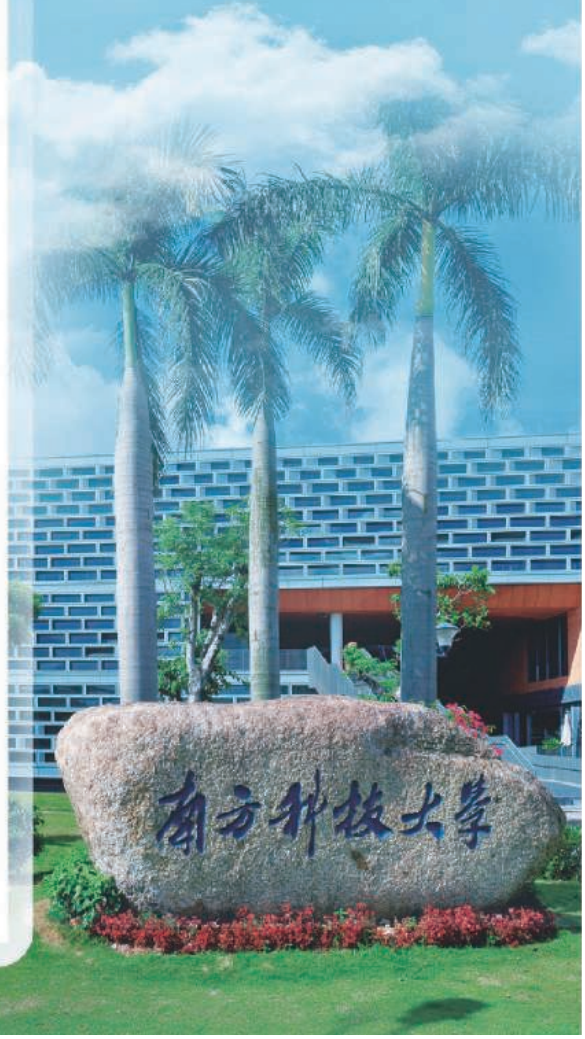


Science Careers online @sciencecareers.org
OPPORTUNITIES IN CHINA

ScienceCareers online @sciencecareers.org

# FUNDING OPPORTUNITIES — U.S. Department of Defense

## Defense Health Program

## Peer Reviewed Medical Research Program

The Peer Reviewed Medical Research Program (PRMRP) funds exceptional research with the goal to improve the health and well-being of all military Service Members, Veterans, and their beneficiaries. The PRMRP received ***$278.7 million*** in fiscal year 2016 (FY16) and seeks grant applications in the following ***topic areas:***

*Acute Lung Injury*
*Antimicrobial Resistance*
*Chronic Migraine and Post-Traumatic Headache*
*Congenital Heart Disease*
*Constrictive Bronchiolitis*
*Diabetes*
*Dystonia*
*Emerging Infectious Diseases*
*Focal Segmental Glomerulosclerosis*
*Fragile X Syndrome*
*Hepatitis B*
*Hereditary Angioedema*
*Hydrocephalus*
*Inflammatory Bowel Disease*
*Influenza*
*Integrative Medicine*
*Interstitial Cystitis*
*Lupus*
*Malaria*
*Metals Toxicology*
*Mitochondrial Disease*
*Nanomaterials for Bone Regeneration*
*Nonopioid Pain Management*
*Pancreatitis*
*Pathogen-Inactivated Dried Plasma*
*Polycystic Kidney Disease*
*Post-Traumatic Osteoarthritis*
*Psychotropic Medications*
*Pulmonary Fibrosis*
*Respiratory Health*
*Rett Syndrome*
*Rheumatoid Arthritis*
*Scleroderma*
*Sleep Disorders*
*Tinnitus*
*Tuberculosis*
*Vaccine Development for Infectious Disease*
*Vascular Malformations*
*Women's Heart Disease*

Descriptions of the FY16 PRMRP Program Announcements and General Application Instructions are anticipated to be posted on Grants.gov by ***mid-March 2016:***

- Clinical Trial Award
- Discovery Award
- Focused Program Award
- Investigator-Initiated Research Award
- Technology/Therapeutic Development Award

*All applications must conform to the Program Announcements and General Application Instructions that will be available for electronic downloading from the Grants.gov website (all viewable under CFDA number 12.420). Execution management support will be provided by the Congressionally Directed Medical Research Programs.*

**For more information, please visit: http://cdmrp.army.mil/funding/prmrp.shtml**
**http://cdmrp.army.mil**

## PRIZES

# 2017 Vetlesen Prize

## Achievement in the Earth Sciences

# Call for Nominations

**Nominations should be sent prior to 1 August 2016 to:**

Sean C. Solomon, Director
Lamont-Doherty Earth Observatory
PO Box 1000
61 Route 9W, Palisades, NY 10964
Tel: 845/365-8729

or via electronic submission to:
vetlesenprize@ldeo.columbia.edu

Lamont-Doherty Earth Observatory
Columbia University | Earth Institute

The Vetlesen Prize, established in 1959 by the G. Unger Vetlesen Foundation, is awarded for scientific achievement that has resulted in a clearer understanding of the Earth, its history, or its relations to the universe. The prize consists of a medal and a cash award of $250,000. Nominations are now open for the next prize, which will be awarded in 2017.

The prize is awarded to a single individual, who can reside and work anywhere in the world. The prize is administered by Columbia University's Lamont-Doherty Earth Observatory.

Nomination packages should include at least two letters that describe the nominee's contributions to a fuller understanding of the workings of our planet, along with a one-paragraph biographical sketch and the full curriculum vitae of the candidate.

**For more information about the Vetlesen Prize:**
http://www.ldeo.columbia.edu/vetlesen-prize

### Past Vetlesen Laureates

2015 Stephen Sparks
2012 Susan Solomon, Jean Jouzel
2008 Walter Alvarez
2004 W. Richard Peltier, Sir Nicholas J. Shackleton
2000 W. Jason Morgan, Walter C. Pitman III, Lynn R. Sykes
1996 Robert E. Dickinson, John Imbrie
1993 Walter H. Munk
1987 Wallace S. Broecker, Harmon Craig
1981 M. King Hubbert
1978 J. Tuzo Wilson
1974 Chaim L. Pekeris
1973 William A. Fowler
1970 Allan V. Cox, Richard R. Doell, S. Keith Runcorn
1968 Francis Birch, Sir Edward Bullard
1966 Jan Hendrik Oort
1964 Pentti E. Eskola, Arthur Holmes
1962 Sir Harold Jeffreys, Felix Andries Vening Meinesz
1960 W. Maurice Ewing

MEDICAL SCHOOL
UNIVERSITY OF MICHIGAN

## Chief Scientific Officer and Executive Vice Dean for Research

**The University of Michigan Health System (UMHS) seeks an internationally renowned biomedical researcher and academic leader to serve as the Chief Scientific Officer and Executive Vice Dean for Research (CSO) of the University of Michigan Medical School (UMMS) and UMHS**. UMHS is a premier academic medical center made up of three hospitals and more than 40 health centers and clinics; the University of Michigan Medical School; and a physician faculty group practice.

The CSO reports to the Executive Vice President for Medical Affairs and Dean (EVPMA/Dean) and will work collaboratively with the EVPMA/Dean and Executive Vice Deans to recruit outstanding leaders to chair the basic science departments and direct the centers and institutes that are primarily focused on research. He or she will work closely with the U-M Vice President for Research in setting the ongoing vision and leadership for the medical school research mission and strategies.

Candidates must have a PhD or a doctoral degree in medicine, have an active research program and qualify for tenure as a full professor in the medical school. The successful candidate will be a proven visionary leader who has developed or grown an innovative program in cutting-edge biomedical research, has been recognized internationally as a scholar and/or academic leader, and has a strong record of scientific accomplishment and administrative, managerial and operational experience in oversight of research programs.

Inquiries, nominations and applications are invited and should be sent electronically to **MichiganMed.CSO@russellreynolds.com**. All applications and nominations will be held in the strictest confidence. Applications should include a CV and a bullet point summary of one's leadership roles and major accomplishments. Review will begin immediately and continue until the position is filled.

The search committee composition and an expanded version of the position description can be found at **http://umhealth.me/CSO_search**.

Additional information about the University Michigan Health System and Medical School can be found at http://www.med.umich.edu/ and https://medicine.umich.edu/medschool/.

*The University of Michigan is an Equal Opportunity/Affirmative Action Employer.*

TEXAS BIOMEDICAL
RESEARCH INSTITUTE
Enhancing Lives Through Discovery℠

## FACULTY POSITION
## VIROLOGY AND IMMUNOLOGY

The Department of Virology and Immunology at Texas Biomedical Research Institute, located in San Antonio, Texas, invites applications for a faculty-level position at the Assistant through full Scientist level (equivalent to an Assistant, Associate, and Full Professor). The successful candidate will show strong potential (Assistant level) or have an established research program (Associate or full Scientist) with emphasis on infectious disease, molecular biology, pathogenesis and/or immune responses. Candidates that demonstrate ability to take advantage of the extensive resources of the Department and Institute are preferred. Departmental resources include the capacity to work with animal models at all levels of containment laboratories (BSL2, BSL3, BSL4), and extensive expertise in nonhuman primate models, for development of vaccines, therapeutics and diagnostics and the study of the immune responses against viral and bacterial infections including several select agents. Collaborations with Texas Biomed's Department of Genetics and the Southwest National Primate Research Center are encouraged. Strong associations with the University of Texas Health Science Center at San Antonio and the University of Texas at San Antonio allow participation in teaching and graduate student programs.

Qualified applicants must have as a minimum a doctoral degree in the biological sciences and/or an M.D. or D.V.M. degree, with a strong research-based publication record.

**Apply online at http://www.txbiomed.org/about/employment. Application packets are accepted electronically or in hard copy. A completed application packet is a requirement for all positions. Incomplete applications will not be accepted.**

*EOE*

## Kuwait University
## Faculty of Science
## Department of
## Biological Sciences

The College of Sciences at Kuwait University invites applications for faculty positions at the academic rank (Associate Professor or Professor) in the Department of Biological Sciences in the field of **Zoology**.

**The following minimum qualifications are required:**

- All Degrees must be from Kuwait University of an accredited university in a traditional residential and on-campus format.
- PhD in one of the following fields: Chordates, Invertebrate, Immunology, Cell Biology
- M.Sc. Zoology from a reputable university
- B.Sc. in Biological Sciences with a GPA not less than 3.00 out of 4 points scale, or equivalent
- The applicant is expected to have research experience and publications in the specified field
- The applicant is expected to have teaching experience of related course in the English language
- Excellent command of the English language

Kuwait University offers an internationally competitive salary and benefits package, salary, rank and benefits will be determined in accordance with the university rules and regulations. The university provides strong support for research. **For consideration, applications should be submitted two months within the announcement date.**

Qualified applications should apply online for open faculty positions using the following web address **http://vpaa.kuniv.edu.kw/en/index.php**.

**For inquiries use: biology@ku.edu.kw**
**Fax: 00965-24836127**

ScienceCareers online @sciencecareers.org

# 10 ways that *Science* Careers can help advance your career

1. Register for a free online account on **ScienceCareers.org**.
2. Search thousands of job postings and find your perfect job.
3. Sign up to receive e-mail alerts about job postings that match your criteria.
4. Upload your resume into our database and connect with employers.
5. Watch one of our many webinars on different career topics such as job searching, networking, and more.
6. Download our career booklets, including Career Basics, Careers Beyond the Bench, and Developing Your Skills.
7. Complete an interactive, personalized career plan at "my IDP."
8. Visit our Career Forum and get advice from career experts and your peers.
9. Research graduate program information and find a program right for you.
10. Read relevant career advice articles from our library of thousands.

Visit **ScienceCareers.org** today — all resources are free

ScienceCareers

FROM THE JOURNAL SCIENCE AAAS

SCIENCECAREERS.ORG

Universität Konstanz

The University of Konstanz, with its "Institutional Strategy to promote Top-Level Research", has been receiving continuous funding since 2007 within the framework of the Excellence Initiative by the German Federal and State Governments.

The Faculty of Sciences of the University of Konstanz, Department of Computer and Information Science, has an immediate opening for a definite-term

## Junior Professorship in "Modelling of Complex Self-organizing Systems" (salary scale W1)

The appointment is initially for 3 years and can be extended to 6 years. We are looking for a renowned expert in data-driven modelling and analysis of spatial and dynamic aspects of complex systems with a clear focus on computer science with applications in the natural sciences.

For further information please visit our website:
http://www.uni-konstanz.de/stellenangebote/?cont=stellausw&id=3

Zertifikat seit 2006 audit familiengerechte hochschule

Please send your digital application (including a CV, letter of motivation etc.) *as a single pdf-file attachment* by e-mail to Prof-2016-105@uni-konstanz.de **until 6 June 2016**. If you have questions about the procedure please contact Hanns Fahlbusch, phone +49 (0)7531 / 88-2413.

## NEUROINFLAMMATION AND NEURODEGENERATION FACULTY POSITION

The Department of Anatomy and Neurobiology (http://www.uthsc.edu/anatomy-neurobiology/) at the University of Tennessee Health Science Center seeks an outstanding researcher in the area of neuroinflammation and neurodegeneration to fill an open rank tenure track position (Assistant, Associate, Full Professor). We seek candidates to complement and extend departmental and campus-wide research on the role of microglia/neuroinflammation in neurodegenerative diseases, especially, but not limited to, traumatic brain injury, chronic traumatic encephalopathy, stroke, Alzheimer's disease, Parkinson's disease, and amyotrophic lateral sclerosis. Successful candidates are expected to have and maintain an independent, extramurally funded research program, and contribute to the department's teaching mission. The department and campus have state-of-the-art laboratories, core facilities, and unique populations of inbred mouse strains for elucidating the pathogenesis and treatment of neurodegenerative diseases (http://cgb.uthsc.edu).

We offer competitive salary and start-up packages, and membership in our vibrant interdepartmental Neuroscience Institute (http://www.uthsc.edu/neuroscience/). Candidates must have a Ph.D. or M.D., with preference given to those with funding. For best consideration applications should be submitted by **July 1, 2016**. Submit curriculum vitae, summary of research interests, and contact information for three references, in a single Word or PDF file to **bjsmith@uthsc.edu**.

*The University of Tennessee is an EEO/AA/Title VI/Title IX, Section 504/ADA/ADEA institution in the provision of its education and employment programs and services.*

UNIVERSITY OF CAMBRIDGE

**www.jobs.cam.ac.uk**

## University Lecturer (2 Posts)

### Department of Physiology, Development and Neuroscience • £38,896-£49,230

Applications are invited for two research-oriented, tenure-track University Lectureships in Physiology, Development and Neuroscience available from 1 January 2017 or as soon as possible thereafter. Based in central Cambridge, we are searching for two outstanding scientists, with excellent publication records, undertaking fundable work with synergies with our research programme (http://www.pdn.cam.ac.uk/research/). The research field is open for one post but, for the other post, we are looking to recruit a Neuroscientist and are particularly interested in candidates working in systems or circuitry.

The successful applicants will have PhDs in relevant subject areas, will have aptitude and enthusiasm for teaching, and be willing to contribute effectively to our undergraduate programmes in preclinical medicine, preclinical veterinary science, and natural sciences (http://www.pdn.cam.ac.uk/teaching). They will be expected to contribute to the design and delivery of undergraduate and graduate lecture courses and to perform other academic duties including administration, examining and assessment.

We welcome applications from all qualified candidates and we strongly encourage women to apply. Appointment will be based on merit alone.

Informal enquiries may be made to Professor Bill Harris, Head of Department (wah20@cam.ac.uk; +44 (0) 1223 766137/333772).

Appointment will be made at University Lecturer level with a probationary period of five years, with appointment to the retirement age thereafter. The pensionable salary scale starts at £38,896 to £49,230 per annum. Once an offer of employment has been accepted, the successful candidates will be required to undergo a health assessment, with a satisfactory outcome determined by the University.

**To apply online for this vacancy and to view further information about the role, please visit: http://www.jobs.cam.ac.uk/job/10262.**

**The closing date for applications is midnight on Sunday 10 July 2016.**

**Please quote reference PM09036 on your application and in any correspondence about this vacancy.**

The University values diversity and is committed to equality of opportunity.

The University has a responsibility to ensure that all employees are eligible to live and work in the UK.

Science Careers online @sciencecareers.org

*By* **Julia MacDougall**

# *My seismic career shift*

About 6 months ago, I sat at work, watching a robot vacuum cleaner glide confidently across the floor—until it dove off a ledge. "Well," my co-worker remarked, "that's not good," as he entered the result into a spreadsheet. Observing such product failures is just one part of my job as the senior scientist for a consumer product testing website, where anything even tangentially related to science ends up on my plate. On any given day, I could be tweaking a data model of smartphone battery life, thinking about how to test the temperature consistency of charcoal grills, or writing a consumer safety article about defrosting a turkey. I love rising to these delightfully unpredictable daily challenges, which I never could have anticipated when I was working on my Ph.D.

As a student, I was drawn to physics and geology, because to me these two disciplines epitomize the many important and varied real-world applications of science. Every experiment I did in my classes, from lighting up a pickle by running an electrical current through it to using Play-Doh to illustrate the major tectonic plate faulting styles, brought new revelations about how integral science is to everyday life.

So, with only vague notions about what I would do afterward, I continued to pursue my love of science by going to graduate school to study geophysics, with a focus on seismology. Once I was there, fulfilling my teaching assistant requirements confirmed my preference to avoid teaching, ruling out a future in academia. Ultimately, my fieldwork provided the biggest clue about a potential career path. The hands-on approach to science that I employed while deploying seismometers deep in the wilds of Georgia and Florida set my thoughts toward a possible career in industry, where research, getting your hands dirty, and real-world applications coexist comfortably.

Yet, I struggled to figure out whether I could do work that wasn't directly related to my degree—and, perhaps more to the point, whether I should. I worried that I would be throwing away years of training—that going into any field that wasn't directly related to earthquakes would make me a highly educated ingrate. But after some soul-searching, I concluded that I would rather try something outside my comfort zone than potentially languish in postdoc purgatory for the next few years.

I cast a wide net and applied for jobs in nuclear seismic monitoring, signal processing, and technical writing, to name a few. But at my interview for my current position, I fell in love with product testing. Since starting my job, I have worn expensive smart watches for a weekend, tasted chocolate melted in a slow cooker, and used smartphones to play with party-themed smart lightbulbs, all in the name of science. My job combines rigorous research with seeing scientific principles play out in real time, and even after a year, I still find this work as fun and engaging as when I started.

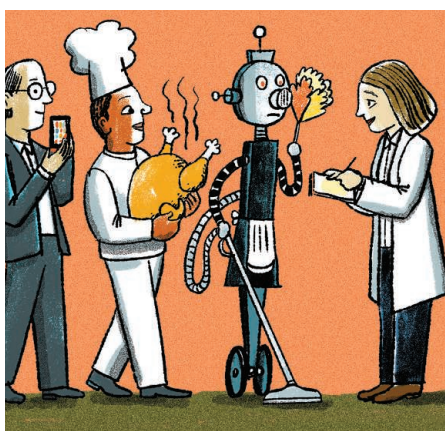

***"Anything even tangentially related to science ends up on my plate."***

When I was in graduate school, I never thought that this is what I would be doing with my Ph.D., but my training hasn't been wasted. My job calls for the mental flexibility, tenacity, and curiosity that I developed as a graduate student, and I am still honing those skills, even though I'm no longer in academia. At times, I even get to draw on some of the specific knowledge I gained as a geophysicist—understanding heat flow, for example, is crucial for oven and cooktop testing—and when this happens, I get a little extra skip in my step. I am still chasing my dream of investigating and sharing science with the world; I'm just approaching it from a different angle than I expected.

Applying my geophysics knowledge to decidedly nongeophysical problems has also broadened my outlook about—and, I hope, my suitability for—the types of jobs that I might pursue in the future. For now, though, I'm happy to be learning and telling the world about the science behind the products we use every day, one robot vacuum testing run at a time. ■

*Julia MacDougall is the senior scientist at Reviewed.com. For more on life and careers, visit sciencecareers.org. Send your story to SciCareerEditor@aaas.org.*

ILLUSTRATION: ROBERT NEUBECKER

Downloaded from http://science.sciencemag.org/ on May 12, 2016



Published by AAAS